

LNF-10/06 (IR)
February 19, 2010



SPARX-FEL

Technical Design Report

Version 2.00

Change history

Date	Version	Requester	Comments
18.06.2008	0.01		Creation of first draft
25.09.2008	0.02	All WPL	Updated of first version
27.09.2008	0.03	Vaccarezza/ Giannessi	Update of parts
24.10.2008	0.04	Various	Insertion Infrastrutture, corrections on Chapter 5,4,6,13
25.10.2008	0.05	Various	Different corrections, insertion of chapter 4.1 and 4.5
29.10.2008	0.06	Various	Minor changes
6.11.2008	0.07	Zema/Gianne ssi/Rossi- Albertini/Ghi go	Corrections
6.11.2008	0.08	Rossi- Albertini/Ghi go	Corrections chapter 9, creation of chapter 11
12.11.2008	0.09	Galerano	Corrections for chapter 2
13.11.2008	0.10	Various	Minor changes on chapter 2
12.1.2009	0.13	Antici	Added International scenario
12.1.2009	0.14	Antici	Added new author list
12.1.2009	0.15	Antici	Inserted foreword
12.1.2009	0.18	Antici	Inserted Comments Rossbach
15.1.2009	0.19	Antici	Corrected Foreword
15.1.2009	0.20	Antici	Corrected Foreword
15.1.2009	0.21	Antici	Forward included in Executive summary
15.1.2009	0.22	Antici	Comments Rossbach on LINAC (dimensions)
15.1.2009	0.23	Antici	Minor changes
15.1.2009	0.24	Ferrario	Updated SPARC experience in Executive summary
16.1.2009	0.25	Palumbo	Revised and reorganized Executive summary
16.1.2009	0.26	Palumbo	Revised and reorganized Executive summary (2 nd version)
16.1.2009	0.27	Antici	Taken out corrected comments
16.1.2009	0.28	Antici	Corrections Exec Summ
19.1.2009	0.29	Antici	Experimental part Exec Summ
19.1.2009	0.30	Antici	Experimental part Exec Summ

23.1.2009	0.31	Antici	Minor corrections
23.1.2009	0.32	Antici	Insertion of Foreword
26.1.2009	0.33	Pellegrini	First Corrections
26.1.2009	0.34	Couprie	First Corrections
28.1.2009	0.35	Couprie	Corrections Ferrario
30.1.2009	0.36	Couprie	Corrections Ghigo
03.2.2009	0.37	Couprie	Corrections Giannessi
05.2.2009	0.38	Antici	Layout
06.2.2009	0.39	Chiadroni	Added paragraph
10.2.2009	0.40	Antici	Minor changes
11.2.2009	0.41	Antici	Minor changes
12.2.2009	0.42	Antici	Minor changes
13.2.2009	0.43	Antici	Update sections
14.2.2009	0.44	Antici	Change of references
18.2.2009	0.45	Migliorati	Swap of table BC2&BC3
19.2.2009	0.46	Gallerano	Referenza Fig Chap 2 e inserzione nome.
20.2.2009	1.00	Antici	Version sendto "Regione Lazio"
18.5.2009	1.01	Palumbo/Antici	Updated Author list
17.6.2009	1.02	Ferrario	Updated SPARC experience with new results
01.07.2009	1.03	Chiadroni	Added contribution Spontaneous Undulator Radiation
07.07.2009	1.04	Rossi-Albertini	Updated Chapter 9
08.07.2009	1.05	Antici	Reduced Font size to 11
12.07.2009	1.06	Antici	New layout
13.07.2009	1.07	Antici	Added Chapter Financing
14.07.2009	1.08	Antici	Minor changes, Layout
15.07.2009	2.00	Antici	Second official version for distribution

Project team

Project Management

Palumbo	Luigi	U. di Roma "La Sapienza" / INFN
Gallerano	Gian Piero	ENEA
Quaresima	Claudio	CNR
Ghigo	Andrea	INFN
Antici	Patrizio	INFN

Project Coordinators

Boni	Roberto	INFN
Di Pirro	Gian Piero	INFN
Esposito	Adolfo	INFN
Ferrario	Massimo	INFN
Ghigo	Andrea	INFN
Giannessi	Luca	ENEA
Poletto	Luca	CNR-INFN, Laboratorio LUXOR
Rossi-Albertini	Valerio	CNR
Sabia	Elio	ENEA
Stucchi	Silvano	U. di Roma "Tor Vergata"
Tommasini	Sandro	INFN
Zema	Nicola	CNR

Authors

Alesini	David	INFN
Antici	Patrizio	INFN
Avaldi	Lorenzo	CNR
Bacci	Alberto	INFN
Bassi	E	ENEA
Barletta	William	ENEA
Bedogni	Roberto	INFN
Bellaveglia	Marco	INFN
Biscari	Caterina	INFN
Bolognesi	Paola	CNR
Boni	Roberto	INFN
Boscolo	Manuela	INFN
Broggi	Francesco	INFN
Castellano	Michele	INFN
Catani	Luciano	INFN
Catone	Daniele	CNR
Cedola	Alessia	CNR
Chiadroni	Enrica	INFN
Cianchi	Alessandro	INFN
Ciocchi	Franco	ENEA
Clozza	Alberto	INFN
Contini	Giorgio	CNR
Cultrera	Luca	INFN
Dattoli	Pino	ENEA
De Martinis	Carlo	U. di Milano / INFN

CONTENT

1	FOREWORD	19
2	EXECUTIVE SUMMARY	21
2.1	FROM SYNCHROTRON LIGHT SOURCES (SLS) TO FREE ELECTRON LASERS (FEL)	21
2.2	DEVELOPMENT OF SYNCHROTRON RADIATION SOURCES AND FEL IN THE FRASCATI AREA.	22
2.3	THE SPARX INITIATIVE	25
2.4	SPARX LAYOUT AND PARAMETERS	26
2.4.1	MACHINE SCHEMATIC AND PARAMETERS	26
2.4.2	SPARX LAYOUT DESCRIPTION	28
2.4.3	THE PHOTO INJECTOR BASED ON THE SPARC EXPERIENCE	30
2.4.4	THE LOW ENERGY BEAM DIAGNOSTICS	33
2.4.5	LINACS, TRANSFER LINES AND COMPRESSORS	34
2.4.6	UNDULATOR LINES	36
2.4.7	PHOTON BEAMLINES	38
2.4.8	BEAM DISTRIBUTION SYSTEM	38
2.4.9	THE THZ BEAMLINE	40
2.5	INTERNATIONAL SCENARIO	40
2.6	SCIENCE AND TECHNOLOGY WITH SPARX-FEL	45
2.6.1	OVERVIEW	45
2.6.2	TIME RESOLVED X-RAY DIFFRACTION	46
2.6.3	COHERENT X-RAY DIFFRACTION IMAGING (CXDI)	47
2.6.4	FEMTOPHYSICS: DIRECT TESTS OF QUANTUM MECHANICS	47
2.6.5	FEMTOCHEMISTRY: REAL-TIME STUDY OF CHEMICAL REACTIONS.	48
2.6.6	SPECTROMICROSCOPY	49
2.6.7	INVESTIGATIONS ON WEAK SCATTERERS	50
2.6.7.1	Dilute solutions	51
2.6.8	NANOPARTICLES AND CLUSTERS.	51
2.6.8.1	Hydrogen-based systems.	52
2.6.9	X-RAY HOLOGRAPHY	52
2.6.10	NON DIFFRACTOMETRIC STRUCTURAL STUDIES	53
2.6.10.1	X-ray reflectometry	53
2.6.10.2	Inelastic X-ray scattering	54
2.6.11	APPLICATIONS TO INERTIAL CONFINED FUSION (ICF) STUDIES	55
2.6.12	MAGNETIC MATERIALS	55
2.7	REFERENCES	56
3	EXPERIENCE WITH SPARC TEST FACILITY	59
3.1	ORIGIN OF THE SPARC PROJECT	59
3.2	GOALS OF THE SPARC PROJECT	59
3.2.1	150 MEV ADVANCED PHOTO-INJECTOR	59
3.2.2	SASE-FEL VISIBLE-VUV EXPERIMENT	60
3.2.3	X-RAY OPTICS/MONOCROMATORS	60

De Padova	Paola	CNR
De Silvestri	Sandro	CNR / Politecnico di Milano
Del Franco	Mario	ENEA
Di Pasquale	Enrico	INFN
Di Pirro	Giampiero	INFN
Dipace	Antonio	ENEA
Doria	Andrea	ENEA
Drago	Alessandro	INFN
Esposito	Adolfo	INFN
Esposito	Marco	INFN
Faillace	Luigi	U. di Roma "La Sapienza"
Ferrario	Massimo	INFN
Ficcadenti	Luca	INFN
Filippetto	Daniele	INFN
Fioravanti	Sandro	INFN
Flammini	Roberto	CNR
Fusco	Valeria	INFN
Gallerano	Gian Piero	ENEA
Gallo	Alessandro	INFN
Gatti	Giancarlo	INFN
Ghigo	Andrea	INFN
Giannessi	Luca	ENEA
Giove	Dario	INFN
Giovenale	Emilio	ENEA
Ippoliti	Alessandro	CNR
Lagomarsino	Stefano	CNR
Ligi	Carlo	INFN
Marcellini	Fabio	INFN
Marchetti	Barbara	U. di Roma "Tor Vergata"
Marolo	Cesare	INFN
Marelli	Chiara	U. di Roma "La Sapienza"
Marinelli	Agostino	U. di Roma "La Sapienza" / UCLA
Migliorati	Mauro	U. di Roma "La Sapienza" / INFN
Mostacci	Andrea	U. di Roma "La Sapienza" / INFN
Nisoli	Mauro	CNR
O'Keeffe	Patrick	CNR
Orlandi	Gianluca	ENEA
Ottaviani	Carlo	CNR
Pace	Elisabetta	INFN
Paci	Barbara	CNR
Palumbo	Luigi	U. di Roma "La Sapienza" / INFN
Pellegrini	Claudio	UCLA
Pellegrino	Luigi	INFN
Petralia	Alberto	ENEA
Petrillo	Vittoria	U. di Milano / INFN
Poletto	Luca	CNR-INFN, Laboratorio LUXOR
Preger	Miro	INFN
Priori	Sandro	CNR
Quaresima	Claudio	CNR
Quattromini	Marcello	ENEA
Reiche	Sven	UCLA
Renieri	Alberto	ENEA

Ricci	Ruggero	INFN
Ronsivalle	Concetta	ENEA
Rosenzweig	James	UCLA
Rossi	Andrea	INFN
Rossi	Franca	CNR
Rossi-Albertini	Valerio	CNR
Sabia	Elio	ENEA
Sansone	Giuseppe	CNR
Sensoli	Roberto	ENEA
Serio	Mario	INFN
Sgamma	Francesco	INFN
Spasovsky	Ivan	ENEA
Spataro	Bruno	INFN
Stagira	Salvatore	Politecnico di Milano/Ultras CNR-INFN
Stecchi	Alessandro	INFN
Stella	Angelo	INFN
Stucchi	Silvano	U. di Roma "Tor Vergata"
Surrenti	Vincenzo	ENEA
Tazzioli	Franco	INFN
Tomassini	Sandro	INFN
Tiburzio	Angelo	INFN
Tondello	Giuseppe	U. Padova
Turchini	Stefano	CNR
Vaccarezza	Cristina	INFN
Venturini	Fabio	LBNL
Vescovi	Mario	INFN
Vescovi	Sandro	INFN
Vicario	Carlo	INFN
Volpe	Luca	INFN
Vozzi	Caterina	CNR
Zema	Nicola	CNR
Zhukowsky	Karl	ENEA
Zobov	Mikhail	INFN

Tecnical Designer

Anelli	Federico	INFN
Baldini	Pietro	INFN
Battisti	Antonio	INFN
Belli	Maurizio	INFN
Brolatti	Massimo	CNR
Cacciotti	Luciano	INFN
Campana	Ezio	ENEA
Cecchinelli	Alberto	INFN
Chimenti	Paolo	INFN
Clementi	Renato	INFN
Coiro	Oscar	INFN
De Giorgi	Maurizio	INFN
Fontana	Gianni	INFN
Grossi	Eleuterio	INFN
Lollo	Valerio	INFN
Martinelli	Moreno	INFN

Pavan	Valerio	INFN
Pieri	Roberto	INFN
Piermarini	Graziano	INFN
Rondinelli	Maurizio	INFN
Sensolini	Giancarlo	INFN
Sorchetti	Rossano	INFN
Zarlenga	Raffaele	INFN
Zolla	Alessandro	INFN

International Advisory board

Coupré	Marie-Emmanuelle	Soleil
Pellegrini	Claudio	UCLA
Prosperi	Tommaso	CNR
Rosbach	Jörg	DESY
Serafini	Luca	INFN

Scientific Secretary

Casarin	Francesca	INFN
Crescentini	Lucilla	ENEA
Giabbai	Manuela	INFN

3.3	SPARC LAYOUT	60
3.4	SPARC PARAMETER LIST	63
3.5	SPARC EXPERIMENTAL ACHIEVEMENTS	66
3.5.1	LOW ENERGY BEAM MEASUREMENTS	66
3.5.1.1	Cathode and Laser system	67
3.5.1.2	RF system and synchronization	70
3.5.1.3	The control system	71
3.5.1.4	Advanced Diagnostic devices: the emittance meter and the RF deflector	71
3.5.2	LOW ENERGY BEAM MEASUREMENTS	74
3.5.2.1	Laser Pulse Shape Studies	78
3.5.2.2	High Brightness Beam	79
3.5.2.3	Double Minimum Oscillation	81
3.5.2.4	Velocity Bunching Experiment	83
3.5.2.5	First observation of Self Amplified Spontaneous Emission at SPARC	87
3.6	REFERENCES	90
4	MACHINE PHYSICS	91
4.1	FEL PHYSICS	91
4.1.1	INTRODUCTION	91
4.1.2	GENERAL SPECTRAL PROPERTIES	91
4.1.2.1	Pulse intensity	92
4.1.2.2	Temporal characteristics	93
4.1.2.3	Polarization	95
4.1.3	FEL SCALING PRINCIPLES	95
4.1.3.1	Limitations on the FEL gain	98
4.1.4	BEAM EMITTANCE AND ACCELERATOR PARAMETERS	99
4.1.5	COMPUTATIONAL TOOLS	100
4.1.5.1	GENESIS 1.3	100
4.1.5.2	PERSEO	101
4.1.5.3	PROMETEO	101
4.1.5.4	Tools validation	102
4.1.6	OPTIONS FOR SPARX FEL ARCHITECTURE	103
4.1.7	OVERALL LAYOUT AND CHOICE OF PARAMETERS	106
4.1.7.1	VUV-EUV beamline (40-124 eV)	106
4.1.7.2	The EUV-Soft X-Ray beamline	116
4.1.7.3	The Hard X-Ray Undulator beamline	139
4.1.8	CONCLUSION	148
4.1.9	SPONTANEOUS UNDULATOR RADIATION	149
4.2	PHOTO-INJECTOR	155
4.2.1	INTRODUCTION	155
4.2.2	HIGH CHARGE WORKING POINT (1 nC)	156
4.2.3	LOW CHARGE WORKING POINT (200 pC)	159
4.2.4	SHORT PULSE WORKING POINT (50 pC)	160
4.2.5	SENSITIVITY TO RF COMPRESSOR PHASE JITTER	162
4.3	ACCELERATOR	163
4.3.1	OVERVIEW	163
4.3.2	LAYOUT	163
4.3.3	LINAC L1-L4	165
4.3.4	WAKE FUNCTION, IMPEDANCE, WAKE POTENTIAL, LOSS FACTOR AND ENERGY SPREAD	167

4.3.5	LONGITUDINAL BEAM DYNAMICS	168
4.3.6	LINAC CAVITIES WAKE FIELDS	169
4.3.7	RESISTIVE WALL	173
4.3.8	X-BAND LINEARIZATION	175
4.3.9	TRANSVERSE BEAM DYNAMICS	177
4.3.9.1	Bunch Compressor system (inside CSR)	177
4.3.9.2	First Bunch Compressor BC1	179
4.3.9.3	Second Bunch Compressor BC2	180
4.3.9.4	Third Bunch Compressor BC3	182
4.3.10	PARTICLE TRACKING 1D	182
4.3.11	PARTICLE TRACKING 3D-1D COMPARISON	186
4.3.12	MICROBUNCHING INSTABILITY	189
4.4	TRANSFER LINES	191
4.4.1	INTRODUCTION	191
4.4.2	LOW ENERGY TRANSFER LINES	193
4.4.2.1	Dogleg and FODO line	193
4.4.2.2	DL1-U1 and DL1-U2	194
4.4.3	HIGH ENERGY TRANSFER LINES	197
4.4.3.1	DL2-U2 and DL2-U3	198
4.5	SEED SOURCES BASED ON HIGH-ORDER HARMONIC GENERATION IN GAS	200
4.5.1	SCALING LAWS FOR EFFICIENT HIGH-ORDER HARMONIC GENERATION.	202
4.5.2	GENERATION AND TRANSPORT OF THE SEEDING RADIATION	204
4.5.2.1	Design of the seeding source.	204
4.5.2.2	Beamline for conditioning and transport of the seeding	205
4.5.3	CHARACTERIZATION OF THE SEEDING BEAM	210
4.5.3.1	Spectral characterization	210
4.5.3.2	XUV intensity measurement	210
4.5.3.3	XUV beam divergence	210
4.5.3.4	XUV source size	211
4.6	APPENDIX: C-BAND OPTION FOR THE SPARX LINAC	211
4.7	REFERENCES	217

5 LINEAR ACCELERATOR **221**

5.1	PRE-INJECTOR	221
5.1.1	RF-GUN	221
5.1.1.1	RF Project	222
5.1.1.2	Coupling and Beam Loading	226
5.1.1.3	RF Pulsed Heating	226
5.1.1.4	Magnetic Quadrupole Component	227
5.1.1.5	Transient Analysis	228
5.1.1.6	Preliminary results	229
5.1.1.7	Thermal Analysis	230
5.1.1.8	Stress Analysis	232
5.1.1.9	Outlook	233
5.1.2	PHOTOCATHODES	234
5.1.2.1	Candidate materials for photocathodes	235
5.1.2.2	Laser energy requirements in operational conditions	236
5.1.2.3	Influence of cathode material on dark current	237
5.1.3	LASER SYSTEM	239
5.1.3.1	Definition of the SPARX laser performances	240
5.1.3.2	Laser system description	241
5.1.3.3	Time pulse shaping	244

5.1.3.4	Spatial pulse shaping and imaging system to the cathode	257
5.2	LINAC DESIGN	264
5.2.1	LINAC LAYOUT	264
5.2.2	ACCELERATING STRUCTURES	265
5.2.3	RF POWER DISTRIBUTION	268
5.2.4	IV HARMONIC SYSTEM	271
5.2.4.1	X-band power source and structure	274
5.2.4.2	Preliminary cavity design	275
5.2.4.3	X-band power sources	280
5.2.5	S-C-X-BAND SYSTEMS COMPARISON	281
5.2.5.1	C-band LINACs	281
5.2.5.2	X-band LINACs	282
5.2.5.3	Summary and conclusions.	283
5.2.6	LOW-LEVEL RF CONTROLS AND FEEDBACKS	284
5.3	ELECTRON BEAM DIAGNOSTICS	288
5.3.1	INTRODUCTION	288
5.3.2	EMITTANCE DIAGNOSTIC	289
5.3.3	ELECTRON BEAM DIAGNOSTIC @ 6 MEV	289
5.3.4	ELECTRON BEAM DIAGNOSTIC @ 150MEV	292
5.3.5	ELECTRON BEAM DIAGNOSTIC @ 1.5 GEV:	295
5.3.6	ALIGNMENT LASER	297
5.3.7	OPTICAL DIFFRACTION RADIATION	297
5.3.8	RF DEFLECTORS	298
5.3.8.1	Bunch length measurements	298
5.3.8.2	Longitudinal phase space measurements	300
5.3.8.3	Horizontal slice emittance measurements	301
5.3.8.4	Beam manipulation with an RFD: ultra-short bunch generation	301
5.3.8.5	Deflector parameters	302
5.3.9	BEAM POSITION MONITORS	306
5.4	CONVENTIONAL MAGNETIC ELEMENTS	309
5.4.1	DESIGN PROCEDURE	309
5.4.2	MATERIAL CHOICE AND CONSTRUCTION	310
5.4.3	SINGLE MAGNETIC ELEMENTS	311
5.5	REFERENCES:	317
6	UNDULATORS SYSTEMS	321
6.1	MAGNET TECHNOLOGY	321
6.2	UNDULATOR DESIGN	325
6.3	UNDULATOR TOLERANCES	327
6.4	UNDULATOR MEASUREMENT SYSTEM	333
6.5	PHASE SHIFTER	336
6.1	REFERENCES	338
7	RADIATION BEAMLINES	339
7.1	GENERAL CONSIDERATIONS	339
7.2	POWER LOAD, RADIATION DAMAGE AND OPTICAL DESIGN	341
7.2.1	DAMAGE	341
7.2.2	MIRRORS AND COATINGS	342
7.3	PHOTON BEAM TRANSPORT	344

7.3.1	FRONT-END	346
7.3.2	VACUUM	347
7.4	BEAMLINES LAY-OUT	350
7.5	SPLITTING, FILTERING, MONOCHROMATIZATION AND FOCUSING	351
7.5.1	GAS ABSORBER	352
7.5.2	SWITCHING MIRROR	353
7.5.3	BEAMLINES FOR SHORT PULSES	354
7.5.3.1	Low-resolution monochromator	354
7.5.3.2	Focussing section	355
7.5.4	DESIGN OF A BEAMLINE FOR THE 1.5-15 NM SPECTRAL REGION	356
7.5.4.1	Effect of the slope errors	357
7.5.4.2	Operative conditions	359
7.5.4.3	Energy density on the optics and exit slit	360
7.5.4.4	Focussing section	360
7.5.5	DESIGN OF THE BEAMLINE FOR THE 1-5 NM REGION	361
7.5.5.1	Focussing section	364
7.5.6	ALTERNATIVE DESIGNS: THE GRATING IN THE OFF-PLANE MOUNT	365
7.5.7	BEAMLINES FOR HIGH-ENERGY RESOLUTION	366
7.5.7.1	High-resolution on ultra short pulses	366
7.5.8	OPTICAL LAYOUT OF THE BEAMLINE	368
7.5.8.1	Pre-focussing section	368
7.5.8.2	Monochromator section	368
7.5.8.3	Focussing section	368
7.5.9	DESIGN OF A BEAMLINE FOR THE 4.5-15 NM RANGE	368
7.5.9.1	Effect of the slope errors	370
7.5.9.2	Operative conditions	370
7.5.9.3	Energy density on the optics and exit slit	370
7.5.10	DESIGN OF A BEAMLINE FOR THE 0.6-1.2 NM RANGE	371
7.5.11	BEAMLINES FOR SPONTANEOUS RADIATION	372
7.6	REFERENCES	375

8 PHOTON DIAGNOSTICS **377**

8.1	RADIATION BASED DIAGNOSTICS IN LINAC	377
8.1.1	BEAM SIZE MONITORS	377
8.1.2	COHERENT RADIATION BUNCH LENGTH SYSTEMS	378
8.2	RADIATION BASED DIAGNOSTICS IN UNDULATORS	380
8.2.1	RADIATION TRANSPORT	381
8.2.2	SPECTRAL MEASUREMENTS	383
8.3	RADIATION BASED DIAGNOSTICS IN BEAM LINES	384
8.3.1	IN-LINE MEASUREMENT OF THE FEL SPECTRUM	385
8.3.1.1	Design for the 1.5-20 nm region	386
8.3.1.2	Design for shorter wavelengths	388
8.3.1.3	Expertise of the team in realization of spectrometers for Free Electron Lasers	389
8.3.2	CONTROLLED ATTENUATION OF FEL RADIATION USING A GAS ABSORBER	389
8.3.3	INTENSITY MONITOR	391
8.3.4	BEAM POSITION MONITOR	392
8.3.5	WAVE FRONT MEASUREMENT	392
8.3.6	FOCUS CHARACTERIZATION	393
8.3.7	MEASUREMENT OF THE TRANSVERSE COHERENCE	393
8.3.8	TEMPORAL CHARACTERIZATION	393
8.3.8.1	Cross-correlation measurements	394

8.3.8.2	Autocorrelation measurements	397
8.4	PROPOSAL OF NOVEL DIAGNOSTIC TECHNIQUES	399
8.4.1	ELECTRON BEAM TRANSVERSE SIZE EFFECTS IN THE TRANSITION RADIATION SPECTRUM AS A POSSIBLE DIAGNOSTIC TOOL IN LINAC FELS	399
8.4.2	PULSE LENGTH MEASUREMENTS USING INCOHERENT SYNCHROTRON RADIATION FLUCTUATIONS	401
8.4.3	DIAGNOSTICS USING FAST IR SINGLE ELEMENT PHOTODIODES AND ARRAY DETECTORS.	404
8.5	REFERENCES	407
9	EXPERIMENTAL ACTIVITY	409
9.1	INTRODUCTION AND PREMISE	409
9.2	STRUCTURAL STUDIES BY USING X-FEL RADIATION	410
9.2.1	BIOLOGICAL SYSTEMS	410
9.2.2	REFERENCES	411
9.3	TIME RESOLVED X-RAY DIFFRACTION: PUMP&PROBE EXPERIMENTS	412
9.3.1	COHERENT DIFFRACTION: X-RAY HOLOGRAPHY	412
9.3.2	REFERENCES	414
9.4	COHERENT DIFFRACTION IMAGING, HOLOGRAPHY AND NANO-PROBES BEAMLINES	414
9.4.1	CXDI	414
9.4.2	HOLOGRAPHY	416
9.4.3	OPTICAL COMPONENTS FOR COHERENT IMAGING	417
9.4.4	BEAM-LINES DESCRIPTION FOR COHERENCE EXPERIMENTS	418
9.5	PLASMA PHYSICS	420
9.5.1	LASER-PLASMA INTERACTION: THEORETICAL MODELS	420
9.5.2	SOME LASER-PLASMA EXPERIMENTS AT SPARX	423
9.6	ATOMS , MOLECULES AND CLUSTERS	426
9.6.1	TWO PHOTON EXCITATION, IONIZATION AND DOUBLE IONIZATION	427
9.6.2	DISSOCIATION FOLLOWING THE MULTIPLE IONISATION OF SMALL POLYATOMIC MOLECULES	432
9.6.3	MAIN CHAMBER, SPECTROMETERS AND TARGETS	434
9.6.4	CHARACTERISTIC OF THE BEAMLINE, MONOCROMATIZATION AND BEAM DIAGNOSTIC	436
9.7	SOME NONLINEAR OPTICS EXPERIMENTS AT SPARX	436
9.7.1	INTENSITY DRIVEN (I.E. NON LINEAR OPTICS) EXPERIMENTS	437
9.7.2	TWO PHOTON ABSORPTION	438
9.7.3	□ ⁽³⁾ EFFECTS	438
9.8	CONDENSED MATTER SPECTROSCOPY	441
9.8.1	SUMMARY	441
9.8.2	X-RAY PHOTON CORRELATION SPECTROSCOPY ON SUPERCONDUCTORS	441
9.8.3	<i>SYNTHESIS AND STUDY OF NANOPHASE MATERIALS</i>	443
9.8.4	<i>TIME RESOLVED SPECTROSCOPY: PUMP-PROBE</i>	444
9.8.4.1	Pump-probe: surfaces and interfaces	445
9.8.4.2	Ultrafast Pump-probe Experiments: Nanostructures	446
9.8.5	EMISSION SPECTROSCOPY AT THE SOFT X-RAY ENERGIES	447
9.8.6	LOW-DIMENSIONAL SYSTEMS	448
9.8.7	HIGHLY CORRELATED SYSTEMS	450
9.8.8	SPECTROMICROSCOPY	451
9.8.9	BIOLOGICAL SAMPLES	452
9.8.10	STUDY OF PHOTOSYNTHETIC COMPLEXES AND PHOTOCHEMICAL PROCESSES.	454
9.8.10.1	The problem of radiation damage	455

9.8.10.2	Magnetic Materials	456
9.8.11	NANOIMAGING	460
9.8.11.1	Generalities	460
9.8.11.2	Optics	460
9.8.11.3	Phase Contrast	461
9.8.11.4	Spectromicroscopy	461
9.8.12	MICRORADIOLOGY	462
9.8.12.1	Introduction	462
9.8.12.2	Current programs	463
9.8.12.3	The future: the SASE-FEL sources	465
9.8.13	NANOLITHOGRAPHY	466
9.9	REFERENCES:	471

10 TIMING AND SYNCHRONIZATION, CONTROL SYSTEM **477**

10.1	TIMING AND SYNCHRONIZATION: INTRODUCTION AND GENERAL ARCHITECTURE	477
10.1.1	REFERENCE MASTER OSCILLATOR (RMO)	479
10.1.2	OPTICAL MASTER OSCILLATOR (OMO)	480
10.1.3	OPTICAL DISTRIBUTION OF THE SYNCHRONIZATION REFERENCE	481
10.2	CLIENT SYNCHRONIZATION	484
10.2.1	SYNCHRONIZATION OF SPARX LASERS	484
10.2.1.1	Laser Timing Description	485
10.2.1.2	Laser triggering scheme	488
10.2.2	SYNCHRONIZATION OF THE SPARX RF CLIENTS	490
10.2.3	SYNCHRONIZATION OF SPARX BEAM DIAGNOSTICS	492
10.2.3.1	RF Macropulses	493
10.2.3.2	High repetition rate optical signals	493
10.2.3.3	Short time pulses	493
10.3	TRIGGERS GENERATION	496
10.3.1	INTRODUCTION AND PRINCIPLES OF OPERATION	496
10.3.2	COMMENTS ON THE MAIN DIVIDER	496
10.3.3	LIST OF MAIN TRIGGER MODULES	497
10.3.4	EVENT AND TIME-STAMP GENERATOR AND RECEIVERS	498
10.4	CONTROL SYSTEM	502
10.4.1	GENERAL DESCRIPTION	502
10.4.2	HARDWARE	503
10.4.2.1	Network	503
10.4.3	SOFTWARE	506
10.4.3.1	Service Programs	506
10.4.4	ELEMENTS	506
10.4.4.1	Laser	506
10.4.4.2	RF	506
10.4.4.3	Magnets	507
10.4.4.4	Vacuum	507
10.4.4.5	Diagnostic	508
10.4.4.6	Motion and positioning	508
10.5	REFERENCES	510

11 VACUUM SYSTEM AND ALIGNMENT **511**

11.1	VACUUM SYSTEM	511
-------------	----------------------	------------

11.1.1	INTRODUCTION	511
11.1.2	GENERAL REMARKS	511
11.1.3	SUBSYSTEMS	512
11.1.3.1	LINAC	512
11.1.3.2	RF-Gun	513
11.1.3.3	Transfer Lines	514
11.1.4	UNDULATORS	515
11.1.4.1	Pumps	515
11.1.4.2	Vacuum diagnostics	515
11.1.4.3	Valves	515
11.1.4.4	Beam transfer lines	515
11.2	ALIGNMENT	516
11.2.1	REFERENCE NETWORK	517
11.2.2	COMPONENT SUPPORTS AND ADJUSTMENT SYSTEMS	519
11.2.3	FIDUCIALIZATION	519
11.2.4	POSITIONING OF COMPONENTS	520
11.3	REFERENCES	521

12 RADIATION SAFETY **523**

12.1	INTRODUCTION	523
12.2	OPERATING PARAMETER	523
12.3	MACHINE PROTECTION	523
12.3.1	ELECTRON LOSSES	523
12.3.2	DOSE MONITORING IN THE UNDULATORS SECTION	523
12.4	RADIATION PROTECTION	524
12.4.1	SHIELDING OUTLINES	524
12.4.2	SHIELDING DESIGN CRITERIA	524
12.5	SOURCE TERM	524
12.5.1	BREMSSTRAHLUNG	524
12.5.2	NEUTRONS	525
12.5.2.1	Giant resonance production	525
12.5.2.2	Pseudo-deuteron production	525
12.5.2.3	Photo-pion production	525
12.5.3	MUONS	526
12.5.4	GAS BREMSSTRAHLUNG	526
12.5.5	INDUCED ACTIVITY	527
12.5.6	MACHINE ACCESSES	527
12.5.7	BEAM LINE RADIATION SHIELDING DESIGN	527
12.5.8	THE OPERATIONAL RADIATION SAFETY PROGRAM	527
12.5.8.1	Interlock design and feature	528
12.6	ELECTRON BEAM DUMP	529
12.7	OTHER RADIATION SOURCES	529

13 INFRASTRUCTURE **531**

13.1	THE SITE	531
13.2	BUILDINGS	533
13.3	SPARX ELECTRICAL POWER SUPPLY	538
13.3.1	REDUNDANCY CRITERIA	539
13.3.2	LOW VOLTAGE POWER DISTRIBUTION	540
13.3.3	ELECTRICAL INSTALLATION FOR THE ACCELERATOR TUNNEL	540

13.3.4	GROUNDING, BONDING AND LOW VOLTAGE DISTRIBUTION SYSTEM	541
13.3.5	ELECTROMAGNETIC COMPLIANCE	541
13.4	ACCELERATOR SPECIAL FLUID PLANTS	541
13.4.1	COLD AND HOT FLUIDS PRODUCTION	541
13.4.2	AIR CONDITIONING AND VENTILATION OF TUNNELS AND HALLS	542
13.4.3	WATER COOLING	542
13.4.4	COMPRESSED GASES	543
13.4.5	ENERGY EFFICIENCY	543
13.4.6	USERS EVALUATION	543
13.4.7	ELECTRICAL CONSUMPTION	550
13.4.8	OPEN POINTS	550
13.4.9	ROOMS AND SPACES	550
13.5	REFERENCES	552
14 PROJECT MANAGEMENT		553
<hr/>		
14.1	OVERVIEW	553
14.2	ORGANIZATION	554
14.2.1	PREMISE	554
14.2.2	STEERING COMMITTEE (COMITATO TECNICO SCIENTIFICO – CTS)	554
14.2.3	PROJECT TEAM - PT	555
14.2.4	DIRECTORATE	555
14.2.5	EVALUATION COMMITTEE	556
14.3	ROLES AND RESPONSIBILITIES WITHIN THE SPARX PROJECT	557
14.3.1	DIRECTORATE	557
14.3.2	PROJECT DIRECTOR	557
14.3.3	DEPUTY DIRECTOR	558
14.3.4	PROJECT MANAGER	558
14.3.5	SCIENTIFIC COORDINATOR	558
14.3.6	TECHNICAL COORDINATOR	559
14.3.7	EXECUTIVE COMMITTEE	559
14.3.8	WORKPACKAGE LEADER (WPL)	560
14.4	PROJECT MANAGEMENT TOOLS AND PROCEDURES	560
14.5	HUMAN RESOURCES AND RECRUITMENT POLICY	561
14.6	SPARX CONSORTIUM AND COLLABORATION AGREEMENTS BETWEEN CONTRIBUTING INSTITUTES	561
14.7	COMMUNICATION	562
14.7.1	TOOLS AND INITIATIVES	562
14.7.2	GENERAL GUIDELINES	563
14.7.3	WEBPAGE DEVELOPMENT AND MAINTENANCE	563
14.7.4	COMMUNICATION AND SCIENTIFIC DISSEMINATION ACTIONS - PRESS AND BROCHURES	563
14.7.5	ORGANIZATION OF WORKSHOPS, SEMINARS AND SCHOOLS	564
14.7.6	IRUVX-FEL	564
14.8	REFERENCES	565
15 PROJECT TIMELINE AND FINANCING		567
<hr/>		
15.1	OVERVIEW	567
15.2	TIMELINE	567
15.3	CONSTRUCTION COSTS	570
15.4	OPERATIONAL COSTS	571

1 FOREWORD

This Technical Design Report (TDR) gives a detailed technical description of the new research infrastructure SPARX (Sorgente Pulsata Autoamplificata Raggi X) FEL.

The TDR and its accompanying Scientific Case, give evidence of the strong motivation for constructing and operating such a facility for a wide and multidisciplinary user community. We are convinced that SPARX-FEL will enrich the landscape of the research infrastructures for the forthcoming decades and will be of great benefit for the development of science and technology.

The manuscripts have been written with the contribution of about two hundred scientists, engineers and designers from different laboratories worldwide, and with the advise of international editors.

I would like to express my gratitude to all of them for their deep commitment and constant effort.

Luigi Palumbo
SPARX-FEL Project Director

2 EXECUTIVE SUMMARY

2.1 From Synchrotron Light Sources (SLS) to Free Electron Lasers (FEL)

Synchrotron Radiation Sources have played a relevant role in the scientific and technological development over the last thirty years, being indeed instrumentation tools for different fields of basic science and applications.

In order to improve experimental accuracy and reduce the measurement exposure time, synchrotron light sources have been designed with higher and higher *brightness* since the use of the first synchrotrons radiation from bending magnets. With the design of ultra low emittance rings and with the introduction of wigglers and undulators this parameter has increased by about nine orders of magnitudes. Today, the so-called third generation sources provide X-ray beams with brightness exceeding 10^{20} photons/sec/0.1% bw/(mm mrad)² – (from now on these units will be referred to as c.u.). It is widely believed that brightness in the region of 10^{23} (c.u.) is an upper limit for the present technology based on storage rings. A new technological step is necessary to go beyond based on linear accelerators and a well-known physical process named SASE (self amplified spontaneous emission).

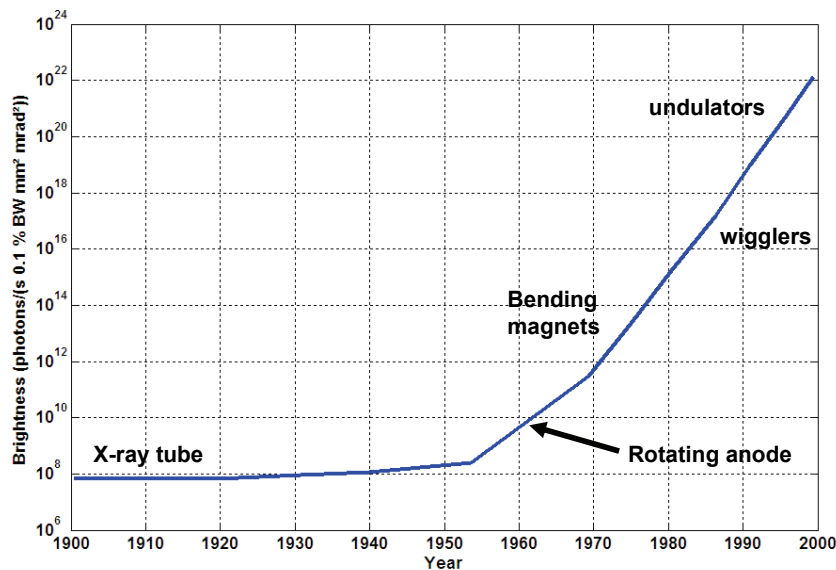


Figure 2.1: Evolution of X-ray source brightness

With these new devices, it is expected that the emission process will deliver a photon brightness eight order of magnitude higher than what is achievable with the spontaneous emission in the last generation of SLS.

Free Electron Lasers (FELs) are sources of coherent electromagnetic radiation having similar optical properties as conventional gas or solid-state lasers. The relevant difference is the lasing medium being, for FELs, an electron beam which moves freely through a magnetic structure, the undulator which causes transverse electron oscillations. While travelling in the undulator, the coupling of electron transverse velocity with an electromagnetic radiation field

results in energy transfer. This causes micro-bunching of the electron beam in dependence of the radiation wavelength and leads to coherent emission. In LINAC based FELs, the micro-bunching instability can be created in a single pass through sufficiently long undulators, where an exponentially growing power radiation is produced. This spontaneous amplifying mechanism is called Self Amplified Spontaneous Emission (SASE), which ensures only the transverse coherence radiation, the longitudinal distribution showing large numbers of spikes generated by the noise in the electron bunch density. "Seeding" the electron beam with an external radiation source, allows to drive the instability and to control the longitudinal properties of radiation.

The generated output radiation is extremely interesting in terms of brilliance, coherence, pulse duration and intensity, these unique features offer new opportunities in many fields of research: material science, chemistry, biology, medical science, industrial applications.

So far few SASE FELs have been tested at LEUTL, VISA and TTF-FEL. This last, named recently FLASH has the record of wavelength (6 nm) and started to operate as user facility in 2007. Many projects are being proposed in the world. The major initiatives concern the American LCLS at Stanford and the European X-FEL at DESY, Hamburg, which are willing to reach the Angstrom region. Nation based initiatives are particularly active in Europe, Asia.

2.2 Development of synchrotron radiation sources and FEL in the Frascati area.

Theoretical and experimental research activity on particle accelerator, as instruments of investigation in nuclear physics, started about forty years ago in the Frascati area with the electron-synchrotron, and have been continuing in recent years with the construction of new accelerator machines mainly for High Energy Physics applications. Since the first observations on the accelerated beams, it was clear that a new type of radiation, available from bending magnets (synchrotron radiation), had those interesting and promising properties, which would allow researchers to probe and investigate matter, and biological samples at the nano-scale level.

The first experiments of synchrotron light in Italy date back to the late fifties when at the Frascati National Laboratory (LNF) a research team, involved in the construction of the first-in-the-world storage ring ADA, measured, for diagnostic purposes, the radiation emitted by less than 100 electrons circulating in the machine. The measurement was accurate enough to detect the light emitted by single electrons.

The high interest about the radiation properties and its application gave birth to a joint Italian-French collaboration aiming at the experimental use of the synchrotron radiation produced by the 1.1 GeV electron-synchrotron in Frascati. In this pioneering time the first experiments on absorption spectroscopy were performed in the spectral region 50 eV – 500 eV.

The experience gained in the pioneering time made possible a further development of the SR applications through a collaboration between INFN and CNR with the project PULS on the storage ring ADONE at LNF. A new era had started and an ever-growing community of Italian physicists approached this new field of research.

The first beam line on ADONE dedicated to SR, completed in 1979, was able to transport UV and X-rays from a dipole magnet to the experimental area. The scientific activity was mainly addressed to X-ray absorption and fluorescence. In the next years PULSE laboratory grew up to 6 beam lines, equipped with monochromators, and delivering a photon flux of 10^{10} - 10^{12} photons per second. Despite the “parasitic” use of the radiation beam lines, the source became soon competitive in the international scenario with the publication of more than 1000 papers on international referred journals. The PULS project became the main road for the development of a national community of synchrotron radiation users.

An important step for the RS source was done with the realization in 1979 of the first “wiggler” magnet, unique source at that time, which started the operation the same year at Frascati and Stanford laboratories. The photon flux and the radiation bandwidth were significantly increased, and three new beam lines, up to the hard X-rays, were installed on the machine. The experimental stations were dedicated to absorption spectroscopy, fluorescence, Mössbauer time resolved. In addition X-ray lithography and digital angiography techniques were tested and developed.

In April 1993 ADONE was switched off and the machine dismantled in order to leave place to a new accelerator complex DAFNE, 1.1 GeV center of mass energy, devoted to high luminosity particle physics experiments. It was designed to host also two SR beam lines (Dafne-light project): the X-ray beam line (1-7 keV) extracts radiation from a wiggler and splits the beam in two separate lines, DRX1 e DRX2; the infrared beam line extracts radiation from a dipole magnet which, because of the high current stored in the ring (1.5 A), produces an extremely high photon flux.

Accelerator physicists and engineers played also a relevant role in the proposal and project of the 3rd generation 5 GeV European Synchrotron Radiation Source (ESRF) and in the design of the Italian SR Source ELETTRA. For the last case it is worth mentioning the construction of 5 beam lines (VUV, XRD, GAPH, POLAR, X-Proximity) done by CNR institutes in Rome and by the Universities of Rome. A collaboration between CNR, INFN and INFN designed and constructed the multi-purpose beam line GILDA at ESRF.

Relevant contribution to the development of synchrotron radiation sources was given by ENEA (at the time CNEN) which, immediately after Madey’s pioneering experiment at the Stanford University in 1976, started the development of low energy accelerators dedicated to Free Electron lasers (FEL). Over the years ENEA built microtrons and LINACs, providing e-beams with suitable characteristics to provide FEL radiation in the IR-FIR region of the e. m. spectrum.

The ENEA researchers also developed the theoretical framework to study the physics of this new coherent source and the first numerical code, giving a significant contribution to the understanding of the processes concerned with gain and saturation along with the major scaling laws, that are nowadays widely exploited in the preliminary design of FEL sources.

A FEL operating in the IR spectral region, based on a 20 MeV electron beam accelerated by a microtron was realized at the beginning of the eighties. Later on a 5 MeV microtron was used to obtain FEL-Cerenkov coherent radiation and, finally, two FELs operating in the sub-mm and Terahertz region have been realized at ENEA Frascati exploiting novel features linked to the waveguide operation, such as the possibility of operating at “zero slippage” and

the “energy-phase correlation mechanism” exploited in the source FEL-CATS to enhance the coherent emission in the widest possible bandwidth.

The competences in the field of FEL and SR grown at ENEA and INFN were merged into common research lines on the study, design and construction of sources of coherent radiation from free electrons.

After the first experiment of FEL done at Stanford by J. Madey, in 1977 at Stanford, three FEL experiments were proposed in Europe: FEL-ACO at Orsay (France), LEDA-F at CNEN (now ENEA) and LELA both in the area of Frascati Labs. (Italy).

The LEDA-F project has been the first example of Storage Ring FEL in which the accelerator has been designed and optimized for the FEL operation.

The LELA undulator installed in 1981 on ADONE storage Ring at LNF, was 2.3 meters long with 20 magnetic periods 11.6 cm each and an optical cavity made of high quality mirrors at 17.5 meters apart. The experiment performed with LELA had at least two important merit

- a) the role of the mirror damage due to the intense flux of X-ray radiation emitted by the electrons in the undulator
- b) the measure of the third harmonic gain

The results obtained on the point a) became successively paradigmatic for all the successive experiments, while, as to the point b), it was clearly shown that the FEL can be used with noticeable flexibility and that FEL operating on higher harmonics can be realized by a suitable design of the optical cavity. The experiment confirmed furthermore the correctness of the theoretical predictions, with respect to gain coefficient and to the enhanced sensitivity to inhomogeneous broadening effects.

Successively ENEA has been involved in different experiments around the world. Strong collaborations occurred with Santa Barbara (CA USA) quantum institute, Stanford (USA CA) University, Dartmouth College (N H USA), Orsay (Fr), Dortmund (GE) and Elettra (Trieste Italy).

In particular the collaboration with Orsay has provided a significant improvement both in theory and in experiments and one of the main achievements was the understanding of the interplay between FEL and different type of beam instabilities, which became of particular interest during the last years for the cure of the micro-bunching instability in bunch compressor devices.

Analogous contributions, both experimental and theoretical, have been given to the realization of the Storage Ring FEL operating at Elettra, whose success has been determined by extensive studies on the mirror technology and radiation induced damage.

In more recent years INFN has significantly contributed to TTF (Tesla Test Facility) at DESY (Germany), in particular with the accelerating modules cryostats, with new semiconductor-type cathodes, diagnostics instrumentation. Up to the recent successes of FLASH, INFN has contributed to the development of the facility, and is presently involved in the construction of the European X-FEL facility.

2.3 The SPARX Initiative

The SPARX (Sorgente Pulsata Autoamplificata di Radiazione X) FEL project is aiming at the realization of a source of coherent X-rays, covering the range of wavelengths (λ) ranging from 0.6 to 40 nm at fundamental harmonics, which will be able to reach the angstrom-region using the third and fifth harmonics where high power is still produced. SPARX covers a radiation region complementary to those of other existing or in construction facilities, such as FLASH ($4 < \lambda < 40$ nm), FERMI ($10 < \lambda < 100$ nm), X-FEL ($0.1 < \lambda < 1.6$ nm), LCLS ($0.15 < \lambda < 1.5$ nm), SCSS ($\lambda > 0.1$ nm), and will produce, with special magnets, radiation up to the THz region. These ranges of wavelengths, showing some convenient overlap, have the advantage of providing sufficient access to users, expected to be proposing experiments in many fields of disciplines, and ensuring at the same time a beneficial level of competitiveness.

The project is planned as an evolutionary research infrastructure exploiting the large site available at the Tor Vergata University campus, an area about 1.5 km long. The machine and the related infrastructures have been designed by a project team in the framework of a collaboration among the major national research institutes, CNR, ENEA, INFN, the University of Roma "Tor Vergata", in strong partnership with many Italian and foreign universities well recognized for their expertise on FELs and their scientific applications. The SPARX facility total length is around 500 m, furthermore, the available site for the construction of SPARX does not limit the expansibility of the facility for future upgrades up to the wavelength of one Angstrom in the first harmonic.

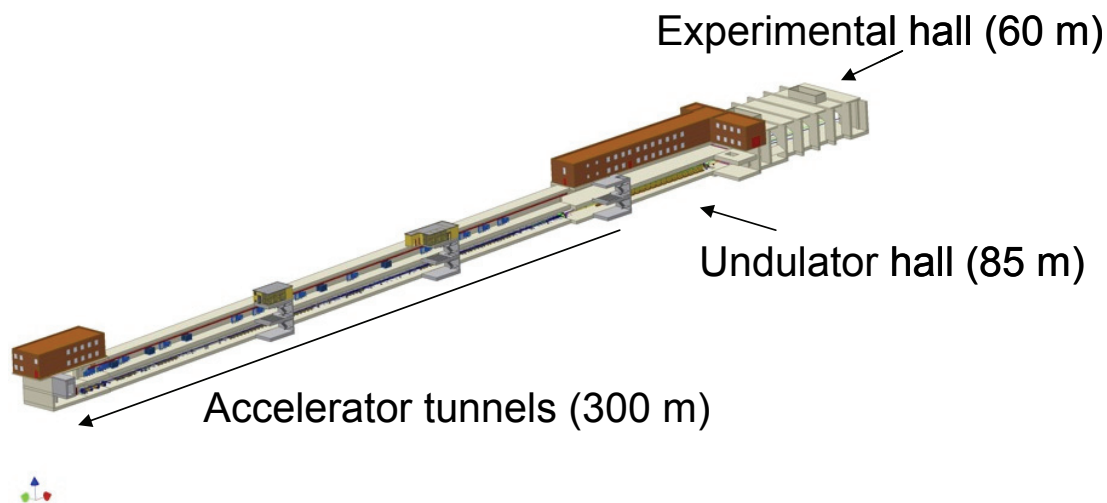


Figure 2.1: The SPARX surface buildings and the LINAC tunnel

SPARX has already seen relevant steps of development, namely in the construction of the Test Facility (SPARC), dedicated to a robust R&D program on ultra-brilliant electron beam LINACs, and on FEL physics. SPARC was approved and funded in 2003 by the Italian Ministry of Research in the framework of the national strategic research program (FISR), and got additional support by the EUROFEL Project within the 6th Framework Programme of the UE. The test facility is now completed, hosting a 150 MeV electron beam LINAC which feeds a 12 meters long undulator. The LINAC has been commissioned and the tests of most critical FEL components have been successfully completed, including

High-Order Harmonic Generation (HHG), based on the interaction between the laser beam and a gas target, used for the seeding experiment. During the last commissioning days the spontaneous emission from the undulators has been observed. In the coming weeks and months an exciting R&D program is expected to be performed in order to generate the classical SASE radiation, and perform the testing of innovative radiation generation schemes based on the “seeding” process” and High Gain Harmonic Generation (HGHG) which can extend the operating wavelength of SPARX-FEL down to sub nano-meter region. First observation of radiation from undulator has been observed recently and an intense R&D program is currently preformed on the generation of SASE and seeded FEL. A complete description of SPARC test facility is given in a chapter 3. It must be said that besides the excellent scientific results achieved with the SPARC test facility, a highly qualified and adequate team of experts - which covers all technical and scientific fields - has grown around this activity.

2.4 SPARX Layout and parameters

2.4.1 Machine schematic and parameters

Due to the availability of a large area at Tor Vergata site, SPARX is conceived as an evolutionary project which foresees with this TDR two additional steps to the already completed SPARC test facility. The main goal is to achieve in the first harmonic the VUV and soft X-Rays spectrum, tuning the machine from 5-6 Å to 30-40 nm

In this way the facility easily covers in its first harmonic the water window spectral region (ranging from 2.3 to 4.4 nm) where the large transmission contrast between Carbon and Oxygen allows to observe biological samples in nm scale and also allows to perform spectroscopic studies on more fundamental materials as solids, surfaces, clusters, molecules, atoms and the interactions among them as, for instance, the study of dynamic processes involved in the heterogeneous catalysis. The subnanometer FEL emission (5-6 Å) is quite suitable for molecular structure studies and it can be further extended down to 1 Å with the use of third and fifth harmonics.

To this end, in order to operate with high flexibility and energy tunability of the electron beam, the electron LINAC has been designed with a maximum energy of 2.64 GeV. This is reached by means of a 150 MeV SPARC-like photoinjector followed by a first LINAC, bringing the operating energy up to 1.5 GeV (which allows to enter the water window region) and the second LINAC for an optimized operating energy of 2.4 GeV (maximum energy is 2.64 GeV) necessary for reaching the subnanometer region. The electron beam, which can be extracted at 1.5 GeV and at 2.4 GeV, feeds three parallel undulators (see Figure 2.2).

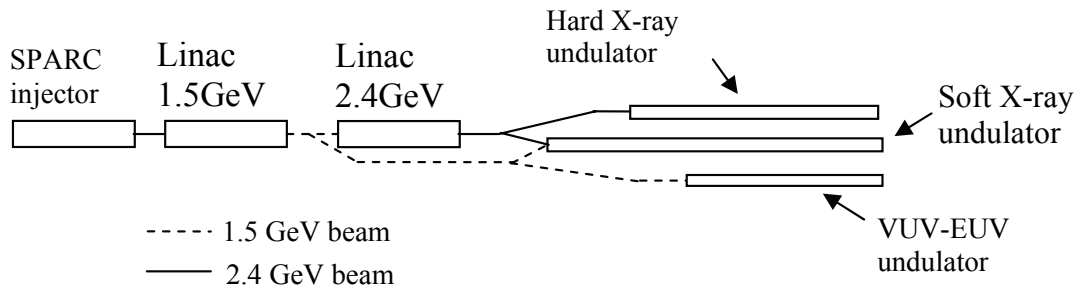


Figure 2.2: Layout of SPARX

The choice of the S-band LINAC with respect to a superconducting L-band LINAC was already made for the test facility SPARC (i.e. the SPARX injector) mainly due to the following reasons:

- 1) compactness of the system
- 2) the lower cost
- 3) existence at LNF of a 800 MeV LINAC, using the same technology
- 4) existing expertise at LNF

The present TDR includes also a comparison between cold S, C and X-band LINAC, showing that X-band LINAC technology is lacking of adequate maturation and can present drawbacks with regard to wakefield interactions between cavity structures and electron beam. On the other side, C-band LINAC looks a good alternative especially after successful tests at SCSS (Japan), however, the choice of S-Band LINAC has been kept since it permits today a technically robust design of the machine and will guarantee with the existing expertise a reliable and efficient operation of the facility.

Two beamlines for each undulator source in order to maximize the users' accessibility. The beamlines, optimized for high photon energy resolution and for short-pulse handling, have been designed for the following energy ranges:

- VUV-EUV beamline: 30 -124 eV (10 -40 nm)
- EUV - Soft X-ray beamline: 88.6 - 1240 eV (1 - 14 nm)
- Soft-X-ray beamline: 1280 eV - 2000 eV (0.6 - 1 nm)

In order to reach SASE saturation in undulators of reasonable length, a peak current $I_{pk} = 1 \div 2.5$ kA is needed for lower and higher energies respectively. The required final beam energy spread is 0.1% in each case and the machine is designed to operate at a repetition rate of 100 Hz. The main parameter list are reported in Table 2.1 and Table 2.2.

Table 2.1: Electron beam parameter list

Energy	(GeV)	E	1 ÷ 1.5	2.4
Peak current	(kA)	I_{pk}	1	2.5
Normalized transverse emittance slice	(μm)	ϵ_n	1	1
Correlated energy spread	(%)	σ_δ	0.1	0.1
Photon Radiation wavelength	(nm)	λ_r	40 ÷ 3	3 ÷ 0.6

Table 2.2: Radiation parameters of the FEL sources

	<i>Units</i>	<i>U1</i>	<i>U2</i>	<i>U2</i>	<i>U3</i>
Electron beam energy	GeV	0.96-1.5	0.96-1.5	1.9-2.4	1.9-2.4
Wavelength	nm	40-10	15-4	4-1.2	1.2 - 0.6
Photon Energy	eV	30-120	80-300	300-1000	1000-2000
Peak power	GW	1.7-3.4	~2	3-20	0.8@2.4GeV
Average power	W	-	0.1-0.2	0.03-0.1	-
Photon beam size (FWHM)	μm	~140	~150	~130	~120
Photon beam divergence (FWHM)	μrad	33	25	19	17
Bandwidth (FWHM)	%	0.2	0.2-0.1	0.15-0.1	0.09@2.4GeV
Pulse duration (FWHM)	fs	200	30-250	70-30	70-80
Repetition rate	Hz	100-50	100-50	100-50	100-50
Number of photons per pulse	#	$1.0 \cdot 10^{14}$	$1.5 - 8.5 \cdot 10^{13}$	$5 \cdot 10^{12}$	$0.5 - 1.5 \cdot 10^{12}$
Peak brilliance*			$\approx 10^{28}$		$\approx 10^{27}$
Average brilliance*			$\approx 10^{20}$		$\approx 10^{19}$
* standard units:	<i>Number of photons (sec·mrad²·mm²·0.1 % BW). Mean values have been considered for the different cases.</i>				

2.4.2 SPARX Layout description

The SPARX X-FEL accelerator will be built in the Tor Vergata campus site, a few km south of the city of Rome. It will be disposed along a line, approximately 0.5 km long. The ground in this area has volcanic origin; it came from the eruption of the Colli Albani volcano more than 600000 years ago. A geological analysis of the territory has been carried out and it has proved that the ground is made of very stable rock.



Figure 2.3: The Tor Vergata Campus Site

The SPARX facility is housed in a complex of civil buildings, part of which is underground. The surface buildings have been reduced at minimum, in order to reduce the visual impact as required by the urbanistic constraints on the Tor Vergata area. The buildings are located at the beginning and the end of the LINAC (Figure 2.4).

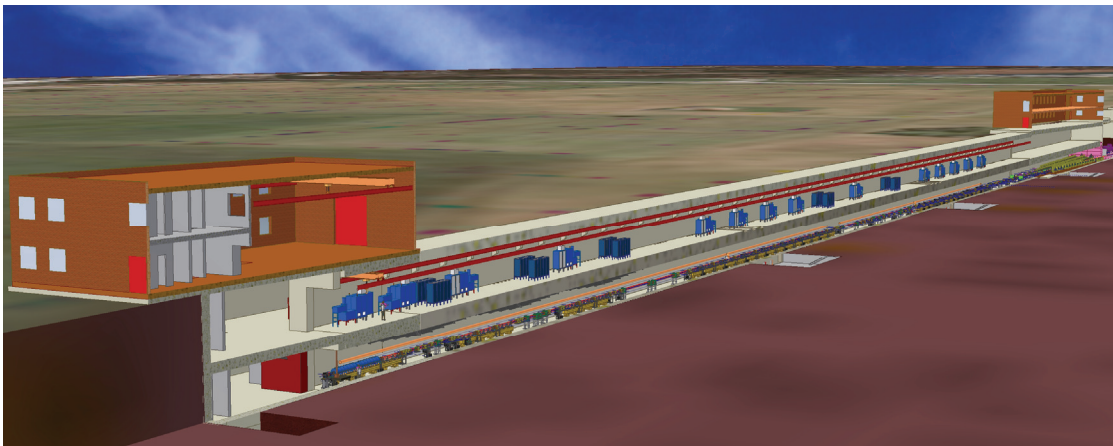


Figure 2.4: The SPARX surface buildings and the LINAC tunnel

The underground buildings consist of a service area at the beginning of the LINAC, two superimposed tunnels (with variable width) for the LINAC and the undulators, and a large experimental hall (measuring 60 x 30 m). Total length is about 400 m see (Figure 2.5 and Figure 2.6). LINAC and undulator halls will be divided in two overlapped tunnels. The lower tunnels will house the accelerator components, while the upper ones will house all the backing equipment such as modulators, klystrons and power supplies.

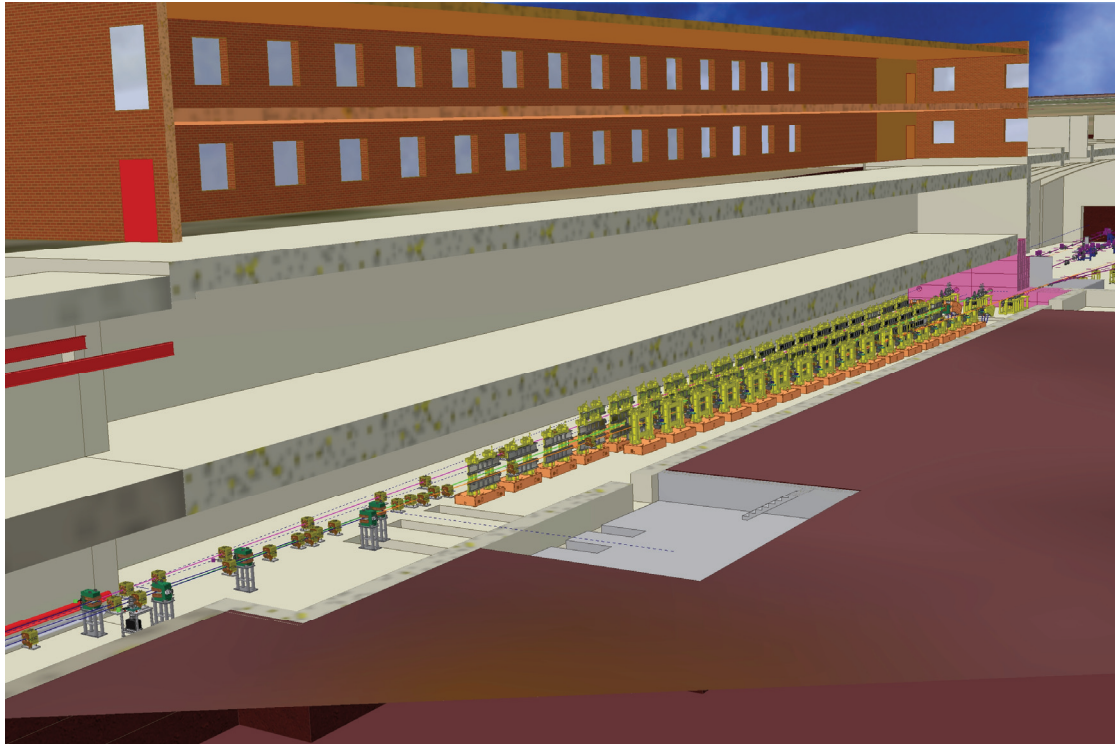


Figure 2.5: The Undulator Hall



Figure 2.6: The Experimental Hall

2.4.3 The Photo injector based on the SPARC experience

The SPARX photoinjector is based on the SPARC photo injector experience and is described in detail in the dedicated chapter 3 [1].

The maximum flexibility is required for the SPARX photoinjector in order to provide different beams for the FEL operation and to satisfy the needs of the FEL users. At this aim additional working points have been identified for SPARX spanning a range of charge between 50 pC and 1 nC. The SPARC installation is now completed including the undulator modules and first tests with the spontaneous radiation are currently under its way. Here we summarize the main parameters and the main results achieved with the SPARC injector at INFN laboratories at Frascati.

The layout of SPARC is shown in Figure 4.50: it consists of a 1.6 cell RF gun (BNL/SLAC/UCLA type) including a Copper photocathode with an emittance compensating solenoid followed by three 3-meters long SLAC-type travelling wave sections operating at 2856 MHz reaching electron energies up to 150 MeV. The first two accelerating sections are embedded in a solenoid in order to allow operation in the velocity bunching mode [2]; each solenoid is composed of 13 coils with the first coil and the other twelve coils in groups of three independently supplied.

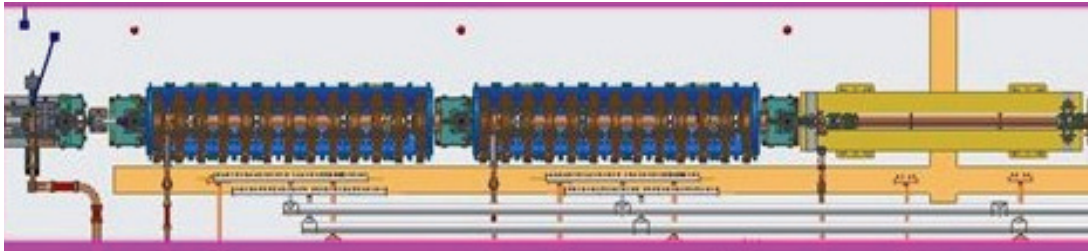


Figure 2.7: Photoinjector layout

The main operating parameters of the SPARC photoinjector are summarized in the following table.

Table 2.3: Main SPARC photoinjector parameters

<i>Parameter</i>	<i>Value</i>
Gun electric field amplitude	120 MV/m
Gun electric field operation phase	32°
Output gun beam energy	5.6 MeV
Amplitude of electric field in the traveling wave sections	23.5 MV/m
Magnetic field in the emittance compensating solenoid	2.72 kgauss
Total photoinjector length	12 m
Charge	1 nC
Bunch length	10 ps
Maximum electron Energy	150 MeV
Maximum current	100 A
Energy spread	0.1 %

Concerning the many scientific achievements during the commissioning phase of SPARC, we can emphasize the following:

1) Flat top laser pulse generation: It has been shown that uniform longitudinal charge distribution strongly reduces non linear space charge effects leading to a higher electron beam brightness. To this end, a dedicated R&D has been performed in order to achieve a 10 ps long UV-flat-top laser pulse illuminating the cathode with rise time shorter than 2 ps, as reported in

[3]. The following figure shows one of the best obtained results with pulse shaping.

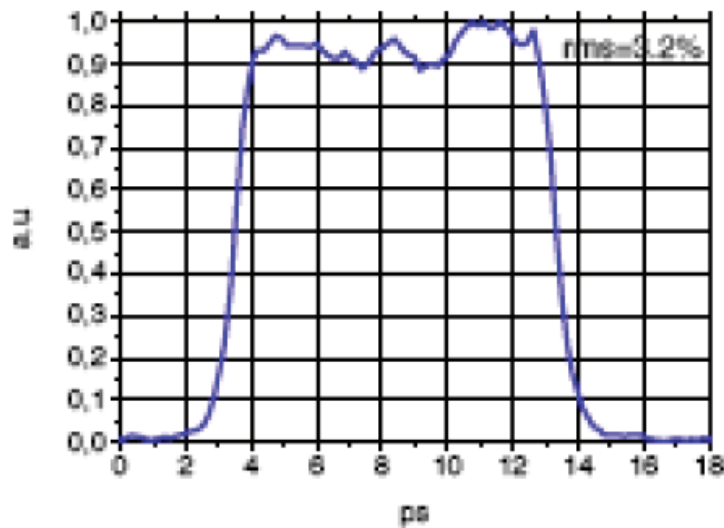


Figure 2.8: Flat top temporal laser pulse shape with 10 ps FWHM and 1.5 ps rise time, retrieved from the spectral measurement.

2) High brightness beam generation and beam dynamics studies. In the following figure are shown most relevant results obtained during the first commissioning run with the Emittance-meter device. Left is shown the emittance and envelope vs z for the highest measured brightness beam (7 1013 A/m²); In the center of the figure the emittance evolution comparison between a gaussian and a flat pulse with the same FWHM for a 740 pC beam; on the right figure the “Double minimum” [4] emittance oscillation: emittance and envelope vs z .

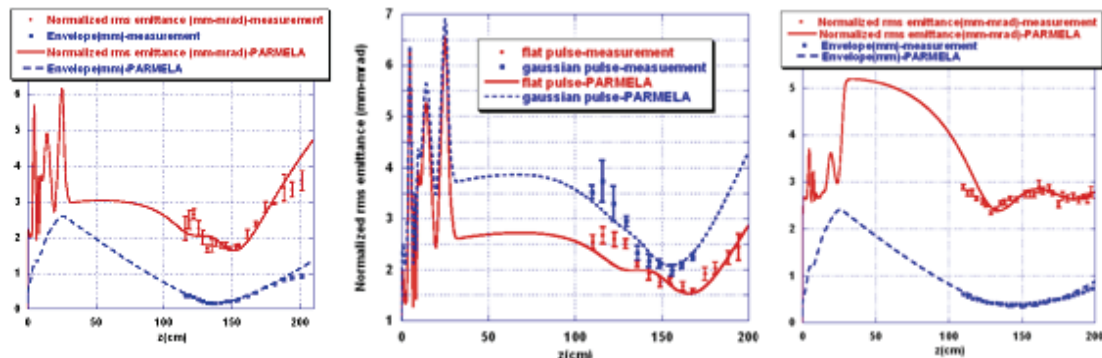


Figure 2.9: Emittance-meter measurements and simulation comparison.

3) The RF compression or “velocity bunching” technique [5].

Tests of beam longitudinal dynamics in the Velocity Bunching (VB) regime have been also performed. VB consists in compressing the beam by injecting it in the first RF structure with a phase near to the zero accelerating phase: the beam slips back up to the acceleration phase undergoing a quarter of synchrotron oscillation and is compressed. The emittance growth occurring during the compression can be taken under control by a proper shaping of the magnetic field of the focusing solenoids embedding the accelerating structures. The following figure shows the measured compression factor for a 250 pC beam vs the phase of the first travelling wave. The reduction of the bunch

length from 5 psec to 2.5 psec for a phase range variation of 20 degrees results to be in good agreement with PARMELA simulations. A more systematic study of velocity bunching is on progress.

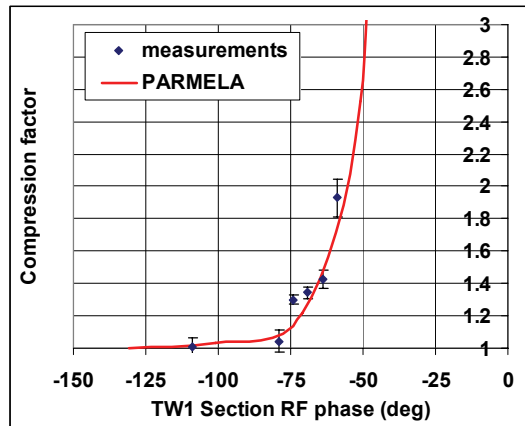


Figure 2.10: First test of velocity bunching: compression factor vs the phase of the first TW section. Comparison between measurements and simulations

Based on the matured experience of SPARC the SPARX photoinjector follows the same basic design and is shown in the following figure.

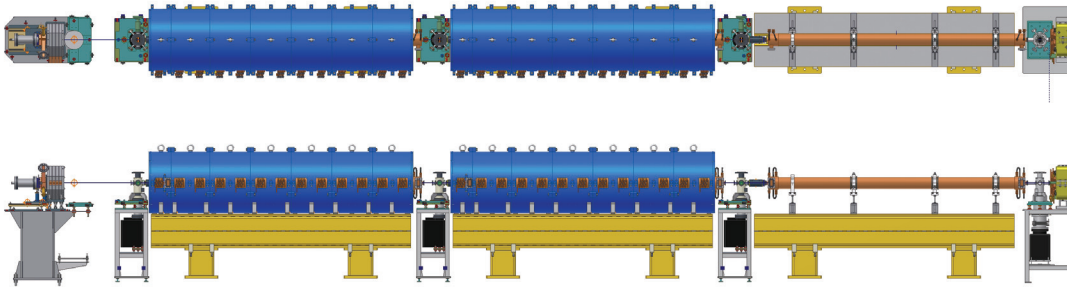


Figure 2.11: Top and side view of the SPARX Photo Injector (total length 12 m).

2.4.4 The low energy beam diagnostics

The 150 MeV beam is characterized by a dedicated diagnostics section, 11 m long that includes the laser heater chicane, the spectrometer for energy and energy spread measurements, emittance and slice emittance measurements and pulselength and longitudinal phase space measurements using an RD deflector. The complete description of the lines shown below are detailed in paragraph 5.4.4.

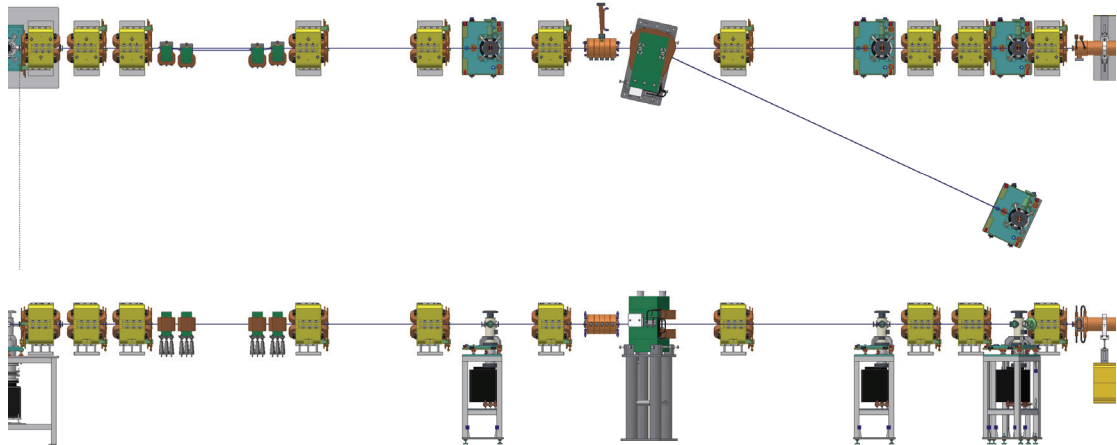


Figure 2.12: The 150 MeV Diagnostics Section (up: top view, bottom: side view)

2.4.5 LINACS, transfer lines and compressors

As shown in Figure 2.13, the 150 MeV beam from the photoinjector is boosted up to 1.5 GeV by three LINACS.

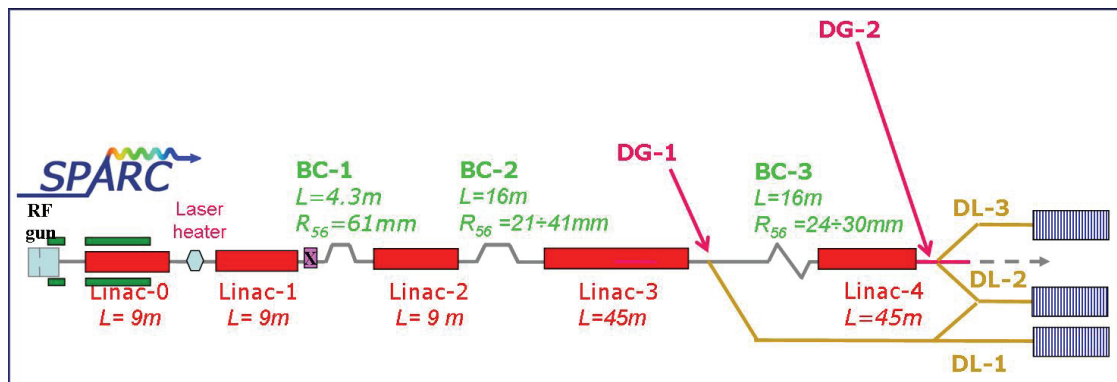


Figure 2.13: SPARX acceleration and compression schematic layout using SPARC injector.

The first LINAC is made of three accelerating structures (LINAC1) and is followed by the first bunch compressor (BC1). The second LINAC (LINAC2) is also made of three accelerating structures and is followed by the second bunch compressor BC2, as shown in Figure 2.14. and Figure 2.15. These two LINACs are 11 m long while the bunch compressors are 12 and 24 m long respectively.

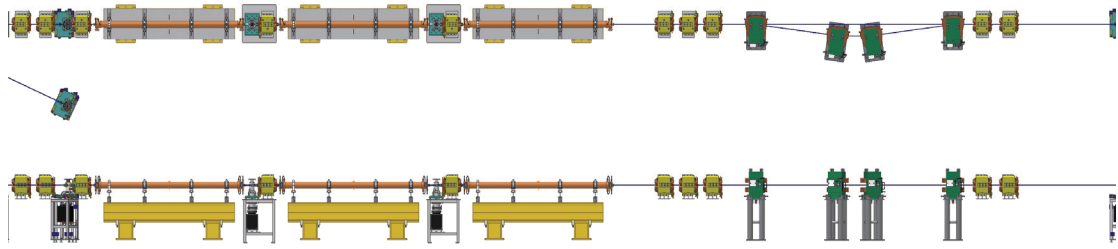


Figure 2.14: LINAC1 and BC1 (up: top view, bottom: side view). Total length: 23 m.

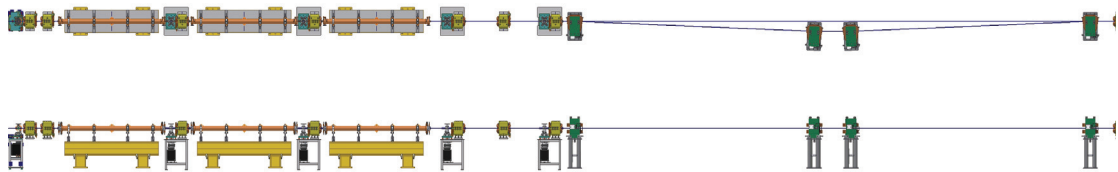


Figure 2.15: LINAC2 and BC2 (up: top view, bottom: side view). Total length: 35 m.

The third LINAC is made of 15 RF structures that accelerate the beam up to 1.5 GeV (Figure 2.16). The total length of this section is 55 m.

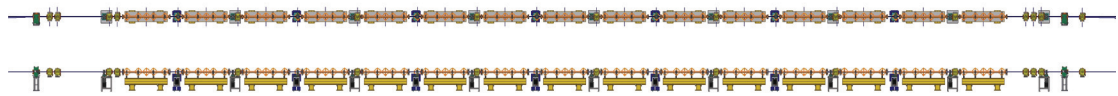


Figure 2.16: Top and side view of LINAC3 (up: top view, bottom: side view). Total length: 55 m.

Figure 2.17 shows details of vacuum pumps and quadrupoles placed in the drifts in between consecutive accelerating structures (quadrupoles are ~30 cm long, accelerating structures 3 m long).

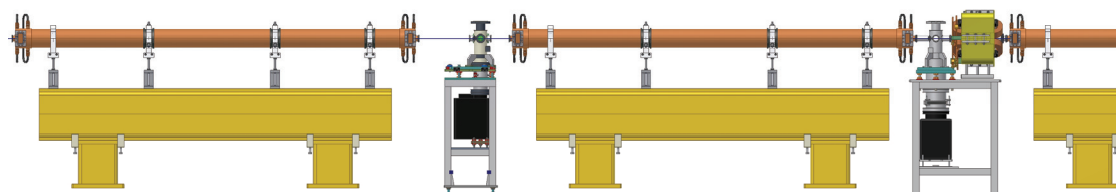


Figure 2.17: LINAC3 Module, detail.

The transfer lines and the third bunch compressor (BC3) downstream the LINAC3 are shown in the following figure; because of the small exit angle the magnetic elements are longitudinally shifted to avoid installation interference. In this section will also host diagnostics devices to measure the electron bunches at 1.5 GeV.

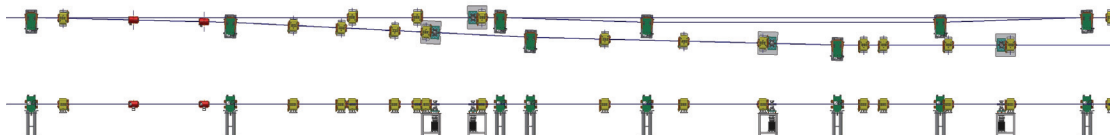


Figure 2.18: TL1 Transfer Line and BC3: total length is 47 m.

The final LINAC (LINAC4), 52 m long, is composed by 15 RF structures, that can accelerate the beam up to 2.64 GeV (Figure 2.19), before being sent into the undulators.



Figure 2.19: LINAC4 (up: top view, bottom: side view). Total length: 52 m

In LINAC4 the quadrupoles are foreseen every three accelerating structures, as shown in (Figure 2.20), therefore the total length is shorter than in LINAC3.

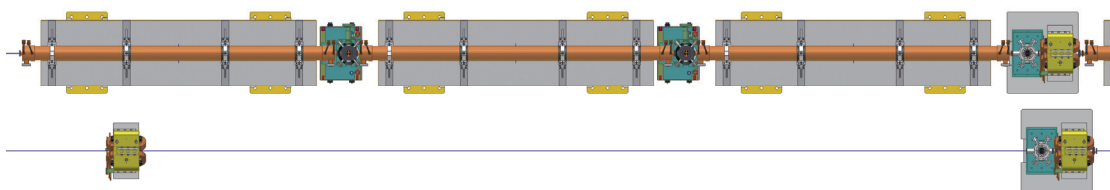


Figure 2.20: Accelerating sections of LINAC4 Module, detail (accelerating sections are 3 m long).

The transfer line designed to sent the beam from the LINAC to the different undulators are shown in the following figure. Because of the small deflecting angles, a special lattice has been designed avoiding conflicts between magnetic elements and electron beam vacuum chambers.

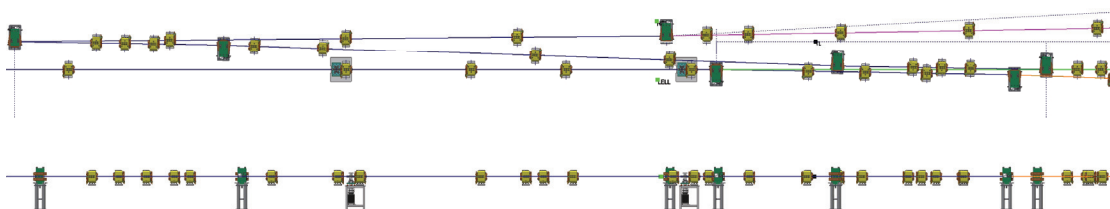


Figure 2.21: Beam distribution transfer lines: total length 45 m.

2.4.6 Undulator lines

Three undulators are foreseen to cover the photon spectral range of the project (see parameter list in dedicated section), the low energy one at 1.5 GeV on the right side following the beam direction (i.e. the undulator that are on the lower part of the Figure 2.22), the high energy one left side following the beam

direction (i.e. the upper side of the figure). The central one is multi-stage undulators in which both low and high energy electron beams can be sent. The three undulator are, from the left to right, about 44 m, 55m and 45 m respectively. Each undulator stadium is long 2.2 m, each gap in between about 60 cm.

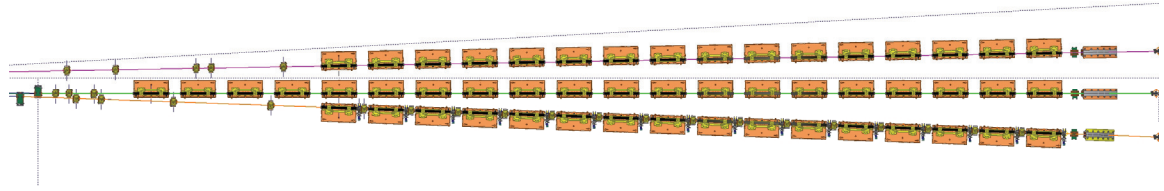


Figure 2.22: Undulators (top view, the electron beam is coming from the left side).

The following picture shows in detail undulators with quadrupole and diagnostics inserted

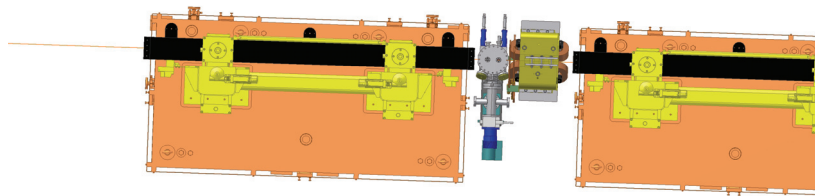


Figure 2.23: Undulator section detail

At the very end of the undulators sections the bending magnets necessary to send the electron beam to the dump are shown together with the photon beam lines front end (see Figure 2.24).

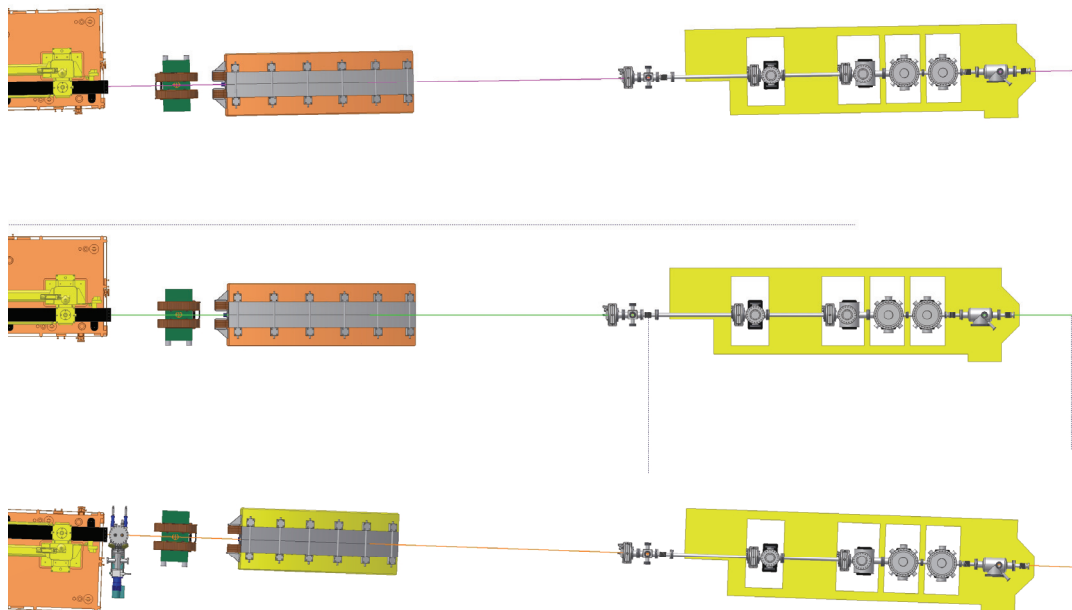


Figure 2.24: Dumping magnets and photon lines front-end.

2.4.7 Photon beamlines

The SASE and Seeded FEL photons produced in the undulators propagate in beam lines with suitable optical components. The optical line configurations allows the simultaneous use of different experimental stations (see Figure 2.25)

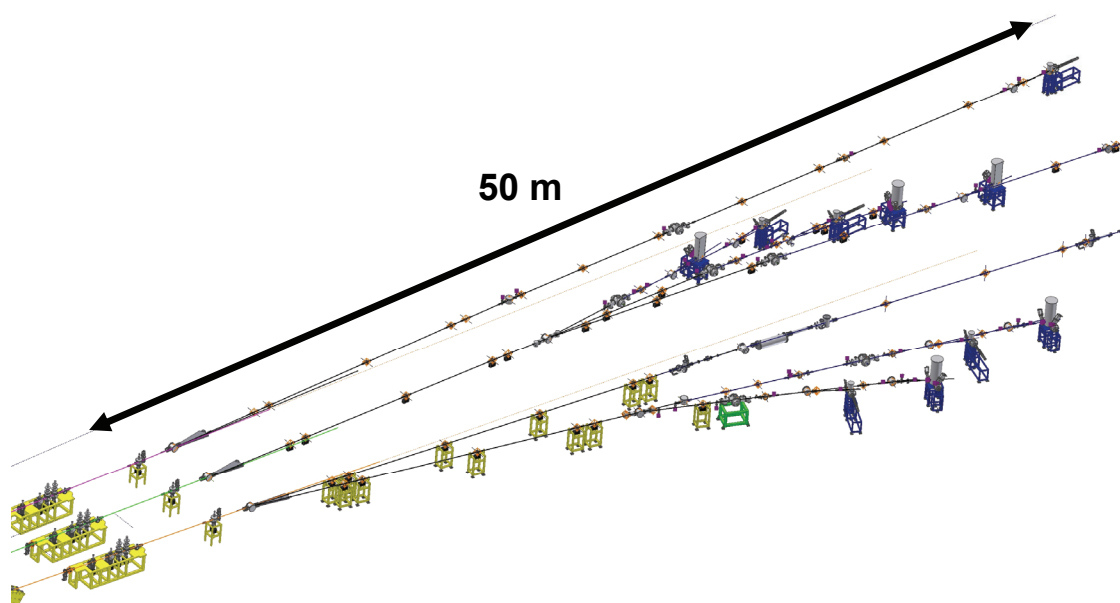


Figure 2.25: Optical beam lines and experimental stations

2.4.8 Beam distribution system

The SASE-FEL operating at SPARX facility will produce photon beams whose first harmonic energy spans from 40 eV to 2000 eV with narrow bandwidth and very short time pulses (femtoseconds regime). The use of higher harmonics (third mainly) will allow to extend the energy interval up to 6 keV. Three undulators will be employed to produce the SASE-FEL radiation: U1 that uses the 1.5 GeV electron beam from LINAC; U3 that uses the 2.4 GeV electron beam; U2 that is designed to operate with both the beams.

The very high peak energy of the photon beam together with the extremely short pulse length can cause ablation of the optical elements, then the beamline design requires modifications respect to the usual SR beamlines as well as the choice of proper materials for optical coating and bulk. Such considerations suggest the use of grazing incidence angles on optical surfaces, to avoid strong focusing of the FEL radiation onto optical elements (slits included), and the use of surface materials with as low as possible ionization cross section. In spite of the extremely high peak power generated by the FEL, the average thermal load results much smaller than what expected in typical SR beamlines (100-1000 W, according to the photon source), making conventional side cooling sufficient to remove the average heat load from optical elements.

The principal characteristics of the FEL radiation is its very short pulsed structure that should be preserved as much as possible passing through the beamline. The mutual dependence of pulse length and energy bandwidth

through the Fourier transform limit relation $\Delta T \Delta E \geq h/4\pi$ determines the limit of the pulse shortness when high resolution is demanding. Furthermore, optical elements as mirrors and gratings may introduce photon path differences that increase the pulse time duration. The contribution of mirrors to the optical path difference is negligible being in the attoseconds domain, while gratings, due to the asymmetry between the incident and the diffracted beams, stretch the pulse up to hundreds of picoseconds [6]. The time expansions due to gratings can be compensated adopting a suitable mirror symmetry for the dispersive elements of the beamline that implies the use of two opposed, identical monochromators with a shared slit. This implies, besides a sensible increase of costs mostly due to the more stringent requests for mechanical tolerances, severe limitations to the photon flux.

These considerations impose the beamlines designer to choose, between high energy resolution and short pulse time duration taking in mind that, in many cases, a compromise may represent the best choice.

In order to maximize the flexibility of the experimental activities the SPARX project foresees for at least two photon-transport beamlines for each undulator. One of the two beamlines acts as a filter with a resolution ΔE wider than the intrinsic bandwidth of the FEL; it serves to eliminate the higher harmonics contribution maintaining practically unchanged the pulse duration and working with resolving power $E/\Delta E$ $1000 \div 2000$. The other beamline is equipped with a more performing monochromator that can reach resolving powers of 10^4 at expenses of the time pulse duration that anyway remains within the fractions of a picosecond. These two types of beamlines have been designed and optimized for the energy ranges of the three FELs: U1: 40 - 120 eV; U2: 100 - 1000 eV; U3: 1000 - 2000 eV. Only one beamline at a time will be used at each FEL, and switching between them is accomplished by means of moveable mirrors. After the exit slit of the generic beamline monochromator the photon beam is focused onto the sample in the experimental equipment. In order to satisfy opposite requests on power density at the sample, two conditions with different focal characteristics (microfocus and $\sim 1 \times 1$ magnification) have been considered.

Each couple of beamlines shares the front-end, the spectrometer and the gas attenuator filter.

The front-end houses the variable aperture diaphragm that can be considered the first optical element of the beamline. It defines the origin and the angular apertures of the photon beam; it also stops most of the spontaneous SR emission. In order to avoid the high peak power to cause ablation, the light must impinge grazing onto the surfaces of the four independent cooled blades forming the diaphragm.

The spectrometer is a multi-function optical element that mainly serves for electron beam diagnostic and for photon beam characterizations operating a non-destructive analysis of the FEL spectrum. It consists of a plane mirror with a small grating ruled at the centre. The grating groove density is made variable to allow the foci at different wavelengths to lie all on a line [7]. This feature allows to acquire the entire spectrum imaged on a fluorescent screen as a single camera frame. Away from the diffracted beam the rest of the photons (more than 98%) is purely deflected by the plane mirror by few degrees. Such reflection serves to put the photons far away the undulator line that contains the extremely dangerous bremsstrahlung emission. The entire spectrometer can be removed from the undulator axes so that the light has the possibility of travelling without any reflection along a third beamline in order to take advantage of the entire spectrum of the spontaneous emission that extends up

to tens of KeV. Such an emission, in spite of the lower brightness respect to the FEL lines, produces a high integrated flux of photons with a short pulsed time structure and should make feasible many experiments of time resolved X-Rays scattering in “white light”.

The gas attenuator is a long pipe (10-20m) equipped, at the two ends, with differential pumping stage. It allows to control the intensity of FEL pulses and the high harmonic content of the “white” FEL photon beam, when working without the monochromator spectral selection.

A deeper description of the beamlines design is reported in chapter 7.

2.4.9 The THz beamline

There are also plans to build a fully separate beamline collecting the Coherent Synchrotron Radiation (CSR) emitted by the bending magnet which deflects the electron beam toward the beam dump at the end of the SPARX electron beam lines after having passed the undulators. This setting will not affect the normal operation of SPARX. Indeed, the coherence in the THz range is essentially ensured by the electron bunches being short enough (bunch length smaller than 1 ps).

CSR [8,9] will be collected by a mirror placed in the bending magnet chamber, looking upwards, under broad acceptance angles (100 - 150 mrad, due to the wide emission cone at millimeter wavelengths) and will present the standard polarization properties of synchrotron radiation: linear in the orbit plane and elliptical (or circular) out of the plane.

The large emission angles in the THz region may imply diffraction effects. Moreover, the THz pulse time structure can be degraded by multiple reflections along the line. Therefore this should be as short as possible. A suitable location for the THz laboratory would be the large experimental hall located above the undulators. In this location, the THz laboratory may also host a self-standing compact THz laser built at the ENEA laboratories in Frascati [10, 11, 12].

2.5 International Scenario

Synchrotron radiation is a powerful research tool in a large variety of scientific and technological fields from spectroscopy to material science, from biology to biomedicine. From the first pioneering activities, which used the light generated in bending magnets of synchrotrons devoted to elementary particles research, in about three decades the field had a dramatic development, evolving through three generations of synchrotron radiation sources. In spite of the excellent performance of the existing sources, there is an increasing demand of more advanced radiation characteristics in the X-ray spectral region (approximately between 10 nm and 1 Å) in terms of peak and average brilliance, transverse and longitudinal coherence, and time structure, aiming at pulse durations well below a picosecond:

- The achievement of higher brilliance will allow an increase in spatial resolution without losing spectral resolution, as well as the use of single-shot techniques in order not to damage samples, which might be quite sensible to the radiation. This will eventually make nano-imaging experiments possible;

Coherence, at least transverse, will be of crucial importance in the development of diffraction and interference techniques and will enrich the signal content by adding phase information to the images;

Ultrashort radiation pulses, on the order of 100 fs, will allow real time measurements which, together with the high peak and average brilliance, will make possible to make measurements in a way faster than any radiation damage process and, eventually, to investigate the damage dynamics itself.

FELs driven by LINAC electron beams in SASE configuration are foreseen to meet the challenging requests for the new generation synchrotron radiation sources (4th generation). The peak brilliance will exceed of about 10 orders of magnitude that produced by the undulators of the 3rd generation sources, while the average one will be larger by a factor $10^3 - 10^4$. In addition the pulse duration could be quite short (of the order of 100 fs) with respect to what is currently attainable with storage ring based radiation source (several ps).

In Figure 2.26 we have reported the evolution during a time span of about one hundred years of X-ray sources. It is evident that the performance offered by FEL high gain sources could exceed in brightness the third generation sources of coherent radiation by ten orders of magnitude or more.

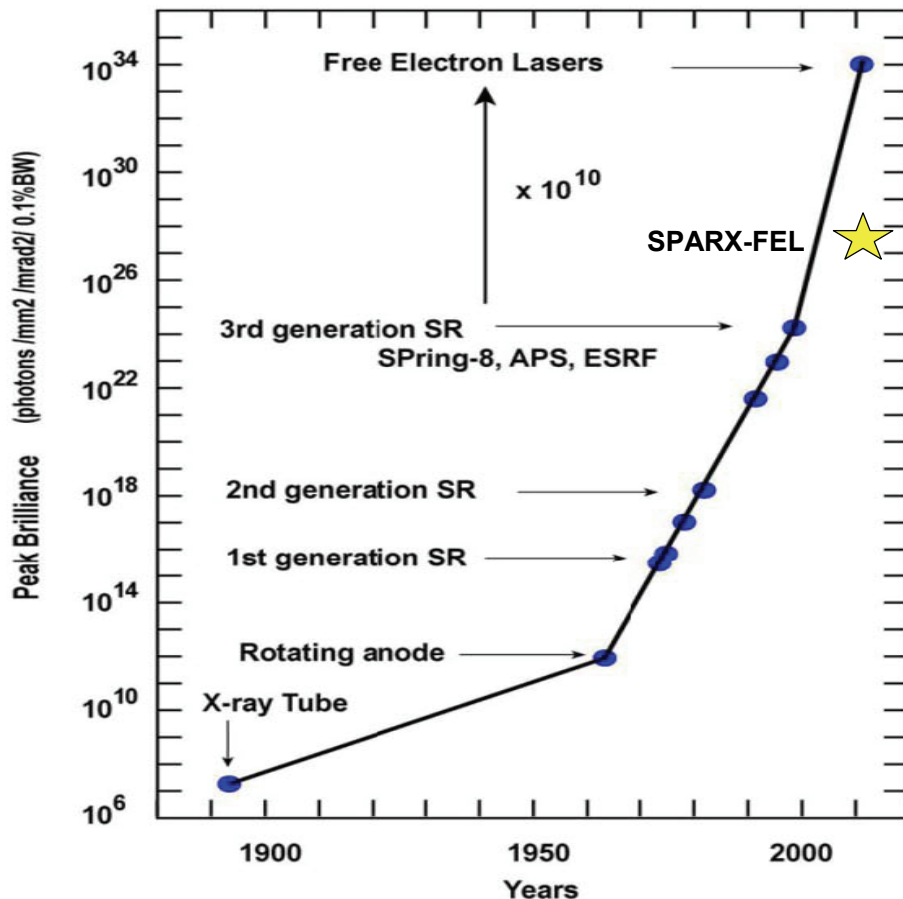


Figure 2.26: Chart of X-Ray source rightness through the years

The perspective of realising FELs with a performance ten order of magnitudes better than the current state of the art is due to the fact that the FEL amplification process guarantees a gain in the emission of photons of eight order of magnitudes, with respect to the spontaneous emission in Wiggler magnets, as it is the case in synchrotron radiation sources operating with Storage Rings. Furthermore the emitting source (namely the electron beam) in a LINAC can be made smaller by a factor 100 with respect the case of a storage ring beam. This aspect of the problem will be treated in more technical details later in this TDR.

The challenge related to the realization of very high brilliance short pulse VUV – X sources is considerable. The cost of this kind of R&D activity is close to that of the so-called “Big Science”. This means that it is not conceivable that just a single laboratory, whatever big it is, can invest in this field the required large amount of money and man power. For this reason the need of a coordinated effort was clear from the very beginning of this research activity. From the analysis of what has been done up to now it is possible to recognise a posteriori a kind of road map in which we can single out the directions along which the past R&D work is gone. In this moment many laboratories are working in a new phase in which a credible road map toward VUV – X spectral region has to be designed. Milestones of this road map must be those of all the laboratories involved in, in order to share at the best the experience and the obtained results. We believe that, in a quite natural way, due to the formal and informal collaborations and mutual interactions within the FEL community, this common road map appears now quite well outlined. In order to summarize what has been done up to now and what are the following steps, the operating photon energy in eV of the main SASE-FEL devices around the world versus the year of start of operation (or expected starting year) have been reported in Figure 2.27. It is worth underlying that FLASH (D) was operated at 13 nm in July 2006 and that the SCSS prototype in Japan (J) firstly generated FEL pulses at 49 nm on 20 June 2006.

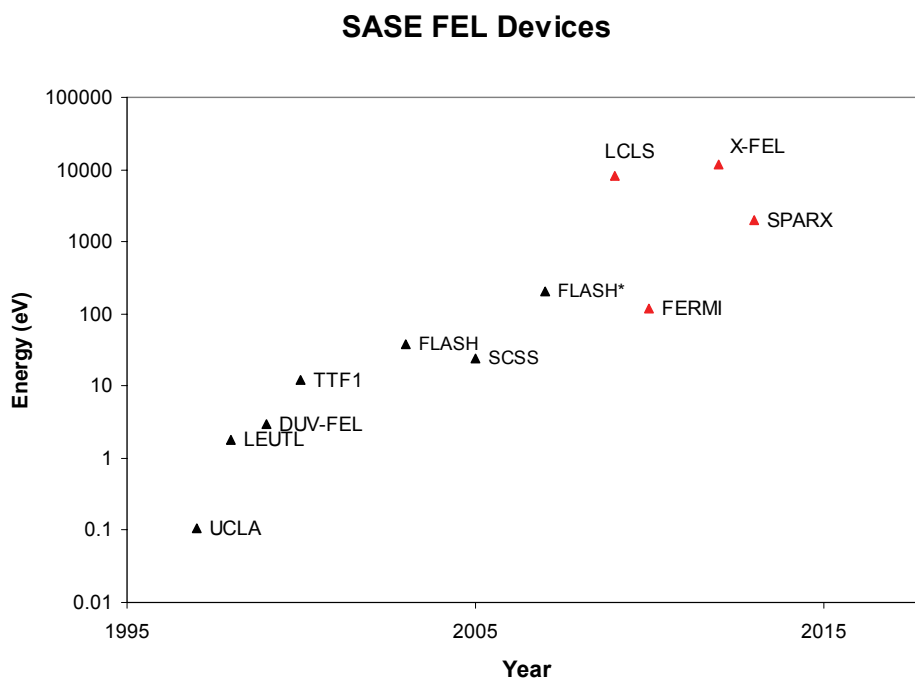


Figure 2.27: SASE FEL photon energy vs. operation year.

Furthermore In Figure 2.28 we have reported the existing or planned sources along with their brightness (achieved or expected) and photon energy, while in Figure 2.24 we have provided the brightness vs. the r. m. s. time duration.

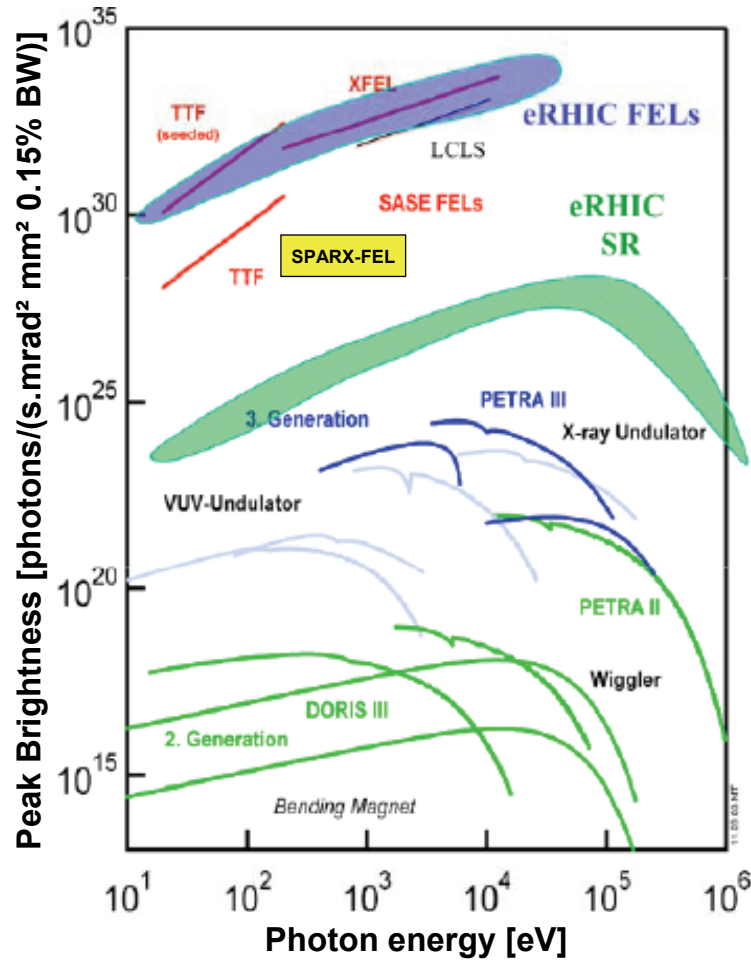


Figure 2.28: SASE FEL Peak Brightness vs. photon energy (in eV). Figures extracted [13].

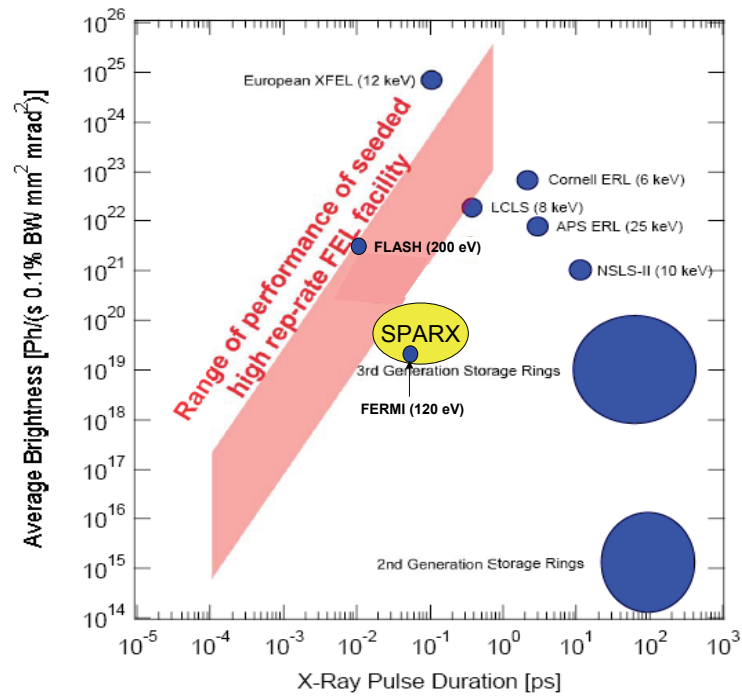


Figure 2.29: Brightness vs. pulse duration

Two strategies for the realization of X-FELs have been developed. The first, aiming at realizing large scale facilities, is going to benefit from the heritage of the big science, dominated for many years by elementary particle Physics. The scientific institutions interpreting this role are listed in Table 2.4 along with the foreseen performances of the X-FEL sources.

Table 2.4: Large scale X-FEL projects (private communications and web sites)

	<i>LCLS</i>	<i>X-FEL</i>	<i>SCSS</i>
Pulse duration	<230 fs	100 fs	80 fs
Wavelength	1.5 Å	1-15 Å	1-50 Å (49 nm, June 2006 result)
Repetition Rate	120 Hz	10 Hz	60 Hz
e.bunches/pulse	1	3000	1
e.b. energy	14.3 GeV	20 GeV	8 GeV
Photons/pulse at 1 Å	1.1 10 ¹²	1.2 10 ¹³	0.8 10 ¹³
LINAC length	10 ³ m	2 10 ³ m	350 m
Estimated start date	2009	2012	2010

For laboratories of “smaller dimensions” the strategy is focused on the development of “smart” solutions based on exotic undulators, seeding, hybrid devices (oscillator-amplifier). The scenario of small-medium size device under

development or proposed, which exploit this kind of “smart technologies” is reported in Table 2.5. In particular it must be stressed that a significant effort has been done towards the realization of mirrors for laser resonators, capable of confining short wavelength radiation in the region below 170 nm. In the next future it will be possible to have optical resonators confining radiation in the range of 150 nm or less. The use of the mechanism of intra-cavity non linear coherent harmonic generation can therefore be exploited to produce a significant amount of coherent radiation in the region of 10 nm without the problems associated with SASE devices. The combined use of intra-cavity harmonic generation and of micro-undulators may provide compact tools reaching short wavelengths with very modest e-beam energies.

Table 2.5: National scale UV to soft-X FEL projects (private communications and web sites)

	<i>SPARX (I)</i>	<i>FERMI FEL-2 (I)</i>	<i>STARS (D)</i>	<i>NLS (UK)</i>	<i>Arc en Ciel seed @ 19nm (F)</i>
Pulse duration [fs]	130	1400	20		200
Wavelength [nm]	40-0.6	10-40	1.24-51		1.2-2.1-6.3
e.b. energy [GeV]	1.5-2.4	1.2	2.3		1
Estimated start date	2013	2009	R&D proposal	R&D proposal	R&D proposal

2.6 Science and technology with SPARX-FEL

2.6.1 Overview

The X-rays are used at present in a wide range of fields, from the fundamental and applied research, to the radiological diagnostic and to the analysis of industrial products. The SPARX source will take most current applications at new excellence levels and towards new directions. The disciplines involved will be numerous and of very different kinds. Novel methodologies based on X-rays imaging and on time-resolved studies in material science, in biology and in medicine will be developed. Many applications of non-linear optics will be extended to new spectral ranges and new directions in the x-rays microscopy will be explored as well as new

methodologies in the field of protein crystallography and of genomics, which is growing very quickly.

The SPARX source will furthermore allow sending a huge energy concentration on small areas of condensed systems. This will make it possible the discovery of new phenomena, which cannot be forecast through a simple extrapolation of what already known. In particular, a series of results in the context of the photochemistry, which may have interesting industrial repercussions, can be expected.

The SPARX source will produce X-rays with absolutely unprecedented characteristics, among which three are particularly important: the space coherence of the radiation; its peak brilliance, about 10^{28} (in conventional units, c. u., that is photons/s/mrad²/mm², 0.1% band width); the duration of each pulse, about 100 femtoseconds. In the final project, possible experimental techniques to obtain even shorter pulses, i.e. few femtoseconds long, will be studied.

Concerning the spectral range, SPARX will be realized in two phases: the first one foresees the emission of radiation with wavelength between 30.0 nm and 4.0 nm; the second phase foresees the emission down to 0.6 nm. The use of higher harmonics (third and fifth) will allow a wide tunability of the energy between 30.0 nm and 0,12 nm.

The parameters of the SPARX source, presented in detail in the next sections, are obviously susceptible of revisions in the advanced phase of the project in order to meet the requirements of new users and new disciplines (together with possible technological improvements). The use of the ultra-short and ultra-brilliant pulses, in the energy interval mentioned above, will find a huge variety of advanced applications in a wide range of scientific and technological disciplines.

Clearly, it is impossible at the moment, even briefly, to evaluate all the possible applications of the new source. Furthermore, three decades of research experience in the synchrotron radiation field teaches that the actual applications of a new X-rays source are much wider than those foreseen.

Here after some techniques of investigation are briefly illustrated together with the most significative experiments to be performed.

2.6.2 Time resolved X-ray diffraction

In the last two decades, a good deal of work have been devoted to the real time evolution of the systems on the time scale of elementary processes. Time resolved chemical reactions [14], molecular motions [15], phase transitions [16], propagation of excitations [17] have been approached in a radically different way from the past.

The development of pulsed laser technology allowed to address the necessary time resolution and a new category of experiments, referred to as femtochemistry, provided a new insight to the world of microscopic transformations [18]. A general description of the method can be given in terms of a disturbance of the sample by a suitable stimulation (pump) and the subsequent detection of the produced effect by means of a probe. The pump disposes the system in a certain initial condition (zero-time reference) and the probe "reads" the configuration the system has assumed after τ . Executing a τ -scan, the time evolution of the sample is obtained. A diffraction-based pump&probe technique would enable a direct connection between the time-resolved diffraction patterns sequence and the "instantaneous" arrangements of sample atoms.

The application to diffraction of the pump&probe technique is both of physical and of chemical interest. It can be utilized either when the measurement concerns the motion of the sample elements or when it is used to follow their transformation. An X-FEL pulse is, in many aspects, an ideal probe to freeze in a diffraction pattern frame the structure of a system previously pumped by a IR, visible, UV laser pulse or by another X-FEL pulse.

2.6.3 Coherent x-ray diffraction imaging (CXDI)

Coherent x-ray diffraction imaging is one of the most promising techniques to study the structure and behaviour of non-periodic single objects or non-periodic assembly of objects at the nanoscale, being able, in principle, to achieve wavelength-limited spatial resolution overcoming the limitations imposed by the optical elements aberrations. This is the reason why CXDI is one of the most appealing methodologies for FEL installations, and the object of a recent striking experiment at FLASH in Hamburg [19].

CXDI was first introduced by Sayre [20], and demonstrated for the first time by Miao et al. [21]. It is based on phase retrieval of the diffraction pattern through iterative algorithms, under suitable oversampling geometry. Chapman et al. [6] have demonstrated at FLASH that even with femtosecond pulses it is possible to record a diffraction pattern before the sample is destroyed by Coulomb explosion.

Important fields of applications of CXDI are material science and bio-medical. In the first case, nanomaterials, as isolated quantum dots or single magnetic particles, can be studied by CXDI exploiting the high brilliance of FEL. Dynamic studies can be carried out using its unique time structure. Even more exciting are the perspectives on studies of single biomolecules, viruses or protein complexes that cannot be crystallized.

2.6.4 Femtophysics: direct tests of quantum mechanics

Although the quantum mechanics is the physical theory that exhibits the best agreement with experimental results, the correctness of its description of the microscopic objects motion have not been directly tested so far. As an example, Pauling representation of resonance among different electronic structures was commonly considered to be a model to describe some chemical bonds and before pump&probe experiments no evidence had been found to affirm that it is the real behavior of bound electrons [22]. In the same way, in the harmonic potential approximation, a molecule in a pure vibrational eigenstate should not move and only when the molecule is sent in a superposition of various eigenstates a non-stationary wave- packet can be formed and an actual motion observed (see Figure 2.30). Indeed, an ensemble of molecules can be prepared in a coherent state (i.e. sharing the same wave-function) in which each molecule is simultaneously excited to the same mixed state [23].

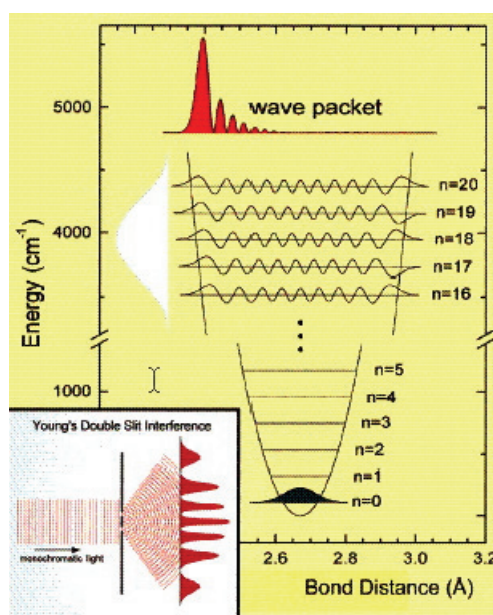


Figure 2.30: Scheme of the simultaneous excitation of several vibrational mode together with the resulting wave-packet. In the insert the analogy with classical optics is shown [22].

A X-FEL pulse has a sufficient intensity and time resolution to provide a diffraction pattern containing the Fourier transform of the instantaneous correlation of the intra-molecular atoms positions, i.e. of the bond lengths. The mechanism of re-distribution of the vibrational energy of a single excited mode to the other ones could be studied. It was found [24] that the re-distribution happens following the classic model of pendulums connected by soft springs. Femtosecond spectroscopy data confirmed that also this mechanism is real and that rotations or other spurious effects are not able to cancel out the phase coherence that enables the recursive energy transfer [25].

Femtosecond diffraction data would provide a picture of the complex molecular movement, decomposing it in a sequence of elementary steps. Also the coherent rotations could be captured with the same technique allowing the study of the inner (Coriolis forces) and external (collisions) perturbations, that finally produce the disappearance of the coherent effects [26].

2.6.5 Femtochemistry: Real-time study of chemical reactions.

The usual picture of chemists who represent the chemical transformations in terms of reagents that convert into products through a transition state (“activated complex”) had a clear confirmation [27]. The transition state, which can be identified neither with the original nor with the final compound, turned out to be a real state of matter and, in spite of its short life time, has to be considered as an independent compound. Also the way in which the energy is transferred from the reagents to the activated complex and, from it, to the products, (together with their characteristic time scales) was spectroscopically investigated by optical pump&probe techniques [28]. A useful application would be the study of laser-initiated time evolution of chemical

reactions. The simplest model of such a process is the bond breakage of a diatomic molecule [29]. A visible laser pulse can be used as a pump to excite a valence electron to an anti-bonding repulsive state.

The molecular wave-packet will follow the monotonically decreasing energy profile broadening and getting further and further from the origin, which corresponds to the progressive separation of the atoms. The separation could be monitored by X-FEL diffraction, showing if this description of the process is realistic or if it is complicated by the crossing of several potential energy surfaces (see *Figure 2.31*).

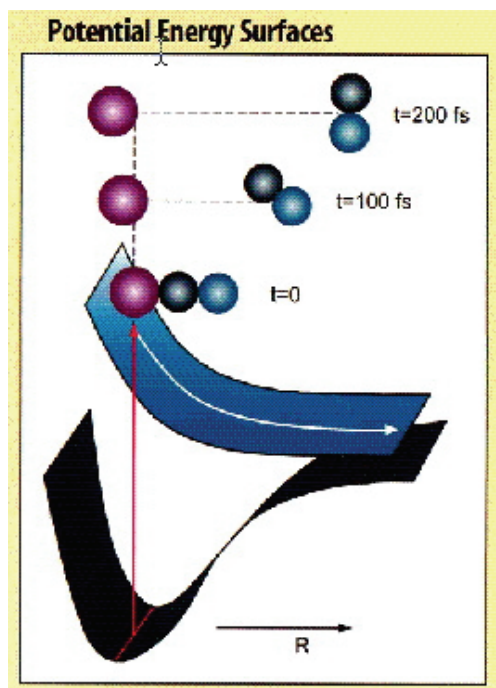


Figure 2.31: Sketch of a tri-atomic molecule photodissociation [27].

2.6.6 Spectromicroscopy

Photoemission techniques like electron spectroscopy for chemical analysis are the leading electronic probes in material science, but their impact in the life science has been minimal. A critical problem is that the lateral resolution in ordinary photoemission is limited to several tens of a micron, which is nearly useless for most of the fundamental problems in biophysics and biochemistry, which deal with microstructures in the submicron range or smaller. This limit has been overcome with synchrotron radiation spectromicroscopy on third-generation soft-x-ray synchrotron sources. Such technique is able to distinguish quantitatively the different physical and chemical behavior with a laterally resolved determination of chemical composition. In fact photon energies in the soft X-ray energy range can be used to study all the chemical elements that have core levels (K or L edges) in this energy range. with a lateral resolution better than 100 nm and a spectral resolution of 0.1 eV. As

examples we can refer to works on diamond, where it has been possible to distinguish quantitatively between carbon phases with different hybridizations in a laterally resolved determination of chemical composition experiment [30], works on dodecahydro-dodecarborate where it has been possible to make chemical mapping images and spectra identifying the chemical contrast between Boron and Silicon by digitally subtracting different images taken with different photon energies [31] and works on neuronal cells to detect specific positions of the cells where metals was clustering after uptaking. This again falls in the study of low dilute systems and the use of the enhanced intensity and brightness from the new XFEL source opens the possibility to put a lot of light into a small spot which, together with the improvement of today available electro-optical systems can reduce the spatial and spectral resolution of a factor 10.

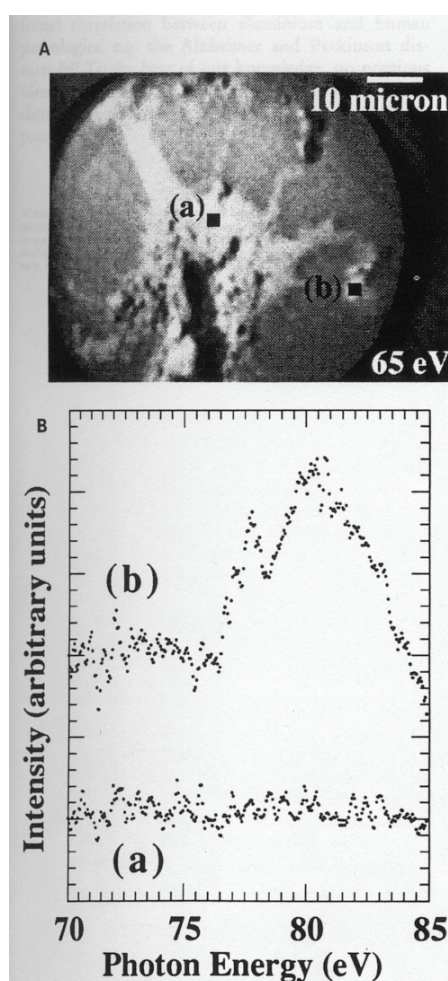


Figure 2.32: Microimage of neuronal cells doped with aluminum. The aluminum absorption spectra refer to different area of the cell. (ref. G. De Stasio et. al. Neuroreport 4, 1175 (1993)).

2.6.7 Investigations on weak scatterers

The extremely high brilliance of the X-FEL beam opens new research fields for all the systems that are not able to effectively scatter X photons. This may be due to either the scarceness of the scattering centers or to the low efficiency of each single scatterer, as in the case of low atomic number atoms. Interesting systems belong to this category and, as an example, the following can be mentioned:

2.6.7.1 Dilute solutions

Dilute solutions are interesting from the fundamental point of view since, as the dilution increases more and more, they tend to behave in the way described by Raoult and Henry simple models (similar to the Boltzmann hypothesis for molecular chaos), which have an enormous importance in analytic chemistry. However, to carry out a diffraction measurement on an extremely dilute solution, i.e. to observe the effect of the small quantity of solute ions in the overwhelming majority of solvent particles, a differential technique must be used. Assuming that the presence of the solute is a small perturbation on the original microscopic arrangement of the pure solvent, the minimal difference in the diffraction pattern of the pure solvent and of the solution should reveal the effect of the solute presence. The huge statistics required for doing this with a satisfying degree of accuracy can be attained by using the high brilliance on the X-FEL source.

2.6.8 Nanoparticles and Clusters.

Extremely small dimension crystals do not produce Bragg peaks when submitted to irradiation because of the finite size effect, of the random distribution of the grains orientation and of the high concentration of defect they often retain. The liquid-like diffraction patterns of such systems require a more sophisticated processing technique than the ordinary Rietveld refinement and a high intensity incident beam is necessary to gain a sufficient statistics on the diffraction signal.

Aggregates having linear dimensions up to 1000Å are referred to as nanocrystals. The interest in nanocrystals is due to their peculiar characteristics and to the role they play in the nucleation processes. Indeed on one side, remarkable catalytic properties connected to the high surface to volume ratio and quantum confinement effects similar to those present in artificial structures (quantum wells, wires and dots) may be observed in the smallest size aggregates. On the other side, the classical theory of crystallization from a saturated solution or from an undercooled macromolecular liquid describes the spontaneous birth and growth of crystalline domains in terms of random formation of small clusters. Only when a cluster exceeds a critical size it gets thermodynamically stable and may constitute the seed for the development of a macrocrystal. This phenomenological description does not include any detail of the cluster size fluctuations and of the dynamics of crystal formation, which could be provided by real-time X-FEL diffraction.

2.6.8.1 Hydrogen-based systems.

A very wide class of compounds both inorganic and organic are partially composed by hydrogen atoms. Among them, polymers and biological molecules play a fundamental role in many different fields of science. However, the structure of such systems could be studied by X-ray diffraction only partially and neutron diffraction have been preferred, despite the fluxes of neutrons, even those produced by nuclear reactors, are several orders of magnitude lower than that of a third generation synchrotron.

Indeed, in usual X-ray diffraction experiments, the hydrogen atoms are generally considered as invisible and their positions in molecules or in crystal lattices have to be obtained on the base of independent chemical knowledge. Indeed, having the neutral hydrogen atoms a single electron only, they are not able to effectively interact with an X-ray beam, because the X-ray intensity scattered elastically by an atom is proportional to the square of its atomic number. Even at low values of momentum transfer, light atoms scatter the radiation mainly inelastically (i. e. incoherently or Compton), so that the detected signal contains a very poor structural information, which is carried by elastically scattered radiation only. A substantial increase of the incident beam is required to improve the statistics in such a way that even the minimal coherent perturbation can be detected and extracted from the incoherent background.

2.6.9 X-ray holography

In analogy with the visible light holography, an X-ray holographic method has been successfully used to investigate the structure of simple crystals, like cobalt oxide (see *Figure 2.33* and *Figure 2.34* [32]).

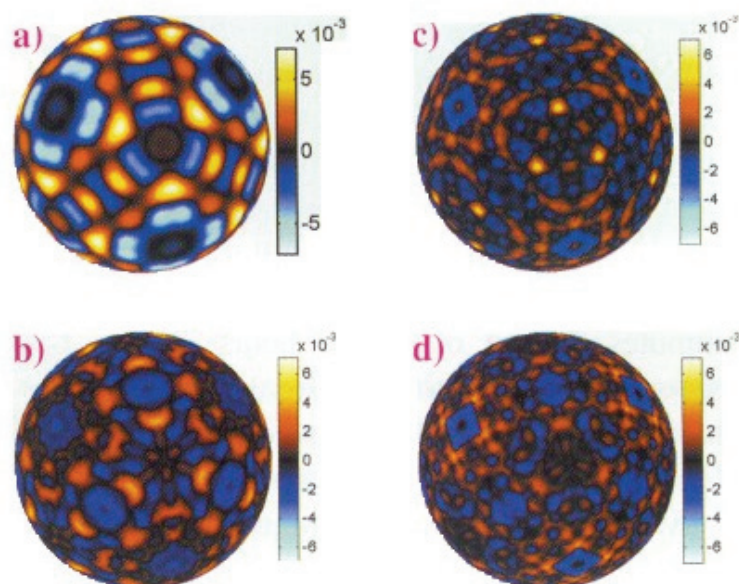


Figure 2.33: Holograms collected at various energies: 6.925, 13.861, 17.444, 18.915 keV. Four holograms were acquired in order to minimize the systematic errors [32].

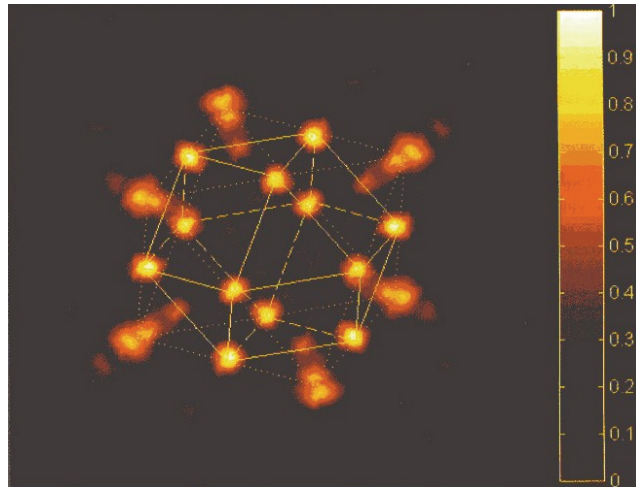


Figure 2.34: Spatial distribution of Co atoms calculated from the previous holograms [32].

To perform an X-ray holography measurement coherent X-ray beam is split and one of the two components is used to directly irradiate a detector, while the second is sent on the sample.. At present, the drawback of this revolutionary technique consists of the difficulty of selecting a portion of the beam inside which the coherent component is not negligible. Indeed, the spatial (transverse) coherence of an X-ray beam emitted by an undulator at a third generation synchrotron is rather low and, to perform experiments of this kind, pinholes diaphragm as small as 10 μm must be used. This reduces the beam intensity very much, enormously dilating the experiment duration, so that a single acquisition currently lasts many hours [33].

Thanks to the full transversal coherence of its higher harmonics, the use of X-FEL for this purpose is the natural solution to this restriction for systems having long bond (or interplanar) distances. Needless to say, to couple the X-ray holography with the pump&probe diffractometric techniques mentioned above would open the way to unprecedented structural studies of the matter.

2.6.10 Non diffractometric structural studies

2.6.10.1 X-ray reflectometry

From Snell law of classical optics, when a light beam passes through the interface between two media having different refractive index, it is deviated from its original direction. In particular, if the index of the second medium is lower, the beam will be totally reflected when the incidence angle is below a critical threshold (critical angle) [34]. In optics, the refraction index is an increasing function of the density, so that the total reflection may occur

passing from a more to a less dense medium (for instance from condensed matter to air). Snell rule still applies in the X-rays energy range. However, the relationship between density and refraction index is inverted, so that the total reflection is observable passing from a less to a more dense material (from air to a condensed matter). This fact consents to use the reflectometry as a tool for physical and material science studies because an X-ray beam impinging on a sample (either in air or under vacuum) can be totally reflected by it. Under total reflection conditions, a stationary wave, whose magnitude decreases exponentially with the depth from the surface, penetrates inside the sample. Since the penetration depth is a function of the incidence angle, a progressively thicker layer of the sample can be explored by scanning the incidence angle from zero (grazing geometry) to the critical value. As a consequence scattering measurements based on the total reflection effect can be executed on soft matter samples, like biological systems, dramatically reducing the irradiation damages.

2.6.10.2 Inelastic X-ray scattering

The inelastic X-ray scattering is usually referred to as Compton scattering. It consists of the energy transfer from the electromagnetic radiation to an atomic electron that, as a consequence, is expelled from the atom, i.e. the original atomic system is broken as a consequence of the interaction.

The possibility that the energy transfer may involve the atom as a whole (with no breaking) is not usually taken into account, since the atomic mass is so big that no significant recoil is expected when a photon is scattered by it. However this picture is an approximation because a small quantity of energy may be actually released to the atoms in the form of an increase of its kinetic energy (mainly of the nucleus) and, hence, the spectroscopy of scattered radiation may give information on the atomic motions [35]. From this viewpoint, information similar to that obtained by neutron spectroscopy can be achieved and the result of the inelastic X-ray scattering spectroscopy is the measurement of the dynamic structure factor $S(\omega, q)$ [36].

The difference is that neutrons are sensitive to the dynamics of atomic nuclei while X-ray to the dynamics of atomic electrons and that different zones of the (ω, q) space are scanned in the two cases.

The main problem of inelastic X-ray scattering is that the energy resolution must be extremely high, exactly because the radiation energy shift is very small. A monochromator in the quasi-backscattering configuration, corresponding to very weak high-order Bragg reflections, must be used for this purpose, which involves a considerable signal loss. The photon flux collected by the detector in such experiments is of the order of one photon per second. The high intensity and collimation of the X-FEL beam will reduce the acquisition times to reasonable duration and will allow the study of high atomic number systems, which was precluded till now by absorption problems. Investigations of interest are the study of the motion in HT_c superconductors electrons, which play a fundamental role in the physical properties of these materials; the dynamic of disordered and / or complex systems, like liquids, glasses, semi crystals (polymers), liquid crystals; elementary excitations that involve charge waves along the system.

2.6.11 Applications to inertial confined fusion (ICF) studies

It is well known that some of the most important diagnostics for the Inertial Confined Fusion rely on x-rays. Usually at least one laser beam is used as back lighter on high-Z target to produce an intense, point-like x-ray source (but incoherent and polychromatic) to perform plasma radiography of the fusion plasma, particularly of the high density region which is crucial to understand the compression dynamics and avoid detrimental instabilities. It is clear that a great deal of advantages can be obtained using, in place of such a source, a coherent x-ray pulse. Techniques as interferometry and holography could be designed and used in the ICF experiments. The feasibility of a soft-X-ray interferometer for plasma density measurements has been proven at Lawrence Livermore National Laboratory [37] using a laser pumped plasma X-ray laser.

However such kind of x-ray lasers have too low intensity and too low photon energy, so far, to be usable as diagnostic tool for the compressed core or fusion pellets. The SASE-FEL X-ray pulse would be a unique resource for such kind of ICF diagnostics.

Fast Ignition of fusion compressed fuel plasmas. One of the presently most promising schemes for ICF was introduced by Tabak et al in 1994 [38]. The basic idea is to avoid the very difficult and unstable volume ignition of the compressed pellet by injecting a localized energy pulse in the dense plasma. Due to the high density, x-rays are among the privileged options. The energy need calculated so far is higher than the one expected by the SASE-FEL single pulse, while the pulse length is the same. This can stimulate the design of specific fast ignition experiments to be scaled to the expected ICF condition.

2.6.12 Magnetic materials

The research on magnetism and magnetic materials has largely profited in the past decade from the development of new investigation methods based on the synchrotron radiation from third generation storage rings. Wide-spread applications of various types of spectroscopy, magnetometry, diffraction, scattering and microscopy techniques have been specifically designed to exploit magnetic dichroic phenomena induced by circularly and linearly polarized x-ray radiation [39-42]. The high brilliance and the time structure of the FEL pulses (with $1 \text{ nm} < \lambda < 100 \text{ nm}$) will lead to developments of these methods, capable of shedding light on the magnetic behavior of materials into yet unexplored microscopic and time domains

See also refs: 39, 40, 41, 42.

2.7 References

- [1] SPARC Project team, "Technical Design Report for the SPARC advanced Photoinjector", <http://www.lnf.infn.it/acceleratori/sparc> (2004)
- [2] L. Serafini and M. Ferrario, Velocity Bunching In Photo-injectors, AIP Conference Proceedings, 581, 87, (2001) also in LNF note LNF-00/036 (P)
- [3] A. Cianchi, Phys. Rev. ST Accel. Beams 11, 032801 (2008)
- [4] M. Ferrario et al., Phys. Rev. Letters 99, 234801 (2007)
- [5] L. Serafini et al., PAC01, Chicago, June 2001
- [6] Paolo Villorosi, Appl. Opt. 38, 28, (1999)
- [7] T. Kita et al, Appl. Opt. 22, 819 (1983)
- [8] A. Doria, R. Bartolini, J. Feinstein, G.P. Gallerano, R. H. Pantell IEEE J.Quantum Electron. QE-29, 1428-1436 (1993)
- [9] G.P. Williams, Rep. Prog. Phys. 69, 301 (2006).
- [10] G.P. Gallerano, A. Doria, E. Giovenale, A. Renieri Infrared Phys. and Tech. 40, 161-174 (1999)
- [11] A.Doria, G.P.Gallerano, E.Giovenale, G.Messina, I.Spassovsky Phys. Rev.Lett 93, 264801 (2004)
- [12] Scientific proposal for the extraction of Terahertz radiation from the SPARX FEL; P. Calvani, A. Nucara, S. Lupi, G. P. Gallerano, A. Doria, M. Ortolani; Contribution to the SPARX Scientific Case", in press
- [13] G.P. Gallerano and A. Renieri, Proceedings of SPIE - The International Society for Optical Engineering 6346 PART 1, art. no. 63461T (2007)
- [14] A. H. Zewail, J. Phys. Chem. (Centennial Issue) 100, 12701 (1996)
- [15] P. M. Felker and A. H. Zewail, Adv. Chem. Phys. 70, 265 (1988)
- [16] J. W.M. Frenken and J.F. van der Veen, Phys. Rev. Lett. 54, 134 (1985)
- [17] P. A. Rigg and Y. M. Gupta, Appl. Phys. Lett. 73, 1655 (1998)
- [18] A. H. Zewail, J. Phys. Chem. 97, 12427 (1993)
- [19] H.N. Chapman et al., Nature Phys., 2, 839 (2006)
- [20] D. Sayre, Acta Cryst., 5, 843 (1952)
- [21] J. Miao et al., Nature 400, 342 (1999)
- [22] A. H. Zewail, J. Phys. Chem. A, 104, 5660 (2000)
- [23] C. Wittig, Dynamics of ground state in molecular reactions, E.R. Bernstein Ed., Oxford, University Press, New York (1996)
- [24] W. R. Lambert et al., J. Chem. Phys., 81, 2209 (1984)
- [25] M Dantus et al., Nature, 343, 737 (1990)
- [26] M. Gruebele et al., J. Chem. Phys, 98, 883 (1993)
- [27] S. Pedersen et al., Science, 226, 1359 (1994)
- [28] S. De Feyter, Chem. Phys. Lett., 303 249 (1999)
- [29] T. S. Rose, J. Chem. Phys., 88, 6672 (1988)
- [30] Ch. Ziethen et al. J. El. Sp. Rel. Phen. 107, 261 (2000)
- [31] G. De Stasio et al. Rev. Sci. Instrum. 69, 2062 (1998)
- [32] M. Tegze and G. Faigel, *Nature*, 380, 49, (1996)
- [33] M. Belakhovsky et al., ESRF Newsletter, October 2000, p. 12
- [34] X.L. Zhou and S. H. Chen, Phys. Rep., 257, 223 (1995)
- [35] G. Gruebel et al., Proceedings of the 4th Generation Light Source Workshop, *Advanced Photon Source*, Argonne, (1997)
- [36] S. Dierker, *NLS Newsletter*, Brookhaven National Lab., (1995)
- [37] L. B. Da Silva et al., Phys Rev Lett. 74, 3991 (1995)
- [38] M. Tabak et al., Phys. Plasmas 1, 1626 (1994)

- [39] B.T. Thole, P. Carra, F. Sette, G. van der Laan, Phys. Rev. Lett. 68, 1943 (1992).
- [40] P. Carra, B.T. Thole, M. Altarelli, X. Wang, Phys. Rev. Lett. 70, 694 (1993).
- [41] F. Nolting, et al. Nature, 405, 767 (2000).
- [42] H. A. Dürr, G. Y. Guo, G. van der Laan, J. Lee, G. Lauhoff, J. A.C. Bland, Science 277, 213 (1997).

3 EXPERIENCE WITH SPARC TEST FACILITY

3.1 Origin of the SPARC Project

Driven by the large interest that 4th generation light sources, *i.e.* X-ray SASE FELs, have raised world-wide in the synchrotron light scientific community, as well as in the particle accelerator community, and following the solicitations arising from several Italian national research institutions, the Italian Government launched in 2001 a long-term initiative devoted to the realization in Italy of a coherent X-ray source in the next decade.

To pursue this program, the Italian Government published two calls for proposals, in March 2001, and in December 2001, staging the initiative in two steps: a 3 year R&D program with a budget of 11 M€, and a subsequent program for a X-ray coherent source planned to be built in the second phase with a budget of 96 M€. The budget is comprised of 70% from the Government and 30% from the proposing institutions.

In March 2002 the SPARC proposal, born from a collaboration among ENEA, INFN, CNR, Università di Roma “Tor Vergata”, Sincrotrone Trieste and three units of the INFN, and strategically oriented to explore both the feasibility of a ultra-brilliant photo-injector and to perform a SASE-FEL experiment at ~500 nm, was approved. The project was funded with 9.5 M€ budget, and the Government funding (70%) was delivered on January 2003, allowing the project to commence.

In 2004 the scientific program was enriched with a Seeding and Velocity Bunching experiments, ad new diagnostics devices, through the participation to EUROFEL, a Design Study Project funded by 7th Framework Programme of EC.

3.2 Goals of the SPARC Project

The overall SPARC project consists of four main lines of activity directed towards several goals; their common denominator is to explore the scientific and technological issues that give rise to the most crucial challenges on the way to the realization of a SASE-FEL based X-ray source. These are:

3.2.1 150 MeV Advanced Photo-Injector

Since the performances of X-ray SASE-FEL's are critically dependent on the peak brightness of the electron beam delivered at the undulator entrance, this activity was conceived with the purpose of investigating two main issues:

generation of a high brightness electron beam by means of an innovative scheme of space charge compensation, able to drive an FEL-SASE experiment at ~530 nm.

generation of a ultra high brightness, high peak current beams, via RF and/or magnetic compressors, suitable for future X-Ray sources.

Due to short schedule and limited budget, the task (1) was given the priority inside the MIUR proposal, and forms what we will refer to as SPARC Phase 1. Nevertheless, the latter task is of urgent importance for the development of ultra-brilliant electron beams. Therefore, although the SPARC injector group is concentrated on the tasks of Phase 1, some strategic activity will continue on the secondary tasks in description 2) in order to perform the necessary work that will enable Phase 2 of the SPARC project to continue with as little delay as possible beyond the successful completion of Phase 1.

3.2.2 SASE-FEL Visible-VUV Experiment

This component of the SPARC initiative foresees: a) performance of a SASE FEL experiment with the 150 MeV photo-injector-derived beam, using a segmented undulator with additional strong focusing, to observe FEL radiation at 530 nm and below; b) investigation of the problems related to matching the beam into an undulator and keeping it well aligned to the radiation beam, as well as the generation of non-linear coherent higher harmonics.

3.2.3 X-ray Optics/Monochromators

Radiation emitted from an X-ray FEL will provide photon beams to users that are unique in terms of peak brightness and pulse time duration (100 fs). Such beams pose severe challenges in implementing the optics necessary to guide and handle the intense radiation. This project will pursue also a vigorous R&D activity on the analysis of radiation-matter interactions in the spectral range typical of SASE X-ray FEL's (from 0.1 to 10 nm), as well as the design of new optics and monochromators compatible with these beams.

Schematic drawings displayed at the end of this report show the exact location inside the Frascati Laboratories, and the layout of the full system, photo-injector plus undulator, inside the SPARC hall.

3.3 SPARC Layout

The proposed system consists of: a 1.6 cell RF gun operated at S-band (2.856 GHz, of the BNL/UCLA/SLAC type) and high peak field on the cathode (≥ 120 MV/m) with incorporated metallic photo-cathode (Copper or Mg), generating a ≥ 5.6 MeV beam which is properly focused and matched into 3 accelerating sections of the SLAC type (S-band, travelling wave) which accelerate the bunch up to 150-200 MeV. The layout of SPARC showing Phase 1 is displayed in Figure 3.1.

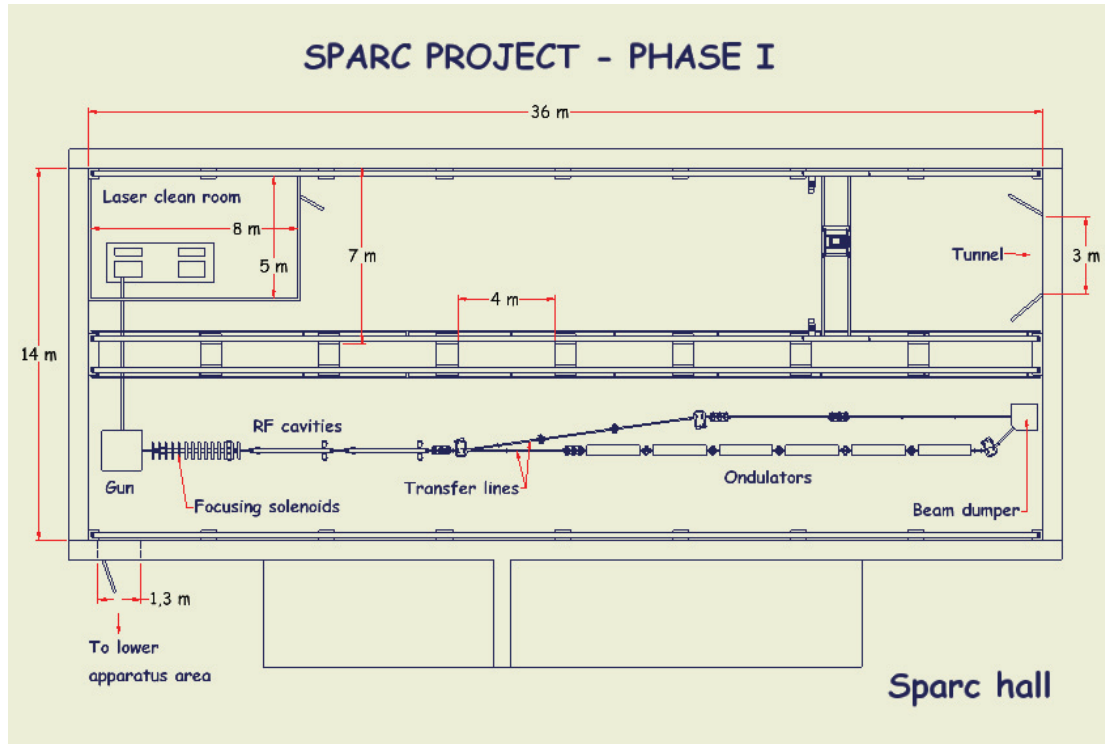


Figure 3.1: Schematic of layout of the SPARC photo-injector complex inside the SPARC experimental hall, including undulator, and by-pass line (Phase 1).

The choice of the S-band LINAC with respect to a L-band is due to compactness of the system, the lower cost, and the existence at LNF of a 800 MeV LINAC based on the same technology, with obvious advantages on the side of the expertise and spares components. Moreover, the higher RF frequency leads to a higher brightness attainable by an optimized photo-injector.

The production of highest brightness electron beams in the photo-injector requires that a temporally-flat, picosecond laser source be used to drive the photo-cathode. The laser system driving the photocathode employs high bandwidth Ti:Sa technologies with the oscillator pulse train locked to the RF (Figure 3.2). The Ti:Sa mode locked oscillator and amplifiers able to produce the requested energy per pulse (500 μJ at 266 nm) have been commercially available. To obtain the desired time pulse shape we tested the manipulation of frequency lines in the large bandwidth of Ti:Sa, in order to produce the 10 ps long flat-top shape. Used a liquid crystal mask in the Fourier plane of the non-dispersive optic arrangement or a collinear acousto-optic modulator for linear frequency manipulation.

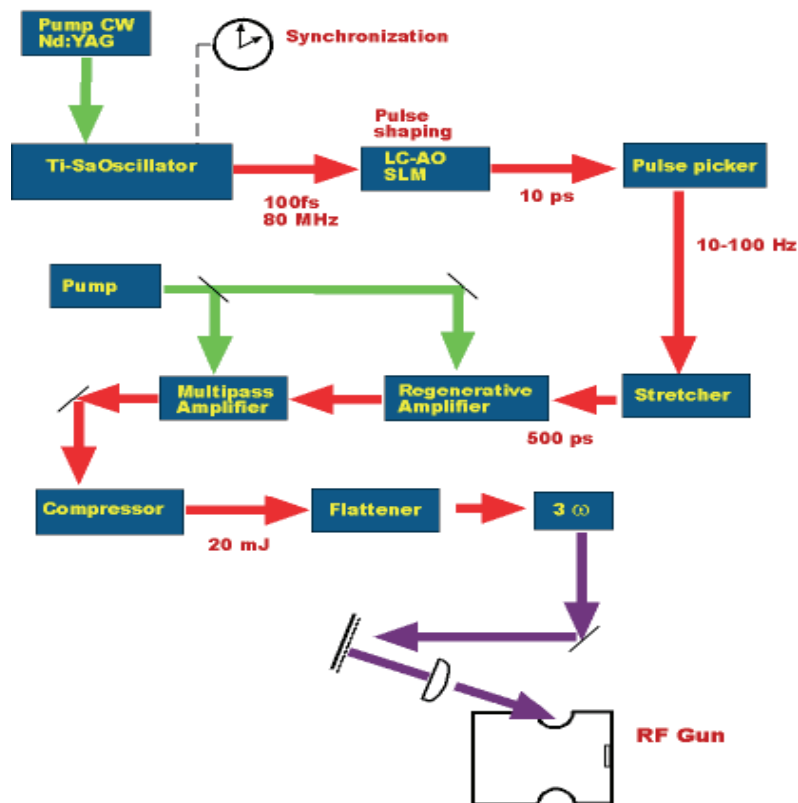


Figure 3.2: Layout of the photocathode laser system.

The SASE FEL experiment uses a permanent magnet undulator made of 6 sections, each 2.13 m long, separated by 0.36 m gaps, and featuring single quadrupoles which focus the electron beam in the horizontal plane. The undulator period is set at 3.0 cm, with an undulator parameter $k_u = 1.4$.

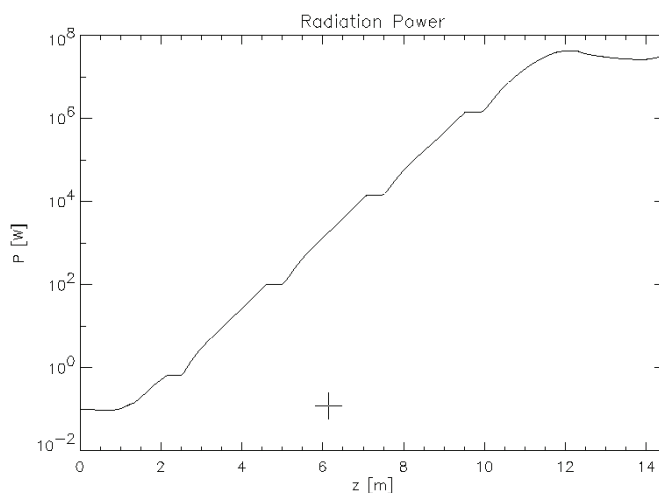


Figure 3.3: Radiation Power at 530 nm growth along the undulator, from GENESIS simulation.

A simulation performed with GENESIS is reported in Figure 3.3, showing the exponential growth of the radiation power at 530 nm along the undulator;

almost 10^8 W can be reached after 14 m of total undulator length. Preliminary evaluations of the radiation power generated into the non-linear coherent odd higher harmonics show that 10^7 and 7×10^5 W can be reached on the third and fifth harmonics, respectively.

The second beam line is envisioned to by-pass the undulator, thus experiments on magnetic pulse compression to be performed. In particular, in Phase 2, it is foreseen to investigate emittance degradation due to CSR induced effects on and surface roughness wake-field effects.

3.4 SPARC parameter list

We present here the parameter lists describing the photo-injector in two slightly different configurations, (A) 155 MeV and (B) 200 MeV operation. The 155 MeV case has been intensively studied for use in driving the FEL. The higher energy operation is of course interesting, as it results to be the maximum allowed beam energy for FEL experiments.

Table 3.1: Ferrario working point, distance 1st section entrance to cathode = 1.5 m, gap between sections 0.5 m, two cases with three accelerating sections at 155 MeV and 200 MeV

ELECTRON BEAM	A	B
Electron Beam Energy (MeV)	155	200
Bunch charge (nC)	1	1
Repetition rate (Hz)	10	10
Cathode peak field (MV/m)	120	120
Peak solenoid field @ 0.19 m (T)	0.273	0.273
Photocathode spot size (mm, hard edge radius)	1	1
Central RF launch phase (RF deg)	35	35
Laser pulse duration, flat top (ps)	12	12
Laser pulse rise time (ps) 10%→90%	1	1
Bunch energy @ gun exit (MeV)	5.6	5.6
Bunch peak current @ LINAC exit (A)	85	85
Rms transverse emittance @150 MeV (mm-mrad)	< 2	< 2
Rms slice norm. emittance (300 μm slice)	< 1	< 1
Rms longitudinal emittance (deg.keV)	1000	1250
Rms total correlated energy spread (%)	0.2	0.2
Rms uncorrelated energy spread (%)	0.05	0.05
Rms beam spot size @ LINAC exit (mm)	0.4	0.3
Rms bunch length @ LINAC exit (mm)	1	1

DRIVE LASER SYSTEM

Laser central wavelength (nm)	780
Laser oscillator rep rate (MHz)	79.3
Laser pulse length @ oscillator exit (fs)	100
Laser pulse energy (IR) @ amplifier output (mJ)	20
Laser pulse energy (UV) @ photocathode (mJ)	0.5
Repetition rate (Hz)	1-10
Laser pulse duration, flat top (ps)	8-12
Laser pulse rise time (ps) 10%→90%	< 1
Phase jitter w.r.t. RF (ps)	< 1
Rms energy jitter in UV (shot-to-shot) (%)	5
Rms pointing stability on cathode (mm)	< 0.1
Flat top uniformity (peak-to-peak) (%)	< 30
Intensity transverse uniformity on photocathode (%)	20
Spot ellipticity on cathode: (1-a/b) (%)	< 10

RF GUN and LINAC	A	B
Maximum peak field at cathode (MV)	120	
Maximum rep rate (Hz)	10	
RF pulse duration (μ s)	4.5	
Gun RF peak power (MW) at 140 MV/m	15	
Operating vacuum - RF, laser on (Torr)	10^{-9}	
Operating temperature (deg C)	45	
Cathode material(s)	Cu, Mg	
Quantum efficiency	$10^{-5}, 10^{-4}$	
Laser incidence angle @ cathode (deg)	72	
Maximum solenoid magnetic field (T)	0.31	
Power supplies for gun solenoid sections	4	
1 st section accel. gradient (MV/m)	25	25
1 st section accel. Phase (RF deg)	on crest	on crest
2 nd section accel. gradient (MV/m)	12.5	25
2 nd section accel. Phase (RF deg)	on crest	on crest
3 rd section accel. gradient (MV/m)	12.5	15
3 rd section accel. Phase (RF deg)	on crest	on crest
RF peak power per section (MW)	55,15,15	55,55,20
# klystrons	2	2
# solenoids on 1 st section	12	12
# LINAC solenoid power supplies	4	4
Magnetic field on 1 st LINAC section (Gauss)	750	750

UNDULATOR & FEL	A	B (seeded)
Slice energy spread (other parameters as above)	$1 \cdot 10^{-3}$	$2 \cdot 10^{-4}$
Undulator period (cm)	2.8	2.8
Undulator sections	6	6
Undulator parameter (k)	2.14	2.14
Undulator field on axis (T)	0.82	0.82
Undulator gap (mm)	8.8	8.8
Undulator section length (m)	2.156	2156
Drifts between undulator (m)	0.364	0.364
FEL wavelength (nm)	500	300
Saturation length (m)	~ 12	~ 12
FEL pulse length (ps)	8	6
FEL power @ saturation (MW)	~ 120	~ 160
Peak Brilliance (photons/sec/0.1 % bw/mm/mrad)	$1.5 \cdot 10^{27}$	$1.5 \cdot 10^{27}$
Peak # Photons/pulse	$7 \cdot 10^{14}$	$5 \cdot 10^{14}$
FEL power @ sat. (MW) 3 rd harm.	> 4	6
FEL power @ sat. (MW) 5 th harm.	> 0.06	0.2

3.5 SPARC experimental achievements

3.5.1 Low Energy Beam Measurements

The first phase of the SPARC project consisted in characterizing the electron beam out of the photoinjector at low energy (5 MeV) before the installation of the three accelerating sections. The design goal in terms of peak current (100 A) and emittance (2 mm mrad) has been successfully achieved during the year 2006. The experimental layout for this phase of the project is shown in Figure 3.4.

The SLAC/BNL/UCLA 1.6 cell S-band RF gun was conditioned up to 10 MW, corresponding to a field of 120 MV/m at the beginning of 2006.

The photocathode drive laser has been characterized in terms of pulse shape and quality and the first generation of an UV flat top laser pulse has been achieved. In combination with a quite high Quantum Efficiency (QE) up to 10^{-4} of the copper photocathode, achieved after a dedicated laser cleaning and with accelerating field of 120 MeV/m, the nominal beam electron beam parameters have been obtained (1 nC, 10 ps long).

In order to study the first few meters of beam propagation where space charge effects and plasma oscillations dominate the electron dynamics, a new sophisticated diagnostic tool has been installed and commissioned: the movable emittance-meter.

Emittance oscillations driven by space charge in the drift downstream the RF gun have been observed, in agreement to what expected from our theoretical model and numerical simulations, and the first experimental observation of the double emittance minima effect, on which is based the optimized matching with the SPARC LINAC, has been achieved [1].

In addition the particular design of the emittance-compensating solenoid with 4 different coils inside the magnetic yoke allowed a study of how different magnetic field configurations affect the electron beam dynamics in particular varying (in sign and absolute values) independently the current setting for each coil power supply.

Additional parallel activities in the framework of future higher energy FEL experiments (SPARX) have been brought ahead and the recent results from R&D on new photocathode materials, X-band RF structures and advanced diagnostic will be also reported.

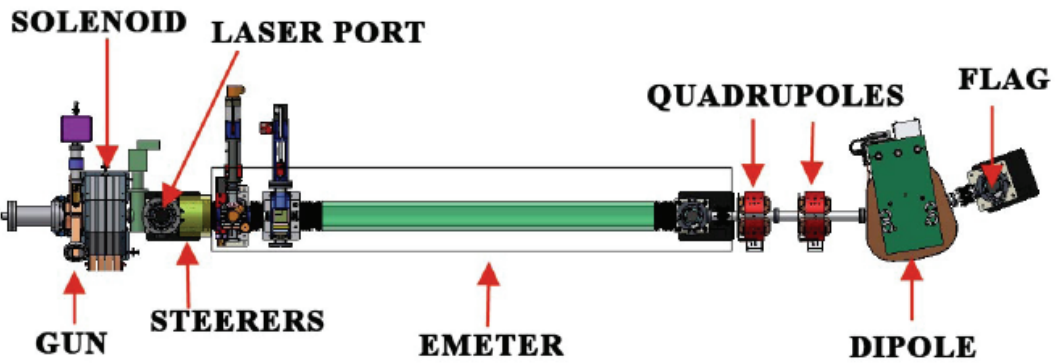


Figure 3.4: (up) Picture of the SPARC photoinjector showing the RF gun with solenoid and emittance meter installed; (down) Schematic layout of the experiment. Emeter is the abbreviation of the emittance meter.

3.5.1.1 Cathode and Laser system

Challenging requests are made on laser temporal pulse profile (flat top pulse with ~ 1 ps rise time and ripples limited to 30%) to minimize the e-beam emittance, consequently the main activity of the laser group has been devoted to optimize pulse shaping techniques. The Laser system layout is shown in Figure 3.5.

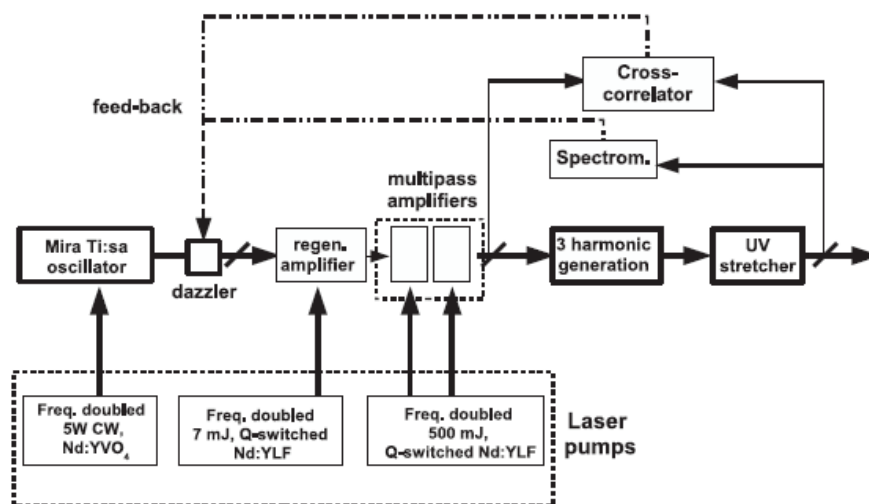
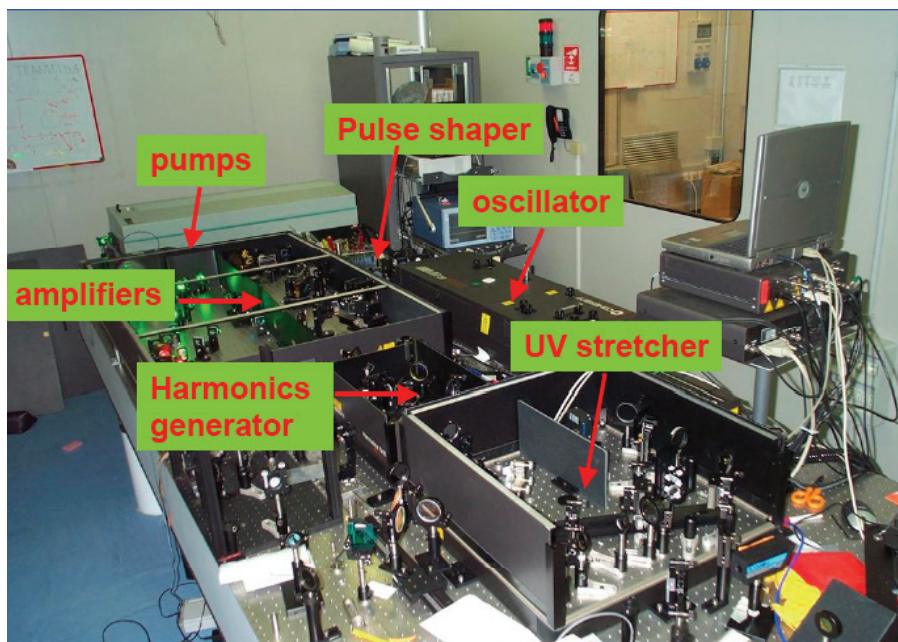


Figure 3.5: (up) Picture of the laser system; (down) laser system layout.

We currently use a Cu cathode with a quantum efficiency (QE) of 10^{-4} at 120 MV/m, achieved after a successful in situ laser cleaning treatment, therefore it is required about $50 \mu\text{J}$ to extract 1 nC at the operating phase.

The SPARC laser is a 10 Hz TW system produced by Coherent. The laser system [2] is composed by a Ti:Sa oscillator that generates 100 fs pulses with a repetition rate of 79.3 MHz and an energy of 10 nJ. An acousto-optic programmable dispersive filter called “DAZZLER”, used to modify the spectral amplitude and phase is placed between the oscillator and the amplifier to obtain the target temporal profile in the UV. The regenerative and two multipass amplifiers delivers pulses with bandwidth of at 10 nm FWHM $\lambda = 800 \text{ nm}$ with energy of $\sim 50 \text{ mJ}$ and divergence less than 1 mrad. The amplified pulses

go to the third harmonic generator (THG) where UV pulses with an energy up to ~ 4 mJ are produced. The THG is characterized by two type-I BBO (Beta Barium Borate) crystals of 0.5 mm and 0.3 mm thickness used to produce respectively the second and third harmonics. The crystal lengths have been chosen to allocate enough bandwidth to preserve the pulse shape and, at the same time, to guarantee good efficiency. The efficiency of the first conversion is about 50% and the overall conversion efficiency is more than 10%. After the THG the pulse is sent to a pair of 4300 g/mm UV parallel gratings, that forms a negative group velocity dispersion two passes stretcher. Varying the distance L between the gratings it is possible to obtain the output pulse length. The energy efficiency of the UV stretcher is about 30 % producing a energy up to 1.5 mJ with an amplitude jitter of 5 % RMS. To characterize the pulse time profile a multishot crosscorrelator with 200 fs resolution was built. The diagnostics uses part of the sub-ps IR pulse to cross-correlate the UV pulse and generating the frequency difference at 400 nm. According with the theory and experimental measurements, when a large chirp is imposed, such as for our the UV stretcher, the pulse spectrum allows the direct reconstruction of the time intensity distribution. For the spectral measurements in the UV it has been designed a spectrometer using a UV grating with 4350 g/mm and a converging lens to focus the different wavelength on a ccd camera. This diagnostic proved a the resolution of 0.02 nm. The optical transfer line to the cathode has been designed to increase the pointing stability, to easily change the spot dimension and to provide a normal incidence on the cathode surface.

In the early commissioning runs, we started with Gaussian pulses which are the natural output of the laser system. Figure 3.6 shows the typical projected transverse profile of the laser spot. The DAZZLER is used to increase the pulse length in order to avoid a transform limited pulse in the output of the amplifier. This was done to prevent damaging the BBO crystal. The UV pulse length on the cathode was controlled by means of the UV stretcher.

Figure 3.7 shows the longitudinal profile obtained from spectral measurement fitted with a 4.4 ps rms width Gaussian.

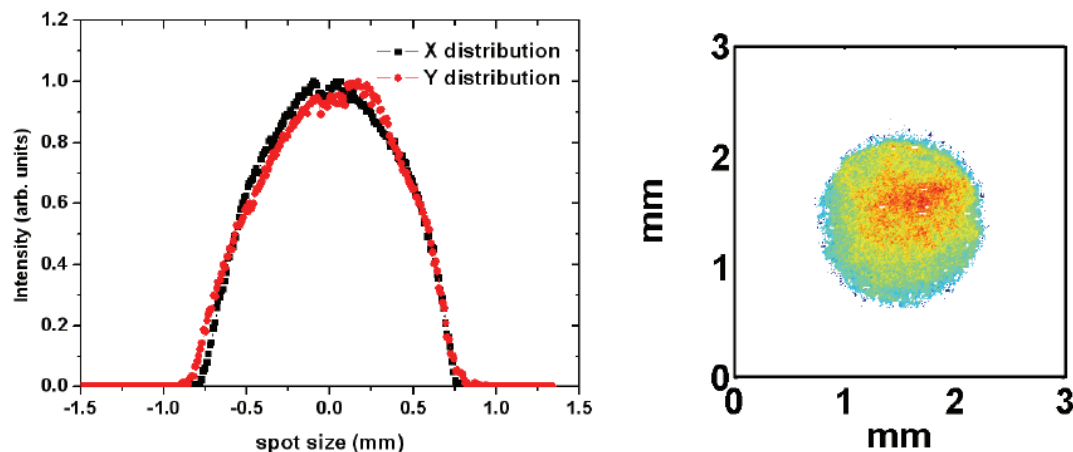


Figure 3.6: *Right: Typical projected transverse profile of the laser spot on the virtual cathode. Right: 2D laser spot profile*

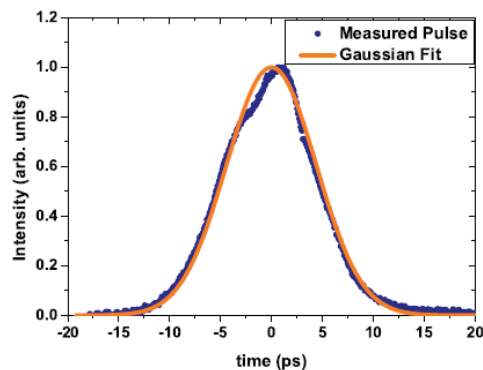


Figure 3.7: Longitudinal shape for a Gaussian-like laser pulse obtained from a spectral measurement.

Studies were performed in order to check the dependence of the beam parameters on RF phase and laser parameters, mainly the pulse shape and pulse length, with particular attention to the laser pulse rise time, defined as the time needed for the pulse intensity to grow from 10% to 90% of the maximum one.

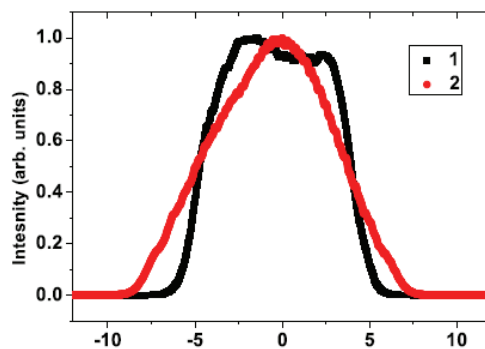


Figure 3.8: Two different pulse shapes with the same FWHM=8.7 ps: (1) Rise time \approx 2.5 ps, (2) rise time \approx 5 ps.

3.5.1.2 RF system and synchronization

The SPARC RF system [3] is mainly constituted by two RF chains. The power sources, are the 45 MW peak, 2856 MHz klystrons TH2128C. The klystron n.1 feeds the RF gun with 3 μ s long pulses and one accelerating section via a 3 dB waveguide coupler and an RF deflecting cavity for beam diagnostic purposes.

The RF gun, has been successfully conditioned without relevant problems and we fed into it more than 10 MW of RF power that corresponds to an accelerating field of about 120 MV/m. Klystron n. 2 and its waveguide distribution lines feeds two high gradient accelerating sections through an energy compressor that allows to obtain a 60 MW - 0.8 μ s RF pulse.

The timing distribution system is installed and it provides the 79.33 MHz reference to lock the laser system to the RF oscillator using a home-designed frequency divider board. It also furnish the 10 Hz repetition rate signal to the machine, synchronous with the external line and to the 2856 MHz internal distribution.

The synchronization diagnostic allows to trace the time jitter from each location of the machine (relative to the main oscillator) and this is displayed in the control room monitors. Also an RF phase feedback system was implemented to correct slow drifts due to temperature. The observed rms time jitter of the accelerating field inside the gun is 250 fs and the laser oscillator rms time jitter is 350 fs.

3.5.1.3 The control system

In order to reduce the time of development of the SPARC control system [4], we decided to use well known Rapid Application Development (RAD) software. Labview became the natural choice because in the collaboration laboratories the use of National Instrument software is very popular. Also Labview is considered as reference software by many hardware manufacturers that write interface drivers in Labview. Other software such as Matlab (whose integration with LabView is very well established) will be introduced and integrated in the control system in order to help the online and offline analysis of the beam during the machine operation. Gigabit Ethernet is used as interconnection bus giving the sufficient bandwidth in the data exchange; PC are used as front-end CPU and operator consoles giving the sufficient computing power.

We have developed also a data acquisition system based on a database with a possibility to communicate via TCP/IP (PostgreSQL). We have each front-end processor running programs that send periodically all data of the controlled elements to the database. We have developed some different interface programs that can correlate the information.

The control system is currently working and it is ready to be extended to the SPARC full configuration. The SPARC main server with a RHEL3 operating system, the consoles standard workstations with Windows XP. The photo-injector device drivers are installed in industrial PCs placed in the bunker. Two process form a connecting bridge from the front-end industrial PCs to the control room consoles. The data server: it accepts a request of information from the consoles and send them the data read from the proper industrial PC. The data can be software variables (that identify the controlled devices), sampled signals, images or information about the status of the computer itself. And the command server: it elaborates the queue coming from the consoles and, once identified legal commands, it delivers them to the front-end PCs to control the photo-injector devices.

3.5.1.4 Advanced Diagnostic devices: the emittance meter and the RF deflector

The measurements of the beam parameters at different positions z , being z the distance from the photocathode, is fundamental to study the beam dynamics. The emittance meter (see Figure 3.9) allows one to follow and completely characterize the transverse phase space evolution along the direction of propagation, for a particular dynamical configuration, i.e., for a given beam density, RF relative phase, and magnetic lens strength.

The beam parameters can be measured in the range from about $z = 1000$ mm to $z = 2100$ mm. The technique [5] of measuring the beam emittance and the phase space in both horizontal and vertical planes makes use of a double system of horizontal and vertical slit masks made of 2 mm thick tungsten. The slit mask must stop, or strongly degrade, the intercepted fractions of the beam. By selecting an array of beamlets by means of an intercepting multislit mask or alternatively by creating one beamlet using a single slit moving transversely over the beam spot, we can divide the space charge dominated incoming beam into emittance-dominated beamlets drifting up to an intercepting screen. Assuming a linear screen response, the intensity of the beamlets spot on the screen is directly proportional to the number of particles in the beamlets hitting the screen. The emittance can be measured estimating the beamlets size [6].

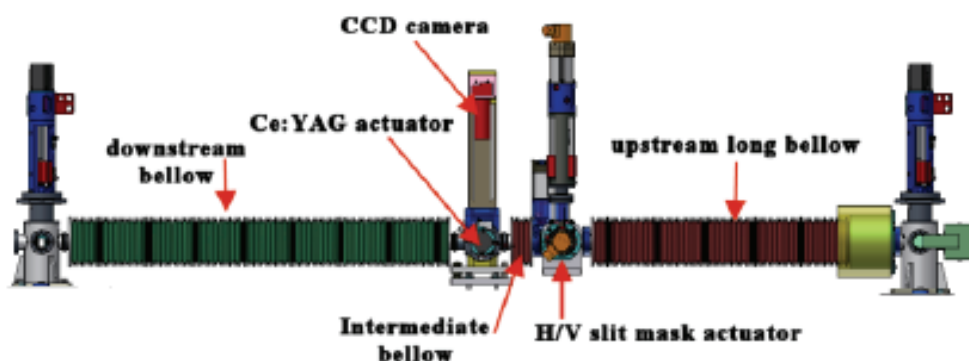


Figure 3.9: Schematic view of the emittance-meter device. Beam direction is from right to left.

Each mask (see Fig. Figure 3.10) consists of a slit array (7 slits, $50 \mu\text{m}$ wide spaced by $500 \mu\text{m}$, 2 mm thick) and two single slits, 50 and $100 \mu\text{m}$ wide. The slits are manufactured by electrochemical etching, which provides, in comparison with mechanical machining, higher precision and improved smoothness of the slit edges. Each individual slit was machined as a component of 0.5 mm height and later assembled into the frame [7]. This configuration allows changes of the geometry of the slit mask simply by reshuffling the single components.

The multislit mask was used for single shot measurements, when the beam size was large enough for an adequate beam sampling by the slit array. Alternatively, a single slit was moved across the beam spot in a multishot measurement. In this case the range of transverse sampling can be freely chosen by adjusting the step between the different positions of the slit. Typical values of the sampling distance between the slit positions range from $110 \mu\text{m}$ to $380 \mu\text{m}$. From 9 to 13 beamlets are collected in a single slit scan. No relevant differences were found between single and multislit measurements performed under comparable conditions.

The beamlets emerging from the slit mask are measured by means of a downstream Ce:YAG radiator. The doping level of cerium in the crystal is 0.18%. The response is linear up to $0.01 \text{ pC}/\mu\text{m}^2$ [8], an order of magnitude larger than the maximum density of our beam. Since beam size and divergence depend on the longitudinal position of the device, also the slit to screen

distance must be properly adjusted in order to optimize the beamlets profile measurement. A bellow, placed between the slit mask and the screen, allows one to change their relative distance from 22 to 42 cm, to optimize the drift according to different measurements conditions (converging beam, diverging beam, single, or multislits).

The radiation emitted in the forward direction from the Ce:YAG crystal is collected by a 45 degrees mirror downstream the radiator, on the same screen holder. We observe the back side of the transparent crystal radiator, thus minimizing the degradation of the spatial resolution due of the optics field depth. The small thickness of the crystal ($100\ \mu\text{m}$) prevents appreciable blurring effects due to the crystal bulk emission, as well as significant multiple scattering.

Images are acquired using 8 bit digital CCD cameras (Basler 311 f) equipped with 105 mm “macro” type objectives from SIGMA. The chosen magnification of about 0.66 yields a calibration factor near to $15\ \mu\text{m}$ per pixel and a field of view of the screen around 9.6 mm times 7.2mm. The angular resolution depends on the drift length between the slits mask and the screen and is in the order of $100\ \mu\text{rad}$. The influence on the beam quality of the bellow has been investigated [9]. The bellow has a length of 1.5 m long, and a diameter of 150 mm. Wake field perturbations due to the corrugated structure were studied using the HOMDYN [10] code. The wake fields were computed using the diffractive model of Bane and Sands [11]. This is particularly important when the beam is not wellaligned on-axis. In the case of 1 mm misalignment from the center of the bellow, the contribution of the wakes to the emittance degradation is negligible (0.05%). It remains around 0.13 % also at a distance of 4 mm, much larger than the estimated misalignment.

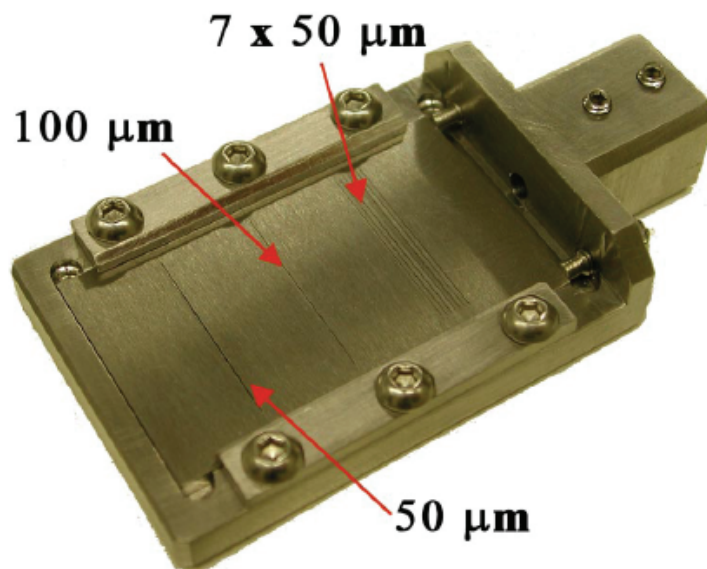


Figure 3.10: Slit mask composed of 7 slits of $50\ \mu\text{m}$ width spaced by $500\ \mu\text{m}$, one slit of $100\ \mu\text{m}$ width and one of $50\ \mu\text{m}$ width.

The six-dimensional beam phase space characterization at the exit of a photoinjector is another important measurement we have conducted in the second phase of the SPARC commissioning. This measurement is based on the use of an RF deflector that allows measuring the temporal profiles of the beam, as well as the complete longitudinal phase space by adding a dispersive system. Using the quadrupole scan technique the horizontal beam slice

emittances as a function of longitudinal position in the beam can also be measured. Simulations made by the ELEGANT code have shown the feasibility of this diagnostic system.

The RF deflector design [12] has been made by the use of the e.m. codes MAFIA and HFSS. The RF deflector proposed is a 5-cell SW structure working on the p mode at 2.856 GHz and fed by a central coupler with $b = 1$. Since the transverse shunt impedance is ~ 2.5 MW and the maximum input power is 2 MW, it is possible to obtain a resolution length of the order of 12 mm. Two small longitudinal rods have been inserted to shift the resonant frequency of the 90 deg rotated polarity modes with respect to the working mode. By the bead-pull technique we have measured the deflecting field on axis. A tuning procedure has been implemented in order to reach a field flatness of the order of a few percents. External quality factor measurements have also been done, showing good agreement with expectations.



Figure 3.11: RF Deflector

3.5.2 Low Energy Beam Measurements

We performed a detailed characterization of the photoinjector, studying the beam dynamics as function of relevant parameters such as the solenoid field, the beam charge and size, the laser pulse length and its shape. First of all we made charge versus gun RF phase measurement (phase scan) that allow us to choose day by day the optimal phase for the electron extraction and to collect information about the accelerating gradient and cathode quantum efficiency. Moreover this kind of measurement allows to obtain a rough estimation of the beam duration. Figure 3.12 shows some phase scans performed in different photoinjector working points.

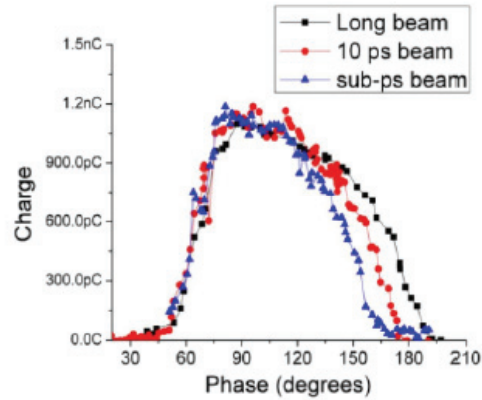


Figure 3.12: Charge vs phase in three different beam configurations

The spectrometer and its transport line (constituted by a FODO cell) are placed at the end of the diagnostics chain to measure energy and energy spread. We performed these measurements in low and high charge configurations versus the launching phase as shown in Figure 3.13 for the case of 1 nC.

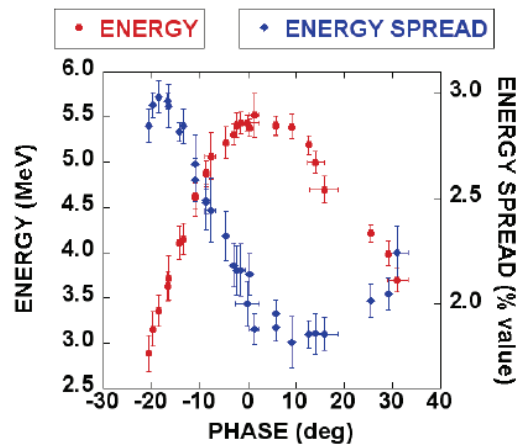


Figure 3.13: Energy and energy spread for low and high bunch charge

The e-meter gives also the possibility to investigate the longitudinal dynamics by inserting a slit and selecting a low charge beam slice at different longitudinal locations.

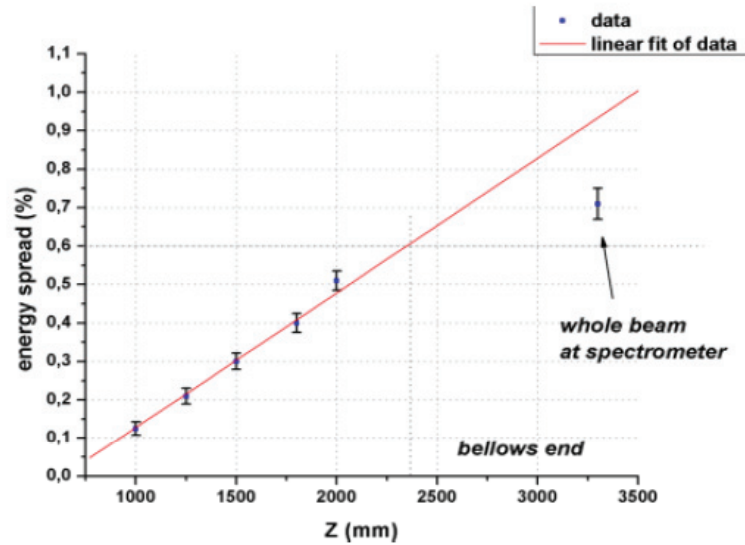


Figure 3.14: Energy spread versus z

By doing so, as shown in Figure 3.14, we can ‘froze’ the space charge contributions to energy spread growth and measure its evolution at different locations along the beamline. Moving the slit over the beam and measuring the energy and the energy spread in the spectrometer gives information of possible correlation between position and energy. Also centering the slit on the beam and moving along the emittance meter allows the measure of the energy spread in different longitudinal positions.

A longitudinal diagnostic, based on Cherenkov radiation produced by the beam passing through a 5 mm thick aerogel slab with index of refraction $n = 1.017$, was installed with the main purpose of studying the photoinjector response to different laser pulses length. A fieldlens narrow band filtering optical system delivers the Cherenkov light to the entrance slit of a 2 ps resolution Hamamatsu streak camera of type C1370 enabling direct pulse length measurements see Figure 3.15.

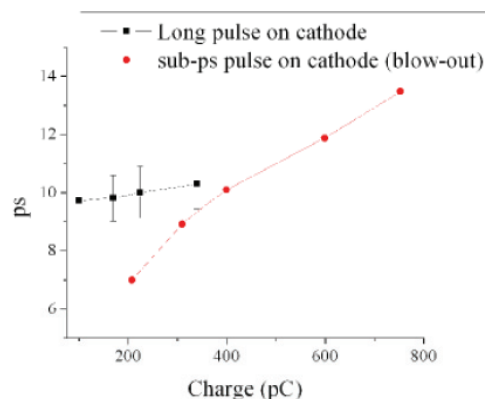


Figure 3.15: Bunch length measurements with streak camera

With the emittance meter it is possible to follow the emittance evolution, and tuning the machine parameters. A typical emittance measurement with the single-slit mask consists of collecting 15 beam images for each slit position.

The center of mass and RMS size of beamlets are then calculated for each image and averaged. From the beamlets images we calculate the projection on the axis, subtract the baseline, try a gaussian fit to find the best position for the distribution center, reduce the number of the relevant points skipping these that are outside the 3 standard deviation from the centre and only on the remaining points we calculate the RMS parameters.

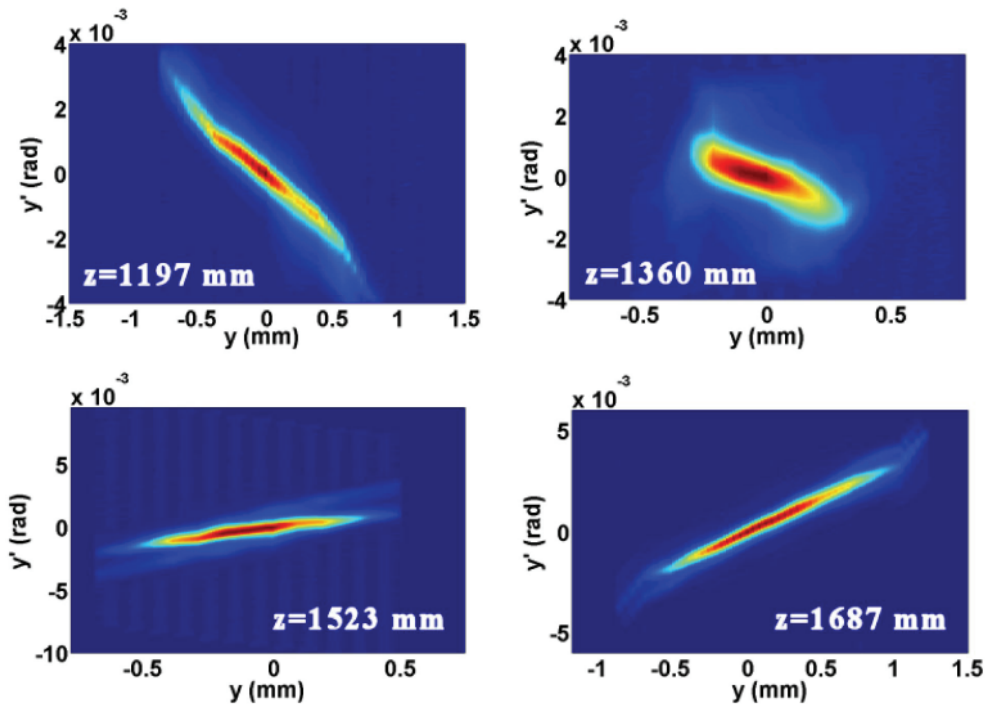


Figure 3.16: Phase space reconstruction

The use of big magnification, an high efficiency YAG and a CCD with a gain remotely controlled give a good signal to noise ratio and large number of sampling point for every beamlet in all the conditions.

The 1-D pepper pot technique [13] allows not only to measure the beam and the Twiss parameters, but also to reconstruct the phase space. In Figure 3.16 the phase space reconstruction in different positions, measured at a charge of 1 nC is shown.

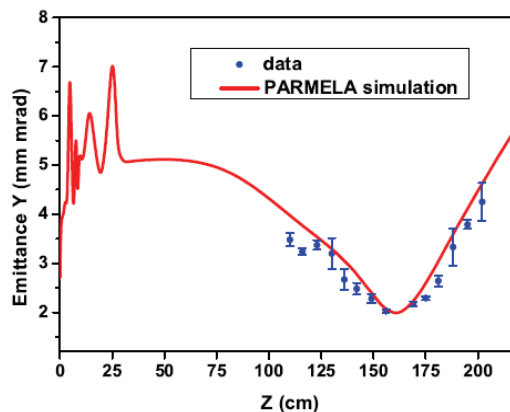


Figure 3.17: Emittance measurement using the longitudinal laser pulse shape of Figure 3.7. A PARMELA simulation is also shown for comparison.

Figure 3.17 shows measurements of the transverse vertical emittance at different z-positions together with a PARMELA simulation. The relevant parameters are shown in Table 3.2.

Table 3.2: Parameters of the beam corresponding to the emittance measurement shown in Figure 3.17.

<i>Parameter</i>	<i>Value</i>
Energy	5.65 MeV
Charge	1 nC
Laser spot size	450 μm
Laser pulse length	10 ps FWHM
Phase ($\varphi - \varphi_{\text{max}}$)	5°

The phase φ_{max} is the RF phase corresponding to the maximum energy measured in the spectrometer.

The value 5 deg means that there is a difference of 5 degrees with respect to the phase where the energy is maximum in the direction of the minimum energy spread. Figure 3.13 shows the values of the energy and the energy spread versus phase to clarify this point.

3.5.2.1 Laser Pulse Shape Studies

Studies were performed in order to check the dependence of the beam parameters on RF phase and laser parameters, mainly the pulse shape and pulse length, with particular attention to the laser pulse rise time, defined as the time needed for the pulse intensity to grow from 10 % to 90 % of the maximum one.

In the following we show the comparison between results obtained with two different longitudinal laser pulses. Figure 3.8 shows the time profiles calculated from spectral measurements.

Table 3.3: Parameters of the two beams corresponding to the emittance measurement shown in Figure 3.18.

<i>Parameter</i>	<i>Value</i>
Energy	5.4 MeV
Charge	0.74 nC
Laser spot size	310 μm
Laser pulse length	8.7 ps FWHM
Phase ($\varphi - \varphi_{\text{max}}$)	8°
Rise time beam 1	2.5 ps FWHM
Rise time beam 2	5.0 ps FWHM

The parameters are reported in Table 3.3. The rise time was about 2.5 ps for pulse shape 1 and about 5 ps for the pulse shape 2 of Figure 3.8. The corresponding emittance evolution in the vertical plane is shown in Figure 3.18. The beam dynamics is different in the two cases because it is strongly

dependent on the laser rise time. The minimum emittance value is about 25 % smaller in the case of shorter rise time, confirming the result of [14].

3.5.2.2 High Brightness Beam

A large number of emittance-meter scans have been done in the drift region after the gun to maximize the brightness, defined as $B=2I/\varepsilon_x\varepsilon_y$, with I representing the peak current and $\varepsilon_{x,x}$ the transverse emittances.

The optimization parameters were the injection phase, the solenoid strength, the longitudinal profile of the laser and the transverse beam spot size.

The design goal was 2 mm mrad for the transverse emittance, 100 A for the beam current and thus $5 \cdot 10^{13}$ A/m² for the brightness.

The plots in Figure 3.19 summarize the results of the measurements showing, in a sample of several runs with a brightness larger than the design value, the peak brightness normalized to its design value and the normalized emittance [15].

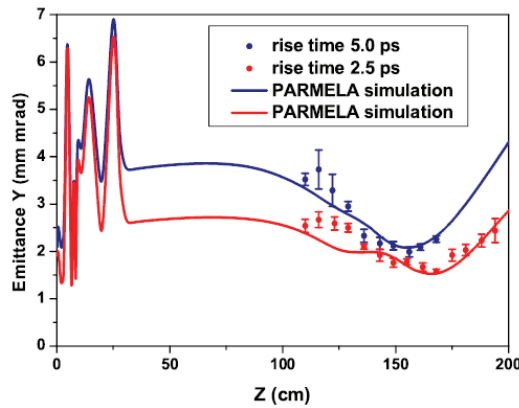


Figure 3.18: Vertical emittance evolution for the beams with the longitudinal profiles of Figure 3.8 and parameters of Table 3.3.

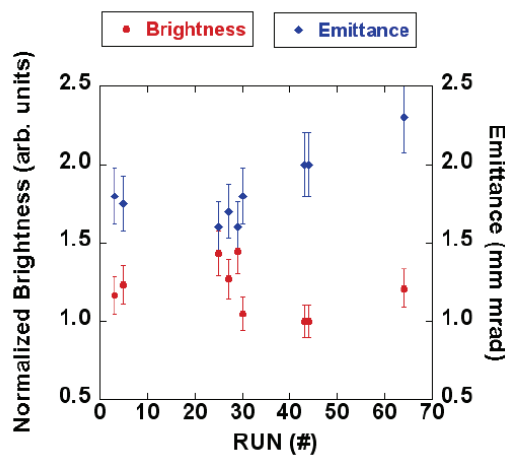


Figure 3.19: Vertical emittance and brightness normalized to their design values, in the cases with peak brightness larger than its design value ($5 \cdot 10^{13}$ A/m²)

In order to find the brightness values we used the laser bunch length measured at the cathode to calculate the beam current and the minimum emittance value measured in the drift. Therefore we neglected the bunch length increase due to the space charge longitudinal defocusing along the drift. Simulations show that in the measurements conditions, the bunch lengthening is less than 10 %, which is within the uncertainty of the charge measurement. We also performed some electron pulse length measurements with the Hamamatsu streak camera (still model C1370) using an aerogel as radiator. The time resolution of this streak camera is around 2 ps as before. We could not distinguish between the lengths of the electron bunch and of the laser pulse.

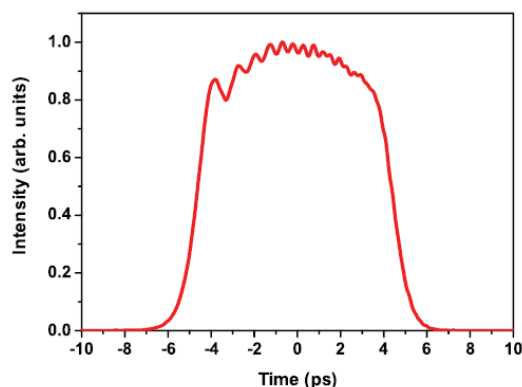


Figure 3.20: Longitudinal laser profile. The pulse length is 9 ps FWHM, and the rise time is about 2.7 ps. The best brightness has been obtained with this profile.

The best brightness has been obtained with the longitudinal profile shown in Figure 3.20; the beam parameters are given in Table 3.4. The results in Figure 3.21 show the measured emittance evolution versus z for a beam of 92 A peak current.

Table 3.4: Parameters of the beam corresponding to the best brightness result.

<i>Parameter</i>	<i>Value</i>
Energy	5.65 MeV
Charge	0.83 nC
Laser spot size	360 μm
Laser pulse length	8.9 ps FWHM
Phase ($\varphi - \varphi_{\text{max}}$)	8°

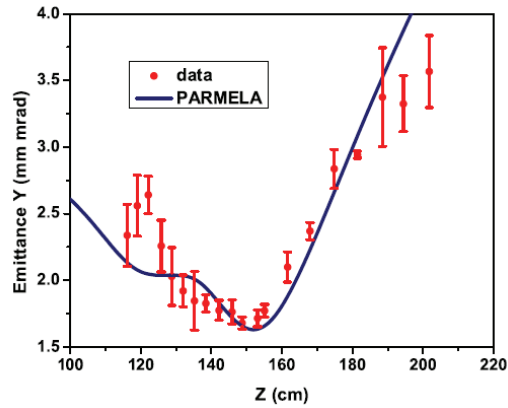


Figure 3.21: Vertical emittance versus z for run #29. This is the measurement with the highest brightness of about $7 \cdot 10^{13}$ A/mm². A PARMELA simulation is also shown.

The minimum emittance value is 1.65 ± 0.06 mm mrad, yielding a peak brightness of $7.0 \pm 0.8 \cdot 10^{13}$ A/m². The injection phase was set to -8.0 ± 0.5 deg with respect to the maximum energy gain phase and the laser RMS spot size was 360 μ m. The solid line in the plot is a simulation made with PARMELA.

3.5.2.3 Double Minimum Oscillation

The emittance oscillation observed in the simulation of a photoinjector is an important feature of the Ferrario working point [16]. Some of the photoinjectors running worldwide (FERMI [17], LCLS [16]) or in the already designed (XFEL [18]) or still in design stage (PAL [19], BESSY FEL [20]) are based on this working point.

The optimized matching with the SPARC LINAC relies on this peculiar space charge regime which works in the flat top pulse mode and guarantees the optimum matching to the invariant envelope in the LINAC sections, yielding therefore the minimum emittance at the LINAC output. Emittance oscillations of this kind have been explained as the effect of a beating between head and tail plasma frequencies caused by correlated chromatic effects in the solenoid 21. We have obtained a direct evidence of this type of oscillation working with short laser rise time (~ 1.5 ps, the longitudinal profile is shown in Figure 3.22). To enhance this effect we move the injection phase above the maximum energy gain phase, thus inducing a higher energy spread (~ 3 %), although the minimum achievable emittance in this case is slightly worse. The parameter of such a beam are given in Table 3.5.

Table 3.5: Parameters of the beam whose emittance measurement is shown in Fig.~\ref{doubleminimum}.

<i>Parameter</i>	<i>Value</i>
Energy	5.5 MeV
Charge	0.5 nC
Laser spot size	450 μ m
Laser pulse length	5.5 ps FWHM
Phase ($\varphi - \varphi_{\max}$)	12°

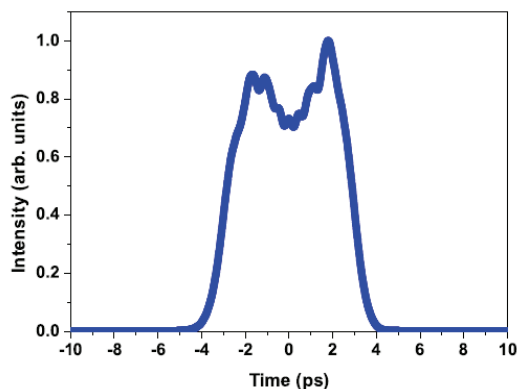


Figure 3.22: Longitudinal profile of the laser for the measurement shown in Figure 3.23. The rise time is 1.5 ps and the FWHM is 5.5 ps.

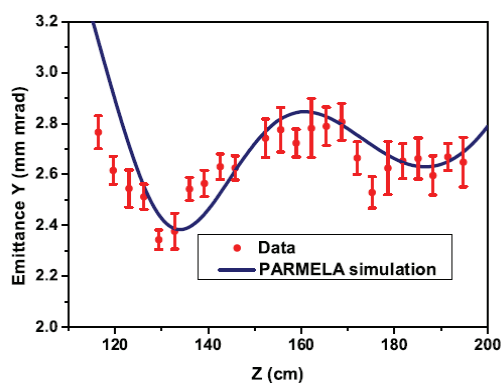


Figure 3.23: Vertical emittance measurement showing a double minimum oscillation. A PARMELA simulation is also shown on the same plot for comparison.

The result of this measurement, showing double minimum oscillation of the emittance is shown in Figure 3.23. It is worth remarking that this is the first direct measurement of double minimum oscillation in a photoinjector ever done. The effect of this oscillation can also be observed in the transverse phase space. In this dynamic regime the head and tail of the bunch experience a different focusing when passing through the solenoid, due to the space charge correlated energy spread which is strongly enhanced at the bunch ends. As a consequence, at the z position of the relative emittance maximum a cross shape structure in the transverse phase space is predicted by simulations with a flat top longitudinal distribution of the laser pulse (see Figure 3.24 on the right). Under laminar conditions, i.e. when the solenoid field is not so high to cause crossover, the space charge dominated waist is reached at different positions by the head and the tail slices of the bunch, so that when the bunch tail is already diverging the bunch head is still converging.

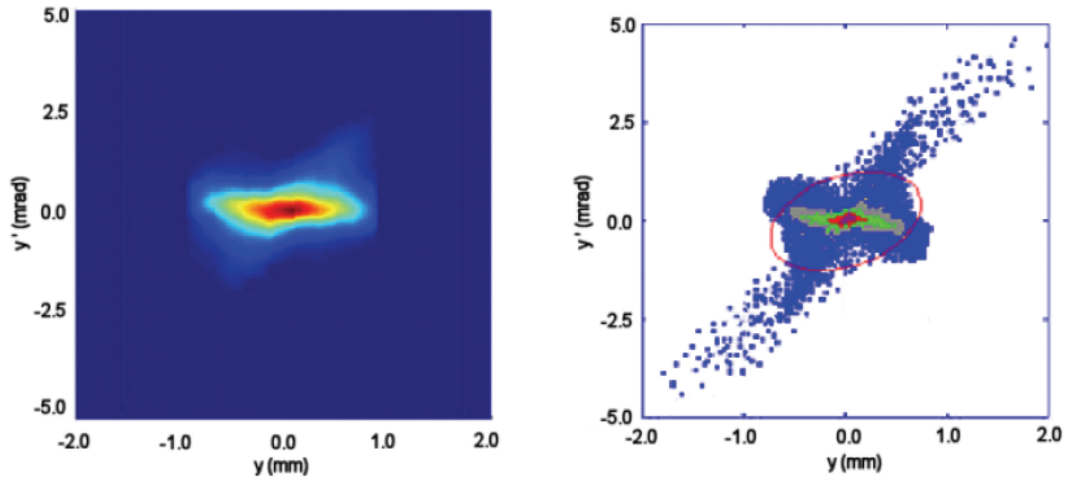


Figure 3.24: *On the left: measured transverse phase space in the vertical plane at $z=1500$ mm from the cathode. On the right: PARMELA simulation obtained with the parameters of the measurement.*

We have measured this effect and the comparison between PARMELA simulation and measured phase space. This is shown in Figure 3.24. Even if it is hard to compare them quantitatively, the measured phase space exhibits this particular cross shape structure as predicted by simulation.

3.5.2.4 Velocity Bunching Experiment

The longitudinal phase space rotation in the Velocity Bunching process is based on a correlated velocity chirp in the electron bunch, in such a way that electrons on the tail of the bunch are faster than electrons in the bunch head. This rotation happens inside the longitudinal potential of a traveling RF wave (longitudinal focusing) which accelerates the beam inside a long multi-cell RF structure and simultaneously applies an off crest energy chirp to the injected beam. This is possible if the injected beam is slightly slower than the phase velocity of the RF wave so that, when injected at the zero crossing field phase, it will slip back to phases where the field is accelerating, but at the same time it will be chirped and compressed. The key point is that compression and acceleration take place at the same time within the same linac section, actually the first section following the gun, that typically, under these conditions, accelerates the beam from < 5 MeV up to 25-35 MeV.

One of the main goals of the SPARC high brightness photoinjector is the experimental demonstration of the emittance compensation process while compressing the beam with the Velocity Bunching technique [xxii]. For this reason the first two S-band travelling wave accelerating structures, downstream the 1.6 cells S-band RF gun, are embedded in long solenoids, in order to keep under control the space charge induced emittance oscillations when the bunch is compressed.

The SPARC beam diagnostic allows rms beam envelope measurements on four YAG screens: three screens are located at the entrance of each RF structure while the fourth one is located at the exit of the linac. On the last screen the rms emittance is measured by a quadrupole scan [xxiii]. A RF deflecting cavity placed at the exit of the third accelerating structure allows bunch length measurements with a resolution of $50 \mu\text{m}$. A photo of the SPARC photoinjector is shown in Figure 3.25.

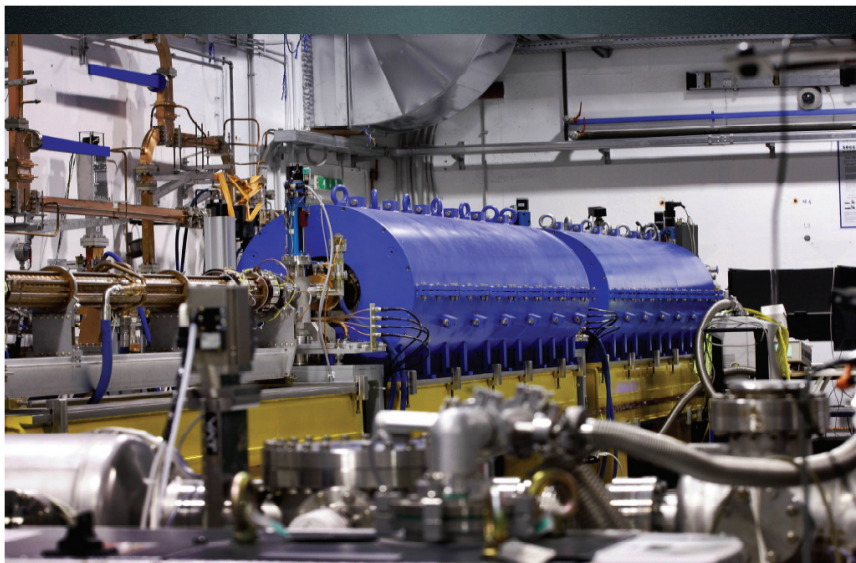


Figure 3.25: Photo of the SPARC photoinjector showing the 3 accelerating structures with 2 long solenoids

During the 2009 winter a preliminary experimental study of the velocity bunching technique has been performed and the main results are reported hereafter.

The first measurements made at SPARC were devoted to study the compression ratio as a function of the injection phase, without any external focusing (solenoids off). We have been operating with a quasi-Gaussian longitudinal laser profile, ~ 7.5 ps FWHM long and with $300 \mu\text{m}$ of transverse spot size. The bunch charge was 300 pC resulting in an initial peak current around 35 A .

When the beam has been accelerated on crest by an accelerating field of 20 MV/m in the first two sections and 10 MV/m in the last section, the final energy was 150 MeV with an energy spread of 0.1% and an energy stability better than 0.1% . The rms bunch length measured at the linac exit was 3.25 ps .

SPARC measurements 2/04/09

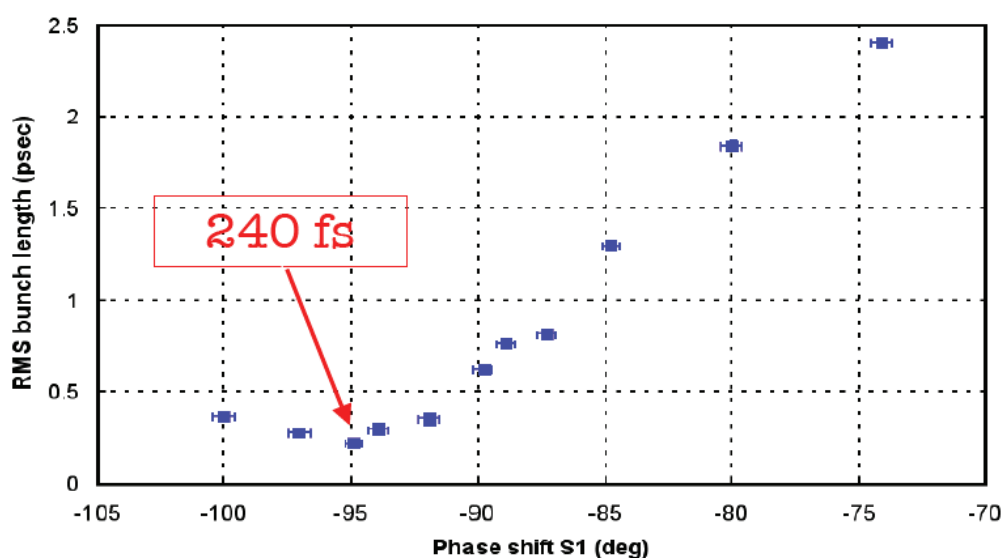


Figure 3.26: Measured rms bunch length of a 300 pC beam versus the phase of the first travelling wave structure.

Figure 3.26 shows the measured rms bunch length versus the injection phase in the first travelling wave structure. The error bars have been calculated over the 10 images collected for each measurement, a more detailed study including jitters effects and systematic error will be the subject of future investigations. A significant bunch compression occurs only after a phase shift of 85 degrees, the beam energy was progressively observed reducing to 100 MeV and the energy spread grows up to 1 %. In the next 10 degrees shift (from -85 to -95) the strong compression regime occurs, as expected, with almost the same final energy and energy spread. The shortest rms bunch length we have measured was 240 fs, (72 μm) limited by the longitudinal beam emittance. During this measurements the minimum spot size with the RF deflector turned off was 30 μm . The last two measurements also show the over-compression effect when the phase setting exceeds -95 deg.

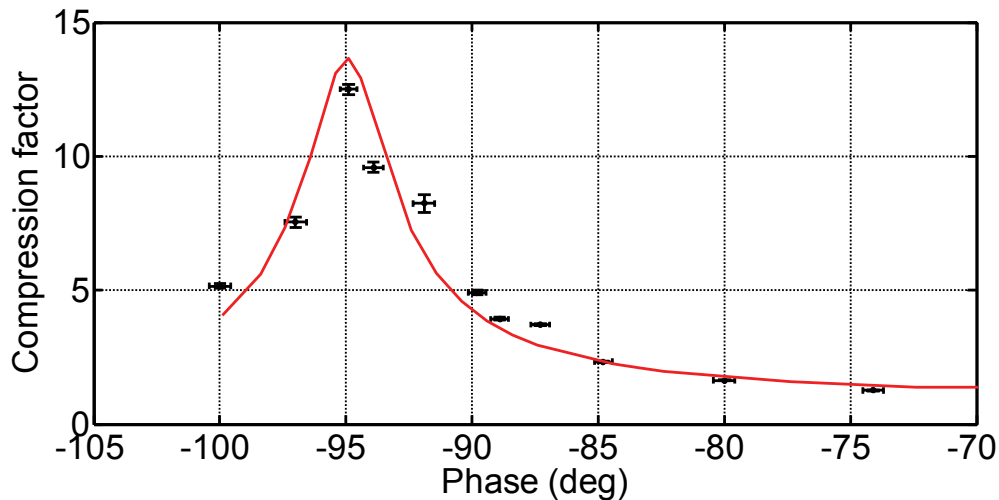


Figure 3.27: Compression factor versus injection phase, PARMELA simulations are also shown (red curve).

In Figure 3.27 the compression ratio versus the injection phase is also shown. The red curve is the results of PARMELA simulation. The agreement is quite satisfactory.

The emittance compensation optimization requires a careful tuning of the solenoid field in order to keep under control the space charge induced emittance oscillations. A systematic study of the emittance compensation process has been done so far only for one case with a moderate compression ratio 3.

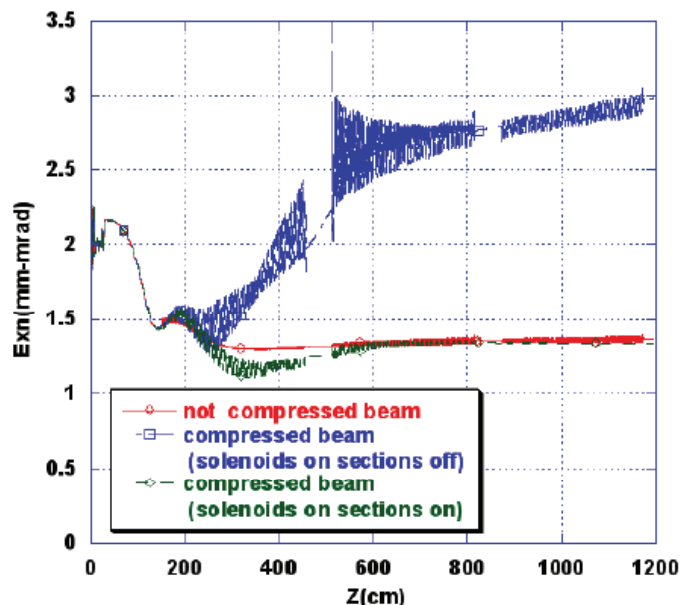


Figure 3.28: Emittance evolution along the linac, PARMELA simulations.

In Figure 3.28 are shown PARMELA simulation of the rms emittances evolution along the linac for three different conditions: no compression (beam on crest), compression with solenoids off, same compression with all solenoids set to 400 Gauss. The effectiveness on the emittance compensation produced by the solenoids is clearly visible from the simulation and it is in good agreement with our measurements.

In Table 3.6 the measured beam parameters are reported. The second column contains the measured data of the uncompressed beam (on crest acceleration) for comparison. The lowest achieved emittances are $\varepsilon_{nx} = 1.7 \mu\text{m}$ and $\varepsilon_{ny} = 1.4 \mu\text{m}$ (to be compared with $\varepsilon_{nx} = 4.3 \text{ mm}$ and $\varepsilon_{ny} = 6.1 \mu\text{m}$ with solenoids off, marked with * in the table). With a peak current of 120 A this bunch exhibits the highest beam brightness so far obtained by SPARC injector.

Table 3.6: Measured beam parameters

	<i>No Compression</i>	<i>Compression ratio 3</i>
Injection phase [deg]	0	-85
Bunch Charge [pC]	300	300
Beam Energy [MeV]	140	100
Energy spread [%]	0.11	1.0
Rms Length [ps]	3.25±0.16	1.03±0.1
ε_{nx} [μm]	2.33 ±0.11	1.74±0.05 4.33 ±0.84 *
ε_{ny} [μm]	1.30 ±0.05	1.44 ±0.03 6.06 ±0.4 *
Solenoid Field [Gauss]	0	400

3.5.2.5 First observation of Self Amplified Spontaneous Emission at SPARC

In this section we report the first observation of the Self Amplified Spontaneous Emission (SASE) at 500 nm in the SPARC FEL.

In Figure 2.29 a picture of SPARC taken from the undulator end is shown. The undulator, realized by *ACCEL GmbH*, is made of six permanent magnet sections with 2.8 cm period, 25 to 6 mm variable gap with maximum undulator parameter $K_{\max} \sim 2.2$.



Figure 3.29: Photo of the SPARC undulator sequence.

During this experiment we have been operating with a laser pulse with Gaussian longitudinal profile, 6-8 ps FWHM long. The bunch charge was in the range of 200 - 300 pC resulting in a peak current around 35 A. The beam has been accelerated up to 150 MeV with an energy spread of 0.1% and an energy stability better than 0.1%. At the linac exit the rms emittance has been measured by a quadrupole scan and the bunch length, slice emittance and slice energy spread have been measured downstream of a high resolution RF deflector [xxiii]. The typical measured rms emittance was around 2 μm in both planes for a 250 pC bunch. In Figure 3.30 the beam current profile together with the slice energy and slice energy spread are shown. These electron beam parameters have been sufficient for the preliminary characterisation of the spontaneous and stimulated radiation in the undulators.

The first clear signature of coherent radiation at SPARC has been observed at 500 nm on February 17th, 2009. In between each of the 6 undulator modules shown in Fig. 3.29, a 36 cm drift hosts quadrupoles for horizontal focusing and radiation diagnostic stations. Each station is equipped with actuators allowing the insertion of Alumina screens and Aluminum mirrors to extract the radiation. At the end of the undulator sequence, an in-vacuum spectrometer built by the LUXOR Laboratory (Padova) is installed. The instrument is a 1 m long normal incidence spectrometer with a Princeton UV grade CCD camera allowing the detection of spectra both in single shot and in the integrated mode in the spectral range 40 - 570 nm. A focusing lens ($f=14\text{cm}$) positioned at a distance f from the entrance slit selects the angular acceptance of the detector. With a slit opening of 800 μm all the radiation is collected and the integrated spectrum provides the information on the pulse energy.

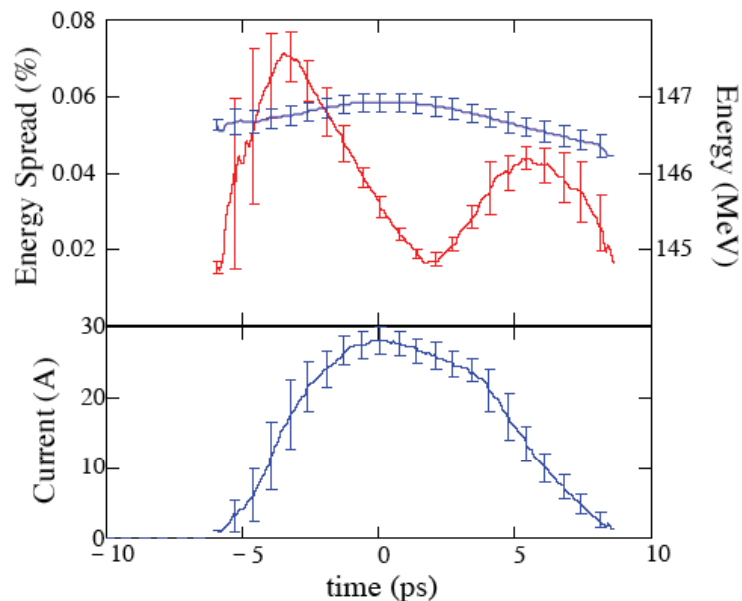


Figure 3.30: Measured electron beam slice parameters: slice energy (red) and slice energy spread (blue) in the upper plot, current profile in the lower plot.

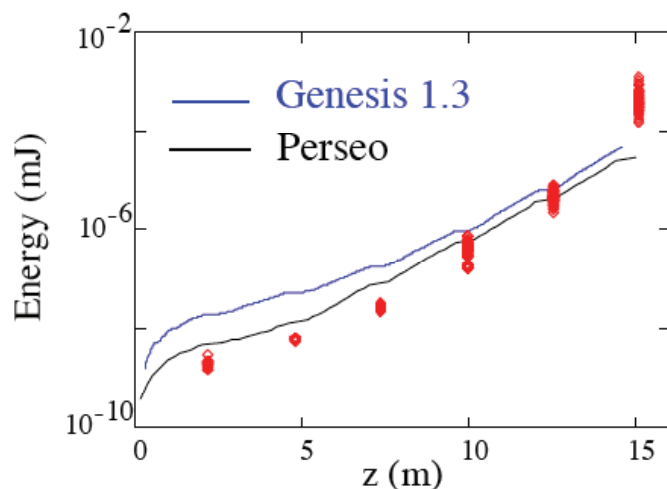


Figure 3.31: Pulse energy measured at the undulator intrasections. The continuous line show simulations obtained with Genesis 1.3 (blue) and Perseo (black).

The evolution of the pulse energy as a function of the position in the undulator sequence is obtained turning off the FEL interaction by progressively detuning the gap of the undulators. The measured pulse energy is shown in Figure 3.31. Each of the data points corresponding to the first three undulator sections (up to $z \sim 7$ m) are the result of an integration over multiple shots (1800 shots). The data corresponding to the 4th, 5th and 6th undulators are instead single shot measurements. We have observed an

amplification factor of about 10^6 and the observed gain length was ~ 1 m. Saturation is expected in these conditions at a pulse energy $\sim 300\mu\text{J}$.

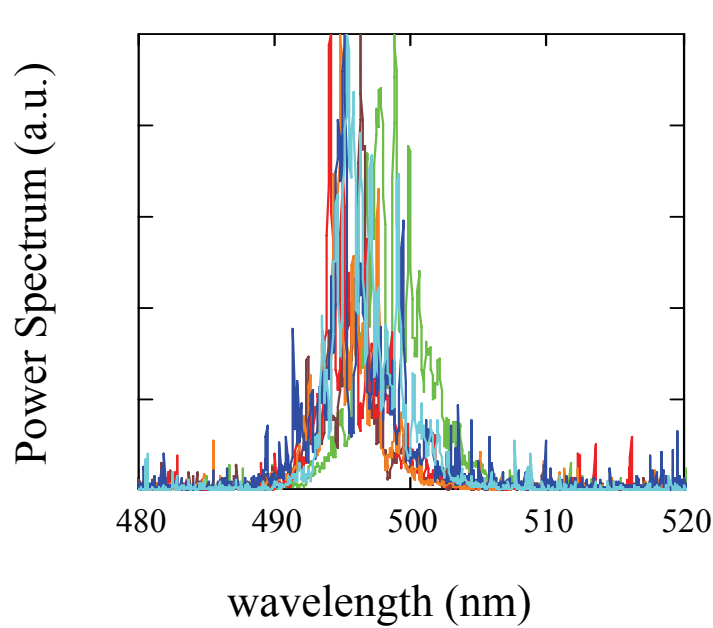


Figure 3.32: Single shot spectra at the end of the undulator sequence

The pulse energy is compared to simulations obtained with Genesis 1.3 [xxiv] (blue) and Perseo [xxv] (black) codes. In Figure 3.32 typical SASE single shot spectra after the sixth undulator are shown. The spectral narrowing associated with the FEL amplification is evident in Figure 3.33, where the behaviour of the spectral width versus the position in the undulator sequence is shown.

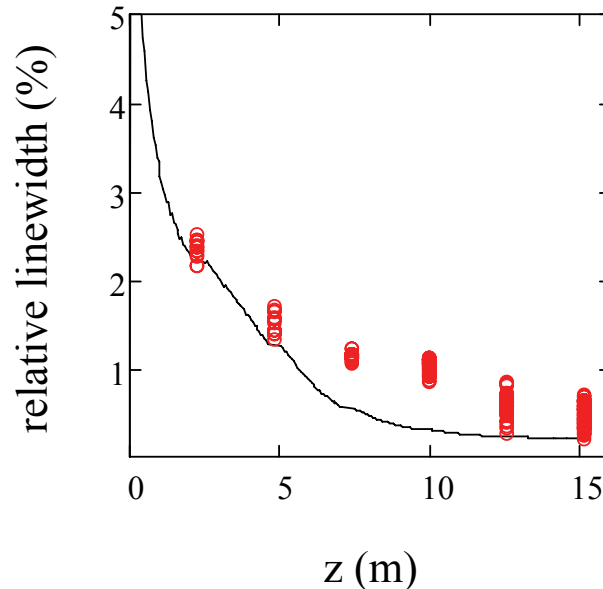


Figure 3.33: Measured Spectral width versus z . The continuous line is the result of a Perseo simulation.

3.6 References

- [1] M. Ferrario, Phys. Rev. Lett. 99, 234801 (2007)
- [2] S. Cialdi, M. Petrarca, C. Vicario High-power third-harmonic flat pulse laser generation, Opt. Lett. Vol 31, 2885 (2006) and Virtual Journal of Ultrafast Science Oct. 2006.
- [3] M. Bellaveglia et al., The RF System of the Sparc Photo-Injector @ LNF, LINAC 06, Knoxville
- [4] G. Di Pirro, F. Anelli, M. Bellaveglia, D. Filippetto, S. Fioravanti, E. Pace, L. Catani, A. Cianchi, Proc. of ICALEPS 2007, pag214-216, Knoxville (Texas, USA)
- [5] B. E. Carlsten, J. C. Goldstein, P. G. O'Shea, and E. J. Pitcher, Nucl. Instrum. Methods Phys. Res., Sect. A 331, 791 (1993)
- [6] C. Lejeune and J. Aubert, Adv. Electron. Electron Phys. Suppl. A 13, 159 (1980).
- [7] L. Catani et al., Rev. Sci. Instrum. 77, 093301 (2006).
- [8] D. Filippetto, Ph.D. thesis, University of Rome; La Sapienza, 2007 (to be published at <http://padis.uniroma1.it/>).
- [9] Cianchi et al., in Proceedings of EPAC 2004, Lucerne, Switzerland (2004), p. 2622.
- [10] M. Ferrario, J. E. Clendenin, D. T. Palmer, J.B. Rosenzweig, and L. Serafini, SLAC-PUB 8400.
- [11] K. Bane and M. Sands, SLAC-Pub-4441.
- [12] D. Alesini et al., NIM A, Vol: 568 Issue: 2 (2006).
- [13] C. Lejeune and J. Aubert, Adv. Electron. Electron Phys. Suppl. A 13, 159 (1980).
- [14] J. Yang, F. Sakai, T. Yanagida, M. Yorozu, Y. Okada, K. Takasago, A. Endo, A. Yada, and M. Washio, J. Appl. Phys. 92, 1608 (2002).
- [15] Cianchi, Phys. Rev. ST Accel. Beams 11, 032801 (2008)
- [16] P.R. Bolton et al., NIM 483, 296 (2002)
- [17] C. Bocchetta et al. (Fermi Collaboration), FERMI@Elettra Conceptual Design Report; (Sincrotrone, Trieste, 2007), <http://www.elettra.trieste.it/docs/FERMIelettra-CDR.pdf>.
- [18] M. Ferrario, K. Flöttmann, T. Limberg, P. Piot, and B. Grigoryan, TESLA FEL 2001-03.
- [19] S. J. Park, J. H. Park, Y.W. Parc, C. B. Kim, C. D. Park, J. S. Oh, J.Y. Huang, I. S. Ko, D. Xiang, and X. Wang, in Proceedings of FEL 2005, Stanford, California, USA (2005), p. 600.
- [20] F. Marhauser, in Proceedings of EPAC 2004, Lucerne, Switzerland (2004).
- [21] M. Ferrario, M. Boscolo, V. Fusco, C. Vaccarezza, C. Ronsivalle, J. B. Rosenzweig, and L. Serafini, The Physics and Application of High Brightness Electron Beam (World Scientific, Singapore, 2002).
- [22] L. Serafini and M. Ferrario, AIP Conference Proceedings, 581, 87, (2001)
- [23] B. Marchetti et al., "Beam Slice Characterization at SPARC High Brightness Photoinjector", Proc. of PAC 2009
- [24] S. Reiche, Nucl. Instr. and Meth. A 429 (1999) 243.
- [25] L. Giannessi, Overview of Perseo, a system for simulating FEL dynamics in Mathcad, , in: Proceedings of FEL 2006 Conference Germany, <http://www.jacow.org>.

4 MACHINE PHYSICS

4.1 FEL Physics

4.1.1 Introduction

The choice of FEL configurations at SPARX is based on user-defined requirements on the spectral properties of the output FEL pulses, i.e., output wavelength, peak output power, X-ray polarization, and required average repetition rate. Typically, users expect an FEL-based light source to deliver $\geq 10^{14}$ photons/sec in a 0.1% bandwidth at a tunable wavelength to the experimental end station. The time structure of the pulse has to be matched to the characteristic timescales of physical processes being studied. For X-ray imaging and other high intensity studies, the photons should be delivered in ultra-short, high intensity pulses. In contrast, spectroscopic studies require limited peak intensity so as to avoid non-linear processes, but also require high repetition rates to collect sufficient data in acceptable experimental periods. Other requirements that drive the SPARX FEL design concern tunability, pulse duration, pulse-to-pulse stability, timing and synchronization, degree of polarization, and repetition rate. The layout of the SPARX FEL is designed with the aim of maximizing the flexibility of the source in order to match the experimental needs in the widest variety of conditions.

4.1.2 General Spectral properties

The SPARX science program requires that the FEL architecture access a large range of wavelengths from 40 eV (120 nm) to ≥ 1 keV (1.2 nm). The fluctuations in the central wavelength, without a monochromator in the beamlines, should be smaller than the pulse line-width.

Bandwidth

Many SPARX users are expected to request spectral bandwidth that is close to Fourier-transform limited. The most demanding experiments are likely to employ Resonant Inelastic X-ray Scattering (RIXS) to study elementary excitations in condensed matter. RIXS will require MeV resolution for studies of such phenomena. Providing ultra-high resolution pulses with $\Delta\lambda/\lambda \sim 10^{-5}$ in the soft X-ray regime is likely to require the passage of the FEL pulse through a monochromator, and might lead to large intensity fluctuations.

Harmonic content

Harmonic generation is an intrinsic process in FEL amplification. The higher order harmonics are an effect of amplification, and constitute a valuable source of radiation at shorter wavelengths. The implementation of an undulator tuned at the second or third harmonic of the main undulator may be used to enhance the higher order harmonics emission induced by residual current modulation. The SPARX FEL exploits a variant of such a high gain harmonic generation (HG) scheme in order to maximize the extension to shorter wavelengths of the spectral range of operation. Furthermore the reconstruction of single pulse, X-ray images generally requires the presence of a reference signal from a scattering source, pinhole, or Fresnel lens with an outermost fringe spacing of the order of the spatial resolution. Recently, researchers at the FLASH FEL have demonstrated an algorithm – called the “shrinkwrap technique [1]” – to reconstruct high resolution images by illuminating the experimental sample with a few percent of third harmonic radiation. The

unscattered harmonic signal provides a phase reference from which the image of a sample on a clean background can be reconstructed from the outer edges of the sample plane inward. Higher order harmonics produced at SPARX may be exploited to provide admixtures of fundamental/harmonic signal at the sample, ensuring optimized conditions for the above diagnostic scheme.

Tunability

Spectroscopic experiments at SPARX will demand the tunability of the FEL output near to and across edge transitions. The undulator system and FEL architecture should allow rapid tuning, fully under user control at the level of the spectral bandwidth of the output pulses. We will design the system to be tunable over tens of eV on the time scale of minutes with minor adjustments of the electron beam characteristics.

Coherence

Most experiments at SPARX, such as single pulse imaging, coherent scattering, studies of nanostructures, and soft X-ray, coherent multidimensional absorption spectroscopy require that the X-ray pulses have a very high degree of spatial coherence [see chapter 1]. Fortunately, the high gain FEL process intrinsically produces pulses that typically contain ~99% of the radiation in the lowest order mode. In other words they are nearly diffraction limited. When operated in seeded (or self-seeded) configurations the SPARX FEL will have the additional intrinsic feature of showing an improved phase coherence temporally as well as spatially. Full temporal coherence is not available in the SASE configuration that will give the furthest reach in X-ray energy, except when producing very short, single spike pulses. As temporal coherence is not a property of the radiation available at synchrotron light sources, the first generation of SPARX users is unlikely to demand full coherence at the shortest wavelengths. Also temporal coherence is not required for imaging.

4.1.2.1 *Pulse intensity*

To meet user requirements the SPARX FELs will have to produce X-ray pulses with a large range ($\sim 10^5$) of intensities. A tunable absorber based on a variable pressure gas chamber in the transfer lines from the undulators to the experimental stations, is foreseen. The light intensity may be however tuned by changing the operation parameters of the FEL.

Linear processes

For the investigations of linear phenomena, minimum single pulse intensities must be consistent with measuring photoemission signals and recording changes in X-ray absorption by the sample, without at the same time damaging the sample. As the single pulse intensity is increased, 1) damage of the sample becomes more and more likely, 2) the electric field associated to the pulse becomes sufficiently strong that broadening of the line spectrum of the sample exceeds line spacing, and multi-photon processes become more likely. Typically, these considerations limit the linear regime to FEL output intensities in the range of $10^7 - 10^8$ photons on the sample. To gather sufficient data in experimental runs commensurate with those that typify synchrotron light sources, users would prefer pulses rates as high as possible limited only by the characteristic relaxation times of the processes under investigation and by removal of heat deposited in the sample.

For many experiments, these requirements imply that producing bursts of FEL pulses spaced by $\sim 0.1 \mu\text{s}$ is acceptable to many users. Pulse trains,

composed of 20/30 pulses, could be achievable if needed with the SPARX LINAC structure.

Pulse intensity: non-linear processes

In contrast with spectroscopy and the study of linear processes, single pulse X-ray imaging and the investigation of multi-photon processes, and non-linear dynamics are likely to require as many as $\geq 10^{12}$ UV/X-ray photons in a single pulse. At such high fluence, X-ray absorption in the sample and the consequent hydrodynamic motion or ablation will destroy the sample, before sufficient signal is received in the experimental detectors. Consequently the duration of the FEL pulse must be less than the ablation time of the sample or the hydrodynamic expansion time over a resolution element. It is giant and short X-ray pulses such as these that have made possible the spectacular imaging experiments at the FLASH free electron laser in Hamburg [1].

Pulse-to-pulse stability at SPARX

Time-resolved spectroscopy and scattering studies of ultra-fast dynamical processes such as phase transitions generally require X-ray probes to be highly stable both in intensity, wavelength and bandwidth. For some experiments jitter in these features is tolerable if the characteristics are measured and recorded on a pulse-to-pulse basis. If, however, the jittering X-ray pulse excite – on the average – too small a fraction of the molecules or materials, the average signal-to-noise at the detector can become unacceptably low. In addition, sufficiently stable pulse characteristics can allow the experimenter to make real time subtraction of backgrounds via pump on/pump off experiments.

Stability levels at synchrotron light sources can be at the level of 0.1% – 1%, stability that seems extremely difficult for pulsed LINAC-based sources to achieve. In the SPARX design we will push toward achieving the highest level of stability practical. Stability at the 5% level seems both practical with respect to FEL design and also acceptable with respect to the requirements for FEL-based experiments (see chapter 1). Detailed analysis of the achieved stability will be carried on with start-to-end simulations and multivaried analysis of the system parameters. However, we expect that users will be able to develop adequate background subtraction techniques if we can achieve stability at the few percent level.

4.1.2.2 Temporal characteristics

Pulse duration at SPARX

The widespread availability of table-top terawatt lasers has made pump-probe (stroboscopic) experiments a ubiquitous approach for studying ultra-fast processes. At wavelengths accessible with lasers, dynamics can be studied with 1 – 10 fs resolution. In such experiments the sample is first excited with a suitable wavelength of radiation – the pump. A subsequent light pulse, with a duration much shorter than the characteristic time of the process under study, then probes the transient state created by the first pulse. By varying the delay time between the pump and probe pulses one can measure the relaxation of the excited state. By generating ultra-fast electron bunches and using an ultra-short seed laser, SPARX will be ideally suited to extend stroboscopic techniques to VUV and X-ray wavelengths.

Stroboscopic studies of solution phase chemistry and biochemistry, of reaction and solvent dynamics, and of magnetization dynamics will require pulses of 20 - 200 fs pulse duration. Likewise single pulse experiments such as molecular imaging and time-resolved coherent scattering with nanometer spatial resolution will require pulse durations in the range from 20 – 30 fs.

Presently a new area of experimental physics is emerging [2] - "attosecond science". In the future, we expect that users of SPARX may request X-ray pulses as short as few hundred attoseconds.

Different electron beam configurations will allow the control of the radiation pulse duration from several hundred to few femtoseconds. An option for sub-femtosecond pulses is under study too. The radiation pulse duration may be controlled by seeding the FEL with a short radiation seed and by exploiting the non-linear pulse evolution after saturation, which can lead to the production of pulses shorter than the FEL cooperation length [3]. Other techniques to generate very short pulses with FELs have been proposed by Fawley and Zholents [4], by Saldin [5] et al. and other authors [6]. The SPARX system of undulators will be laid out to permit implementing one of such schemes of attosecond pulse generation should sufficient demand arise from users.

Coherent synchrotron radiation (CSR) occurs when synchrotron radiation emitted from the back of electron pulse can propagate through the vacuum chamber to overtake and interact strongly with the head of the pulse as the beam passes through a dipole. For multi-GeV electron beams pulses with a duration < 1 ps, carrying 1 nC, the emission of CSR when the beam passes through bending magnets can rapidly create an energy chirp from head to tail of the beam. It can also increase beam emittance. The design of the beam spreaders, which direct the full energy SPARX beam to different FEL lines, takes careful account of the potential.

Timing and synchronization

As discussed above, stroboscopic experiments initiate a time-evolving process in the sample with another laser or UV/X-ray pulse. To maximize the useful data collection rate in pump-probe experiments, especially when the dynamics are to be followed with the highest possible temporal resolution, the laser pump (or probe) must be synchronized with an accuracy that is (ideally) an order of magnitude smaller than the duration of the probe pulse. In principle, data can be taken without active synchronization of the pump and probe if the arrival time at the sample can be measured with an sufficient accuracy ~ 10 fs.

Timing and synchronization controls using both time domain and frequency domain techniques have been demonstrated at the <20 fs level by groups at MIT and Lawrence Berkeley Laboratory (LBNL) respectively. The stabilized optical fiber systems such as those developed and tested at LBNL could be used to measure pulse arrival times when SPARX is operated in a Self-Amplified Spontaneous Emission (SASE) or self-seeded mode. The SPARX FEL systems using seed laser pulses will be designed to assure active synchronization the possibility of auxiliary laser pulses to within <20 fs of the UV/X-ray pulse.

A large class of experiments such as single pulse imaging and coherent scattering require no synchronization signal beyond the trigger pulse that activates the photocathode laser at the front end of the SPARX LINAC.

Pulse repetition rate

The radiofrequency (RF) repetition rate of the SPARX LINAC is limited to 100 Hz. In standard operation conditions a single electron bunch per RF pulse train is expected.

From the point of view of the users, the pulse repetition rate would be ideally limited by the relaxation time of the physical process being studied. Consequently, rates as high as ~ 10 MHz are interesting for a large class of experiments. Such high rates could be provided in a burst mode at SPARX where higher repetition rates could be achieved by filling a larger number of bucket in the RF pulse. Practical considerations such as thermal damage or ablative processes in the sample may preclude even short bursts of pulses at relaxation-limited rates; such is, for example, the case for RIXS experiments. In those experiments that require single pulses so intense as to damage or ablate the sample, the relevant maximum useful repetition rate will be governed by how fast the sample can be replaced or annealed.

4.1.2.3 Polarization

Over specific range of photon energies the SPARX FELs will offer full control over the choice of the polarization of the radiation. User-controlled variation from right-handed to left-handed circular polarization is needed for dichroism spectroscopy and studies of magnetic structures in condensed matter. The implementation of polarization rotation schemes on specific undulator beamlines will be the subject of future analysis.

4.1.3 FEL Scaling principles

When an electron bunch with a relativistic factor, γ , traverses a periodic array of dipole magnets (an undulator), the Lorentz force leads to transverse oscillations of the bunch about the direction of motion causes the beam to emit narrow band quasi-monochromatic radiation (see Figure 4.1). In the beam frame the wavelength of the radiation is the backscattered value, λ_w/γ , of the Lorentz contracted period, λ_w of the undulator field, B_w . Transforming to the laboratory frame, one observes the radiation Doppler upshifted by a factor $2\gamma/(1+\theta_{\text{rms}}^2)$, where θ_{rms} is the rms angle by which the electron trajectory is bent in the undulator.

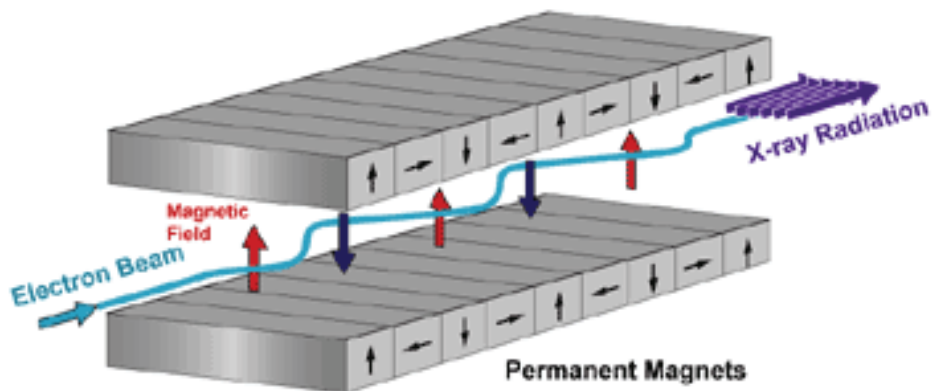


Figure 4.1: Electron trajectory in the field of a linearly polarised undulator

By reducing the mean longitudinal velocity of the bunch, the transverse undulations thereby enhance the rate at which the emitted radiation slips past the electrons in the bunch. If that rate is such that the radiation slips one optical wavelength per undulator wavelength, then the electrons will oscillate in

phase with the field, continually lose energy to the field. The growth of the field increases the rate of energy loss by the electrons.

As the signal grows, the ponderomotive potential created by the undulator field and the radiation field, bunches the electrons into thin packets spaced by the resonant wavelength. The bunched electrons begin to radiate coherently leading to an exponential growth of the radiation field that co-propagates through the undulator along with the electron beam. The result is an exponentially growing radiation field with a power that grows as [7, 8, 9, 10]

$$P = \alpha P_n e^{z/L_g} \quad (4-1)$$

In equation (4-1) P_n is the initial signal strength, α is a coupling coefficient between the signal strength and the dominant mode, and z is the distance along the undulator. L_g is the gain length, that is, the distance for an e-folding of the radiation intensity.

The resonance condition that links the radiation wavelength, λ_r , the undulator wavelength and the energy of electrons beam is

$$\lambda_r = \frac{\lambda_u}{2\gamma^2} (1 + K_{rms}^2) \quad (4-2)$$

where $K_{rms} = K/\sqrt{2} = a_w$ for a planar undulator and equals K for a helical undulator. The numerical value of K can be derived from (4-3). The energy of the electron beam is $\gamma m_e c^2$. The dimensionless vector potential of the undulator field, a_w , is set by the maximum magnetic field on axis, B_w and the undulator period, λ_u . In physical units,

$$a_w = 0.667 \lambda_u [cm] B_w [T]. \quad (4-3)$$

The gain of the FEL and the speed of the bunching process in a cold (zero emittance) beam with no incoherent energy spread is described by the universal scaling parameter, ρ [9, 9, 10];

$$\rho = \left(\frac{a_w \omega_p \lambda_u}{8\pi c} \right)^{2/3} \propto \frac{I^{1/3} B_w^{2/3} \lambda_u^{4/3}}{\gamma} \quad (4-4)$$

where ω_p is the relativistic plasma frequency,

$$\omega_p^2 = \frac{4\pi n_e r_e c^2}{\gamma^3} \quad (4-5)$$

and a_w is the dimensionless vector potential of the undulator. In equation (4-5) n_e is the electron density and r_e is the classical radius of the electron. The electron density is related to the beam radius r_b and the beam current by

$$I = \pi c e n_e r_b^2 \quad (4-6)$$

In a linear undulator the FEL scaling parameter may be expressed as

$$\rho = \frac{1}{4\pi\gamma} \left[(f_B(\xi(K)) \lambda_u K)^2 \frac{I}{I_A} \frac{2\pi^2}{\Sigma_B} \right]^{\frac{1}{3}} \quad (4-7)$$

where Σ_b is the electron beam cross section, I is the e-beam peak current and $I_A = ec/r_e$ is the Alfvén current. The function $f_b(\xi) = J_0(\xi) - J_1(\xi)$ where $\xi = K^2/4(1 + K^2/2)$, is the Bessel factor arising from the average over the longitudinal fast motion typical of linear undulators.

The e-folding (gain) length, L_G , for the power carried by the electromagnetic field as computed from the 1-dimensional theory in the cold beam limit is given by the general expression,

$$L_G = \frac{\lambda_w}{4\pi\rho \operatorname{Im}(2\mu)} \quad (4-8)$$

where $\operatorname{Im}(\mu)$ is the solution to the (cubic) eigenvalue equation for the FEL instability written for the field intensity. In the cold-beam, 1-D limit, $\operatorname{Im}(\mu) = \sqrt{3}/2$. After ~ 20 gain lengths (in a distance L_{sat}) the FEL output signal saturates at a power, $P_{sat} \sim \rho P_{beam}$.

The line width, $\Delta\lambda/\lambda$, of the output radiation from the SASE process in the classical regime is the root mean square of the homogeneous and inhomogeneous broadenings¹. The homogeneous width is equal to ρ and is related to the temporal spikes that characterize SASE output. Inhomogeneous broadening arises from errors in the beam energy, undulator field and undulator wavelength; their contribution to $\Delta\lambda/\lambda$ can be found by differentiation of the resonance condition.

If one desires a temporally coherent pulse, an input seed with a power level substantially larger than the shot noise must be provided. An estimate of the shot noise equivalent power is given by [10,11,12]

¹ Assuming the inhomogeneous broadenings over the uncorrelated current distribution. Increasing the gain length the local (slice) inhomogeneous broadenings could paradoxically have the opposite effect.

$$P_{noise} \approx \frac{8\pi c}{5} \frac{\rho^2 E_{beam}}{\lambda_0} \quad (4-9)$$

where $E_{beam} = m_0 c^2 \gamma$ is the electron beam energy. Experiments based on frequency up-conversion of the Ti:Sapphire fundamental wavelength in rare gas atoms have demonstrated the possibility of generating high-order harmonics in the EUV region of the spectrum [13, 14, 15, 16, 17]. Such sources, providing sufficient power density to overcome the electron beam shot noise exist up to photon energies of about 100 eV. The high-order harmonics result from the strong non-linear polarisation induced in the rare gases atoms, such as Ar, Xe, Ne and He, by the focused intense electromagnetic field of the "pump" laser. This method represents a promising technique to seed FEL amplifiers at short wavelengths [18]. Successful seeding experiments have been recently realized at SCSS Test Acc [19] and the SPARC test facility will provide important information on the viability of such a scheme [20]. A detailed analysis of the seed source characteristics required for SPARX and the expected seeded FEL performances is given in Sec. 4.5. At photon energies higher than 100 eV the possibility to improve the longitudinal coherence properties of the radiation is provided by self seeded/regenerative amplifiers schemes, which are based on the injection of part of the radiation generated by the FEL or by regenerative amplifiers.

4.1.3.1 Limitations on the FEL gain

The cold beam limits seems highly idealistic. In realizable electron beams, three principal effects can act to suppress the bunching process in the FEL with the consequence that the gain will be reduced [21]. With respect to the FEL design such effects will increase the gain length from the value given in Eq. (4-8). The potentially deleterious effects are 1) instantaneous (incoherent) energy spread in the beam, $\Delta\gamma/\gamma$. 2) beam emittance, ε , i.e. the spread in electron radial position and angles, and 3) diffraction of the radiation out of the beam.

Both instantaneous energy spread and beam emittance lead to a spread in the mean longitudinal velocity $\langle v_z \rangle$ of the beam electrons. As $\langle v_z \rangle$ increases to the level that that the longitudinal drift of electrons is a large fraction the radiation wavelength as the beam traverses one gain length as computed from Eq. (4-8), the gain will be strongly suppressed. Quantitatively, the FEL will be insensitive to the energy when

$$f_1 = \frac{4 \Delta\gamma}{\rho \gamma} < 1 \quad (4-10)$$

The condition on normalized beam emittance, ε_n , is a combination of energy spread and diffraction considerations. Often this condition is stated as requiring that the phase area of the electron beam should not exceed that of the diffraction-limited radiation; i.e.,

$$f_2 = \frac{4\pi\epsilon_n}{\lambda_r\gamma} < 1 \quad (4-11)$$

Finally, the non-linear coupling of the radiation field and the beam implies that the bunching rate (and therefore the gain) will be decreased if the radiation diffracts out of the electron beam too rapidly. Therefore, Rayleigh range of the radiation should be greater than the gain length;

$$f_3 = \frac{L_G}{Z_R} < 1 \quad (4-12)$$

The parameters, f_i are linked by the resonance condition; [22] has shown that

$$f_1 = f_2^2 f_3 / 4 \quad (4-13)$$

and have characterised [22] the sensitivity of the FEL gain to the variations these dimensionless parameters. Figure 4.2 from [22] shows examples of the gain surface for the case of weak and strong diffraction.

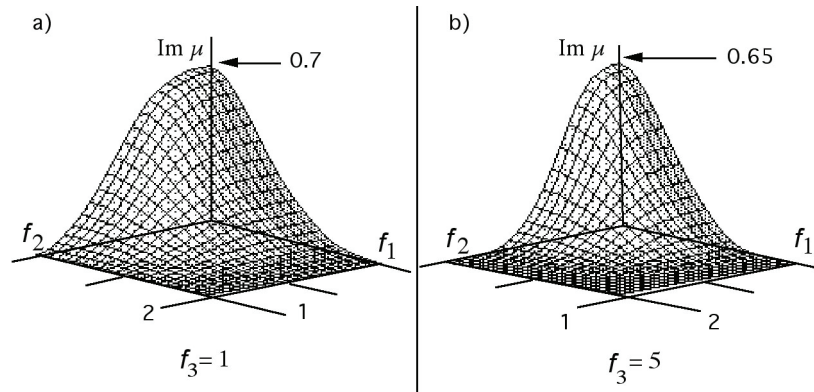


Figure 4.2: Gain surface, $Im \mu$, versus scaled emittance and energy spread for a) small and b) large values of the diffraction parameter, f_3

4.1.4 Beam emittance and accelerator parameters

The diffraction and the beam size depend on both the emittance of the beam and on the strength of the focusing provided by the undulator and associated quadrupoles. These characteristics are related by the optical functions (Twiss parameters) of the beam transport. The motion of a beam through a linear focusing channel can be described as the solution of the Hill's equation,

$$u'' + k(s)u = 0 \quad (4-14)$$

where u represents the transverse motion of beam particles and $k(s)u$ is the magnetic restoring force as a function of the distance along the transport, s . The solution to the transport equation can be written as a quasi-periodic function

$$u(s) = \sqrt{\varepsilon\beta(s)} \cos[\varphi(s) - \phi(0)] \quad (4-15)$$

Eq.(4-15) connects oscillation of particles in the beam with the beam emittance and with the beta function, $\beta(s)$, which is $(2\pi)^{-1}$ times the local wavelength of the oscillatory motion of the particles. The beta function. Defining two functions $\alpha(s)$ and $\gamma(s)$ by

$$\begin{aligned} \alpha(s) &\equiv -\frac{1}{2} \frac{d\beta(s)}{ds} \\ \gamma(s) &\equiv \frac{1 + \alpha^2(s)}{\beta(s)} \end{aligned} \quad (4-16)$$

one has equations for the beam envelope and beam divergence,

$$\begin{aligned} E(s) &= \sqrt{\varepsilon\beta(s)} \\ A(s) &= \sqrt{\varepsilon\gamma(s)} \end{aligned} \quad (4-17)$$

respectively.

4.1.5 Computational tools

The optimization of the FEL in terms of saturation length is obtained by using scaling laws of the gain length L_g vs. undulator/beam parameters and by cross comparing the results with those of simulation codes solving the particles/fields evolution equations. Different scaling functions describing the gain depression in presence of non-ideal beam parameters are available [23,24] and have been implemented in order to evaluate the required undulator length to reach saturation with a given set of beam parameters. The problem may be reversed, i.e. given the undulator length which may be constrained by other considerations as those related to costs and space, we may optimize the undulator characteristics and define the required beam parameters in order to reach saturation within its length. On the other side, the codes have been used to validate the scaling laws and to estimate parameters as radiation size, divergence, spectrum and other quantities which may be only qualitatively inferred from a theoretical point of view.

4.1.5.1 GENESIS 1.3

GENESIS 1.3 [25] is a time-dependent three-dimensional FEL code. Its focus is to simulate single-pass free-electron lasers, both FEL amplifiers and

SASE FELs, although the flexible input can easily be used to extend the capacity of GENESIS 1.3 to cover FEL oscillators or multistage configurations.

GENESIS 1.3 has its origin in the steady-state 2D code TDA3D, although the two codes no longer have much in common except for some naming conventions. Macro particles represent the electron beam in all dimensions of the 6D phase space. The differential equations for energy and phase are solved by a 4th order Runge-Kutta solver, in which the field amplitudes of the discretized radiation field and electrostatic field are interpolated to the particle positions. Distinct from the main undulator field, the quadrupole and dipole fields combine many field sources such as the natural focusing of the undulator, strong focusing quadrupoles, undulator field errors and corrector magnets (steering magnets). The radiation field is described in the paraxial approximation, in which the field is separated into a dominant, fast oscillating term and an amplitude, which varies slowly in magnitude and phase. The transverse profile of the field is discretized on a Cartesian grid with uniform spacing. The Alternating Direction Implicit (ADI) solver guarantees an unconditionally stable, fast, and memory-efficient method to advance the radiation field at each integration step. GENESIS 1.3 supports two modes of calculations: steady-state and time-dependent simulations. Steady-state simulations are based on the assumption of an infinitely long electron bunch and a radiation field with no longitudinal variation of any parameter. The longitudinal description can be reduced to a single wavelength (bucket) with periodic boundary condition in the ponderomotive phase of the macro particles.

4.1.5.2 PERSEO

PERSEO [26] is a library of functions devoted to the simulation of FEL dynamics in the MathCAD environment. Functions for the generation of phase space variables, for the solution of the pendulum-like FEL equation and for manipulating the phase space in a number of devices are available. These functions can be combined in MathCAD worksheets, to model more complicated situations as time dependent simulations, three-dimensional simulations, oscillator FEL configurations, optical klystrons, cascaded FELs.

The core of the library consists of a routine that solves the pendulum-like FEL equations coupled with the field equations. This routine self-consistently includes the field variables for the higher order harmonics. In an oscillator FEL, in a seeded FEL, and more generally when the transverse properties of the radiation may be considered as a constraint of the problem, the coupling coefficient in the pendulum equation must be corrected by a proper filling factor. In general when the radiation size is the result of the balance between diffraction and focusing induced by the gain, as in a single pass FEL, a filling factor coefficient may be derived from the Xie scaling laws [23] by calculating the ratio between the Xie factor with and without diffraction effects. PERSEO and GENESIS have been compared in different situations and despite of the different physical assumptions a remarkable agreement has been observed [27].

4.1.5.3 PROMETEO

PROMETEO is a standalone simulation code with similar characteristics of PERSEO. It is capable of simulating higher order harmonics and of simulating FELs in cascaded configurations. It has been used mainly in the preliminary set-up of the SPARX configurations.

PROMETEO is a 1D, multiparticle code [28] based on a modified version of the Prosnitz, Szoke, and Neil formulation of the FEL dynamical equations [29, 30]. The original model has been generalized to include the effect of beam emittance and the undulator errors. The code is capable of accounting for the evolution of the fundamental harmonics and for the coherent generation of higher-order harmonics in SASE or oscillator FELs, including optical klystron and segmented undulators. It has been used in the preliminary set-up of the SPARX configurations as well as in the analysis of specific cases of interest for SPARX.

4.1.5.4 Tools validation

The scaling formulae do not account for a number of effects which are, in contrast, implicitly included in the models reproduced by the simulations (segmented wigglers, betatron oscillations and pulse propagation effects). Therefore, we have selected a set of parameters close to the parameter space of SPARX and have compared the results of the Xie scaling [23] and the DOP (Dattoli, Ottaviani, Pagnutti [24]) scaling with the predictions of GENESIS 1.3 and PERSEO, both run in “time dependent” mode. The parameters used in the simulations are shown in Table 4.1.

Table 4.1: Test case beam parameters

<i>Beam Energy</i>	<i>1.2 GeV</i>
Peak Current	1 kA
Normalized emittance	1 mm mrad
Energy Spread	$2 \cdot 10^{-4}$
Twiss β	6 m
Undulator period	28 mm & 42 mm
K min - max	1.07 - 2.26 (28 mm) 1.30 - 2.32 (42 mm)

The undulator strength K has been varied consistent with the resonance condition. Good agreement is found by multiplying the Xie output by the numerical factor 1.3 and the DOP output by the factor 1.2².

² Part of the observed difference is related to the definition of saturation, which is the peak power saturation in the analytical cases and the bunch energy saturation in time dependent simulations.

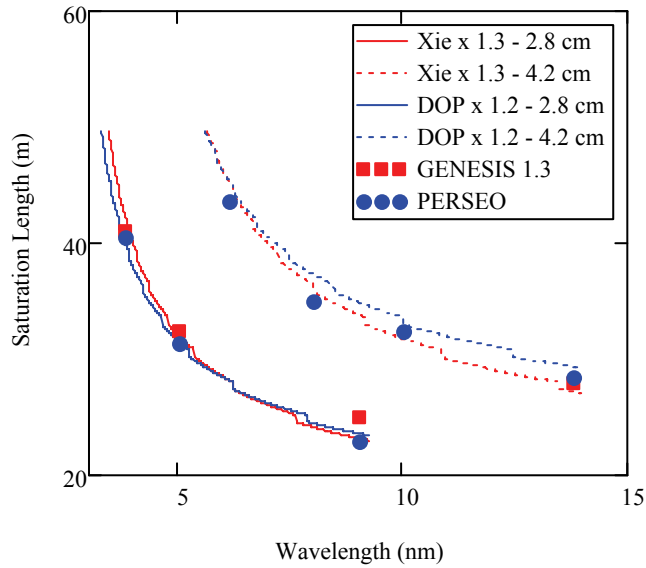


Figure 4.3: Comparison between GENESIS 1.3 and PERSEO simulations with Xie/DOP analytical models. The analytical models are corrected to account for the presence of segments between the undulator and are multiplied by an empirical factor /1.3 for Xie, 1.2 for DOP) to improve the matching with the simulations.

4.1.6 Options for SPARX FEL architecture

To achieve high power FEL output over a large range of X-ray energies from 40 eV to 2 keV, we design the family of SPARX undulators to be able to run in multiple configurations.

The fundamental architectures of the SPARX system are

- 1) SASE operation: The simplest and most common FEL architecture is self-amplified spontaneous emission (SASE) in which the radiation starts from shot noise of the electron beam and amplifies as the beam passes through the undulator. This process produces short wavelengths without the requirement of an external master oscillator source. The SASE output has high peak power and a high degree of transverse coherence. However, the temporal coherence of the generated pulses is only partial, and the intensity fluctuations are important.
- 2) SASE operation with the option of harmonic up-conversion: If the SASE amplifier is interrupted when the bunching is maximum – at roughly 80% of saturation – the bunched beam will contain large Fourier components of the current at the harmonics of the SASE fundamental frequency. If this bunched beam is immediately injected into a radiator (undulator) that is tuned to an harmonic, the beam will emit strong, coherent synchrotron radiation to that harmonic.
- 3) An important option in extending the SASE FEL operation range to short wavelengths is by minimizing the beam emittance by reducing the bunch charge. Extremely short radiation pulses with

sub-fs duration and high peak power may be obtained in these conditions.

- 4) Seeded, single-step High Gain Harmonic Generation (HGHG). An alternate configuration for a single pass FEL is High Gain Harmonic Generation (HGHG) [31, 32, 33]. This proven approach is more compact and can produce radiation with the same properties of SASE radiation but with fully temporally coherent pulses and small energy fluctuations [34, 35]. In this configuration, an external laser source is injected as a seed into a first undulator where it induces an energy modulation on the electron beam. This energy modulation is converted into a spatial density modulation as the electron beam crosses a dispersive section. Passing then through an other undulator – the radiator – the microbunched electron beam coherently emits at the n th harmonic of the laser fundamental frequency. The tuning of the radiator selects the amplified harmonic. The properties of the output radiation are determined by the seed laser, which can have a high degree of temporal coherence. Seeded FEL amplifier operation in combination with harmonic generation has been demonstrated experimentally at both mid-infrared and VUV wavelengths. The advantages of this scheme in the EUV Soft-X-ray spectral range have still to be proven. A complication of using a seeded architecture is that the electron beam energy, which sets the central wavelength of the gain-bandwidth, must be stabilized to well within the gain bandwidth of the FEL process. That is, the energy should be stable on a pulse-to-pulse basis to $\sim\rho/3$.

- 5) HHG plus HGHG: As anticipated in the previous section, an alternate way to reach shorter wavelengths is to use a seed laser in operating in the VUV domain. Developments in femtosecond laser technology are making possible new, coherent, short wavelength sources. One such source, called High-Order Harmonics Generation (HHG), is based on the interaction between the laser beam and a gas target. Fraction of a microjoule energies can be obtained at wavelengths down to 25 nm. The HHG could be used as seed to inject an undulator, either in the amplifier or in the HGHG configuration to extend the operating wavelength of FELs down to sub nm. A critical question is whether the intensity and phase stability of the HHG harmonics at short wavelength is sufficient for the FEL output to satisfy the stability requirements of users. Such questions will be investigated at SPARC [36] to quantify issues related to the injection of an external radiation seed in a single pass FEL and the analysis of the coupling efficiency of the electron and photon beams in terms of the input parameters [37].

- 6) Multi-stage HGHG cascade: In the multiple step harmonic cascade the radiation output from the first radiator is used as a high power seed to be injected into a downstream modulator-radiator section. Several aspects related to such scheme will be investigated in experiments at SPARC [20] and will be considered in the SPARX layout.

- 7) Multi-bunch regenerative amplifier either self-seeded or externally seeded: In EUV FELs driven by bunch trains from a LINAC with peak currents of $\sim 100 - 200$ A and with an emittance in the range of $1 - 2 \pi$ mm-mrad, a 10 -15 m undulator can produce an overall gain of 20 -30% even in a four mirror resonator. Such a multi-pass, self-seeded Regenerative Amplifier FEL (RAFEL) has been tested at infra-red wavelengths by Nguyen et al. [38] at Los Alamos. In the RAFEL the initial signal grows from noise and is amplified by the SASE process. However, unlike a conventional oscillator, the RAFEL does not store optical energy in the cavity to be switched out after the system reaches saturation. Instead the low-Q ring resonator cavity serves to re-inject a small fraction of the optical power into the undulator as the seed for the next pass. The Los Alamos experiment, consisting of a simple ring resonator with two imaging paraboloids and two annular mirrors had a radiation out-coupling ~ 50 % of the generated radiation. This configuration allowed the RAFEL to come to saturation after few passes through the undulator. The SPARX LINAC is suited for the generation of train of pulses within the same RF macropulse, to be delivered to multiple undulator beamlines to simultaneously serve a larger number of users. As suitable multi-layer mirrors are available in the EUV, a RAFEL may be consistent with the SPARX LINAC operation in a multi-bunch mode with a pulse spacing of several ns. A second injector optimized to deliver longer train of pulses could be implemented as a second option. This would allow a substantial increase of the laser repetition rate and would make particularly interesting the regenerative amplifier scheme.

- 8) Single Spike operation: An ultra-short beam, with very small charge, may have very high brightness, and thus may efficiently drive the SPARX FELs producing ultrashort radiation pulses [39]. We have therefore investigated the creation, through initial velocity bunching [40] at low energy and subsequent chicane bunching, of ultra-low-charge (~ 1 pC) beams of sufficient quality to support strong FEL gain. These beams can drive the FEL in single (or few) spike mode; one may therefore obtain SASE sources with improved coherence X-rays that are both quite stable and have pulse lengths at or below the femtosecond scale.

4.1.7 Overall layout and choice of parameters

The SPARX linear accelerator is configured to provide the beam at energies ranging between 0.96 GeV and 2.64 GeV. A schematic layout of the accelerator structure is shown in Figure 4.4.

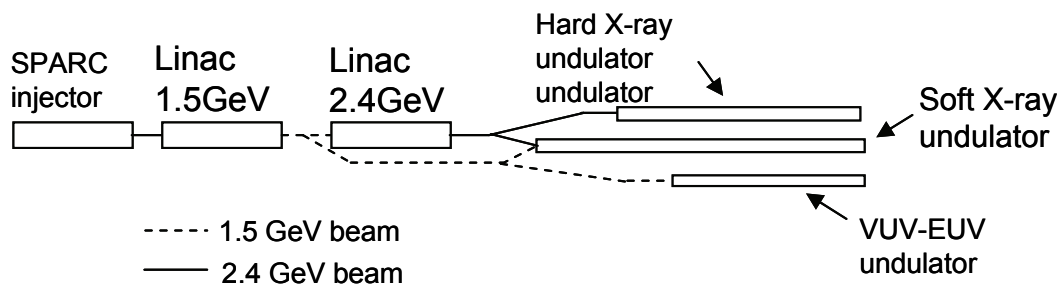


Figure 4.4: Layout of SPARX

A bypass at the first exit, with a nominal energy of 1.5 GeV allows the extraction of the electron beam into the first undulator beam line. The second beam exit at the end of the structure provides the beam at full energy (2.4 GeV).

Three undulator beamlines provide photons in the following photon energy ranges:

- 1) VUV-EUV beamline (30 eV/40 nm - 124 eV/10 nm)
- 2) EUV - Soft X-ray beamline (88.5 eV/14 nm - 1000 eV/1.2 nm)
- 3) X-ray beamline (1000 eV/1.2 nm - 2 keV/0.6 nm)

The large range planned for the soft x-ray beamline is made possible by allowing the line to be fed with the electron beam coming from either the low or high energy exits.

The electron beam energy may be varied over the range from 0.96 GeV to 1.5 GeV at the “low” energy exit and over the range from 1.70 GeV -2.64 GeV at the LINAC exit.

The expected beam parameters depend on the specific conditions of operation - i.e. energy, charge and pulse duration - which may be varied according to the specific needs of the users. In the following sections we will provide more detailed descriptions of the undulator beamlines and the electron beam parameters required to achieve SASE operation over the three specified ranges of photon energy.

4.1.7.1 VUV-EUV beamline (40-124 eV)

For the FEL to operate in SASE mode the undulator length must exceed the saturation length, as described in Sect.4.1.3. The undulator characteristics such as the period length, number of periods, and the strength K, must be optimized as function of the target wavelength range of operation. An analysis of the energy spread induced by the resistive wall wakefield (see sec. 4.3.7) shows that the inner diameter of the vacuum chamber through the undulator should not be smaller than 7 mm. For mechanical strength, the wall thickness

of the beam pipe is 0.5mm. Consequently, the minimum acceptable undulator gap is 8 mm (8.1mm). The undulator field in a pure permanent magnet planar undulator in the Halbach configuration (four blocks per period), scales with the gap opening as

$$B(\lambda_u, g, B_r) = \frac{8B_r}{\pi} \sin\left(\frac{\pi}{4}\right) \exp\left(-\frac{\pi g}{\lambda_u}\right) \quad (4-18)$$

Assuming a remnant field of 1.2 T (a reasonable value after shimming and correction of the undulator poles to achieve the required field quality (see chapter 1), we have plotted in Figure 4.5 the K parameter defined in Eq.(4-3) and the undulator period, vs. the resonant wavelength at the minimum gap of 8.1mm. The plot is computed for a beam energy of 0.96 GeV. An even lower beam energy could be obtained by reducing the gradient in the LINAC, but doing so would degrade the beam quality because of the non-optimized longitudinal phase space balance between the energy chirp required for longitudinal compression, RF fields and longitudinal wakes (see 4.3.7). The lowest photon energy of 40eV is obtained with an undulator period of 34mm.

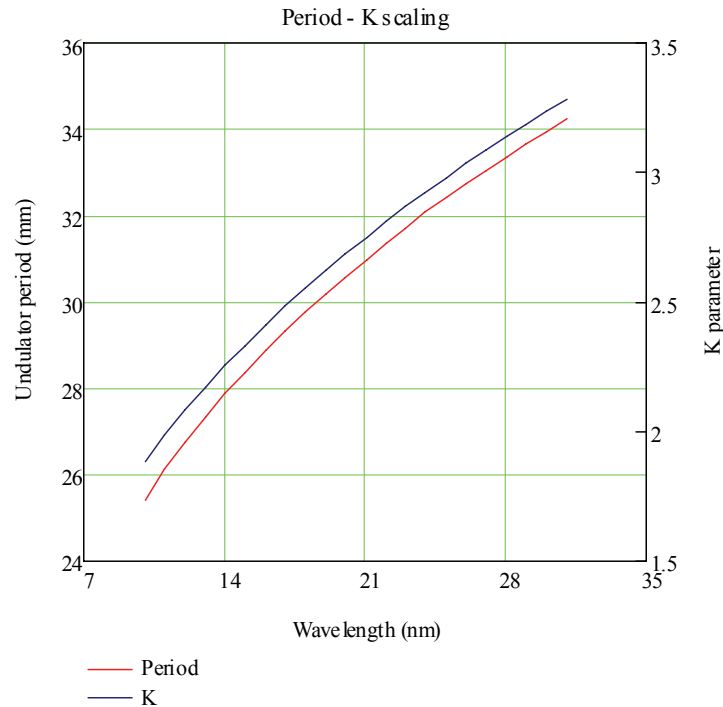


Figure 4.5: Undulator period and strength calculated at the minimum gap of 8.1 mm at the beam energy of 0.96 GeV vs. the wavelength matching the resonance condition

In Figure 4.6 the K parameter vs. the undulator gap is shown.

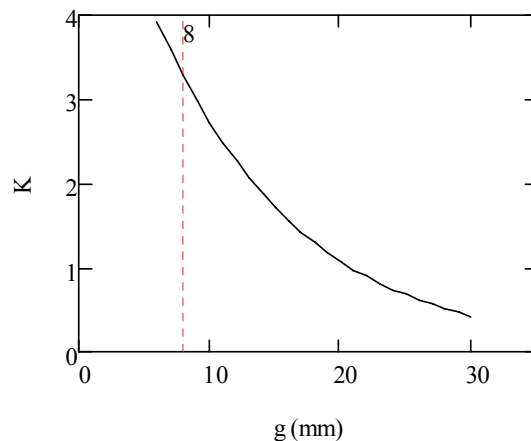


Figure 4.6: K parameter vs. undulator gap with a period of 34 mm.

As reaching saturation of the FEL output becomes more challenging as the wavelength decreases, the undulator length has been optimized for the shortest required wavelength for this beamline. The cold-beam gain length at 10 nm at the nominal beam energy of 1.5 GeV is ~ 70 cm for 1 kA peak current, assuming a rms transverse beam size of 50 microns. As previously described, under non-ideal beam conditions the saturation length depends on the emittances and energy spread of the electron beam. Based on the modified Xie/DOP models, in Figure 4.7 we have estimated the saturation length as a function of the average Twiss parameter in the undulator beamline. The estimate assumes that the beam has the reference parameters of 1 kA, 1 mm-rad transverse emittances, and 2×10^{-4} relative energy spread.

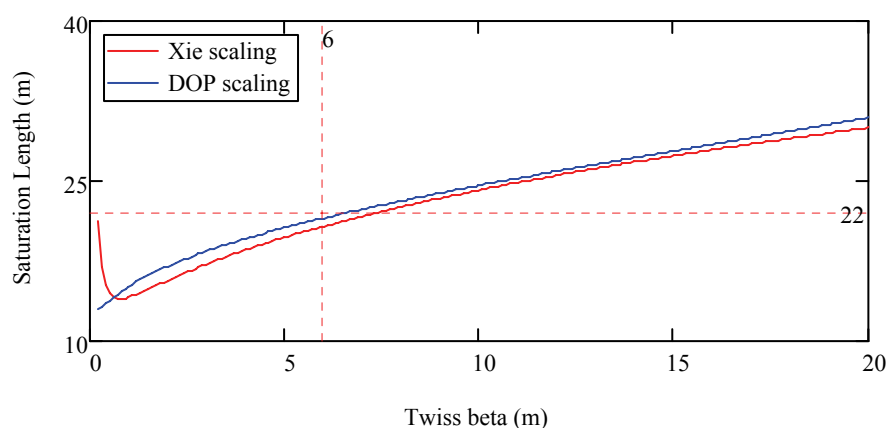


Figure 4.7: Saturation length vs. average β Twiss parameter estimated with Xie and DOP (both corrected) scaling relations

At value of $\beta = 6$ m the FEL saturates within ~ 21 meters of magnetic length. The beam transport in this case is realized with a FODO lattice with alternate gradient quadrupoles located between the undulators. The quoted value of the Twiss β coefficient is compatible with an undulator length of 2.2 m. A more detailed analysis of the undulator optics ensuring the correct matching of the beam is given in the paragraph “Undulator parameters and Undulator optics”. Table 4.2 summarizes the principal undulator parameters .

Table 4.2: List of the main VUV undulator parameters

<i>VUV-EUV Undulator parameters</i>	
Period (mm)	34
Min. gap (mm)	8.1
K (max-min)	3.275-0.3
Periods/segment	65
# of Segments	11

The contour plot in Figure 4.8 shows dependence of the saturation length on the beam quality. The plot has been obtained assuming a peak current of 1kA and an average betatron function, $\beta \sim 6$ m.

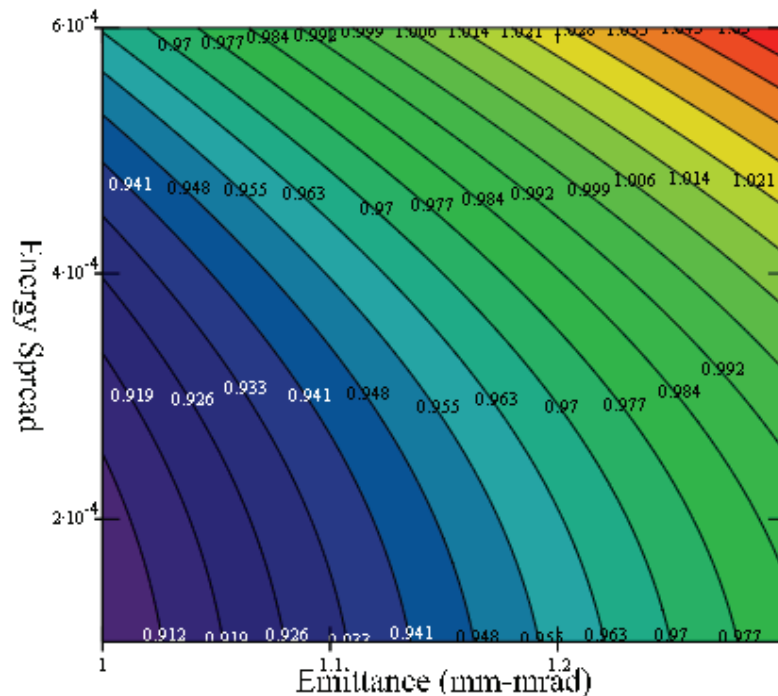


Figure 4.8: Saturation length normalized to undulator length vs. energy spread and transverse emittances for a peak current of 1kA at the wavelength of 10nm/124 eV.

Table 4.3 presents a set of the principal (slice) beam parameters required for reaching saturation with the specified number of undulator segments.

Table 4.3: VUV FEL beam parameters for 5% undulator length contingency for reaching saturation

VUV-EUV FEL Beam parameters operating range

Energy (GeV)	0.96-1.5
Peak Current	> 1 kA
Emittances (slice)	< 1.1 mm mrad
Energy spread (slice)	< 3 10^{-4}

The dependence of the saturation length vs. wavelength, assuming a wavelength variation obtained by gap and energy tuning is shown in Figure 4.9.

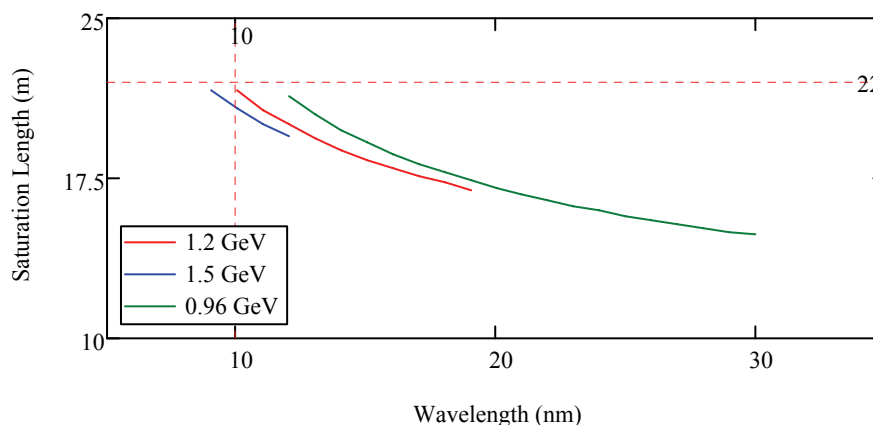


Figure 4.9: Saturation length vs. wavelength at different electron beam energies.

4.1.7.1.1 Undulator parameters and Undulator optics

The VUV-EUV undulator beamline is composed by 11 permanent magnet undulators in the Halbach configuration, with the parameters listed in Table 4.4.

Table 4.4: VUV-EUV Undulator parameters

Period	3.4 cm
Undulator length	2.278m
No. of Periods	67
Gap (min/max)	8.1 / 25 mm
K max	3.275
Remanent field (effective)	1.2 T
Blocks per period	4

A detailed description of the undulator design, mechanical tolerances and field characterization is given in chapter 1. The undulator sections are separated by empty gaps dedicated to the installation of quadrupoles for the beam transport, phase correctors for the compensation of the phase advance between electrons and fields in the longitudinal phase space and for the installation of diagnostics for both the e-beam and the FEL radiation. The electron beam transport in the undulator is realized with a FODO lattice, with alternated gradient quadrupoles. The undulator field introduces an horizontal/vertical asymmetry. We have sketched a layout of one period of the lattice in Figure 4.10.

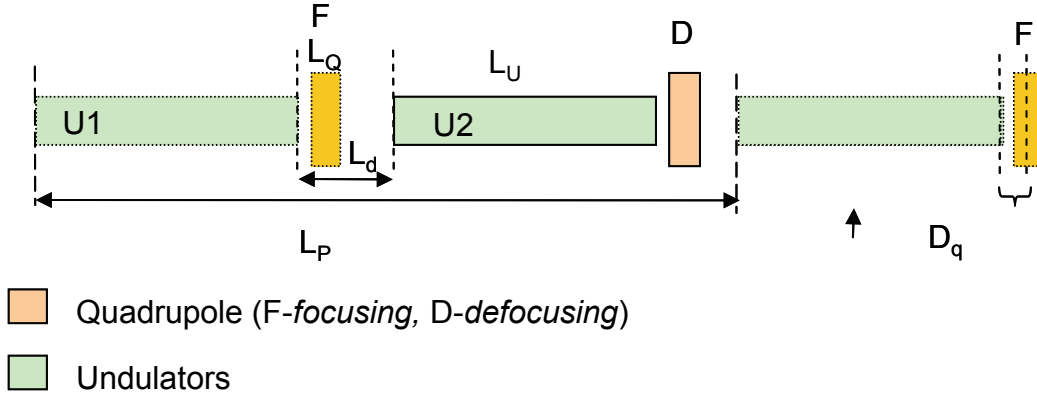


Figure 4.10: Layout of the undulator FODO lattice

The lattice period L_p includes two undulator sections. The quadrupole design has been based on the idea of minimizing the longitudinal space occupation in the gap between the undulators and steering correctors are included in the quadrupoles design as additional coils. A list of the main parameters of the beam line is summarized in Table 4.5.

Table 4.5: Parameters of the VUV-EUV undulator beam line

Lattice period	L_p (m)	5.712
Drift length	L_d (m)	0.578
Quadrupole distance from UM (center of Q.)	D_q (m)	0.204
Beamline Length	L_B (m)	31.058

We have considered non-symmetrically centred quadrupoles within the drifts between the undulators to facilitate the insertion of the diagnostics. We define the average Twiss β_{xy} parameters in (*vertical-y/horizontal plane-x*) the undulator region as

$$\bar{\beta}_{x,y} = \frac{1}{L_{u1}} \int_0^{L_{u1}} \beta_{x,y}(z) dz + \frac{1}{L_{u2}} \int_{L_{u1}+L_d}^{L_{u1}+L_{u2}+L_d} \beta_{x,y}(z) dz \quad (4-19)$$

The matching condition is obtained by imposing the following conditions:

- 1) the Twiss beta parameters in the horizontal and in vertical plane, averaged over the undulator U1 and U2 lengths are equal to the design parameter

$$\bar{\beta}_{x,y} = \beta_d \quad (4-20)$$

- 2) the difference between the Twiss beta parameters in the horizontal and in vertical plane, averaged over the undulator U1 and U2 is minimized.

$$\left| \frac{1}{L_{u1}} \int_0^{L_{u1}} \beta_{x,y}(z) dz - \frac{1}{L_{u2}} \int_{L_{u1}+L_d}^{L_{u1}+L_{u2}+L_d} \beta_{x,y}(z) dz \right| = \min \quad (4-21)$$

The matched Twiss parameters at the undulator entrance depend on the undulator strength K and the e-beam energy. The limitation to the K range of variation is imposed by the vertical size of the vacuum chamber that will not allow the gap to be smaller than 8.1mm. For this reason the matching condition has been calculated at three different K values and at two beam energies. We have considered the maximum and minimum energy and the maximum K , an intermediate K value and $K=0$, i.e. corresponding to the condition of a pure FODO. The highest Quadrupole Integrated Gradient (QIG) is found in the pure FODO mode at the highest energy (*label F in Table 4.6*). The corresponding Twiss parameters α and β at the undulator entrance are given in Table 4.6.

Table 4.6: Characteristics parameters of the undulator beamline, $\alpha_{X-Y}, \beta_{X-Y}$ are the transverse twiss parameters, QIG the quadrupole integrated gradient and K the undulator strength. The undulator period is 34 mm.

Case	Energy (GeV)	K	λ (nm)	QIG (T)	α_x	β_x (m)	α_y	β_y (m)
A	0.96 GeV	3.275	30.64	0.363/-0.733	0.837	7.407	-0.593	4.808
B		2.144	15.89	0.84/-0.99	1.315	8.259	-0.701	4.175
C		-	-	1.11/-1.11	1.567	8.687	-0.73	3.847
D	1.5 GeV	3.275	12.55	1.332/-1.56	1.328	8.281	-0.703	4.159
E		2.8	9.7	1.447/-1.612	1.4	8.402	-0.713	4.067
F		-	-	1.735/-1.735	1.572	8.694	-0.73	3.842

In Figure 4.11 the Twiss β in the X and Y plane along the undulator are plotted for the FODO lattice, in case E of Table 4.5.

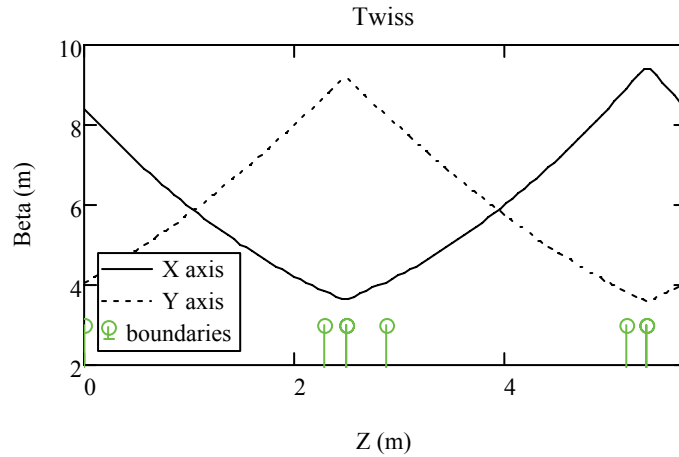


Figure 4.11: Twiss β in the X and Y plane along the undulator (coordinate Z) for the FODO lattice case E of Tab.2. The green marks represent the boundaries of the magnetic elements in the beamline.

4.1.7.1.2 Preliminary simulations

Assuming the beam parameters in Table 4.3, we have simulated the FEL behaviour in a set of reference cases in the requested wavelength range. As resulting from the plot in Figure 4.9 the wavelength tuning of this beamline may be realized with both energy and undulator strength K tuning. Energy tuning at constant (high) K parameter allows the best efficiency and the shortest saturation length, but at the same time involves the simultaneous tuning of several accelerator parameters. Wavelength tuning via undulator strength on the other side, allows to scan a given wavelength range with the same beam conditions. The simulations have been done with PERSEO (1D with correction of diffraction effects) and GENESIS 1.3, (3D, time dependent mode, no harmonics version). In order to provide figures of the pulse energy and number of photons we have assumed a Gaussian bunch current distribution with a charge of 1 nC. Examples with lower charge (200 pC and 50 pC) with the peak current and all the other parameters as listed in Table 4.3 have been considered in the highest energy/shortest wavelength case.

The simulation with two codes ensures additional reliability to the results and provide complementary information. The simulations with PERSEO (black in the table) do not provide information on the beam size and divergence, while the simulations in GENESIS (*grey italic*) do not provide the number of photons at the third harmonic of the fundamental. All the FEL radiation parameters are listed at the saturation position and the peak power is an “average power” in a bunch of Gaussian shape with the pulse energy and r.m.s. duration obtained in the simulation. For this reason it may differ substantially from the instantaneous peak power affected by the spiky nature of the SASE FEL source.

In Figure 4.12 the pulse energy evolution vs. the longitudinal coordinate in the undulator in the 1nC/10 nm case (first line in the table) is shown. Saturation is reached at the end of the beamline, at about 30 m. This correspond to about 22 m of magnetic length as listed in Table 4.7.

Table 4.7: VUV-EUV beamline main parameters. Simulations done in GENESIS 1.3 (grey italic) and PERSEO (black). Pulse parameters are calculated at saturation

	Charge (nC)	Beam Energy (GeV)	Und. K	Wave- length (nm)	Photon Energy (eV)	Magnetic Sat.Length ³ (m)	Peak power (GW)	Pulse Energy (mJ)
A	1	1.5	2.86	10.04	123.47	21.5	3.4	1.7
B	<i>1</i>	<i>1.5</i>	<i>2.86</i>	<i>10.04</i>	<i>123.47</i>	<i>22.5</i>	<i>2.5</i>	<i>1.4</i>
C	0.2	1.5	2.86	10.04	123.47	21.7	3.4	0.37
D	0.05	1.5	2.86	10.04	123.47	21.4	3.3	0.09
E	1	1.25	2.55	12.08	102.7	20.3	2.9	1.5
F	<i>1</i>	<i>1.25</i>	<i>2.55</i>	<i>12.08</i>	<i>102.7</i>	<i>20.6</i>	<i>2.1</i>	<i>1.0</i>
G	1	1.25	2.86	14.46	85.74	19.2	3.0	1.5
H	1	1.25	3.27	18.03	68.76	18.1	3.0	1.6
I	<i>1</i>	<i>1.25</i>	<i>3.27</i>	<i>18.03</i>	<i>68.76</i>	<i>18.8</i>	<i>2.4</i>	<i>1.2</i>
J	1	0.96	2.55	20.48	60.55	17.1	2.6	1.4
K	1	0.96	2.86	24.52	50.57	16.4	2.8	1.5
L	1	0.96	3.27	30.57	40.56	15.6	3.2	1.6
M	<i>1</i>	<i>0.96</i>	<i>3.27</i>	<i>30.57</i>	<i>40.56</i>	<i>15.7</i>	<i>1.7</i>	<i>0.8</i>

	Bandwidth (% - rms)	Duration (rms - fs)	Phot./pulse	Div. (rms μ rad)	Size (rms μ m)	3 harmonic Phot./pulse
A	0.17	200	9×10^{13}	-	-	3×10^{11}
B	<i>0.17</i>	<i>220</i>	<i>7×10^{13}</i>	<i>22</i>	<i>120</i>	-
C	0.18	40	2×10^{13}	-	-	5×10^{10}
D	0.19	10	4×10^{12}	-	-	1×10^{10}
E	0.18	200	9×10^{13}	-	-	3×10^{11}
F	<i>0.18</i>	<i>195</i>	<i>6×10^{13}</i>	<i>27</i>	<i>156</i>	-
G	0.2	200	1×10^{14}	-	-	4×10^{11}
H	0.2	210	1.4×10^{14}	-	-	8×10^{11}
I	<i>0.19</i>	<i>205</i>	<i>1.1×10^{14}</i>	<i>33</i>	<i>140</i>	-
J	0.22	210	1.4×10^{14}	-	-	7×10^{11}
K	0.24	210	1.8×10^{14}	-	-	1×10^{12}
L	0.25	200	2.5×10^{14}	-	-	2×10^{12}
M	<i>0.20</i>	<i>180</i>	<i>1.1×10^{14}</i>	<i>42</i>	<i>198</i>	-

The transition from the exponential regime to the saturated regime is characterized by a sudden increase of the pulse linewidth, a growth of the pulse length and an increase of the beam size and divergence. In Figure 4.13-

³ An arbitrariness in the definition of the saturation position is one of the reasons of the differences between the GENESIS 1.3/PERSEO results. The saturation length has been estimated as the length where the pulse energy reaches 1/e of the maximum energy over the simulation range in z, plus one gain length. This definition is correct if saturation is effectively reached in the simulation range and reduces the arbitrariness in the saturation length parameter calculation.

a,b the pulse structure and spectrum at saturation are shown. The simulation has been obtained with GENESIS and corresponds to line B of Table 4.7.

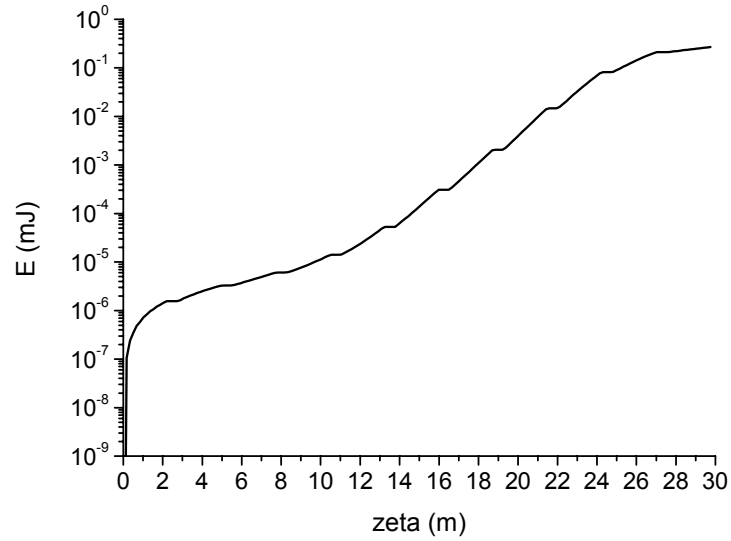


Figure 4.12: Radiation pulse energy as a function of the position along the undulator zeta for a charge of (1 nC).

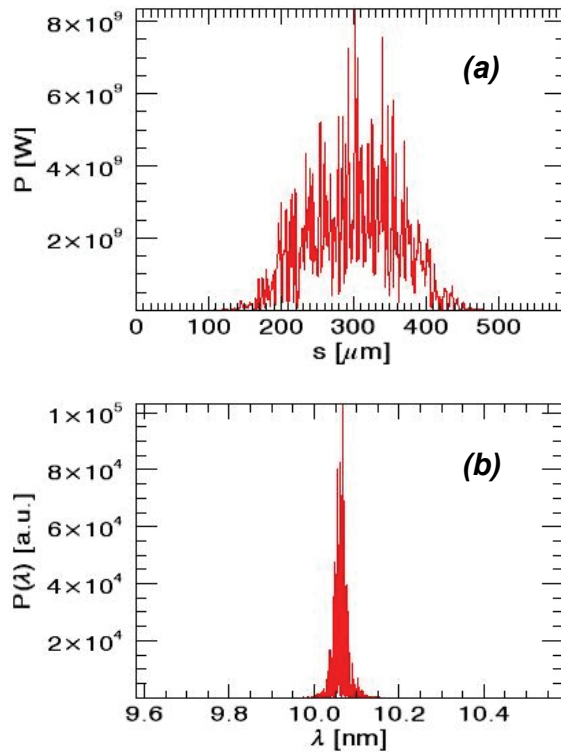


Figure 4.13: Temporal (a) and spectral (b) pulse structure at saturation (at the end of the undulator, 29.75 m). Rms pulselength is ~ 220 fs and rms bandwidth 0.17 %.

The specific example considered has been obtained with an ideal beam with a smooth Gaussian shape and with the slice parameters as indicated in Table 4.3. These parameters constitute the constraint to reach saturation within the available undulator length at the shortest wavelength foreseen for

this beamline (10 nm). An accurate modelling of the accelerator/compressor system which has to ensure the required beam quality is the subject of Sect. 4.3. Finally in section 4.2 the start-to end simulation of the FEL operating with the beam as resulting from the LINAC will be discussed.

4.1.7.2 The EUV-Soft X-Ray beamline

The photon energy range required from the EUV-Soft X-Ray beamline spans from 88.5 eV (14 nm) to 1.24 keV (1 nm). Despite the fact that the EUV-Soft X-ray beamline may be fed with both the high energy and the low energy electron beams, even exploiting the full beam energy variation available from SPARX, the simple energy tuning is not sufficient to ensure such a wide wavelength variation.

As in the previous case, it would be possible to increase the wavelength tuning range by changing the undulator strength. Figure 4.14 plots the undulator strength parameter K as a function of the undulator period calculated ensuring the resonance condition at the shortest wavelength (1nm), with the maximum available energy of 2.64 GeV (2.4GeV+10%) and at the longest wavelength, with the minimum beam energy of 0.96 GeV.

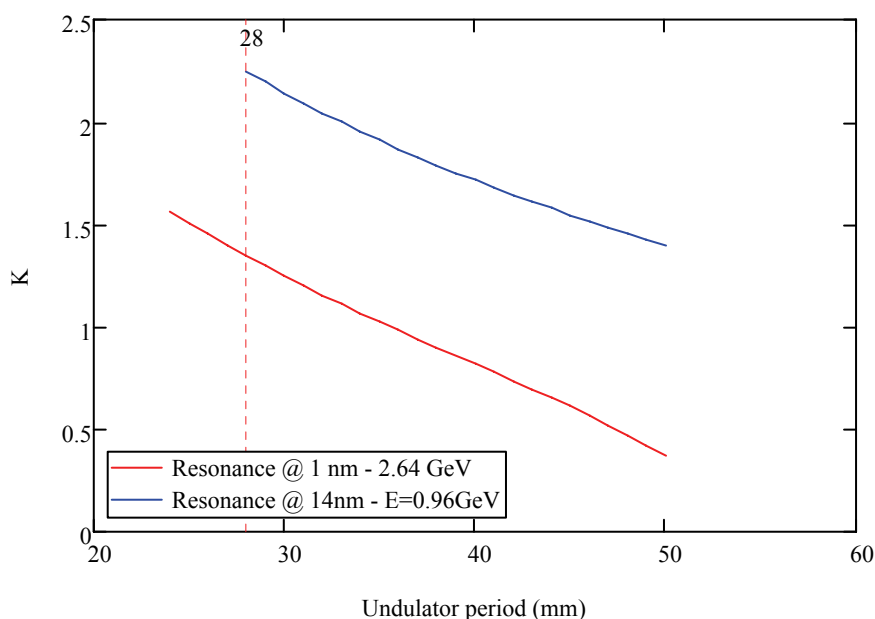


Figure 4.14: Undulator strength K vs the undulator period length at 1nm/2.64GeV and at 14nm/0.96GeV

In Figure 4.14 the limiting value of the K parameter assuming a resonant field of 1.2 T (as explained in the previous section), occurs at the minimum gap of 8.1 mm. The minimum undulator period that fulfills the FEL resonance condition at both sets of wavelength/energy is 28 mm. This value of the undulator period simultaneously permits FEL resonance at the lowest wavelength with the minimum beam energy and also maximizes the undulator

strength at the shortest wavelength. Moreover, this choice matches exactly the period of the existing SPARC undulators.

Further optimization is possible if one abandons the idea that the undulator must have the same period over its entire length. We explain this concept by considering two reference sets of beam parameters at the high and the low energy exits. The parameters are listed in Table 4.8.

Table 4.8: List of test beam parameters for the low energy (LE) and the high energy (HE) SPARX beams.

<i>Test beam parameters</i>		
Set name	Low energy beam (LE)	High energy beam (HE)
Beam energy	0.96 GeV - 1.5 GeV	1.92 GeV - 2.64 GeV
Peak Current	1 kA	3.3 kA
Energy spread (slice)	$3 \cdot 10^{-4}$	$2 \cdot 10^{-4}$
Emittances (slice)	1.1 mm mrad	1 mm mrad
Twiss β	6 m	10 m

While the (LE) beam parameters are the same as those listed in Table 4.3, the HE beam parameters represent a very high quality beam that will be challenging to produce. The (magnetic) saturation length calculated according to the Xie model with the period of 28 mm, at the wavelength of 1 nm, is $L_{sat} \sim 35\text{m}$. We assume that this value is the undulator length L_u required to satisfy the condition of lasing over the entire wavelength range. In Figure 4.15 we plot the ratio of undulator length divided by the saturation length vs. the output wavelength. Wavelength tuning is obtained by varying the beam energy and undulator K parameter in the permitted ranges.

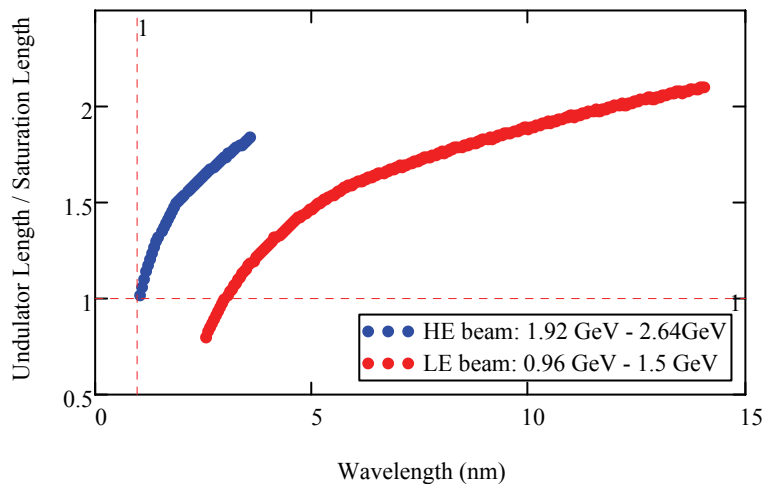


Figure 4.15: L_u/L_{sat} vs. the resonant wavelength in the SPARX EUV-Soft X-ray spectral range with the HE and the LE beams. (Reference value for $L_u=35\text{ m}$).

When the curve drops below the unity, the undulator length is not long enough for the FEL to reach saturation. By definition, at 1 nm the ratio $L_{sat}/L_u = 1$. At shorter wavelengths the ratio may grow by a factor 1.5 with the HE beam. At the longest wavelength with the LE beam the ratio grows by about 2.2 despite the lower beam quality. Thus in the case of operation at 14 nm, the undulator is ~ 2.2 times longer than required. To reduce this inefficiency in undulator design, we can consider the alternative undulator configuration with the same overall magnetic length, but composed of two different segments. The segments are characterized by an undulator period that decreases toward the end of the structure. The scheme considered is shown in Figure 4.16-B.

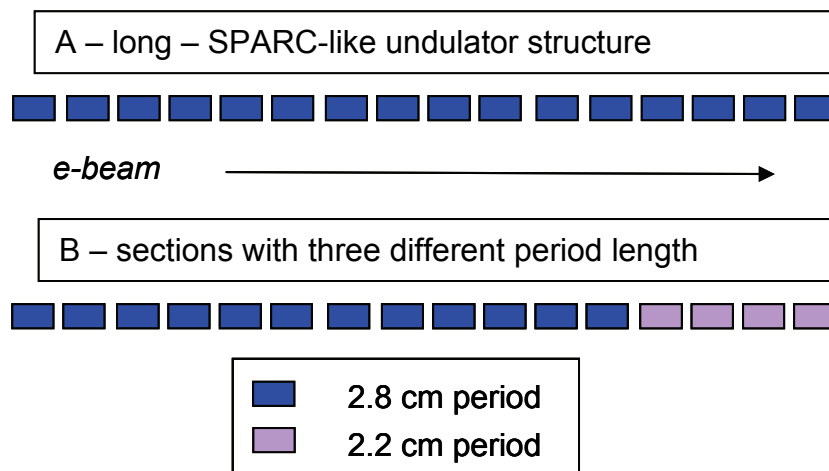


Figure 4.16: Comparison of the 16 equal undulator segments scheme (A) with the multi-period undulator scheme (B)

In both cases we assume a segmented undulator composed of 16 segments of 2.2 m of length each. The only difference between (A) and (B) is that in the latter the four last undulator segments have a shorter period – 22 mm instead of 28 mm. The saturation length is a function of both the beam parameters and the undulator parameters. We may impose the condition that the two different undulators are matched at the same resonant wavelength, where Eq. (4-2) links the undulator strength to the undulator period. We define a relative undulator efficiency,

$$\eta(\lambda_0, \lambda_{u,1}, K_1, \lambda_{u,2}, K_2) = \frac{L_{sat}(\lambda_0, \lambda_{u,2}, K_2)}{L_{sat}(\lambda_0, \lambda_{u,1}, K_1)} \quad (4-22)$$

that is the ratio between the saturation length with the parameters of undulator 1 with respect to undulator 2 in Eq. (4-2). This function allows one to compare quantitatively the effectiveness in reaching saturation at a given wavelength λ_0 , of an undulator with one set of period and K parameters, with respect to another. As an example in Figure 4.17 we have calculated the undulator efficiency as a function of the period length at three resonance wavelengths for a beam with parameters listed in the first column of Table 4.8

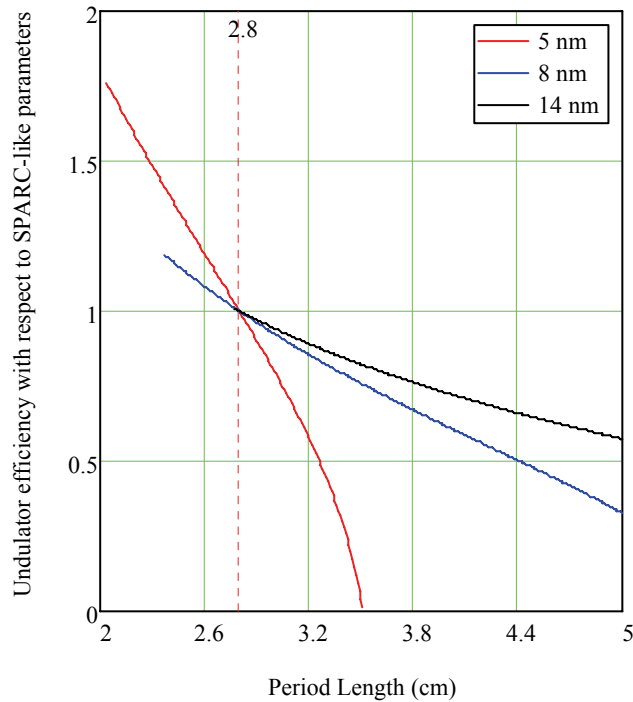


Figure 4.17: Undulator efficiency Eq. (3.1.17) compared to the SPARC-like undulator parameters vs. the undulator period length at three reference wavelengths (0.96 GeV)

All the curves intersect at $\eta = 1$ when the period is 28 mm, corresponding to the reference SPARC-like period. At 14 nm (black line) the resonance condition cannot be satisfied with a period shorter than 28mm; a longer period leads to a lower efficiency. At the shorter wavelengths, 8nm and 5 nm, a shorter period leads to a substantially higher undulator efficiency > 1.5 for a period length of 22 mm at 5nm. Choosing the configuration in Figure 4.16 (B) which has the same undulator magnetic length as (A), we may still reach saturation at 1nm while reducing the peak current from 3.3kA to 2.6kA (leaving the other parameters unchanged – corrected Xie scaling). In Figure 4.18 the plot as in Figure 4.15 has been reproduced with the high energy beam parameters (Table 4.8) except for the peak current, set at 2.6 kA .

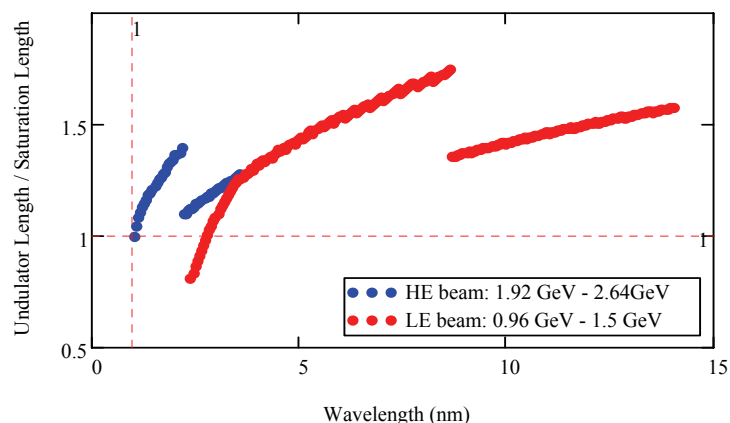


Figure 4.18: L_u/L_{sat} vs. the resonant wavelength in the SPARX EUV-Soft X-ray spectral range with scheme B of Figure 4.16 and with the HE and the LE beams. The beam energy and undulator K have been varied to optimize the saturation length.

Discontinuities in the curves of the same colour represent the wavelengths at which the short period undulator can no longer be matched to the resonance condition as the wavelength increases. This fact is fully compensated by the increasing gain which scales favourably with the wavelength. The result is a more efficient undulator which can operate over the same spectral range with relaxed beam parameters.

4.1.7.2.1 Seeding and cascaded configuration at the EUV-SoftX-Ray beamline

The SPARX FEL is also designed to operate as an amplifier of high-order harmonics generated in gas. Substantial energy from this type of source is available in the VUV. Figure 4.19 shows the energy per pulse obtained with the HHG technique as a function of the wavelength. The peak power can be estimated by considering that the harmonics are generated with laser pulse durations of ~ 50 fs. The dashed line represents the beam shot-noise-associated energy (multiplied by $10^{4(4)}$), obtained from assuming the same pulse duration and constant K, period and ρ . The FEL shot noise power rapidly grows with decreasing wavelength; hence, an ever higher seed energy is required.

⁴ The numerical factor 10^4 is the result of an estimate of the losses due to transport optics to the FEL (x5) the matching with the electron beam (x2) the frequency matching (x10) and the contrast ratio (x 10^2). A more detailed analysis is given in Sect. 4.4

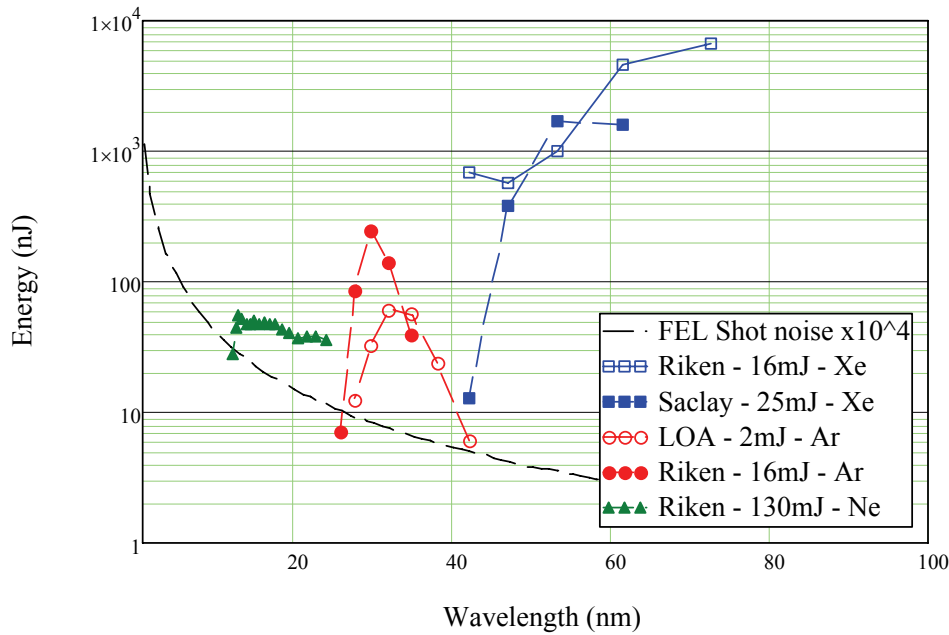


Figure 4.19: Energy per pulse (typical laser pulse duration 50 fs) obtained from HHG sources vs. wavelength compared to electron beam shot noise energy $\times 10^4$ (black dashed line) [41].

Of particular interest is the spectral range in the region of 30nm; this region corresponds to the 27th harmonic of the Ti:Sa generated in *Ar* for which the HHG peak power is much larger than the beam's shot noise power. An analysis of the issues related to the HHG source and to the optics to match the source to the FEL is given in a dedicated section. Implementing an FEL cascade with harmonic multiplication requires modulating the beam at a long wavelength and injecting this beam into a radiator resonant with the one of the higher order harmonics. As was illustrated in Figure 4.14, the resonance in a SPARC-like undulator (period: 28 mm) cannot be matched at 30 nm even at the lowest SPARX energy. For this reason, we need an additional larger period undulator in order to set the fundamental resonant wavelength to the seed wavelength. A higher order harmonic of this undulator can be matched to the undulator sequence in Figure 4.16B. Figure 4.20 shows the variation of the undulator gap and K parameter vs. the beam energy, assuming the same remnant field and the condition of resonance at 29.63 nm (27th harmonic of the Ti:Sa) with an undulator period of 40 mm.

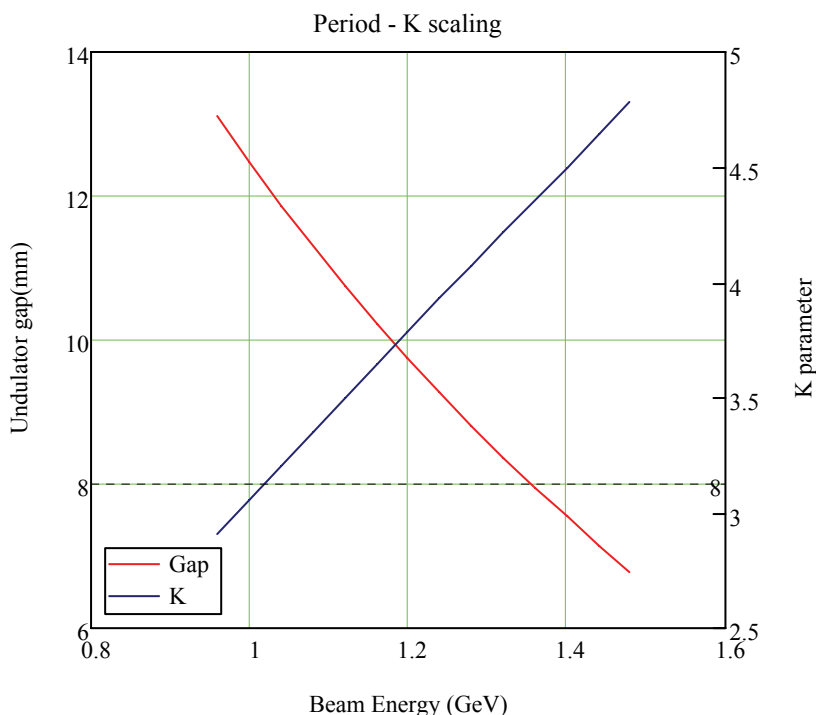


Figure 4.20: undulator gap and the K parameter vs. the beam energy, assuming the same remnant field (1.2T) and the condition of resonance at 29.63nm with an undulator period of 4 cm.

With this period length the energy required (~ 1 to 1.36 GeV) to satisfy the resonance condition at the desired harmonic with a gap larger than 8 mm, matches the SPARX LE beam energy range. The gain length at 29.6 nm with the parameters of the first column of Table 4.8 is almost independent of the beam energy and is ~ 60 cm. At this wavelength four undulator modules constitute $2/3$ of the saturation length, ensuring an amplification factor up to 10^6 . When the FEL is operated in seeded mode, exploiting the improvement in spectral purity associated with the seed, requires attention to the shape and uniformity of the e-beam longitudinal phase space. The compression factor implicitly assumed to reach the peak current in Table 4.8 must be relaxed resulting in a smaller amplification factor. The detailed investigation of the seeded mode SPARX operation is presented in a dedicated section. The undulator layout including the seeding option with HHG is shown in Figure 4.21.

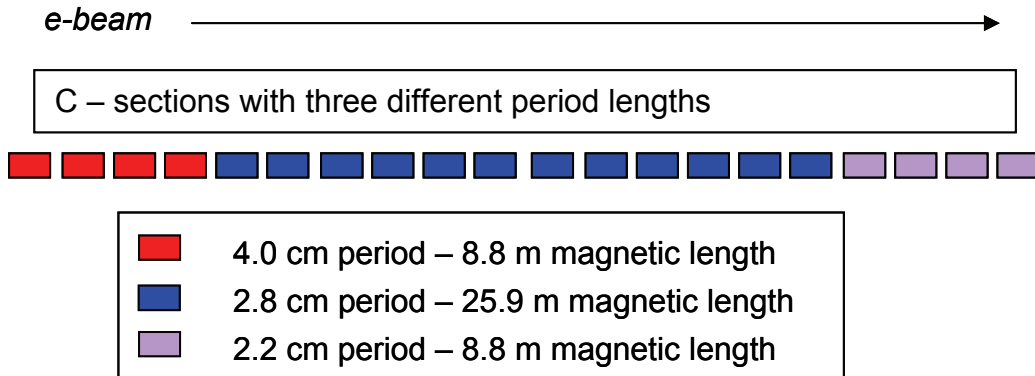


Figure 4.21: 16 Multi-period undulator scheme (C) including four sections with a larger period matching the resonance at the 27th harmonic of the Ti:Sa (29.6 nm).

4.1.7.2.2 SASE with the multi-period segmented undulator option (C)

The relatively large K of the four undulator modules added to the SPARX structure allows a wide wavelength tunability. We may therefore expect these modules to contribute to the saturation length even at shorter wavelengths (in the range 1-14 nm). Figure 4.22 shows the saturation efficiency vs. wavelength (Equation (4-22)) calculated by comparing the period of 40 mm and 28 mm at 1.5 GeV, i.e. the full energy of the LE beam. The efficiency is larger than 50% down to 7 nm.

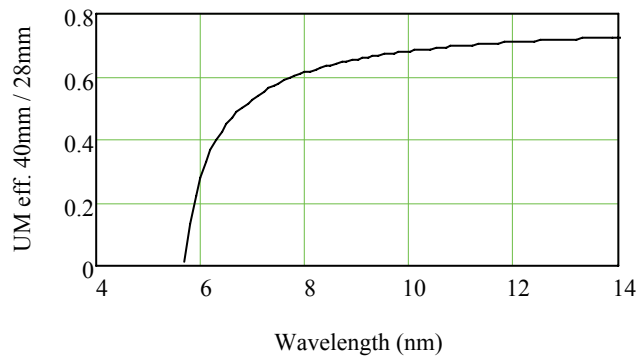


Figure 4.22: Efficiency of the 40mm undulator period with respect to the SPARC-like 28mm vs. operation wavelength at 1.5 GeV.

The additional 4 undulator sections with $\lambda_u=40$ mm allow a reduction of the peak current required for saturation at 1nm at the maximum energy (2.64 GeV) to about 1.9 kA. The condition for saturation vs. beam quality is deduced from the contour plots in Figure 4.23 and Figure 4.24 where the ratio L_{sat}/L_u is plotted vs. emittance and energy spread. For the HE beam (2.64 GeV) at 1 nm we have considered $I_{peak}=2.3$ kA, with average $\beta_{Twiss}=10$ m (Figure 4.23) and for the LE beam (1.5 GeV) at 3nm we have $I_{peak}=1$ kA and $\beta_{Twiss}=6$ m (Figure 4.24).

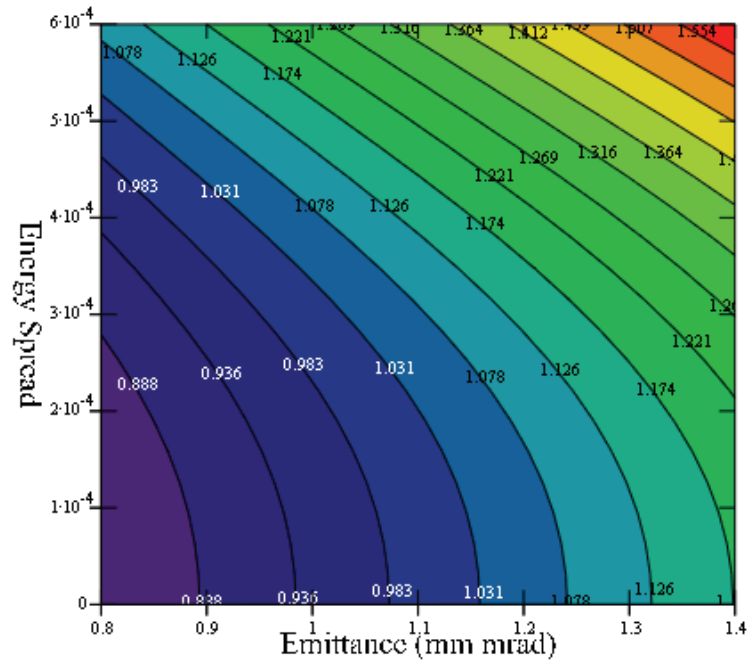


Figure 4.23: Saturation length normalized to undulator length vs. energy spread and transverse emittances for a peak current of 2.3kA at the wavelength of 1nm/1240eV (HE beam, 2.64GeV)

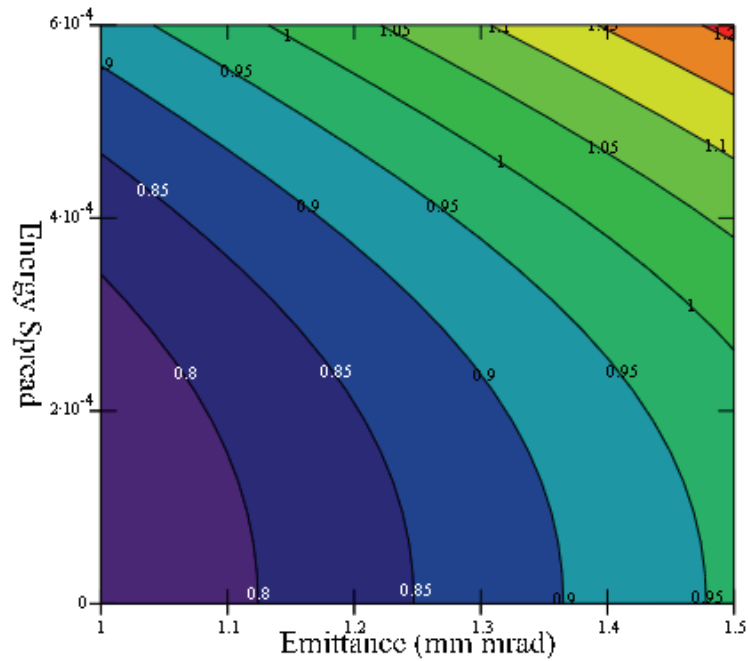


Figure 4.24: Saturation length normalized to undulator length vs. energy spread and transverse emittances for a peak current of 1kA at the wavelength of 3nm/413eV (LE beam, 1.5GeV)

In **Figure 4.25** we have represented the behaviour of the saturation length normalized to the undulator length in the 2.64 GeV/1 nm case (as in **Figure 4.24**) with peak current and emittances as independent variables. The slice

energy spread considered is $2 \cdot 10^{-4}$. The red mark (A) corresponds to the set of beam parameters listed in Table 4.9 (HE beam). The red dashed line identifies the condition where saturation is reached at the end of the undulator. The working set of parameters along this line are equivalent in terms of gain length and saturation efficiency and may be considered in the working point optimization of the accelerator system. Operation at low charge indeed allows to reach a substantially smaller beam emittance at expense of a lower peak current. The set of parameters labelled with A, B and C indicated in Figure 4.25 and listed in Table 4.9 will be considered as possible options in the beam dynamics optimization. In Figure 4.26 the analogous of Figure 4.25 for the LE beam (1.5 GeV) at 3nm is represented.

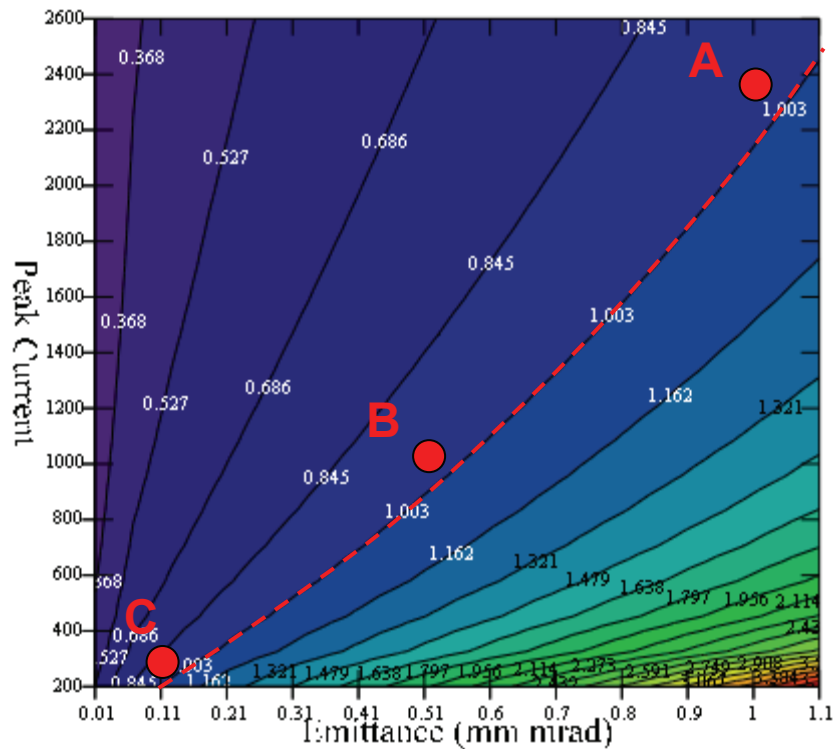


Figure 4.25: Saturation length normalized to undulator length vs. peak current and transverse emittances at the wavelength of 1 nm/1240 eV (HE beam, 2.64 GeV, energy spread $2 \cdot 10^{-4}$). The marks A, B, C correspond to the three sets of parameters listed in Table 4.9, cases HE A, HE B, HE C.

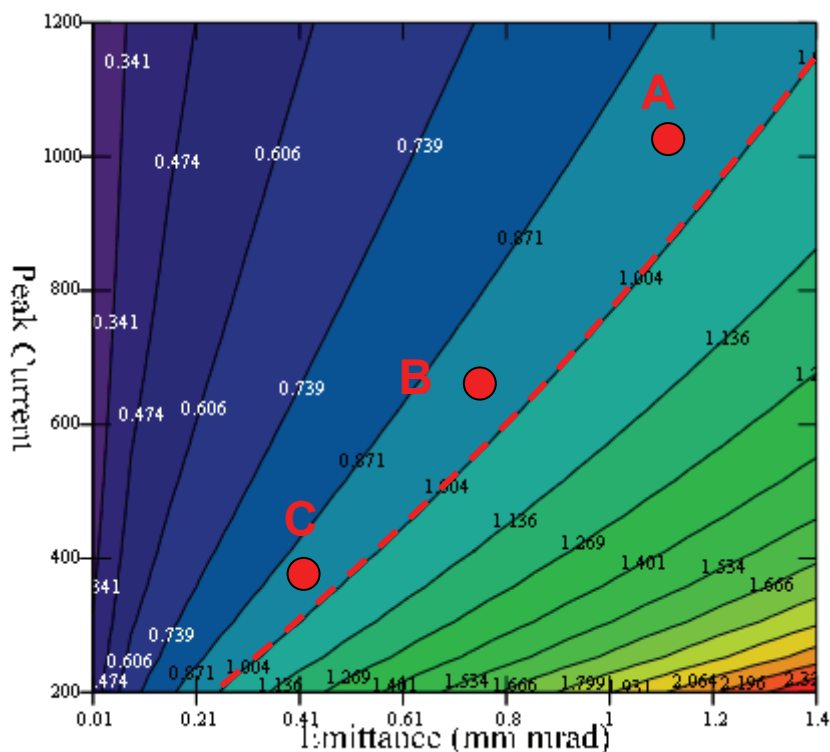


Figure 4.26: Saturation length normalized to undulator length vs. peak current and transverse emittances at the wavelength of 3 nm/413 eV (LE beam, 1.5 GeV, energy spread 3×10^{-4})

Table 4.9: Reference beam parameters for the EUV soft X-ray SPARX beamline (slice).

<i>Reference beam parameters</i>						
	Low energy beam			High energy beam		
Set name	LE-A	LE-B	LE-C	HE-A	HE-B	HE-C
Beam energy (GeV)	0.96 - 1.5			1.92 - 2.64		
Peak Current (kA)	>1	>0.6	>0.4	>2.3	>1.0	>0.3
Energy spread (slice)	$<3 \times 10^{-4}$			$<2 \times 10^{-4}$		
Emitt. (slice, mm-mrad)	<1.1	<0.7	<0.4	<1	<0.5	<0.1
Twiss β (m)	~6			~10		

In Figure 4.27 we have recalculated the ratio L_u/L_{sat} versus the resonant wavelength in the SPARX-Soft X ray spectral range with the high energy and low energy beam parameters (listed in Table 4.9) using the undulator structure C of Figure 4.21.

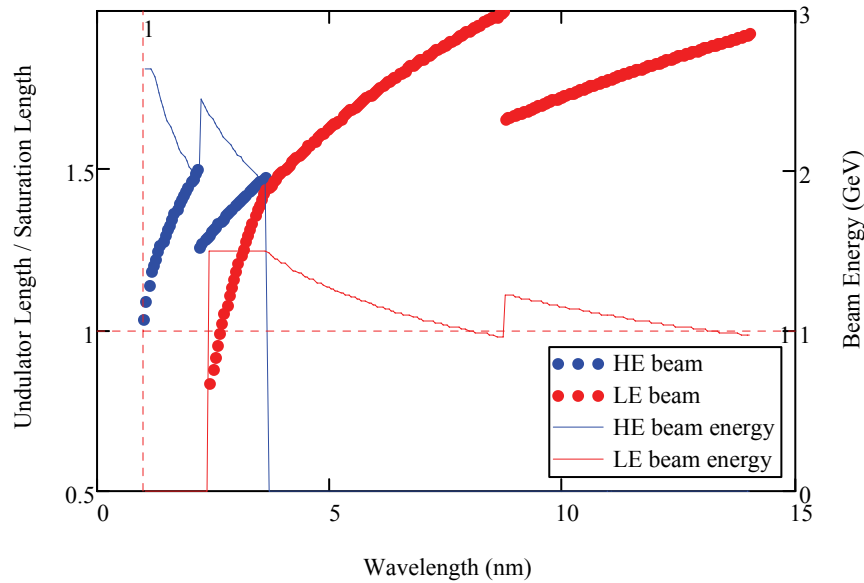


Figure 4.27: L_u/L_{sat} vs. the resonant wavelength in the SPARX EUV-Soft X-ray spectral range with the HE-A and the LE-A beams

The more stringent condition on the beam parameters is the one related to the operation at the shortest wavelength in each energy range. When the inequalities in Table 4.9 are fulfilled, the entire wavelength range is covered by the combined tuning of the undulator gap and beam energy.

4.1.7.2.3 Undulator parameters and undulator optics

The EUV-Soft-Xray undulator beamline is composed by three undulator sequences with different period lengths. The undulators are all variable gap permanent magnet undulators in the Halbach configuration, with the parameters listed in Table 4.10.

Table 4.10: EUV-Soft X-ray Undulators parameters

<i>UM1 - Undulator sequence (4 segments)</i>	
Period	4 cm
Undulator length	2.278 m
No. of Periods	55
Gap (min/max)	8.1 / 25 mm
K max	3.27
Remanent field (effective)	1.21 T
Blocks per period	4

<i>UM2 - Undulator sequence (12 segments)</i>	
Period	2.8cm
Undulator length	2.156m
No. of Periods	77
Gap (min/max)	8.1 / 25 mm
K max	2.3
Remanent field (effective)	1.21 T
Blocks per period	4

<i>UM3 - Undulator sequence (4 segments)</i>	
Period	2.2cm
Undulator length	2.20m
No. of Periods	100
Gap (min/max)	6.1 / 25 mm
K max	1.9
Remanent field (effective)	1.21 T
Blocks per period	4

A detailed description of the undulator design, mechanical tolerances and field characterization is given in chapter 1. The undulator sections are separated by empty gaps dedicated to the installation of quadrupoles for the beam transport, phase correctors for the compensation of the phase advance between electrons and fields in the longitudinal phase space and for the installation of diagnostics for both the e-beam and the FEL radiation. As in the VUV-EUV beamline, the electron beam transport in each of the undulator sequences is realized with a FODO lattice, with alternated gradient quadrupoles as sketched in Figure 4.28. At the transition between the different undulator sequences (UM1 to UM2 and UM2 to UM3) the FODO parameters have to be adapted to match the beam to the next undulator sequence. As shown in Figure 4.28, four quadrupoles at the transition are sufficient to match four independent Twiss parameters from UM1 to UM2.

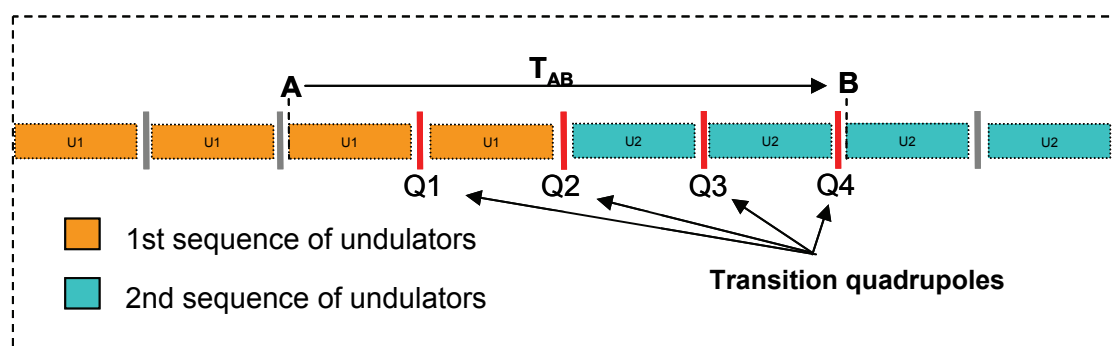


Figure 4.28: Layout of the undulator FODO lattice in a transition from UM1 to UM2 (analogous to the transition from UM2 to UM3)

A list of the main parameters of the beam line with the notation defined in Figure 4.28 is summarized in Table 4.11.

Table 4.11: Parameters of the EUV/Soft-X undulator beam line

UM1 - Undulator sequence (4 segments)		
Lattice period	$L_p(m)$	5.712
Drift length	$L_d(m)$	0.6
Quadrupole distance from UM (center of Q.)	$D_q(m)$	0.12
Beamline Length	$L_B(m)$	11.2

UM2 - Undulator sequence (12 segments)		
Lattice period	$L_p(m)$	5.712
Drift length	$L_d(m)$	0.588
Quadrupole distance from UM (center of Q.)	$D_q(m)$	0.112
Beamline Length	$L_B(m)$	32.928

UM3 - Undulator sequence (4 segments)		
Lattice period	$L_p(m)$	5.712
Drift length	$L_d(m)$	0.594
Quadrupole distance from UM (center of Q.)	$D_q(m)$	0.11
Beamline Length	$L_B(m)$	10.582

Each undulator sequence is matched to ensure the desired average Twiss beta parameter. We have considered non-symmetrically centred quadrupoles within the drifts between the undulators to facilitate the insertion of diagnostics/other magnetic elements. The lattice period is composed by two undulator sections and the average Twiss β_{xy} parameter is defined according to Eq.(4-19). Three different matching conditions for the three different periodic undulator sequences are obtained by imposing the same conditions defined in dedicated section, i.e. that the Twiss beta parameters in the horizontal and in vertical plane, averaged over the undulator lengths are equal to the design parameter

$$\begin{aligned}
 \bar{\beta}_{x,y}|_{UM1} &= \beta_d \\
 \bar{\beta}_{x,y}|_{UM2} &= \beta_d \\
 \bar{\beta}_{x,y}|_{UM3} &= \beta_d
 \end{aligned}
 \tag{4-23}$$

The quadrupole settings of the transitions between the undulator sequences UM1→UM2 (and UM2→UM3) are obtained by imposing that the transfer matrix from position A to position B in Figure 4.42 transforms the beam Twiss parameters matched for the UM1 (or UM2) lattice in the beam Twiss parameters matched for the UM2 (UM3) lattice, i.e.

$$\begin{pmatrix} \alpha_x \\ \beta_x \\ \alpha_y \\ \beta_y \end{pmatrix}_B = T_{AB}(Q1, Q2, Q3, Q4) \begin{pmatrix} \alpha_x \\ \beta_x \\ \alpha_y \\ \beta_y \end{pmatrix}_A \quad (4-24)$$

A small detuning of the *Q1-Q4* quadrupoles with respect to their nominal gradient is generally sufficient to ensure the matching between contiguous undulator segments. As in the VUV-EUV beamline case previously analysed, the matched Twiss parameters depend on the undulator strength *K* and the e-beam energy. The limitation to the *K* range of variation is imposed by the vertical size of the vacuum chamber that will not allow the gap to be smaller than 8.1 mm (6.1 mm in the last undulator sequence). For this reason the matching condition has been calculated at three different *K* values and at two beam energies. We have considered the maximum and minimum energy and the two values of *K* plus the special case of *K*=0, i.e. the condition of a pure FODO. The highest Quadrupole Integrated Gradient (QIG) is found in the pure FODO mode at the highest energy. The corresponding QIG for the three sections and Twiss parameters α and β at the first undulator entrance are given in Table 4.12.

In Figure 4.29 the Twiss β in the X and Y plane along the undulator are plotted for the FODO lattice, with the parameters labelled (*K*) in Table 4.12.

The matching condition in the three undulator sections is only slightly modified by the different period/undulator parameters and a small tuning of the quadrupoles is sufficient to ensure proper matching in the transition from one undulator sequence to another.

Table 4.12: Characteristics parameters of the undulator beamline optics

Case	Energy (GeV)	λ (nm)	α_x	β_x (m)	α_y	β_y (m)
<i>Twiss parameters at injection</i>						
A	0.96	14	-0.67	4.07	1.30	8.32
B		12	-0.68	4.04	1.36	8.38
C		-	-0.72	3.92	1.53	8.60
D	1.2	8	-0.69	4.00	1.41	8.45
E		5	-0.71	3.95	1.49	8.55
F		-	-0.72	3.92	1.52	8.60
G	1.5	3.5	-0.71	3.94	1.49	8.56
H		3	-0.72	3.94	1.51	8.57
I		-	-0.72	3.92	1.52	8.60
J	2.4	2	-0.80	8.04	1.20	12.22
K		1.2	-0.81	8.00	1.24	12.29
L		-	-0.82	7.98	1.25	12.30

	<i>1st Undulator séquence</i>			<i>2nd Undulator séquence</i>			<i>3rd Undulator séquence</i>		
	$\langle\beta_{xy}\rangle$ (m)	K	QIG (T)	$\langle\beta_{xy}\rangle$ (m)	K	QIG (T)	$\langle\beta_{xy}\rangle$ (m)	K	QIG (T)
A	6	1.715	1.05/-0.98	6	2.249	0.87/-0.64	6	-	1.11/-1.11
B	6	1.495	1.06/-1.01	6	2.013	0.93/-0.74	6	-	1.11/-1.11
C	6	-	1.1/-1.1	6	-	1.1/-1.1	6	-	1.11/-1.11
D	6	1.553	1.34/-1.3	6	2.074	1.24/-1.08	6	-	1.38/-1.38
E	6	0.87	1.37/-1.35	6	1.393	1.32/-1.25	6	1.736	1.23/-1.04
F	6	-	1.38/-1.38	6	-	1.38/-1.38	6	-	1.38/-1.38
G	6	1.008	1.71/-1.7	6	1.519	1.67/-1.60	6	1.866	1.59/-1.42
H	6	0.765	1.72/-1.71	6	1.301	1.68/1.63	6	1.643	1.62/-1.49
I	6	-	1.72/-1.72	6	-	1.72/-1.72	6	-	1.73/-1.73
J	10	-	1.58/-1.56	10	-	1.48/-1.40	10	-	1.62/-1.62
K	10	-	1.61/-1.60	10	-	1.56/-1.53	10	-	1.48/-1.39
L	10	-	1.62/-1.62	10	-	1.62/-1.62	10	-	1.62/-1.62

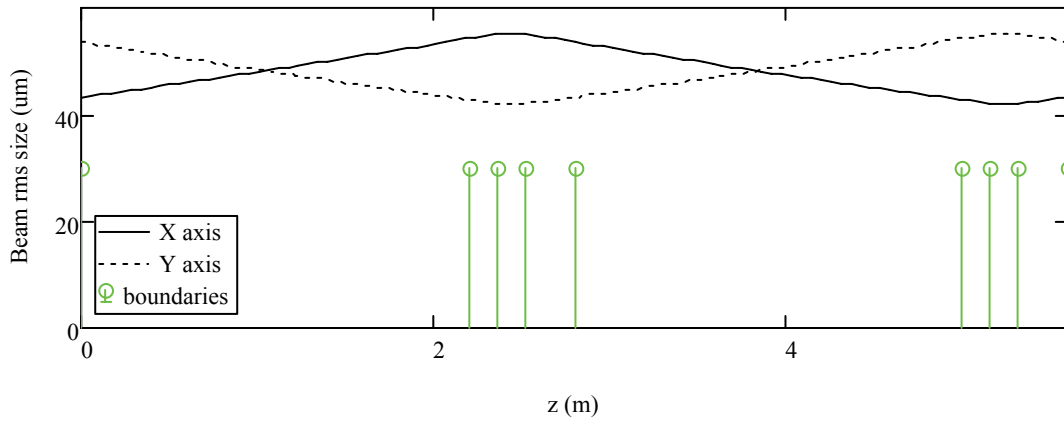


Figure 4.29: Twiss β in the X and Y plane along the undulator for the FODO lattice in Table 4.12 (K), first undulator section. The green marks represent the boundaries of the magnetic elements in the beamline.

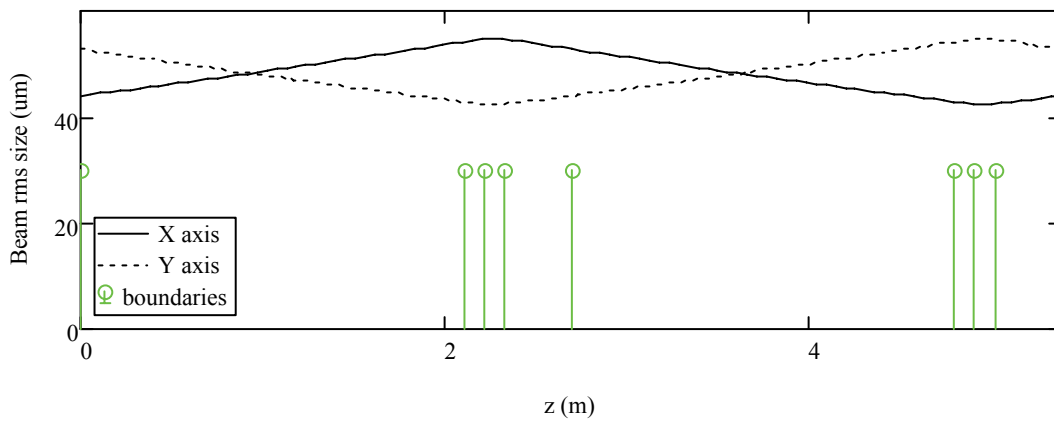


Figure 4.30: Twiss β in the X and Y plane along the undulator for the FODO lattice in Table 4.12 (K), second undulator section.

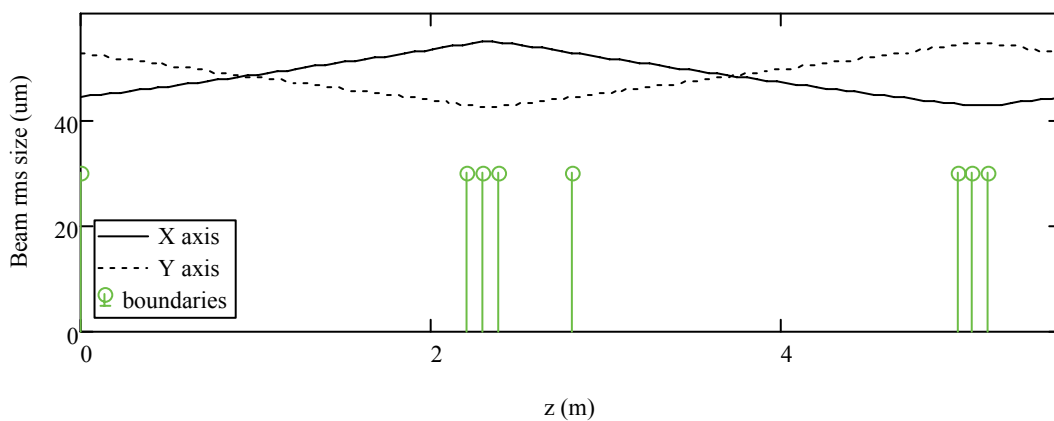


Figure 4.31: Twiss β in the X and Y plane along the undulator for the FODO lattice in Table 4.12 (K), third undulator section

4.1.7.2.4 Preliminary simulations

Extensive simulations of the FEL dynamics in the three undulators sequences have been done with GENESIS 1.3 and PERSEO. With the same consideration drawn in Sect. 4.1.7.1.2 previously treated, the wavelength tuning may be obtained by both varying the undulator gap and the beam energy. An additional possibility is offered by the layout based on the three different undulators. The third undulator sequence may be indeed tuned at one of the harmonics of the preceding sections in order to enhance the harmonic emission. This is effective when saturation is reached at the end of the UM2 sequence. In Table 4.13 and Table 4.14 the simulations results with the HE and LE beam parameters respectively, are listed. The simulations have been obtained by assuming a Gaussian current distribution with the beam parameters listed in Table 4.9 (LE-A and HE-A) corresponding to a 1nC e-bunch charge. Examples at lower charge have been studied with GENESIS 1.3 only at the shortest wavelength (3nm in the LE beam case and 1nm in the HE beam case). The listed saturation length corresponds to the magnetic saturation length, i.e., without including the gap between the undulators. The saturation position has been estimated with the same method as explained in Sect. 4.1.7.2.4. The peak power has been estimated as the average power in a gaussian pulse with the same pulse length and energy as listed in the table. The peak power associated to characteristic spikes of SASE is significantly higher than the average power calculated with this definition.

Table 4.13: List of the main FEL parameters for the Soft-X-ray beamline in the range 90/400 eV. Simulations done with PERSEO (black, LE-A beam - 1nC) and GENESIS 1.3 (gray/italic LE-A beam - 1nC, 0.05nC).

	Q (nC)	E (GeV)	K ₁	K ₂	K ₃ ⁵	λ (nm)	Ph. En. (eV)	S.Len. ⁶ (m)	P ⁷ (GW)	P. En. (mJ)
A	1	1.5	0.77	1.305	1.648	3	412.02	41	1.7	1.2
B	<i>1</i>	<i>1.5</i>	<i>0.77</i>	<i>1.305</i>	<i>1.648</i>	<i>3</i>	<i>412.02</i>	<i>39.3</i>	<i>5</i>	<i>0.56</i>
C	<i>0.05</i>	<i>1.5</i>	<i>0.77</i>	<i>1.305</i>	<i>1.648</i>	<i>3</i>	<i>412.02</i>	<i>36</i>	<i>3.4</i>	<i>0.056</i>
D	1	1.5	1.008	1.519	0.862*	3.5	354.22	34.8	2.3	1.0
E	1	1.5	1.205	1.712	1.067*	4	309.48	30.8	2.4	1.1
F	1	1.5	1.52	2.039	0.783*	5	247.8	26.9	2.6	1.3
G	1	1.25	1.261	1.77	-	6	206.65	26.8	2.2	1.3
H	1	1.25	1.67	2.2	-	8	154.92	22.9	2.5	1.3
I	1	0.96	1.237	1.744	-	10	123.96	22.4	2.0	1.2
J	1	0.96	1.495	2.012	-	12	103.33	20.7	2.0	1.2
K	1	0.96	1.715	2.25	-	14	88.56	19.6	2.2	1.2

	Δλ/λ (%)	δt (fs)	#Phot. ⁸	Div. (rms μrad)	Size (rms μm)	h	#Phot. (h)	Δλ/λ (3h,%)
A	0.09	170	1.8×10 ¹³	-	-	3	1 × 10 ¹⁰	0.08
B	<i>0.13</i>	<i>200</i>	<i>8.5×10¹²</i>	<i>23</i>	<i>150</i>	-	-	-
C	<i>0.17</i>	<i>30</i>	<i>8.5×10¹¹</i>	<i>21</i>	<i>140</i>	-	-	-
D	0.09	180	1.8×10 ¹³	-	-	2*	1 × 10 ¹¹	0.21
E	0.11	190	2.2×10 ¹³	-	-	2*	4 × 10 ¹¹	0.25
F	0.13	200	3.3×10 ¹³	-	-	3*	2 × 10 ¹¹	0.22
G	0.14	200	3.3×10 ¹³	-	-	3	5 × 10 ¹⁰	0.11
H	0.16	210	5×10 ¹³	-	-	3	1 × 10 ¹¹	0.14
I	0.17	215	5.7×10 ¹³	-	-	3	1 × 10 ¹¹	0.15
J	0.18	220	7.1×10 ¹³	-	-	3	2 × 10 ¹¹	0.17
K	0.2	230	8.8×10 ¹³	-	-	3	3.5×10 ¹¹	0.2

⁵ The third undulator sequence resonance may be tuned to enhance the harmonic emission when saturation is reached before the end of the second undulator sequence. In this examples the h harmonic has been considered and the specific cases are indicated with an asterisk in the h and K_3 column.

⁶ The magnetic saturation length is indicated. When the saturation length is shorter than the undulator length an improvement of FEL performances may be obtained by tapering the remaining undulator sections. This is not accounted in the

⁷ Peak power calculated as the “average power” in a bunch of Gaussian shape with the pulse energy and r.m.s. duration obtained in the simulation.

⁸ Photons per pulse

Table 4.14: List of the main FEL parameters for the Soft-X-ray beamline in the range 350/1240 eV (HE-A beam - 1 nC)

	Q (nC)	E (GeV)	K ₁	K ₂	K ₃ ⁹	λ (nm)	Ph. En. (eV)	S.Len. ¹⁰ (m)	P ¹¹ (GW)	P. En. (mJ)
A	1	2.64	0.81	1.34	1.682	1	1246	42.8	4.8	1.8
B	1	2.4	0.81	1.34	1.682	1.2	1030	42.8	6	1.8
C	1	2.4	1.15	1.657	1.01(*)	1.5	1030	33.4	3.3	1.3
D	1	2.4	1.553	2.074	-	2	619.9	28.2	8.5	4.1
E	1	1.92	1.237	1.744	-	2.5	495.8	27.3	7	3.4
F	1	1.92	1.495	2.012	-	3	413.0	25.2	7.8	4.1
G	1	1.92	1.715	2.25	-	3.5	354.24	24.0	7.9	4.1

	Δλ/λ (%)	δt (fs)	#Phot. ¹²	Div. (rms μrad)	Size (rms μm)	h	#Phot. (h)	Δλ/λ (3h,%)
A	0.07	150	9x10 ¹²	-	-	3	3 x10 ⁹	0.07
B	0.09	200	2x10 ¹³	-	-	3	4 x10 ¹⁰	0.08
C	0.09	175	2.5x10 ¹³	-	-	2(*)	2x10 ¹¹	0.27
D	0.11	180	4x10 ¹³	-	-	3	5 x10 ¹⁰	0.1
E	0.12	190	4x10 ¹³	-	-	3	6x10 ¹⁰	0.1
F	0.18	200	6 x10 ¹³	-	-	3	1 x10 ¹¹	0.12
G	0.14	200	7.2x10 ¹³	-	-	3	2 x10 ¹¹	0.12

Figure 4.32 illustrates the energy growth vs the distance z along the undulator calculated with GENESIS 1.3 (1 nC - second line of Table 4.13. Saturation is reached in 50 meters (effective length) at 0.56 mJ. Figure 4.33 shows the power profile vs. the bunch coordinate and the radiation spectrum. at saturation.

⁹ The third undulator sequence resonance may be tuned to enhance the harmonic emission when saturation is reached before the end of the second undulator sequence. In this examples the h harmonic has been considered and the specific cases are indicated with an asterisk in the K_3 column and in the harmonic order column (h)

¹⁰ The magnetic saturation length is indicated. When the saturation length is shorter than the undulator length an improvement of FEL performances may be obtained by tapering the remaining undulator sections. This is not accounted in the

¹¹ Peak power calculated as the "average power" in a bunch of Gaussian shape with the pulse energy and r.m.s. duration obtained in the simulation.

¹² Photons per pulse

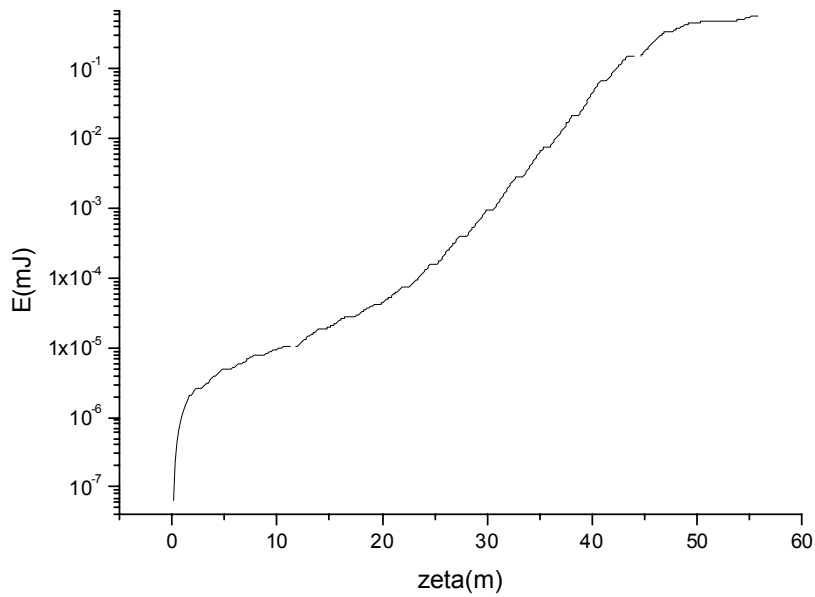


Figure 4.32: Average energy in the radiation pulse vs. undulator length at 3 nm wavelength (1 nC).

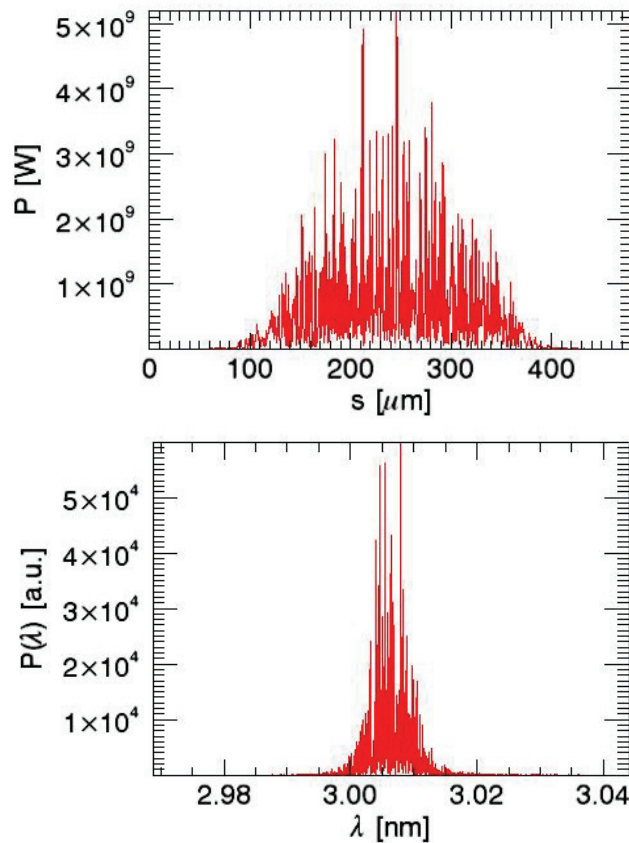


Figure 4.33: Temporal (top) and spectral (bottom) structure for 3 nm radiation from UM2 at saturation (50 m).

The plot in Figure 4.34 shows the evolution of the laser power vs the e-bunch coordinate s (horizontal) and the undulator position z (vertical). The plot is relevant to the low charge case (charge 50 pC, beam parameters as in Table 4.9, LE-B beam). The power is normalized at each z in order to allow the observation of the SASE spikes formation occurring mainly in the first undulator module, the exponential power growth in the intermediate undulator sequence and the saturation, reached in the last undulator sequence. The electron bunch length considered allows a drastic reduction of the number of spikes with respect to the 1nC case plotted in Figure 4.33, but is not sufficiently short to ensure the selection of a single spike. At saturation the pulse length is approximately 17fs (5 μ m). In Figure 4.35 the power profile and the spectrum are shown at saturation (45 m).

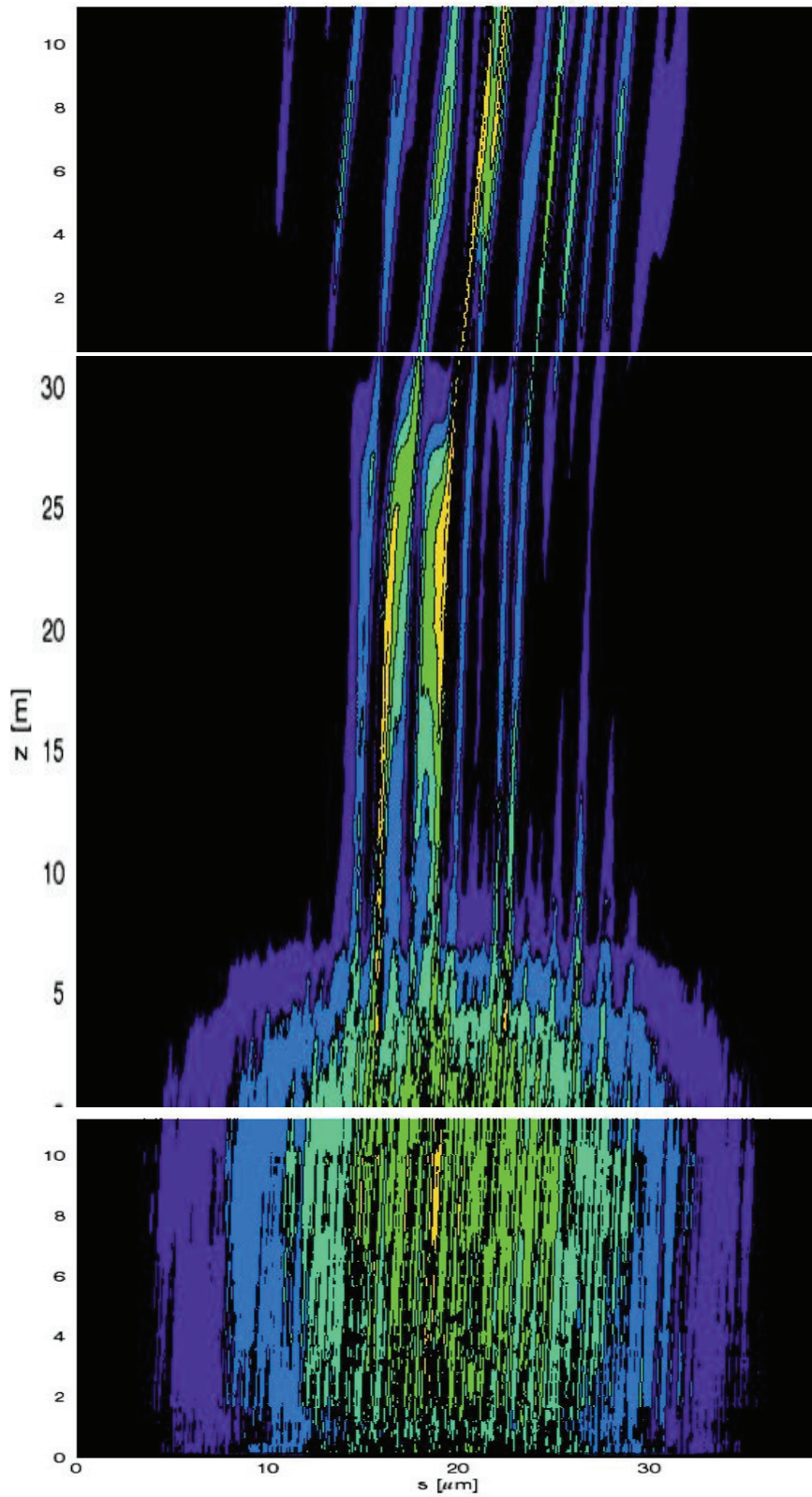


Figure 4.34: Normalized power level curves in the (s, z) plane for the ideal case at 50 pC, 3 nm

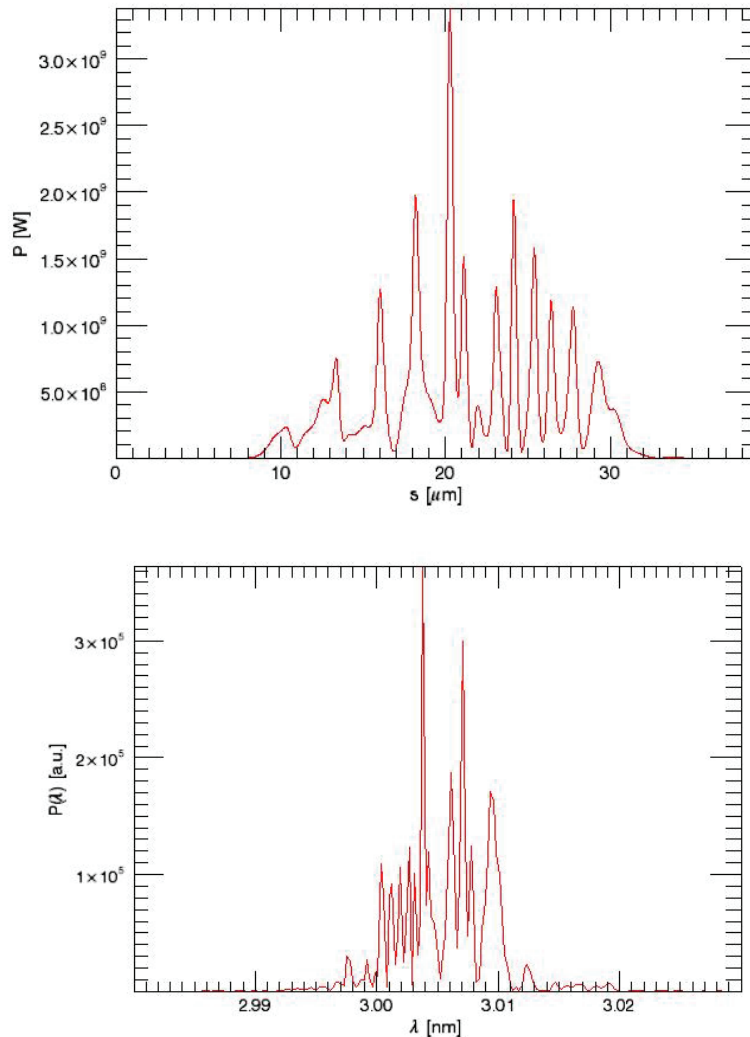


Figure 4.35: Temporal (top) and spectral (bottom) structure for 3nm radiation from UM2 at saturation (~ 45 m)

4.1.7.3 The Hard X-Ray Undulator beamline

This beamline is designed to cover the hard X-ray photon energy range at SPARX with a maximum photon energy of 2keV (0.62nm). The production of hard X-ray photons using conventional undulator technology, in which the remnant magnetic field is ~ 1.2 - 1.3 T, requires relatively long period lengths to yield a sufficiently large K parameter. This choice implies a relatively high beam energy and a long undulator structure. The HE beam nominal energy is 2.4GeV (with an upper limit of 2.64 Gev due to RF constraints). The requirement on the spectral range suggests the following different strategies with respect to the beamlines discussed so far.

- 1) The undulator must be optimized for the shortest wavelength; wavelength tunability must be realized by tuning the beam energy and not by tuning the undulator strength.

- 2) The undulator must be in vacuum, to maximize the undulator field vs. gap.
- 3) High field technology must be implemented to maximize the remnant field. As it will be explained in chapter 1, alternatives exist to enhance the peak field on axis in a periodic undulator structure. Examples are provided by hybrid structures or cryo-cooled undulators in which the low temperature permits an increase of the remnant field thereby allowing a reduction of the undulator period while keeping the undulator strength at a reasonable value. For a detailed study of magnetic undulator technology see chapter 1.

The physical gap of the undulator coincides with the aperture used to estimate the longitudinal wake function. The analysis of the wake fields in Sect. 4.3.7 shows that the energy spread induced by the energy wake in a square vacuum chamber with vertical aperture of 5 mm leads to an induced (correlated), energy spread per unit length $dE/dz \approx 15$ keV/m (at 1 nC). This value leads to a total correlated energy spread of 400 keV in an undulator beamline with an overall length of ~ 30 m. In terms of relative energy spread, at 2 GeV (HE beam), this corresponds to the limit indicated in the “Slice energy spread” in Table 4.9. At this point, the correlated energy spread induced by the wake in the undulator poses a constraint on the saturation length that must be verified during the optimization procedure. In Figure 4.36 we have calculated the undulator period λ_u and K parameter for a gap of 5 mm vs the operating wavelength at the nominal HE beam energy (2.4 GeV). The remnant field is 1.45 T, which is well within the capabilities of these new materials.

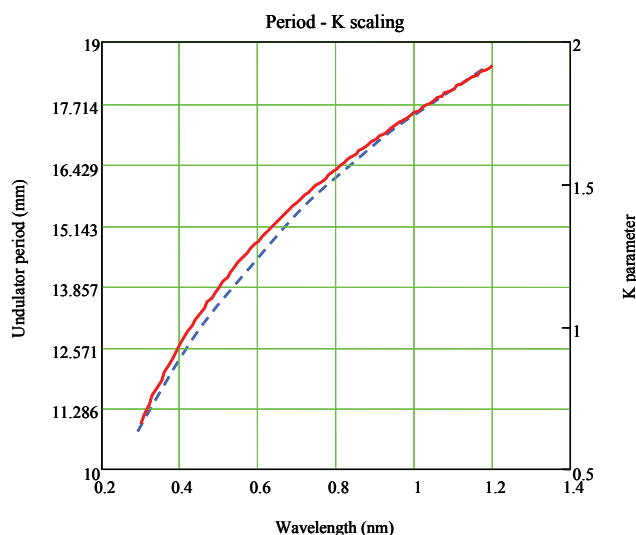


Figure 4.36: Period (continuous-red) and strength K (dashed-blue) vs. wavelength operation with a gap of 5mm and remnant field of 1.45T

At 0.62 nm (2 keV) we have $\lambda_u=15$ mm and $K=1.283$. A shorter period would require a higher K parameter which could be obtained with a

smaller gap (or a larger remnant field) only. A longer period would require a lower K and would lead to an increased saturation length. Following the same procedure of the previous sections, we have calculated the (magnetic) saturation length vs. the beam parameters at the shortest wavelength. In Figure 4.37 we have calculated the saturation length vs. energy spread and emittances at 0.62nm with $I_{peak}=2.3kA$.

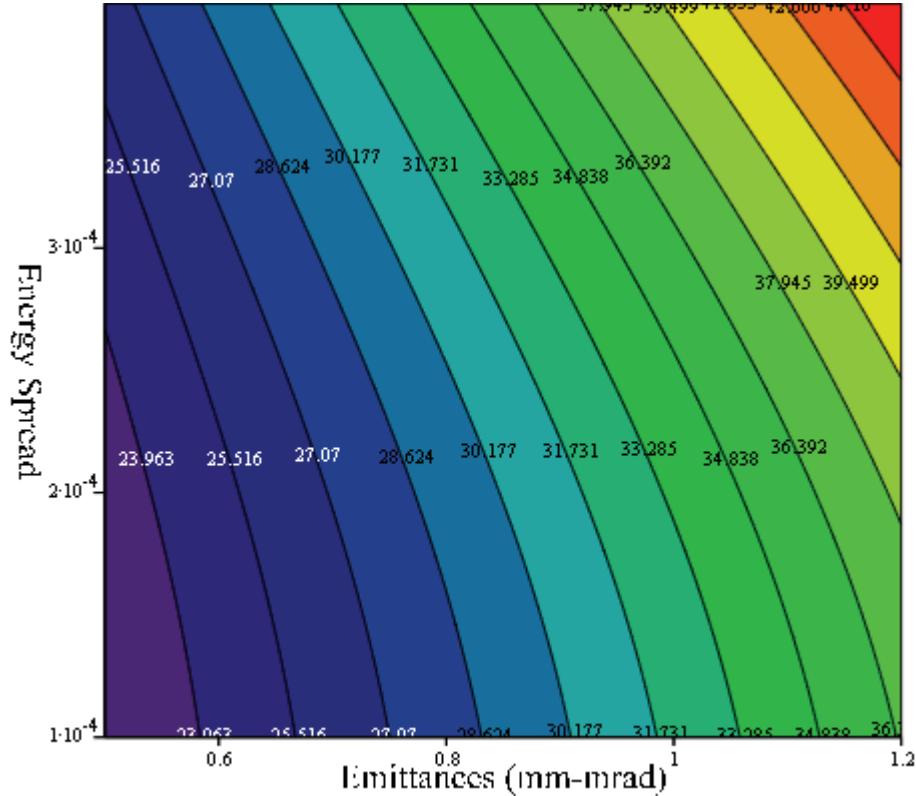


Figure 4.37: Saturation length vs. emittances and energy spread at 0.62nm for 2.3kA peak current ($\beta_{Twiss}=10m$).

The (magnetic) saturation length with the beam parameters in Table 4.9 (HE beam) is about 33-34m. At this wavelength the saturation length is quite sensitive to the beam emittance, and a saturation length below 30m can be obtained with a normalized transverse emittance (slice) lower than 0.8mm-mrad. An energy spread of the order of 10^{-4} is comparable to the correlated energy spread induced by the longitudinal wake ($\sim 300keV$). The local (slice) energy spread due to the wake is significantly smaller and its effect should still be negligible over this undulator length.

In Figure 4.38 we have calculated the saturation length vs. the resonant wavelength in the HE energy range (2.64GeV- 1.96GeV) using the parameters in Table 4.9 (red line). The blue line has been obtained with 0.8 mm mrad of normalized slice emittance. In the latter case, with an undulator of 30m, saturation is even achieved at 0.512 nm (2.42keV) at 2.64 GeV.

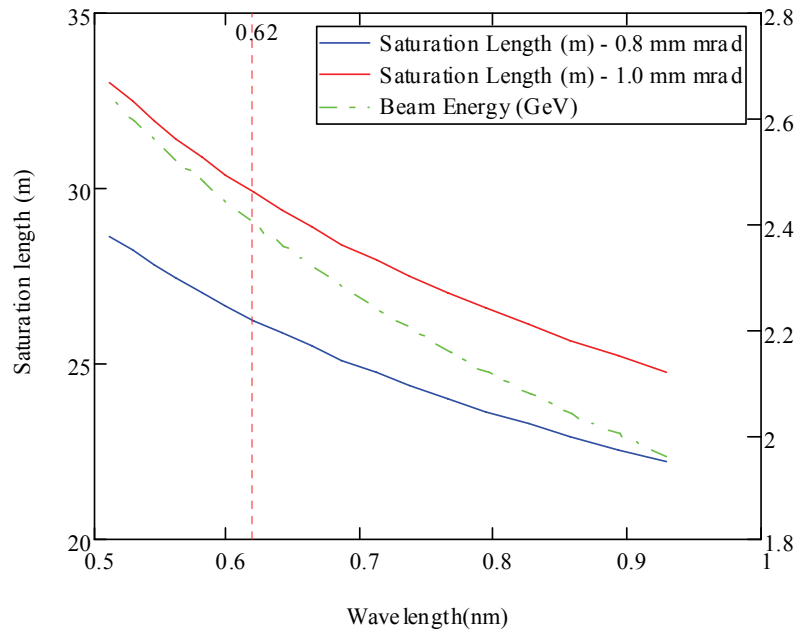


Figure 4.38: Saturation length vs. resonant wavelength with the beam parameters of Table 4.9 (HE beam) except for the normalized transverse emittances which are 0.8mm-mrad (blue line) and 1.0 mm-mrad (red line).

In Figure 4.38 we illustrate the behavior of the saturation length vs. beam current and transverse emittances (at 0.62 nm, 2.4 GeV with average Twiss $\beta=10\text{m}$).

The three beam parameters set HE-A, HE-B and HE-C have been marked with red dots. The dashed line represents the undulator length corresponding to an undulator composed by 14 modules of 180 periods each. Saturation is reached at the shortest wavelength of 0.62nm in all the three cases considered.

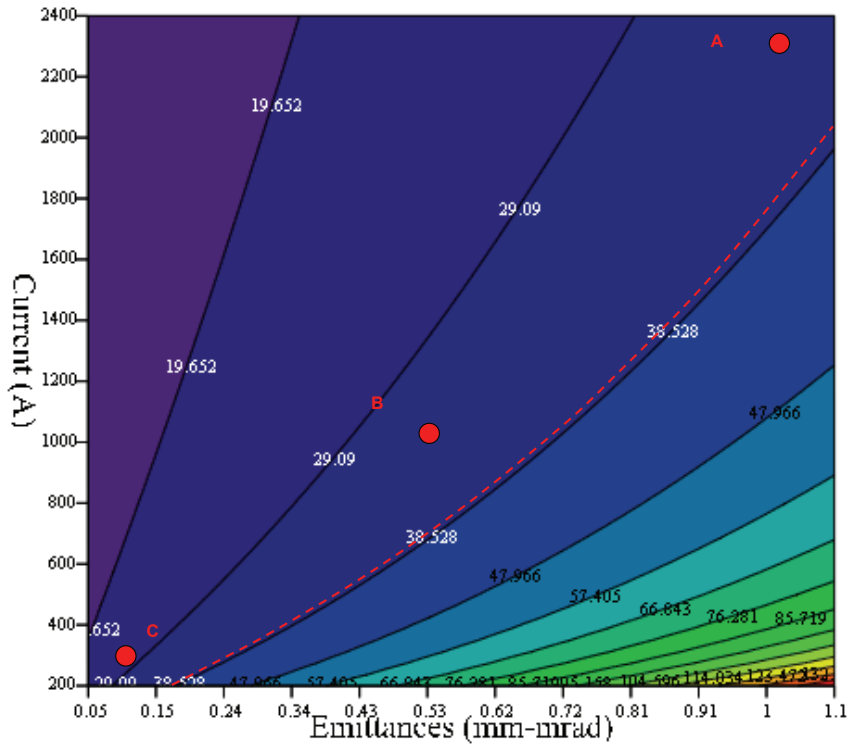


Figure 4.39: Saturation length vs. peak current and beam emittances (at 0.62 nm, 2.4 GeV with average Twiss $\beta=10m$).

4.1.7.3.1 Undulator parameters and undulator optics

The beamline is composed by 11 undulator sections, with the parameters listed in Table 4.17

Table 4.15: X-ray undulator beamline

Period	1.5 cm
Undulator length	2.7 m
No. of Periods	180
Gap	5 mm
K	1.283
Remanent field (effective)	1.45 T

The electron beam transport in the undulator is realized with a FODO lattice, with alternated gradient quadrupoles, with the difference from the previously analysed cases that the undulator is a fixed gap device where the focusing properties depend only on the beam energy. We have sketched a layout of one lattice period in Figure 4.40, where the relevant parameters are defined.

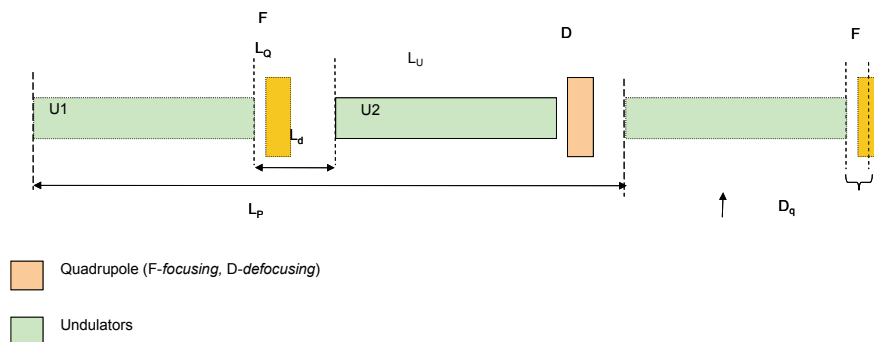


Figure 4.40: Layout of the undulator FODO lattice

The lattice period L_p extends to two undulator sections. A list of the main parameters of the beam line is summarized in Table 4.16.

Table 4.16: Parameters of the X-ray undulator beamline

Lattice period	L_p (m)	6.6
Drift length	L_d (m)	0.6
Quadrupole distance from UM (center of Q.)	D_q (m)	0.12
Beamline Length	L_b (m)	45.6

As in the previous cases we have considered non-symmetrically centred quadrupoles within the drifts between the undulators to facilitate the insertion of the diagnostics. The average Twiss β parameters in (vertical-y/horizontal plane-x) is defined in Eq. (4-19). The matching condition is obtained by imposing that the Twiss beta parameters in the horizontal and in vertical plane, averaged over the undulator U1 and U2 lengths are equal to the design parameter ($\bar{\beta}_{x,y} = \beta_d$), minimizing the difference between the Twiss beta parameters in the horizontal and in vertical plane (see eq. (4-20)). In Figure 4.41 the saturation length vs. the average Twiss $\langle \beta \rangle$ parameter is shown. The $\langle \beta \rangle$ optimizing the gain length is about 6 - 8m but a larger value of $\langle \beta \rangle$ reduces the sensitivity to transverse alignments and is not particularly detrimental in terms of the gain length increase.

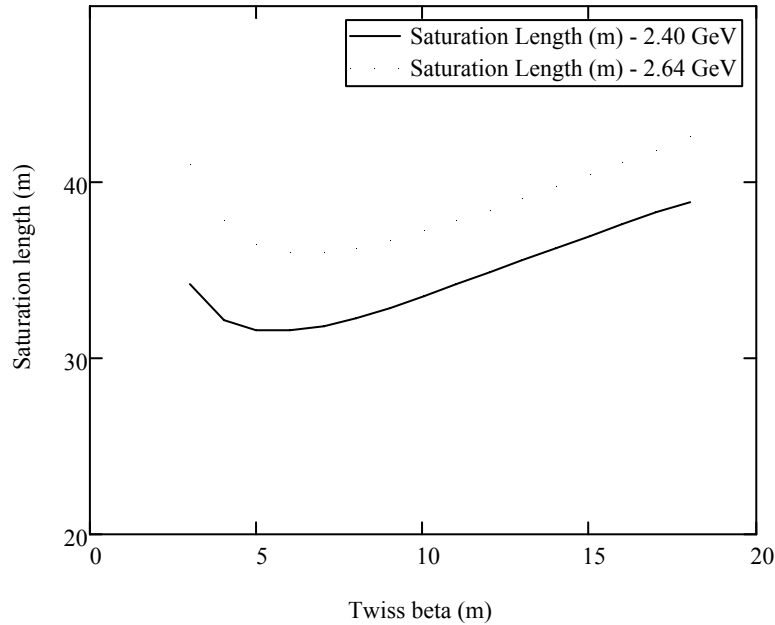


Figure 4.41: Saturation length vs. Twiss $\langle\beta\rangle$ with the HE-A beam parameters at 2.4 GeV and 2.64 GeV

The matched Twiss parameters at the undulator entrance depend on the e-beam energy and on the desired average β . The corresponding Twiss parameters α and β at the undulator entrance at the beam energy of 2.64 GeV, 2.4 GeV and 1.92 GeV are given in Table 4.17 for $\beta_d = 10m$ and $\beta_d = 6m$.

Table 4.17: Characteristics parameters of the undulator beamline

Case	Energy (GeV)	$\langle\beta_{xy}\rangle$ (m)	λ (nm)	QIG (T)	α_x	β_v (m)	α_y	β_y (m)
A	1.92	10	0.97	0.905/-1.079	1.02	12.04	-0.71	8.17
B	2.4	10	0.62	1.323/-1.461	1.13	12.28	-0.75	7.96
C	2.64	10	0.51	1.517/-1.642	1.17	12.35	-0.76	7.92
D	1.92	6	0.97	2.03/-2.19	1.62	8.99	-0.71	3.62
E	2.4	6	0.62	2.66/-2.79	1.67	9.08	-0.72	3.54
F	2.64	6	0.51	2.96/-3.08	1.69	9.1	-0.72	3.5

In Fig.(below) the Twiss β in the X and Y plane along the undulator are plotted for the FODO lattice, in case F of Table 4.17.

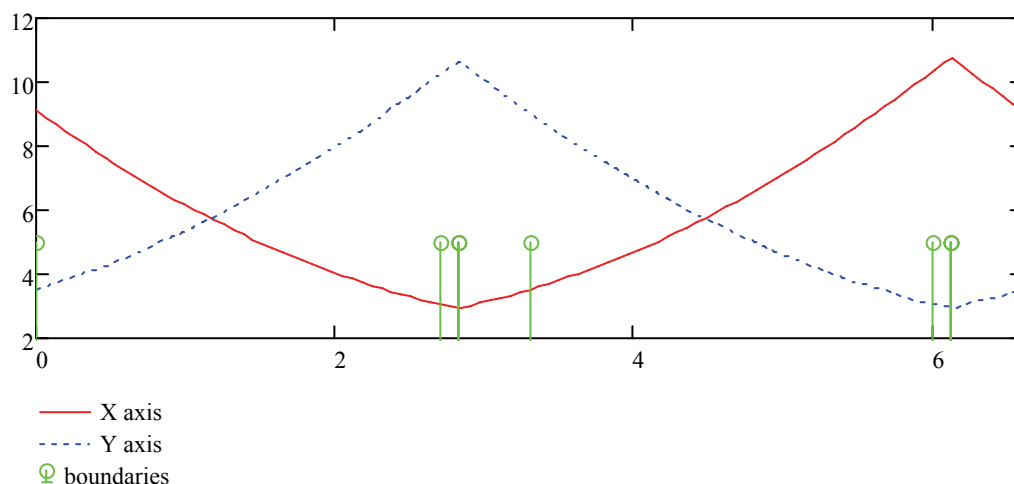


Figure 4.42: Twiss β in the X and Y plane along the undulator for the FODO lattice case F of Table 4.17. The green marks represent the boundaries of the magnetic elements in the beamline.

4.1.7.3.2 Preliminary simulations

As in the previously analysed cases, simulations of the FEL performances have been done with GENESIS 1.3 and PERSEO. This undulator is characterized by the operation at fixed gap, with a strength parameter $K=1.283$. The wavelength tuning is obtained by varying the beam energy. The simulation results are listed in Table 4.18 (below). The simulations have been done assuming a Gaussian electron beam with the parameters in Table 4.9. (HE-A column).

Table 4.18: List of the main FEL parameters for the X-ray beamline in the range 1.28/2.42 keV. Simulations done with PERSEO (black, HE-A beam - 1nC) and GENESIS 1.3 (gray/italic LE-A beam - 1nC).

	Q (nC)	E (GeV)	λ (nm)	Ph. En. (keV)	S.Len. (m)	P^{13} (GW)	P. En. (mJ)
A	1	2.64	0.512	2.42	39.8	4	0.7
B	1	2.4	0.62	2.00	34.8	4.1	0.8
C	<i>1</i>	<i>2.4</i>	<i>0.62</i>	<i>2.00</i>	<i>39.8</i>	<i>0.8</i>	<i>0.12</i>
D	1	2.2	0.738	1.68	31.4	4.1	0.86
E	1	2.0	0.893	1.39	27.7	4.1	0.84
F	1	1.92	0.968	1.28	26.9	4	0.87

¹³ Peak power calculated as the “average power” in a bunch of Gaussian shape with the pulse energy and r.m.s. duration obtained in the simulation.

	$\Delta\lambda/\lambda$ (%)	δt (fs)	#Phot. ¹⁴	Div. (rms μrad)	Size (rms μm)	#Phot. (3h)	$\Delta\lambda/\lambda$ (3h,%)
A	0.053	70	1.8×10^{12}	-	-	8×10^8	0.05
B	0.055	77	2.5×10^{12}	-	-	1×10^9	0.05
C	0.09	-	3.7×10^{11}	17	120	-	-
D	0.062	83	3.2×10^{12}	-	-	2×10^9	0.05
E	0.063	82	3.7×10^{12}	-	-	2.2×10^9	0.05
F	0.069	86	4.2×10^{12}	-	-	2.9×10^9	0.05

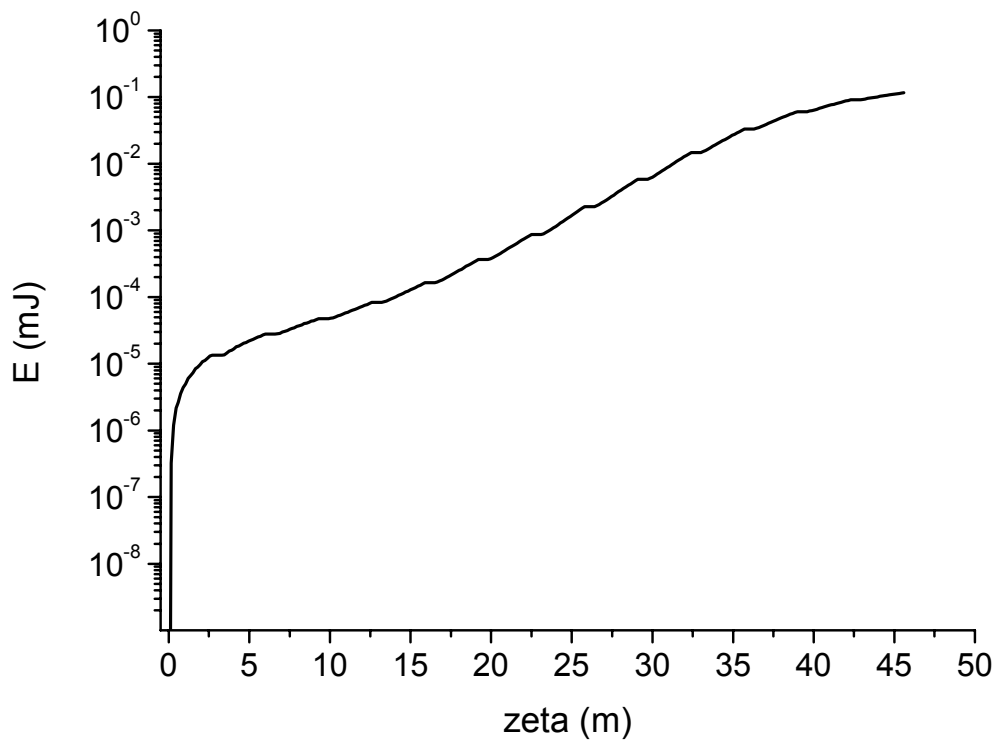


Figure 4.43: Average energy in the radiation pulse as a function of the position along the undulator

¹⁴ Photons per pulse

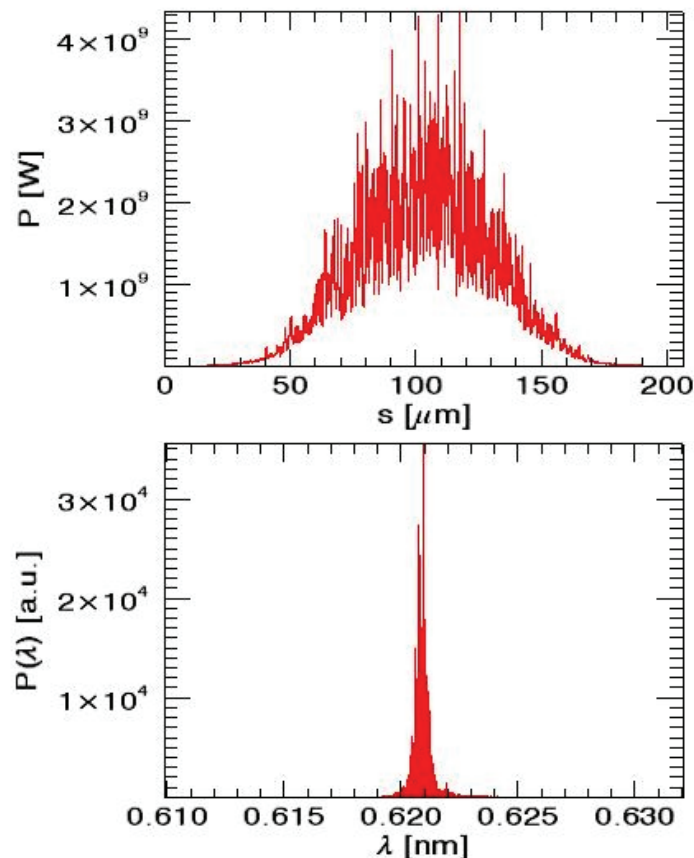


Figure 4.44: Temporal (top) and spectral (bottom) structure for 0.62 nm radiation at the end of undulator, close to saturation.

4.1.8 Conclusion

In this section we have presented an overview of the basic calculations which lead to the definition of the general parameters of the three undulator beamlines. A set of electron beam parameters fulfilling the requirements for FEL saturation with the given undulators beamline have been also discussed. The problem of matching optics and transport of the electron beam through the undulator has been analysed and preliminary simulations of the FEL performances in the various cases has been presented.

In the next sections the analysis will be focused on the problem of generating an electron beam with the required characteristics. The possibility of operating the FEL in different conditions of peak current/transverse emittances, which has been analysed in this section will be exploited to study different working points of the accelerator device, which may be optimized to produce a large number of photons in the high charge mode, or a short pulse in low charge mode. These two operation modes are indeed characterized by complementary optimization parameters in terms of peak current/normalized (slice) emittance.

The calculations presented in this section have provided the basic set of electron beam/undulator parameters ensuring operation of the three beamlines in the required wavelength ranges. In section 4.3.10 the beam parameters obtained from simulations will be implemented in full start to end calculations of the FEL radiation properties. Summary tables can be found in chapter 2 (Table 2.1 and Table 2.2).

4.1.9 Spontaneous Undulator Radiation

As any undulator, the SASE FEL one will also emit a spontaneous radiation spectrum.

Though the brilliance and spectral flux of the spontaneous emission are several orders of magnitude smaller than those of the stimulated emission, they however can be competitive with those of third generation light sources. Furthermore, the fact that the angular distribution spectrum is nearly a continuum, extending to higher energies, up to tens of keV for SPARX beamlines, might be advantageous.

For a planar undulator, the on-axis spectrum consists of the peaks of the odd harmonics, whose numbers and energy depends on the electron beam energy and the magnetic gap.

Detailed calculations of the average and peak properties of the undulator spontaneous radiation have been performed for the three undulator beamlines, i.e. VUV-EUV, EUV-Soft X-ray and Hard X-ray (cfr. Figure 4.4) and fully described in the document dedicated to the SPARX scientific case.

The RF repetition rate of the SPARX linac is limited to 100 Hz. In standard operation conditions a single electron bunch per RF pulse train is expected.

Table 4.19, Table 4.20 and Table 4.21 summarize both machine parameters and the calculated photon beam characteristics for the three cases considered.

Table 4.19: VUV-EUV beamline – UM1.

Machine design	Energy [GeV]	1.5
	Current [nA]	100
	Charge [nC/bunch]	1
	$\varepsilon_{x,y}$ [mm-mrad]	1
	Bunch FWHM τ [ps]	0.517
	# of bunches/s $\rightarrow f_{rep}$ [Hz]	100
Insertion device	Undulator L [m]	24.31
	λ_u [cm]	3.4
	# of periods N_u	65*11
	$\beta_{x,y}$ [m]	6
	K (@ $\lambda_r = 10$ nm)	2.86
	1 st harmonic energy [eV]	123.721
Beamline & optics	$\sigma'_{x,y}$ (FWHM) [μ rad]	53
	$\sigma_{x,y}$ (FWHM) [μ m]	141
DC experiments	Ave. flux F_n [ph/s/0.1%BW]	$9.6 \cdot 10^9$
	Ave. brilliance B [ph/s/mm ² /mrad ² /0.1%BW]	$1.3 \cdot 10^{14}$
Pulsed experiments	Photons/bunch	$9.6 \cdot 10^7$
	Peak flux [ph/s/0.1%BW]	$1.9 \cdot 10^{20}$
	Peak brilliance B [ph/s/mm ² /mrad ² /0.1%BW]	$2.2 \cdot 10^{24}$

To show the potential of an undulator at every energy, it is worthwhile to introduce the so-called tuning curves, which trace out how the peaks of the harmonics move as the K value changes.

For the UM1 undulator, the tuning curves which show how the average brilliance varies with the photon energy (i.e., with the K parameter) are displayed in Figure 4.45 (straight lines). The starred points plotted on the curves represent the values of the average brilliance obtained with K fixed at 2.86 corresponding to a fundamental wavelength of 10 nm and its 3rd and 5th harmonics, respectively.

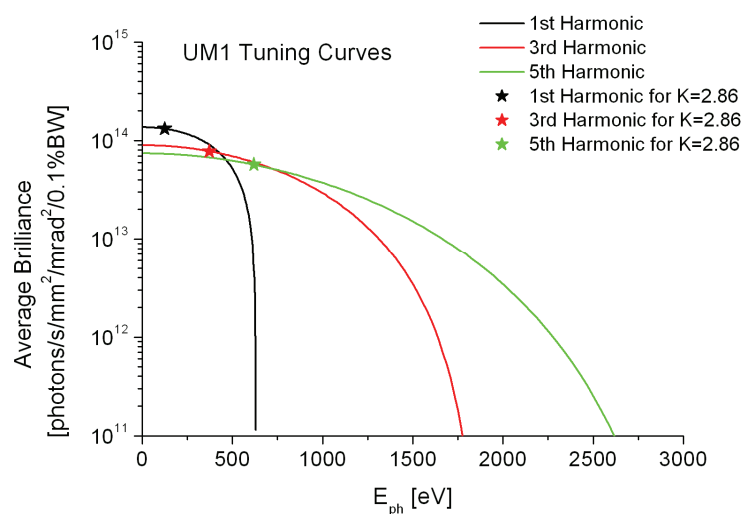


Figure 4.45: Tuning curves for UM1. The black star represents the average brilliance of the UM1 tuned with the fundamental wavelength at 10 nm, corresponding to 123.7 eV photon energy. The red and green stars depict its 3rd and 5th harmonic, whose energy is 371.2 eV and 618.6 eV, respectively.

The peak flux of the spontaneous radiation at 10 nm has been compared with the one from SASE emission at the same wavelength. The SASE line in Figure 4.46 is superimposed on a base of spontaneous emission showing how the spontaneous radiation properties are several orders of magnitude smaller than the laser values.

It is worthwhile to note that the EUV – Soft X-ray beamline (UM2) consists of three undulator magnets with different period: the long period (4 cm) undulator, the SPARC-like undulator ($\lambda_u = 2.8$ cm) and the short period (2.2 cm) undulator. For the spontaneous undulator radiation studies, each undulator, considered separately, is tuned with the fundamental wavelength at 3 nm. Table 4.20 summarizes photons characteristics for this wavelength and electron beam parameters common to the three sections.

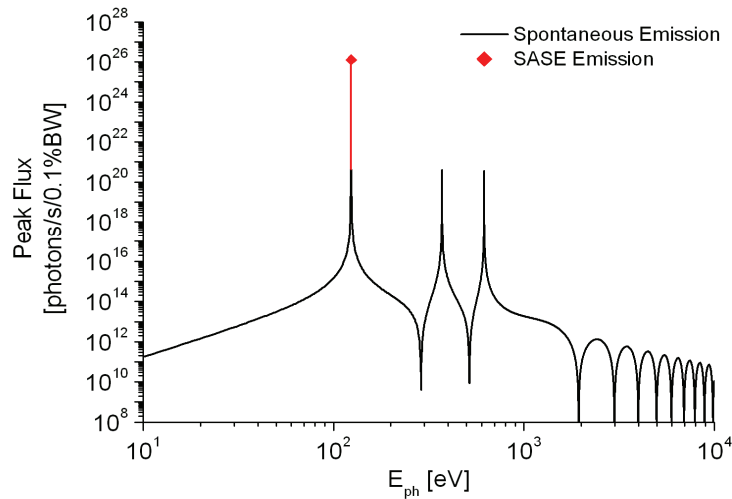


Figure 4.46: On-axis peak flux of the spontaneous VUV-EUV undulator radiation for the first three harmonics compared to the on-axis peak flux of the SASE emission at the fundamental wavelength, i.e. 10 nm.

Table 4.20: EUV - Soft X-ray, UM2.

Machine design	Energy [GeV]	1.5		
	Current [nA]	100		
	Charge [nC/bunch]	1		
	$\varepsilon_{x,y}$ [mm-mrad]	1		
	Bunch FWHM τ [ps]	0.517		
	# of bunches/s $\rightarrow f_{\text{bunch}}$ [Hz]	100		
Insertion device	Undulator L [m]	8.8	25.2	8.8
	λ_U [cm]	4.0	2.8	2.2
	# of periods N_U	55*4	75*12	100*4
	$\beta_{x,y}$ [m]	6		
	K (@ $\lambda_r = 3$ nm)	0.76	1.3	1.63
Beamline & optics	1st harmonic energy [eV]	415.3		
	$\sigma'_{x,y}$ (FWHM) [μ rad]	49	35	49
	$\sigma_{x,y}$ (FWHM) [μ m]	110	118	111
DC experiments	Ave. flux F_n [ph/s/0.1%BW]	$1.2 \cdot 10^9$	$9 \cdot 10^9$	$4.6 \cdot 10^9$
	Ave. brilliance B [ph/s/mm ² /mrad ² /0.1%BW]	$3.3 \cdot 10^{13}$	$4 \cdot 10^{14}$	$1.2 \cdot 10^{14}$
	Photons/bunch	$1.2 \cdot 10^7$	$9 \cdot 10^7$	$4.6 \cdot 10^7$
Pulsed experiments	Peak flux [ph/s/0.1%BW]	2.4	1.7	$8.9 \cdot 10^{19}$
	Peak brilliance B [ph/s/mm ² /mrad ² /0.1%BW]	10^{19}	10^{20}	$2 \cdot 10^{24}$
	Peak brilliance B [ph/s/mm ² /mrad ² /0.1%BW]	$5.5 \cdot 10^{23}$	$7 \cdot 10^{24}$	$2 \cdot 10^{24}$

Figure 4.48 shows the tuning curves for the average brilliance of the SPARC-like undulator magnet only.

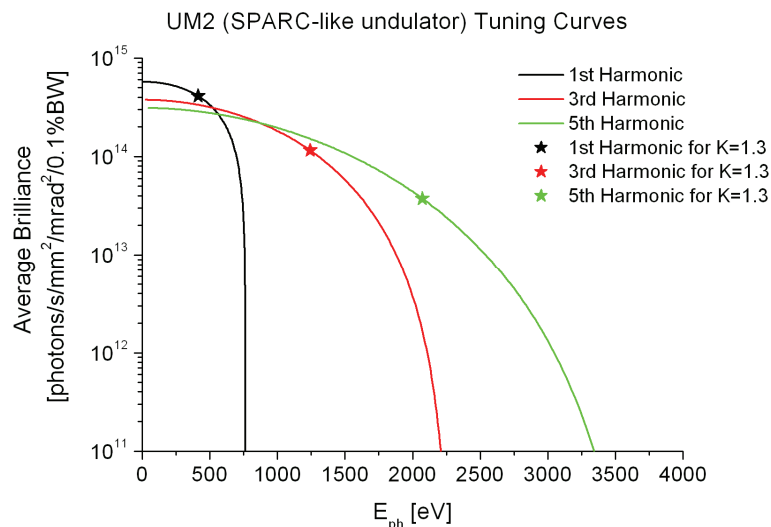


Figure 4.47: UM2 Tuning curves: the SPARC-like undulator magnet is tuned at 3 nm.

Table 4.21 summarizes electron and photon beam parameters concerning the hard X-Ray beamline.

Table 4.21: Hard X-ray beamline, UM3.

Machine design	Energy [GeV]	2.4
	Current [nA]	100
Insertion device	Charge [nC/bunch]	1
	$\varepsilon_{x,y}$ [mm-mrad]	1
	Bunch FWHM τ [ps]	0.2
	# of bunches/s $\rightarrow f_{rep}$ [Hz]	100
	Undulator L [m]	37.8
	λ_U [cm]	1.5
	# of periods N_U	180*14
	$\beta_{x,y}$ [m]	6
	K (@ $\lambda_r = 0.62$ nm)	1.28
	1st harmonic energy [keV]	2
Beamline & optics	$\sigma'_{x,y}$ (FWHM) [μ rad]	25
	$\sigma_{x,y}$ (FWHM) [μ m]	90
DC experiments	Ave. flux F_n [ph/s/0.1%BW]	$2.5 \cdot 10^{10}$
	Ave. brilliance B [ph/s/mm ² /mrad ² /0.1%BW]	$3.8 \cdot 10^{15}$
Pulsed experiments	Photons/bunch	$2.5 \cdot 10^8$
	Peak flux [ph/s/0.1%BW]	$1.2 \cdot 10^{21}$
	Peak brilliance B [ph/s/mm ² /mrad ² /0.1%BW]	$1.7 \cdot 10^{26}$

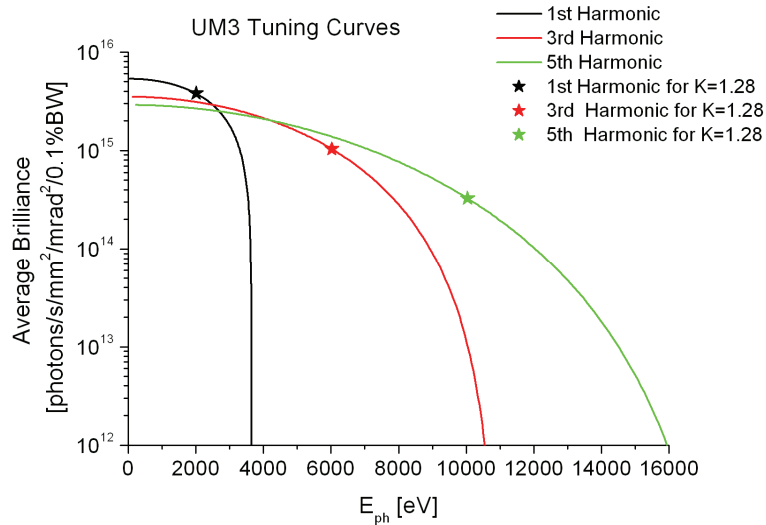


Figure 4.48: Tuning curves for the hard X-ray beamline. With the K parameter fixed at 1.28 the fundamental wavelength is 0.62 nm (2 keV) and the 3rd and 5th harmonic are 2Å (6 keV) and 1.2 Å (10 keV), respectively.

Figure 4.48 shows the average brilliance for the hard X-Ray beamline as a function of the photon energy and highlights the potential of this undulator. The tuning curve for the 5th harmonic of 0.62 nm (1.2 Å, corresponding to 10 keV) extends up to 16 keV indeed. The values of the average brilliance corresponding to the first three odd harmonics for K fixed at 1.28 are plotted on the straight line curves with the star symbols.

From the point of view of the users, repetition rates as high as ~10 MHz are interesting for a large class of experiments. Such high rates could be provided in a burst mode at SPARX where higher repetition rates could be achieved by filling a larger number of bucket in the RF pulse.

At this regard, we studied the properties of the spontaneous undulator radiation in the case of multi-bunch operation for the high energy hard X-ray beamline. We considered a train of electron bunches, each bunch having a 200 fs pulse width and repetition rate of 10 MHz. Machine parameters and the calculated photon beam properties are presented in Table 4.22.

Table 4.22: Hard X-ray beamline, multi-bunch operation.

Machine design	Energy [GeV]	2.4
	Current [A]	0.01
	Charge [nC/bunch]	1
	$\varepsilon_{x,y}$ [mm-mrad]	1
	Pulse train length [ns]	390
	Macro-pulse Rep. Rate f [Hz]	100
	Bunch Rep. Rate f_0 [MHz]	10

Insertion device	Bunch FWHM τ [fs]	200
	Undulator L [m]	37.8
	λ_u [cm]	1.5
	# of periods N_u	180*14
	$\beta_{x,y}$ [m]	6
Beamline & optics	K (@ $\lambda_r = 0.62$ nm)	1.28
	1st harmonic energy [keV]	2
	$\sigma'_{x,y}$ (FWHM) [μ rad]	25
	$\sigma_{x,y}$ (FWHM) [μ m]	90
DC experiments	Ave. flux F_n [ph/s/0.1%BW]	$2.5 \cdot 10^{15}$
	Ave. brilliance B [ph/s/mm ² /mrad ² /0.1%BW]	$3.8 \cdot 10^{20}$
Pulsed experiments	Photons/bunch	$2.5 \cdot 10^8$
	Peak flux [ph/s/0.1%BW]	$1.2 \cdot 10^{21}$
	Peak brilliance B [ph/s/mm ² /mrad ² /0.1%BW]	$1.7 \cdot 10^{26}$

Figure 4.49 shows the average brilliance from spontaneous undulator radiation in the hard X-ray beamline when SPARX is operated in the standard single bunch mode (black curve) compared to the multi-bunch operation (red curve). It is clear that due to the higher average beam current (10 mA instead of 100 nA), the average photon beam parameters are enhanced with respect to the single bunch case by several orders of magnitude.

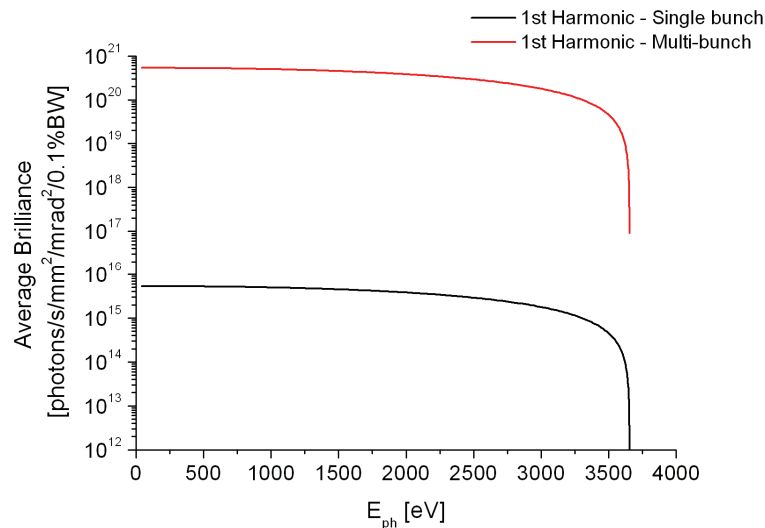


Figure 4.49: Hard X-ray beamline The average brilliance for the single bunch operation is compared to the multi-bunch one. The tuning curve of the 1st harmonic only is depicted.

4.2 Photo-Injector

4.2.1 Introduction

The SPARX photoinjector is based on the SPARC facility [42] now in phase of commissioning at INFN laboratories at Frascati. It is mainly devoted to FEL SASE-seeding experiments in the visible light, but is intended also to be used as a test prototype of the SPARX photoinjector.

The layout is shown in Figure 4.50: it consists of a 1.6 cell RF gun (BNL/SLAC/UCLA type) including a Copper photocathode with an emittance compensating solenoid followed by three 3-meters long SLAC-type travelling wave sections operating at 2856 MHz. The first two accelerating sections are embedded in a solenoid; each solenoid is composed of 13 coils with the first coil and the other twelve coils in groups of three independently supplied.

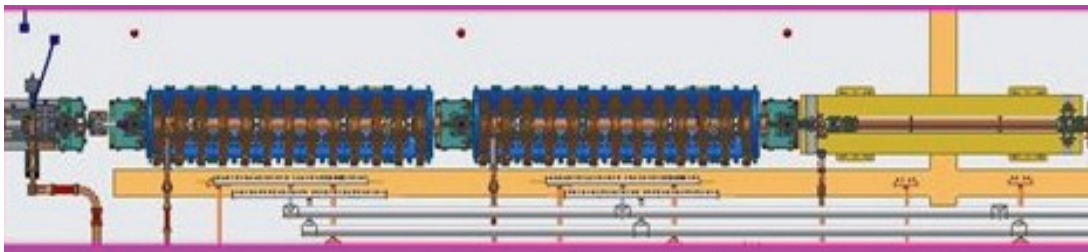


Figure 4.50: Photoinjector layout

The main operating parameters of the SPARX photoinjector are summarized in Table 4.23.

Table 4.23: Main photoinjector parameters

Parameter	Value
Gun electric field amplitude	120 MV/m
Gun electric field operation phase	32°
Output gun beam energy	5.6 MeV
Amplitude of electric field in the traveling wave sections	23.5 MV/m
Magnetic field in the emittance compensating solenoid	2.72 kgauss
Total photoinjector length	12 m

The maximum flexibility is required in order to provide different beams for the FEL operation to satisfy the needs of the FEL users. At this aim different working points have been identified spanning a range of charge between 50 pC and 1 nC.

The experimental observation of the so called “double minimum oscillation” [43] in the first phase of SPARC commissioning confirmed for the working point at 1nC in the SPARX photoinjector the same choice done for SPARC. It consists in placing the LINAC in the position where the local maximum of the emittance oscillation occurs and then matching properly the beam with the accelerating structures according to the “invariant envelope” condition [44]. This working point was originally proposed in the context of the LCLS Project [45] and later has been adopted also by X-FEL collaboration at DESY [46].

Starting from the parameters of the working point at 1 nC, the transverse and longitudinal rms sizes of the beam for lower values of charge are scaled with the power 1/3 of the charge. In this way the conditions of injection (gun electric field amplitude and phase and the emittance compensating solenoid strength) are the same for all the working points and what is changed passing from one working point to another is only the focusing on the accelerating structures and the RF phase of the structures.

As to the RF compression or “velocity bunching” technique [47], it consists in compressing the beam by injecting it in the first RF structure with a phase near to the zero accelerating phase: the beam slips back up to the acceleration phase undergoing a quarter of synchrotron oscillation and is compressed. The emittance growth occurring during the compression can be taken under control by a proper shaping of the magnetic field of the focusing solenoids embedding the accelerating structures. The simulations show that compression factors larger than three require an accurate tuning of the coils composing the solenoids embedding the structures.

The beam dynamics for each working point has been extensively studied and optimized by using the PARMELA (LANL version) code according to the above design criteria. In the simulations a number of particles of 50K has been used in phase of optimization after increased to 200K to be used with a good statistics in the start-to-end simulations. A cylindrical symmetry has been assumed with a number of mesh intervals equal to 20 in radial direction and 200 in longitudinal direction. For the working point with the maximum RF compression an optimization genetic algorithm combined with ASTRA code has been also tested [48]. As to the thermal emittance a typical value of 0.6 mm-mrad/mm of an hard edge beam radius has been considered in all simulations.

4.2.2 High charge working point (1 nC)

This working point, based on a 1 nC beam, is splitted in three operation modes depending on the use or not of the RF compression. The input and output beam parameters are listed in Table 4.24 and Table 4.25.

Table 4.24: Input beam parameters

Parameter	Value
Charge, Q	1 nC
RMS transverse size, σ_{xv}	550 μm
Temporal structure	Flat top, FWHM=10 ps, rise time=1 ps
Thermal emittance	0.66 mm-mrad

Table 4.25: Output beam parameters

Parameter	No RF compression	Moderate RF compression	High RF compression
Charge (nC)	1	1	1
Energy (MeV)	216.7	163	148.6
RMS bunch length (μm)	904	280	108
RMS normalized emittance (mm-mrad)	0.98	1.19	1.6
Correlated energy spread (%)	0.15	1.037	0.737
Peak current (A)	94	309	800
RMS size, σ_{xy} (μm)	270	162	163
Twiss parameters, α_{xy}, β_{xy}	-1.28, 31.6	-0.71, 7.1	-0.6, 5

For the three operation modes Figure 4.51 shows the computed behaviour of the rms emittance and transverse and longitudinal envelopes along the photoinjector. It can be observed that the emittance increases with the compression, but the growth is always limited and kept under control. Figure 4.52 shows the expected longitudinal phase space at 12 m from the cathode: in the operation mode without RF compression the phases on the three booster sections have been set in order to minimize the output energy spread, whilst in the other two operation modes the phase of the first section has been moved toward the zero phase in order to compress the bunch.

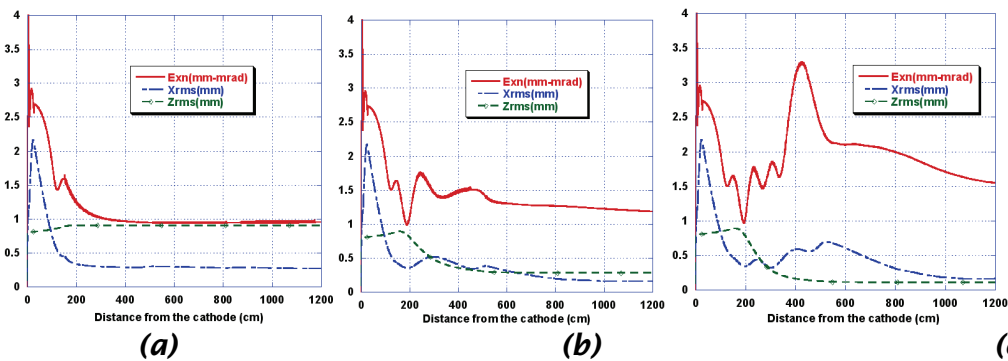


Figure 4.51: Evolution of normalized transverse emittance, transverse envelope and longitudinal envelope from the cathode to the injector exit for the high charge working point: (a) no RF compression (b) moderate RF compression (c) high RF compression

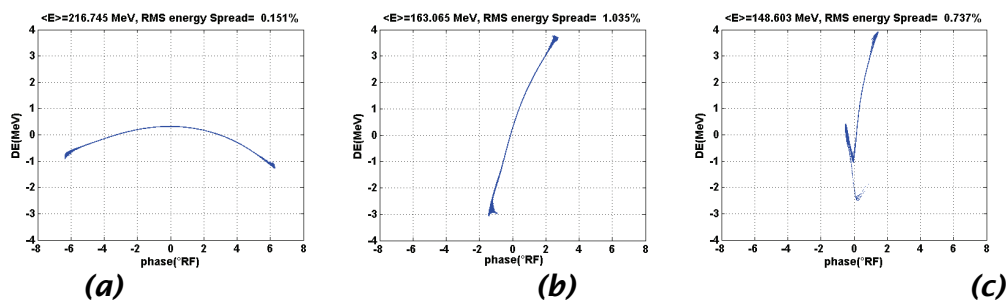


Figure 4.52: Longitudinal phase space at the injector exit for the high charge working point: (a) no RF compression (b) moderate RF compression (c) high RF compression

The operation mode with moderate compression ($\varphi(TW1) \sim -85^\circ$) foresees the use of the high charge beam in a hybrid RF-magnetic compression scheme: a RF compression factor of 3 has been chosen because for larger values the deteriorating of the longitudinal emittance induced by the uncompensated nonlinearities due to the space charge (third order non linearity) and to the effect of RF curvature (fourth order non linearity) prevents an effective use of the magnetic compression. The operation mode with high RF compression ($\varphi(TW1) \sim -89.5^\circ$) uses a compression factor around 7: for this high value a high current spike is produced that can be used for lasing at high energy without any further magnetic compression. Of course this high compression factor requires an accurate shaping of the magnetic field especially in the first TW section, where the RF compression occurs: an increase of the magnetic field (Figure 4.53) with the bunch current is required in order to control the projected emittance that at 12 m from a cathode is limited to 1.6 mm-mrad. A spike with a very high normalized brightness ($2 \cdot 10^{15} \text{ A}/(\text{m}\cdot\text{rad})^2$) can be produced in such way (Figure 4.54). This result has been obtained by an interplay between a manual optimization based on PARMELA aimed to move the minimum number of parameters and different solutions found by an optimization genetic algorithm [48] interfaced with ASTRA.

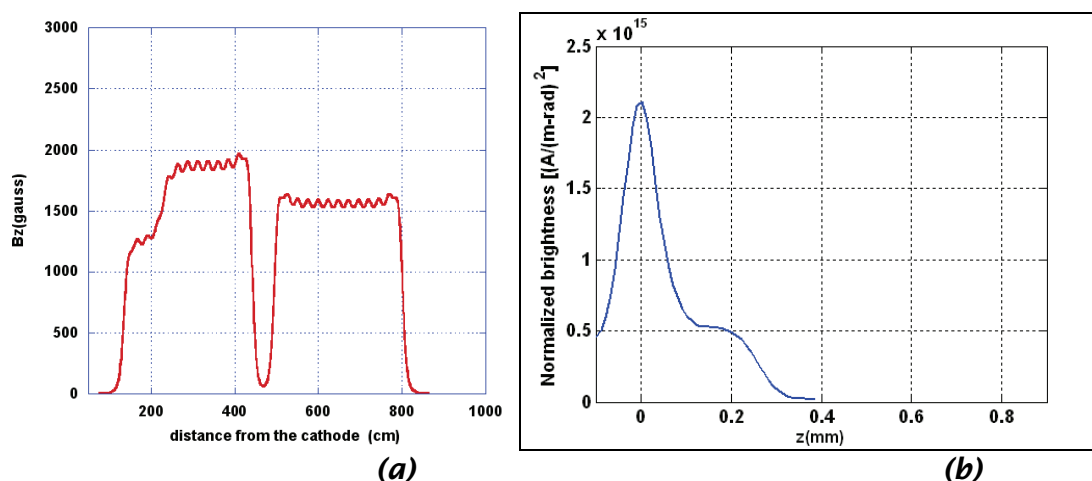


Figure 4.53: High RF compression-high charge working point: (a) on-axis magnetic field of the solenoids embedding the first 2 TW sections (b) Brightness along the bunch (the bunch head is on the left)

4.2.3 Low charge working point (200 pC)

This working point uses a 0.2 nC beam and is splitted in two operation modes with and without RF compression to be used respectively in a scheme with full magnetic compression and in an hybrid RF-magnetic compression scheme. As it can be seen in tables 3.2.4 and 3.2.5 the peak current that is only 32 A without RF compression can be raised to 96 A by using the RF compression with a lower emittance respect to the 1nC working point with the same peak current.

Table 4.26: Input beam parameters

Parameter	Value
Charge, Q	0.2 nC
RMS transverse size, σ_{xy}	300 μm
Temporal structure	Flat top, FWHM=6 psec, rise time=1 psec
Thermal emittance	0.36 mm-mrad

Table 4.27

Parameter	No RF compression	With RF compression
Charge (nC)	0.2	0.2
Energy (MeV)	216.94	161.96
RMS bunch length (μm)	539	182
RMS normalized emittance (mm-mrad)	0.53	0.62
Correlated energy spread (%)	0.056	0.6
Peak current (A)	32	96
RMS size, σ_{xy} (μm)	209	158
Twiss parameters, α_{xy}, β_{xy}	-1,35.5	-1.3,12.7

In addition to the reduced level of emittance in the photoinjector the use of a low charge level is expected to give more stable performances with negligible resistive wakefields, greatly reduced CSR effects and no transverse wakefield dilution in the LINAC [49].

Figure 4.54 compares the two operation modes of this low-charge working point respect to the evolution in the photoinjector of envelopes and transverse emittance. The longitudinal phase spaces are compared in Figure 4.59: as for the high charge working point the RF compression factor has been chosen in order to get a longitudinal phase space that is enough linear and suitable for the following magnetic compression.

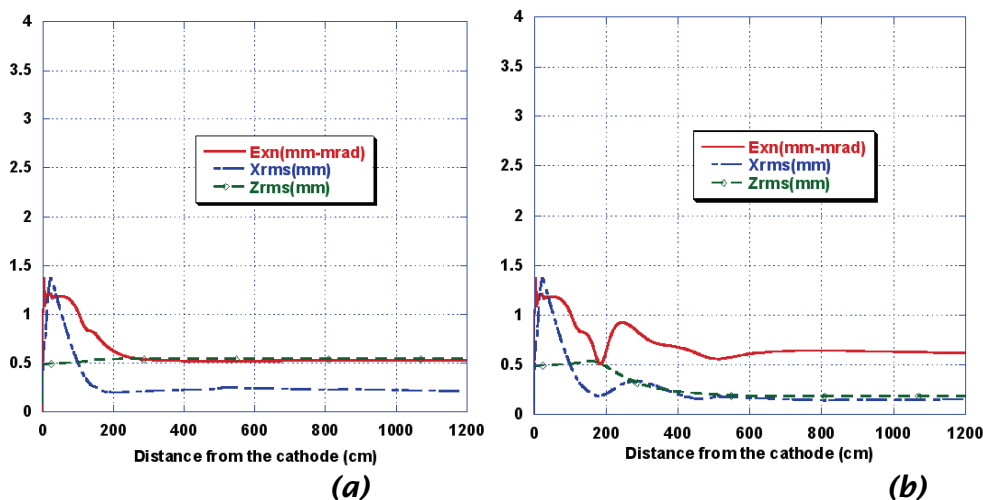


Figure 4.54: Evolution of normalized transverse emittance, transverse envelope and longitudinal envelope from the cathode to the injector exit for the low charge working point: (a) no RF compression (b) RF compression on

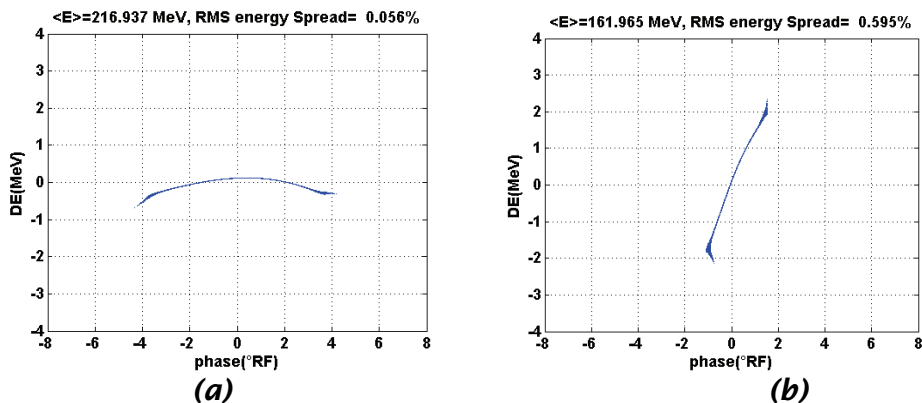


Figure 4.55: Longitudinal phase space at the injector exit for the low charge working point: (a) no RF compression (b) RF compression on

4.2.4 Short pulse working point (50 pc)

This working point has been selected for the FEL applications requiring a very short pulse with a RMS length around $5 \mu\text{m}$. This goal can be achieved by using an hybrid compression scheme based on the use of the RF compression in the photoinjector producing a short bunch with a rms length of about $50 \mu\text{m}$ and then applying a further compression of about a factor ten in the magnetic compressors. The input and output beam parameters are reported in Table 4.28 and Table 4.29: the charge of 50 pC is compatible with the SPARX diagnostics.

Figure 4.56 shows the evolution of the rms emittance and transverse and longitudinal envelopes along the photoinjector. The longitudinal phase space is shown in the plots of Figure 4.57: the scale on the left plot is the same used for the others working points putting in evidence the shortness of the pulse in comparison with the other working points.

Table 4.28: Input beam parameters

Parameter	Value
Charge, Q	0.05 nC
RMS transverse size, σ_{xy}	180 μm
Temporal structure	Gaussian, $\sigma_t=1$ ps
Thermal emittance	0.22 mm-mrad

Table 4.29: Output beam parameters

Parameter	With RF compression
Charge (nC)	0.05
Energy (MeV)	161.3
RMS bunch length (μm)	45
RMS normalized emittance (mm-mrad)	0.47
Correlated energy spread (%)	0.235
Peak current (A)	96
RMS size, σ_{xy} (μm)	126
Twiss parameters, α_{xy}, β_{xy}	-0.77, 10.7

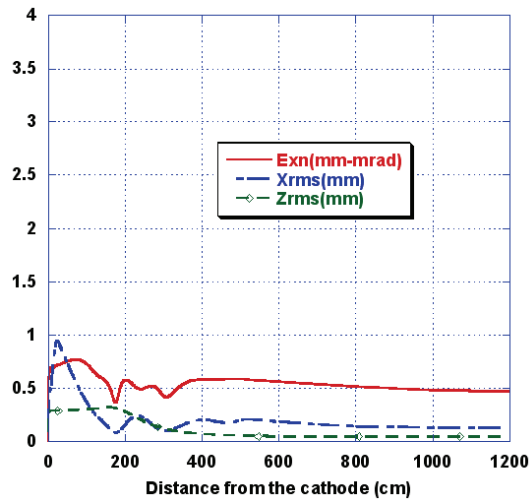


Figure 4.56: Evolution of normalized transverse emittance, transverse envelope and longitudinal envelope from the cathode to the injector exit for the short pulse working point

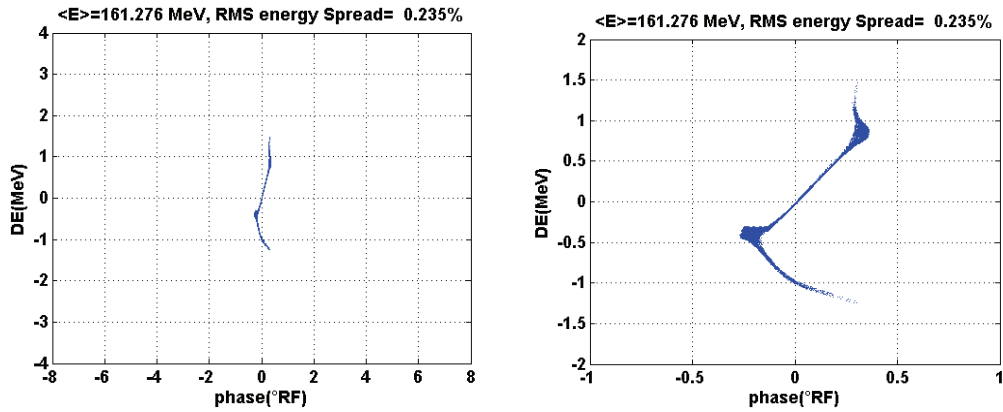


Figure 4.57: Longitudinal phase space at the injector exit for the short pulse working point on two different scales: the left scale is the same used for the other working points.

4.2.5 Sensitivity to RF compressor phase jitter

In the previous paragraphs it is shown that the largest part of the SPARX photoinjector operation modes employs the technique of the RF compression. So a study of sensitivity of beam parameters to the RF compressor phase jitter has been done. The analysis shows that the most sensitive beam characteristic to this parameter is the RMS bunch length. The plot in Figure 4.58 of the percentage variation of the RMS bunch length versus the RF compressor phase error indicates that, as it is expected, rising the compression requires a better phase stability and that in order to limit the rms bunch length variation below 10% a phase stability of 0.25 RF degrees is required.

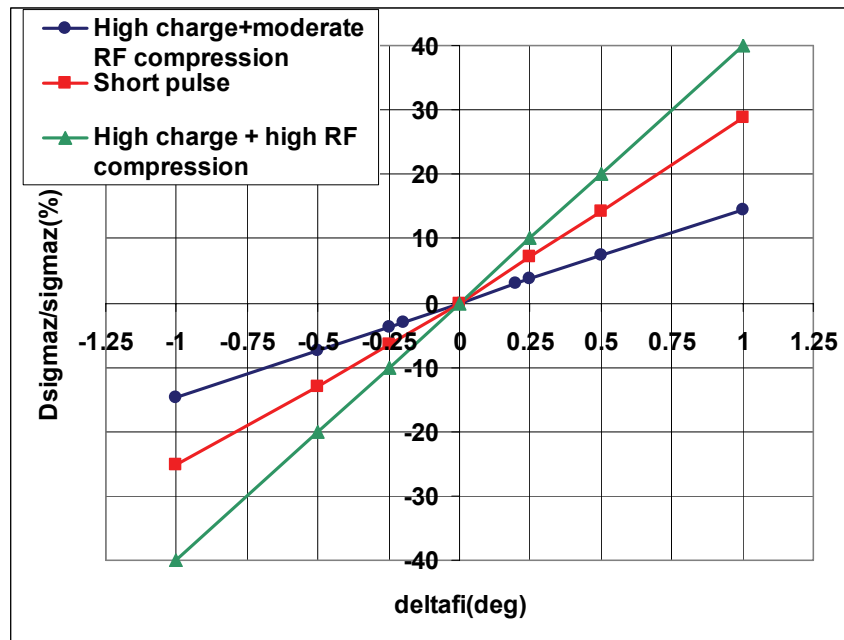


Figure 4.58: Percentage variation of the rms bunch length vs RF compressor phase error.

4.3 Accelerator

4.3.1 Overview

The SPARX accelerator is meant to be realized in two phases providing a radiation wavelength in the following ranges: $\lambda_r \approx 40 \div 10$ nm, $\lambda_r \approx 15 \div 3$ nm, $\lambda_r \approx 4 \div 1.2$ nm, $\lambda_r \approx 1.2 \div 0.6$ nm at different electron beam energies around 1 GeV, 1.2 GeV, 1.5 GeV, 2.4 GeV. To reach SASE saturation in reasonable length undulators a peak current $I_{pk} \approx 1 \div 2.5$ kA is needed for lower and higher energies respectively. The required final beam energy spread is 0.1% in each case and the machine is designed to operate at a repetition rate of 100 Hz. The main parameter list is reported in Table 4.30 and a schematic drawing of the accelerator is shown in Figure 4.59 where the nominal beam energy, rms bunch length σ_z and rms energy spread σ_δ are indicated.

Table 4.30: Electron beam general parameter list

Energy	(GeV)	E	1 \div 1.5	2.4
Peak current	(kA)	I_{pk}	1	2.5
Normalized transverse emittance <i>slice</i>	(μm)	ϵ_n	1	1
Correlated energy spread	(%)	σ_δ	0.1	0.1
Radiation wavelength	(nm)	λ_r	40 \div 3	3 \div 0.6

4.3.2 Layout

The SPARX accelerator is composed of five S-band LINAC sections ($f_{rf} = 2.856$ GHz, $E_{acc} = 23.5$ MV/m), one short X-band section ($f_{rf} = 11.424$ GHz), and six separate bending sections (three compressor chicanes and three “doglegs”). The first LINAC LINAC-0 (L0) is composed of three 3m long accelerating sections: it belongs to the SPARC photoinjector system previously described. A diagnostic section follows in the transport line prior LINAC-1 providing energy and beam emittance diagnostic. A laser heater chicane is also included upstream to rise the uncorrelated beam energy spread [50]. The following LINAC-1 includes three accelerating sections, operating at $\Phi_{rf} = -18 \div -28^\circ$, and rises the beam energy up to ≈ 350 MeV before the first magnetic compressor BC-1; a short X-band section is also provided to linearize the beam longitudinal phase space before the bunch compression [51]. The BC-1 magnetic chicane, with $R_{56} \approx 61$ mm, should bring the peak current from 100 to 350 \div 400 A. The BC-1 magnets are foreseen to be switched off when the beam current from the photoinjector is $I_{pk} \geq 300$ A, i.e. when the velocity bunching technique [52] is adopted in the photoinjector system and the magnetic compression occurs in BC-2-3 only. The RF-compression technique is presently under test at the SPARC photoinjector facility at LNF [53], and from this point of view SPARX will be the first FEL facility to operate with the hybrid (RF plus magnetic chicane) compression scheme.

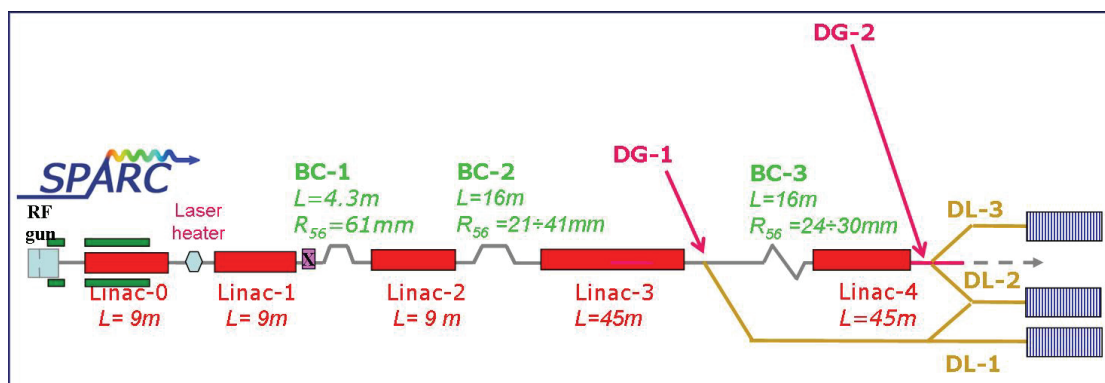


Figure 4.59: SPARC acceleration and compression schematic layout. Two beam delivering energies are foreseen with two doglegs DL1-2 having no effect on the bunch length; the compressors BC1-2-3 are four-dipole chicanes, the on crest acceleration is defined at $\Phi_{rf}=0$.

The LINAC-2 is composed of three accelerating sections operating at $\Phi_{rf} = -18 \div -28^\circ$, it brings the beam energy up to 500 MeV and the projected energy spread up to $\sigma_\delta \approx 0.7\%$. The BC-2 magnetic chicane with an $R_{56} \approx 22$ mm compresses the bunch length up to a peak current of 1 kA and the LINAC-3 (fifteen sections) increases the beam energy up to 1.5 MeV, while compensating the projected beam energy spread down to $\sigma_\delta \approx 0.1\%$. The DL1-2 doglegs are a four-six dipole bypass beamline with $R_{56} = 0$ that extracts the 1.5 GeV beam and deliver it to the entrance of the low-medium energy undulators U1 and U2 respectively. A diagnostic section DG-1 is provided downstream the LINAC-3 for the complete electron beam characterization.

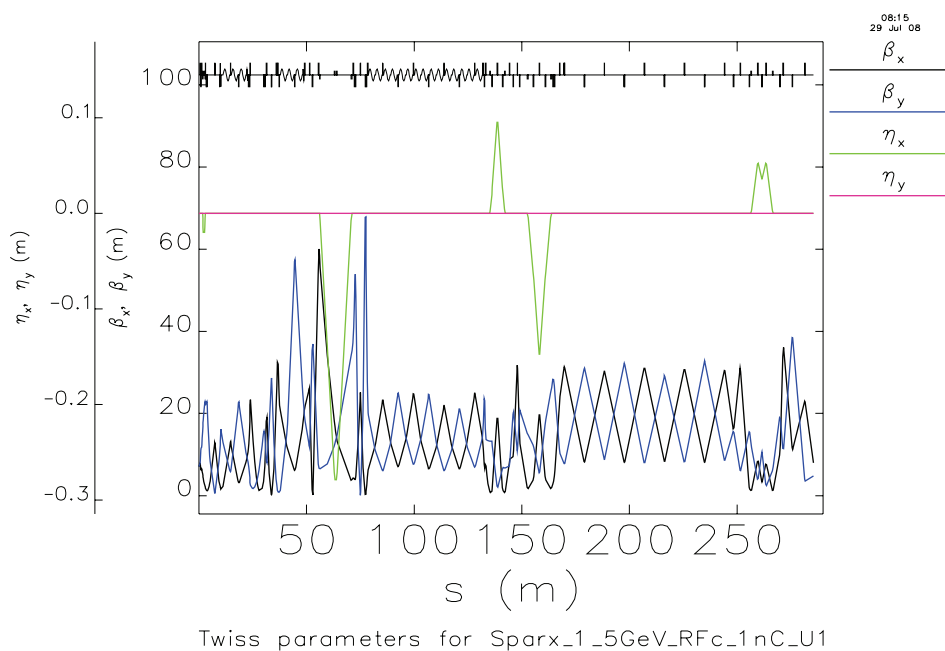


Figure 4.60: Twiss Parameters for the 1.5GeV and DL1-U1 channel. Here only BC2 is switched ON.

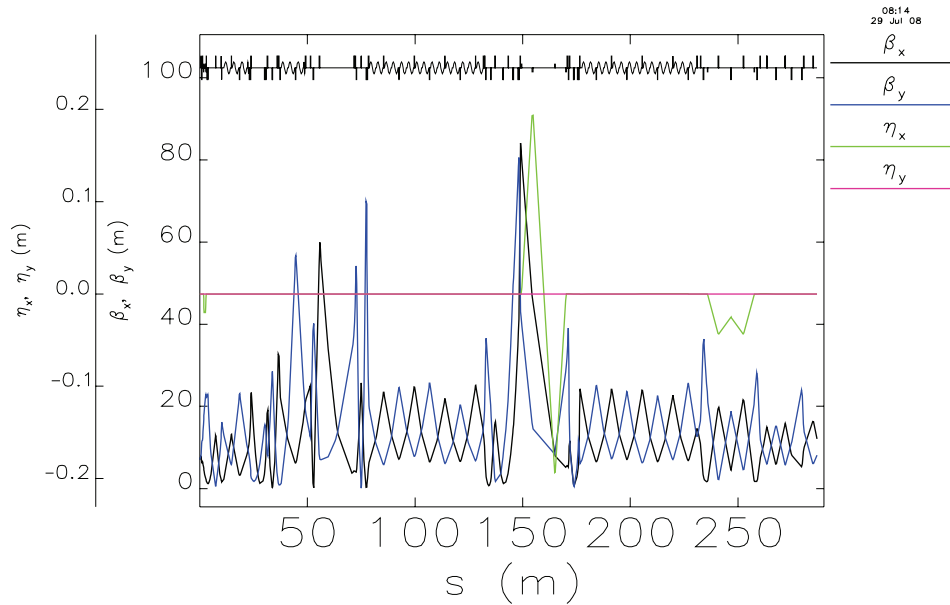


Figure 4.61: Twiss Parameters for the 2.4 GeV and DL2-U3 channel. Here only BC3 is switched ON

With an off-phase of $\Phi_{rf} = -28^\circ$ the LINAC 3 injects an energy chirped 1.5 GeV beam in the BC-3 s-shaped magnetic chicane, $R_{56} \approx 30$ mm, that performs the final compression on the electron beam rising the bunch current up to $I_{pk} \approx 2.5$ kA. Then the LINAC-4 (fifteen sections) accelerates the electrons up to 2.4 GeV and the high energy DL-2 dogleg delivers the beam to the medium-high energy undulator.

In Figure 4.60 and Figure 4.61 the Twiss parameters are reported for the 1.5-2.4 GeV LINAC from the photoinjector exit down to the undulators entrance.

4.3.3 LINAC L1-L4

The four LINAC sections L1-L4 are based on the S-band ($f_{rf}=2856$ MHz, $L=3$ m) accelerating structures. The maximum accelerating gradient is $E_{acc}=23.5$ MV/m. The L1 LINAC is composed by three RF structures and starts the bunch compression process accelerating off crest the beam from 150 MeV up to 350 MeV, generating the required linear energy-z correlation to compress the 100A beam in BC1, with a final energy spread of 1.1 %. In the same way the L2 LINAC accelerates off crest the beam up to 500 MeV reaching an energy spread of about 0.7 % for the second compression stage taking place in BC2. When the BC1 chicane is switched off both the L1-L2 LINACs operate off crest at the same phase to reach the required correlated energy spread before BC2. The L3 LINAC is composed by fifteen structures and can accelerate the beam up to 1.5 GeV. The L1 LINAC provides a quadrupole between each of the three sections. For the L2-L3-L4 LINAC a 6 m quadrupole spacing has been chosen in order to place quadrupole and beam steering pairs after each pair of RF structures, in a 80 cm drift. The 70.2° betatron phase advance per cell has been considered in order to smoothly vary the beam envelope through the accelerating sections easing the beta's matching upstream and downstream the

magnetic compressors. Nevertheless optimization of this preliminary adopted lattice is in progress to minimize element misalignment effectiveness on the emittance dilution. In Figure 4.62 the Twiss parameters are reported along the L4 LINAC. For the 2.4 GeV beam the BC2 chicane is turned off and the compression is operated in BC3 only. The L3 LINAC is operated off crest to reach a correlated energy spread of $\approx 0.7\%$ before the BC3 compression, then the L4 accelerates the beam at 2.4 GeV. Upstream the BC1 compressor chicane a X-band short section is located to counteract the second-order term in the beam longitudinal phase space distribution. In Table 4.31 the beam parameters for the four LINAC sections and the X-band structures are reported for the 2.4 GeV SPARX beam.

Table 4.31: Beam parameters of the four S-band LINAC sections plus the X band (case for $Q=1nC$, $E=2.4$ GeV, with BC1 and BC2 OFF)

Beam Parameter	unit	L1	X1	L2	L3	L4
Initial energy	GeV	0.163	0.347	0.321	0.508	1.433
Final energy	GeV	0.347	0.321	0.508	1.433	2.416
Active linac length	m	9.00	0.60	9.00	15.00	15.00
RF phase (crest at 0)	deg	-28.5	180.0	-28.2	-28.2	22
Initial rms energy spread	%	1.06	0.81	0.89	0.78	0.66
final rms energy spread	%	0.86	0.89	0.78	0.66	0.25
rms bunch length	mm	0.244	0.244	0.244	0.244	0.049

Beside the beam transport in the LINAC through a FODO lattice another scheme has been recently approached for beams propagating in transition regime, i.e. from space charge to emittance dominated dynamics [54], as it is the case for the SPARX beam from the exit of the magnetic compressors up to the final delivery energy. In this regime the electron beam can be properly matched to the LINAC accelerating sections under invariant envelope conditions, and it has been shown in the reference that an equilibrium between RF focusing forces and space charge emittance defocusing forces can be obtained without external focusing along the LINAC (no quadrupoles needed), thus reducing alignment problems and mitigating emittance dilutions due to misalignments and beam parameter jitters.

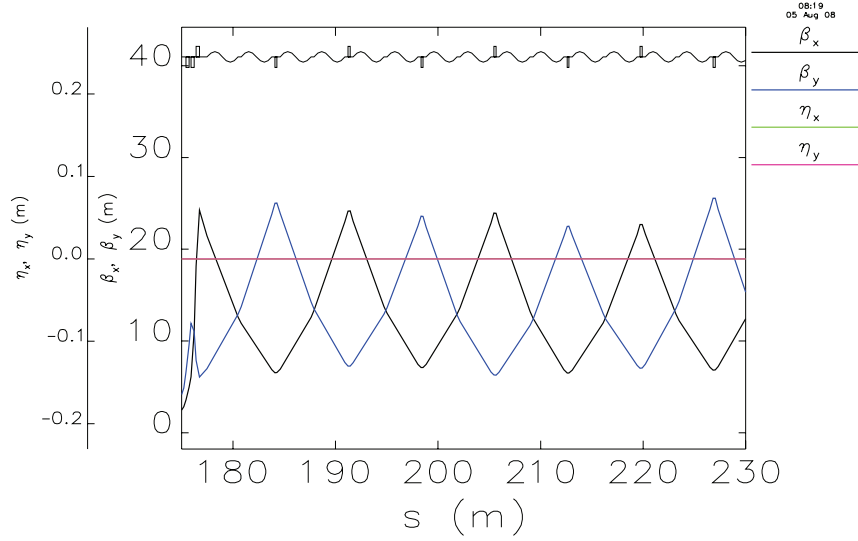


Figure 4.62: Twiss Parameters for the L4 LINAC

4.3.4 Wake function, impedance, wake potential, loss factor and energy spread

When a charge q_1 travels inside a vacuum chamber or, more in general, in a machine device, it produces electromagnetic fields that act on the other charges of the same bunch modifying their energy and their trajectory. The energy variation of a test charge due to the electromagnetic forces of q_1 is obtained by integrating the longitudinal Lorentz forces along the whole structure, while the integration of the transverse ones gives rise to a deflecting momentum.

The longitudinal $w_{\parallel}(z)$ and transverse $w_{\perp}(z)$ wake functions are defined respectively as the energy variation and the deflecting momentum divided by the test charge and q_1 .

In order to study the effects of the wake fields on the beam dynamics, it is convenient to define also the coupling impedance. The longitudinal and transverse coupling impedances are the Fourier transforms of the corresponding wake functions:

$$Z_{\parallel}(\omega) = \frac{1}{c} \int_{-\infty}^{\infty} w_{\parallel}(z) e^{-i\omega z/c} dz \quad (4-25)$$

$$Z_{\perp}(\omega) = -\frac{i}{c} \int_{-\infty}^{\infty} w_{\perp}(z) e^{-i\omega z/c} dz$$

By the knowledge of the coupling impedance, it is possible to obtain, with the inverse Fourier transform, the wake function. In the longitudinal case, for example, we have

$$w_{\parallel}(z) = \frac{1}{2\pi} \int_{-\infty}^{\infty} Z_{\parallel}(\omega) e^{i\omega z/c} d\omega = \frac{2}{\pi} \int_0^{\infty} \text{Re}[Z_{\parallel}(\omega)] \cos(\omega z/c) d\omega \quad (4-26)$$

In the case of the longitudinal beam dynamics, the wake potential, that depends on the longitudinal bunch distribution $\lambda(z)$, and it is defined as

$$W_p(z) = Q_{tot} \int_{-\infty}^{\infty} w_{||}(z') \lambda(z'+z) dz' \quad (4-27)$$

allows to derive easily the loss factor and the energy spread induced by the wake fields, respectively

$$k_l = \int_{-\infty}^{\infty} W_p(z) \lambda(z) dz \quad (4-28)$$

$$\sigma_\varepsilon = \sqrt{\int_{-\infty}^{\infty} W_p^2(z) \lambda(z) dz - k_l^2} \quad (4-29)$$

The wake potential can also be written in terms of the coupling impedance as

$$W_p(z) = Q_{tot} \frac{c}{2\pi} \int_{-\infty}^{\infty} Z_{||}(\omega) \lambda(\omega) e^{i\omega z/c} d\omega \quad (4-30)$$

so that the loss factor becomes

$$k_l = Q_{tot} \frac{c^2}{2\pi} \int_{-\infty}^{\infty} Z_{||}(\omega) \lambda^2(\omega) d\omega = Q_{tot} \frac{c^2}{\pi} \int_0^{\infty} \text{Re}[Z_{||}(\omega)] \lambda^2(\omega) d\omega \quad (4-31)$$

From the above equations it is clear that when the wake fields are generated by two different effects (superposition principle), also the corresponding loss factors can be summed up, but not the energy spread. It is however possible to sum quadratically the energy spread generated by two uncorrelated effects.

4.3.5 Longitudinal beam dynamics

The particles of the input beam from the SPARC photoinjector have been tracked through the SPARX accelerator in order to optimize the working point robustness and flexibility. Three codes have been used for this purpose: Litrack [55], for the longitudinal beam dynamics analysis, Elegant [56] for particle tracking with wake fields in the accelerating structures and 1-D CSR effect approximation in the chicanes, and CSRtrack plus TStep [57,58] for accurate 3-D CSR effect computation including space charge contribution. With the Litrack code the first assessment of the accelerator is performed, tuning the RF-phase of the LINAC sections, the X-band accelerating field, the momentum compaction of the magnetic chicanes, in order to minimize the sensitivity of the channel to phase errors, charge fluctuations and so on. As an example in Figure 4.63 the Litrack longitudinal tracking starting from the SPARC input beam is shown up to $E=2.4$ GeV and $I_{pk} \approx 2.5$ kA; this case refers to 1nC charge

beam and hybrid compression scheme: velocity bunching in the photoinjector plus magnetic chicane in the LINAC.

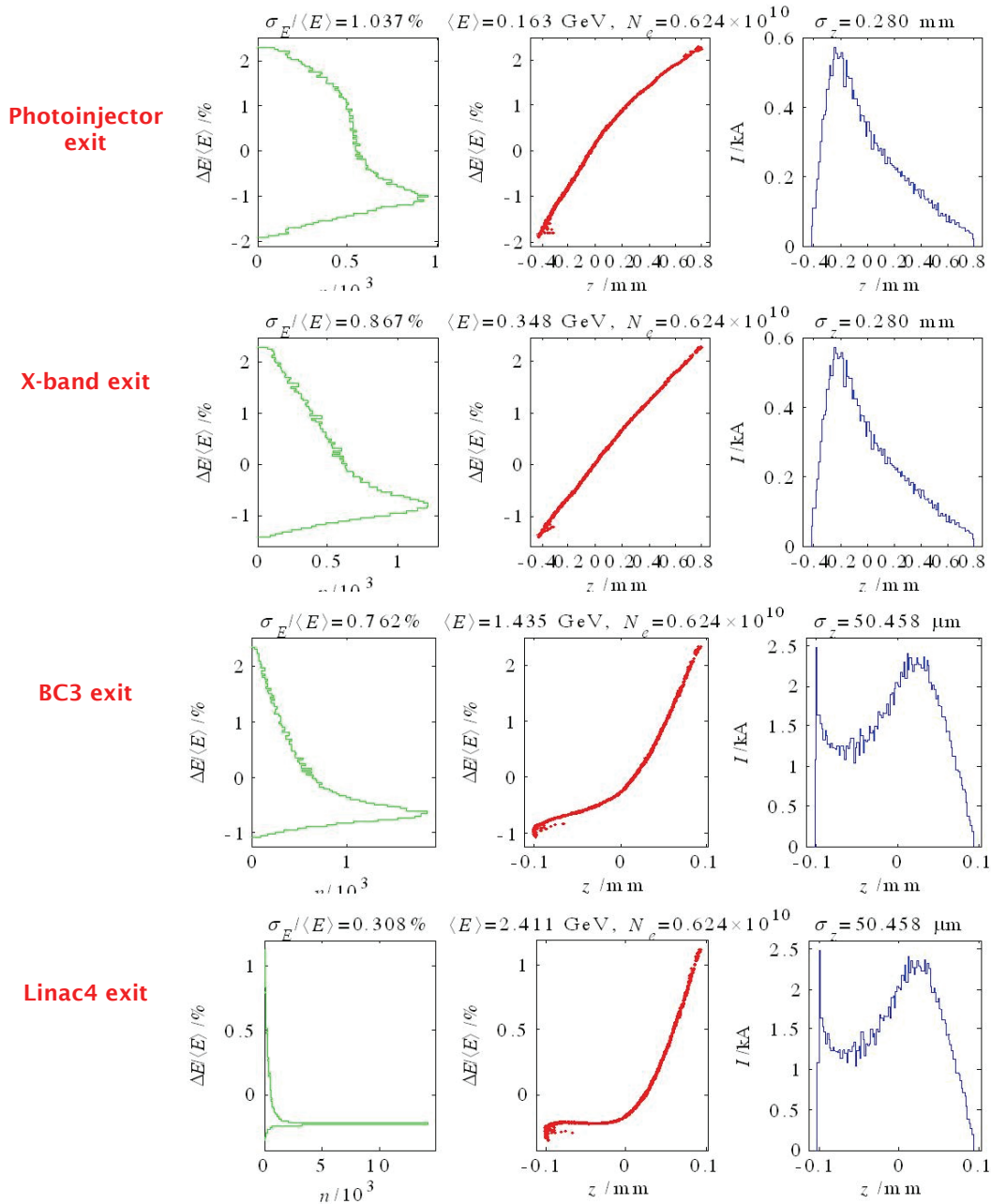


Figure 4.63: Longitudinal tracking and analysis of the 2.4 GeV channel from the SPARC beam compressed with the velocity bunching technique : $I_{pk} = 300\text{A}$, $\sigma_z = 280\mu$, $Q = 1\text{nC}$.

4.3.6 LINAC cavities wake fields

When the bunch's length σ is much smaller than the beam pipe radius a , $\sigma \ll a$, methods of diffraction theory [59] are used to calculate the impedance at high frequencies, $\omega \gg c/a$, where c is the speed of light. The model supposes each structure as a pill box cavity, whose geometric dimensions are: a the beam pipe radius, b the cavity radius and g its length (see Figure 4.64). When a bunch reaches the edge of the cavity, the electromagnetic field is just the one

that would occur when a plane wave passes through a hole; with this hypothesis it is possible to use the classical diffraction theory of optics to calculate the fields.

According to it, the longitudinal and transverse wake fields are respectively:

$$\begin{aligned} W_{\parallel 0}(s) &= \frac{Z_0 c}{\sqrt{2\pi^2 a}} \sqrt{\frac{g}{s}} \\ W_{\perp 0}(s) &= \frac{2^{3/2} Z_0 c}{\pi^2 a^3} \sqrt{gs}. \end{aligned} \quad (4-32)$$

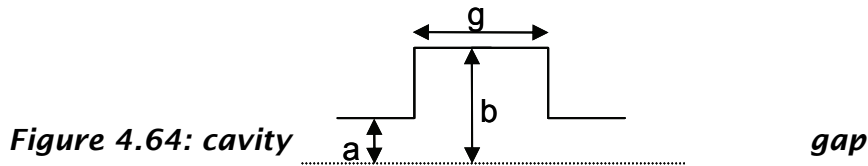
where Z_0 is the characteristic impedance and s the longitudinal coordinate inside the bunch, being $s=0$ the bunch's head.

Eqs.(4-32) are the fields produced by a point charge on a test charge at a distance s : they represent Green functions. One can calculate the longitudinal and transverse wake potential of an arbitrary distribution by making the convolution of the bunch distribution with the Green functions.

For a uniformly charged cylinder, we can obtain the wake potential and finally the wake fields [60]:

$$\begin{aligned} E_{\parallel}^w(s) &= \frac{q}{L} \frac{2}{\sqrt{2\pi^2 a \epsilon_0}} \sqrt{\frac{s}{g}} \\ E_{\perp}^w(s, x) &= \frac{q}{L} \frac{2^{5/2}}{3\pi^2 a^3 \epsilon_0} \frac{s^{3/2}}{\sqrt{g}} x \end{aligned} \quad (4-33)$$

where q is the bunch's charge, L its length and x is the bunch transverse displacement from the nominal axis.



For a collection of cavities, Equation (4-33) can't be used anymore because the wake fields, along the cavities, do not sum in phase and the result would be a high overestimation of the effects. An asymptotic wake field, for a periodic collection of cavities of period p , obtained numerically at SLAC [61] and then fitted to a simple function, is used instead. Such wake field is thus valid after a certain number of cavities given by:

$$N_{crit} = \frac{a^2}{2g(\sigma + \frac{2a}{\gamma})} \quad (4-34)$$

The Green functions are:

$$\begin{aligned}
 W_{\parallel 0}(s) &= \frac{Z_0 c}{\pi a^2} e^{-\sqrt{s/s_1}} \\
 W_{\perp 0}(s) &= \frac{4Z_0 c s_2}{\pi a^4} \left[1 - \left(1 + \sqrt{\frac{s}{s_2}} \right) e^{-\sqrt{s/s_2}} \right].
 \end{aligned} \tag{4-35}$$

Eqs. (4-35) are valid when $s/p \leq 0.15$, $0.34 \leq a/p \leq 0.69$ and $0.54 \leq g/p \leq 0.89$. Such constraints are fulfilled for the SLAC cavities to be used in SPARX where $a=11.6$ mm $g=29.2$ mm and $p=35.0$ mm. Furthermore the value of N_{crit} is of the order of a few units, so that we can use Eqs. (4-35) for the whole accelerating structure.

Following the same procedure of a single cavity one can obtain [62] the longitudinal and transverse wake potential from the Green functions and thus the wake fields for a uniform charge distribution:

$$\begin{aligned}
 E_{\parallel}^{\text{wake}}(s) &= \frac{2Z_0 c s_1 q}{\pi a^2 L} \left[1 - e^{-\sqrt{s/s_1}} \left(1 + \sqrt{\frac{s}{s_1}} \right) \right] \\
 E_{\perp}^{\text{wake}}(s, x) &= \frac{4Z_0 c s_2^2 q x}{\pi a^4 L} \left[-6 + \frac{s}{s_2} + 2e^{-\sqrt{s/s_2}} \left(3 + 3\sqrt{\frac{s}{s_2}} + \frac{s}{s_2} \right) \right].
 \end{aligned} \tag{4-36}$$

In this case the displacement x is, as for the single cavity, the offset at the position s .

For a Gaussian bunch distribution, it is possible to obtain the wake potentials by the numerical integration of the convolution of eqs. (4-35) with the distribution function.

With an rms bunch length of .28 mm and a charge of 1 nC, the longitudinal wake fields induce in a single accelerating section of either L1 and L2 an energy spread of about 140 MeV, while in the L3 LINAC, since the bunch length is about 0.1 mm, the induced energy spread becomes about 170 MeV. These results agree with those obtained with Elegant and are fully compatible with the project parameters.

In the transverse case, the wake fields in resonance with betatron oscillations cause an increase of the oscillation amplitude that can produce a head tail instability called beam break-up.

The transverse wake potential of a Gaussian bunch is represented in Figure 4.65.

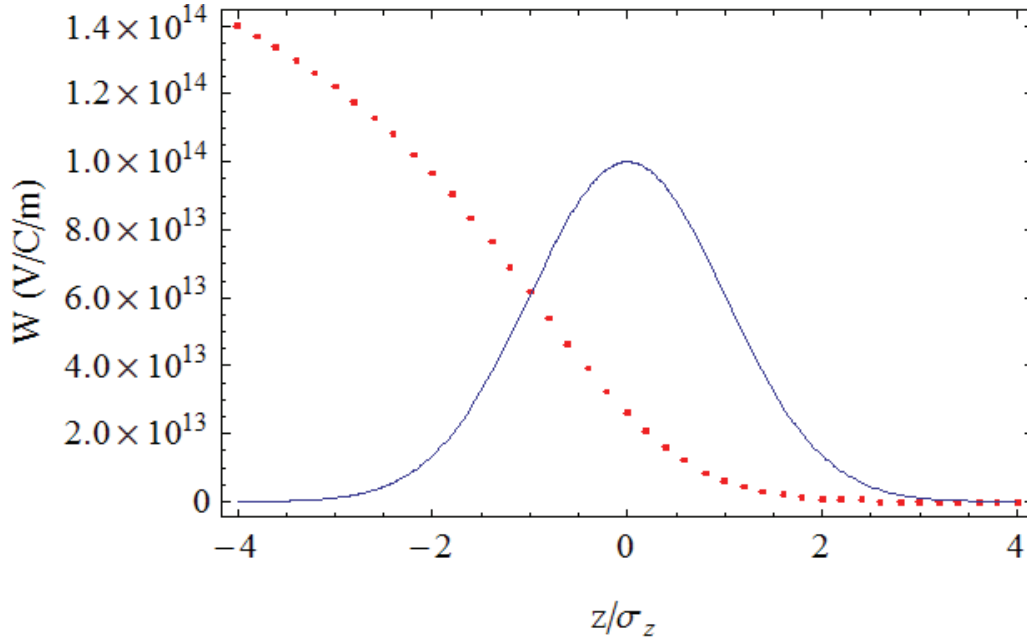


Figure 4.65: Transverse wake potential of a LINAC cavity.

The differential equation governing the motion of a bunch in presence of the transverse wake potential can be solved under particular conditions [63].

A first order solution is found through a perturbation approach if the beam break-up effect is not too strong. In such a case, it is sufficient to consider the maximum transverse wake potential inside the bunch (conservative assumption), that, from the figure, has been chosen equal to 10^{14} V/Cm. With the perturbation method, by using the WKB theory, under the only assumption of moderate s -dependence of $\gamma(s)$, $k_{\beta}(s)$ and $\gamma(s)k_{\beta}(s)^2$, the first order solution to the equation of motion is:

$$\frac{x^1(s, z)}{x(0)} = -\frac{e^2 N_p}{2E_0 L_{str}} \sqrt{\frac{k_{\beta 0} \gamma_i}{k_{\beta}(s) \gamma(s)}} \sin[\psi(s)] \int_0^s \frac{1}{k_{\beta}(s') \gamma(s')} ds' \int_z^{\infty} W_{\perp}(z'-z) \lambda(z') dz' \quad (4-37)$$

If we consider 1 nC of bunch charge with an initial energy of 150 MeV and 18 m of LINAC, we end up with a transverse relative displacement of 0.3, a very small effect that can be considered negligible.

Homdyn simulations give analogous results, as shown in Figure 4.66.

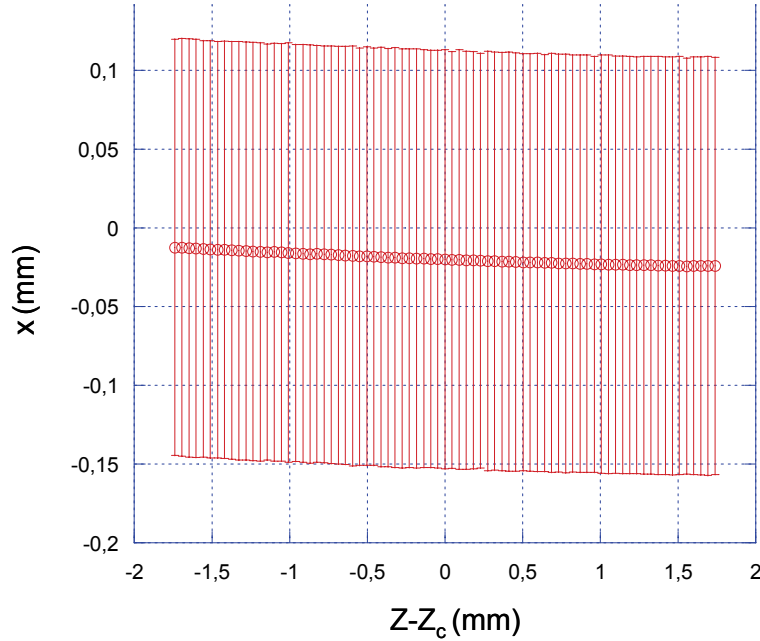


Figure 4.66: Homodyn transverse beam slice displacements x due to the geometric wake fields of 18 m long LINAC cavities at 150 MeV. Horizontal axis is the longitudinal position with reference to the center of the bunch Z_c .

4.3.7 Resistive wall

The resistive wall wake fields are caused by the finite conductivity of the chamber walls. Wake fields, as well as coupling impedances, can be obtained for a circular beam pipe and for parallel plates, that represents an approximation of a rectangular vacuum chamber. Expressions are derived either for a simple frequency independent conductivity and in the more general case of a dependence of the kind

$$\sigma_c(\omega) = \frac{\sigma_{c0}}{1 - i\omega\tau}$$

with σ_{c0} the zero frequency conductivity and τ the relaxation time. These quantities for the aluminum are respectively $\sigma_{c0} = 4.22 \times 10^7 \Omega^{-1} \text{m}^{-1}$ and $\tau = 8 \times 10^{-15} \text{s}$, while for copper they are $\sigma_{c0} = 6.45 \times 10^7 \Omega^{-1} \text{m}^{-1}$ and $\tau = 2.7 \times 10^{-14} \text{s}$.

For a circular beam pipe of radius b the longitudinal wake function per meter is written as

$$w_{\parallel}(z) = \frac{4Z_0c}{\pi b^2} \left[\frac{1}{3} \exp(-z/s_0) \cos(\sqrt{3}z/s_0) - \frac{\sqrt{2}}{\pi} \int_0^{\infty} \frac{x^2 \exp(-x^2 z/s_0)}{8 + x^6} dx \right]$$

with

$$s_0 = \left(\frac{2b^2}{\sigma_c Z_0} \right)^{1/3}$$

If s_0 is very small compared to the bunch length, the wake function can be simplified by using the asymptotic expression:

$$w_{\parallel}(z) = -\frac{Z_0 c}{4\pi^{3/2} b^2} \left(\frac{s_0}{z}\right)^{3/2}$$

The coupling impedance per meter is

$$Z(\omega) = \frac{Z_0}{2\pi b \left(\lambda(\omega) \frac{c}{\omega} - i \frac{\omega b}{2c} \right)}$$

with

$$\lambda(\omega) = \sqrt{\frac{Z_0 \sigma_c |\omega|}{2c}} (i + \text{sgn}(\omega))$$

For parallel plates, the wake function can be derived from the coupling impedance

$$Z(\omega) = \frac{Z_0}{4\pi} \int_{-\infty}^{\infty} \left[\frac{\lambda(\omega)c}{\omega} \cosh^2(bx) - \frac{i\omega}{cx} \cosh(bx) \sinh(bx) \right]^{-1} dx \quad (4-38)$$

with b the half gap.

These wake fields cause energy loss and correlated energy spread in the bunch. They exist in the LINAC cavities, in the transfer lines, and in the undulator sections.

For what concern the LINAC cavities, as it can be seen in Figure 4.67, these wakes can be considered as a small perturbation of the geometric wake fields and therefore they are negligible.

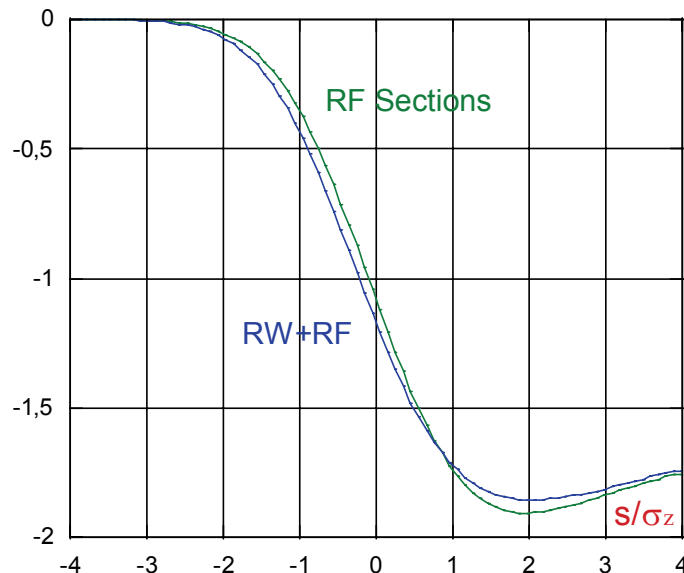


Figure 4.67: Comparison between geometric RF and resistive wall wake fields.

In the transfer lines, since the beam pipe radius is quite large (20 mm), the induced energy spread and the loss factors are small: for 50 m of beam

pipe, they both varies between 80 and 100 keV depending on the bunch distribution (Gaussian or rectangular with rms bunch length of 70 μm), that means a relative energy spread of about $5 \times 10^{-5} - 6.3 \times 10^{-4}$ at 1.5 GeV. In the calculations we have considered aluminum vacuum chamber and 1 nC of bunch charge. If the rms bunch length increases up to 110 μm , the above numbers halve the values since the energy spread for a Gaussian bunch is approximately proportional to $\sigma_z^{-3/2}$.

For what concerns the undulators, the vacuum pipe in the VUV and the EUV Soft X-ray beamline has a vertical inner aperture of 7 mm. The impedance in equation (4-38) in the case of Aluminum and for a bunch of maximum charge 1 nC leads to an induced energy-spread $\sigma_{\text{RW}} < 10$ keV/m. A total relative correlated energy spread $< 3 \cdot 10^{-4}$ is expected from the wakes in the 55 m of the long EUV Soft X-ray beamline and 31 m of the VUV-EUV beamline for the LE beam (1.5 GeV). In the vacuum chamber in the hard X-ray beamline has a vertical aperture of 5 mm. The energy spread induced by the wake is in this case $\sigma_{\text{RW}} < 13$ keV/m and the relative correlated energy spread at the end of the 45m of the high energy undulator beamline is $2.3 \cdot 10^{-4}$

This values are comparable to the incorrelated energy spread assumed in Table 4.9 and may be considered acceptable.

4.3.8 X-band linearization

One short X-band RF section ($f_{\text{RF}}=11.424$ GHz) is foreseen in the SPARX layout to linearize the compression by removing the quadratic energy-time bunch correlation generated in the LINAC structures before the magnetic bunch compressors. It operates at 180° before BC1 magnetic chicanes [16] at a relatively low gradient, $\approx 33 \div 45$ MV/m, and decelerate the beam of $\approx 20 \div 27$ MeV. A more linear correlation allows the bunch to be compressed to a much smaller length than in the case without the X-band section, without heavily affecting the longitudinal bunch current profile, i.e. without giving rise to sharp temporal spikes that may drive unwanted collective effects such as Coherent Synchrotron Radiation (CSR) and longitudinal wakefields in the undulators. Furthermore the level of the final compression is also made much less sensitive to the bunch arrival time errors (timing jitter).

The magnetic compressor chicane transforms the energy deviation $\Delta E/E_0$ to a path-length deviation [27] and it is used to compress the energy chirped bunch:

$$z = z_0 + R_{56}(\Delta E/E_0) + T_{566}(\Delta E/E_0)^2, \quad (4-39)$$

Where the momentum compaction (R_{56}) of a chicane made up of rectangular magnets with small bending angle and for ultra-relativistic electrons can be written as:

$$R_{56} \equiv \frac{\partial z}{\partial \delta} \approx -2\theta_B^2 \left(\Delta L + \frac{2}{3} L_B \right), \quad (4-40)$$

and where $\delta = \Delta E/E_0$, θ_B is the bending angle, L_B the bending magnet length, ΔL the drift length between the magnets and bunch head at $z < 0$. The second-order momentum compaction (T_{566}) of a rectangular-bend chicane (no quadrupole magnets) is $T_{566} \approx -3/2 R_{56}$. The relative energy deviation after a LINAC S-band accelerating section and an X-band structure can be written at the second order as:

$$\Delta E/E_0 \approx \left(\frac{-eV_0 k_s \sin \varphi_s}{E_0} \right) z_0 + \left(\frac{-eV_0 k_s^2 \cos \varphi_s - eV_x k_x^2 \cos \varphi_x}{2E_0} \right) z_0^2 \approx a z_0 + b z_0^2 \quad (4-41)$$

substituting (4-41) into (4-39) we can write:

$$z = (1 + a R_{56}) z_0 + (b R_{56} + a^2 T_{566}) z_0^2 \quad (4-42)$$

To linearize the transformation the second term must be set to zero:

$$b R_{56} + a^2 T_{566} = 0 \quad (4-43)$$

with the IV harmonic RF section this second order term in the compression can be cancelled applying (4-41) for $\varphi_x = \pm\pi$ ($eV_x \geq 0$):

$$b = -\frac{T_{566}}{R_{56}} a^2 \approx \frac{3}{2} a^2, \quad (4-44)$$

$$\frac{-eV_0 k_s^2 \cos \varphi_0 + eV_x}{2E_0} = -\frac{T_{566}}{R_{56}} \left(\frac{-eV_0 k_s \sin \varphi_0}{E_0} \right) \quad (4-45)$$

The second order effect is to be compensated so the RF phase of the harmonic section should be chosen at decelerating crest.

In Figure 4.68 the severe effect on the longitudinal bunch distribution of a compression scheme without X-band correction is shown for the BC1 SPARX chicane.

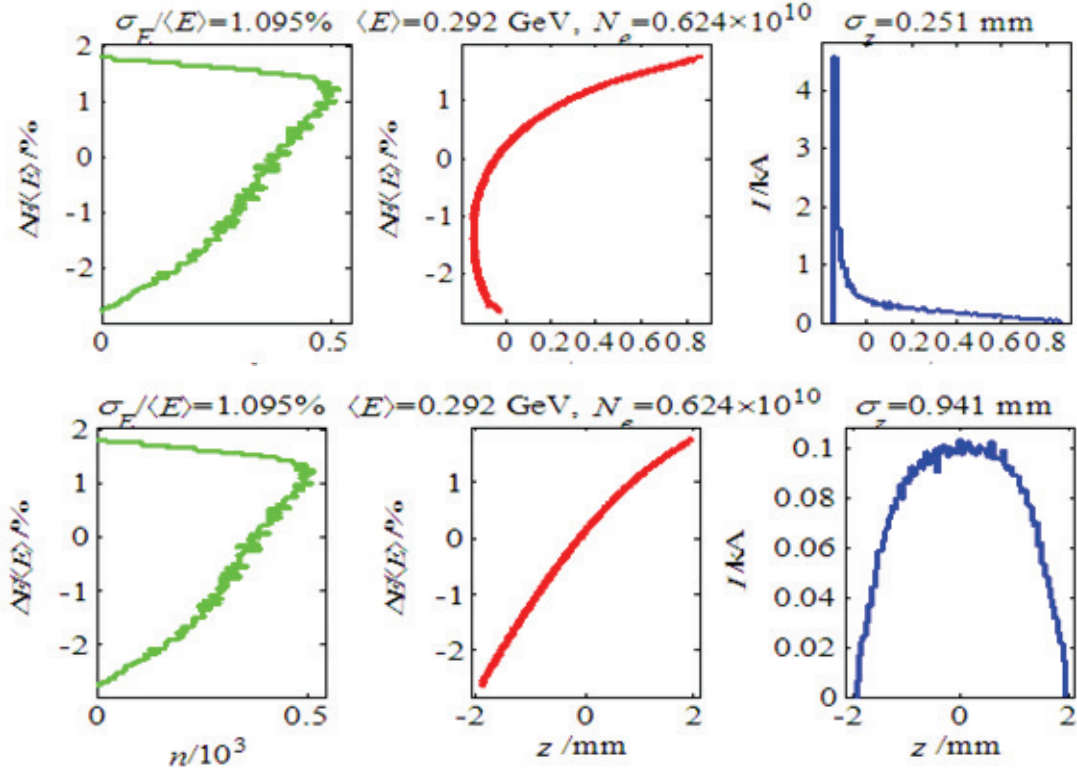


Figure 4.68: Energy profile, (left), longitudinal phase space (center), and temporal profile (right), after L1 SPARX LINAC, prior to BC1 compressor, X-band switched ON (figure above) –OFF (figure below). Bunch head at $z \leq 0$.

4.3.9 Transverse beam dynamics

4.3.9.1 Bunch Compressor system (inside CSR)

The high value of the bunch peak current necessary for the SASE experiment requires the bunch length compression taking place in magnetic chicanes with the proper energy dependence of the particles' path length:

$$\Delta z = R_{56} \delta E / E_0 \quad (4-46)$$

where the momentum compaction R_{56} for a chicane made up of rectangular bending magnets is expressed in equation (4-40), where the symbol definitions are those expressed in Table 4.28 and the approximation is valid for ultra relativistic particles and small bending angles. The second order momentum compaction T_{566} of a rectangular bending magnet chicane with no quadrupoles is $T_{566} \approx -3/2 R_{56}$ [62, 64].

For very short bunches the coherent synchrotron radiation can significantly worsen the transverse emittance by generating energy spread in the dipoles.

In our study we will consider the case of the steady state radiation of an ultra relativistic particle in a long magnet, and we neglect the screening effects of conducting walls [64, 65]. In such a case, the CSR wake fields is

$$w_{\parallel}(z) = \frac{1}{4\pi\epsilon_0} \frac{2}{R^{2/3}} \frac{1}{(3z)^{4/3}} \quad \text{for } z > 0 \quad (4-47)$$

with R the magnet bending radius and $w_{\parallel}(z) = 0$ for $z \leq 0$. It is important to observe that, unlike the other wake fields, this radiation wake field is localized in front of the generating charge. In the above equation we have neglected the transient effects occurring at the entrance and at the exit of the magnet.

The coupling CSR impedance is

$$Z(\omega) = Z_0 \frac{\Gamma(2/3)}{3^{1/3} 4\pi R} \left(\sqrt{3} + i \right) \left(\frac{\omega}{c} R \right)^{1/3} \quad (4-48)$$

For a rms bunch length σ_z , dipole length L_B , bend radius R ($\approx L_B/\theta_B$) and N particles per bunch, from the above equations we can obtain the CSR-induced energy rms relative energy spread per dipole for a Gaussian bunch under steady state conditions is [65]:

$$\sigma_{\delta} \approx 0.22 \frac{N r_e L_B}{\gamma R^{2/3} \sigma_z^{4/3}} \quad (4-49)$$

where r_e is the classical electron radius and γ is the Lorentz energy factor. The above formula is valid for a dipole magnet where the radiation shielding of the conducting vacuum chamber is not significant, namely for a full vertical vacuum chamber height h satisfying:

$$h \gg \left(\pi \sigma_z \sqrt{R} \right)^{2/3} \equiv h_c \quad (4-50)$$

Since the bunch length is reduced through the chicane the local energy spread induced at each dipole increases especially at last one.

Emittance increase is due to the longitudinal CSR in the dispersion region of the bunch compressor. The energy variation induced by the CSR on a particle is transformed at the exit of a magnet in a deflection angle [66] and, as second order effect, in a transverse displacement. The rms horizontal emittance after a single chicane can be written as:

$$\begin{aligned}
 \Delta x &= \int_{\text{bends}} R_{16}(s) \frac{d\delta}{ds} ds, & \Delta x' &= \int_{\text{bends}} R_{26}(s) \frac{d\delta}{ds} ds \\
 \varepsilon^2 &= \varepsilon_0^2 \left[\beta \langle \Delta x'^2 \rangle + 2\alpha \langle \Delta x \Delta x' \rangle + (1 + \alpha^2) \langle \Delta x^2 \rangle / \beta \right] + \langle \Delta x^2 \rangle \langle \Delta x'^2 \rangle - \langle \Delta x \Delta x' \rangle^2 \\
 &= \varepsilon_0^2 + 2\zeta \varepsilon_0 \Delta \varepsilon + \Delta \varepsilon^2 \geq (\varepsilon_0 + \Delta \varepsilon)^2, & \zeta &\geq 1
 \end{aligned} \tag{4-51}$$

where the $R_{16}(s)$ and $R_{26}(s)$ are the transfer matrix elements from point s to the last dipole end, α and β are the nominal Twiss parameters at the end of the chicane and ε_0 and ε are the initial and final rms horizontal emittance. The second moments Δx and $\Delta x'$ are ensemble averages over the entire bunch and ζ is the Courant-Snyder invariant. In the ideal unshielded, steady state conditions $\langle \Delta x^2 \rangle \langle \Delta x'^2 \rangle \approx \langle \Delta x \Delta x' \rangle^2$ and the relative emittance growth for the last bend of a single chicane, using the previous equations and a constant Gaussian bunch length σ_z in the last magnet is:

$$\frac{\varepsilon}{\varepsilon_0} \approx \sqrt{1 + \frac{(0.22)^2}{36} \frac{r_e^2 N^2}{\gamma \varepsilon_N \beta} \left(\frac{|\theta|^5 L_B}{\sigma_z^4} \right)^{2/3} [L_B(1 + \alpha^2) + 9\beta^2 + 6\alpha\beta L_B]} \tag{4-52}$$

where $\varepsilon_N (\equiv \gamma \varepsilon_0)$ is the initial normalized (invariant) emittance. This is nevertheless an underestimation of the emittance growth since it does not introduce radiation effects in the chicane nor the time domain treatment including field transients at the entrance and at the exit of the bends, its relevance lies in the focusing of the main parameters involved in this effect. More complete calculation of the CSR effect has been carried on through the three magnetic compressors BC1-3 with the help of codes like Elegant and CSRtrack [56, 57]. The last is a 3D full-field treatment including x-z correlations in the beam at high dispersion points, the space charge forces, longitudinal and transverse forces. The results of the simulations for the three considered input cases from photoinjector are reported in the following chapters

4.3.9.2 *irst Bunch Compressor BC1*

The first bunch compressor BC1 is a magnetic chicane designed to compress the bunch length from 1 mm down to 200-300 μm . The four dipole lattice has been chosen because it adds no net beamline angle or offset, generates no chromaticity or high order dispersion (with rectangular bends) since it contains no quadrupole magnets, and the R_{56} tuning is achieved with a single power supply [62]. To counteract the space charge effects the energy has been chosen around $E=350$ MeV. The transverse emittance dilution due to the CSR (Coherent Synchrotron Radiation) effect has been minimized keeping the bending angle below 8 degrees and providing a total length of about 5 m. In Table 4.32 the BC1 parameter list is reported, while in Figure 4.69 the Twiss parameters are shown. It has to be pointed out that the one-stage compression

scheme has also been explored, i.e. compressing the beam only in BC2 from 900 to 90 μm , but it turns out so far that it is not possible without unbearably diluting the beam transverse emittance, in agreement with the adopted schemes for LCLS and FLASH [62,67].

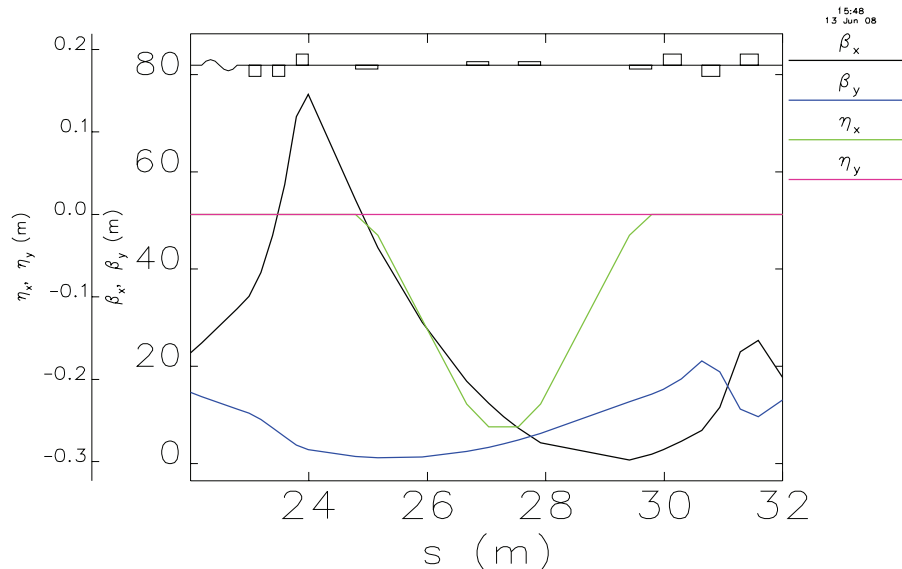


Figure 4.69: Twiss parameters for BC1 compressor chicane.

Table 4.32: Parameter list for the first bunch compressor BC1

Parameter	Symbol	Unit	Value
Beam Energy	E	GeV	0.35
Initial rms bunch length	σ_{zi}	mm	0.9
Finale rms bunch length	σ_{zf}	mm	0.24
Rms total incoming energy spread	σ_{δ}	%	0.98
RMS uncorrelated relative energy spread	$\sigma_{\delta u}$	10^{-5}	1.1
Momentum compaction	R_{56}	mm	-61*
Second order momentum compaction	T_{566}	mm	92
Total chicane length	L_{total}	m	5.02
Length of each dipole magnet	L_B	m	0.38
Length of drift between 1 st and last two dipoles	ΔL	m	1.50
Length of drift between center two dipoles	ΔL_C	m	0.50
Bend angle of each dipole	$ \theta_B $	deg	7.77
Maximum dispersion	$ \eta_{max} $	m	0.26
Projected CSR emittance dilution	$\Delta \varepsilon_{est} / \varepsilon_0$	%	30

4.3.9.3 Second Bunch Compressor BC2

The second bunch compressor BC2 is again a four-dipole magnetic chicane that compresses the bunch length from 200÷300 μm down to 70÷100 μm , namely raising the average peak current up to $I_{pk} \approx 1 \div 1.2$ kA. The chicane

* Bunch head at $z \leq 0$.

parameters have been chosen in order to minimize the CSR contribution to the transverse emittance dilution here more severe than in the BC1 case. The momentum compaction is $R_{56} \approx 22$ mm for the considered case. In Table 4.33 the BC2 chicane parameters are reported, while in Figure 4.70 the Twiss parameters are shown.

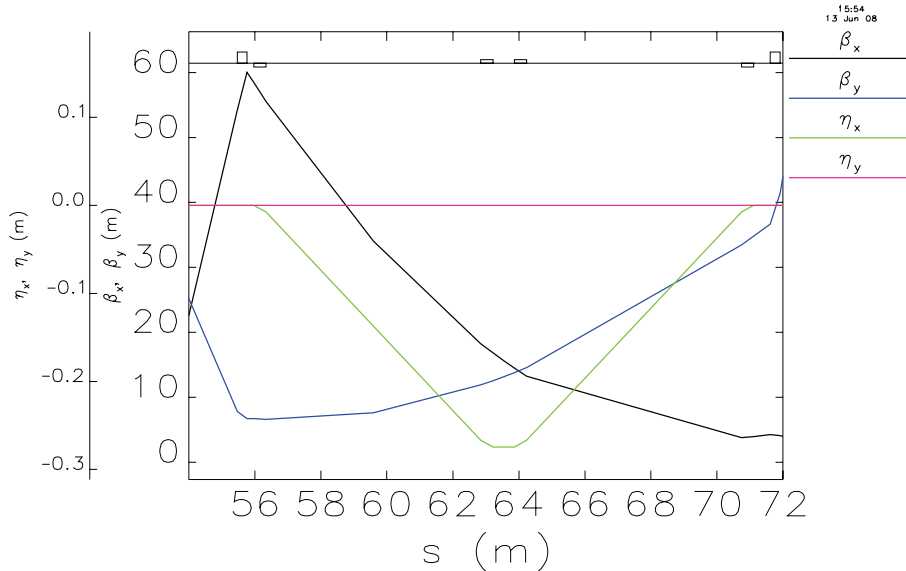


Figure 4.70: Twiss parameters for BC2 compressor chicane.

Table 4.33: Twiss parameters for the second bunch compressor BC2

Parameter	Symbol	Unit	Value
Beam Energy	E	GeV	0.53
Initial rms bunch length	σ_{zi}	mm	0.24
Finale rms bunch length	σ_{zf}	mm	0.110
Rms total incoming energy spread	σ_{δ}	%	0.60
RMS uncorrelated relative energy spread	$\sigma_{\delta u}$	10^{-5}	0.5
Momentum compaction	R_{56}	mm	-22.2*
Second order momentum compaction	T_{566}	mm	33.3
Total chicane length	L_{total}	m	15.18
Length of each dipole magnet	L_B	m	0.38
Length of drift between 1 st and last two dipoles	ΔL	m	6.84
Length of drift between center two dipoles	ΔL_C	m	0.58
Bend angle of each dipole	$ \theta_B $	deg	2.30
Maximum dispersion	$ \eta_{max} $	m	0.29
Projected CSR emittance dilution	$\Delta \varepsilon_{esi} / \varepsilon_0$	%	24

Table 4.34: Parameter list for the third bunch compressor BC3

Parameter	Symbol	Unit	Value
Beam Energy	E	GeV	1.44
Initial rms bunch length	σ_{zi}	mm	0.242
Finale rms bunch length	σ_{zf}	mm	0.049
Rms total incoming energy spread	σ_{δ}	%	0.66
RMS uncorrelated relative energy spread	$\sigma_{\delta u}$	10^{-5}	0.2
Momentum compaction	R_{56}	mm	-30.1*
Second order momentum compaction	T_{566}	mm	45.3
Total chicane length	L_{total}	m	21.12
Length of each dipole magnet	L_B	m	0.38
Length of drift between 1 st and last two dipoles	ΔL	m	4.8
Length of drift between center two dipoles	ΔL_C	m	10.0
Bend angle of first and fourth dipole	$ \theta_B $	deg	2.22
Bend angle of second and third dipole	$ \theta_B $	deg	4.4
Maximum dispersion	$ \eta_{max} $	m	0.19
Projected CSR emittance dilution	$\Delta \epsilon_{csr} / \epsilon_0$	%	16

4.3.9.4 Third Bunch Compressor BC3

The third bunch compressor BC3 is a four-dipole magnetic chicane s-shaped in such a way to compensate the transverse emittance dilution due to the CSR effect [68,69]. The bunch length is reduced here down to 50÷60 μm and the peak current reaches the value $I_{pk} \approx 2\div 2.5$ kA. In Table 4.34 the BC3 chicane parameters are reported, while in Figure 4.71 the Twiss parameters are shown.

4.3.10 Particle tracking 1D

The particles of the input beam from the SPARC photoinjector have been tracked through the SPARX accelerator in order to optimize the working point robustness and flexibility. Five codes have been used for this purpose: Litrack [55], for the longitudinal beam dynamics analysis as reported before, Elegant [56] for particle tracking with wake fields in the accelerating structures and 1-D CSR effect approximation in the chicanes, CSRtrack and TStep [57,58] for accurate 3-D CSR effect computation including space charge contribution. The reference case for tracking is the 1nC charge, with velocity bunching applied at photoinjector, namely compressing the beam only in BC2 or BC3 magnetic compressors for 1.5 and 2.4 GeV extractions respectively. In Figure 4.72 the beam rms size and bunch length are reported as obtained with Elegant ($N_p=200$ k) for the 1.5 GeV case at the exit of the DL1 dogleg. The 2.4 GeV case is illustrated in Figure 4.73; in Figure 4.74 and Figure 4.75 the slice analysis is shown for the two energy beams.

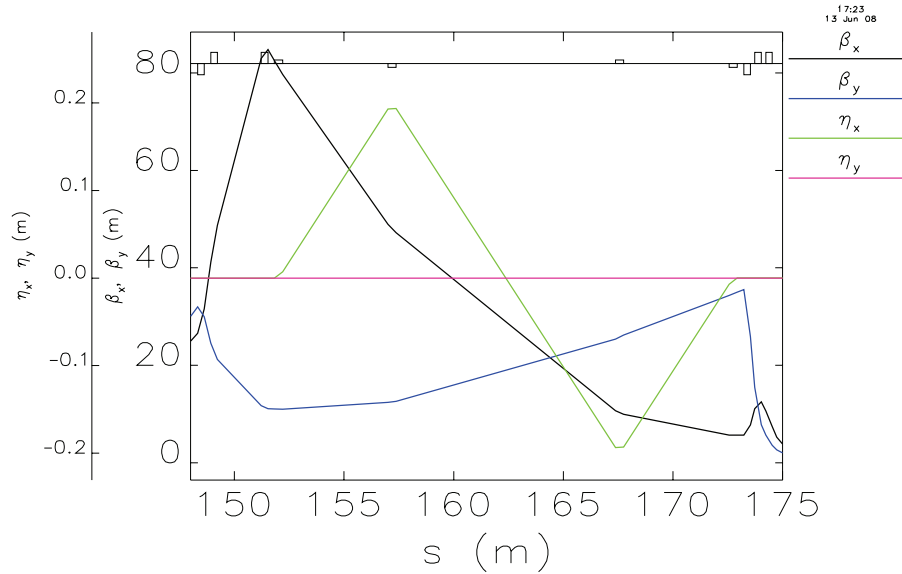


Figure 4.71: Twiss parameters for BC3 compressor chicane.

Different input cases have been studied varying the final energy around the central value or the input beam charge and in Table 4.35 the results are reported.

Table 4.35: Sparx output beam parameters in the energy range of 1-2.4 GeV. The final rms bunch length σ_z , the horizontal normalized emittance ε_{nx} , the energy spread σ_δ and the peak current I_{pk} are reported together with the three compressor bending angles.

Energy final (GeV)	σ_z (μm)	ε_{nx} (μrad)	σ_δ (%)	ε_{nx} slice (μrad)	σ_δ slice (%)	I_{pk} (kA)	θ_1 (m rad)	θ_2 (m rad)	θ_3 (m rad)
1nC RfC 1.5- 2.4 GeV central									
0.96	107	1.8	0.20	0.9	0.01	1.50	0	40.5	0
1.20	110	1.6	0.15	0.9	<0.02	1.40	0	40.5	0
1.56	110	1.5	0.11	0.9	0.01	1.40	0	40.5	0
2.40	50	1.5	0.25	0.9	0.03	2.50	0	0	38.7
50pC RfC 1.5 GeV central									
1.5	13	0.6	0.04	0.5	0.03	0.6	0	41.8	0

It is worthwhile to notice that in each output case the horizontal normalized slice emittance is kept below the 1 mm-mrad value, and that the

slice energy spread lies around the $0.01 \div 0.02$ % in the beam brightness region of interest.

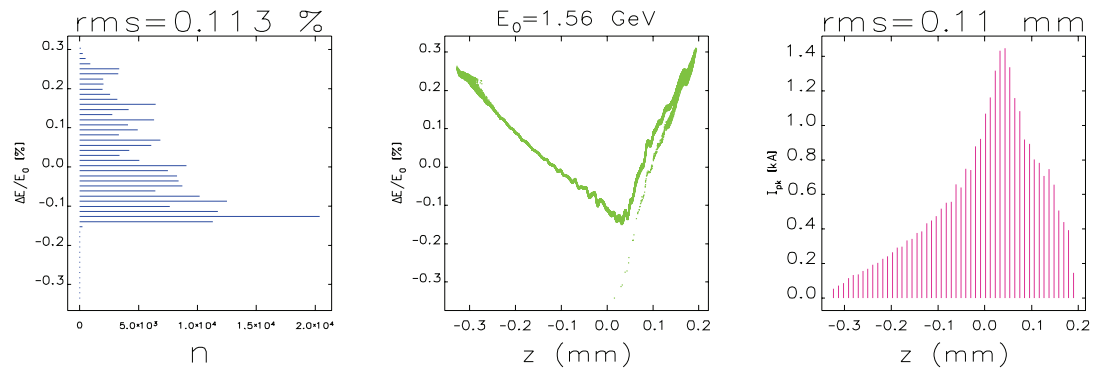


Figure 4.72: Longitudinal output beam features at the dogleg exit at 1.5 GeV; input beam: SPARC with velocity bunching $I \approx 300A$. From the left: energy spread, energy and current distribution.

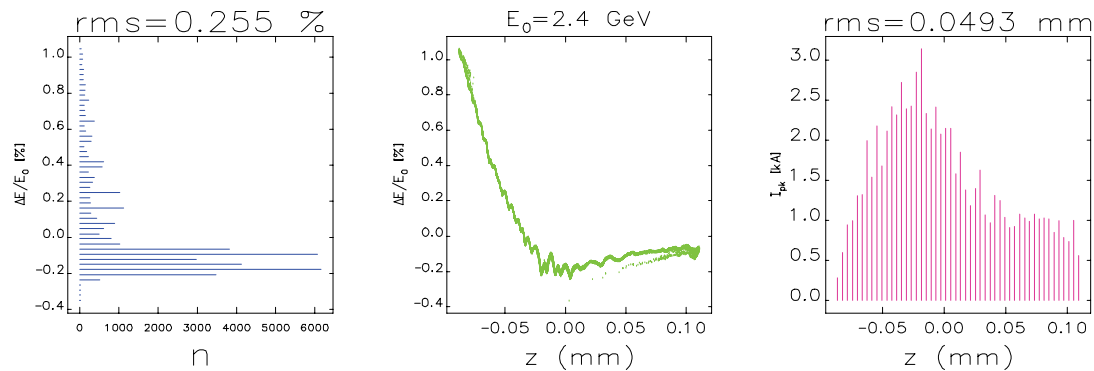


Figure 4.73: Longitudinal output beam features at the dogleg exit at 2.4 GeV; input beam: SPARC with velocity bunching $I \approx 300A$. From the left: energy spread, energy and current distribution.

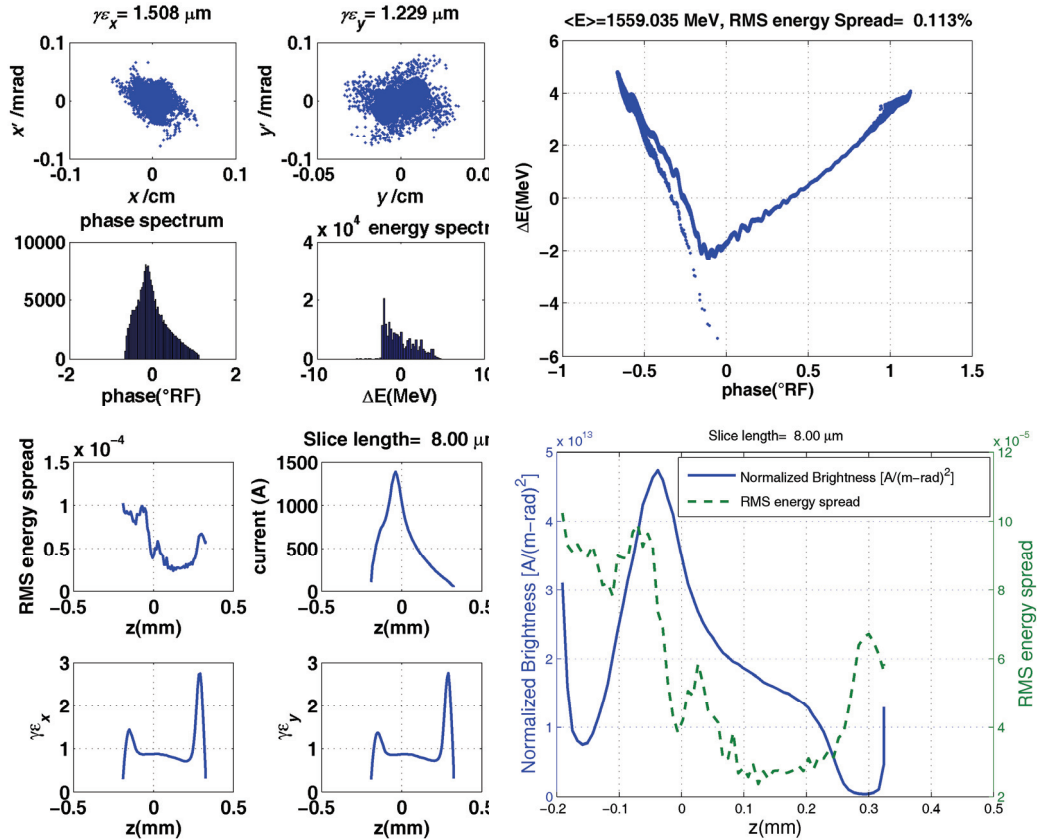


Figure 4.74: Output beam features at the dogleg exit at 1.5 GeV; input beam: SPARC with velocity bunching $I \approx 300\text{A}$. Top left: transverse phase space, Top right: particle distribution in phase and energy. Bottom left: slice analysis of energy spread, current and transverse emittance, Bottom right: beam brightness and energy spread.

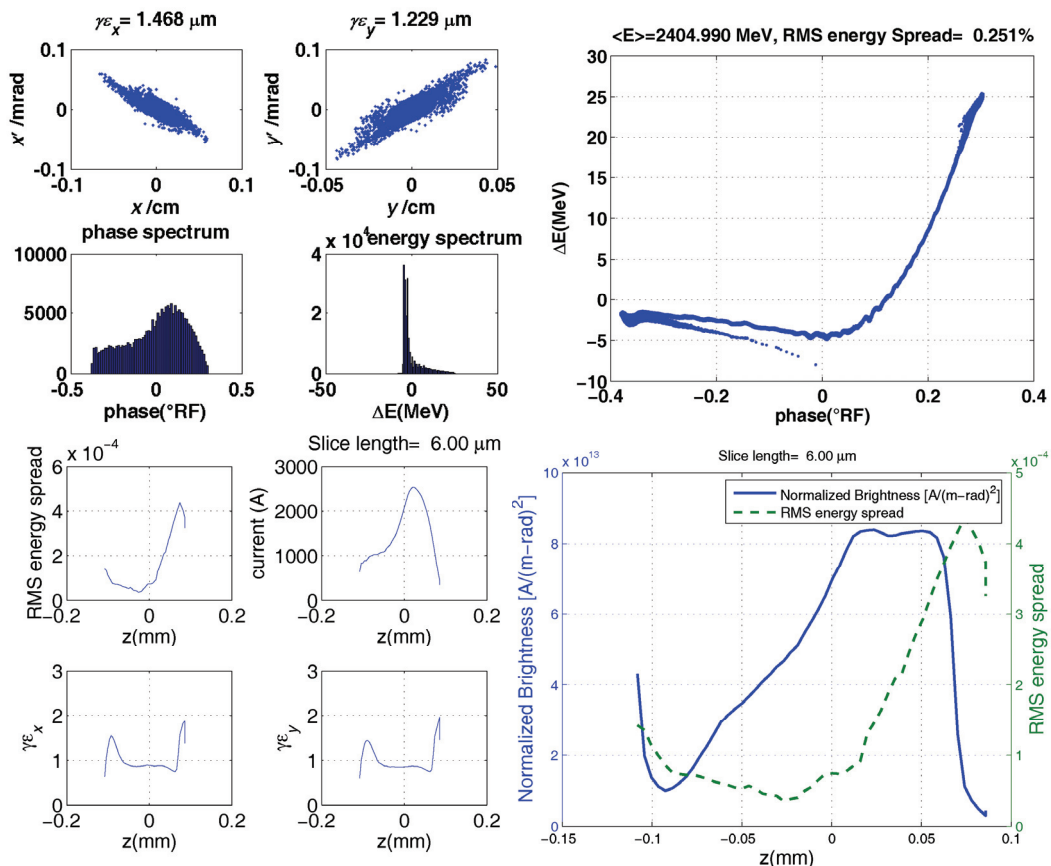


Figure 4.75: Output beam features at the dogleg exit at 2.4 GeV; input beam: SPARC with velocity bunching $I \approx 300\text{A}$. Top left: transverse phase space, Top right: particle distribution in phase and energy. Bottom left: slice analysis of energy spread, current and transverse emittance, Bottom right: beam brightness and energy spread.

4.3.11 Particle tracking 3D-1D comparison

Starting from the exit of the injector the SPARX accelerator has been optimized by using the ELEGANT code [56] that is able to track the particles with longitudinal and transverse wakes in the accelerating structures and 1-D CSR effects approximations in the chicanes, but doesn't take into account the effect of space charge, usually assumed negligible above the energy of 150 MeV due to the $1/\gamma^2$ space charge suppression factor. Nevertheless especially when a hybrid RF-magnetic compressor scheme is employed space charge effects together with CSR in the magnetic compressors can affect the beam quality also in the high energy part. In order to evaluate accurately these collective effects other two codes have been used CSRTRACK [56] and TStep [58], both able to handle space charge and CSR affects using different models. The capabilities and limitations of the three codes are summarized in Table 4.36.

Table 4.36: Simulation codes employed in the SPARX accelerator design

Code	Space charge	CSR	Longitudinal wakes in the accelerating structures	Transverse wakes in the accelerating structures
ELEGANT	No	Yes (1D model)	Yes	Yes
TSTEP	Yes (3D)	Yes (1D model)	Yes	No
CSRTRACK	Yes (3D)	Yes (3D model)	No	No

TStep code is the last evolution of the LANL version of PARMELA code with a much improved space charge 3D calculation characterized by the use of the shifted integrated Green function method according to the description of ref. [70], that allows to reduce the sensitivity to the very large aspect ratios assumed by the beam at high energy in the rest frame where the space charge fields calculation is done according to the “static approximation” on a Cartesian grid. Besides space charge effects TStep includes longitudinal wake functions in the accelerating structures and for the CSR uses the same approximation employed in ELEGANT based on the Saldin 1-D model [71].

A more accurate evaluation of the CSR in the beam dynamics is done by CSRTRACK code that works with three main tracking algorithms: (1) a fast one-dimensional projection method, (2) a more accurate 3D calculation based on a sub-bunch test with a Green’s function method and (3) a point-to-point (p-p) algorithm keeping into account all the retarded potentials. The CSRTRACK simulations for the SPARX accelerator used the 3D method, that is hundred times faster than the point-to-point (p-p) algorithm and, by using a convolution [72] to reduce the 3D integration of retarded source (spherical Gaussian sub-bunch) to a 1D integral, is able to manage ten times more macro particles than the p-p algorithm.

Being the accelerating structures not implemented in CSRTRACK this code has been used only in the compressor chicanes and in the drifts immediately following the magnets, using as input the particles coordinates computed by TStep in the rest of the accelerator.

The simulations reported in this paragraph refer to the high charge working point (1 nC) with RF compression occurring in the photoinjector and have been based for all the three codes on 50K macro-particle beam. The RF-compressed 300 A beam has been transported up to the exit of BC2, where the magnetic compression is done before the final acceleration to a maximum energy of 1.5 GeV foreseen for the first part of SPARX.

The results of TStep computations in Figure 4.76a show that CSR in the laser-heater magnets give an emittance growth in the horizontal plane and that emittance oscillations due to residual space charge effects are visible up to an energy around 400 MeV inside LINAC-2. The further increase of emittance up to 1.6 mm-mrad in the 8 m drift between LINAC2 and BC2 is not due to space charge but to a chromatic effect (particles with different energies receive different kicks in the quadrupole) in the strong horizontal focusing of a

quadrupole placed at $z \sim 64$ m (this effect is not taken into account by ELEGANT), as it can be seen in the plot of Figure 4.76b where the comparison between space charge on and off in this region shows that an increase of emittance up to 1.6 mm-mrad is present also in absence of space charge effects. An adjustment of the optics in this drift space with a reduction of this quadrupole strength can avoid this additional emittance growth.

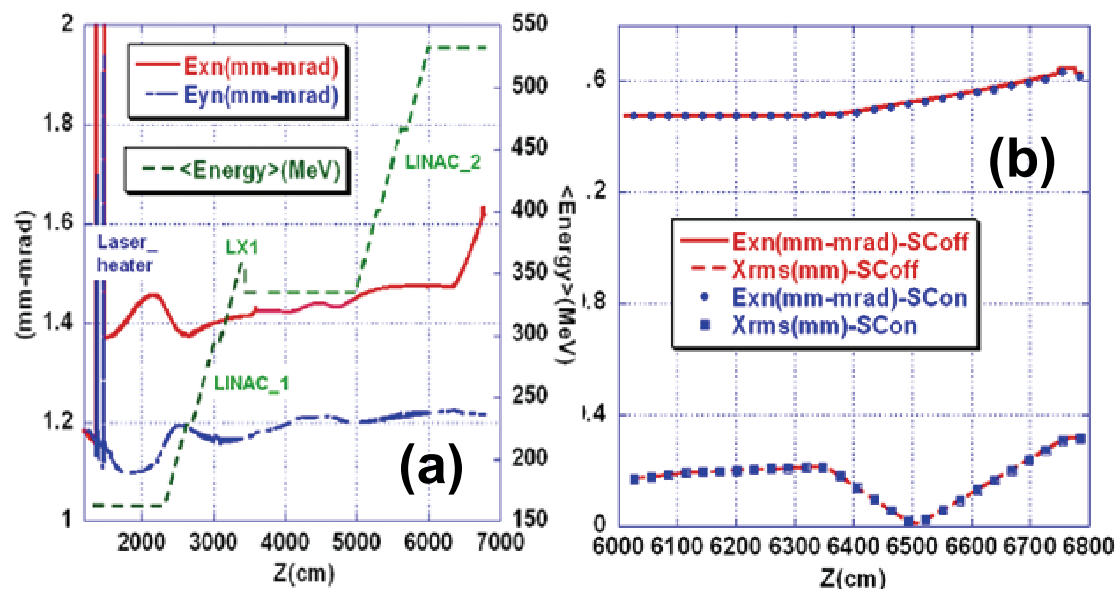


Figure 4.76: TStep beam transport from the injector exit up to BC2 entrance: (a) evolution of beam transverse emittance and energy vs z (b) beam envelopes and emittance evolution vs z in the drift between LINAC-2 and BC2 with space charge on and off.

Figure 4.77 compares the behavior of the horizontal emittance in BC2 as computed in the ELEGANT design with the results obtained with CSRTRACK with and without CSR effects. CSRTRACK computation started from the particle coordinates computed by TStep taking into account the evolution of the beam (including space charge effects) in the whole previous part of the accelerator, whilst ELEGANT starts from the coordinates at the injector output. CSRTRACK with CSR effect included and gives at the output of BC2 an emittance of 2.1 mm-mrad instead of the ELEGANT value of 1.5 mm-mrad.

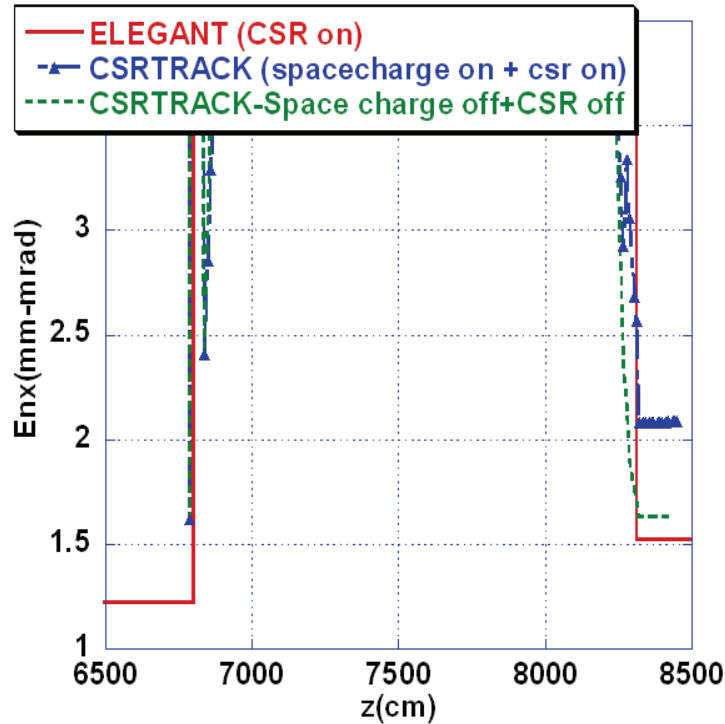


Figure 4.77: Horizontal emittance behavior in the BC2 region: comparison between CSRTRACK results with SC+CSR on and ELEGANT

The analysis of the emittance behavior along the LINAC performed with the different codes described above points out the relevance of the space charge effect contribution to the beam dynamics: this is due to the fact that through all the SPARX LINAC the beam experiences a continuous transition between the space charge to the emittance dominated regime. Nevertheless the differences in the horizontal emittance values, as coming from the simulation results, do not seem so severe to affect the performance of the SPARX FEL. A further optimization is in progress looking also at the slice emittance evolution through the LINAC channel.

4.3.12 Microbunching instability

Longitudinal space charge (LCS) in the LINAC structures causes an energy modulation that is converted in longitudinal modulation in the magnetic compressor. Due to the CSR effect, this longitudinal modulation is amplified and can cause the microbunching instability. The effect of the microbunching has been evaluated either by the linear theory [73] or by the use of a Vlasov solver in 2D phase space [74]. By considering a LINAC from 150 to 540 MeV where the LSC acts and then the BC2 compressor, with a transverse beam size of 0.4 mm and an emittance of 10^{-6} mm mrad, the linear theory predicts a gain of a given initial wavelength modulation as reported in Figure 4.78.

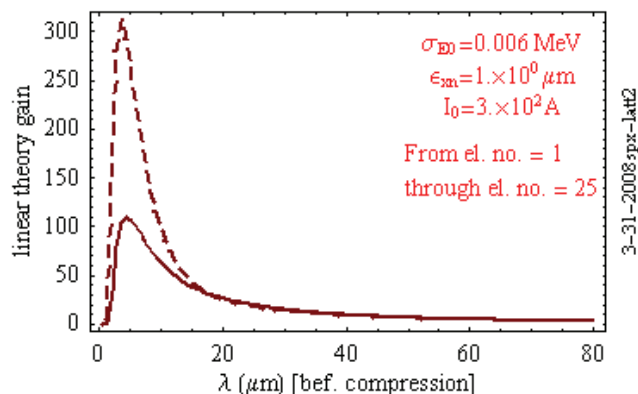


Figure 4.78: Modulation gain in BC2 compressor due to CSR and LCS effects.

To counteract this effect, i.e. to rise the value of the uncorrelated energy spread a small laser heater chicane is foreseen upstream the L1 LINAC ($E \approx 150$ MeV) [50]. In Table 4.37 the parameter list is reported for a laser heater chicane suitable to be inserted before LINAC 1 and presently under study. The study on the instability effectiveness and on the beam “heating” optimization is in progress exploring also other remedy possibilities.

Table 4.37: Laser heater chicane parameter list

<i>Parameter</i>	<i>Symbol</i>	<i>Unit</i>	<i>Value</i>
Beam Energy	E	GeV	0.15
Total chicane length	L_{total}	m	1.90
Length of each dipole magnet	L_B	m	0.10
Length of drift between 1 st and last two dipoles	ΔL	m	0.15
Length of drift between center two dipoles	ΔL_C	m	0.80
Bend angle of each dipole	$ \theta_B $	deg	6

4.4 Transfer Lines

4.4.1 Introduction

In this section we give a short description of the design guidelines for the beam transfer lines which transport the beam from the LINAC to the undulators.

Two different energies are foreseen for SPARX operation, and three undulator lines will be fitted in the same hall.

The low energy beam at 1.5 GeV is extracted from the LINAC with an almost isochronous dogleg towards a long transfer line which runs parallel to the high energy part of the LINAC and which splits into two branches injecting the beam into two undulators, named hereafter U1 and U2.

The last part of the LINAC further compresses and accelerates the beam to higher energy (2.4 GeV). The transfer line which extracts this beam is again divided into two different branches injecting in the undulator U2 and in the third undulator U3.

All the lines are therefore displaced from the LINAC main axes in order to protect the undulators from potential beam halo and dark currents. Furthermore, this arrangement allows to add more accelerating structures, in a further construction phase, to increase the beam energy.

Figure 4.79 shows a schematic layout of the transport lines.

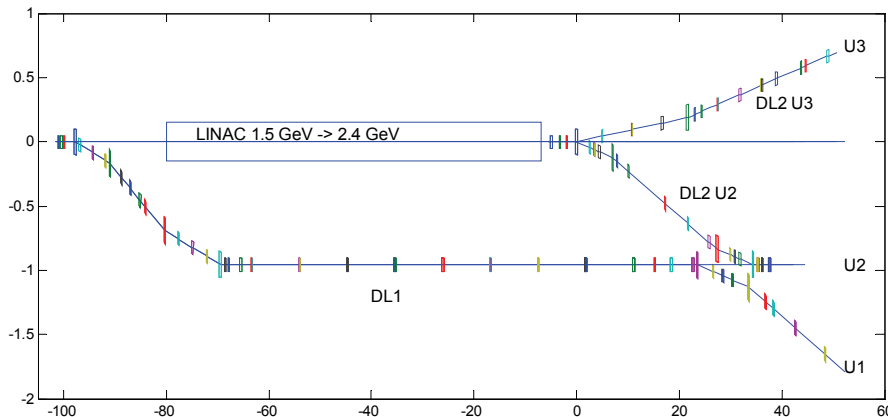


Figure 4.79: Schematic layout of the whole transport line complex. The transverse element dimension are not to scale.

Requirements for the beam transport are essentially the same for the low and the high energy lines.

The transport lines should keep the bunch length and peak current unchanged, that is, they should be nearly isochronous. The path length deviation ds , for electrons moving on a curved trajectory, can be expressed in linear approximation by:

$$ds = R_{56} \frac{\delta E}{E_0} \quad (4-53)$$

where $R_{56} = \int \eta(s) / \rho ds$ is the first order momentum transfer matrix element relating position and energy spread, depends on the bending radius ρ of the dipole magnets and the (first order) dispersion function η .

To be isochronous, the beam transport lines should have a small or vanishing R_{56} ; Chasman-Green [75] type cells are used in order to have very little path length energy dependence. Each period of the Chasman-Green lattice contains focusing quadrupoles magnets symmetrically located between a pair of identical dipoles. The horizontal dispersion function reaches a maximum in the center of each cell and it reverses sign in half of the bends.

The use of a double bend achromat lattice allows to generate minimal emittance dilution due to synchrotron radiation too. The FEL process requires high brilliance electron beams with an extremely high peak current, high electron density with a small energy spread and a low transverse emittance. However in the bends of the doglegs, the extremely short bunches emit synchrotron radiation which superimposes coherently with the already emitted synchrotron radiation when the radiation wavelength exceeds the electron bunch length. An infra-red radiation field is so built up in the dipole magnets, travelling faster than the electrons: this radiation overtakes the previous bunch and can so interact with the electrons and generate a position dependent momentum modulation. In a 1-dimensional approximation we have:

$$\frac{dp_{csr}}{ds} \approx \int_{s-\rho\phi^3/24}^s w_{csr}(s-s')\lambda(s')ds' \quad (4-54)$$

$$w_{csr}(s-s') = -\frac{2}{(3\rho^2)^{1/3}} \frac{\partial}{\partial s'} \frac{1}{(s-s')^{1/3}} \quad (4-55)$$

where ρ is the magnet bending angle, ϕ is the passed angle, w_{csr} the CSR wake function and $\lambda(s)$ the longitudinal charge density. The CSR induced momentum modulation in the dispersive section changes instantaneously the reference trajectory of the electron beam and the electrons start to perform betatron oscillations equivalent to an increase in the single particle emittance.

The resulting CSR induced emittance growth can be estimated from:

$$d\mathcal{E}(s)_{csr} = H(s)(dp(s)/p)_{csr} \quad (4-56)$$

$$\Delta\varepsilon_{csr} = \int H(s)(dp(s)/p)_{csr} ds \quad (4-57)$$

$$H(s) = \gamma(s)\eta(s)^2 + 2\alpha(s)\eta(s)\eta'(s) + \beta(s)\eta'(s)^2 \quad (4-58)$$

where α , β , γ are the Twiss parameters.

To avoid strong CSR induced emittance dilutions in the SPARX transfer lines only weak dipole magnets have been used, with a maximum bending angle of 1.4° , and the dogleg optics have been designed to keep the dispersion and the beta function in the magnets as small as possible.

The CSR effects along the lines have been studied with the simulation code ELEGANT, which takes into account the effects within the 1-D model introduced above.

All the lines end with a flexible beta-matching section for the undulator-input.

All dipoles are C type and all have the same magnetic length.

There are three types of quadrupoles, depending on the space constraints. Where there are no interferences among the lines the quadrupoles have a simple design, as shown in paragraph 5.4. For those quadrupoles placed in the zones where two beam lines are nearer than 10 cm the two lines will be fitted inside the poles, which will be slightly separated, while when the distance is larger than 10 cm thin and long magnets will be used. For the optical design up to now all quadrupoles are considered equivalent, with a magnetic length of 30 cm.

4.4.2 Low energy transfer lines

The low energy line (DL1) transport the 1.5 GeV beam from the LINAC to the Undulators U1 and U2.

4.4.2.1 Dogleg and FODO line

The first part of the line is a double-bend dog-leg which displaces it about 95 cm horizontally from the main LINAC axis (see Figure 4.80).

It is then followed by a straight section, about 100m long, composed by two matching sections at both ends and a central FODO lattice. Figure 4.80 shows the detail of the layout, while Figure 4.81 a and b show the betatron and the dispersion function respectively. The small bending angle of each dipole (24.5 mrad) and the lattice optics produce an R_{56} of only -0.146 mm.

The effect of the second order momentum compaction T_{566} is even less. It can be seen in the figure that the horizontal betatron function in all dipoles is small. One triplet before and one after ensure the matching with the LINAC and the FODO respectively.

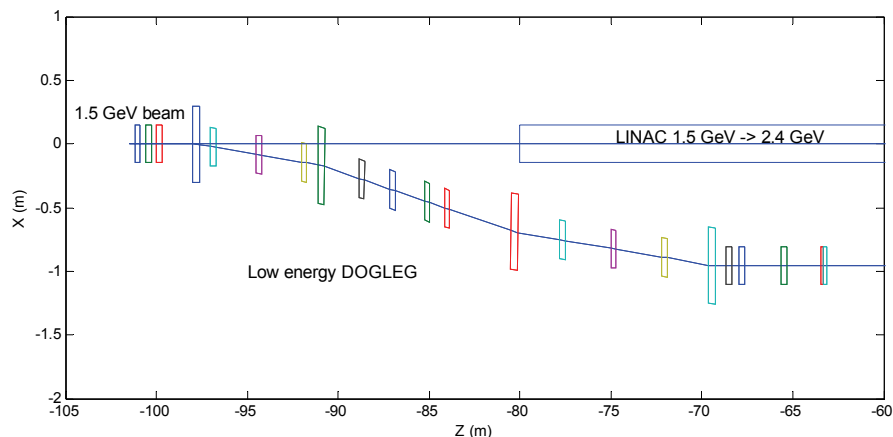


Figure 4.80: Schematic layout of the low energy dogleg with the initial part of the FODO line.

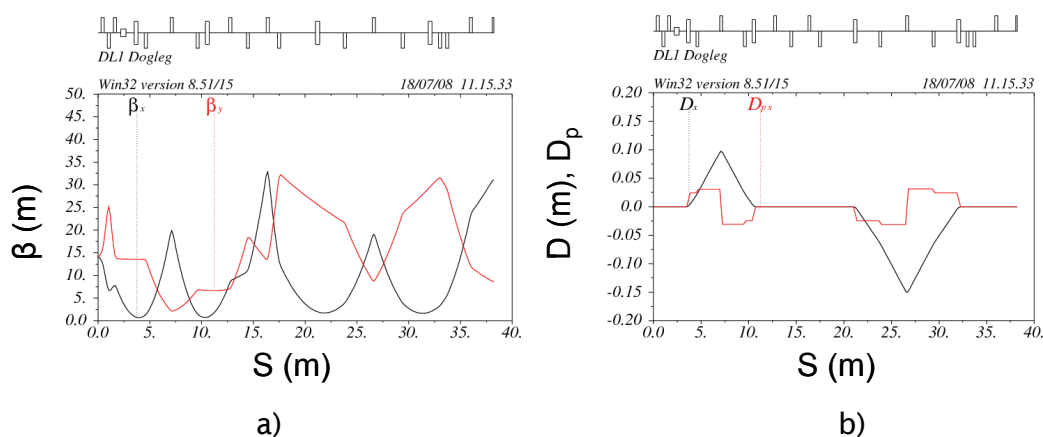


Figure 4.81: Betatron functions (a) and Dispersion function (b) in the low-energy dogleg.

4.4.2.2 DL1-U1 and DL1-U2

After the FODO line a matching section precedes a double bend achromat which takes the beam to the undulator U1. When the achromat is switched off the beam goes straight to the undulator U2. Matching sections are in front of each undulator entrance. The matching section of U2 is shared by the low and high energy beams. Figure 4.82 shows a schematic layout, and the last part of the line coming from the high energy part is also shown.

The global first order momentum compaction is about -0.171 mm for the DL1-U1, with a second order momentum compaction of -0.024 m.

The dispersion and beta functions along the low energy lines are shown in Figure 4.83 and Figure 4.84 for the DL1-U1 and the DL1-U2.

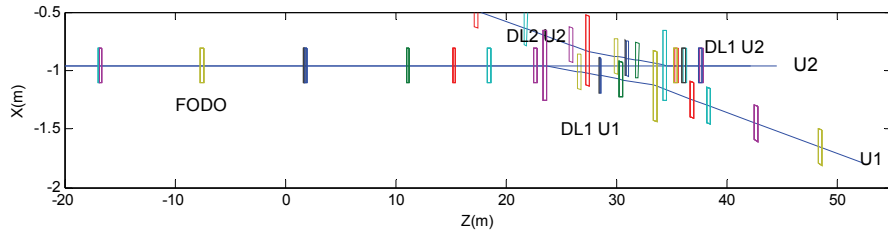


Figure 4.82: Schematic layout of the low energy lines DL1-U1 and DL1-U2.

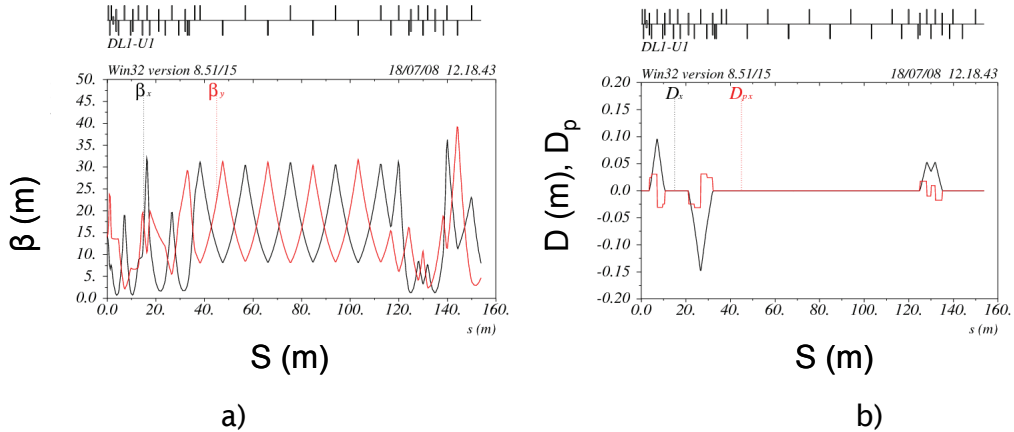


Figure 4.83: Optical functions of DL1-1 from the LINAC to the undulator U1.

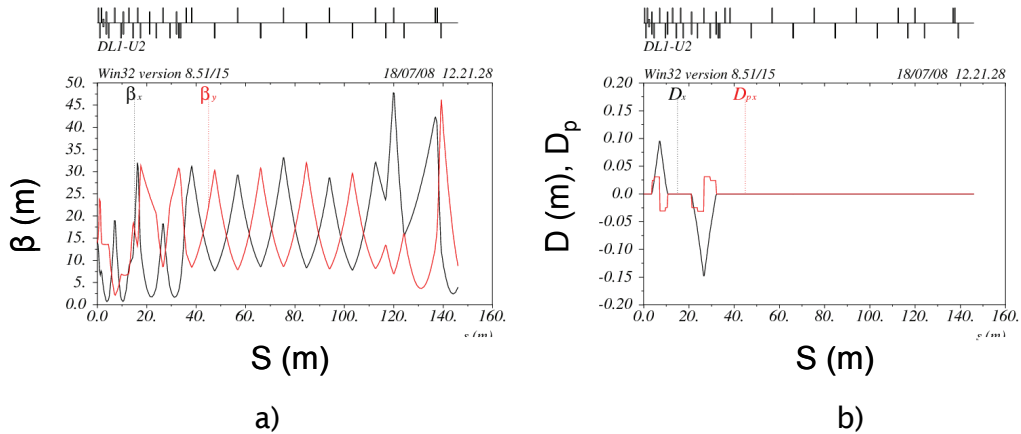


Figure 4.84: Optical functions of DL1-2 from the LINAC to the undulator U2.

In Figure 4.85 the RMS normalized horizontal emittance along the low energy line is shown. The CSR induced horizontal emittance dilution, computed with ELEGANT, is negligible.

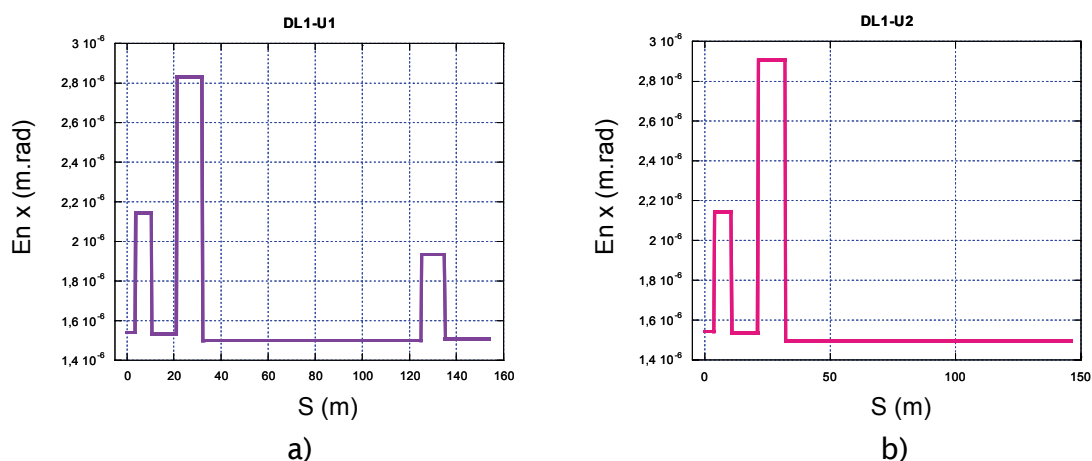


Figure 4.85: Normalized horizontal emittance along low energy line DL1-U1 (a) and DL1-U2 (b). The point $s=0$ is the end of the LINAC.

The main DL1 parameters are summarized in Table 4.38:

Table 4.38: DL1 parameters

Parameter	Symbol	Unit	Value
Beam energy	E	GeV	1.5
DL1 total horizontal deflection	Δx	m	0.95
DL1-U1 total horizontal deflection (sum of six bends)	θ_B	deg	2
DL1-U1 total horizontal deflection	Δx	m	1.79
DL1-U2 total horizontal deflection (sum of four bends)	θ_B	deg	0
DL1-U2 total horizontal deflection	Δx	m	0.95
RMS bunch length	σ_z	mm	0.11
RMS energy spread DL1-U1	σ_δ	%	$1.1 \cdot 10^{-3}$
RMS energy spread DL1-U2	σ_δ	%	$1 \cdot 10^{-3}$
DL1-U1 R56	R_{56}	mm	-0.171
DL1-U2 R56	R_{56}	mm	-0.146
DL1-U1 second order T566	T_{566}	m	-0.024

DL1-U2 second order T566	T_{566}	m	-0.021
Length of each dipole magnet	L	m	0.375
DL1-U1 total length	L	m	153.86
DL1-U2 total length	L	m	145.99
Bend angle for each of first four DL1-U1 dipoles	$ \theta_B $	deg	1.4
Bend angle for each of last two DL1-U1 dipoles	$ \theta_B $	deg	1
Bend angle of each DL1-U2 dipole	$ \theta_B $	deg	1.4
Maximum DL1-U1 dispersion	$ \eta_{\max} $	m	0.147
Maximum DL1-U2 dispersion	$ \eta_{\max} $	m	0.147
DL1-1 projected CSR emittance dilution	$\Delta\mathcal{E}_{csr} / \mathcal{E}_0$	%	0
DL1-2 projected CSR emittance dilution	$\Delta\mathcal{E}_{csr} / \mathcal{E}_0$	%	0
Total number of quadrupoles in DL1-U1 plus DL1-U2	-	-	38
Maximum integrated gradient	$ k_1^* L_{\text{mag}} $	m^{-1}	0.948
Average integrated gradient	$ k_1^* L_{\text{mag}} $	m^{-1}	0.307

4.4.3 High energy transfer lines

The high energy beam transport line extracts the beam at 2.4 GeV and leads it to undulator U2 and U3. The line is splitted in two branches: the DL2-U3 goes to undulator U3 with a single achromat, while the DL2-U2 transports the beam to the undulator 2 matching section, shared with the low energy line. Figure 4.86 shows a schematic layout of the lines, and the interference with the low energy ones.

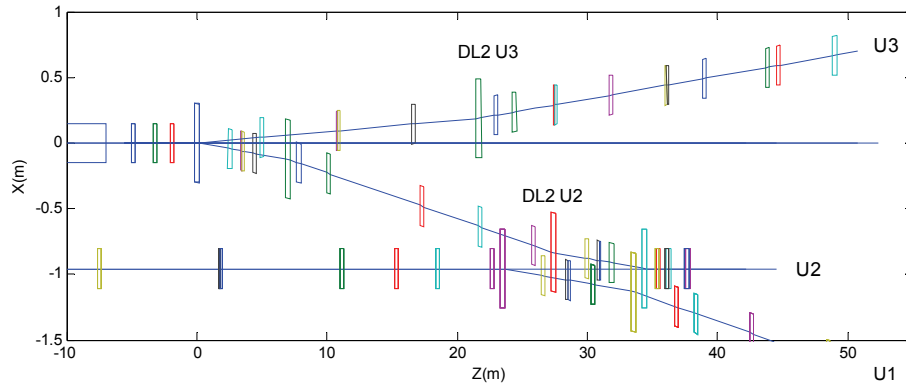


Figure 4.86: Schematic layout of the high energy lines DL2-U2 and DL2-U3.

4.4.3.1 DL2-U2 and DL2-U3

The DL2-U3 gives the beam an angle of 1° with respect with the main axis. A 29 m long lattice leads then the beam to undulator U3 with the required beta and alpha functions. The first bending magnet of the DL2-U3 achromat is shared with the high energy line to U2, that leads the beam to the central undulator matching section with a double bend achromat lattice.

A triplet before the first dipole ensures the matching with the LINAC in the two cases.

The global first order R_{56} is about -0.007 mm for the DL2-U3, and -0.074 mm for the DL2-U2 with a second order T_{566} of -0.0013 m and -0.0047 m respectively.

The dispersion and beta functions along the high energy lines are shown in Figure 4.87 and Figure 4.88 for the DL2-U2 and the DL2-U3, while Figure 4.89 shows the horizontal normalized emittance along the two lines computed by ELEGANT.

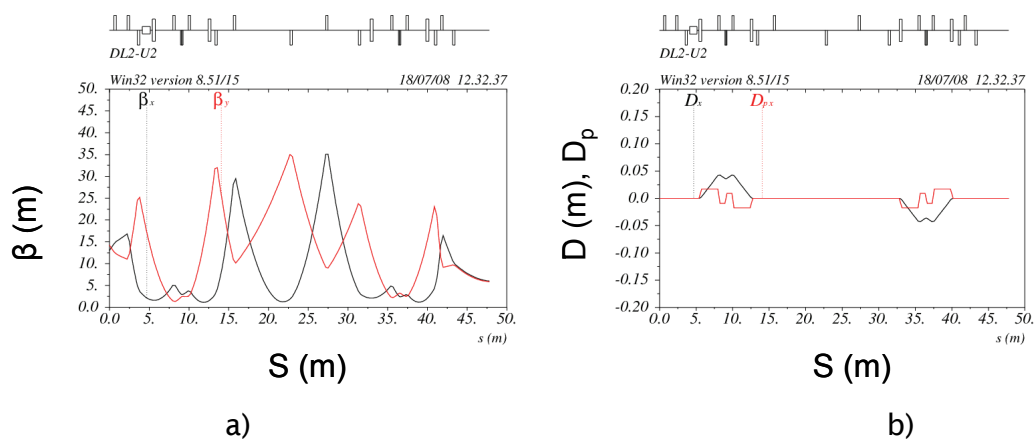
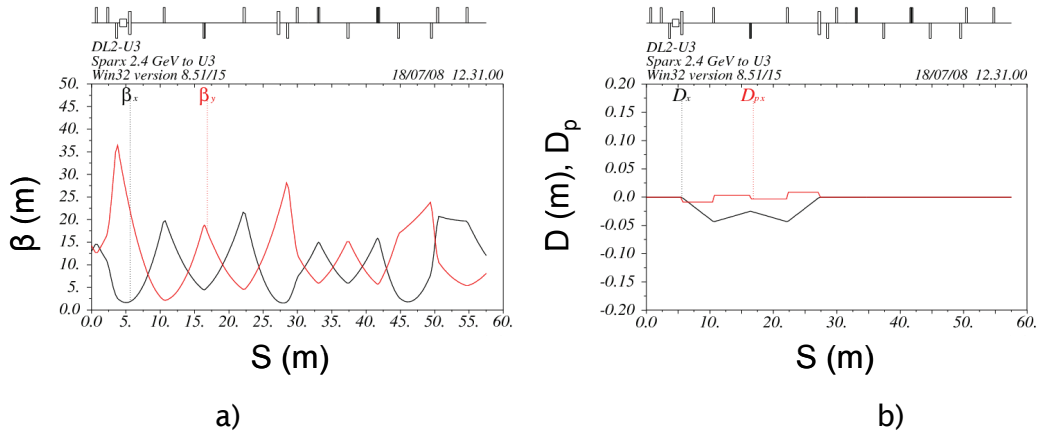
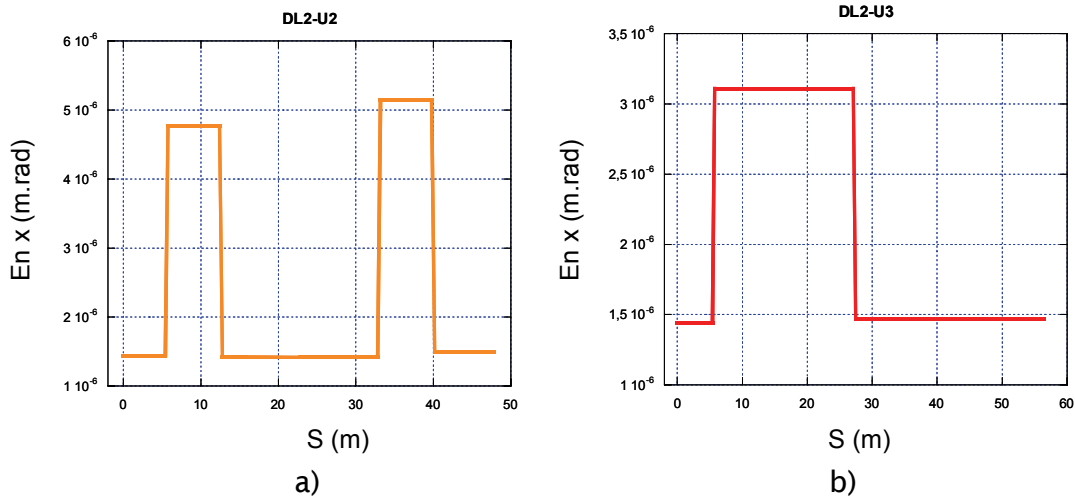


Figure 4.87: Optical functions along high energy line DL2-U2.



a) b)
Figure 4.88: Dispersion and beta functions along high energy line DL2-U3.



a) b)
Figure 4.89: Normalized horizontal emittance along high energy line DL2-U2 (a) and DL2-U3 (b). The point $s=0$ is the end of the LINAC.

The main DL2 parameters are summarized in Table 4.39:

Table 4.39: DL2 parameters

<i>Parameter</i>	<i>Symbol</i>	<i>Unit</i>	<i>Value</i>
Beam energy	E	GeV	2.4
DL2-U2 total horizontal deflection (sum of two bends)	θ_B	deg	2
DL2-U2 total horizontal deflection	Δx	m	0.95
DL2-U3 total horizontal deflection (sum of two bends)	θ_B	deg	1
DL2-U3 total horizontal deflection	Δx	m	0.7
RMS bunch length	σ_z	mm	0.049

RMS energy spread DL2-U2	σ_δ	%	$2.46 \cdot 10^{-3}$
RMS energy spread DL2-U3	σ_δ	%	$2.48 \cdot 10^{-3}$
DL2-U2 R56	R_{56}	mm	-0.074
DL2-U3 R56	R_{56}	mm	-0.007
DL2-U2 second order T566	T_{566}	m	-0.0047
DL2-U3 second order T566	T_{566}	m	-0.0013
Length of each dipole magnet	L	m	0.375
DL2-U2 total length	L	m	47.8
DL2-U3 total length	L	m	56.4
Bend angle of each DL2-U2 dipole	$ \theta_B $	deg	1
Bend angle of each DL2-U3 dipole	$ \theta_B $	deg	0.5
Maximum DL2-U2 dispersion	$ \eta_{\max} $	m	0.04
Maximum DL2-U3 dispersion	$ \eta_{\max} $	m	0.04
DL2-U2 projected CSR emittance dilution	$\Delta\epsilon_{csr} / \epsilon_0$	%	3.4
DL2-U3 projected CSR emittance dilution	$\Delta\epsilon_{csr} / \epsilon_0$	%	1.6
Total number of quadrupoles in DL2-U2 plus DL2-U3	-	-	29
Maximum integrated normalized gradient	$ k_1 * L_{\text{mag}} $	m^{-1}	0.78
Average integrated normalized gradient	$ k_1 * L_{\text{mag}} $	m^{-1}	0.37

4.5 Seed sources based on high-order harmonic generation in gas

High-Order Harmonic Generation (HHG) in gases is one of the most promising methods for generating ultrashort pulses of coherent radiation in the XUV (30-300 eV) - soft X (300-3000 eV) region of the spectrum, to seed short wavelength Free Electron Lasers. High-Order harmonics (HH) result from the strong, non-linear optical response induced in the target (for instance a noble gas) by the focused intense electromagnetic field of an ultra-short, intense "pump" laser pulse. The process can be understood in terms of the three-step semi-classical model [76, 77] illustrated in *Figure 4.67*.

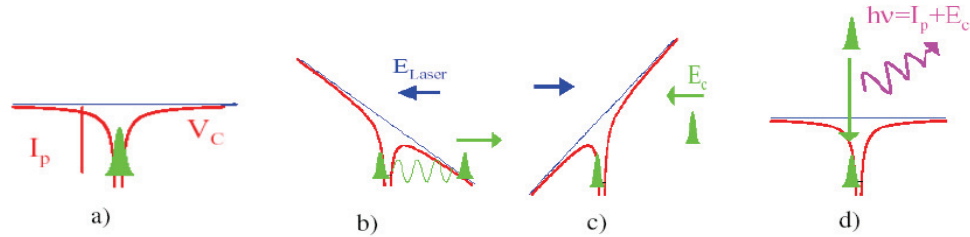


Figure 4.90: Three-step semi-classical model: a) initial state of the gas atom at zero field, V_C : Coulomb potential, I_p : ionization potential; b) electron tunneling induced by the laser electric field; c) electron acceleration back to the parent ion and gain of kinetic energy E_C ; d) radiative recombination and emission of a XUV burst.

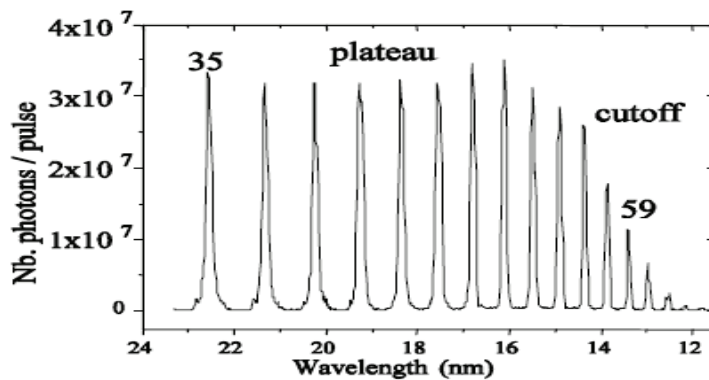


Figure 4.91: High-Order Harmonics spectrum in Neon.

As the external electromagnetic field strength is comparable to the atomic Coulomb field, the atom ionizes by tunnelling of electrons. The ejected electrons, far from the core, are then accelerated in the external laser field and gain a kinetic energy E_C . Those which are driven back close to the core can either be scattered or can recombine to the ground state emitting a burst of XUV photons every half-optical cycle. Correspondingly, the harmonic spectrum (see Figure 4.91) includes the odd harmonics of the fundamental laser frequency. The characteristic distribution of intensities is almost constant with harmonic order in the "plateau" region where, depending on the generating gas, the conversion efficiency varies in the range 10^{-4} - 10^{-7} . For higher orders, the conversion efficiency decreases rapidly in the "cut-off" region. The upper spectral limit is given by the so-called "cut-off law", $E_{cutoff} = h\nu_{cutoff} = I_p + 3.17 U_p$, where I_p is the gas ionization potential and $U_p \propto I \lambda_{pump}^2$ is the ponderomotive potential (I the focused intensity, λ_{pump} the wavelength of the pump). According to the three-step model and the cut-off law, the higher the ionization potential of the gas target (thus the higher the laser intensity which can be applied without ionizing the atom), the higher is the cut-off energy. Moreover, for the same gas target and laser intensity, longer pump wavelengths correspond larger cut-off extensions.

High-Order harmonics of an ultrashort laser pulse show high temporal [78] and spatial [79] coherence and are characterized by a time duration shorter than that of the driving source. Single XUV pulses with 130 attosecond duration have been recently produced and measured by exploiting a polarization gating technique [80]. At a longer temporal scale, XUV pulses with

durations ranging from 8 to 13 femtoseconds have been generated by spectral selection of a single harmonic with a suitable time-compensated monochromator [81].

Unfortunately, HH sources are inherently inefficient; among all the electron trajectories starting from the atom at ionization time, few of them collide back with the parent ion and emit radiation. For this reason, exploiting HHG for FEL seeding requires powerful laser sources and suitable techniques to boost the XUV emission to the required peak powers. Among the numerous techniques proposed for the optimization of HH yield [82], one can cite the coupling of the drive laser beam to corrugated capillaries [83], the use of two-colour laser pulses [84], the use of mixed gases as target [85], the spatial [86] and temporal [87] optimization of the drive laser by suitable optical shapers, and the interference of counter-propagating laser pulses in the gaseous target [88].

At the moment, the largest HH energies have been achieved by exploiting the loose focusing of a powerful drive laser in a static gas cell [89].:

- 1 μ J pulses have been generated at the 15th harmonic (54 nm) in xenon using 15-mJ, 35 fs laser pulses from a Ti:Sapphire source at 800 nm [90];
- 0.3 μ J pulses have been generated at the 27th harmonic (29.6 nm) in argon using almost the same laser pulses [91];
- 25nJ pulses have been generated at the 59th harmonic (13.5 nm) in neon using 50-mJ, 30 fs pulses from a Ti:Sapphire laser with wavefront correction of the drive beam [92].

Thus the loose focusing technique appears to be a natural candidate for XUV seeding in SPARX.

4.5.1 Scaling laws for efficient High-Order Harmonic Generation.

To achieve the required peak power for XUV seeding, the HHG process must be properly optimized. The main parameters governing the harmonic generation that must be optimized can be outlined as follows:

i) Drive laser source and operating wavelength (pump).

Although not yet completely addressed in the literature, the dependence of harmonic yield on the laser wavelength (pump appears to scale as $\sim \lambda^{-5.5}$ at constant laser intensity and target ionization potential [93]). Thus, with respect to wavelengths in the plateau region, shorter (pump seems more suitable for larger XUV yield. In contrast, the cut-off law states that longer (pump allows extending the spectral cut-off; thus a compromise between the two requirements must be chosen. Ti:Sapphire sources (working at 800 nm) provide a good compromise between spectral HH extension and yield.

It is worth noting that a new class of laser sources, based on parametric processes pumped by Ti:Sapphire lasers in nonlinear crystals, have recently emerged. Such sources show large tunability and flexibility and are already suitable for HHG [94], though limited at the moment to the millijoule energy level. Indeed, scaling parametric sources to tens of millijoules and more, as required by HHG in loose focusing, needs completely different approaches such as the Optical Parametric Chirped Pulse Amplification (OPCPA) technique. That goal is demanding, but is already in the development stage [95]. At the moment, Ti:Sapphire lasers are the more reliable, mature, and stable sources suitable for the FEL seeding application.

ii) Gas target.

The XUV emission strongly depends on the nature of the target: as a general rule, the lower the atomic ionization potential, the higher is the polarizability of the target and the emission yield of harmonics. Nevertheless, large ionization rates should be avoided. Therefore, one must compromise between maximum ionization and harmonic yield. According to references [83-92], Xenon and Krypton are good choices for HHG in the 50-80 nm region; Argon is the best candidate for XUV emission in the 25-50 nm spectral band, and Ne should be considered for wavelengths between 10 and 25 nm.

iii) Coherence length L_{coh} .

HHG is a coherent generation process; thus the XUV field amplitudes (not the emitted intensities) emerging from different regions of the laser-excited medium add up along the propagation direction. Maximizing the seed peak power requires constructive interference among all these contributions. The coherence length L_{coh} is the distance beyond which the XUV contributions no longer interfere constructively. For this reason, L_{coh} must be of the same order of magnitude as the length of the generating medium, L_{med} . When this condition is satisfied and the absorption is negligible, the number of emitted XUV photons scales as $SL_{med}^2 p^2$, where S is the laser beam spot area and p is the gas pressure [96]. The coherence length depends strongly on the laser beam profile and intensity, the focusing geometry, the target nature and ionization level, and the laser wavelength.

Harmonic yield cannot be improved by arbitrarily increasing the product $L_{med} p$. Indeed in such case the coherence length decreases [96] and the absorption of the medium increases. The increase of HH energy can instead be obtained by increasing the laser beam spot area S . Since the laser peak intensity must be kept at an optimal level, this scaling must be achieved by an increase of the laser pulse energy.

iv) Ionization level and laser pulse duration.

In general, L_{coh} is maximized when a low ionization level (lower than 5%) is present in the target; ionization must also be minimized to reduce the medium depletion, which lowers the efficiency of the drive laser pulse. For a constant peak laser intensity and a fixed target, a lower ionization level is achieved for shorter laser pulse durations [97].

The low ionization condition cannot be satisfied, even in gases like Neon or Helium, when very high harmonics (namely, for XUV emission below 10 nm) must be generated, since higher laser intensities are required (see the aforementioned cut-off law). For this reason, suitable techniques for phase matching improvement must be applied for efficient very-high-order harmonic generation [82,83,88].

v) Absorption length L_{abs} .

As XUV radiation is absorbed by the generating medium, the HH yield does not benefit from a medium length L_{med} longer than a few times the absorption length L_{abs} ; beyond such a value, the yield saturates [96,98]. For a gas target with a pressure of 1 torr, L_{abs} (in the XUV spectral region) is of the order of few centimetres.

4.5.2 Generation and transport of the seeding radiation

4.5.2.1 Design of the seeding source.

The parameters governing high-order harmonic generation (HHG) must be properly chosen to provide simultaneously a good XUV emission yield, a small divergence, and a smooth XUV beam profile to be delivered to the FEL.

This optimization should be performed experimentally, since it is strongly sensitive to the laser beam profile, temporal pulse duration, central wavelength, pulse energy and focusing conditions.

While a preliminary optimization can be performed numerically, the computational load required for a full numerical simulation [99,100,101] is huge and precludes a complete numerical optimization of the XUV output across the all the spatial, spectral and temporal domains for medium lengths longer than few millimetres. A partial pre-optimization can be performed in the spatial domain, determining the optimal phase matching conditions and treating the XUV emission as a continuous-wave generation process [102]. The results of such simulations must be considered only as guidelines for the experimental optimization.

As previously mentioned, the generation of high-order harmonics in a gas cell is the most convenient technique for FEL seeding: it provides larger XUV intensity and a more stable XUV energy level with respect to gas jets since it avoids target density fluctuations. It is also more reliable in comparison with the XUV generation in straight or corrugated capillaries, since it is less sensitive to misalignment of the laser beam. For these reasons, the HHG FEL seeder will consist of a static gas cell (length L_{med}) containing the gas target at pressure p , in which the drive laser beam propagates through small apertures. The cell input is located downstream of the laser focus (where the intensity beam radius is w_0 at $1/e^2$), at a distance z_{input} from the focal point. This choice allows one to select only the portion of XUV emission well collimated along the propagation direction.

The SPARX design will be limited to a seeder operating at about 30 nm; the following guidelines will be considered:

- a) drive laser wavelength: $\lambda_{pump} = 800 \text{ nm}$ (Ti:Sapphire source);
- b) gas target and pressure: Argon, $p < 10 \text{ torr}$ [96];
- b) laser pulse duration at full with half maximum of intensity (gaussian envelope): $\tau_{pump} = 35 \text{ fs}$;
- c) gaussian laser beam profile;
- d) maximum laser intensity on target I_{max} : corresponding to a maximum ionization level $\eta = 4\%$ in the target [96];
- e) minimum laser intensity on target: $I_{min} > I_{cs}$, where I_{cs} is the cut-off intensity for the chosen seed harmonic. This condition imposes inside the gas target a laser intensity that always exceeds the minimum value required for the seed generation;
- f) laser focusing: focal lengths $f < 8 \text{ m}$ (for practical reasons).

Table 4.40 shows a set of parameters, corresponding to a laser pulse energy $E = 7 \text{ mJ}$ focused by a lens with $f = 5 \text{ m}$ focal length, assuming an initial beam diameter $D = 1 \text{ cm}$ at $1/e^2$ of the intensity profile:

Table 4.40: Laser parameters for XUV FEL seeding at 29.63 nm.

I_{seed}	I_{pump}	I_{res}	Cut-off	λ_{seed}	HH	p	w_0	L_{med}	z_{inout}
W/cm^2	W/cm^2	W/cm^2	nm	nm		torr	μm	cm	cm
$1.8 \cdot 10^{14}$	$1.5 \cdot 10^{14}$	$1.4 \cdot 10^{14}$	24	29.6	27th	0.1	250	6	6

These conditions correspond to a coherence length $L_{coh} \sim 3 \text{ cm}$ and an absorption length, $L_{abs} \gg L_{med}$.

Through numerical simulations these parameters were optimized in the spatial domain, to achieve the smallest XUV beam divergence and a smooth intensity profile. The resulting harmonic field profile $A_q(r)$ was determined according to the relation [102]:

$$A_q(r) \propto \int_0^{L_{med}} [1 - \eta(r, z)] I^m(r, z) \exp[i\Phi(r, z)] \exp\left[\frac{z - L_{med}}{2L_{abs}}\right] dz$$

where $q = 27$ is the harmonic order, $m = 5$ accounts for the laser intensity dependence of the nonlinear dipole emission [102]. $\Phi(r, z)$ is the phase mismatch accumulated along the propagation direction, owing to the dispersion of neutral atoms and plasma, the focusing geometry and the intrinsic nonlinear dipole phase [102].

Figure 4.92 (left panel) shows the calculated intensity profile of the XUV beam at the 27th harmonic (29.63 nm); at the output of the gas cell the XUV beam diameter is about 100 μm at FWHM of the intensity profile; the far field divergence (shown in the right panel) is lower than 0.7 mrad FWHM. Experimental results reported in the literature are in agreement with the simulated beam diameter and divergence [96].

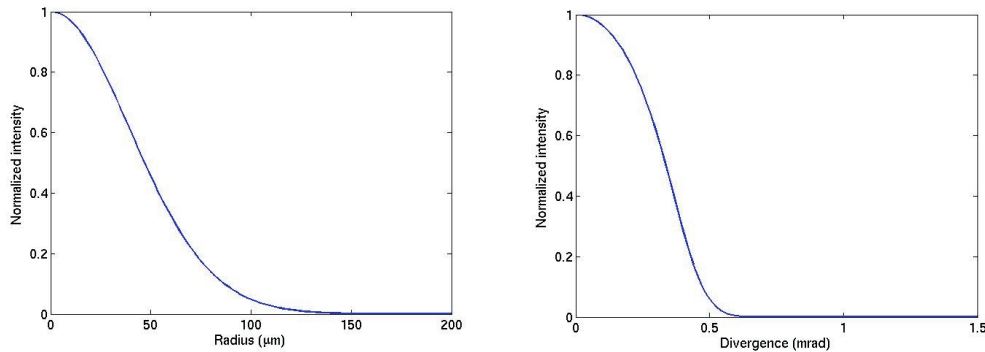


Figure 4.92: Calculated XUV beam profile (left) and divergence (right) at 29.63 nm at the output of the Argon cell.

The parameters reported in Table 4.40 are only as a starting point for an experimental optimization of the XUV emission as a function of laser energy and focusing condition as well as of the gas pressure.

4.5.2.2 Beamline for conditioning and transport of the seeding

The radiation generated by the seeding source will be delivered to the Free Electron Laser through a suitable beamline that has to perform the following tasks:

- Separation of the IR pump beam from the XUV beam
- Possible monochromatization of the seeding beam

- Alignment of the seeding beam with the undulator sections
- Focusing of the seeding beam

In the following, the tasks will be analyzed separately.

a) Separation of the IR pump beam from the XUV beam

As the high-energy IR pump beam co-propagates with the generated XUV radiation and may damage the XUV optics of the beamline or disturb the experiment, it must be blocked by a suitable beam separator before being focused. The main requirements for the separation system are: high damage threshold, high attenuation of the pump pulse, and high throughput in the XUV spectral region.

A simple method to separate the IR laser beam from the XUV radiation is to use a thin metal foil which is opaque to the visible and IR and partially transparent in the XUV: such a filter typically consists of a foil with thickness of few hundred nanometers deposited on an electroformed nickel mesh [103]. The most commonly used materials are aluminum, zirconium and palladium. The filter transmits XUV radiation (the typical transmission is ≈ 0.5) and attenuates the visible and near-IR radiation by a factor 10^{-6} - 10^{-7} . However, the damage threshold for a 150-nm-thick Al filter is about 40 mJ/cm² for a 5-ns laser pulse (i.e. $8 \cdot 10^6$ W/cm²). Therefore, this method can be applied only for low-intensity pulses.

High-throughput, high-damage-threshold beam separation has recently been demonstrated by using two plane plates set at the Brewster angle with respect to the pump wavelength [104,105]. The XUV light is reflected toward the experiment, while the IR pump pulse, that is linearly polarized, is attenuated. For radiation at wavelengths longer than 30 nm generated by a Ti:Sapphire laser system centred at 800 nm, silicon plates at 75° are used with a transmission of about 0.5 in the XUV and attenuation of the IR beam of 10^{-4} [102]. For wavelengths in the 10-30 nm region, the beam separator is realized by two silicon plates coated by a 10-nm-thick niobium nitride film and operated at 78°, with a transmission exceeding 0.4 in the 13-18 nm region and an attenuation of 10^{-2} [105]. The beam splitters have been proved to have a damage threshold of at least 0.8 TW/cm² for a 30-fs pump pulse. The two-plate design is simple to align, can be operated over a broad spectral region with high throughput, and does not alter the phase of the XUV pulse. Unfortunately it has been applied only for wavelengths longer than 10 nm. In fact, applying the same design to the 3-10 nm region requires operating the optics at a significantly higher incidence angle ($\approx 84^\circ$ - 87°) to guarantee high throughput. At present, no material has been suitable for operation at such extreme incidence angles with almost zero reflectivity in the near-IR for linearly polarized light.

A method that can be applied for radiation below 10 nm is the use of two plane gratings at grazing incidence in a compensated configuration [106]. The first grating acts as the beam separator: it diffracts the XUV light into the first order while reflects the visible and near-IR light into the zero order. The zero-order light can then be stopped after the grating by a suitable light trap. The diffracted light impinges on a second grating that is operated in a compensated configuration respect to the first: it compensates both the spectral dispersion given by the first grating and the temporal broadening that the XUV ultrashort pulse undergoes after the diffraction in the first grating. The system can be designed for any wavelength in the 3-10 nm XUV region. Since the gratings are operated at extreme grazing incidence, the area of the optical surface that is illuminated by the fundamental laser pulse is quite large. Consequently there is

no risk of damage to the optical surface even in the case of very powerful laser sources. It can be shown that the group delay given by such a system is not constant for broad band XUV pulses. Therefore the output pulse is broadened in time from few to several femtoseconds. This makes such a system suitable as beam separator at wavelengths below 10 nm for femtosecond pulses.

We will limit the spectral range of operation of the beamline to wavelengths longer than 10 nm using silicon or niobium-nitride-coated plates as beam separator. The separator will absorb most of the energy of the drive laser while it will reflect the XUV radiation. The separator will be placed at a distance from the XUV generation point far enough to limit the power density on the optical surfaces and avoid the risk of damage them. A suitable distance is in the 2-4 m range.

Since the divergence of the XUV radiation is significantly reduced, as compared with that of the drive laser, due to phase matching, a small circular aperture will be placed in front of the beam separator to stop the portion of the laser IR radiation with high divergence before the silicon mirror.

b) Focusing mirror

The XUV beam must be focused on the undulator section to co-propagate with the electron beam. The size of the XUV focus is expected to be of the order of 200 μm with a divergence as small as possible to propagate almost collimated for a long distance within the undulator. This condition is obtained through a proper magnification of the seeding beam.

Assume a source with 100 μm FWHM size and 0.4 mrad FWHM divergence. The focusing section could introduce a magnification of a factor 2. This increases the effective size to 200 μm FWHM, and correspondingly decreases the divergence to 0.2 mrad FWHM. The ideal focusing surface would be an ellipsoid, but the focusing requirements are so relaxed and the beam divergence so low that a simple grazing-incidence toroidal mirror can be used. The mirror is placed after the beam separator and has a sufficiently long exit arm to leave space for the accommodation of the aligning section.

Assume the toroidal mirror is placed 4 m from the source. For a magnification of 2, the exit arm is at 8 m. The radii of such a mirror used at an incident angle of 88° are 153 m (tangential) and 0.19 m (sagittal). The reflecting area is 50 mm (tangential) \times 2 mm (sagittal).

c) Alignment section

The seeding beam must be precisely aligned with the electron beam within the undulator sections. Considering a spot size on the HH focus within the undulator of $\sim 200 \mu\text{m}$ and a superposition length of ~ 4 m to ensure a proper interaction between electrons and photons, the required precision is better than ~ 0.05 mrad. This precision implies the remote control of alignment in both the spatial directions. The control is performed in each of the two directions through two plane mirrors at grazing incidence, for a total of four reflections. The first mirror of the alignment section is rotated around an axis passing through the mirror center and perpendicular to the plane of incidence. The second mirror is rotated and is also translated along a linear axis laying on the plane of incidence and parallel to the mirror surface.

The rotation of the second mirror changes the direction of the beam, the simultaneous rotation of both mirrors plus translation of the second mirror changes the position of the source point as seen from the undulators.

Since the input of the focusing mirror has to be kept constant in space, the alignment section is placed after the focusing section.

d) Coatings of optics

The reflectivity of some standard coatings at grazing incidence in the 10-40 nm region are shown in Figure 4.93. Obviously, the higher the incident angle, the higher the reflectivity. Since the total number of reflections is five, i.e., the toroidal focusing mirror and four plane mirrors for the fine alignment in the two spatial directions, the selection of the proper coating has a fundamental role in maximizing the total efficiency. For example, to increase the single reflectivity from 0.85 to 0.90 increases the total efficiency from 0.44 to 0.60.

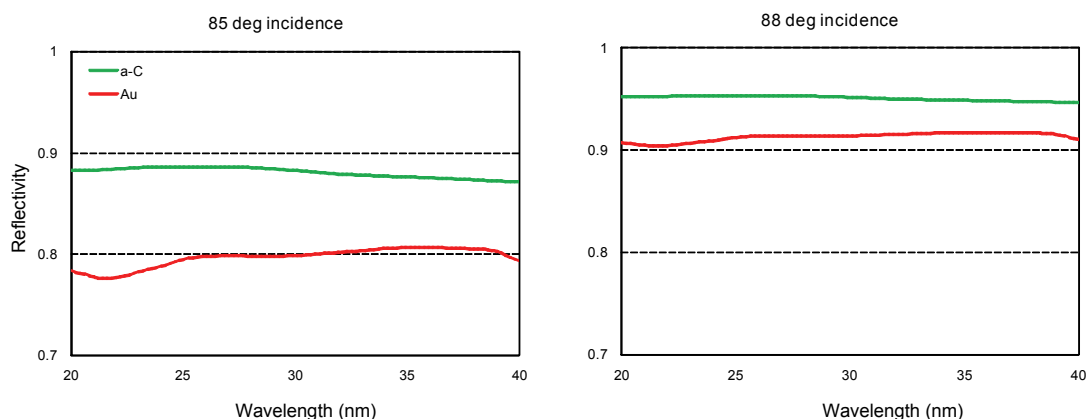


Figure 4.93: Reflectivity of Au and C at grazing incidence in the 20-40 nm region.

The reflectivity of some standard coatings in the 20-40 nm region is shown in Figure 4.93. If carbon-coated mirrors at 88° are used, the efficiency of the five grazing-incidence reflections is about 0.77. The total efficiency of the beamline, which includes also the beam separator with a single silicon plate, is about 0.50 at 30 nm.

e) Polarization

The polarization of the FEL beam is changed by the different values of reflectivity R_s and R_p in the s and p planes. This is true for any reflection on an optical surface. As the grazing angles used for the mirrors, R_s and R_p differ by less than 0.5%, the influence on the beam polarization is negligible.

f) Monochromatization

The intrinsic bandwidth of the harmonics generated around 30 nm is few percent. One could request to seed the FEL with a narrower spectral pulse, at

the expense of a lower photon flux of the seeding beam and a longer pulse duration due to spectral clipping.

A grating monochromator is used to increase the spectral purity of the source. Beyond the altering the pulse duration due to the clipping of its bandwidth, the major mechanism that alters the pulse duration is the difference in the lengths of the optical paths of the rays diffracted by different grating grooves. In fact, a single grating inevitably stretches of the ultrafast pulse due to diffraction: the total difference in the optical paths of the rays diffracted by N grooves illuminated by radiation at wavelength λ is $Nm\lambda$, where m is the diffracted order. This effect is negligible for picosecond or longer pulses, but is dramatic for femtosecond pulses. The monochromator has to be designed to give an instrumental temporal broadening that is comparable to the intrinsic Fourier limit.

One can design grating monochromators that do not alter the temporal duration of an ultrafast pulse by using at least two gratings in a subtractive configuration to compensate for the dispersion [107]. In such a configuration, the second grating compensates for the time and spectral spread introduced by the first one. Such a configuration has already been demonstrated to be effective in the spectral selection of pulses as short as 8 fs [81]. The drawback of the time-delay compensated monochromator is the complexity of the design and the lower throughput with respect to an equivalent single-grating monochromator.

In the case of the seeding signal, the intensity of the harmonics must be preserved as much as possible. Therefore a single-grating uncompensated design will be adopted. For a spectral resolution in the few-thousand range the parameters of the monochromator (i.e. grating groove density, incident angle, geometry) will be selected so that the number of illuminated grooves is as close as possible to the required spectral resolution. For the case of 1000 illuminated grooves, the corresponding instrumental broadening is 100 fs at 30 nm.

The optical design (either concave mirror and plane grating or spherical grating) will be defined once the characteristics of the source and the tuning interval have been defined. The monochromator will be inserted before the focusing mirror.

g) Photon output

An energy of 0.02 μJ /pulse at 29.6 nm is a reasonable initial target value for the output of the FEL seeder, using argon as generating medium. The chosen seed wavelength corresponds to the 27th harmonic of a Ti:Sapphire laser emission. The target energy is well within the present experimental capabilities in the generation of high-intensity harmonics [91], as more than 10 times larger energies have been demonstrated at 30 nm.

The duration of the single harmonic pulse is estimated to be about half the laser pulse duration [81]. Assuming a temporal duration of the drive laser pulse of ~ 35 fs, a conservative estimate of the seeding XUV pulse duration is 20 fs, corresponding to an initial peak power of about 1 MW.

The total transmission of the beamline is estimated to be 0.5, which includes the beam separator and the mirrors (without monochromator). The resulting peak intensity at the undulator input will be 500 kW, which is high enough to seed the FEL process.

The situation is different in case of monochromatization of the seed, since the total efficiency of the beamline decreases to about 0.2. Moreover, assuming

a seed monochromatization with a spectral resolution $\lambda/\Delta\lambda$ of 1000, one can predict a reduction of the photon flux of about 20 times. The pulse focused at the output of the beamline would be longer than the original pulse due to the spectral clipping and to the grating response. A temporal duration of the order of 100 fs can be assumed, which corresponds to a further ten-fold decrease of the peak power. Thus, the initial peak power at the output of the seeder would be reduced by a factor 500 at the undulator input.

Assuming an initial seed energy of 0.3 μJ /pulse at 29.6 nm (that is the highest energy reached up to now at that wavelength [15]) and an initial pulse duration of 20 fs, the resulting peak power at the undulator input would be about 30 kW.

4.5.3 CHARACTERIZATION OF THE SEEDING BEAM

The seeding beam has to be characterized in terms of:

- Spectrum
- Intensity
- Divergence
- Source size

4.5.3.1 *Spectral characterization*

The XUV beam will be spectrally monitored by a XUV flat-field spectrometer equipped with a spherical grating with variable groove-spacing [108]. The grating gives an almost flat spectrum in the 10-40 nm region by an appropriate choice of the variation of the groove density. The spectrum is acquired by a MCP intensifier with phosphor screen optically coupled to a low-noise cooled CCD camera [109]. The MCP is completely solar blind, so any IR radiation from the generation beam entering the spectrometer detector will not disturb the acquisition. In addition, the MCP gain can be adjusted to increase the dynamic range of the detector. The response of the spectrometer will be calibrated within the spectral region of operation.

The spectrometer will be connected to the beamline for the transport of the seeding beam through a lateral flange. A plane mirror which can be inserted in the optical path will deflect the beam toward the entrance slit.

4.5.3.2 *XUV intensity measurement*

The absolute intensity of the XUV beam will be measured by a calibrated XUV photodiode. The diode will give the integral number of photons within the spectrum, then the response of the spectrometer will give the number of photons per harmonic.

4.5.3.3 *XUV beam divergence*

In addition to the acquisition of the spectrum, the spectrometer will also provide a measure of the divergence as a function of the harmonic order. In fact, the spectrometer is astigmatic, i.e. the radiation is focused only in the

spectral dispersion plane. The size of the image on the plane perpendicular to this is proportional to the divergence of the beam, once the distance between the source and the detector is known [110].

4.5.3.4 XUV source size

The size of the source will be measured by mounting a 2D detector (that could be the same detector used for the spectrometer) on the focal plane of a grazing incidence toroidal mirror which creates an image of the high-order harmonic source in a 1:1 configuration. The measurement is sufficiently accurate since the pixel size of the detector is in the 20-25 μm range and the size of the source is expected to be in the 50-100 μm range.

4.6 Appendix: C-band option for the SPARX LINAC

In this section it is described a possible designs of a high frequency LINAC based on C-band technology and a hybrid solution using both a S-band and C-band technology, able to produce beams with brightness as high as 10^{15} A/m² directly from the injector.

As a reference design the S-band (2856 MHz) SPARC photo-injector has been chosen. In its ideal configuration the beam consists in a uniform charge distribution inside a cylinder of length L and radius R. Its parameters (charge Q, beam sizes R and L, peak RF field \hat{E} and solenoid field B) have been scaled to its second (C-band) harmonic frequencies (5.712 GHz) [111] according to the following wavelength scaling laws [112]:

$$Q \propto \lambda_{RF}, \quad R, L \propto \lambda_{RF}, \quad \hat{E} \propto \lambda_{RF}^{-1}, \quad \hat{B} \propto \lambda_{RF}^{-1}$$

As discussed in [2] both the space charge and RF contributions to the total rms emittance scale with λ_{rf} , in addition since the thermal emittance contribution scale with the beam radius a similar scaling can be expected also for $\varepsilon_{th} \propto \lambda_{rf}$. Hence operation at shorter wavelength results a very convenient choice also for the beam brightness: $B_n \propto \lambda_{rf}^{-2}$.

Table 4.41: Original and scaled parameters

<i>Freq.</i> <i>[GHz]</i>	<i>Q [nC]</i>	<i>R</i> <i>[mm]</i>	<i>L</i> <i>[ps]</i>	<i>E_{peak}</i> <i>[MV/m]</i>	<i>B</i> <i>[T]</i>
2.856	1	1	10	120	0.275
5.712	0.5	0.5	5	240	0.55

A direct application of the previous scaling laws leads to the set of new parameters, reported in table I. In addition, to fulfil the scaling approach, also the solenoid length has to be scaled with λ_{rf} , from the original 20 cm long solenoid for the S-band gun design to 10 cm for the C-band case, see Figure 4.94.

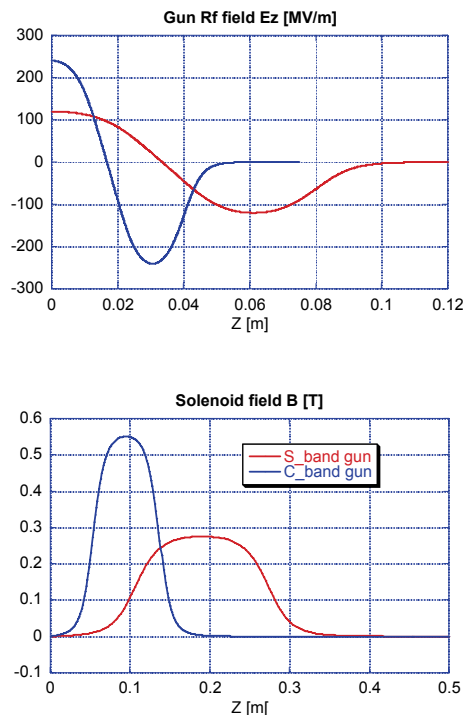


Figure 4.94: Gun RF fields (upper plot) and solenoid fields (lower plot) for the original S-band gun design (red line) and the C-band design (blue line).

The scaled parameters result to be close to the state of the art for a C-band gun option. A beam dynamics study has been performed with the HOMDYN code. The beam chosen is 3.68 ps long with a radius of 0.4 mm and a charge of 200 pC. The assumed thermal emittance is 0.6 mm mrad for a copper cathode.

Figure 4.95 shows the SPARX LINAC layout with the C-band option: a C band photo-injector with 240MV/m peak field, followed by the scaled solenoid, provides a first compensation to the emittance growth. The injector is followed by a C-band accelerating structure operating at 40 MV/m accelerating field, in the RF compression (velocity bunching) configuration, that drives the beam up to 138 MeV with a current of 200 A. Solenoids around the accelerating structures are foreseen to keep under control the emittance oscillations.

The beam is then accelerated in LINAC 1 up to 548 MeV; it is injected in the RF structures following the invariant envelope condition to damp emittance oscillations and it is transported out of crest to gain at the end of LINAC 1 an energy spread of 0.4%. In this way the downstream magnetic compressor ($R_{56} = 15$ mm) compresses the beam to a 0.04 mm length. Finally the last LINAC (LINAC2) drives the beam up to 1.5 GeV energy with a final current of 455 A. The energy spread is reduced to 0.1% by driving the beam out of crest and taking advantage of the wake fields induced along the structures. The length of the linear accelerators is about 35 m.

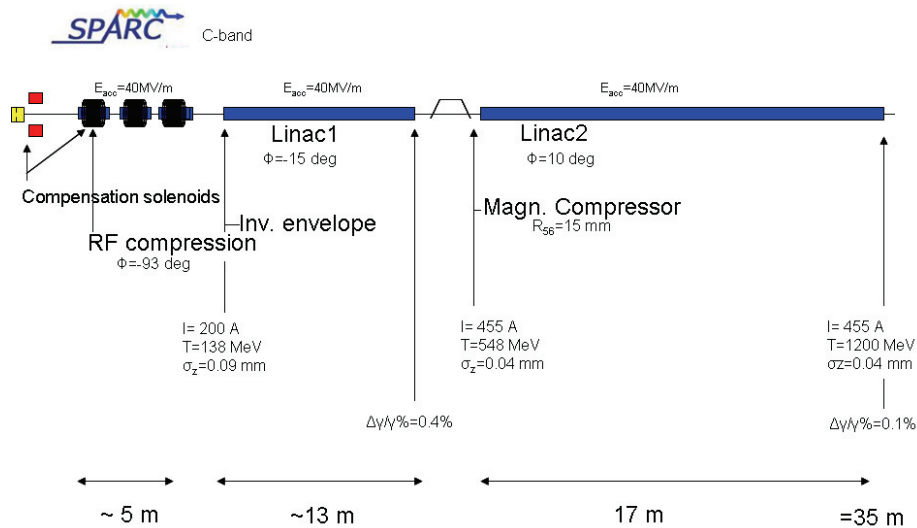


Figure 4.95: Schematic layout of a Sparc C-band photo-injector and C-band LINAC to 1.5 GeV.

The following Figure 4.96 shows the emittance and rms spot size of the beam along the whole accelerator. The solenoids around the three sections have been turned on to compensate the emittance growth with the following values: 0.160 T, 0.120 T and 0.120 T respectively. An emittance of about 0.43 mm mrad has been obtained giving a B_{\perp} of about $5 \cdot 10^{15}$ A/m².

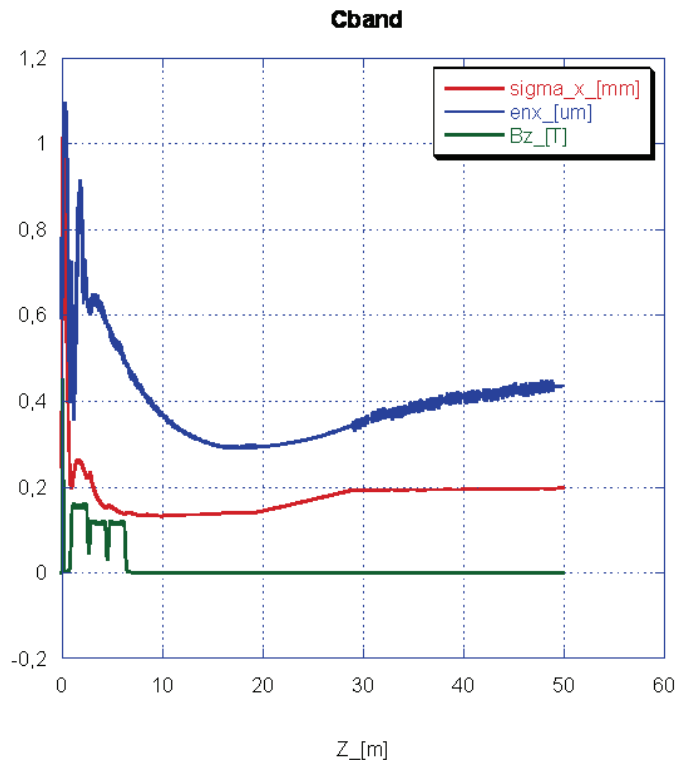


Figure 4.96: Emittance, rms spot size and the solenoid fields along the accelerators up to 1.2 GeV.

Figure 4.97 represents the current, the rms length and the energy spread of the beam as a function of horizontal coordinate z .

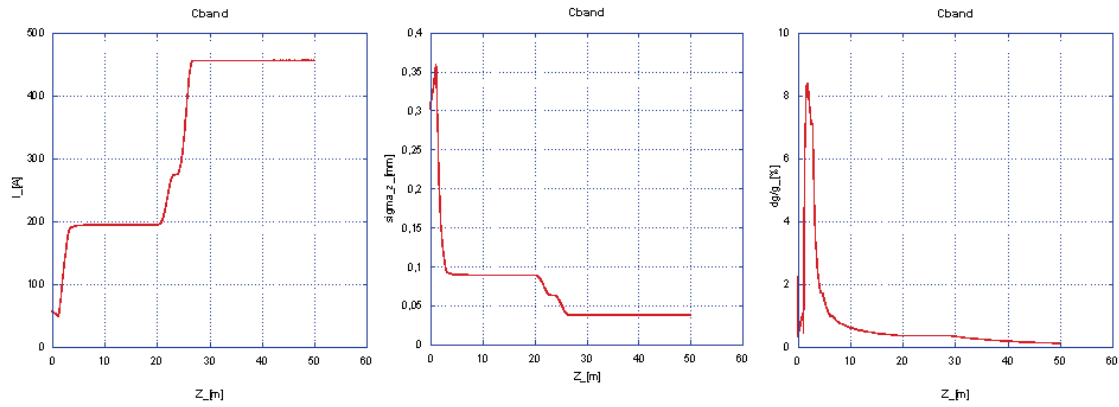


Figure 4.97: From the left hand side: current, rms length, energy spread versus z .

An hybrid solution with S- band and C-band technology has been studied as well. The beam chosen is 5.67 ps long with a radius of 0.64 mm and a charge of 200 pC. The assumed thermal emittance is 0.6 mm mrad for a copper cathode.

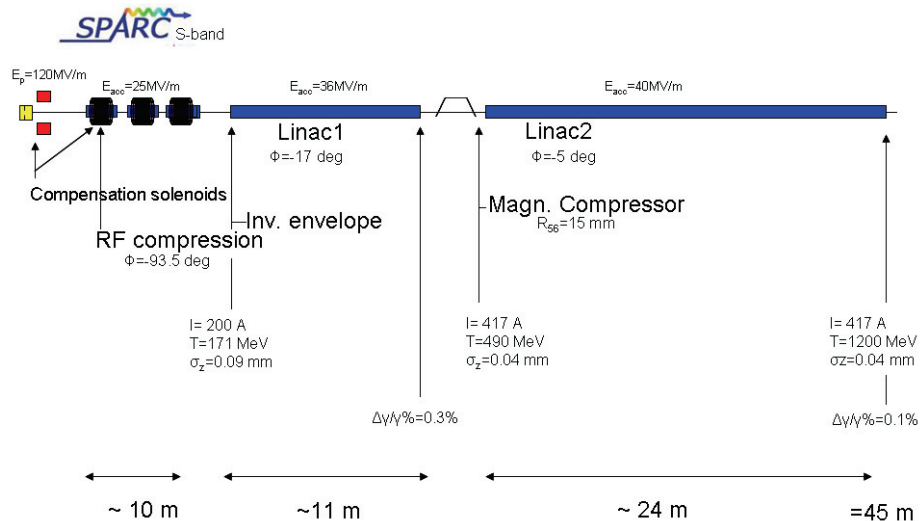


Figure 4.98: Schematic layout of the Sparc S-band photo-injector and C-band LINAC to 1.2 GeV.

In Figure 4.98 an S-band photo-injector, exactly the same as the one foreseen in SPARC, operating at 120 MV/m, together with the gun solenoid, compensate the emittance growth. The beam is then injected in the S-band accelerating structures operating at 25 MV/m, driving the beam to an energy of 171 MeV. The bunch is compressed with the velocity bunching technique and then injected in the following C-band accelerating structures (LINAC 1) up to 490 MeV. As in the previous case the beam is driven along LINAC 1 out of phase to fulfil the following magnetic compressor requirements: the energy spread gained is 0.3% thus allowing the magnetic compressor ($R_{56} = 15$ mm) to compress the beam to 0.04 mm length. The last accelerating structure (LINAC2) in the C-band configuration drives the beam to a current of 417 A and to an energy of 1.2 GeV. The energy spread previously induced is compensated to 0.1% at the end of LINAC 2.

In this case the whole linear accelerators are 45 m long.

The following Figure 6 shows the emittance and rms spot size of the beam along the whole accelerator. The solenoids around the three sections

have been turned on also in the hybrid solution to compensate the emittance growth. An emittance of about 0.56 mm mrad has been obtained giving a B_{\perp} of about $2.6 \cdot 10^{15}$ A/m².

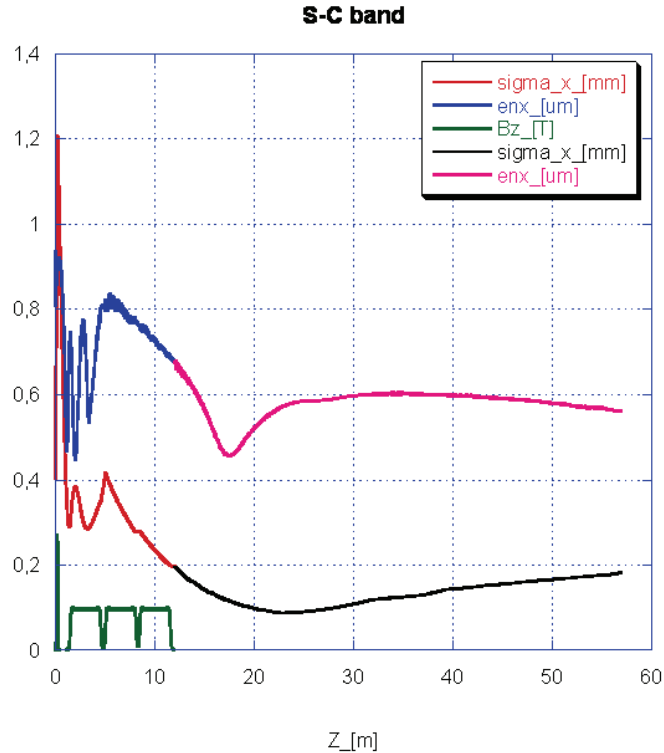


Figure 4.99: Emittance, rms spot size and the solenoid fields along the accelerators up to 1.2 GeV.

Figure 4.100 shows the current, the rms length and the energy spread of the beam as a function of horizontal coordinate z .

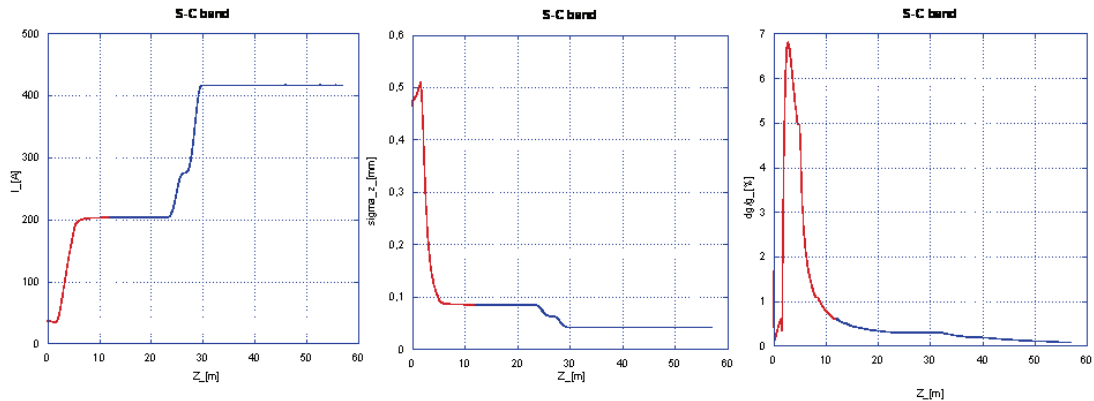


Figure 4.100: From the left hand side: current, rms length, energy spread versus z .

In Table 4.42 are reported for comparison the RF parameters for the S and C guns. As one can see the required peak power from RF source are within the state of the art C-band klystron development.

Table 4.42: S-band and C-band RF parameters

ν [Ghz]	2.856	5.712
R_{sh} [M Ω /m]	46	65
Q	15335	10843
E_{peak} [MV/m]	120	240
P_{RF} [MW]	10	14
P_d at 10 Hz [kW/m]	4.7	
τ [μ s]	4	1.4
L_{cav} [mm]	86	43
R_{iris} [mm]	12	6

4.7 References

- [1] H. N. Chapman et al. *Nature Physics* **2**, 839-843 (2006)
- [2] D.T. Reid, *Science* **291**. No. 5510, 9 March 2001, pp. 1911 - 1913 and M. Drescher, M. Hentschel, R. Kienberger, G.
- [3] R. Bonifacio et al., *Phys Rev. A*, **40**, 4467 (1989); L. Giannessi et al., *Journ. Appl Phys* **98**, 043110 (2005)
- [4] Alexander A. Zholents and William M. Fawley , "Proposal for Intense Attosecond Radiation from an X-Ray Free-Electron Laser," *Phys. Rev. Lett.*, V. 92, Number 22, 4 June 2004.
- [5] E.L. Saldin, E.A. Schneidmiller, and M.V. Yurkov, "Attosecond Pulses from X-Ray FEL with an Energy-Chirped Electron Beam and a Tapered Undulator," *Proceedings of FEL 2006*, BESSY, Berlin, Germany
- [6] L. Giannessi, P. Musumeci, S. Spampinati *Journal of Appl. Phys.* **98**, 043110 (2005)
- [7] P. Sprangle et al. *Phys. Rev. A* **21**, 302 (1980)
- [8] G. Dattoli et al. *IEEE Journal of Quantum Electronics* QE-17, 1371 (1981)
- [9] R. Bonifacio, C. Pellegrini, L.M. Narducci, *Optics Comm.* **50**, 373 (1984)
- [10] H. Haus, *IEEE Journal of Quantum Electronics* QE-17, 1427 (1981).
- [11] G. Dattoli, P.L. Ottaviani, *Journal of Appl. Phys.* **86**, 5331 (1999)
- [12] L. Giannessi, *Proc. of 2004 FEL conference*, www.jacow.org, 37 (2004)
- [13] A. McPherson et al., *J. Opt. Soc. Am. B* **4**, 595 (1987).
- [14] M. Ferray et al., *J. Phys. B: At. Mol. Opt. Phys.* **21**, L31(1988)
- [15] J.F. Hergott et al., *Phys. Rev. A* **66**, 21801 (2002).
- [16] E. Takahashi, N. Y., and M. K., *Opt. Lett.* **27**, 1920 (2002)
- [17] T. Brabec, F. Krausz, *Rev. Mod. Phys.* **72**, 545(2000)
- [18] D. Garzella et al., *Nucl. Instrum. Methods A* **528**, 502 (2004).
- [19] G. Lambert et al. *Nature Physics* **889**, 1 (2008)
- [20] L. Giannessi et al. *NIM A* **593**, 132 (2008)
- [21] G. Dattoli et al. *Il Nuovo Cimento* **11**, 393 (1989)
- [22] W. A. Barletta, A. M. Sessler, L-H Yu, *Nucl. Inst. and Meth.* **A331** (1993) 491-495);
- [23] M. Xie, *Proceedings PAC 1995 IEEE* No. 95CH3584, 183 (1996)
- [24] G. Dattoli, P. L. Ottaviani, and S. Pagnutti, *J. Appl. Phys.* **97**, 113102 2005.
- [25] S. Reiche, *NIM A* **429**, 243 (1999), see also <http://corona.physics.ucla.edu/~reiche/>
- [26] L. Giannessi, *Proceedings of the 2006 FEL conference*, www.jacow.org , 91 (1996)
- [27] L. Giannessi, H. P. Freund, P. Musumeci and S. Reiche, *NIM A* **593**, 143 (2008)
- [28] G. Dattoli, M. Galli, P.L. Ottaviani, 1-dimensional simulation of FEL including high gain regime saturation, Prebunching, and Harmonic Generation, ENEA Internal Report RT/INN/93/09, 1993.
- [29] D. Prosnitz, A. Szoke, V.K. Neil, *Phys. Rev. A* **24** 1436 (1981)
- [30] T. Scharlemann, *J. Appl. Phys.* **58**, 2154 (1985)
- [31] I. Boscolo, V. Stagno, *Il Nuovo Cimento* **58**, 267 (1980)
- [32] L. H. Yu *Phys. Rev. A* **44**, 5178 (1991)
- [33] G. Dattoli et al. *Phys. Rev. E* **49**, 5668 (1994)
- [34] L. H. Yu et al. *Science* **289**, 932 (2000)
- [35] L. H. Yu et al. *Phys. Rev. Lett.* **91**, 074801 (2003)

- [36] L. Giannessi et al., NIM A 593, 132 (2008)
- [37] L. Giannessi et al., Proc. FEL Conference 2006, pag. 95, Berlin
- [38] D. C. Nguyen, L. M. Earley, N. A. Ebrahim, C. M. Fortgang, J. C. Goldstein, R. F. Harrison, W. A. Reass, J. M. Kinross-Wright, R. L. Sheffield, and S. K. Volz, "Regenerative Amplifier FEL," Proc. XX International Linac Conference, Monterey, California (2000)
- [39] J. Rosenzweig, NIM A 593, 39 (2008)
- [40] M. Boscolo, NIM A 593, 137 (2008)
- [41] Data from: B. Carré, talk presented at the slicing ARC-EN-CIEL Workshop, 3-4 February 2004, Orsay
- [42] SPARC Project team, "Technical Design Report for the SPARC advanced Photoinjector", <http://www.Inf.infn.it/acceleratori/sparc> (2004)
- [43] M. Ferrario et al., Phys. Rev. Letters 99, 234801 (2007)
- [44] L. Serafini, J.B. Rosenzweig, Phys. Rev. E 55 (1997) 7565
- [45] M. Ferrario et al. ,Report No, SLAC-PUB-8400
- [46] K. Flottmann et al., Proceedings of the 19th Particle Accelerator Conference, June 18-22, 2001, Chicago, Illinois, p. 2236
- [47] L. Serafini et al., PAC01, Chicago, June 2001
- [48] A. Bacci et al., Nuclear Instruments and Methods B 263 (2007), 488-496
- [49] P. Emma et al., PAC05, Knoxville (2005), p. 344
- [50] Z. Huang, et al, Phys. Rev ST-AB 7 074401, 2004.
- [51] P.Emma, "X-band RF Harmonic Compensation for Linear Bunch Compression in the LCLS", LCLS-TN-01-1, Nov. 14, 2001.
- [52] L. Serafini and M. Ferrario, "Velocity Bunching in PhotoInjectors" , AIP CP 581, 2001, pag. 87.
- [53] http://www.Inf.infn.it/acceleratori/sparc/SPARC_TDR.pdf
- [54] V. Fusco, et al, New J. Phys. 8 295, 2006
- [55] K.L.F. Bane, P. Emma, "LiTrack: A Fast Longitudinal Phase Space Tracking Code with Graphical User Interface", Proc. PAC05, Knoxville(TN).
- [56] M. Borland, "Elegant: A Flexible SDDS-Compliant Code for Accelerator Simulation" Advanced Photon Source LS-287, September 2000.
- [57] M. Dohlus, T. Limberg, CSRtrack: Faster Calculation of 3D CSR effects, FEL 2004, 2004.
- [58] L. Young, private communication.
- [59] K.Bane and M.Sands, "Wakefields of very short bunches in an accelerating cavity". In Proc. Workshop on Impedances Beyond Cut-off, 1987, 1987
- [60] M. Ferrario, V. Fusco, M. Migliorati, L.Palumbo, Int. Journal of Modern Physics A Vol. 22, No. 23 (2007) 4214-34
- [61] K. Bane, SLAC-PUB 9663, (2003).
- [62] Arthur et al, "Linac coherent light source (LCLS) conceptual design report",SLAC-0593, Apr 2002.
- [63] A. Wu Chao, Physics of Collective Beam Instabilities in High Energy Accelerators, 1993
- [64] F. Zimmermann, "longitudinal Single Bunch Dynamics and Synchrotron Radiation Effects in the Bunch Compressor", NLC-Note-3, SLAC, October 1994
- [65] Ya. S. Derbenev, et al, „Microbunch Radiative Tail-Head Interaction“, TESLA FEL 95-05, DESY, Sep. 1995
- [66] G. V. Stupakov, Proc. of Nonlinear and Collective Phenomena in Beam Physics, p. 334, Arcidosso, 1998

-
- [67] The TESLA Test Facility FEL team; SASE FEL at the TESLA Facility, Phase 2, TESLA-FEL-2002-01, 2002.
- [68] A. Lolergue, A. Mosnier, Proc. EPAC 2000, Vienna, Austria
- [69] F. Stulle, A. Adelman, M. Pedrozzi, Phys. Rev. ST-AB 10 031001, 2007
- [70] J. Qiang et al. "A 3D PARALLEL BEAM DYNAMICS CODE FOR MODELING HIGH BRIGHTNESS BEAMS IN PHOTOINJECTORS", PAC2005 p. 3316
- [71] E. L. Saldin, E. A. Schneidmiller, and M. V. Yurkov, Nucl. Instrum. Methods Phys. Res., Sect. A398, 373 (1997).
- [72] M. Dohlus, A. Kabel, T. Limberg: Efficient Field Calculation of 3-D Bunches on General Trajectories. NIM A445 (2000) 338-342.
- [73] S. Heifets, G. Stupakov, S. Krinsky, Phys. Rev. Spec. Topics - A&B 5, 064401 (2002).
- [74] M. Venturini, R. Warnock, and A. Zholents, Phys. Rev. Spec. Topics - A&B 10, 054403 (2007).
- [75] R. Chasman and K.Green, BNL Report, BNL 50505 (1980)
- [76] P. B. Corkum, Phys. Rev. Lett. 71 (1993) 1994-1997.
- [77] M. Lewenstein et al., Phys. Rev. A 49 (1994) 2117-2132.
- [78] P. Salières et al., Science 292 (2001) 902-905.
- [79] L. Le Déroff et al., Phys. Rev. A 61 (2000) 043802.
- [80] G. Sansone et al., Science 314 (2006) 443-446.
- [81] L. Poletto et al., Opt. Lett. 32 (2007) 2897-2899.
- [82] C. Winterfeldt et al., Rev. Mod. Phys. 80 (2008) 117-140.
- [83] A. Paul et al. Nature 421 (2003) 51-54 ; M. Zepf et al., Phys. Rev. Lett. 99 (2007) 143901.
- [84] I. Kim et al., Appl. Phys. Lett. 92 (2008) 021125.
- [85] E. Takahashi et al., Phys. Rev. Lett. 99 (2007) 053904.
- [86] P. Villorosi et al., Opt. Lett. 29 (2004) 207-209.
- [87] T. Baumert et al., Appl. Phys. B 65 (1997) 779-782.
- [88] X. Zhang et al., Nature Physics 3 (2007) 270-275.
- [89] Eiji J. Takahashi et al, IEEE J. Sel. Top. Quantum Electron. 10 (2004) 1315
- [90] E. Takahashi et al., Opt. Lett. 27 (2002) 1920-1922.
- [91] E. Takahashi et al., Phys. Rev. A 66 (2002) 021802(R).
- [92] E. Takahashi et al., Appl. Phys. Lett. 84 (2004) 4-6.
- [93] J. Tate et al., Phys. Rev. Lett. 98 (2007) 013901.
- [94] C. Vozzi et al., Optics Express 14 (2006) 10109-10116
- [95] F. Tavella et al., Opt. Lett. 32 (2007) 2227-2229.
- [96] E. Takahashi et al., J. Opt. Soc. Am. B 20 (2003) 158-165.
- [97] T. Brabec and F. Krausz, Rev. Mod. Phys. 72 (2000) 545-591.
- [98] E. Constant et al., Phys. Rev. Lett. 82 (1999) 1668-1671.
- [99] Data from www-cxro.lbl.gov.
- [100] M. V. Ammosov et al., Sov. Phys. JETP 64 (1986) 1191-1194.
- [101] E. Priori et al., Phys. Rev. A 61 (2000) 063801.
- [102] C. Altucci et al., Phys. Rev. A 68 (2003) 033806.
- [103] F. R. Powell et al, Opt. Eng. 29 (1990) 614.
- [104] E.J. Takahashi et al, Opt. Lett. 29 (2004) 507.
- [105] Y. Nagata et al, Opt. Lett. 31 (2006) 1316.
- [106] F. Frassetto et al, JOSA A 25 (2008) 1104.
- [107] L. Poletto, Appl. Phys. B 78 (2004) 1013
- [108] L. Poletto et al, Rev. Sci. Instr. 75 (2004) 4413.
- [109] L. Poletto et al, Opt. Eng. 40 (2001) 178.
- [110] L. Poletto et al, Rev. Sci. Instr. 72 (2001) 2868.

- [111]M. Ferrario et al., "High brightness C-band and X-band photoinjector concepts and related technological challenges", proc. of FEL 2007, Novosibirsk, Russia.
- [112]A. Fukasawa et al., "Charge and wavelength scaling of the UCLA/URLS/INFN hybrid photoinjector", Proc. of PAC 2007, New Mexico, USA.

5 LINEAR ACCELERATOR

5.1 PRE-INJECTOR

The SPARX electron bunches are generated by the 150 MeV pre-injector which consists of a 1.6 cells cavity RF Gun, followed by three accelerating structures. The system operates at the frequency of 2.856 MHz that is the same frequency of the SPARC photo-injector test facility already built and commissioned at LNF. The RF Gun is equipped with a photocathode, located in the high-field region of cavity and illuminated by 10 psec short laser beams at the repetition rate of 100 Hz.

5.1.1 RF-GUN

The peak electron beam brightness is a crucial requirement, one which in order to meet the demands of average FEL flux should also be achieved at high repetition rate. To this end, a 1.6 cell RF Gun with a 100 Hz repetition rate, working in S-band, has been studied and designed while balancing optimization of the RF parameters and the beam dynamics requirements. The RF design has been carried out using the 2D and 3D modelling codes SUPERFISH [1] and HFSS [2] respectively.

Electromagnetic field higher multipole components inside the gun have been shown [3] to contribute to beam emittance growth, resulting in beam brightness decrease and concomitant degradation of FEL performance. The dipole field component is completely eliminated by using a dual feed system of external coupling to the waveguide, while a “race track” geometry is exploited in order to strongly decrease the quadrupole mode. The minimization of the quadrupole transverse magnetic field components, which couple most strongly to the beam dynamics, has been considered as the figure of merit in the design optimization process.

This race-track geometry is naturally suited to the external coupling employed in the gun, which differs from that used, e.g., on the SPARC injector. This external coupling optimization, which must be set also considering the possibility of beam loading derived power losses, has been performed, with the proper coupling coefficient simulated in HFSS. Further, couplers represent critical area for both RF heating and related thermal stress and breakdown problems, since they are the region where surface RF magnetic fields reach their maximum value in the structure. Thus the RF dissipation, along with the narrowness of the copper in the vicinity, causes large temperature rise [3,4]. The irises themselves are areas where the surface electric field is locally intense. Thus, in order to mitigate possible breakdown, a thorough study of the iris shape choice on the electric field has been carried out. Additionally, the cell-to-cell iris thickness and radius has been chosen to achieve a high enough value of frequency difference between the two gun coupled resonant (0 and π) modes.

With this design in hand, a transient analysis of the RF gun response has also been carried out, allowing a comparison of the simulated fill-time with theoretical prediction. Similarly the RF model of the gun is employed in the code PARMELA to allow preliminary beam dynamics simulations. Finally, and

most critically for the purpose of understanding the maximum repetition rate of the gun itself, thermal and stress analysis of the cavity are carried out by using the code ePhysics [5]. We have studied several geometries, for cooling channels, including a novel channel shape that is allowed only using advanced conformal fabrication techniques. These techniques, typified by using Direct Metal Free Form Fabrication (DMF³), are seen to yield qualitatively and quantitatively superior cooling efficiency. In addition to cooling channels, we have also taken into account the need to make the structure more mechanically robust, so that thermal stresses that still result after optimization of the cooling are managed as well as possible. This analysis approach, taken in tandem with a perturbative calculation of the cavity response in the presence of thermo-mechanical deformations, allows us to predict the adequacy of this RF, thermal and mechanical design for repetition rates well in excess of the peak foreseen in the context of SPARX, 100 Hz.

5.1.1.1 RF Project

The RF Gun consists of one full cell and a half cell. The electromagnetic field inside the structure is excited by a dual RF feed power that flows into the full cell through two identical holes, 180°- opposite to each other. The 3D model is shown in Figure 5.1. This type of feed causes the dipole field component to vanish. Moreover, a “race track” geometry has been designed in order to minimize the quadrupole component of the field (results are discussed in paragraph 4). Higher order modes may be considered negligible. As shown in Figure 5.1, the coupling geometry chosen is a “z-coupling” design in order to reduce the temperature rise at the power-coupling ports (see paragraph 3). The numeric code used for the simulations is HFSS (High Frequency Structures Simulator).

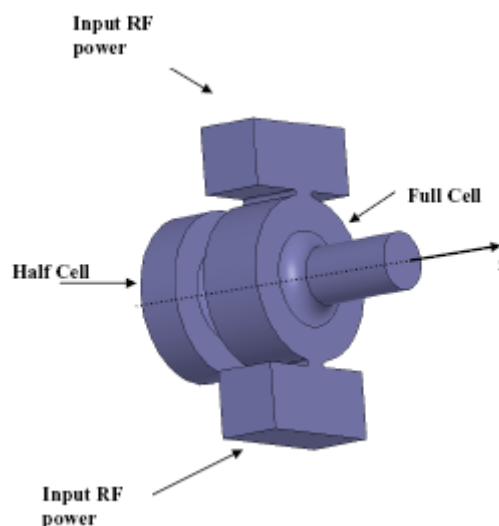


Figure 5.1: 3-D HFSS model of the Gun.

The geometric dimensions of the RF Gun are presented in Figure 5.2, with a close-up of the rounded coupling window. In Figure 5.3, the main parameters

of the RF Gun are shown together with plots of the amplitude and phase of the axial electric field of the π -mode resonant at 2.856 GHz with a quality factor (Q_0) value of about 13500. The two mode separation (0 and π -mode) is approximately 15 MHz. The value of the coupling coefficient $\beta = 1.17$ is due to "beam loading" considerations (see paragraph 2). At the cathode position, the electric field peak is nearly 120 MV/m for 10MW input RF power.

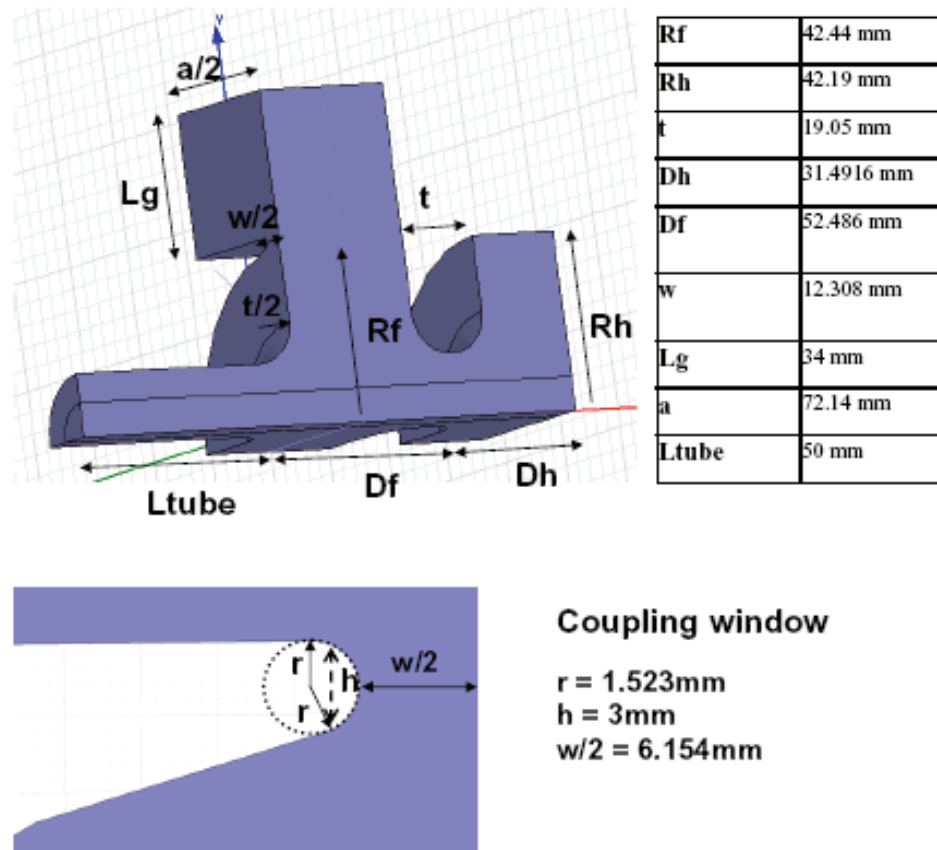


Figure 5.2: (above) a quarter of the RF Gun with all the geometric dimensions; (below) the coupling window.

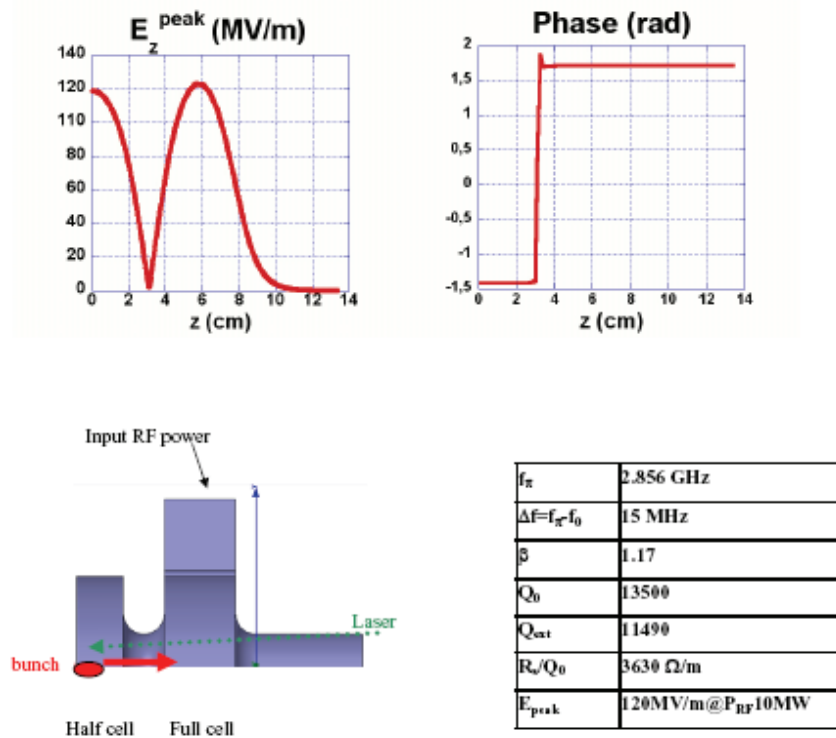


Figure 5.3: above, amplitude and phase profiles of the electric field along the accelerating axis; below, table of the Gun electromagnetic parameters of interest.

By plotting the electric field on all the surfaces of the Gun using the 2D-code SUPERFISH, as shown in figure Figure 5.4a, it is evident that the irises (with radius named “ag”) represent critical areas (in particular the one connecting the half and the full cell), where the E-field,

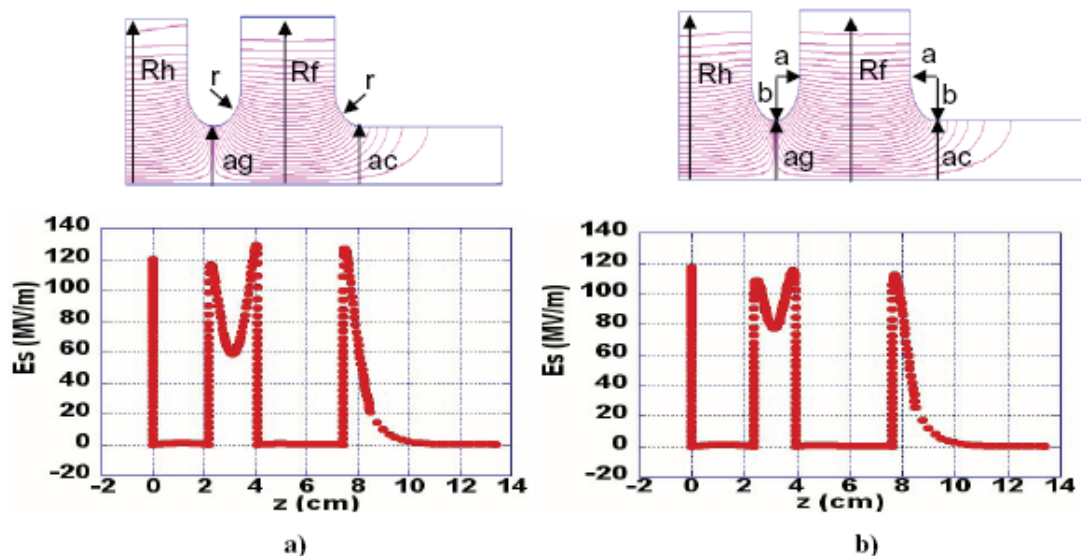


Figure 5.4: Peak surface E-field along the Gun boundaries with a) circular irises and b) elliptical irises.

with a peak of 130 MV/m, has a value bigger than that on the cathode. In S-band structures, the upper limit to consider for avoiding breakdowns is about 150 MV/m. In order to reduce the surface electric field, elliptical irises have been used instead of circular. In figure Figure 5.4b, irises have elliptical shapes

($a=0.8$ cm, $b=1.1$ cm). Peak surface E-field is nearly 10% lower than the previous case and the frequency difference between the two Gun resonant modes increases from 14 MHz to 20 MHz. Nevertheless, in this new configuration, the average electric field increases, but the most important parameter for the structure is the maximum value of the field.

Another geometric parameter that contributes to the mode separation is the radius of the cell-to-cell iris. In Figure 5.5, the same configuration as in Figure 5.4b with $a_g=1.585$ cm is shown. It can be seen that the peak E-field decreases slightly and the mode separation is nearly 26 MHz.

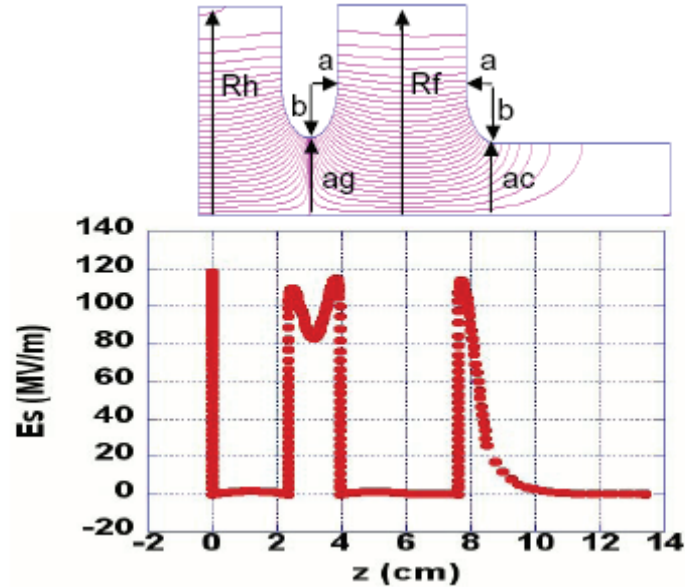


Figure 5.5: Peak surface E-field along the Gun boundaries with elliptical irises.

Since the use of elliptical irises as well as the change of the irises thickness and radius cause a variation of the resonance frequency of the structure, the half cell and full cell radii have been modified in order to keep the mode resonant at 2.856 GHz. In Table 5.1, the three cases explained above are listed, with particular stress of the peak electric field values and mode separations

$a(cm)$	$b(cm)$	$t=2a$ (cm)	$a_g(cm)$	$ac(cm)$	$Rh(cm)$	$RF(cm)$	$E_{speak}(iris)$	$\Delta f (0-\pi)$
0.9525	0.9525	1.905	1.485	1.485	4.219	4.2665	130 MV/m	14 MHz
0.8	1.1	1.6	1.485	1.485	4.2135	4.253	120 MV/m	20 MHz
0.8	1.1	1.6	1.585	1.485	4.239	4.269	117 MV/m	26 MHz

Table 5.1: Peak surface electric field on the iris between the two cells, for different geometric parameters, and the correspondent frequency separation between the two Gun resonant modes.

5.1.1.2 Coupling and Beam Loading

The two waveguide-to-coupler-cell iris dimensions are chosen in order to achieve the value of the coupling coefficient β set by potential beam loading considerations, in which one may allow operation at an average extracted beam power, near RF flat-top, of 1.4 MW (average current of 286 mA, or 1 nC every 10 RF periods). By comparing the power lost to beam acceleration and that dissipated in the cavity wall, an estimate of the external coupling coefficient is [6] $\beta = 1.17$. The parameters of the 2.856 GHz high power RF system feeding the gun and the relevant beam parameters are listed in Table 5.2.

Table 5.2: Klystron and electron beam parameters.

τ_{RF} (pulse length)	3 μ s
f_{RF} (repetition rate)	100 Hz
T_{RF} (pulse period)	10 ms
DC_{RF} (τ_{RF}/T_{RF}) (RF duty factor)	$3 \cdot 10^{-4}$
P_g (Peak power)	10 MW
f_b (beam frequency)	286 MHz
Q_b (beam charge)	1 nC
I_b (beam current)	286 mA

5.1.1.3 RF Pulsed Heating

It is critical to minimize the RF heating of the metal surfaces in the gun in order to allow 100 Hz or higher operation. The limiting sector of the structure is apparently found at the edges of the power-coupling ports. In order to keep the temperature rise below 60°, rounded coupling iris shapes have been used. Moreover, the use of a Z-coupling geometry simplifies fabrication and reduces pulsed heating since edges are only along one dimension (see Figure 5.1 and Figure 5.2), and the narrow copper regions found in Θ -coupling are avoided. The rounding radius of the Z-coupling iris is 1.5mm. In order to quantify the temperature rise, a useful formula [3,4] is employed:

$$\Delta T = \frac{|H_{||}|^2 \sqrt{\tau_{RF}}}{\sigma \delta \sqrt{\pi \rho' c_g k}} \quad (5-1)$$

where τ is the pulse length, σ is the electrical conductivity, δ is the skin depth, ρ' is the density, c_g is the specific heat and k is the thermal conductivity of the metal. In present case, the value of $H_{||}$ is obtained by plotting the H field, provided by simulations, on all the surfaces of the RF Gun: the critical areas are the coupling windows, where the magnetic field reaches a peak equal to $H_{max} = 3.9 \cdot 10^5$ A/m for an input RF power of 10 MW. This field value causes a temperature gradient of about 56°, close to the threshold of 60°, that is

considered the upper limit. Problems arise if the power is much higher than 10 MW.

5.1.1.4 Magnetic Quadrupole Component

The asymmetry of the gun geometry results in a modification of the field distribution inside. In particular, the field component the most sensitive to this asymmetry is the azimuthal one of the magnetic field $H(r, \phi)$. Therefore a thorough study has been performed in order to quantify how much the H-field deviates from the monopole behaviour. The resulting deviation is minimized by using a “race track” geometry.

Only the quadrupole component of the magnetic field has been studied, considering higher order components negligible, and a quarter of the whole structure has been simulated, since HFSS allows to exploit the symmetric distribution of the field inside the Gun. In Figure 5.6, a cross section of the full cell is shown and the field is calculated along circumferences (from 0° to 90°) with different radii R and for different values of the offset D , by which the two cell arcs are drifted apart.

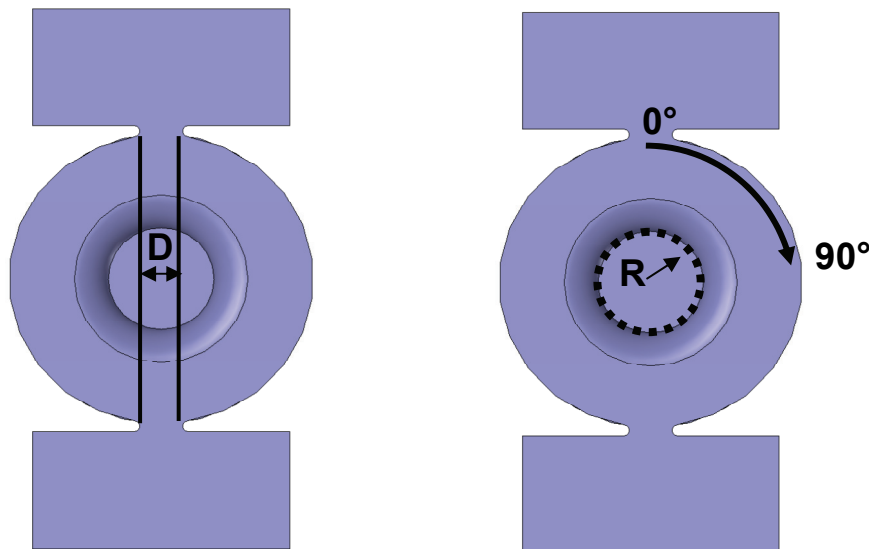


Figure 5.6: Cross-section of the full cell: D is the offset and R is the radius of axis concentric circumferences.

The field $H(r, \phi)$ is a 2π -periodic function of ϕ . It is also real and even, and thus it can be expanded as a Fourier series of cosine functions:

$$H(r, \phi) = \sum_{m=0}^{\infty} H_n(r) \cos(n\phi) \quad (5-2)$$

where the terms H_n , representing the magnetic field components, are equal to

$$H_n(r) = \frac{2}{\pi} \int_0^{\pi} H(r, \phi) \cos(n\phi) d\phi \quad (5-3)$$

For differing values of n , we obtain all of the components of the magnetic field: H_0 is the monopole, H_1 the dipole, and H_2 the quadrupole component, respectively. As noted above, since $H(r, \phi)$ is an even function also in the interval $0 < \phi < \pi$, one directly obtains $H_1=0$, (dipole component of the field) that is eliminated because of the dual feed symmetry. If the mesh density in the region very near the axis of the gun is small, then it is very difficult to obtain an accurate $H(r, \phi)$ profile. In order to overcome this problem, three values of r (10,13,17 mm) have been chosen and a fit has been made to obtain H_2 near the axis ($r=0$ mm). The quadrupole component of the magnetic field, by linear interpolation, is shown in Figure 5.7 for different values of D (0,1,2,3mm). It is clear that the optimum for the value of the offset D is approximately 2 mm, where tends towards vanishing.

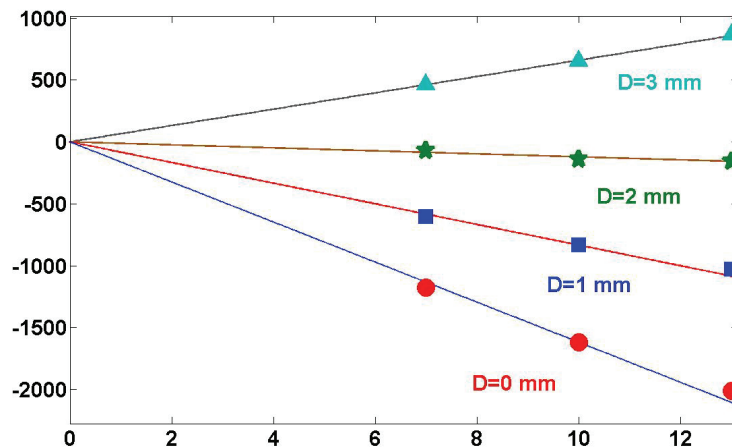


Figure 5.7: Magnetic quadrupole component for four values of the offset D (0,1,2,3mm).

5.1.1.5 Transient Analysis

A transient analysis has been performed on the gun response to the RF pulse generated from the klystron. For this study, we have chosen a total pulse length is $4 \mu\text{s}$, with (linear) rise and fall times both equal to $0.3 \mu\text{s}$. In Figure 5.8, the envelope of the RF voltage pulse (in red) and the envelope of the cavity response (in blue) are plotted. The fill time agrees well with its theoretical value, and is nearly $\tau = 700 \text{ ns}$.

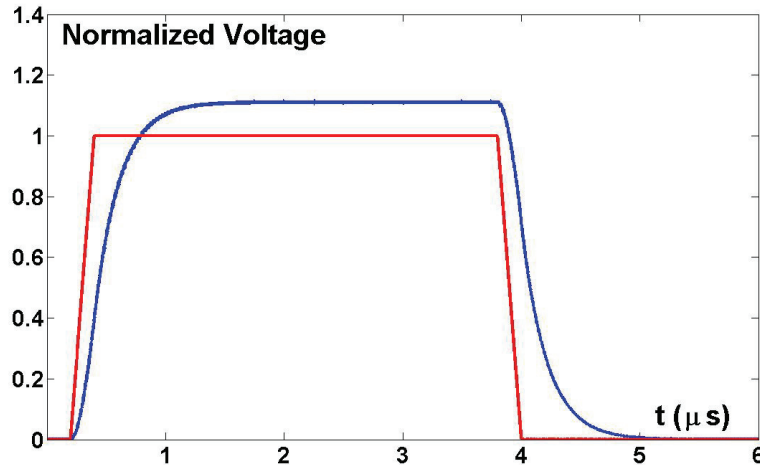


Figure 5.8: envelope of the pulse (in red) and envelope of the cavity response (in blue)

5.1.1.6 Preliminary results

Preliminary beam dynamics simulations using the code PARMELA have been performed. The 2D electromagnetic field distribution given as input to PARMELA is exported from SUPERFISH. The RF gun is examined without a solenoid around it to provide beam size control and emittance compensation. Considering the beam parameters listed in Table 5.2 (beam charge $Q=1$ nC, average beam current $\langle I \rangle=0.286$ A) and a flat-top bunch, the average energy gain of the electrons at the end of the RF gun is about 5.5 MeV with an energy spread equal to 0.25%.

Figure 5.9: Average beam energy gain along the axis (red) and its derivative with respect to the position z (blue).

In Figure 5.9, we plot of the evolution of the electron beam energy gain (in red) along the z axis, from the cathode position to the exit of the gun. In the same plot, the blue line represents the energy gain derivative with respect to the position: it is evident that it is proportional to the axial electric field, as expected. Simulations of the precise behavior of the beam's emittance evolution, including both solenoid focusing, and post-acceleration in a travelling wave LINAC, are now underway. As this design does not deviate in RF acceleration and focusing (and anticipated solenoid design) from previous UCLA and LCLS designs, we do not anticipate that any degradation of the performance of the so-called Ferrario working point, in which <1 mm-mrad transverse emittance may be obtained.

5.1.1.7 Thermal Analysis

The thermal analysis of the 100 Hz RF Gun has been carried out by using ePhysics2. A quarter-section of the structure, with standard cooling channels, is shown in Figure 5.10, above. Note that mechanisms for frequency tuning of each cell are also displayed. To provide cooling, there are six axisymmetric channels and four around the coupling iris region. The circular cross-section diameter is 6 mm in this fairly standard geometry (which might have a rectangular cross-section to be machinable). In order to keep the peak temperature below a certain value, the location of the channels must be optimized. This optimization is achieved by simulating the surface power loss (proportional to H^2) effects. The average power inside the gun is 3 kW, considering the power source parameters in Table 5.2 for a 100 Hz repetition rate.

The calculation of the (RF dissipated) heat flux inside and outside the RF gun is performed by assuming two different thermal boundary conditions, corresponding to the two different heat transport mechanisms operating on the copper structure:

1. Free (natural) convection on the copper outer walls, with a room temperature of 24 °C;
2. Forced convection on the channels walls, considering an input water temperature of 24 °C flowing with a velocity of 4 m/sec.

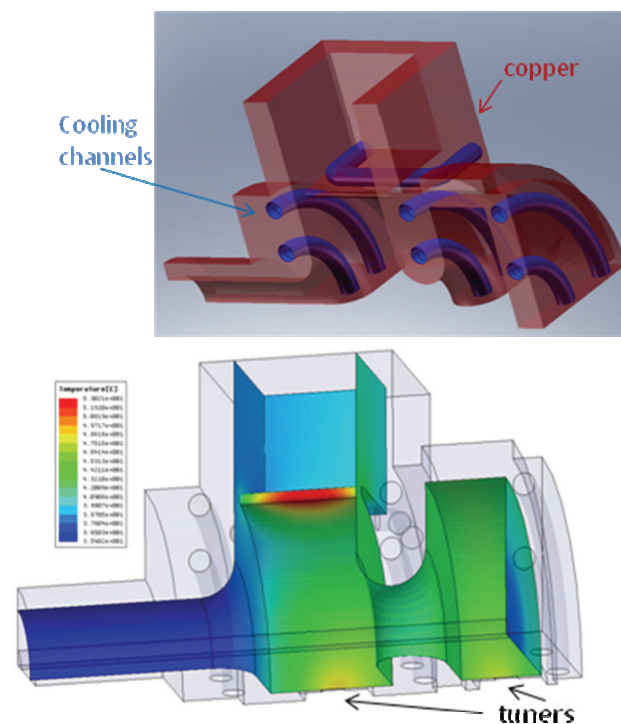


Figure 5.10: Above, section view of the RF gun with cooling channels; below, temperature profile on the inner walls of the RF gun.

The temperature profile on the inner cavity walls for a dissipated average power of about 3 kW is plotted in Figure 5.10, below. The hottest spot of about 53 °C is at the coupling window, as expected due to the high surface magnetic field.

In order to illustrate what improvements can be obtained by using the novel DMF process, we show channel cross-sections that are star-shaped in Figure 5.11. This type of channels, which may not be fabricated using standard machining, acts to increase the heat transfer between water and copper, by both increasing the transfer surface, and by potentially provoking higher turbulence in the water flow. In choosing the flow rate in the simulations, we have balanced this enhanced thermal efficiency with the prospect of mechanical degradation of the channels due to the enhanced turbulence. The star-shaped cross section allows to the cavity wall temperatures to be kept significantly lower than case with cylindrical channels, by 15 °C (see Figure 5.12).

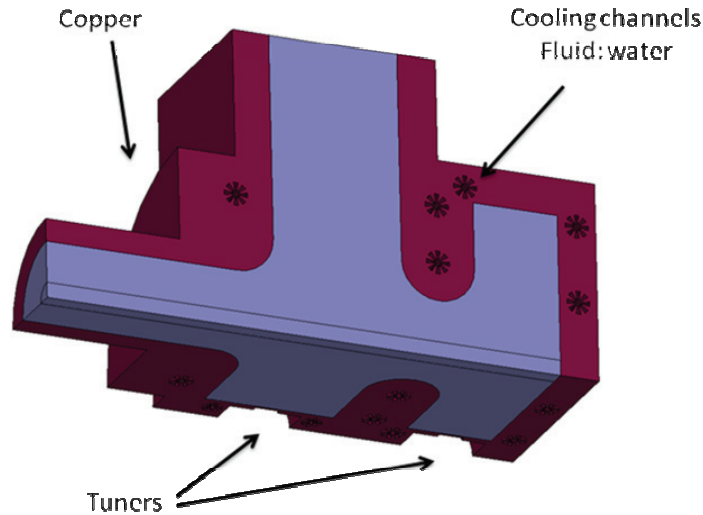


Figure 5.11: RF Gun with star-shaped cooling channels.

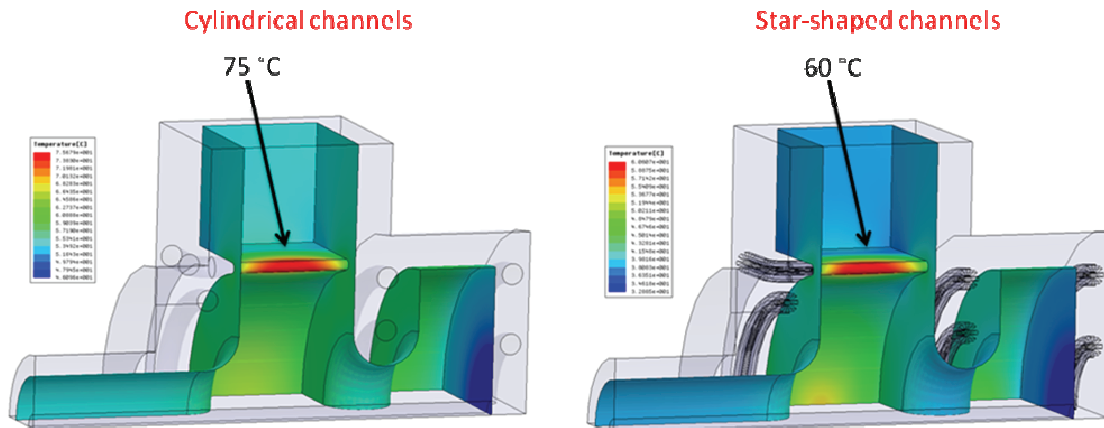


Figure 5.12: Temperature distribution on the cavity inner walls.

It is possible to consider, with such novel fabrication approaches, great improvements in the overall repetition rate. We further optimize the cooling by using a snake-like channel near the coupling irises, as shown in Figure 5.13. In this case, the peak temperature is diminished to 50 °C. Thus, considering the same overall temperature increase, this result immediately yields the possibility of a 170 Hz repetition rate. If we further consider a lower peak accelerating field (than 120 MV/m) operation, we deduce that, using our somewhat conservative design criteria, one may achieve ~245 Hz operation. With further

refinements in the cooling channel design, as well as the mechanical robustness of the structure as a whole, one may anticipate significant further improvements, as discussed below.

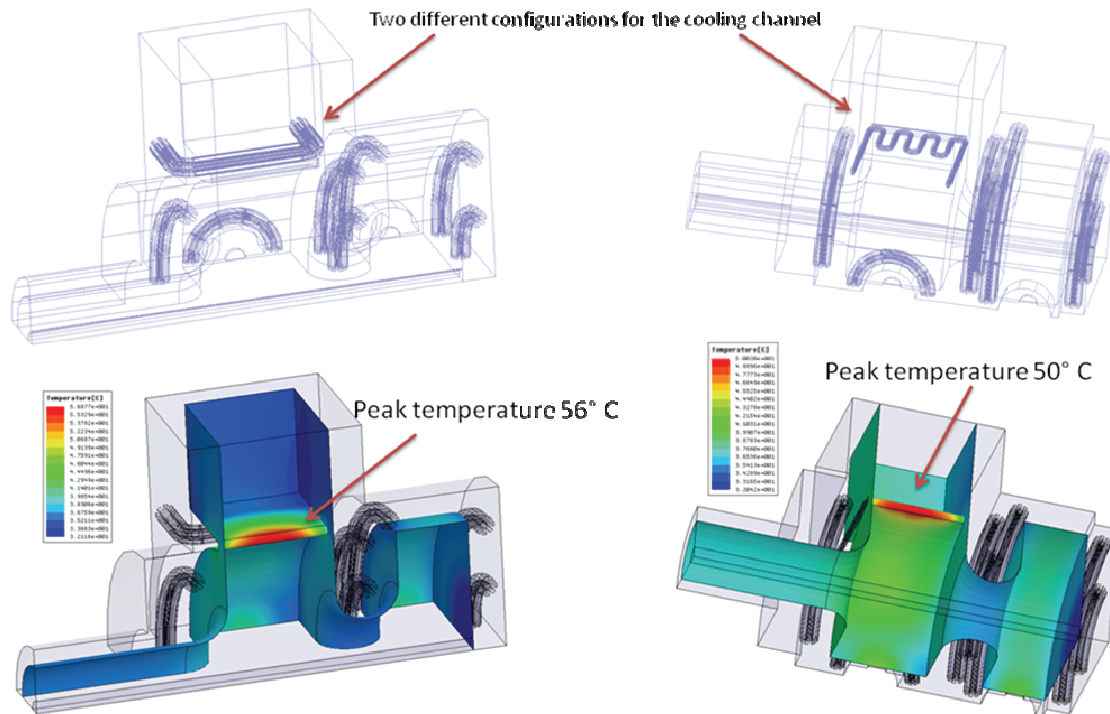


Figure 5.13: Above, sketch of the cooling channels inside the RF gun walls; below, the temperature distribution on the cavity inner cavity walls.

5.1.1.8 Stress Analysis

The stress analysis for the structure, considering the case more standard cylindrical channels as well as that with the star-shaped channels has been also performed by using ePhysics2. Due to the temperature increase of the copper and the presence of the cooling channels, the entire structure undergoes a mechanical deformation, which results in detuning of the RF resonance. In the first case, for an average input power of 3 kW and considering the cathode plate and the waveguide sides fixed, and zero deflection where external clamps are present, a peak displacement of about 32 μm is located at the coupling window and on the sides of the full cell. The deformed structure is shown in Figure 5.14.

By using the Slater perturbation theory, which relates the lost or gained volume and the relative electric and magnetic energy densities to the overall frequency shift of the mode in question, we deduce a detuning in the standard case nearly +350 kHz. This is relatively small, corresponding to a change in nominal operating cooling water temperature of approximately 8° C, which is only ~60% of the maximum allotted LCLS gun temperature change from the no-RF to full power operation condition. Thus, using the LCLS design philosophy as a guideline, one may also consider augmenting the average power by approximately 1.62. This implies that the repetition rate envelope that we may infer rises to ~400 Hz. We note that the total frequency shift condition obtained from this analysis is also sufficient to guarantee

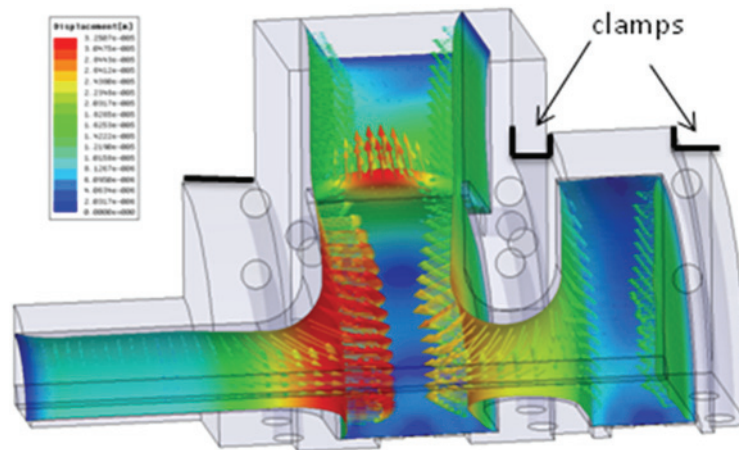


Figure 5.14: Displacement amplitude with vector representation, standard case.

that, particularly given the forgiving nature of the high cell-to-cell coupling, the full-to-0.6 cell field balance is not notably changed by thermo-mechanical structure distortions.

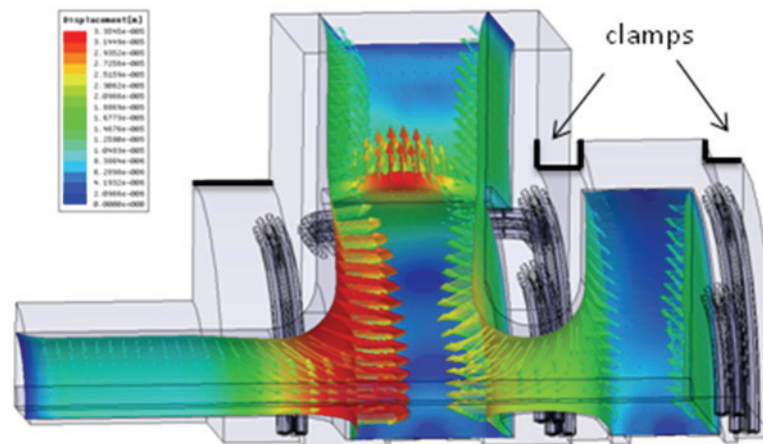


Figure 5.15: Displacement amplitude, with vector representation, star-shaped channel.

In the second case, for an average input power of 5 kW and also considering the cathode plate and the waveguide sides fixed and zero deflection where clamps are present, the peak displacement is similar (see **Figure 5.15**). Thus, concerning mechanical deformation, star-shaped channels allow to use higher RF drive power. We are continuing the study of this structure, as well as the cooling channel with the snake-like shape, to further optimize its performance.

5.1.1.9 Outlook

The design of the RF gun for SPARX has many intersecting elements: RF field optimization and symmetrization, beam dynamics, RF heating (pulsed and average), and thermo-mechanical distortion, and RF performance in the presence of distortions. This study we have reported here presents a first pass at addressing all of these design constraints together, with extremely promising results. In the future one may further refine the overall RF design by choosing an even larger radius of curvature for the waveguide coupling iris port structure, to mitigate RF heating. This would also serve to ease the cooling and the mechanical distortion problems in the neighborhood of the iris.

One may also mitigate the overall power dissipated in the RF gun by using a larger coupling β , and by using a larger RF drive power. The gun may be filled much more quickly in this way, as discussed by Schmerge [7], resulting in a prospective drop of a factor of 3 in duty cycle, and therefore average RF power. By changing the RF phase and driving the gun out of phase, one might also empty the gun more quickly, diminishing the average power even further. Without considering the details of this final point, we can thus point to a path to operating the RF gun at over 1 kHz.

While this is not strictly needed for the present generation of RF guns for FELs such as SPARX, it would provide a critical component of an optimized inverse Compton scattering source, which naturally may be operated at ~ 1 kHz, due to the increasing availability of appropriate laser technology.

We can see that the DMF³ approach can provide wide flexibility in cooling channel design and fabrication, which has already allowed us to consider 1 kHz RF gun operation. With such innovations as star-shaped cross-sections, and arbitrary channel paths, one can design the cooling system even more aggressively. In this regard, we note that the density of water channels in our preliminary design here is smaller than in many previous attempts at high average power RF gun designs. Thus the tool of conformal, shaped cooling channels has yet to be fully exploited. This task remains for the next step in planned work.

5.1.2 Photocathodes

The requirement of short response time of the cathode with respect to the laser beam for the generation of the photoelectrons limits in the case of SPARX photoinjector the choice of the cathode materials to metals that usually present response time of the order of few tens of fs [8].

This choice is also justified because metals usually do not require operating vacuum levels lower than 10^{-9} mbar and can withstand high electric fields gradient at the cathode surface [8].

Moreover, the uniformity of emission characteristics of these materials has been proven to be adequate to the requirements of the SPARX injector [9, 10].

Based on the results since now obtained worldwide in different laboratories, the most promising candidates metals that can be used as sources for electron beam in SPARX are copper, magnesium and yttrium.

One of the parameters that is critical for the final choice and operation of the photocathode is represented by the Quantum Efficiency (QE) at the drive laser wavelength. The QE of these metals has been measured under similar

condition under UV laser irradiation at 266 nm and resulting in values of about 2.5×10^{-5} , 1×10^{-3} and 3×10^{-4} respectively for Cu, Mg and Y [11, 12, 13].

5.1.2.1 Candidate materials for photocathodes

5.1.2.1.1 Copper

Copper is the metal that mostly has been used for long time as source for photoelectron in RF-gun. The choice of using this metal is principally based on the fact that a photocathode based on this metal is in principle easy to be prepared. Cu is used to build the backflange of the RF-gun half-cell cavity as in the case of SPARC photoinjector [14]. Moreover, the chemical reactivity of the Cu with residual gases is quite low and thus the stability of emission properties of Cu photocathode should be preserved at the operational vacuum level of SPARX RF-gun (10^{-9} mbar). Such type of cathode was successfully operated during the commissioning of SPARC photoinjector. At the high electric field gradient of 120 MV/m the *Schottky effect* and the *in situ* laser cleaning treatment of the Cu cathode surface allowed to obtain QE value of about 10^{-4} with uniformity of emission of about 20% with irradiation at 266 nm [10].

5.1.2.1.2 Magnesium

The main advantage of photocathodes based on magnesium with respect to those based on copper lies with the higher QE that they offer. In particular recent results showed that QE as higher than 10^{-3} can be obtained in low DC electric field with photons at 266 nm [2].

In order to develop a reliable photocathode based on Mg an intense R&D program has been carried out within the framework of SPARC and EUROFEL projects. The main aspects that have been investigated covered a wide range of activities: the realization of the photocathode material, the improvements on the *in situ* surface laser cleaning technique to remove oxidised or polluted layers, the test of the cathode in high gradient RF-fields [10, 15].

While some experiments were carried out using sputtered Mg film [16] or friction welded bulk disk [17] onto the Cu back-flange of the RF-gun a new approach based on the deposition of pure Mg film by laser ablation technique showed promising results [10]. Moreover preliminary test of photocathode based on Mg films grown by pulsed laser ablation have been successfully performed in a real RF-gun at PEGASUS laboratories [15]. With respect to Cu, Mg showed stronger reactivity with respect to the chemical species contained in residual gases even at UHV conditions. The surface reactivity of Magnesium may lead to short term instability of the QE because the chemisorption of chemical species on the metallic surface may originate variations on the work function and thus on the QE of the photocathode [18].

5.1.2.1.3 Yttrium

While copper and magnesium have been extensively studied a few research activities were devoted to study the photoemission properties of yttrium and to explore the feasibility of a photocathode based on this metal. Few data have been since now reported in literature. The QE at 266 nm was measured to be about 3×10^{-4} and the work function value is about 3 eV [13, 16]. While the QE is remarkably higher than that of Cu at the same wavelength, the low value of its work function makes this material very interesting because the extraction of photoelectron may be achieved even with photons at 400 nm. This wavelength correspond in fact to the 2nd harmonic of a Ti:Sa laser. The opportunity to use the 2nd harmonic instead of the 3rd presents obvious advantages in terms of the final energy deliverable to the cathode even after spatio-temporal manipulation. Unfortunately at the present the knowledge on the emission properties of Yttrium is limited and only in a future, with a dedicated R&D activities, is reasonable to imagine the use of this material as photocathode in the SPARX RF-gun.

5.1.2.2 Laser energy requirements in operational conditions

Assuming the values of the cathode and laser parameters reported in Table 5.3 it is possible to evaluate the laser energy necessary for the generation of 1nC electron bunches with a launch phase of about 30 degree [17]. The simulated charges extracted vs. the relative phase between laser pulse and RF electric field are reported in Figure 5.16 for Cu, Mg and Y respectively.

Table 5.3: Parameters used to perform phase scan simulation.

<i>Metal</i>	Copper	Magnesium	Yttrium
Work function [eV]	4.5	3.6	3.1
β	2	2	2
QE	2.5×10^{-5}	1×10^{-3}	3×10^{-4}
Laser wavelength [nm]	266	266	266
Laser spot radius [mm]	1	1	1
Laser pulse FWHM [ps]	10	10	10
Laser pulse energy [μ J]	140	0.5	0.9
Electric field [MV/m]	120	120	120

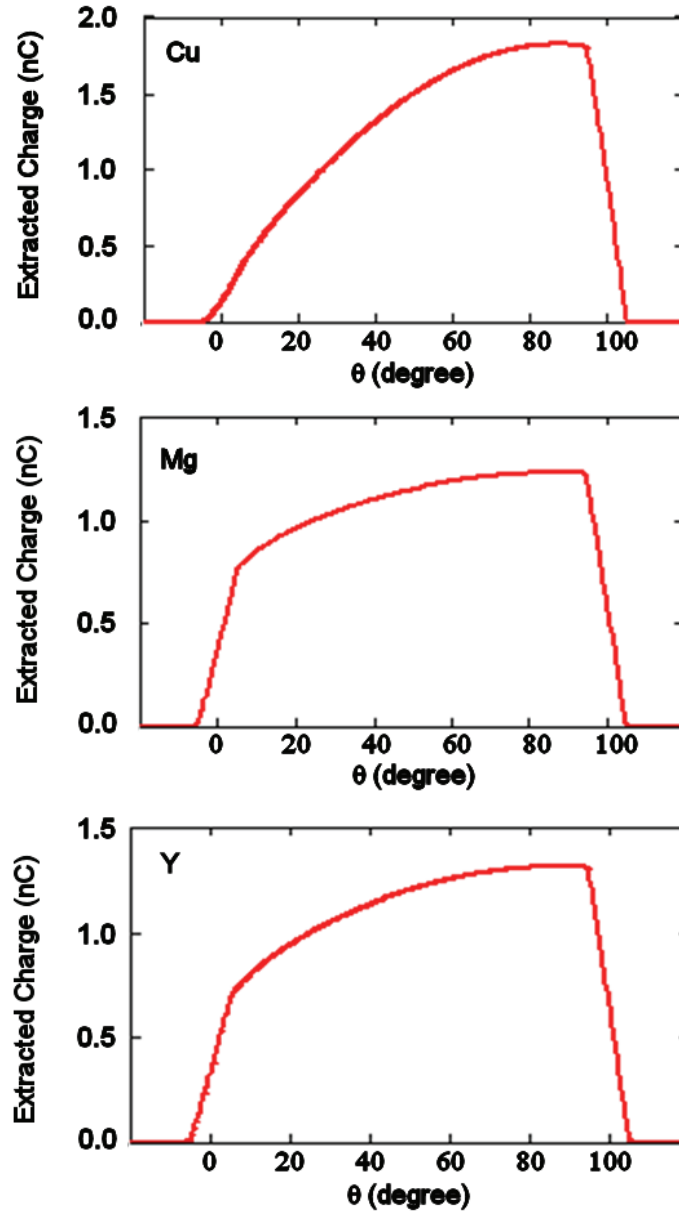


Figure 5.16: Phase scan simulation for Cu, Mg and Y cathodes.

5.1.2.3 Influence of cathode material on dark current

Due to high electric field gradient that is achievable in normal conducting RF-guns similar to that one that is foreseen to be used in SPARX photoinjector, an accurate evaluation of the dark current expected with respect to different cathode materials has been performed. A mathematical model that takes in account the Density of States of different metals allowed the evaluation of the tunneling of electrons through the potential barrier and consequently the evaluation of the field emitted charge expected from the cathode (Figure 5.17).

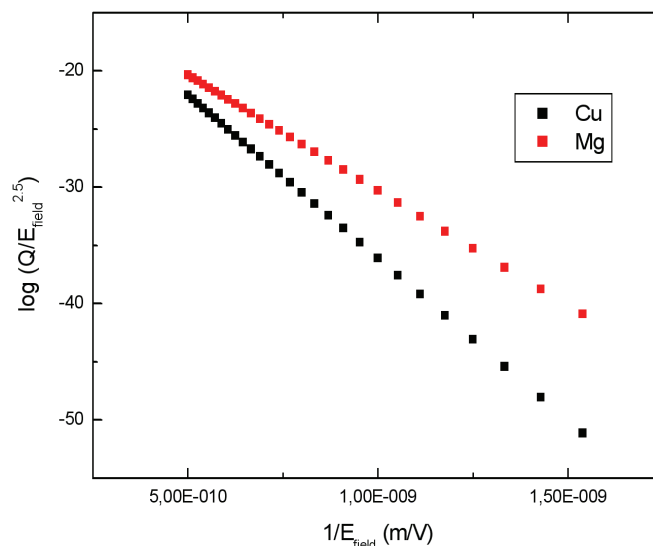


Figure 5.17: Fowler-Nordheim plot of the dark charge expected in SPARX from the central part of the cathode encircled by a circle having a radius of 5 mm for Cu and Mg cathode.

Making use of the field enhancement factor deduced from Fowler-Nordheim plot obtained from SPARC experimental data reported in Figure 5.18, the evaluation of the ratio of the dark charge expected to be emitted from Mg with respect to the one expected to come from Cu cathode has been performed and is reported in Figure 5.19.

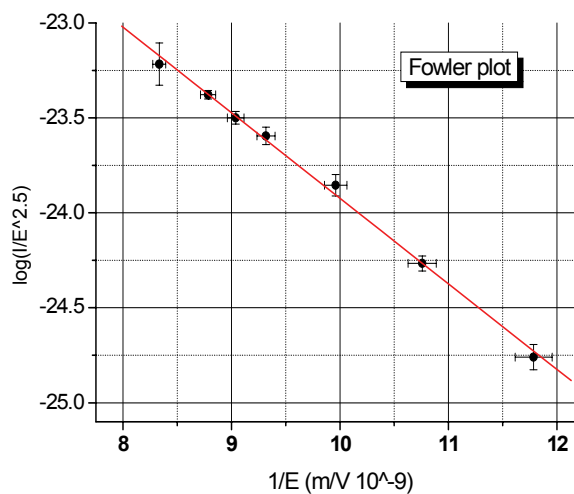


Figure 5.18: Fowler-Nordheim plot of the dark current measured with SPARC RF-gun. The field enhancement factor has been evaluated to be in range between 60 and 80.

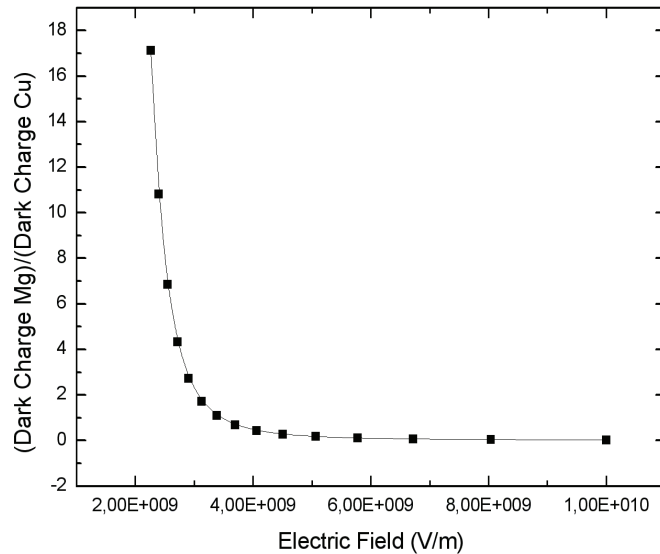


Figure 5.19: Ratio of the dark charge expected from Mg and Cu cathode as a function of the electric field.

From the data reported in Figure 5.19, it is evident that the use of an Mg cathode should not be detrimental from the point of view of the dark current levels. Assuming field enhancement factors similar to those obtained with SPARC RF-gun (between 60 and 80) the local field should range between 5 and 10 GV/m. In this region the field emitted charge of Mg cathode evaluated by our model should be less than that emitted by Cu cathode. Nevertheless such evaluation should be confirmed by dedicated measures with real cathodes in high electric field because the strong influence of the field enhancement factor that is originated from the geometrical microstructure of the cathode surface.

5.1.3 Laser system

Here we report the technical design of the laser system proposed for the SPARX photo-injector with all the ancillary elements used to manipulate, characterize and control the output performances. A dedicated R&D have been devoted for the design of the photoinjector drive laser system. In fact the lasers for high brightness electron applications must exhibit special performances: the low photoemission efficiency for robust photocathodes requires high UV pulse energy; the emittance compensation process and therefore the maximization of the beam brightness is achieved with uniform temporal and spatial energy distribution. Very low amplitude and time jitters from pulse to pulse and pointing stability are challenging demands for repeatable SASE-Fel performances.

Moreover, the emitted pulses have to be synchronized with the SPARX master oscillator to extract electrons at the exact phase of the RF wave. Other laser systems will be used at the SPARX FEL machine for the seeded FEL, for electron and photon diagnostic and finally for a variety of possible pump and probe experiments. All these lasers are required to be synchronous within very tight tolerance. The timing and the synchronization of the lasers will be discussed in another chapter.

5.1.3.1 Definition of the SPARX laser performances

The SPARX LINAC is required to produce a single 1nC electron bunch, high current and a normalized emittance of < 2 mm-mrad. Other working points associated at lower bunch charge are also foreseen. For reduced charge, the laser pulse length and the transverse dimension has to scaled as $Q^{1/3}$ to keep invariant the space charge forces. To reduce the charge it is possible to use a variable attenuator in proximity of the gun table. The pulse length could be continuously varied using a UV stretching system and the transverse dimension can adjusted using a three lenses telescope.

The performances of X-Ray SASE-FEL are critically dependent on the beam peak brightness delivered at the undulator entrance. So the laser pulses have to be tailored to minimize the beam emittance and, at the same time, have enough power to produce relative high current bunches.

The laser system for SPARX is required to deliver excess of 150 μ J energy per pulse at a wavelength of 266 nm to the photocathode at a repetition rate up to 100 Hz. This energy requirement comes out from the typical quantum efficiency of copper photocathode.

As said before, the emittance compensation scheme requires that the laser pulse must show uniform transverse and longitudinal profile in order to compensate the non-linear space charge field with an proper magnetic focusing. The temporal and spatial flat top laser energy distribution on cathode has been demonstrated to reduce the emittance [19,20]. We foresee to change the pulse length on a range between 2 to 10 ps to explore different machine working points.

In order to define in details the operational performances required to the laser system a parametric beam dynamic study has been carried out [21] within the definition of the beam dynamic for the SPARC photoinjector. The first 150 MeV of the SPARX accelerator are directly derived from the SPARC design and most of the considerations for the beam dynamic and laser specification can be extrapolated here. The effect of amplitude variation determines a proportional variation of the emitted charge and can change the optimal beam matching. The time jitter can influence the emittance compensation and the time of fly for the electron beam. Elliptical or asymmetric laser spot distribution are deleterious since not cylindrical space charge forces cannot be perfectly compensated. Finally the effect of the temporal non uniformity and pulse's steepness has been also simulated [21]. In the following table are summarized the laser specifications at the cathode derived by beam dynamic simulation and practical consideration.

Table 5.4: Laser requirements on cathode.

PHOTOCATHODE LASER SPECIFICATIONS	
Central wavelength	260-267 [nm]
Bandwidth in the UV	1.5-2 [nm]
Pulse length FWHM	2-12 [ps]
Pulse energy	150 [μ J]
Repetition rate	>100 [Hz]
RMS energy jitter	< 1.5% [rms]
Laser pulse rise time (10-90%)	< 1 [ps]
Laser pulse longitudinal ripples	<20% ptp
Transverse intensity profile	Top hat
Time jitter respect to a ref oscillator	< 0.3 [ps] rms
Spot dimension sigma rms	0.2-0.5 mm
Centroid pointing stability	<50 μ m
Spot ellipticity (1-x/y)	<5% rms

The temporal pulse shaping and the energy required can be obtained only from large bandwidth (or short pulses) and high damage threshold laser. Commercial Ti:Sa lasers associated with custom system are the natural candidate for fulfill most SPARX specifications. The wavelength is obtained through third harmonic generation (THG) in a non-linear medium. To have low jitter and good stability, the use of diode pumped solid state lasers (DPSSL) is recommended to excite the Ti:Sa stages as well as to ensure a controlled laser environment. Variable pulse length and transverse top hat profile can be achieved with dedicated optical system downstream the laser. Energy level requested demands for amplified laser system, and high efficiency in THG and successive manipulation. Finally a transport over more than 10 meters must preserve the laser pulse characteristic to the cathode.

5.1.3.2 Laser system description

5.1.3.2.1 Oscillator and synchronization unit

The laser system we propose for SPARX photoinjector is a commercial frequency tripled Ti:Sa laser. The active medium, Ti:Sa crystal, is able to produce a bandwidth large enough to perform the time pulse shaping, and can produce the high energy required in SPARX application without optical damage and significant non-linear effect. The Ti:Sa ($\text{Ti:Al}_2\text{O}_3$) crystal has the optical absorption peak between 490 and 540 nm. The relative short fluorescence lifetime (< 3 μ s) requires the medium is pumped by another laser system

operating in Q-switch mode, increasing the complexity of the laser layout. The emitted wavelength can be tuned on a large fluorescence band but the most efficient wavelengths are between 780 and 800 nm.

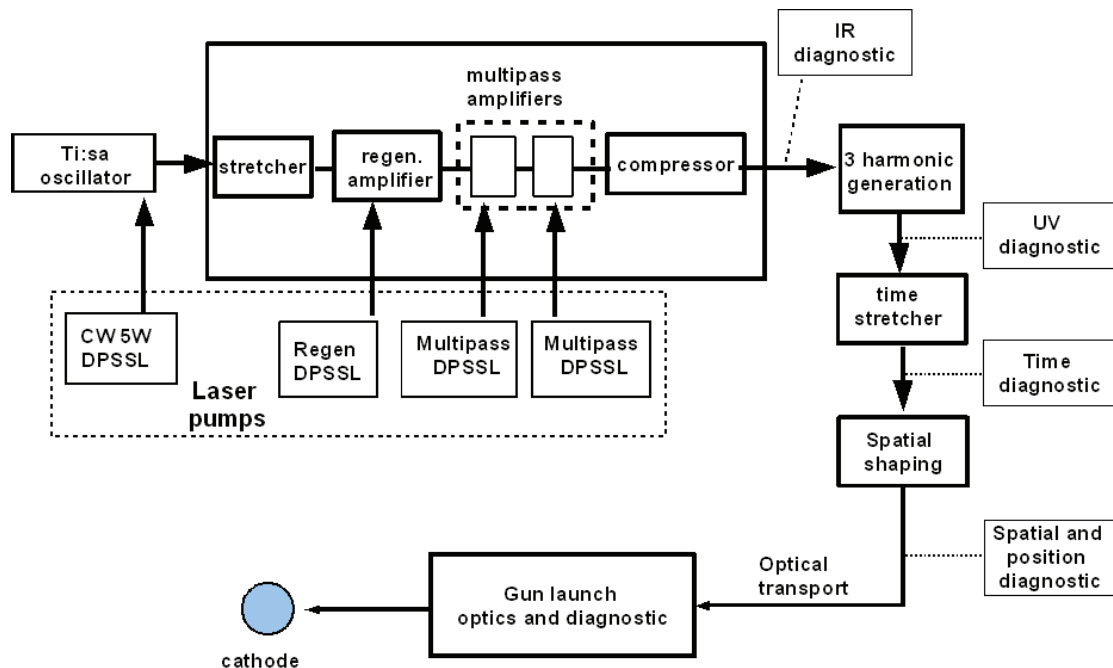


Figure 5.20: Laser conceptual layout

The proposed layout for SPARX (Figure 5.20) laser consists of an intracavity frequency-doubled CW 5 W diode pumped Nd:YVO₄ to stimulate the Ti:Sa oscillator. Inside oscillator, mode-locking regime is generated by a passive Kerr lens nonlinear process inside the Ti:Sa crystal, in a solid state ultra-stable fashion [22, 23]. A GVD (Group Velocity Dispersion) compensation scheme inside the cavity balances the time enlargement of pulses due to positive dispersion inside optical elements and air. The oscillator output provides a train of very short pulses (130 fs) at 89,25 MHz repetition rate (1/32 of RF accelerating field) with an energy of 10 nJ and central wavelength 800 nm; transverse pattern is a TEM₀₀ mode. Repetition rate of laser pulses in modelocking regime is only dependent on the length of the cavity through the relation $f=c/2L$, (L is equal to 1.68 m).

A run-time synchronization between laser and RF master clock is made by controlling the optical cavity length: if the oscillator pulse train is in fact synchronized, the successive amplification stage and frequency conversion can introduce an overall delay, but will not affect repetition rate and in the ideal case will not produce a time jitter. Control of cavity length can be made through different resolution actuator used to move an end cavity mirror. The active feedback is driven by the phase error of the oscillator pulse respect to the SPARX master oscillator, for more details see the time and synchronization chapter.

5.1.3.2.2 Chirped pulse amplification

The amplification stage is made in a Chirped Pulse Amplification (CPA) topology, as conventional Ti:SA amplification of such short pulses would provide too high power, capable of damaging optical components or produce strong distortion on the output properties [24, 25].

In CPA, the pulse is stretched through a positive dispersion line to decrease its peak power; after that, the pulse can be safely amplified, and then it is compressed again to the original length through a negative dispersion line. Both pulse stretcher and compressor are in general implemented using all-reflective gratings and optics to avoid further dispersion introduced by refractive elements [25].

The amplification Ti:SA active medium is pumped by the second harmonic of a Nd:YAG or a Nd:YLF laser at 532 nm with pulse duration ranging from 10 to 100 ns. The diode pumped solid state laser (DPSSL) are preferable diode pumped for not high power system. The diode pump laser assures the required amplitude jitter stability (<1%), the transverse mode purity and the repetition rate required for the SPARX photoinjector. The diode pump system can be implemented by CW diode pump Q-switch system or pulse diode. The first solution assure less energy jitter (<1% rms) and better thermal stability, instead the second due to higher energy output can be used to reduce the number of stages. The present limitation to the maximum energy per pulse can be produced using such a system has been demonstrated to be 20 mJ using 7 W regenerative pump plus 2 DPSSL of 45 W for the successive multipass [26]. The DPSSL can potentially guarantee also the SPARX repetition rate upgrade to 1 kHz.

After the pulse is stretched up to hundred of picoseconds it goes inside a regenerative pre-amplifier (RGA). Here only some pulses are selected inside the 89.25 MHz train from the laser oscillator to be amplified and obtaining repetition frequency up to 100 Hz. Despite the fonal frequency the repetition rate for the pumps is fixed and usually is 1 kHz for the regen DPSSL.

Pockels cells provide the picking of the right pulse to be amplified to get to final repetition rate, and extraction of the pulses after a proper number of round trips for the needed amplification. Out of the RGA pulses energy up to 2.5mJ can be achieved. The energy can be increased with one or two multipass successive stages. One multipass would deliver a maximum energy of 10 mJ and a second multipass between 15 mJ and 20 mJ for DPSSL. After the amplifier the pulses are compressed again to transform limited duration through the grating-based compressor stage.

The result is a very high power so that it is necessary to operate up-conversion as soon as possible, to avoid undesirable nonlinear effects in the pulse free propagation. For SPARX purpose the energy specified at the amplifier exit is 20 mJ.

When the seed pulse enters the amplifiers, Pockels cells and different pumps must be synchronized for the right pulse picking and to deliver maximum gain inside the amplifiers through the correct pump time arrival for more details see the Time and Synchronization section.

5.1.3.2.3 Third harmonic generation

At the output of the amplifier the IR pulses go to a third harmonic generator, where UV pulses with an energy of up to are produced. The up-

conversion is required to generate photon with energy larger than the photoemission work function of the metal cathode. The third harmonic generator is characterized by two type I beta barium borate (BBO) crystals of 0.5 and 0.3 mm used to produce first the second harmonic signal and then the third harmonic signal by frequency sum.

The harmonic process efficiency depends proportionally to the input pulse power density and is proportional to the non-linear crystal length [22]. The overall efficiency expected for the SPARX specification is 20%, due to aging processes occurs in the non linear crystal a more conservative value can be assumed (15-18 %). Amplitude jitter are slightly enhanced due to the non-linear behavior of the harmonic generation process, anyway a still acceptable 2% rms amplitude fluctuation can be estimated. The harmonic generation can be achieved with no perfect transform limited pulse in order to generate enough UV pulse stretcher for time pulse shaping purpose. In the reference [27] the theoretical and experimental characterization of the spectral distortion in the harmonic generation has been reported. Figure 5.21 reports the measurement and the simulated second and third harmonic spectra as function of the linear chirp applied to the IR input pulse.

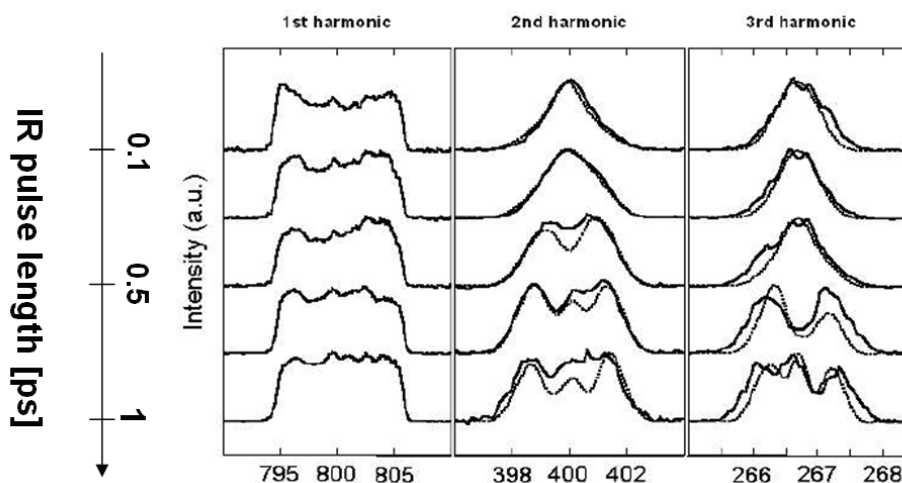


Figure 5.21: From left to right: measured (solid curve) and simulated (dashed curve) IR, BLUE, and UV spectra. Starting from a transform-limited pulse, the input pulse length has been increased through a DAZZLER programmable quadratic phase. The acousto-optical filter applies also an amplitude modulation in order to achieve an amplified square spectrum.

5.1.3.3 Time pulse shaping

For optimum driving a photocathode of a S-band RF cavity, such as the SPARX photoinjector, one desires ideally a relatively high energy ($> 100 \mu\text{J}$) UV laser pulse 2 to 10 picoseconds long, with a flat top temporal profile having fast ($\sim 1\text{ps}$) rise and fall times. The current techniques to manipulate the bell shape laser pulse employ devices that work in the IR, in general before the amplification. This set up requires the pulse shapers are able to compensate the unavoidable distortions caused by the amplification and the harmonic conversion. To perform this pre-compensation it is in general advisable to work with programmable shapers. Two most widespread techniques are here

presented: one is based on a programmable dispersive acousto-optic modulator (the DAZZLER) [28] while the other is based on a liquid crystal mask spatial light modulator (LCM-SLM) placed in a 4-f optical setup [29]. The limited rise time achieved with IR pulse shaper can be improved using two stages pulse shaper scheme, where the programmable shaper is associated to a 4f stretcher in the UV [30]. This device allows to freely change the pulse length, without variation in the peak power and the efficiency of the THG, and to impose a amplitude or phase modulation to the UV pulse spectrum.

Recently, a UV DAZZLER has been proposed and will be briefly described with the foreseen performance and the present limitation [31]. So far we described pulse shaper working in the spectral domain, it is also possible to obtain the uniform intensity profile, directly in the time domain, stacking several short pulse replica properly delayed [32,33].

The principle of laser pulse shaping operated in the spectral domain is based on the amplitude and phase modulation of the spectral components. The field of a light pulse has, in the time and frequency domains, respectively, the expressions:

$$E(t) = \sqrt{I(t)} e^{i\Phi(t)} e^{-i\omega_0 t} \quad \tilde{E}(\omega) = \sqrt{\tilde{I}(\omega - \omega_0)} e^{i\tilde{\Phi}(\omega - \omega_0)} \quad (5-4)$$

The pulse shaping manipulation is a linear filtering process. In the time domain the filter action of the shaper is represented by an impulsive response function $h(t)$; in the spectral domain the filter action is represented by the Fourier transform $H(\omega)$ of $h(t)$. The output electric field $E_{out}(t)$ is the convolution of the input $E_{in}(t)$ and the response function $h(t)$: $E_{out}(t) = h(t) \otimes E_{in}(t)$. In the frequency domain we can write: $\tilde{E}_{out}(\omega) = H(\omega) \cdot E_{in}(\omega)$.

In general $H(\omega)$ is a complex function that can be decomposed as an amplitude and phase terms: $H(\omega) = T(\omega) e^{i\phi(\omega)}$. Appropriate $T(\omega)$ and phase $\phi(\omega)$ modulation can lead to any kind of output signal compatible with the original spectral width. When the input and output fields are given and it is possible to introduce both amplitude and phase modulation the solution of the problem is unique. This solution can be computed by using those particular functions $T(\omega)$ and $\phi(\omega)$ that make the Fourier transform of the input equal into the Fourier-transformed output. Nevertheless, in order to obtain the target pulse, it is possible to introduce only an appropriate phase function modulation; in this case there are multiple solutions to the problem [34].

5.1.3.3.1 IR acousto-optic programmable dispersive filter: the DAZZLER

The “DAZZLER”, an “Acousto Optic Programmable Dispersive Filter” (AOPDF) is a system designed by FASTLITE to manipulate the spectral phase and amplitude of ultrafast laser pulses [28]. A RF signal within 40 to 50 MHz excites a piezo transducer which generates an acoustic wave inside an bi-refrangent acousto-optic TeO_2 crystal. The acoustic wave propagates along the crystal spatially reproducing the RF signal. Being the optical wave velocity much greater than the acoustic wave velocity, the input optical pulse propagates as trough a fixed dielectric grating inside the crystal. The two linear optical modes

of the crystal can be efficiently coupled by an acousto-optic interaction when the phase matching condition, energy and momentum conservation, between the acoustic wave and the two optical modes are satisfied. The coupling assures a partial energy transfer from the input and the output optical mode. The two modes emerge out of the crystal at different angle and the part of the optical pulse interacted with the acoustic grating can be easily separated from the un-diffracted one, and then it can be amplified. The efficiency of the interaction for an optical wavelength depends on the amplitude of the corresponding acoustic frequency. By controlling the amplitude of the acoustic spectrum it is then possible to perform an amplitude modulation of the optical frequencies.

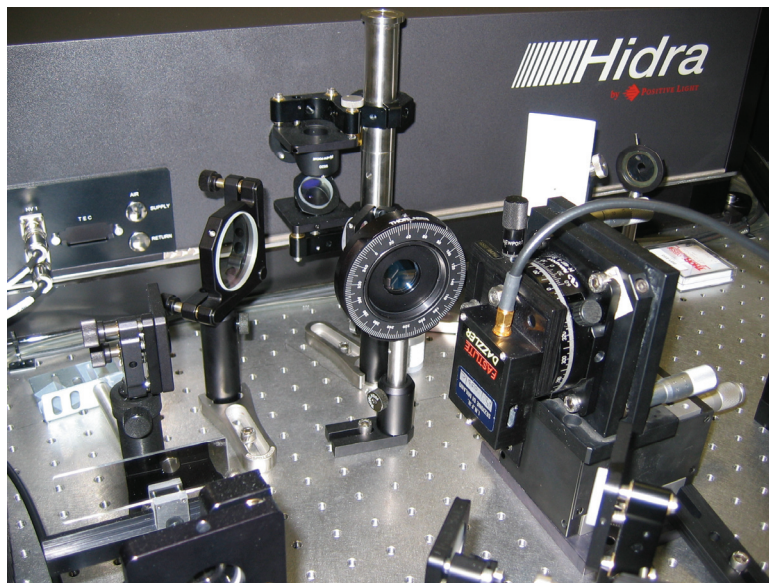


Figure 5.22: Dazzler crystal set up.

Sending a frequency RF chirped signal in different position z along the crystal there will correspond different acoustic frequencies. Since locally, for a given z , there is just one spatial frequency in the acoustic grating, only the optical frequency that satisfies the phase matching condition, can be diffracted in that position z . In this way it is possible to diffract different frequencies at different depths. Due to the TeO_2 birefringence two wavelengths experience diverse propagation time and are subjected to different phase modulation.

The high resolution Dazzler is composed by a 2.5 cm acoustic material. It has a resolution of 0.3 nm and work over a bandwidth of 200 nm around 800 nm. The maximum programmable chirp it can apply produce a laser pulse up to 6 ps.

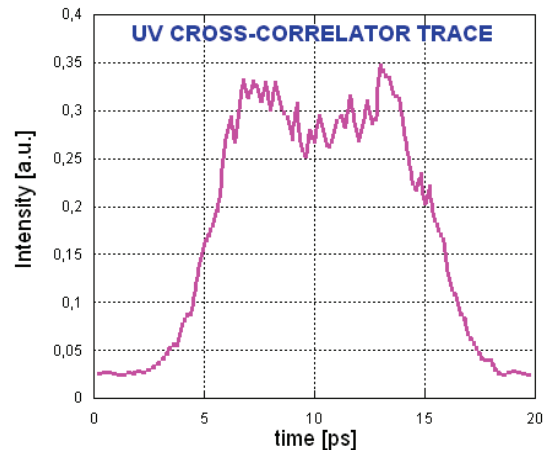


Figure 5.23: cross-correlation trace of the UV flat top pulse obtained with the DAZZLER pulse shaper.

Due to the damage threshold (maximum peak power is 1 MW/mm^2) the DAZZLER is mounted at the oscillator's exit prior to send the beam into the amplifier where the energy losses. Adopting this layout the relative high insertion losses of the acoustic filter, up to the 50%, are easily recovered by the amplification.

The Dazzler is able to produce the desired pulse form in the IR [35], but the distortions induced by the amplification and the third harmonic conversion, especially for high efficiency THG, worsen the rise time. The best rise time measured, as shown in the Figure 5.23, give rise time of $2.5\div 3$ ps [27]. A possible strategy to achieve the desired flat top profile was to produce a square UV spectrum at the UV stretcher. The pulse expander introduce a linear chirp and therefore a direct correlation between spectral and temporal intensity.

5.1.3.3.2 Liquid crystal based spatial light modulator

The mask is an array of pixels interleaved with small gaps (Figure 5.24). Commercial masks, for instance Jenoptick model SLM-S 640/12, have the following features: the dimensions of the pixels and gaps are, respectively, 97 and $3\ \mu\text{m}$ wide, and the number of pixels is 640.

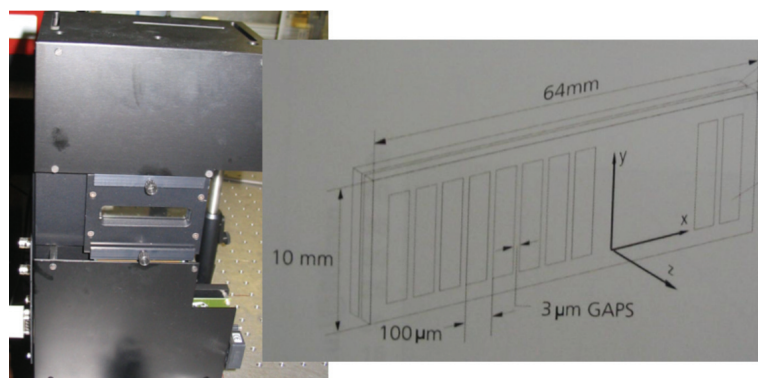


Figure 5.24: Picture of the Jenoptick SLM-S 640/12 and, on the right, the sketch of the liquid crystal array.

By changing the voltage applied to a single pixel it is possible to change the refraction index for that particular pixel. In this way, it is introduced a wanted phase shift in the radiation travelling through the pixels. The pulse shaping with the LCM-SLM is carried out introducing a proper spectral phase in order to obtain the wanted pulse intensity in the time domain.

To introduce the proper phase on the pulse it is necessary to propagate the different pulse wavelengths through the individual pixels of the array. This is possible by using an optical layout called 4f which is sketched in Figure 5.25.

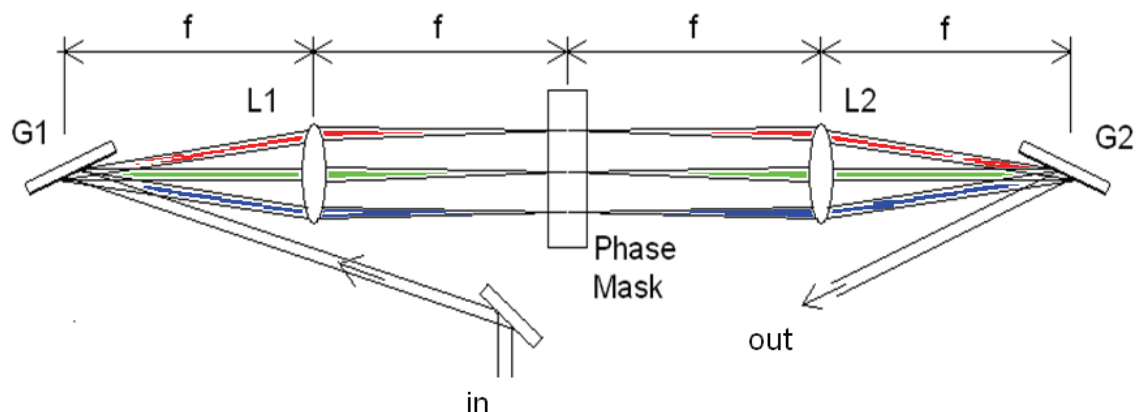


Figure 5.25: 4f optical setup. The diffraction grating G1 is used in order to apply a linear angular dispersion onto the input wavelengths. L1 is used to focus the spectral component at the Fourier plane where the mask is placed. The second lens and the output grating are positioned in a symmetric position and are used to recombine the wavelengths at the exit.

The optical system is composed by two anti-parallel identical gratings and two focusing lenses with focal length f . The optical elements are placed as reported in the figure. The wavelengths are dispersed by the first grating, and then the first lens collimates the laser frequencies. The second lens and the last diffractive optics are used to recombine the wavelengths with no residual spatial chirp and without temporal dispersion. The mask is located at the Fourier plane of the system where the spectral components of the pulse are linearly dispersed and focused. The overall energy losses are comparable with the DAZZLER ones.

The phase function introduced by the mask and which is simulated is changed by modifying the coefficient of the following polynomial function

$$\phi(\omega) = \alpha \cdot (\omega - \omega_0) + \frac{1}{2} \beta \cdot (\omega - \omega_0)^2 + \frac{1}{3!} \gamma \cdot (\omega - \omega_0)^3 + \dots \quad (5-5)$$

The first order coefficient “ α ” of the polynomial function brings a time shift of the pulse without changing its shape, the second order “ β ” induces a linear dispersion effect stretching or compressing the pulse and “ γ ” introduces a right or left asymmetry on the pulse shape. For our purposes the first four term of the polynomial function are sufficient.

For the liquid crystal mask, the phase function modulation can be quickly introduced and it is possible to see in real time the changes of the UV

spectrum. This characteristic makes this device suitable to be integrated with an adaptive algorithm.

A critical point of LCM-SLM is the alignment of the system. In fact, it is not easy to perfectly align the 4f configuration in order to remove any undesired effects such as spatial chirp and beam divergence of the output beam. This consideration is true especially when the optical setup is realized in a small room. The residual spatial chirp out of the 4f system is particularly deleterious since the output pulse seeds the regenerative laser amplifier. This stage is characterized by its own cavity's spatial and longitudinal modes. So, to avoid undesirable amplitude modulation of the amplified IR pulses, it is absolutely necessary that all the spectral components of the pulse coming out of the 4f be well matched with the spatial modes of the RGA cavity. It is then clear that a diagnostic device for the IR before and after the RGA is mandatory to correctly align the 4f apparatus, the output spectrum is very sensitive to even small misalignment of the seed beam and suggests for a real time control.

A comparison between the two techniques shows that the acousto-optic solution performs a continuous frequency modulation, and is able to allocate a bandwidth one order of magnitude larger than the capability of liquid crystals technique [36]. The alignment of an acousto-optic crystal is less critical than a liquid crystal mask. Both types of shaper can be driven dynamically by measuring the pulse profile after the amplifier to pre-compensate gain and conversion distortions.

As reported in Figure 5.25 and Figure 5.26 the resulting pulse shapes achieved with the two techniques appear to be comparable.

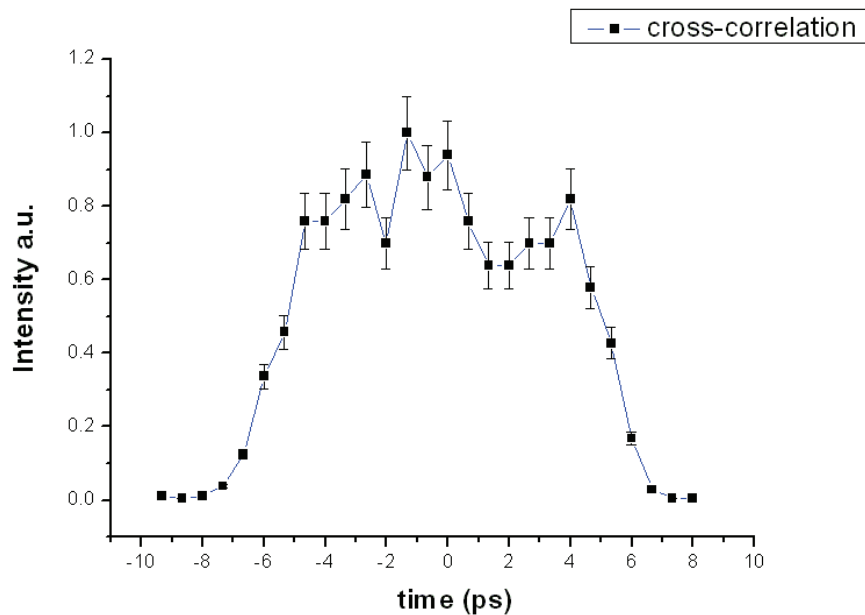


Figure 5.26: cross-correlation trace of the UV flat top pulse obtained with the LCM-SLM shaper.

5.1.3.3.3 UV stretcher for ps rise time

The measured pulses, and the simulations show limitations on the minimum rise time that can be obtained. As shown in Figure 5.23 and Figure 5.26, the rise time is about 2.5 ps, and the ripple is within 20 % ptp. In fact, due to the finite bandwidth of the non-linear crystals, the steepness of the rise and fall time of the resulting flat-top pulses cannot be pre-compensated by the DAZZLER. The correspondence between spectral and temporal pulse profiles experimentally observed [27], suggests that to improve the rise time the spectral tail has to be sharply clipped. For this purpose the UV stretcher can be modified including the possibility to clip the spectrum [37].

After the third harmonic generation the beam can be sent through a specially built optical system in order to shape the longitudinal pulse profile. Basically it is a particular version of the classical 4f optical scheme with two anti-parallel gratings and two lenses of focal distance f respectively separated by a distance f Figure 5.27 [30]. In fact on the lens focal plane there is full correlation between wavelength and transverse position. This allows any desired amplitude or phase modulation on the spectrum simply placing a filter or mask at this plane. Moreover the shift h of the second grating introduces a chirp on the outgoing beam and therefore it can be used to continuously change the output pulse duration on several ps. As shown in Figure 5.27 after the second pass the fraction of the beam reflected by the grating is focalized by a positive lens onto the plane of a CCD camera. In this way a high-resolution (≈ 0.05 nm) spectrometer is integrated in the shaping system [37]. Summarizing, the functions of the described optical system are: i) introduction of a frequency chirp in order to change the pulse length; ii) introduction of an amplitude modulation on the spectrum by placing a mask at the Fourier plane; iii) single shot measurement of the spectrum of the output pulse. Here we focus on the ability of the system to reduce the pulse rise time

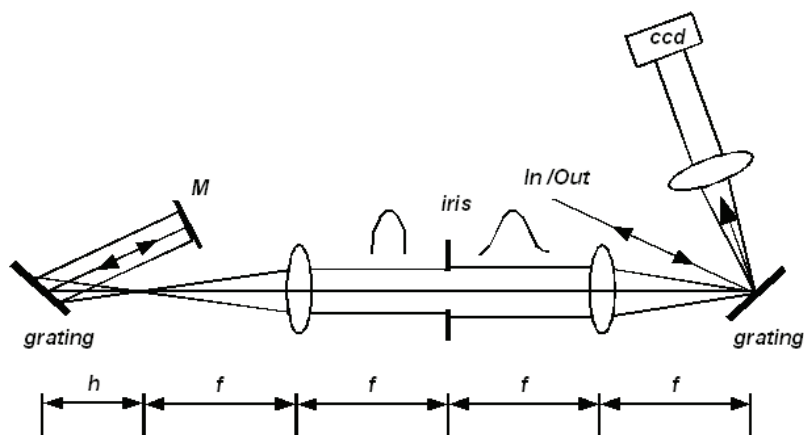


Figure 5.27: Schematics of the UV pulse shaper. The CCD and the lens on the beam reflect reflected composed an high resolution spectrometer.

In Figure 5.28, in the upper plot, it is reported how the simulated improvement on the rise time when the spectrum is clipped as shown in the corresponding lower curves. Starting from the black spectrum we remove the tails increasing the steepness of the curve. As shown in the time profile the rise time can be reduced down to 1.2 ps (green curve). At this point sharper cut in the spectrum induce larger ripples but don't improve anymore the rise time due to the given bandwidth.

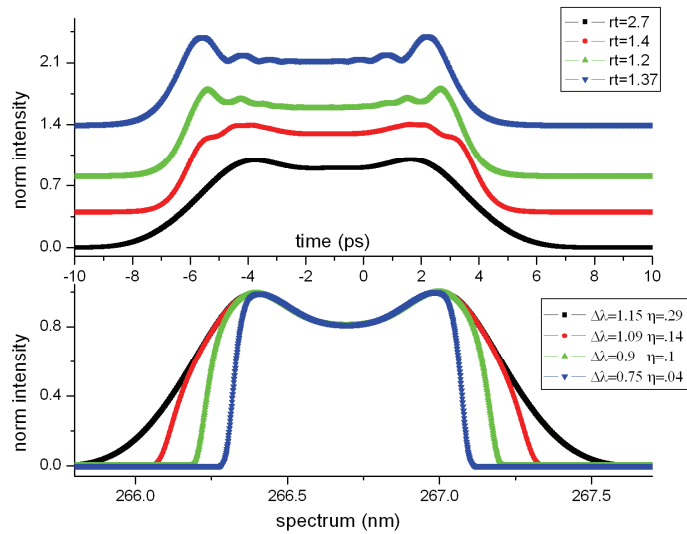


Figure 5.28: Effect of the clip of the spectral tails. In the lower plot are reported different spectra obtained by increasing the steepness of the spectra and the correspondent time intensity profile.

Also experimentally a net improvement on the rise time has been observed. In Figure 5.29 the cross-correlation measurement on the pulse produced clipping the tails of the spectrum with the described apparatus. The pulse length is about 10 ps FWHM and the rise time is about 1.8 ps. The cross-correlation has been measured using a relatively long IR gate pulse of about 0.6 ps FWHM. The long pulse induces a smoothing in the pulse reconstruction and produces an overestimation on the rise time. According to our calculation the achieved rise time is 1.5 ps. The black curve is obtained when one simulates the real output profile and then calculates the cross correlation with the IR pulse we used. As shown in the figure, there is an excellent agreement between simulation and measurement.

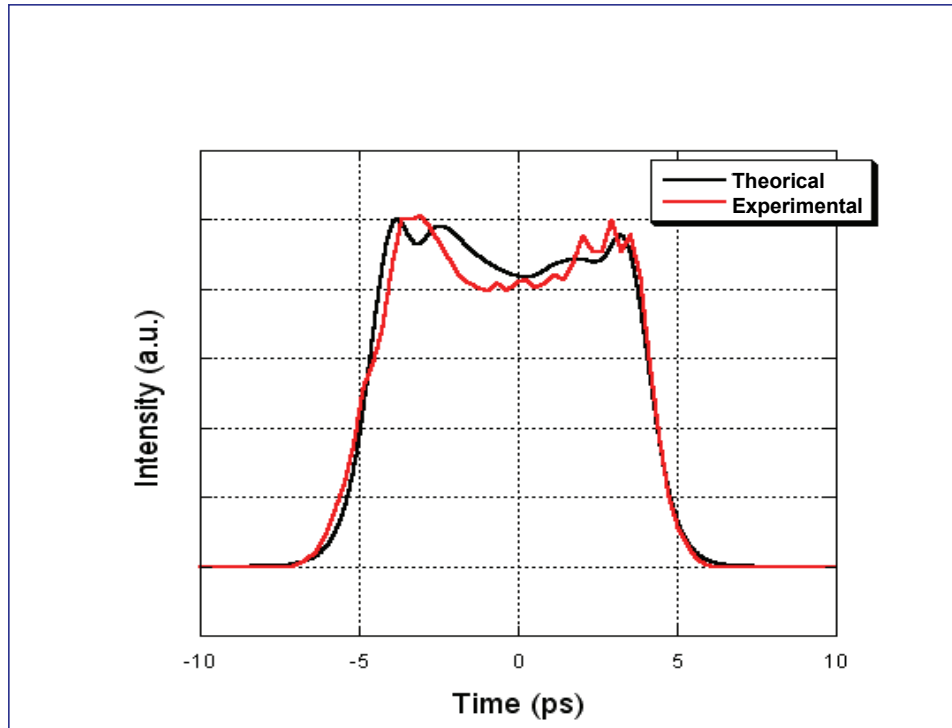


Figure 5.29: Simulated and measured pulse profile when the UV stretcher is used to reduce the rise time.

Numerical simulations [30] indicate that to further reduce the rise time it is important to increase the spectral width of the UV pulse, Figure 5.30. This requires a dedicated design for the harmonic conversion stage and the amplification.

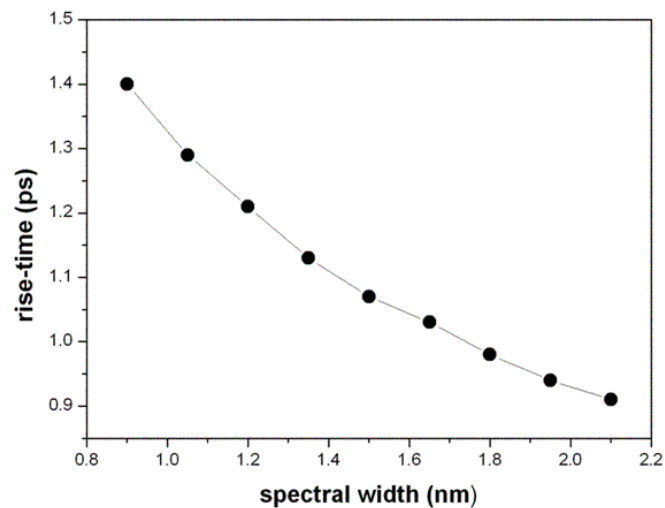


Figure 5.30: Simulated rise time as a function of spectral bandwidth after the cut of the spectral tails.

5.1.3.3.4 UV DAZZLER

Recently an UV version for the DAZZLER with operation range between 400 and 250 nm has been proposed [31]. The filter demonstrated a resolution of 0.05 nm. The acousto optics crystal adopted is, in this case, KDP. The two photons absorption for this crystal limits the maximum energy transmitted by the filter. This paragraph is focused to two typical working points for the SPARX machine. We report results of simulations aiming to attain the nominal SPARX charge CASE 1 (1nC) and lower charge regime CASE 2 (250 pC) keeping constant the density of the electron beam. The design considerations and simulation reported in the following has been produced in collaboration with FASTLITE [38]. The UV DAZZLER can be operated in single or double passes using a fold mirror to retro-reflect the output beam. In the second case the dynamic range of the filter is doubled and the output pulse length can be the doubled respect to the single pass case (in the order of 3 psec).

The simulation design is based on the following considerations:

- 1) Adding external GVD is necessary because of the limited pulse shaping capacity of the DAZZLER and to reduce the power density in the DAZZLER.
- 2) Two photon absorption in the DAZZLER yields a transmission coefficient of the form:

$$t_2 = \frac{1}{1 + kI} \quad (5-6)$$

where $k=2.5 \text{ cm}^2/\text{GW}$ for a 5 cm long crystal, and I is the input intensity on the DAZZLER.

Intense two photons absorption has a pulse shaping effect, both spectrally and spatially. The output pulse is squarer than the input pulse. A simulation program which incorporates the following features have been developed:

- a) Phase shaping using even order polynomials in order to generate a symmetric shape output
- b) Amplitude shaping with super-gaussian shapes
- c) One or two passes through DAZZLER set up
- d) Additional external linear chirp to simulate an external stretching
- e) Input signal with super-gaussian spectrum
- f) Spectral modification due to two photon absorption
- g) Output energy computation including two photon absorption, DAZZLER diffraction efficiency and spectral clipping by the DAZZLER.

The used beam area is 0.3 cm^2 (4x8 mm), which is the absolute maximum achievable with the present FASTLITE device. The characteristics according to the SPARX working points aimed at the specifications listed in the Table 5.5.

Table 5.5: Laser requirements on cathode. Characteristic of the UV laser pulse foreseen for the SPARX photocathode laser system.

	<i>Case 1 (1 nC)</i>	<i>Case 2 (250 pC)</i>
Pulse length	10 ps	6.3 ps
Rise time	1 ps	0.6
Central wavelength	266 nm	266 nm
Bandwidth	1.4-2 nm	1.4-2 nm
Input pulse length*	>1 ps	>1 ps
Input energy	< 1.5 mJ	<1.5 mJ
Energy output required	≥ 150 μJ	≥ 40 μJ
Spot diameter input	Adjustable	Adjustable
Spot diameter @ cathode	2 mm	1.2 mm

In general, we have found that:

1. Case 1(1nC) is not achievable in two passes, because of the strongly reduced DAZZLER efficiency in this setup.
2. Case 1 in one pass and case 2 in two passes are only marginally achievable.
3. Case 2 is achievable in one pass.

The main disadvantage of the one pass scheme, is the absence of compensation of the walk-off¹⁵. This is of the order of 1.3 mm, whereas the beam width would be of order 8 mm. The following Table 5.6 gives some characteristics of solutions found in simulation.

Table 5.6: Simulated parameters for the UV DAZZLER. Case 1 refers to the high charge working point and case 2 to the 250 pC per bunch.

<i>Case</i>	<i>Pass</i>	<i>Extern (ps)</i>	<i>Duration (ps)</i>	<i>Rise time (ps)</i>	<i>E out (mJ)</i>	<i>Cut (%)</i>	<i>Diffract (%)</i>	<i>Two photons (%)</i>	<i>Global (%)</i>
2	2	1.64	6.38	0.61	0.029	94	26.01	7.91	1.93
2	1	4.16	6.29	0.52	0.126	97	34.00	25.47	8.40
1	2	5.43	10.01	0.72	0.04	92	15.21	19.06	2.67
1	1	7.58	10.01	0.64	0.167	94	32.00	37.01	11.13

¹⁵ Spatial walk off in a birefringent medium, such as the UV DAZZLER, is the angular drift associated to two polarizations, that in our case correspond to the input and the diffracted beam. If the diffracted and undiffracted beams are retroreflected after the second pass in the Dazzler they overlap again.

All simulations are done with a pure Gaussian spectrum input signal of 1.5 mJ with 1.4 nm width at 266 nm. The external column gives the amount of stretch required prior to the DAZZLER (at half maximum amplitude). The pre-stretching can be achieved with a standard UV stretcher or with a dispersive glass. The duration of the exit pulse is computed with the criterion “above 90% of maximum”. The last columns give indication of the throughput of different processes reducing efficiency: Cut is the energy reduction by the spectral intensity shaping. Diffract is the effect of DAZZLER diffraction efficiency. Two photons is the energy loss induced by two photons absorption.

In Red, the value that is clearly out of specifications is reported, making Case 1 not achievable using two passes setup. In blue the values close to the specifications are shown: these results have been achieved only through compromise.

The resulting time shapes for these simulations are reported in the following 4 figures (Figure 5.31 to Figure 5.34). They are not ideally flat top, mainly due to the limited time shaping capacity of the DAZZLER and the necessity to add significant stretching externally. They could be made somewhat better by introducing more flexibility in the spectral amplitude programming of the DAZZLER (currently limited to super-gaussian in the simulation).

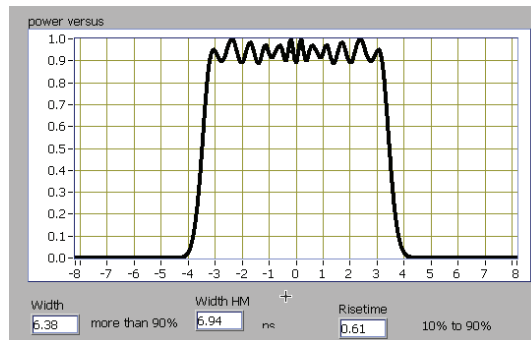


Figure 5.31: Low charge case pulse shape achieved through 2 passes in the DAZZLER (vertical axis: normalized intensity, horizontal axis: time in ps).

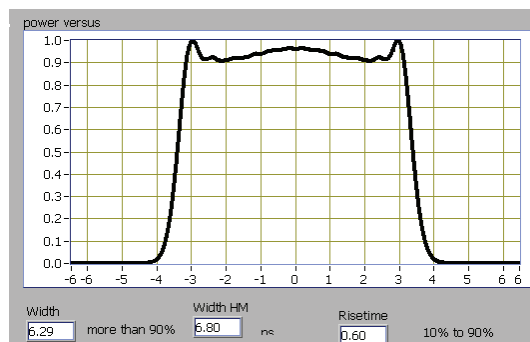


Figure 5.32: Low charge case pulse shape achieved through 1 pass in the DAZZLER (vertical axis: normalized intensity, horizontal axis: time in ps)

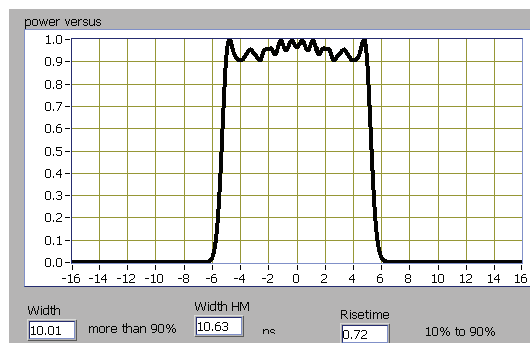


Figure 5.33: High charge case pulse shape achieved through 2 pass in the DAZZLER (vertical axis: normalized intensity, horizontal axis: time in ps).

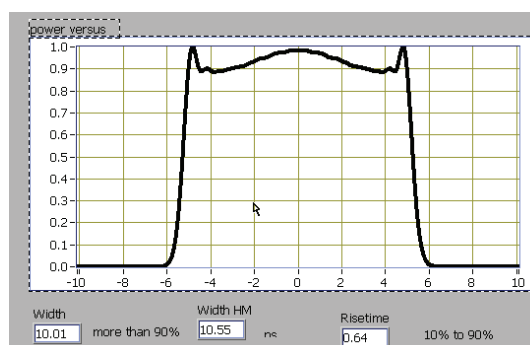


Figure 5.34: High charge case pulse shape achieved through 1 pass in the DAZZLER (vertical axis: normalized intensity, horizontal axis: time in ps)

5.1.3.3.5 Pulse staking

The temporal shaping of the photocathode pulses can be achieved directly in the UV by a temporal shaper called UV Stacker. The concept is to split a UV pulse into two replicas in orthogonal polarization states, provide different temporal delay times and combine (stack) them into a single longer output pulse with a variable polarization state over its temporal evolution. By iterating this procedure one can generate a temporal splitting of the original pulse into many more pulses by pairs while keeping the beam path identical.

The delay lines have been originally proposed using Michelson interferometer. This solution implies a complex and troublesome spatial beam combination scheme especially when the target pulse is required to be shaped with high resolution. The use of a bi-refringtont glass such as MgF_2 or CaF_2 for differential delay is more promising solution to realize entirely collinearly stable pulse shaper.

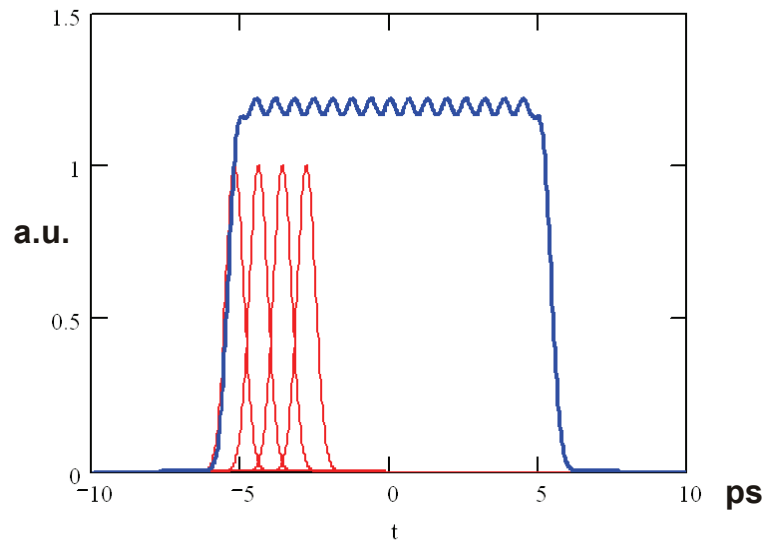


Figure 5.35: Simulated pulse obtained with pulse stacking of 0.5 ps short pulses.

A variable number of crystals up to 16 pairs of pulse replicas stacked together allows to change the output pulse length, dividing by a factor two (for instance it is possible to have duration of 10 ps, 5 ps, 2.5 ps and so on, as shown in Figure 5.35). The pulses separation and the adjustment the peak-to-peak (ptp) variations can be in principle done using a wedges crystals and therefore a different delay. Additionally the rotation of the crystals allows amplitude control of each pairs of pulses, and also of the s-polarized relatively to the p-polarized pulses in the UV stack to ensure the best flatness top-hat UV pulse. The temporal profile foreseen at the photocathode is characterized by a ripple on the plateau <20% ptp variations. The transmission of the proposed UV Stacker can be estimated to be >90% if antireflection coating are used for the stacked glasses. The transverse profile and the energy stability is determined by the incoming pulse.

The pulse staking scheme will not work so well with much shorter initial UV pulse because of the following reasons:

a) many more pairs of pulses will need to be stacked together (128 pairs of replicas for sub-200 fs long initial UV pulse) increasing the amount of optical components placed in the beam path and reducing the UV Stacker overall transmission.

b) not negligible deterioration of the UV beam profile after passing the much greater number of optical material components in the UV Stacker due to filamentation process.

The pulse staker scheme has the advantage of very low insertion losses compared with the other pulse manipulation techniques. The limitation derives from the poor flexibility in term of pulse length and shape achievable.

5.1.3.4 Spatial pulse shaping and imaging system to the cathode

5.1.3.4.1 Homogenizer system: aspheric lenses telescope

The spatial mode generated naturally by the laser systems are in general Gaussian or bell shaped. The use of an aperture and the successive imaging transport to the cathode is associated to unavoidable energy losses and is

useful only when a super-gaussian input is provided in the UV. Therefore a dedicated optical system is required for changing the transverse intensity profile. The beam profile can be static or programmable. The static beam shaper has a fixed transfer function that produces the desired pulse when a well defined input is present. When the input mode diverges for the optimal shape, the output is not anymore flat top. The final consideration is that only the a collimated beam where the flat top intensity is kept over relative long distance (1-2 meters) can be transported over the several meter transfer line and imaged on the cathode.

A static beam shaper that demonstrated the ability to convert a Gaussian input in a flat top one is based on a proper designed aspheric lenses telescope [39]. The use of Galilean design, thus there is no intermediate focusing of a beam, is very useful to avoid non-linear effect due to high intensity reached at the focus of a Newtonian telescope. The principle of operation is described as follows: the first lens is used to defocus the central part of the beam and focus the outer tails, the second lens is used to collimate the beam and produce a plane output wave. The telescope length can be varied to change the focal length of the static shaper.

To simulate the effect of the aspheric lenses telescope on a input, Gaussian beams have been simulated using Zemax optical design code [40]. The input and the output transverse distribution are reported in the Figure 5.36.

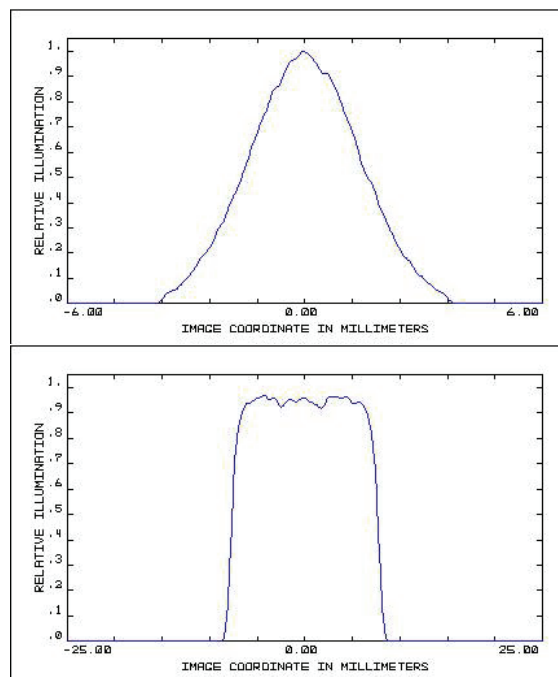


Figure 5.36: Zemax simulation of the aspheric beam homogeneizer.

The ideal output deviate from the flat top shape also for misalignment of the telescope. In fact a transverse displacement of ± 1 mm is specified or angular tilt of 0.5° introduce a asymmetric shape in the output flat top. This consideration means a proper 4 axis mount has to be adopted for the telescope alignment.

5.1.3.4.2 Homogenizer system: deformable mirror

Piezoelectric deformable mirror is a more complex, but more powerful solution, can also be used for beam profile variation. Due to its programmable nature, a myriad of beam forms can be selected, in addition optimization loop can be run to improve the beam shape on the photocathode to maximize electron yield. The deformable mirror can be realized with metal or dielectric coating. The fused silica piezoelectric deformable mirror have the advantage of high-reflection dielectric coating with $R > 99\%$ for optimum shaper transmission. A wave-front sensor is advisable for constantly measuring the output of the spatial shaper and use it as a feedback to the deformable mirror optimization software. This software will simulate the spatial shape on the target 15-20 meters away and will feed this simulation as a feedback to the deformable mirror optimization algorithm. This simulation will be regularly calibrated by a test CCD camera, which will need to be placed at the position of the photocathode target in the time of installation and later on when required for maintenance.

The deformable mirror introduces a phase only transmission function by varying the surface position over a few wavelengths. Using the Fresnel propagator and assuming a cylindrical coordinate system, it has been possible to study the effect of polynomial phase transfer function after a arbitrary propagation [41]. Figure 5.37 reports the calculated input and the output beam profile when a optimizing phase function is applied.

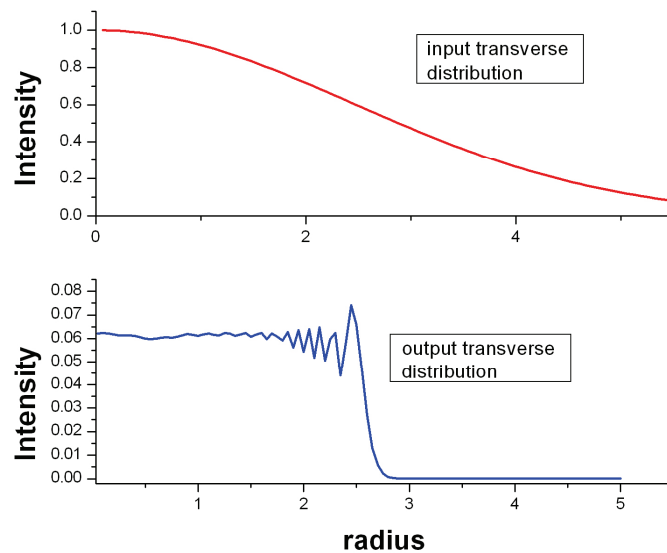


Figure 5.37: Radial distribution of the input and output pulse. The phase-only transfer function has been found using a optimization procedure.

5.1.3.4.3 Imaging and transport system

A dedicated design of the transfer line from the exit of the laser system to the cathode has to be realized. In fact the required performances on the cathode need a compensation of the pointing instability over more than ten meter propagation. It will be used an evacuated beam pipe to the gun for preservation of the spatial and temporal pulse's profile.

The transport to the cathode has to assure a stable beam and the faithful reconstruction of the laser spot at the object plane. The optical transfer line is foreseen to transport the beam from a laser room to a table positioned as close as possible to the gun with an optical path of about 12 meters. A top view of the laser and the transfer line to the cathode are shown in the Figure 5.38. The object plane is located at the exit of the transverse beam shape in the laser room. To reconstruct at the cathode the exact transverse distribution from the object plane, we will adopt a Fourier relay optic scheme. This layout allows also to significantly reduce the pointing stability at the cathode.

This scheme foresees two focusing lenses L_1 and L_2 with focal f_1 and f_2 ; the first lens is mounted at distance f_1 from the object and L_2 is at f_1+f_2 from the first optic, the Fourier relay forms the image on a plane at distance f_2 behind L_2 . The transfer line will also carry out proper demagnification with a variable zoom to match the electrons density required for optimal beam manipulation for several working points.

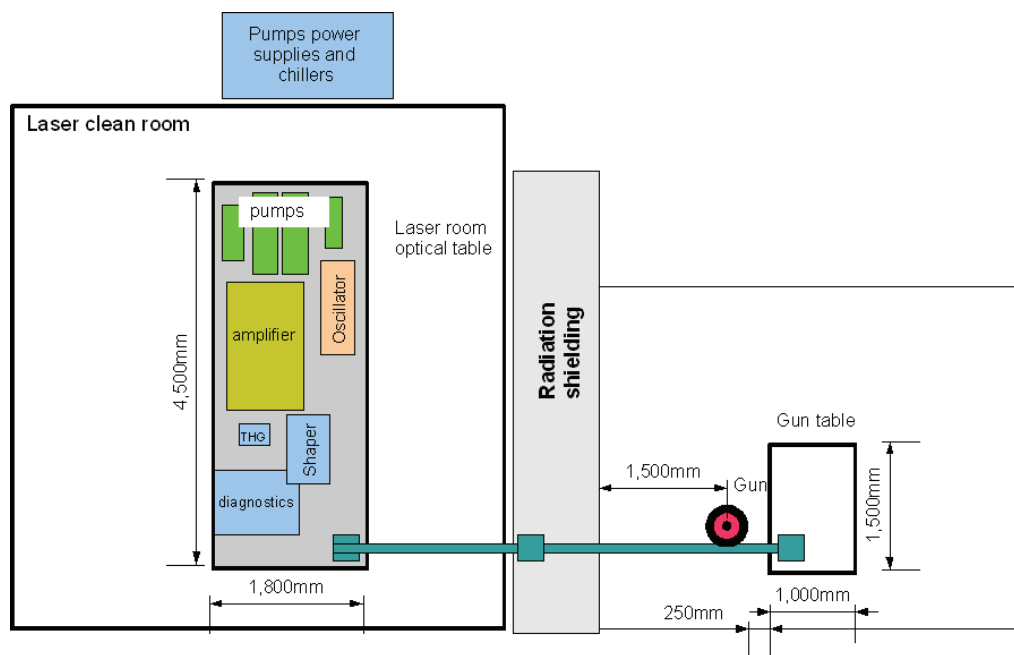


Figure 5.38: Layout of the photocathode laser room and the transport to the cathode (top view).

The magnification of the Fourier relay optic is the ratio f_2/f_1 . In the SPARX case the demagnification will be $\frac{1}{4}$ and the focals are $f_1=6$ m and $f_2=1.5$ m. Figure 5.39 depicts the layout of the transfer line: L_1 is installed on the radiation shielding and the second lens on the gun optical table. After the first lens the

laser is focalized and to avoid high power density in air and consequent distortions it is advisable to keep the transfer-line in low vacuum (10^{-3} mbar) or in nitrogen overpressure.

A three lenses telescope can be used to continuously change the dimension of the beam, typical design allow the magnification from 0.5 to 2, without varying the natural divergence of the beam before the optical transport.

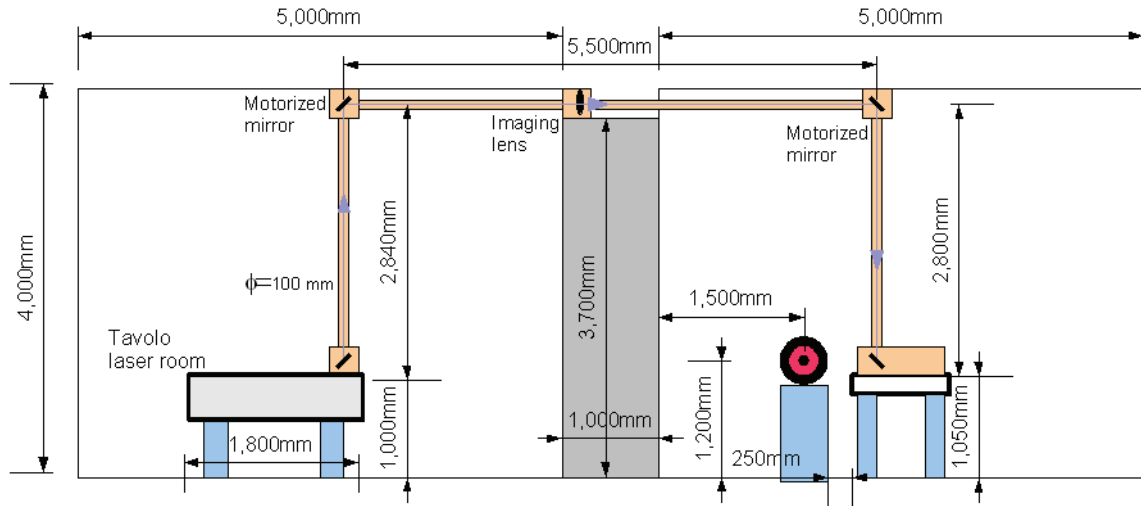


Figure 5.39: Layout of the photocathode laser transport to the cathode (side view).

Figure 5.38 shows the laser room as dedicated environment for the best operating conditions of the laser. In fact, to improve the time and the energy stability of the system it is useful to control the temperature of the environment. We plan to build a dedicated 10^4 class clean laser room with temperature stabilization at $\pm 1^\circ\text{C}$. The Thermal stability of $\pm 1^\circ\text{C}$ is a typical value required for laser environment for reliable and drift-free operation. Furthermore it is important to limit with designed air shielding and enclosures, the turbulences introduced by the temperature stabilization system. The removal from the laser room of chillers, power supplies and or potential sources of heating will help to reduce the speed of the conditioning system.

Figure 5.40 depicts the main optical elements that will be installed close to the photocathode. The laser beam exit from the evacuated pipe and is steered by a series of dielectric mirrors. The motorized mirrors are driven by the signal derived by a quadrant photodiode. The detector is divided in 4 independent sectors, and the output signals allow to reconstruct the relative position of the beam respect to the center of the detector. Two wedge beam splitters will be used to send a fraction of the beam to the on-line diagnostics necessary to continuously monitor the properties of the laser at the cathode. The time of arrival photodiode is used to measure the time jitter between the laser and the RF field. The energy photodiode is a calibrated detector used to measure the pulse-to-pulse energy. Finally a CCD camera is positioned at the virtual cathode, a particular symmetric plane respect to the cathode, to record the transverse beam impinging on the photocathode. Finally a remotely controlled variable attenuator is used to control the energy on the cathode and on the virtual cathode.

When the spectral phase is known, the measurement of the spectral intensity leads also single shot information on the time profile. In the case that large stretching is applied to the UV pulse, the spectrum corresponds directly to the time intensity [30]. Commercial compact spectrometer allows the monitoring of the spectral components before and after the amplification and in the UV. For a high resolution spectral reconstruction it is possible to built a dedicated spectrometer based on a high density grating and a CCD camera.

5.1.3.4.4.2 Spatial profile

For the diagnostic of the spatial characteristics CCD at different positions are useful tools. Special care we have to devote to the measurements of the center's position, of the transverse profile and spot's diameter jitter at the cathode's conjugate plane. Commercial CCD without the usual UV-protective windows can be used for the UV pulse. The best resolution of the spatial measurements is related to the pixel dimensions. Commercial CCDs have an active area up to 10 mm and pixel dimensions of 6-10 μm . A CCD camera with a demagnification system is necessary also to measure the beam transverse distribution after the transverse pulse shaper system.

5.1.3.4.4.3 Beam position measurements and feedback

A transverse feedback, to maintain the laser spot in a fixed position after commissioning optimization, is mandatory. As explained before two quadrants photodiode (formed by four photodetector sectors) is useful or fast control of the beam centroid position at the gun table. After alignment, the horizontal and vertical difference signals from the quadrants can drive feedback loop that will drive the mechanical actuators of selected mirrors, as shown in Figure 5.40, in order to correct unwanted displacements. A quadrant photodiode can be used also on the laser room table to produce repeatable laser beam direction.

5.1.3.4.4.4 Energy diagnostic

To satisfy the energy requirement on the cathode it is mandatory to control the pulse energy in different points of the laser system and the transfer line. The pulse's energy can be measured with piroelectric joulemeter or calibrated photodiode on a fraction of the laser beam reflected by a beam splitter. Joulemeter and photodiode are available from infrared to ultraviolet and shows a linear response up to two orders of magnitude. The pulse energy will be monitored at the exit of the amplifier, after the third harmonic generator and close to the virtual cathode. To change the pulse's energy on the cathode a proper variable filter can be inserted in the optical line.

5.1.3.4.4.5 Phase noise measurement

Phase error of the laser pulse arrival time with respect the RF field on cathode must be corrected to maintain the best performance of the

photoinjector. The time jitter is due to the optical path variation in the laser oscillator length, and can be compensated at sub-ps level with active control of the cavity length. In the laser amplifier and in the transfer line a slow drift can be caused by temperature variations. The relative phase error measurement must be performed close to the gun by mixing the RF field signal coming from a gun probe with a pseudo-sinusoidal signal created passing the fast photodiode signal in RF cavity tuned at $\frac{3}{4}$ of the master frequency [43]. With the mixing signal the laser pulse arrival time can be monitored and eventually corrected by acting on the gun phase shifter. An indirect measurement of the laser pulse jitter with respect to the RF system is also possible adopting a resonant cavity on the beam line after the gun or using an electro-optical sampling.

5.2 LINAC DESIGN

The heart of the SPARX complex is the S-band (2.856 GHz) electron linear accelerator (LINAC) with the nominal design energy of 2.4 GeV, operating at the average accelerating gradient of 23.5 MV/m. It utilizes the normal-conducting radio frequency (RF) technology, which is in operation successfully in numerous High Energy Physics and Synchrotron Light Source Laboratories worldwide.

The choice of the normal-conducting RF comes mostly with the long experience of the LNF accelerator division in operating S-band room-temperature LINACs. Moreover, the choice of an S-band, instead of a C or even an X-band LINAC, derives furthermore from considerations about cost and industrial availability, as reported in detail in the next paragraph 5.2.7.

5.2.1 LINAC Layout

The 1.5 GeV section of the SPARX RF system consists of 9 RF stations, 7 for the main LINAC and two for the pre-injector. Further 7 RF stations must be added to achieve the nominal design full energy of 2.4 GeV. The RF stations provide RF pulses of 50 MW/peak and 0.8 μ sec width to each of 3 accelerating sections. The average accelerating field gradient of 23.5 MV/m is therefore possible in travelling wave (TW), constant gradient (CG), $2\pi/3$, 3 m long, S-band accelerating structures, usually known as SLAC-type sections [44]. The energy gain per power station is about 215 MeV. To ease the maintenance and reduce the spare units, it is proposed to use 60 MW peak klystrons for all the stations including that for the RF gun and two RF deflectors, used for beam diagnostics (see par. 5.6), although these devices require less power. An extra S-band 60 MW power station feeds the RF deflector for the 2.4 GeV beam. The RF layout of the accelerator SPARX is schematically shown in Figure 5.41:

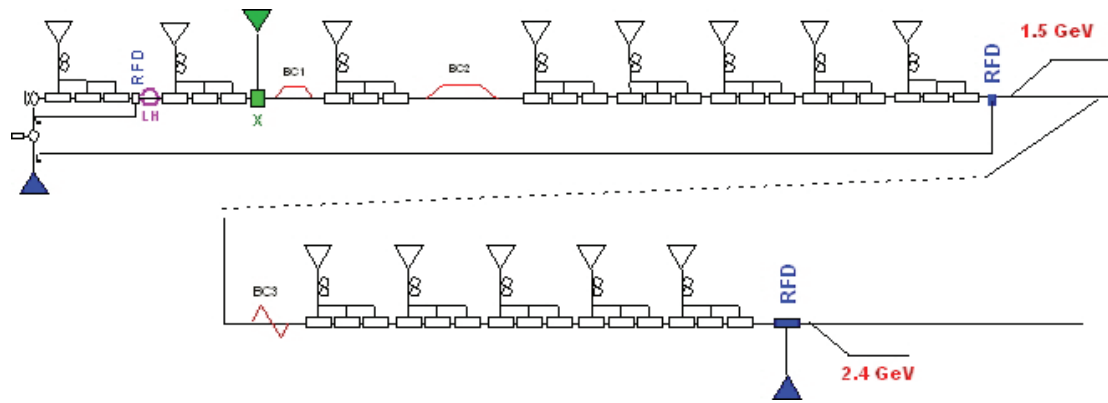


Figure 5.41: RF Layout of the SPARX accelerator

The choice of feeding 3 accelerating sections with one single source is not common in linear accelerators. Nevertheless, it minimizes the number of the RF power stations and allows to operate the LINAC at rather high field gradient as well. Pulse compressor systems (SLED) enable to increase the klystron RF pulse power by about a factor 3.5 and reduce the pulse duration from 4 to 1 μsec , to match the accelerating sections filling time. It is proposed to use the energy compressor developed at KEK [45] with dual-side wall coupling which reduces the electric field at the iris-edges of the cylinder cavities and, as a result, allows to operate the SLED at higher peak power with lower discharge rate. The SLED system is not used for the RF gun power station as the gun filling time is 2.5 μsec . As reported with more details in the above paragraph 5.1.1, the RF gun will be equipped with two symmetric RF inputs to compensate for the distortion of the accelerating field in the first cavity-cell. An option to use the SLED for feeding the gun is foreseen. This solution would permit, with higher peak power, to reach the flat-top field in a shorter time, reducing the average gun RF power but requires to use a more powerful and, therefore, more expensive circulator or isolator to protect the klystron against the reflected RF gun power.

One X-band TW section, installed before the bunch compressor BC1, linearizes the beam longitudinal phase space. The energy gain provided by the X-band structure is of the order of 25 MV/m. The system makes use of high power 11.424 GHz station, described in the paragraph 5.2.4.

5.2.2 Accelerating Structures

The electron beam is generated in the laser-driven photocathode 1.6-cell standing-wave (SW) RF cavity and accelerated to 150 MeV. In order to operate in the decelerating mode, three accelerating sections will be used instead of 2.

The accelerating structures of the SPARX LINAC are travelling wave (TW), constant gradient (CG), $2\pi/3$, 3 m . long, 2.856 GHz units. They are made of a series of 86 RF copper cells, joint with a brazing process performed in high temperature, under vacuum furnaces. The cells are coupled by means of on-axis circular irises with decreasing diameter, from input-to-output, to achieve the constant-gradient feature. The RF power is transferred to the accelerating section through a rectangular slot coupled to the first cell. The power not dissipated in the structure (about 1/3rd) is coupled-out from the last RF cell and dissipated on external load.

To meet the severe emittance requirements for the injector, the single-feed couplers of the pre-injector accelerating structures will be replaced by a

dual-feed design [46] to minimize the multipole field effects generated by the asymmetric feeding, which induces transverse kicks along the bunch, causing beam emittance degradation.

The industrial companies, which can develop the accelerating structures, are only a few in the world. The fabrication is a complex task that requires specialized know-how, availability of very advanced equipment and facilities, top-level organization.

The maximum achievable accelerating gradient is the most important parameters of such devices. The SPARX project operates at an average gradient of 23.5 MV/m that is a medium level accelerating field. Nevertheless, it requires the use of selected materials, precise machining, high-quality brazing process, surface treatments and cleaning, ultra-pure water rinsing, careful vacuum and RF low power tests. The

Figure 5.42 shows an S-band accelerating structure utilized in the Frascati SPARC injector while being installed on the beam-line. The Table 5.7 gives the main parameters of the sections.

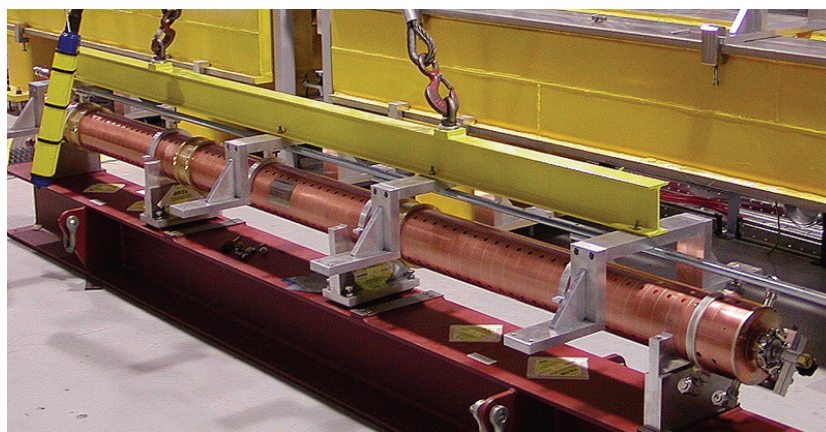


Figure 5.42: S-band accelerating structure

In order to maintain the structure tuned to the $2\pi/3$ mode, that guarantees the necessary cumulative energy gain for the beam particles, the accelerating sections are kept at very constant temperature ($\Delta T = \pm 0.1^\circ\text{C}$) by means of regulated cooling water systems.

Table 5.7: Technical specifications of the accelerating sections

<i>Frequency</i>	<i>2.856 GHz</i>
Type	TW, CG
Structure	Disk-loaded
Mode of operation	$2\pi/3$
Phase velocity	velocity of light in vacuum
Period	3.499 cm
Number of cells	86 (including couplers)
Attenuation constant	0.57 nepers
Normalized group velocity	0.0202 to 0.0065 (v_g/c)
Shunt impedance	53 to 60 M Ω /m
No load energy (50 MW input)	70 MeV (theoretical)
Bandwidth (VSWR \leq 1.2)	\geq 4 MHz
Phase shift per cell	120°
Filling time	0.85 μ sec
Q of structure	13400 (approx)
In/Out VSWR	\leq 1.1

5.2.3 RF Power Sources.

The RF power sources for SPARX consist of 60 MW peak S-band klystrons. Three manufacturers, Thales (F), CPI (US) and Toshiba (JP), develop klystrons which meet the requirements of the SPARX LINAC.

A set of klystron parameters is given in Table 5.7. RF power sources of comparable specifications are being used in other accelerator laboratories. The pulse repetition rate of 100 Hz would not be a problem since already, at SLAC, S-band klystrons operate at 120 Hz. Each klystron, equipped with beam focusing coils, will be supplied by a High Voltage (HV) Modulator and installed in the upper tunnel of the LINAC.

Table 5.8: SPARX klystron main specifications

<i>Frequency</i>	<i>2.856 GHz</i>
RF Pulse Duration	4 μ sec
Repetition Rate	100 pps
Cathode Voltage	350 \div 370 kV
Beam Current	400 \div 420 A
HV Pulse Duration	6 μ sec
RF Peak Power	60 MW

Basically, a HV Modulator consists of an HV charging unit, a Line-Type Pulse Forming Network (PFN) and a 1/n HV pulse transformer, immersed in a tank filled with insulating oil. The system, schematically shown in Figure 5.43, generates almost rectangular HV pulses, applied to the klystron cathode, after the PFN discharge that occurs when the HV switch, that can be a thyatron or a

solid state device, is operated by a trigger signal. The nominal HV pulse duration is 6 μsec FWHM with rise and fall time, determined by the PFN parameters, respectively of 0.5 and 1 μsec .

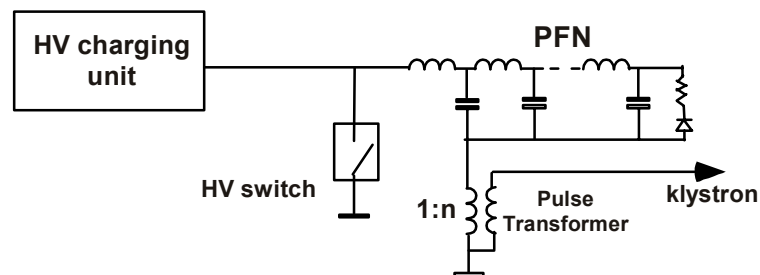


Figure 5.43: Schematic layout of a Pulsed Power Modulator

Recently it is proposed to replace the line-type PFN with a series of solid-state switching boards. The goal is to make compact the modulator size and lower the primary voltages but the long term reliability of this solid state solution is still to be proved. The HV Modulators for scientific applications are very special systems produced by a few specialized industries. The main features are the very high voltage of the modulator pulse needed to drive the klystron and some tight requirements regarding amplitude and pulse-to-pulse phase stability.

Table 5.9 gives the parameters for a SPARX modulator.

Table 5.9: SPARX klystron main specifications HV Pulsed Modulator parameters

Modulator Pulse Voltage transformer primary	25 kV
Pulse transformer secondary voltage/klystron gun	370 kV
Pulse transformer secondary current/klystron gun	420 A
Pulse transformer ratio	1/15
High voltage pulse duration (FWHM)	6 μsec
High voltage rise/fall time (0 to 90%)	0.5 / 1 μsec
Pulse flatness during flat-top	$\pm 0.1 \%$
Pulse to pulse Voltage fluctuation	$\pm 0.3 \%$
Pulse repetition rate	$\leq 100 \text{ Hz}$

5.2.3 RF Power distribution

The layout of the standard RF power station proposed for SPARX is depicted in Figure 5.44. The 60 MW klystron sources feeds, through the KEK-type energy compressor, 3 SLAC-type accelerating structures (with dual symmetric feeding for the pre-injector). To divide equally the RF power among 3 units, a 4.8 dB directional coupler is used to draw 1/3rd of the full power for feeding the first section. A 3 dB directional coupler split to half the remaining power to the following sections.

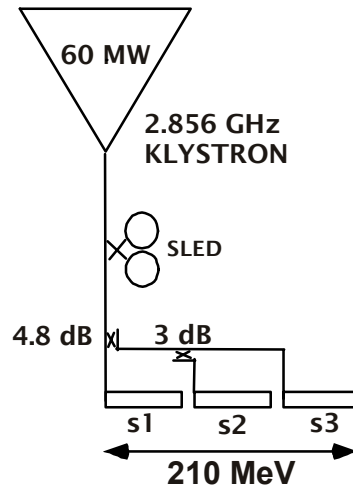


Figure 5.44: Layout of the SPARX RF Power Station

About 50 MW peak are available to each accelerating structure after the energy compressor. Such a power level produces an average accelerating gradient of 23.5 MV/m that means an energy gain of about 215 MeV per RF station.

The Figure 5.45 shows the layout of the 150 MeV pre-injector. The first klystron RF pulse, by means of shunt or series-tee, is divided in 2 equal amounts. The RF pulses are then re-combined with an hybrid-junction or a magic-tee. The use of an hybrid-junction (HJ) to split the RF power, like those used in SLED devices, allows to change freely the gun input power level without dissipating RF power in dummy loads as those employed in waveguide attenuators. This is accomplished by varying the phase of one input HJ signal with a 180° waveguide phase-shifter. The second output port of the hybrid unit supplies the 1.5 GeV RF deflector (RFD-2) that is a travelling-wave unit and therefore a circulator is not required to protect the klystron-1 from reflected power. The 1.5 GeV RFD-2 is supplied with a 130 m. long rectangular WR280 waveguide. The power loss in WR284 waveguides at 2.856 GHz is about 2dB/100m so that, to feed 12 MW to the RFD, a power of about 22 MW must be drawn from the hybrid-junction second port. By adjusting the phase of the input HJ port, it is possible to switch off the deflector when not in use. Complete power dividers are manufactured by the RF industry too (see sketch in Figure 5.46) and provide continuously variable division of input power from insertion loss to -30dB. The RF power may be split between the output ports in any desired ratio. One of the outputs of the power divider may be equipped with a phase shifter to provide two outputs that are continuously variable in both power and relative phase up to 360 degrees. However, hybrid devices have usually an isolation not much greater than 30 dB.

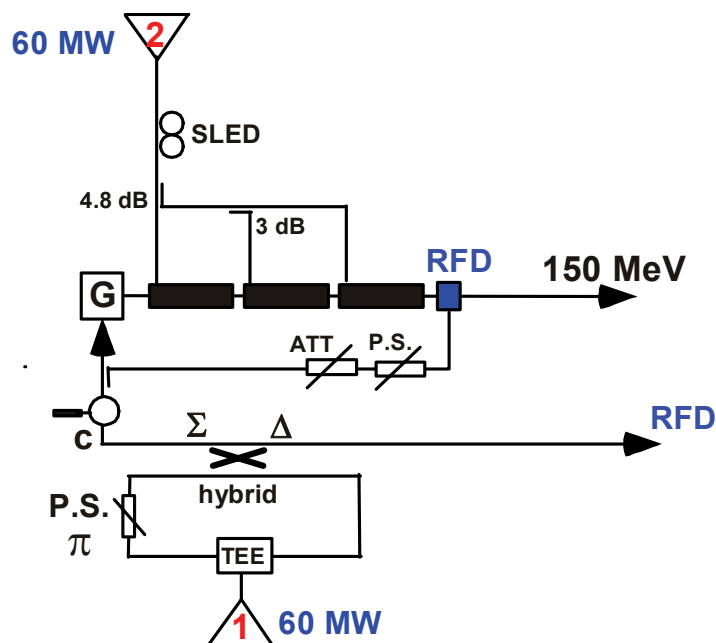


Figure 5.45: SPARX pre-injector layout

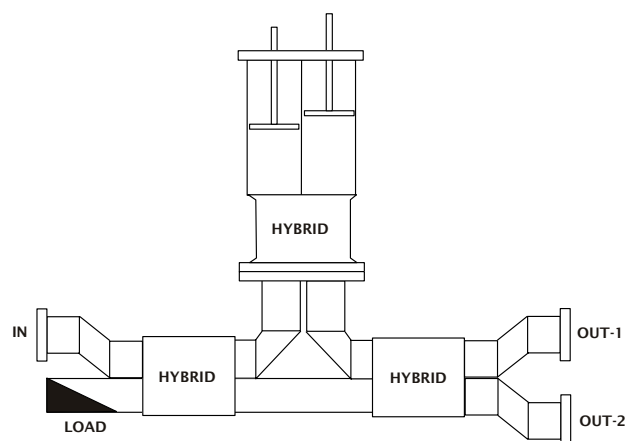


Figure 5.46: Sketch of a variable S-band power-divider

Therefore, a residual deflecting RF power ≥ 6 kW will be available at the RFD-2 input port. It can perform negatively on the beam parameters and must be additionally damped to a few watts with a variable waveguide attenuator sited before the RFD-2. If this were not enough, the use of a dedicated station for the deflector must be foreseen.

A power circulator protects the klystron#1 against the power reflected by the RF gun, that is a SW cavity. Moreover, one-tenth of the gun power is drawn with a 10 dB coupler to feed the first RF deflector RFD-1. The second 60 MW klystron, through the pulse compressor (SLED), feeds three accelerating structures.

The 60 MW RF station configuration is repeated, according to the Figure 5.2.1.2, for 7 units up to > 1.5 GeV and for further 7 stations up to > 2.4 GeV.

A network of rectangular WR284 copper waveguides distributes the RF power to the SLED's and to the accelerating structures. The waveguides are pumped down to 10^{-8} mbar with a distributed pumping system and are

connected to the accelerating structures through ceramic windows to protect the beam line vacuum.

Precise RF phasing of the LINAC will be achieved by means of motorized waveguide-phase-shifters positioned before 2 sections over 3 of a power station, being the third one regulated at low RF level. The RF power at the most significant locations of the power distribution network are monitored by means of waveguide 60 dB directional couplers. The main points to be monitored are the klystron outputs and the input/output ports of the accelerating structures.

5.2.4 IV HARMONIC SYSTEM

One X-band RF section ($f_{rf}=11.424$ GHz) is foreseen in the SPARX layout to linearize the compression by removing the quadratic energy-time bunch correlation generated in the LINAC structures before the magnetic bunch compressors [47]. It operates at 180° before BC1 and BC2 magnetic chicanes [48] at a relatively low gradient, $\approx 33\div 45$ MV/m, and decelerates the beam of $\approx 20\div 27$ MeV. A more linear correlation allows the bunch to be compressed to a much smaller length than in the case without the X-band section, without heavily affecting the longitudinal bunch current profile, i.e. without giving rise to sharp temporal spikes that may drive unwanted collective effects such as Coherent Synchrotron Radiation (CSR) and longitudinal wakefields in the undulators. Furthermore the level of the final compression is also made much less sensitive to the bunch arrival time errors (timing jitter).

The magnetic compressor chicane transforms the energy deviation $\Delta E/E_0$ to a path-length deviation [47] and it is used to compress the energy chirped bunch:

$$z = z_0 + R_{56}(\Delta E/E_0) + T_{566}(\Delta E/E_0)^2, \quad (5-7)$$

Where the momentum compaction (R_{56}) of a chicane made up of rectangular magnets with small bending angle and for ultra-relativistic electrons can be written as:

$$R_{56} \equiv \frac{\partial z}{\partial \delta} \approx -2\theta_B^2 \left(\Delta L + \frac{2}{3} L_B \right), \quad (5-8)$$

and where $\delta = \Delta E/E_0$, θ_B is the bending angle, L_B the bending magnet length, ΔL the drift length between the magnets and bunch head at $z < 0$. The second-order momentum compaction (T_{566}) of a rectangular-bend chicane (no quadrupole magnets) is $T_{566} \approx -3/2 R_{56}$. The relative energy deviation after a LINAC s-band accelerating section and a X-band structure can be written at the second order as:

$$\Delta E/E_0 \approx \left(\frac{-eV_0 k_s \sin \varphi_s}{E_0} \right) z_0 + \left(\frac{-eV_0 k_s^2 \cos \varphi_s - eV_x k_x^2 \cos \varphi_x}{2E_0} \right) z_0^2 \approx a z_0 + b z_0^2 \quad (5-9)$$

substituting (5-9) in (5-7) we can write:

$$z = (1 + aR_{56})z_0 + (bR_{56} + a^2T_{566})z_0^2 \quad (5-10)$$

To linearize the transformation the second term must be set to zero:

$$bR_{56} + a^2T_{566} = 0 \quad (5-11)$$

with the IV harmonic RF section this second order term in the compression can be cancelled applying (5-11) for $\varphi_x = \pm\pi$ ($eV_x \geq 0$):

$$b = -\frac{T_{566}}{R_{56}}a^2 \approx \frac{3}{2}a^2, \quad (5-12)$$

or

$$\frac{-eV_0k_s^2 \cos\varphi_0 + eV_x}{2E_0} = -\frac{T_{566}}{R_{56}} \left(\frac{-eV_0k_s \sin\varphi_0}{E_0} \right) \quad (5-13)$$

The second order effect is to be compensated so the RF phase of the harmonic section should be chosen at decelerating crest.

In the Figure 5.47 and Figure 5.48 the severe effect on the longitudinal bunch distribution of a compression scheme without x-band correction is shown for the BC1 SPARX chicane; in figures Figure 5.49 through Figure 5.51 the same final bunch compression case with the X-band applied can be compared.

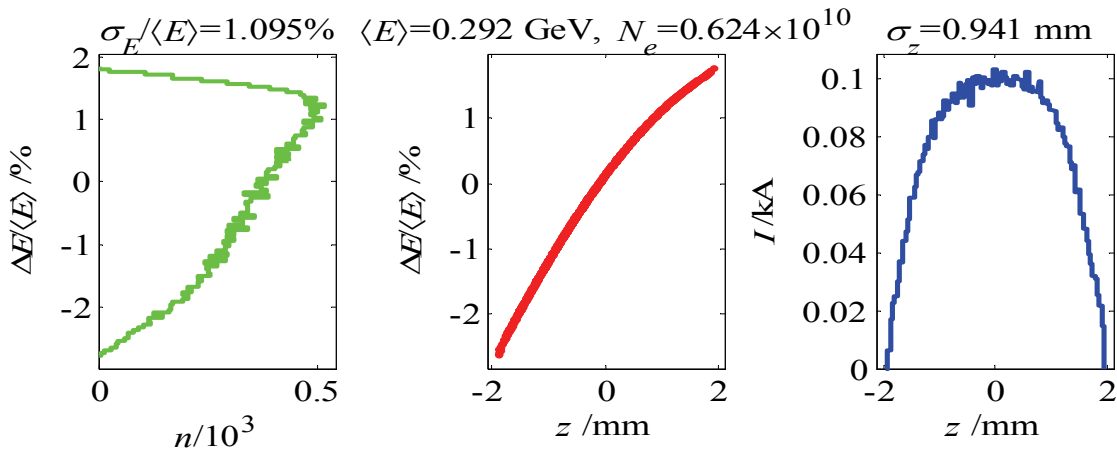


Figure 5.47: Energy profile, (left), longitudinal phase space (center), and temporal profile (right), after L1 SPARX LINAC, prior to BC1 compressor, X-band switched OFF (bunch head at $z \leq 0$).

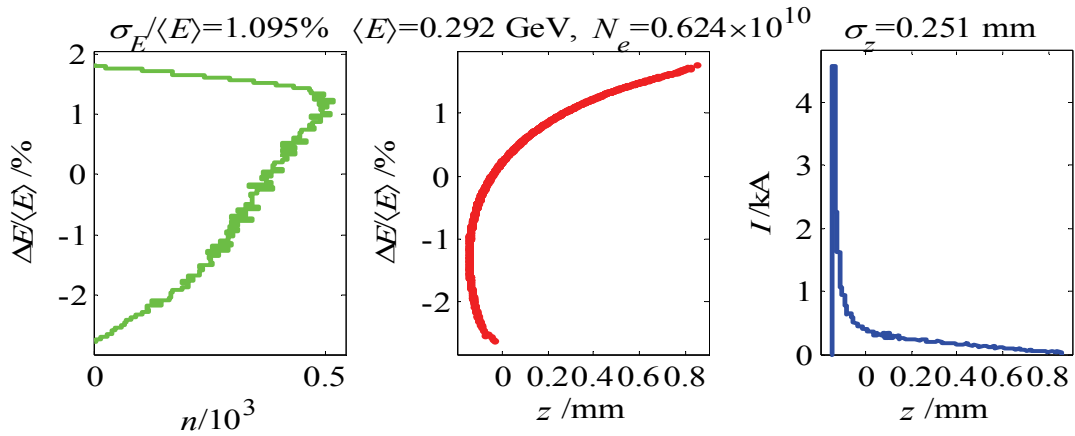


Figure 5.48: After BC1 compressor with x-band RF switched OFF.
 The sharp current spike is evident at the bunch head.

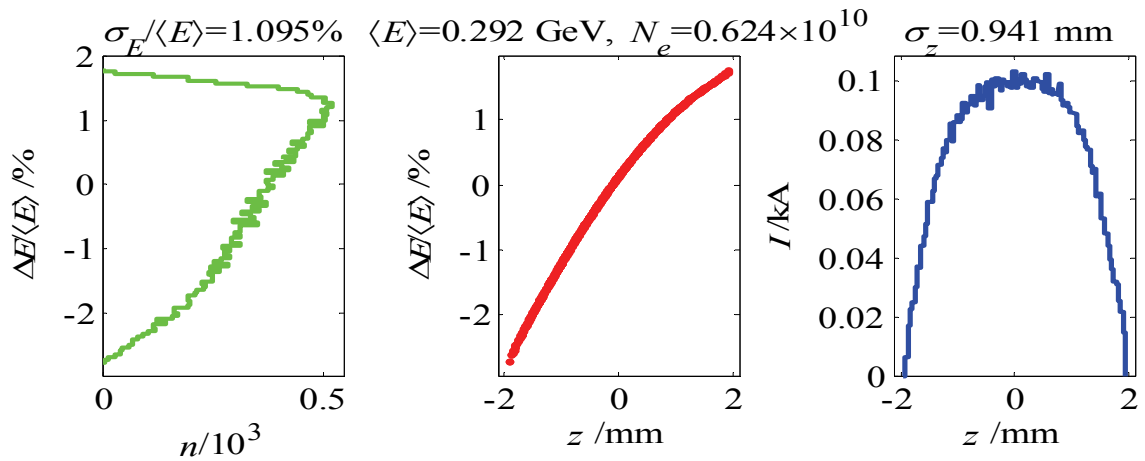


Figure 5.49: Phase space after L1 LINAC prior to X-band RF section.

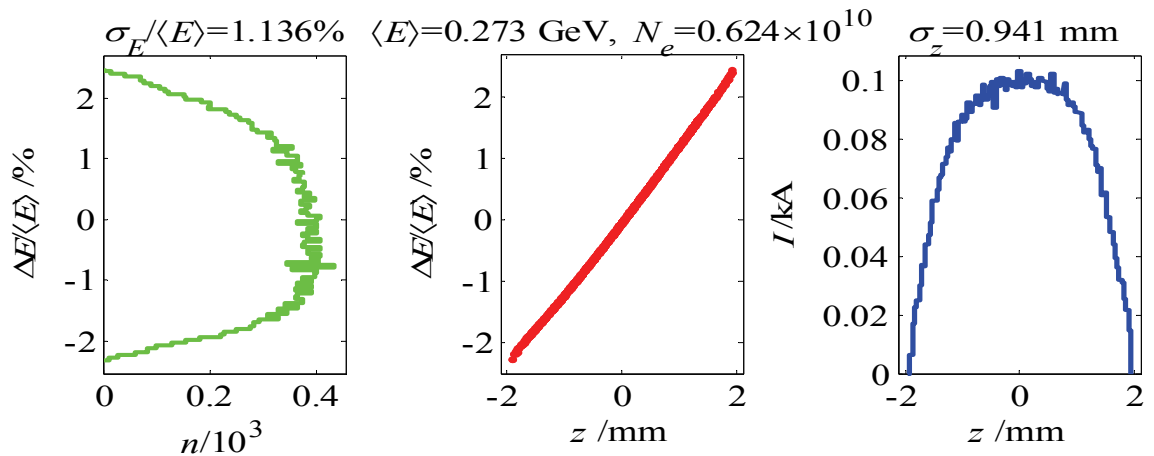


Figure 5.50: Phase space before BC1 but after X-band RF switched on at 20 MV.

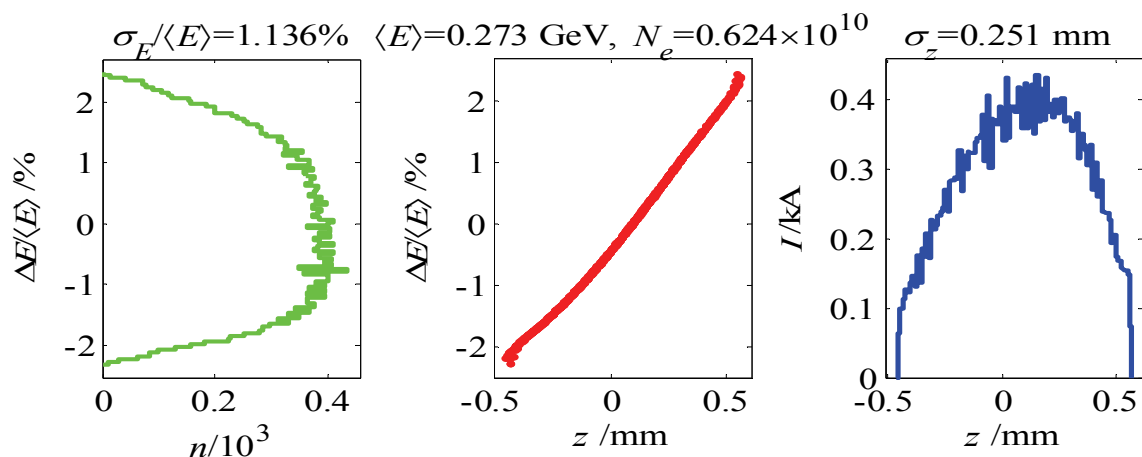


Figure 5.51: Phase Space after BC1 chicane, with X-band RF ON. The compressed temporal distribution at right is nearly the same as the initial profile of Fig. 3.

5.2.4.1 X-band power source and structure

One X-band RF section working at 11.424 GHz (i.e. the 4th harmonic of the LINAC frequency), is foreseen in the SPARX layout.

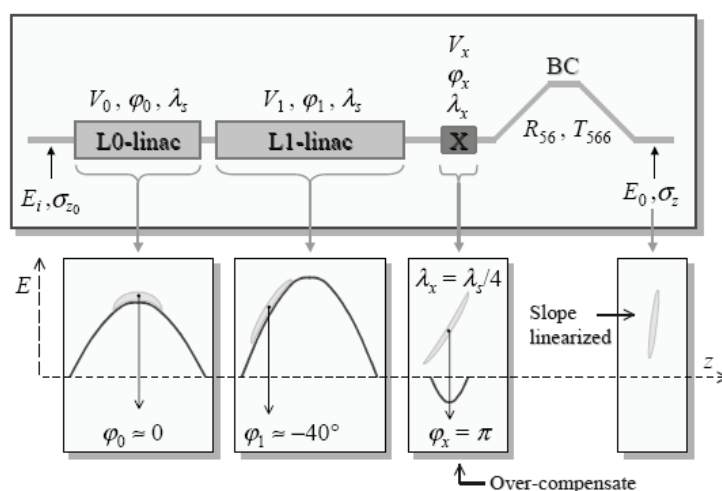


Figure 5.52: Schematic of two LINAC segments followed by harmonic RF and compressor chicane. The bunch is compressed from an initial σ_{z0} rms length to a final length σ_z with initial energy E_i and final energy E_0 (bunch head at left: $z < 0$).

A decelerating field in the X-band structure will be achieved by operating at -180° off the RF crest. To provide this decelerating field, the structure needs to operate at a gradient of 45 MV/m, that is a decelerating voltage of 27 MV. The beam will then be decelerated from 277 MeV down to 250 MeV before entering the first bunch compressor chicane BC1. Table 5.10 shows the X-band RF system requirements to achieve the required deceleration for SPARX.

Table 5.10: SPARX X-band RF requirements

<i>Parameter</i>	<i>Value</i>	<i>Units</i>
Structure Length	0.6	m
Structure Voltage	27	MV
Structure Gradient	45	MV/m
RF phase	-180	deg
RF power at the structure	20 to 40	MW
Repetition Rate	100	Hz
RF Pulse Length	0.4	μ s

5.2.4.2 Preliminary cavity design

Preliminary studies on the 60 cm long TW Constant Impedance structure have been made. The operational frequency is 11.424 GHz and the cell-to-cell phase variation is $2\pi/3$. This choice has been guided by many years of experience devoted at SLAC and KEK in the development of X-band RF components. The device consists of 66 RF cells coupled through on-axis irises with dual-side input-output coupling cells to match the structure with the X-band rectangular waveguides and compensate for the transverse kick caused by single couplings [49].

5.2.4.2.1 Single period consideration

With the HFSS simulation code we have estimated the RF parameter sensitivities at the geometry variations and the possibility to reach the needed voltage within the RF breakdown limit of such structure on the basis of the SLAC studies [50]. The irises thickness has been fixed to 2 mm and the period length to 8.75 mm. From the sensitivities analysis the iris aperture radius is the parameter most sensitive. We have choose to varying the iris radius from 3 mm to 5 mm, consequently the single cell radius must be varied to tune the single period at the operating frequency. A sketch of single period with the electric field magnitude normalized to the equivalent axis gradient of the TM_{010} -like mode is visible in Figure 5.53.

Table 5.11

<i>Dimentions</i>	<i>Value [mm]</i>
P	8.75
r_i	3 ÷ 4
r_c	10.393 ÷ 11.163

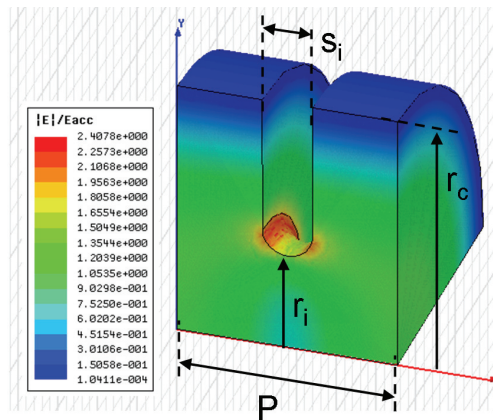


Figure 5.53: A quarter of single period with geometry dimensions.

The longitudinal series impedance per unit length, the attenuation constant (due to copper losses), the group velocity and the filling time of the entire 66+2 cells structures at different iris radius values are reported in Figure 5.54. A strong variation in efficiency and filling time is evident from the diagrams. Structures with small irises are more efficient but have longer filling times and more losses, furthermore, smaller irises lead to more intense wakefields. Greater efficiency geometries involve a careful study of the effects of the wakefields.

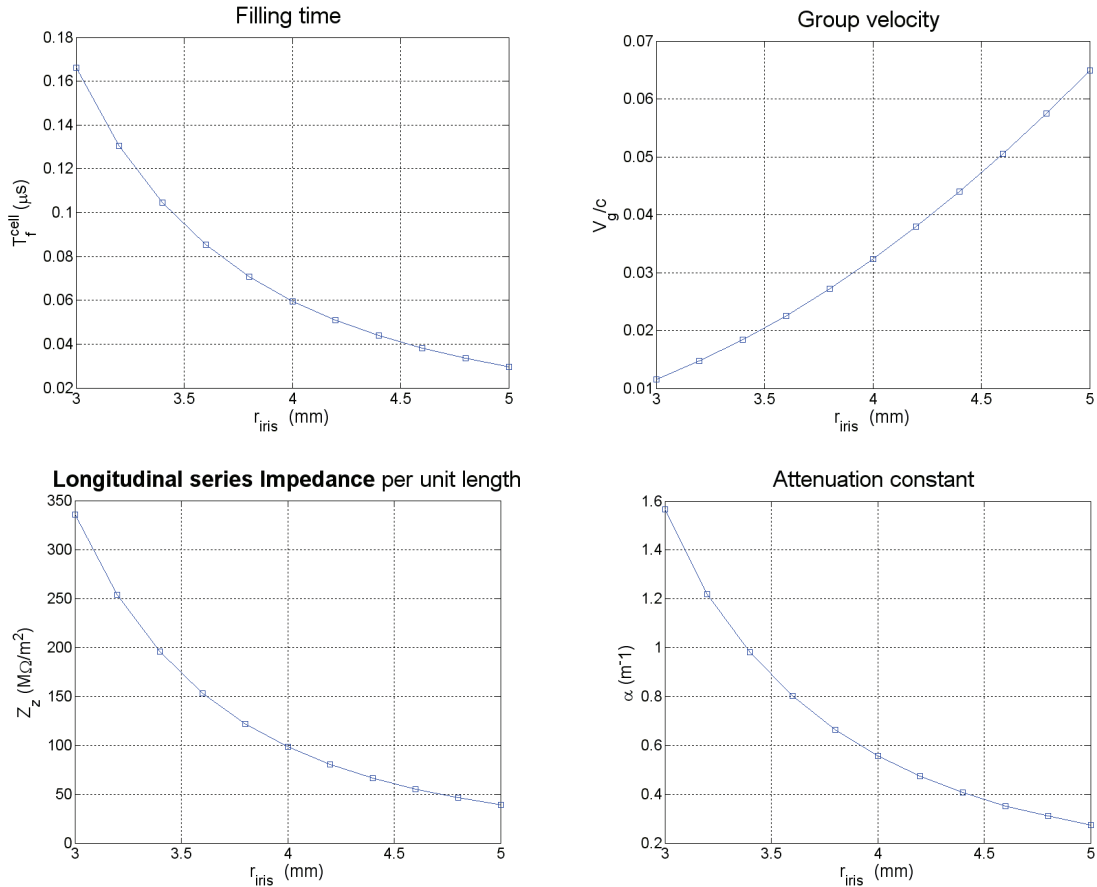


Figure 5.54: RF parameters at different iris aperture radius.

The power required to reach 27 MV accelerating voltage on crest in an area of 0.6 m at different iris radius is depicted in Figure 5.55. By choosing a radius equal to 3.6 mm requests deceleration of the SPARX beam can be met using a power not exceeding 20 MW, much less of 50 MW available power at the klystron output already tested at SLAC and KEK.

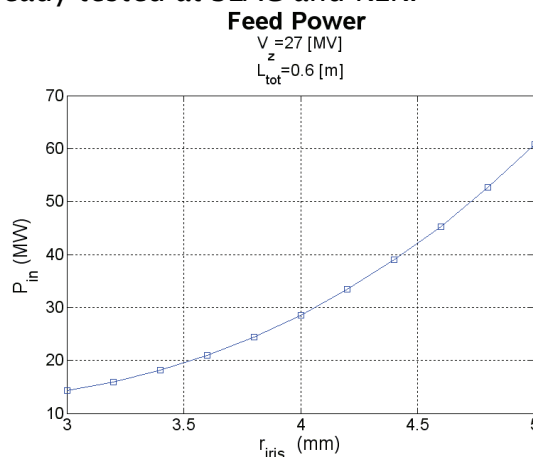


Figure 5.55: Required power at the cavity input port.

After choosing the right geometry, the average accelerating voltage is obtained at different input power for a given total length or at different structure length for a given input power. With a 3.6 mm iris radius, the following curves are given in Figure 5.56.

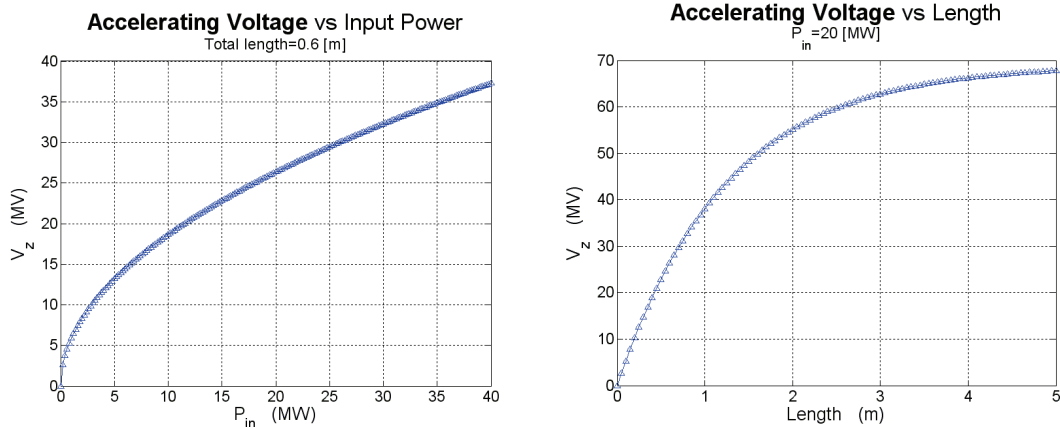


Figure 5.56: Accelerating voltage vs available power and section length.

The maximum surface electric field normalized to on axis equivalent accelerating field has been calculated and reported in Figure 5.57. The maximum surface field is approximately constant and 2.5 times the equivalent on axis field for all iris dimensions.

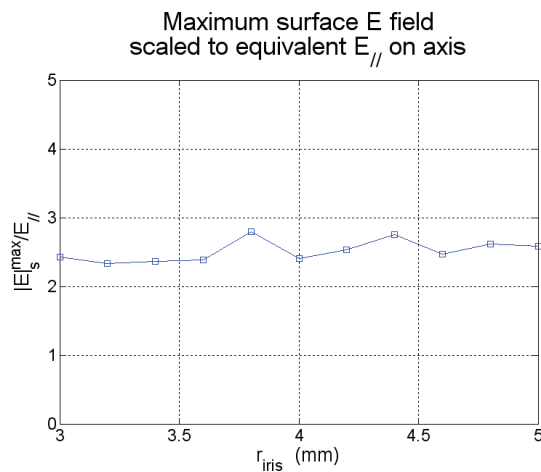


Figure 5.57: Normalized maximum surface electric field vs iris radius.

5.2.4.2.2 Coupler cell consideration

An example of a multi-cell TW accelerating structure with the input and output dual-side coupler cells is sketched in Figure 5.58. The dual feed coupling was chosen to minimize the transverse electric component of the field on axis due to azimuthal coupler asymmetries.

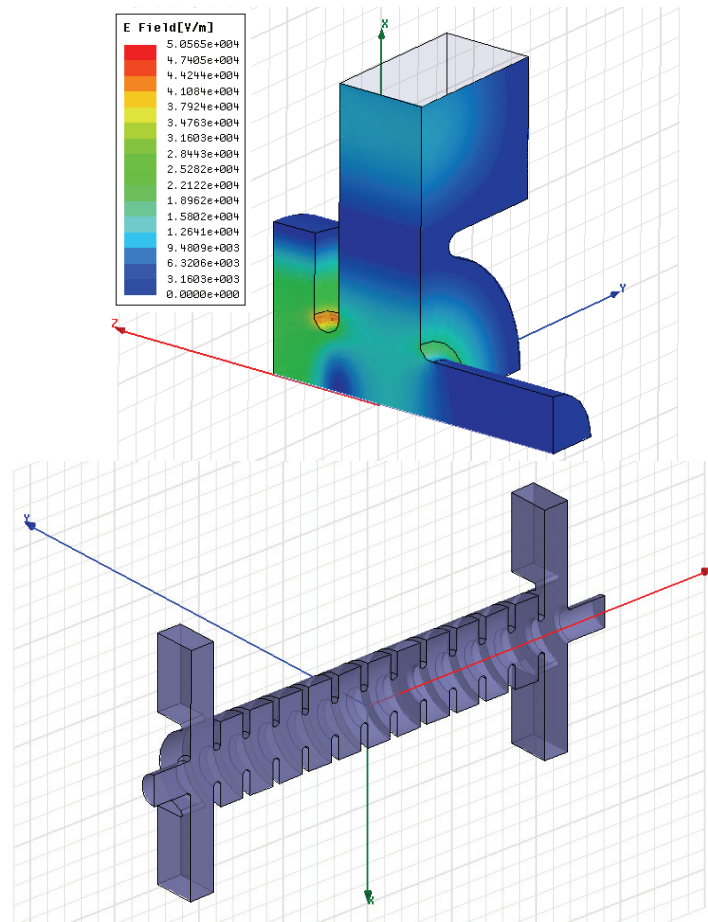


Figure 5.58: (Left) A quarter of coupling cell having rounded window edges; (Right) An example of multi-cell TW structure.

The coupler radius and window aperture must be dimensioned to match the input power to the correct cell-to-cell phase variation (120°). Preliminary coupler cell simulations with coupler windows without mating edges but with rounded connections show that it is possible to limit the maximum surface electric field below the maximum field of the rest of the cavity, by increasing the curvature radius of the coupler window edges. The maximum input power is limited by the maximum surface field already analyzed in Figure 5.57.

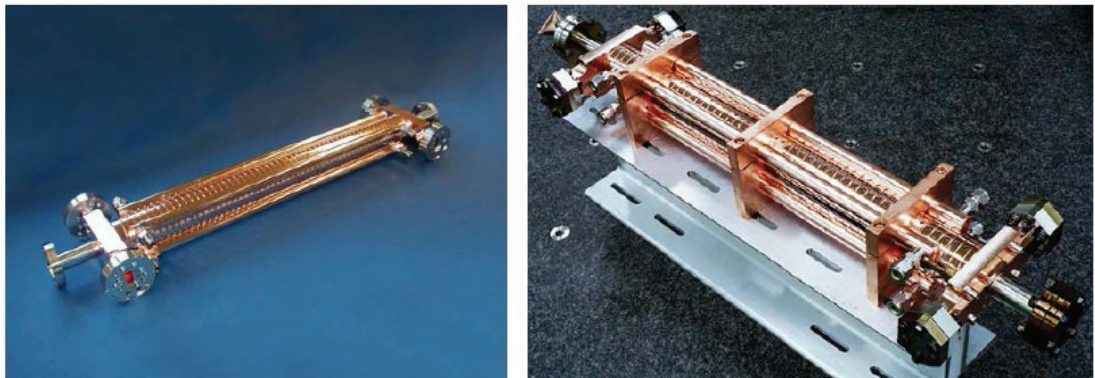


Figure 5.59: X-band TW sections manufactured and power tested at SLAC (left) and KEK (right)

5.2.4.3 X-band power sources

The X-band RF power source for SPARX is a 50 MW peak klystron. Two manufacturers, SLAC and Toshiba (JP) can develop klystrons [51,52,53] which meet the requirements of the SPARX LINAC. The X-band klystron development program at KEK was originally designed for 80 MW peak power at 400ns pulse length. The main parameters of the klystron needed for SPARX are given in Table 5.12.

Table 5.12: Specifications of X-band klystron for SPARX

Frequency	11.424 GHz
RF Pulse Duration	0.4 μ sec
Repetition Rate	100 pps
Cathode Voltage	460 kV
Beam Current	237 A
Gain	53 dB
RF Peak Power	50 MW

To date, 13 XL-4 X-band klystrons (shown in Figure 5.60) have been manufactured at SLAC in the frame of the NLC/JLC collaboration. Their successful operation up to 50 MW RF power, at repetition rates of 60 Hz and pulse length of 1.5 μ s make it a good candidate for SPARX. Upgrading these sources to 100 Hz rep. rate, needed for SPARX, does not seem a difficult task.

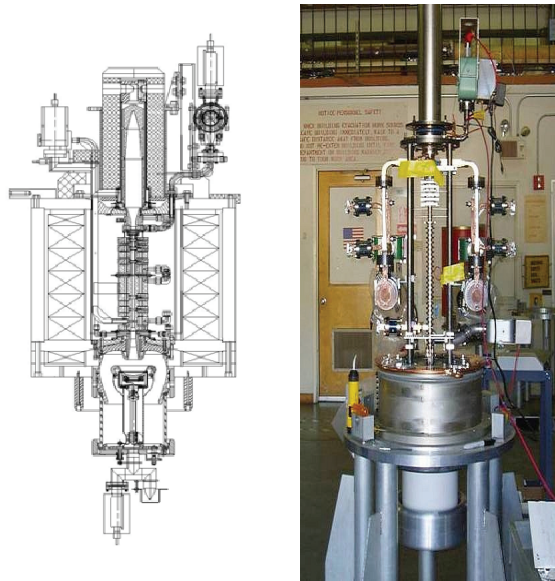


Figure 5.60: The XL-4-X klystron developed at SLAC

5.2.5 S-C-X-BAND SYSTEMS COMPARISON

The normal conducting accelerator at S-band frequency is still commonly used because of its well established technology and lower development cost. The main features of the SPARX LINAC based upon the S-band technology are described in previous paragraphs.

Most challenging accelerator based on the normal conducting technology are C-band (twice of S-band frequency) and X-band accelerator systems (four times the S-band frequency).

5.2.5.1 C-band LINACs

The C-band (5712-MHz) is used in the main accelerator of the Japanese X-ray free electron laser (X-FEL) facility, SPring-8 [54].

The C-band Spring-8 LINAC complex consists of two choke-mode accelerating structures, an RF pulse compressor, a 50-MW klystron, and a 110-MW compact modulator power supply.

These units have been operated in the SCSS (SPring-8 Compact SASE Source) 250-MeV accelerator. After RF conditioning, the achieved accelerating gradient is 35 MV/m.

The accelerating structures (1.8 m long) are quasi-CG sections composed of 91 RF cells. They operate in the $3\pi/4$ traveling wave mode. The average shunt impedance is 54 M Ω /m while the attenuation parameter and the filling time are respectively 0.53 and 300 nsec. The choke mode design eliminates the wakefield generated by the beam in multi-bunch operation. The frequency is finally adjusted by a very efficient feedback system control of the cooling water temperature. The fabrication of the C-band accelerating units has been made by Mitsubishi Heavy Industries.

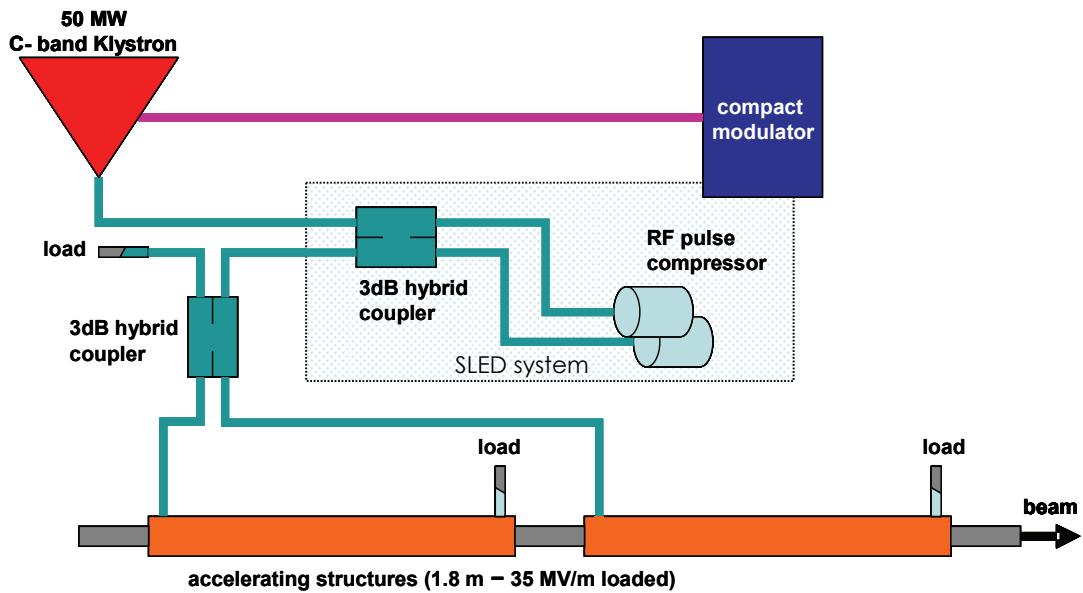


Figure 5.61: Layout of the S-pring8 C-band LINAC, Japan

The RF pulse compressor system consists of one pair of high-Q cavities and one 3-dB coupler. Considering the average in 300-nsec filling time, the power gain is about 3 in conservative operation, when spike peak of output pulse are suppressed.

The klystrons, manufactured by Toshiba, provide 50 MW output power and their reliability has been proved after a rather long operation.

The schematic layout of the S-Pring8 C-band LINAC is shown in Figure 5.61.

5.2.5.2 X-band LINACs

The X-band (11.424 GHz) was originally developed for main accelerator technology in the e+e- linear collider joint project NLC/JLC. The interest on X-band LINACs is today growing again because of the decision to adopt this technology for the CTF3/CLIC project at CERN.

In the mid-1990's, accelerator groups of SLAC and KEK begin started R&D on X-band RF technology. Significant advances in pulsed HV and RF power generation, high gradient acceleration and wakefield suppression have been made until now.

The accelerating structures considered for the NLC/JLC are conventional traveling wave sections. The cell dimensions are about one-fourth of those of S-band LINACs. The phase shift per cell was at first $2\pi/3$, but in the present design it is set at $5\pi/6$. The accelerating gradient is roughly constant over the structure length. Each RF unit includes one pulsed modulator which drives two klystrons of 75 MW peak power each and 1.6 μ s pulse width at 120 or 150 Hz. The klystrons feed an RF compression system that generates higher peak power (by about three times) in shorter (four times) pulses to match the accelerator structure requirements.

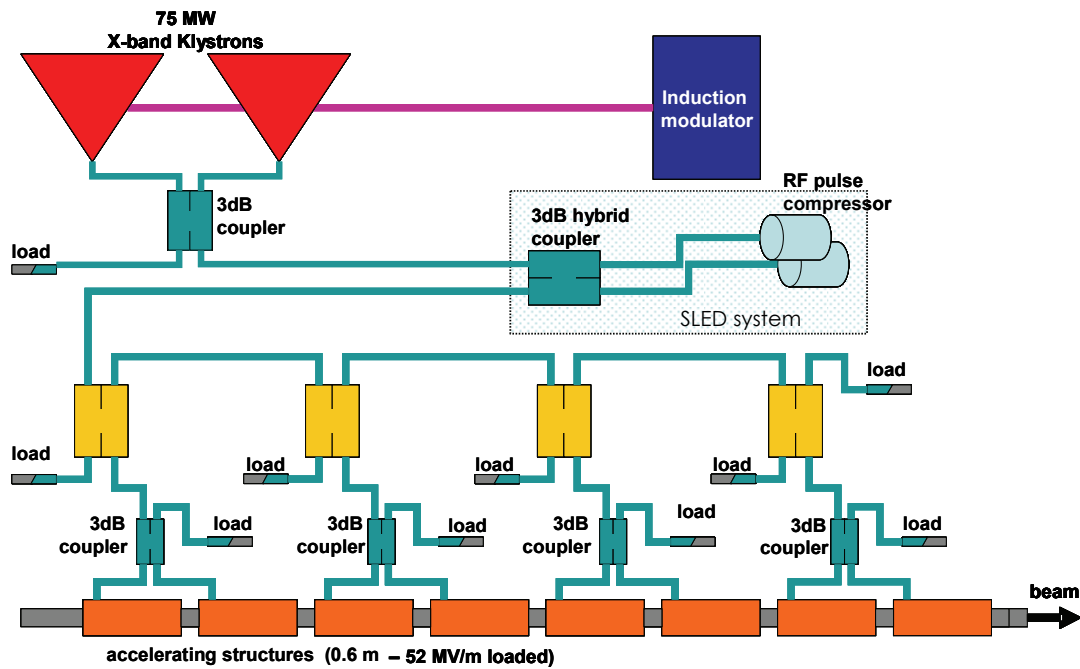


Figure 5.62: Scheme of the X-band LINAC developed for the JLC/NLC linear collider projects.

The resulting 400 ns, 475 MW pulses feed eight, 0.6 m accelerator structures, producing 65 MV/m unloaded gradient in each structure as shown in Figure 5.62.

5.2.5.3 Summary and conclusions.

The following comparison Table 5.13 summarizes the most significant parameters for the 3 LINAC technologies described above. The comparison is for 1 GeV module. Special microwave power components and accessories have been developed and tested at very high gradients both for C and X-band. These components are mainly klystrons, SLEDs, hybrid-junctions, directional couplers, accelerating structures. RF guns are not yet available at C and X bands.

C and X-band devices are, in general, not commonly available by the RF industry, but mainly offered by the original manufacturers, that are KEK or Mitsubishi, Toshiba and SLAC.

Table 5.13: Specifications of X-band klystron for SPARX Comparison of S-C-X band parameters for 1GeV module.

<i>Band</i>	<i>S</i>	<i>C</i>	<i>X</i>
Frequency [GHz]	2.8	5.7	11.4
Accelerating gradient [MV/m]	20	32	65
Number of klystrons	8	8	6
Kly peak power [MW]	60	50	75
Pulse compression ratio	3	3.5	3
Rep rate [Hz]	100	60	100
Kly pulse length [μ s]	4.5	2.5	1.6
RF pulse length at LINAC [μ s]	1.2	0.5	0.4
Section length [m]	3	1.8	0.6
Number of sections	16	16	24
Active length [m]	48	30	14.4

5.2.6 Low-level RF controls and feedbacks

The SPARX low-level RF system is a complex analog/digital/computer control system aimed to:

- Generate the proper RF pulses to drive the RF power plants, both in the S and X bands;
- Acquire and monitor signals sampled in many different selected locations in the RF waveguide network or directly in the high-power RF devices;
- Generate proper control signals, either manually (console settings) or automatically (feedback loops), to set required levels and phases of the RF fields in individual RF devices or groups of them. This part of the job can be also considered as a Timing and Synchronization task;
- Gather interlock signals coming from various machine sub-systems (RF, vacuum, safety, ...) to switch-off the RF under dangerous or improper conditions;
- Communicate with the machine central control system for operator interface and for information exchange. Actually, the control of the SPARX low-level RF system will be conceived and designed as a fully integrated part of the machine central computer control system.

From a logistic point of view the low-level RF system consists of an assembly of parallel units, each dedicated to the control of a single RF power station. A schematic of a typical SPARX RF power station equipped with its low-level control is shown in Figure 5.63. The scheme of each unit is very similar to the whole SPARC low-level RF control.

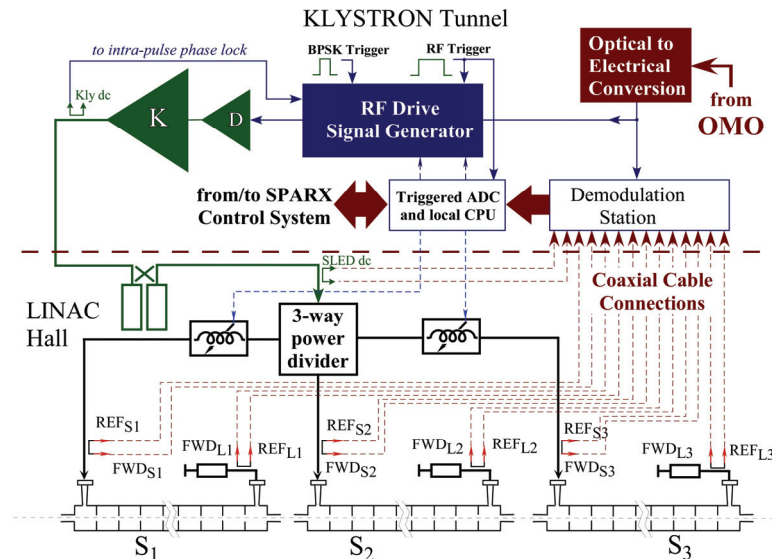


Figure 5.63: Schematics of the RF power station control system

A more detailed sketch of the RF drive pulse generator board is reported in Figure 5.64.

A CW RF reference tone extracted from the optical reference, transported to the RF station through a glass-fibre stabilized link, is the input of the analog RF chain generating the driving pulse for the power station. This low-level control section allows to set the phase and the level of the station, receive the main RF trigger and the phase inversion trigger from the Timing system to generate the proper RF pulse to feed a SLED equipped station, receives a sample of the klystron forward power to implement intra-pulse amplitude and phase feedback loops to correct wideband station noise.

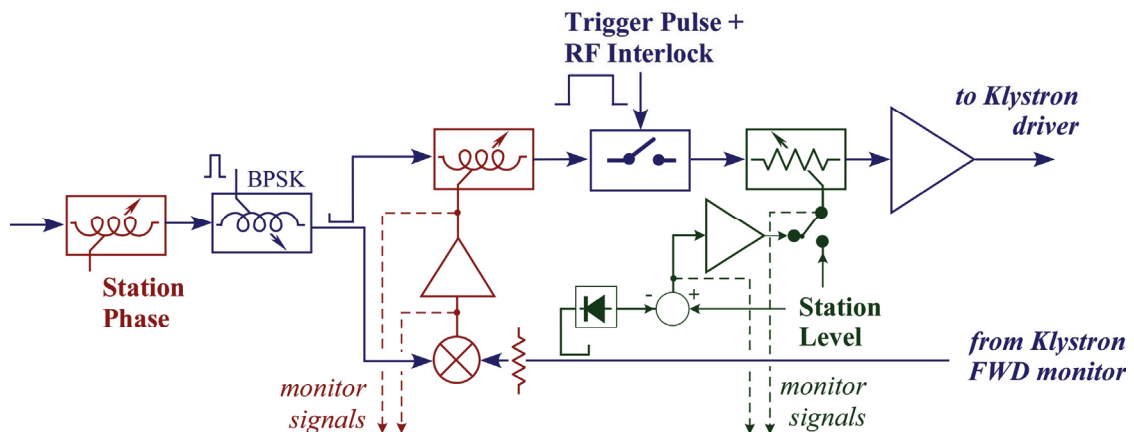


Figure 5.64: RF pulse generator board scheme

The RF pulse generated by the described analog driving line is sent to an RF pre-amplifier (a solid state driver for S-band plants, a TWT amplifier for the X-band plant) and from there to the klystron input. From the klystron output window the RF power is distributed to the various devices through a waveguide network incorporating the pulse compression section (SLED cavities, only in the S-band plants). Signals are sampled by directional couplers and RF probes in the vicinity or directly inside the high power RF devices, transported by low attenuation, temperature compensated coaxial cables. and collected by a main

demodulation station to monitor the field levels and the phase of the RF within the pulses. To extract the required information the signals are base-band converted by I&Q mixers and/or diode peak detectors, as schematically shown in figure 5.2.7.3. The I&Q components of the signals allow an amplitude independent, 4-quadrant phase demodulation. In order to increase the signal-to-noise ratio in the demodulation process it is convenient to exploit the large peak voltages of the sampled signals (> 1 W typically) by using high level mixers (for instance level +27 dBm, as in the SPARC case). However, this implies the presence of an additional RF amplification stage to generate all the required LO reference signals at the specified level.

Peak detectors are used for phase independent RF level measurements. They are also used for level monitoring of all the RF signals that require only amplitude demodulations, such as RF reflected power at the input and output ports of the TW accelerating sections. Referring to the Figure 5.65, each RF signal entering the demodulation station is connected to an I&Q mixers and/or to a peak detectors, and produces from 1 to 3 base-band signals. Therefore, being N and M the number of RF signals and LO copies entering the board, and P the number of base-band signals produced, we always have $M < N < P$. A quite detailed evaluation on the type of demodulation needed by the signals sampled in a standard SPARX RF power station is reported in the Table 5.14. In this case the numbers of signals are $N=16$, $M=9$, $P=33$.

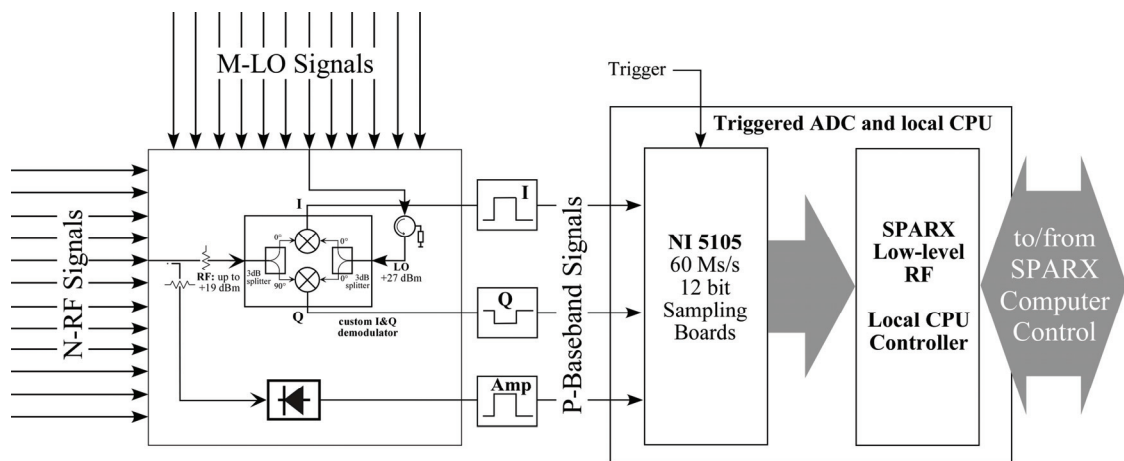


Figure 5.65: Scheme of amplitude/phase detection system of the RF signals

Table 5.14

<i>Signal</i>	<i># of demod. channels</i>	<i>Fit type</i>	
Klystron FWD	3 (I, Q, Diode)	Amplitude:	square pulse
		Phase:	square pulse
Klystron FWD	2 (I, Q)	Amplitude:	square pulse
		Phase:	square pulse
SLED FWD	2 (I, Q)	Amplitude:	piecewise exponential
		Phase:	piecewise linear
SLED RFL	1 (Diode)	Amplitude:	piecewise exponential
		Phase:	---
S1 IN FWD	3 (I, Q, Diode)	Amplitude:	piecewise exponential
		Phase:	piecewise linear
S1 IN RFL	1 (Diode)	Amplitude:	piecewise exponential
		Phase:	---
S1 OUT FWD	2 (I, Q)	Amplitude:	piecewise exponential
		Phase:	piecewise linear
S1 OUT RFL	1 (Diode)	Amplitude:	piecewise exponential
		Phase:	---
S2 IN FWD	3 (I, Q, Diode)	Amplitude:	piecewise exponential
		Phase:	piecewise linear
S2 IN RFL	1 (Diode)	Amplitude:	piecewise exponential
		Phase:	---
S2 OUT FWD	2 (I, Q)	Amplitude:	piecewise exponential
		Phase:	piecewise linear
S2 OUT RFL	1 (Diode)	Amplitude:	piecewise exponential
		Phase:	---
S3 IN FWD	3 (I, Q, Diode)	Amplitude:	piecewise exponential
		Phase:	piecewise linear
S3 IN RFL	1 (Diode)	Amplitude:	piecewise exponential
		Phase:	---
S3 OUT FWD	2 (I, Q)	Amplitude:	piecewise exponential
		Phase:	piecewise linear
S3 OUT RFL	1 (Diode)	Amplitude:	piecewise exponential
		Phase:	---
Fast Phase Loop	2 (monitor)	Error signal:	square pulse
		Working point:	square pulse
Fast Amplitude Loop	2 (monitor)	Error signal:	square pulse
		Working point:	square pulse

The resulting devices needed for single standard demodulation station are listed in Table 5.15.

Table 5.15

<i>Devices</i>	<i>Number</i>	<i>ADC channels</i>
I&Q mixers	9	18
Diodes	11	11
Baseband signals	4	4
		Total: 33

5.3 Electron Beam Diagnostics

5.3.1 Introduction

The SPARX-FEL performances are strictly related to the electron beam characteristics, so all the parameters of electron bunch have to be very precisely measured and controlled all along the accelerator and undulator sections.

The saturation length of the SASE FEL process is inversely proportional to the peak current and brightness of the electron beam, therefore electron bunches of high charge, short duration and small transverse sizes and energy spread are requested.

In this chapter the diagnostic tools are presented together with procedures used to perform the measurements on the electron bunches.

The normalized emittance produced in the injector is of the order of 10^{-6} mrad and it will be preserved all along the accelerating structures, the bunch compressors, the transfer lines and the undulators sections. High resolution beam profile monitors are placed in strategic positions to measure transverse beam sizes and emittances and are described in paragraph 5.3.3-5.3.5.

Another important characteristic of the electron beam produced in the accelerator is the very short bunch length; time resolved experiments using tens of femtoseconds bunch duration will be feasible in the FEL lines. The bunch length is measured with different methods: depending on the bunch length region, the visible or near UV light produced in the dipole, the synchrotron radiation, or in special screens, Optical Transition Radiation (OTR) is collected and measured by using a streak camera. A second method is the measure of the high frequency spectral component extracted via a waveguide inserted in the vacuum chamber; the electron bunch field is transferred in an outside lab and the amplitude of filtered frequencies are measured with a spectrum analyzer.

An alternative method is the use of an RF deflector that “streaks” directly the electron bunch on a screen and measuring the transverse size the bunch length is obtained. The combination of this device with the spectrometer line, composed by a dipole magnet and an OTR screen permits to measure the longitudinal phase space: on the screen is simultaneously projected the energy spread along the bunch length.

Slice emittance is also measured by using the RF deflector and OTR analyzing the transverse slice of streaked bunch (see paragraph 5.3.8.3).

The electron beam must pass at the center of the accelerating structure and e magnetic elements to maintain the emittance and to avoid undesirable dynamic effects. Precise alignment of the beam is performed by using beam position monitors to detect the position of the beam and steering magnets to correct the transverse misalignment

The beam trajectory has to be measured and controlled with a resolution of 10 μm along the accelerator and transfer lines and 2-3 μm in the undulator sections. Two different beam position monitor will be employed according the resolution requested: in the accelerator the strip line monitors, composed by 4 electrodes 13 cm long, are used. (see paragraph 5.3.9).

Table 5.16: Electron beam parameters

Energy [MeV]	6	2400
Charge [pC]	10	1000
σ_x, σ_y [μm]	10	1000
σ_z [ps]	0.1	10
$\Delta E/E$ [%]	1	0.01
$\epsilon_{nx}, \epsilon_{ny}$ [μrad]	1	1
ϵ slice [μrad]	1	1
Δq [pC]	1	100
Phase stability [fs]	10	10

5.3.2 Emittance diagnostic

Several diagnostic techniques will be used being mainly state of the art, plus few new developing tool to cross check the results.

The transverse projected emittance is one of the fundamental parameter to measure. The control of the beam emittance and the prevention of its dilutions are mandatory in the high brilliance light source. The longitudinal phase space contains also valuable information about the all the process of the emittance compensation, the acceleration and the space charge effects.

There will be three principal positions for these measurements: at low energy (5 MeV) just after the gun, at 150 MeV just after the first accelerating modules and the laser heater, the other at 1.5 GeV at the end of the LINAC. Further measurements can be also done in several other positions after both bunch compressors.

5.3.3 Electron beam diagnostic @ 6 MeV

The low energy beam is space charge dominated. In this regime the usual way to measure the emittance is to use a mask placed in the beam trajectory

We plan to measure the beam emittance and the phase space in both horizontal and vertical planes making use of a double system of horizontal and vertical slit masks made of 2 mm thick tungsten. The slit mask must stop, or strongly degrade, the intercepted fractions of the beam. By selecting an array of beamlets by means of an intercepting multislit mask or alternatively by creating one beamlet using a single slit moving transversely over the beam spot, we can divide the space charge dominated incoming beam into emittance-dominated beamlets drifting up to an intercepting screen. Assuming a linear screen response, the intensity of the beamlets spot on the screen is directly proportional to the number of particles in the beamlets hitting the screen. The emittance can be measured estimating the beamlets size [54]. Each mask (see Figure 5.66) consists of a slit array (7 slits, 50 μm wide spaced by 500 μm , 2 mm thick) and two single slits, 50 and 100 μm wide.

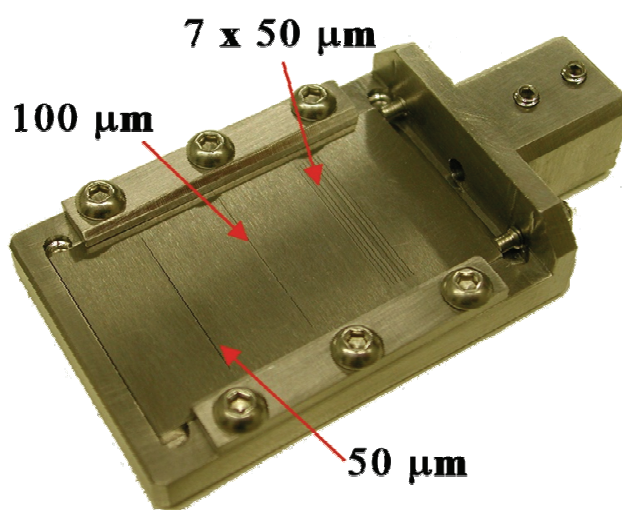


Figure 5.66: Slit mask composed of 7 slits of 50 μm width spaced by 500 μm , one slit of 100 μm width and one slit of 50 μm width

The slits will be manufactured by electrochemical etching, which provides, in comparison with mechanical machining, higher precision and improved smoothness of the slit edges. Each individual slit can be machined as a component of 0.5 mm height and later assembled into the frame. We have already used this system for the SPARC low energy measurements [55]. This configuration allows changes of the geometry of the slit mask simply by reshuffling the single components. The multi-slit mask can be used for single shot measurements, when the beam size is large enough for an adequate beam sampling by the slit array. Alternatively, a single slit can be moved across the beam spot in a multi shot measurement. In this case the range of transverse sampling can be freely chosen by adjusting the step between the different positions of the slit. The beamlets emerging from the slit mask can be measured by means of a downstream Ce:YAG radiator. The radiation emitted in the forward direction from the Ce:YAG crystal is collected by a 45 degrees mirror downstream the radiator, on the same screen holder. We observe the back side of the transparent crystal radiator, thus minimizing the degradation of the spatial resolution due of the optics field depth. The small thickness of the crystal (100 μm) prevents appreciable blurring effects due to the crystal bulk emission, as well as significant multiple scattering.

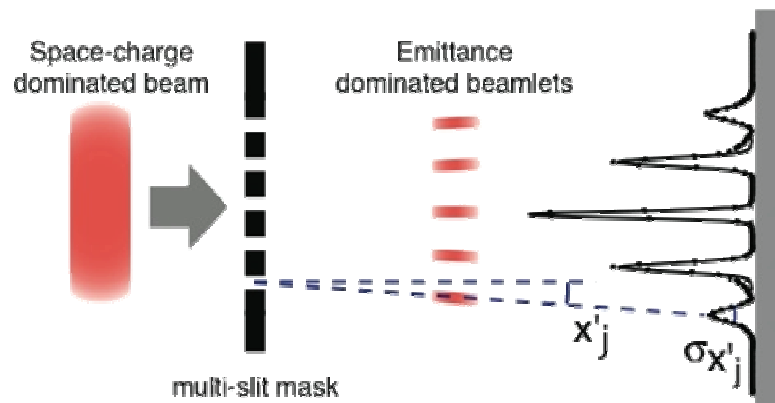


Figure 5.67: Sketch of the measurement geometry. A space charge dominated beam becomes a emittance dominated beamlets after the mask and drift to a fluorescent screen.

The 1D slit technique has several advantages respect to the pepper pot: the data analysis is simpler, the mask is easier to machine and the detail that can be measured on the beam are smaller because it is possible to arrange the steps between the slit positions.

The results produced by the analysis of the beamlets are samples of the beam phase space. These samples can be used to reconstruct, by interpolation, the phase space of the entire beam (see Figure 5.68), the accuracy depending on the number of the collected samples.

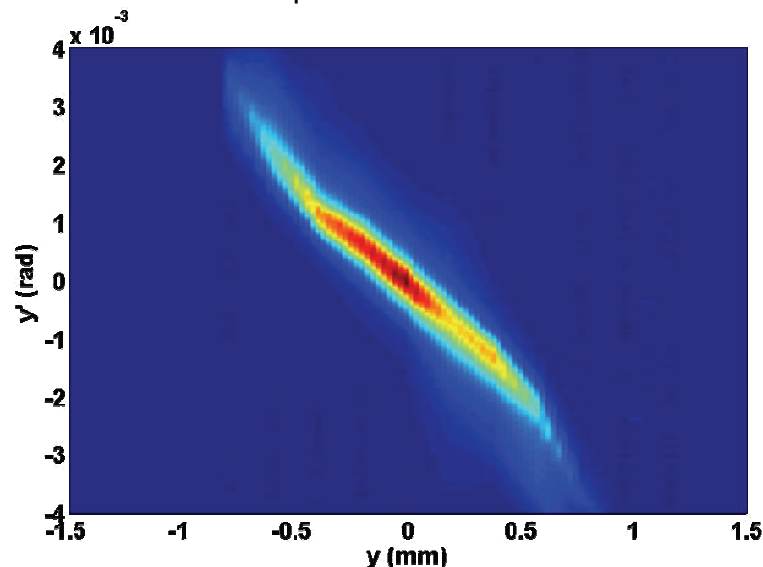


Figure 5.68: Reconstructed SPARC beam phase space from a slits measurements

The beam size, and in this case the beamlets size also, will be measured by intercepting screens, metallic for the production of the OTR, or scintillator. Stepper motor will be used to allocate several screens in one actuator. In the Figure 5.69 the drawing of such actuator with a YAG screen on the bottom part. The crystal will be normal respect to the beam direction with a 45 degrees mirror on the back.

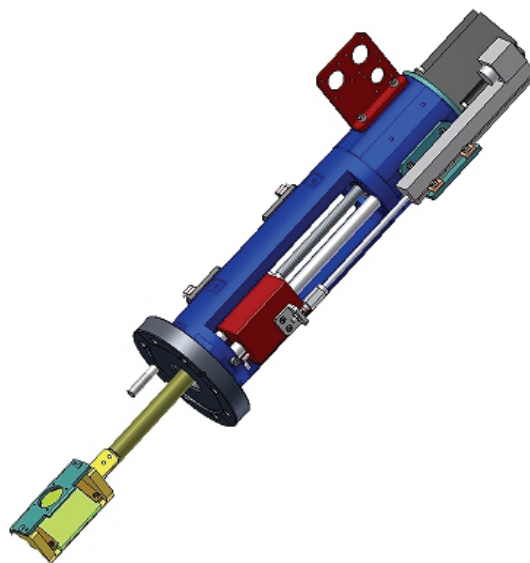


Figure 5.69: Actuator drawing with a YAG crystal mounted with a 45 degrees mirror

The use such geometry allows to look in the back side of the crystal without any problem regarding the depth of field.

The radiation coming from the screens in the beam line and leaving through vacuum windows will be collect by optical systems. The 2D image, single shot, contains valuable information of the incoming beam, such shape, centroid and rms beam size. TV lenses are wide used for light collection, giving a simple, robust and flexible solution.

Digital CCD camera with at least 12 bit depth will be used for signal digitalization. Lead shield screen will also prevent the damage of the CCD due to X-Ray exposure. These cameras will be connected by Firewire interfaces with the control system industrial PC all around the LINAC, using the same system that we have realized for FLASH at DESY [56] and that is working in stable and reliable mode from several years.

Both lenses that CCD will be motorized to change the magnification and gives the maximum flexibility in order to measure beams with different sizes.

5.3.4 Electron beam diagnostic @ 150MeV

The transfer line between the first LINAC section and the second one has been designed to fulfill the acceleration matching conditions. On the other hand this is a perfect zone to make a first complete diagnosis of the photo-injector beam properties.

The electron beam energy will be around 150 MeV at this point. The line layout has been studied to have the possibility of exploring different charge ranges. Furthermore it gives the possibility of either measuring the transverse emittances in the operating conditions with the “four screen method” (FS11, FS12, FS13, FS14), or carry on a deeper beam characterization. The quad scan

technique [57] can be used to retrieve information on the transverse brightness or can be coupled with the streaking of the RF deflector to measure the slice emittance (Figure 5.70). The presence of a deflecting cavity followed by a dispersive section, allows the beam time and energy structure to be measured at the same time (longitudinal trace space picture) or separately (time structure, mean energy and energy spread).

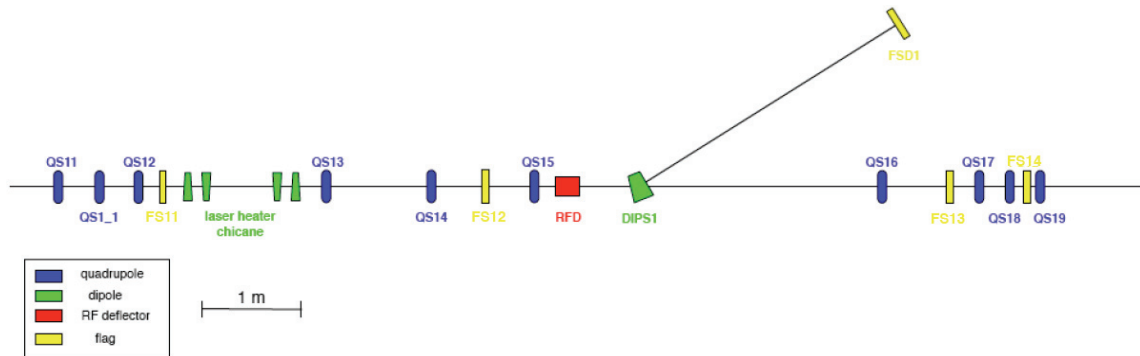


Figure 5.70: 150MeV Transfer line layout.

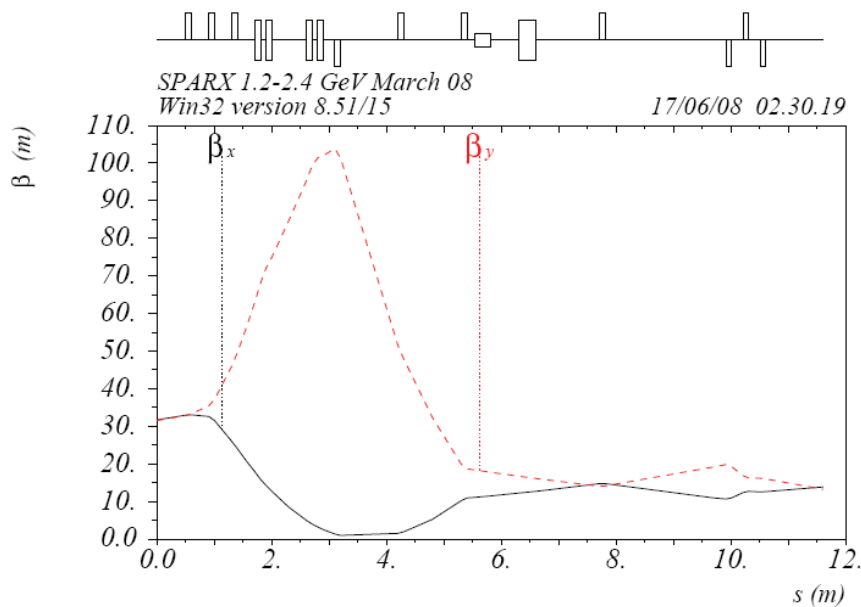


Figure 5.71: beta function along the transfer line in the operating conditions.

The first triplet of quadrupoles (QS11, QS1_1, QS12) on the line is dedicated to the matching between the TWISS parameters at LINAC exit and the “laser heater” device entrance. They can not be changed indeed to perform measurements on the beam, unless the chicane is bypassed. A change in the matching conditions between the laser and the electrons in the chicane could lead to dramatic changes of beam properties, far from operating conditions. The choice in designing the line has been that of maintain this triplet fixed during measurements.

The second triplet is designed to diagnose the beam properties. The FS13 target cross has been used to simulate the measurements of projected

emittance, slice emittance, and time structure, and the positions of QS13 QS14 and QS15 have been optimized to have a small waist on the target, and a variation of beam size compatible with measurements. The smaller round waist achievable is about 80 μm RMS. A round waist is needed, especially for measurements of slice and projected emittance. In this last measure indeed, the measurement procedure allows to measure horizontal and vertical emittances at the same time by variation of two quadrupoles (typically QS14 and QS15).

The space limit is such that after the laser heater chicane only three screens with 180 degrees of phase advance fit in. The “four screens” method [58] can indeed be fully applied only when the laser-electron beam interaction does not take place in the chicane, since a detailed matrix of the interaction would be needed. However an “on the fly” measurement is possible by using three screens, without information on the measurement errors.

To simulate the beam length measurement either 1 and 2 MW of RFD (Radio-Frequency Deflector) input power have been used. It turns out that, at these beam energies, the 1 MW case better fit the practical diagnostic requirements in the case of 1 nC beam. The deflected beam on the screen has a width of 0.951 mm RMS, about 12 times bigger than in absence of deflection. This gives a good setup resolution, and at the same time does not limit the magnification of the optical imaging system needed to detect the image. In the low charge cases (200 and 50 pC), due to the much smaller beam length, the a deflector input power of 2.5 MW has been used to reach a good measurement resolution (ratio between 5 and 10 between the beam RMS with deflector on and off),

The imaging system at this position has to be designed with care. Depending on the particular measurement the beam can have a wide range of dimensions. For measurements making use of RFD the electron density on the screen is relatively low, and a sensitive screen is needed (Ce:YAG, 0.18% of dopant). On the other hand, in a projected emittance measurement, (hypothesis of transversely bigaussian beam distribution with 79 μm RMS on both planes) the beam at waist has an electron density close or even above the saturation limit of the scintillation screen (about 0.01 pC/ μm^2 for a 0.18% doped crystal). Optical Transition Radiation screens does not have such a limitation. The price to pay is a much smaller photon yield, i.e. a smaller SNR, and a more critical hardware alignment.

The same is valid for the system optical magnification. A fixed focal length optical system has been chosen, so the magnification has to be a compromise between the need of have enough resolution to see 80 μm beams, but keeping the whole beam on the image when it is deflected by the RFD. A typical magnification of 1:1.5 has been chosen, with a real pixel size of 9.9 μm square and a 640x480 pixel matrix. The virtual pixel is about 15 μm , and the full image dimensions are 9.6x7.2 mm.

One meter after the RFD cavity a dispersive section has been added to perform energy distribution measurements. A dipole can eventually steer the beam by 30 degrees respect to the straight trajectory. A cross with a Ce:Yag screen has been positioned 2 meters away the dipole center, in such a way that the distance between QS15 and the spectrometer screen is equal to the distance between QS15 and FS13.

Simulations show that beams with typical energy spread (0.1-0.2 %) would be dispersed by the dipole in a beam with 1-2mm sigma on the screen. The beam width ratio between no energy spread case (80 μm RMS) and real energy spread case is less than 1/10 in the worst case, leading to a good measurement resolution (better than 1 %).

By the contemporary use of RFD and the dipole magnet, the full longitudinal trace space picture can be directly seen on the spectrometer screen. For the measurement errors, the considerations made before on the time and energy resolutions hold.

In order to avoid systematic errors in the measurements beam position monitor striplines and beam steerers have been positioned all along the transfer line, inside each quadrupole and just before the dipole entrance, allowing also the magnet beam based alignment procedure.

5.3.5 Electron beam diagnostic @ 1.5 GeV:

The transfer line between the 1.5 GeV and the 2.4 GeV LINAC has been designed as another beam diagnostic section, in addition of providing the matching between the two LINAC structures. The first dipole (DIP_DL1_1) injects the beam through the dogleg into a long transfer delivering the 1.5 GeV beam to the undulator sections.

On the other hand when the dipole DIP_DL1_1 is off, the beam passes through a magnetic compressor and it is then injected in the 2.4 GeV LINAC.

Both these beamlines need adequate diagnostic tools. Projected emittance measurements will be possible without changing the accelerator matching conditions, by means of the "four screens method" (FS01-FS04). Such measurement allows the characterization of the beam at the exit of the 1.5 GeV LINAC, without taking into consideration the chicane\dogleg effect. The triplet of quadrupoles just after the chicane is used with the FS06 screen to perform emittance measurements after the compressor, via the quad scan technique. This station makes possible the study of the magnetic compression effects on the emittance degradation.

Other emittance measurement stations will be installed along the transfer line to undulators, to experimentally test the dogleg contribution to the beam degradation.

Energy and energy spread can be measured either by using the first dogleg dipole or the first chicane dipole (screens for such measurements have to be added in the layout of Figure 5.72).

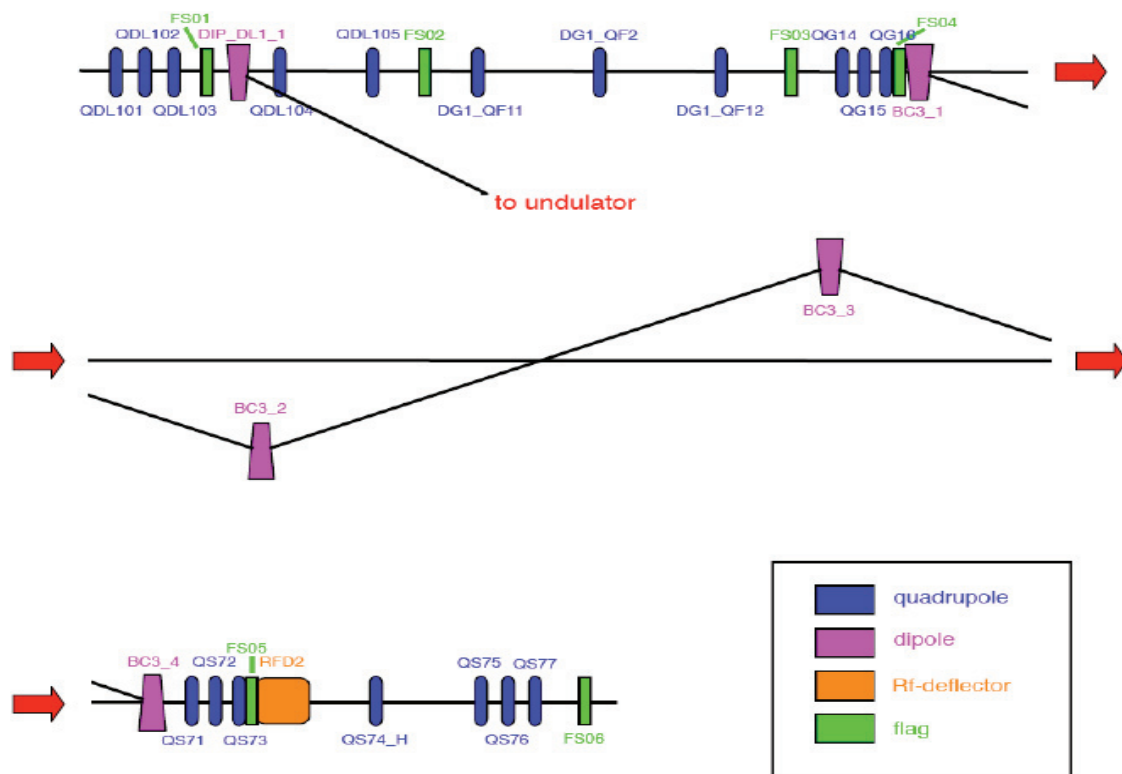


Figure 5.72: Transfer line schematic layout for electron beam at 1.5 GeV.

The position of the RF deflector has to be chosen with care. In the actual layout it has been positioned after the magnetic compressor and the quad triplet QS71-QS73. By the use of the screen FS06 (4 meters from the RFD center) the beam longitudinal structure and its slice emittance can be measured. The triplet just before the deflecting cavity is used to make a round waist at the screen when the deflector is off; by feeding the deflecting cavity, the longitudinal profile can be automatically reconstructed by the image on the FS06 screen. A travelling-wave structure 1.5 meters long has been designed to obtain a good resolution also in case of low charge and short bunches (table IV, V, and VI). In case of horizontal slice emittance measurements (assuming the RFD kick to be along the vertical direction) the horizontal beam dimension is varied by the use of two of the three quadrupoles before the RFD (typically the second and the third one) while maintaining constant the vertical one.

The position of the deflecting cavity allows to carry out longitudinal beam properties measurements either with or without the effect of the magnetic compression, looking for microstructures tail formation in the longitudinal profile.

The drawback of such layout is that there are no points for longitudinal phase space measurements, so that the behavior of the energy spread along the longitudinal coordinate can not be retrieved. This lack can be filled adding an energy line made of a dipole that could be positioned between QS74_H and QS75 and giving to the electron beam an angle of 20 degrees, plus a diagnostic

cross after 2 meters of beamline. With this angle and space between the magnet and the target a good resolution can be achieved.

However in the first phase of the project only the 1.5 GeV line will be installed with the beam passing through the dogleg and the transfer line until the undulators. The straight line will be dedicated only to the beam diagnostic, without any problem of space.

5.3.6 Alignment LASER

A large number of view screens will be implemented as shown in chapter 8. The main devices will be aluminium foils to generate Optical Transition Radiation (OTR). The emission of the OTR is not isotropic, being concentrated in a narrow cone of semi aperture in the order of $1/\gamma$. At high energy (more than several hundreds of MeV) the radiation is so collimated that it is mandatory a precise alignment of the optics, outside the beam pipe, that receive the radiation.

The direction of the emission depends of course from the angle of the metallic foil. Being this screen moving on an actuator a mechanical control of the angle is not possible better than few degrees.

With beam size in the order of 50 μm RMS or less the optic magnification is set to 1:1. The depth of field in this condition is in the order of few hundreds of μm . So it is crucial that the optics field of view looks as much as possible in the centre of the screen, being the centre of the beam line.

For all of these reasons it is important to have a tool to identify the centre of the beam line and to align the optics. A laser beam will be introduced in the sector at 150 MeV just after the accelerating structures. A movable in-vacuum mirror will be used to send the beam to the end of the straight part of the LINAC where a second mirror will produce a round trip of the beam. With this system all the metallic screen can be aligned respect to the optics looking at the reflection of the laser beam.

5.3.7 Optical Diffraction Radiation

The development of non-invasive and non-intercepting diagnostics is strongly encouraged because of the high power density of ultra-high brilliant electron beams and for the possibility of monitoring the beam properties parasitically during the FEL operation.

A non-intercepting measurement of transverse beam emittance is based on the observation of Diffraction Radiation (DR) emitted by a charged particle beam going through a slit in a metallic foil due to the interaction of the charge electromagnetic (EM) field with the screen surface.

The transverse beam size and divergence are measured from the analysis of the angular distribution of the Optical Diffraction Radiation (ODR) produced by the interference of radiation from both edges of the slit. The visibility of the interference fringes is correlated to the beam size (see Figure 5.73 left). The dependence is also affected, in a slightly different way, by the angular divergence of the beam: the ODR angular distribution becomes wider and the intensity of the minimum higher, when the beam divergence increases (see Figure 5.73, right). A dedicate analysis of the radiation angular distribution allows then to separate the two effects. If the beam is in a waist on the DR

screen, the transverse emittance can be derived with a single non-intercepting measurement [59].

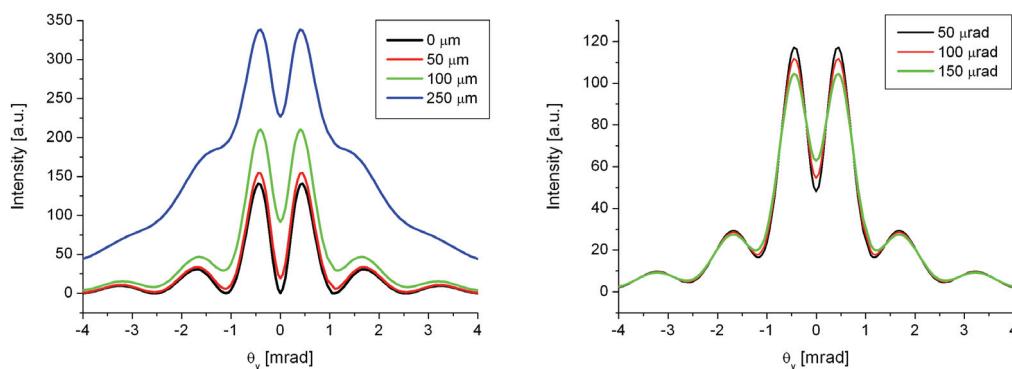


Figure 5.73: Optical Diffraction Radiation angular distribution for different beam sizes (left) and divergences (right).

The ODR station will be located in the 1.5 GeV sector. Due to the very low radiation intensity, a cooled, high sensitivity, 16-bit CCD camera (Hamamatsu C4742-98-LGLAG2) will be used. The camera main features are the very high quantum efficiency on the whole visible spectrum, in particular at 800 nm, the negligible thermal noise and the long exposure time, up to 2 hours, that allows to integrate on chip several pulses.

5.3.8 RF Deflectors

With the use of RF deflectors it is possible to measure the bunch length in different LINAC positions and, if one uses the orthogonal (non deflection) direction, one may perform a wide variety of time-slice measurements. Moreover by adding a dispersive system after the deflector, the longitudinal beam phase space can be completely reconstructed.

The different types of measurements that can be done with RFDs are based on the property of the transverse voltage¹⁶ (V_T) to introduce a correlation between the longitudinal coordinate of bunch and the transverse one (Figure 5.74). The phase of the deflecting voltage with respect to the bunch passage is tuned in order to have zero crossing of V_T in the center of the bunch giving a linear transverse deflection from the head and to the tail of the bunch. After the deflector the transverse kick (vertical, for example) results into a transverse displacement of the centroid of each bunch slice, proportional to the slice longitudinal position with respect to the bunch center.

See also references: 60, 61.

5.3.8.1 Bunch length measurements

¹⁶ The integrated transverse Lorentz force per unit charge.

The longitudinal beam distribution is projected along the vertical coordinate at a detector flag. As illustrated in Figure 5.74 the transverse distribution of the bunch at the detector position is the convolution between the displaced slices and the proper transverse slice sizes at the detector position.

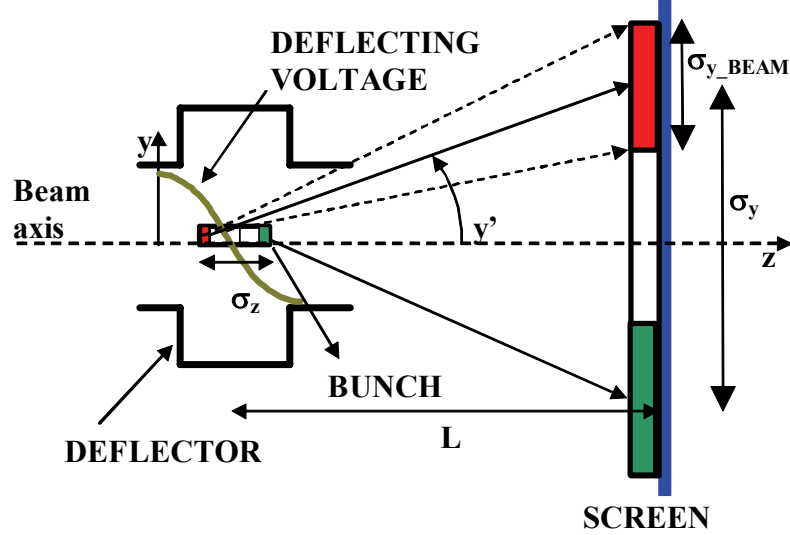


Figure 5.74: Longitudinal to transverse correlation induced by the RFD transverse voltage putting in evidence that the transverse profile after the deflector is given by the superposition of the deflected beam profile and the vertical proper dimensions of the bunch slices at the screen position.

Neglecting the transverse slice sizes of the beam, the rms value (σ_{y_RFD}) of the beam at the detector position is given by:

$$\sigma_{y_RFD} \cong \left| R_{34} \right| \frac{V_T}{E/e} \frac{\omega_{RF}}{c} |\cos \varphi_{RF}| \sigma_z \quad (5-14)$$

where ω_{RF} is the angular frequency of the deflecting voltage, V_T is the peak transverse voltage, E is the beam energy in eV units, φ_{RF} is the RF phase with respect to the bunch passage (at perfect zero crossing $\varphi_{RF} = 0, \pi$) and R_{34} is the optical transfer function given by:

$$\begin{cases} R_{34} = \sqrt{\beta_{y_defl} \beta_{y_screen}} \sin \Delta\Phi & \text{(general expression)} \\ R_{34} = L & \text{(simple drift space)} \end{cases} \quad (5-15)$$

where β_{y_defl} and β_{y_screen} are the vertical β -functions at the deflector and screen position, respectively, $\Delta\Phi$ is the phase advance between the deflector and the screen and L is the drift space of length L .

In the real case, the transverse distribution of the bunch at the screen position is the superposition between the deflected beam profile and the

vertical size of the bunch slices at the screen position (σ_{y_BEAM}). It is possible to demonstrate that, at the screen position, the measured vertical rms distribution is given by:

$$\sigma_y = \sqrt{\sigma_{y_RFD}^2 + \sigma_{y_BEAM}^2} \quad (5-16)$$

with $\sigma_{y_BEAM} = \sqrt{\beta_{y_screen} \varepsilon_y}$ where ε_y is the transverse vertical emittance of the beam.

In order to measure the bunch length with the proper accuracy, σ_z has to be bigger than σ_{y_BEAM} . One can define the resolution length σ_{z_RES} as the bunch length that gives, on the screen, a distribution with rms vertical size exactly equal to $\sqrt{2}\sigma_{y_BEAM}$. From the previous expressions it is easy to verify that:

$$\sigma_{z_RES} = \frac{c(E/e)\sqrt{\varepsilon_y}}{V_T \omega_{RF} |\cos \varphi_{RF}| \sqrt{\beta_{y_defl}} |\sin \Delta\Phi|} \quad (5-17)$$

In the case of a simple drift space this expression becomes:

$$\sigma_{z_RES} = \frac{c(E/e)\sqrt{\beta_{y_screen} \varepsilon_y}}{V_{\perp} \omega_{RF} |\cos \varphi_{RF}| L} \quad (5-18)$$

5.3.8.2 Longitudinal phase space measurements

The conceptual scheme to measure the longitudinal phase space is sketched in Figure 5.75. In this scenario, the bunch is deflected vertically by the RFD and horizontally by a magnetic dipole. The dispersion properties of the dipole allow to completely characterize the energy distribution of each bunch slice enabling the reconstruction of the bunch longitudinal phase space. In this case the energy spread resolution is simply given by:

$$\left. \frac{\Delta E}{E} \right|_{res} = \frac{\sqrt{\varepsilon_x \beta_{x_screen}}}{D_{screen}} \quad (5-19)$$

where ε_x , β_{x_screen} and D_{screen} are the horizontal emittance, the horizontal β -function and dispersion at the screen position.

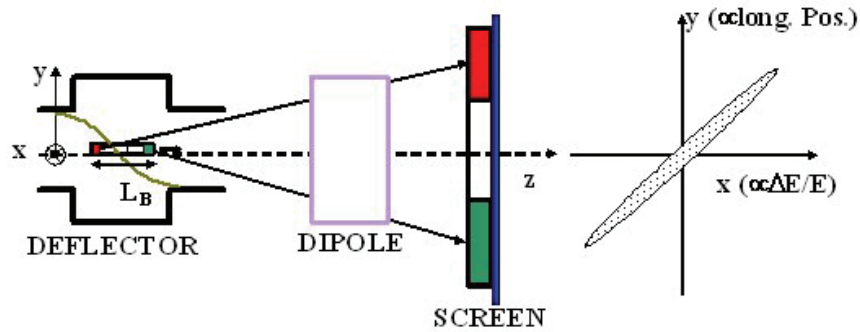


Figure 5.75: Conceptual scheme of the longitudinal phase space measurement setup using an RFD.

5.3.8.3 Horizontal slice emittance measurements

With the deflector it is also possible to measure the horizontal beam slice emittance. In this case the deflecting voltage gives the correlation between the longitudinal slice position and the vertical coordinate at the screen while the horizontal emittance can be measured with the quadrupole scan technique. The conceptual scheme is shown in Figure 5.76.

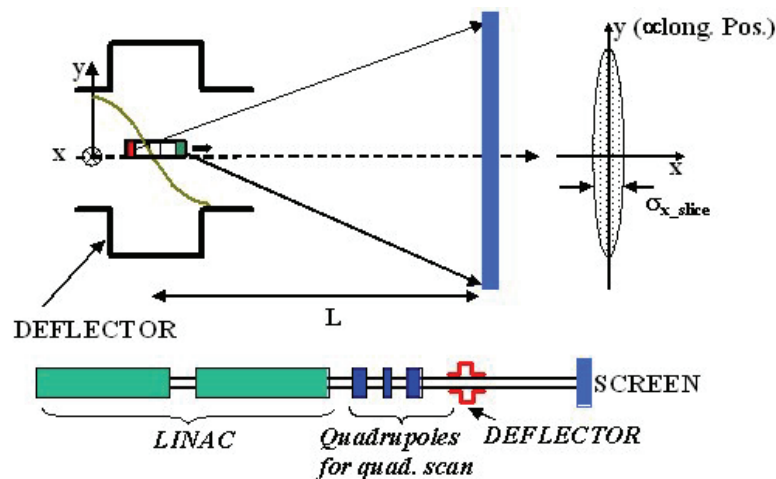


Figure 5.76: Conceptual scheme of the horizontal beam slice emittance measurement using an RFD.

5.3.8.4 Beam manipulation with an RFD: ultra-short bunch generation

RFDs allow to manipulate the beam in order to obtain, for example, ultra-short bunches. The conceptual scheme is given in Figure 5.77. With the plot of the beam shape in the planes zy and zy' . The bunch deflected by the first RFD is cut by the collimator. The correction of the zy' correlation is finally realized by the second RFD.

With a simple calculation it is possible to demonstrate that the bunch length after the process is given by:

$$\sigma_z = \frac{wcE/e}{2V_{T1}\omega_{RF}R_{34_1}} \quad (5-20)$$

where V_{T1} is the transverse deflecting voltage of the first RFD, w is the full width of the collimator aperture and R_{34_1} is the optical matrix element between the RFD1 and the collimator. Moreover the deflector voltages and the optical functions must satisfy the following relations:

$$\begin{aligned} V_{T2} &= -R_{44_2}V_{T1} \\ R_{34_2} &= 0 \end{aligned} \quad (5-21)$$

where R_{44_2} and R_{34_2} are the optical matrix elements between RFD1 and RFD2.

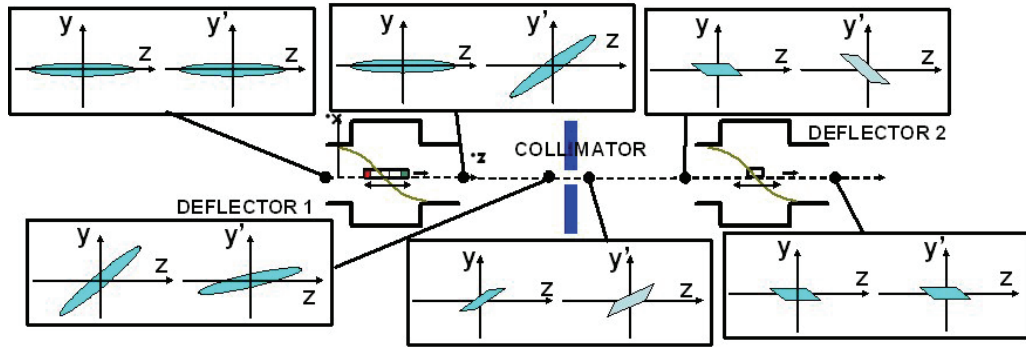


Figure 5.77: Conceptual scheme of the ultra-short bunch generation using an RFDs.

5.3.8.5 Deflector parameters

In the SPARX LINAC three RF deflectors are foreseen for the beam characterization at 150 MeV, 1.5 GeV and 2.4 GeV (phase II) respectively. Two possible solutions, at each energy, have been considered: a standing wave (SW) and a travelling wave (TW) solution while the frequency has been considered constant and equal to the main LINAC frequency 2.856 GHz. For the SW case we have considered multi-cell structures operating on the pi-mode. A single SW cell with the E and B field profiles is sketched in Fig. 5a (z is the beam propagation direction). In this case both E and B field components contribute to the total deflection. The main parameters of the single cell SW deflecting cavity are reported in Table 5.17. In the table we have defined the *transverse shunt impedance* R_T as:

$$R_T = \frac{\left| \int_0^L (E_x - cB_x) e^{j\omega_{RF}z/c} dz \right|^2}{2P_d} [\Omega] \quad (5-22)$$

where P_d is the average dissipated power in the cavity, ω_{RF} is the angular RF frequency, z is the longitudinal coordinate of the travelling wave and \tilde{E}_x, \tilde{B}_y are the transverse complex components of the electric and magnetic field on axis.

The example of a 5 -cell structure with input coupler is shown in Figure 5.78b.

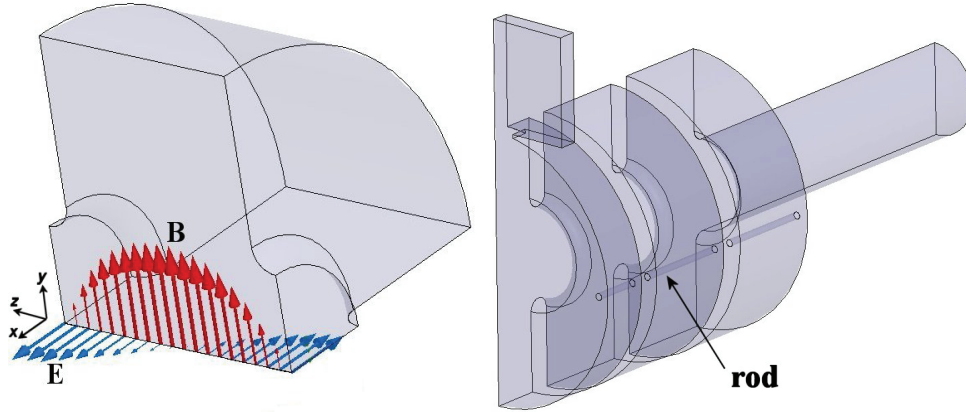


Figure 5.78: (a) Single cell of a standing wave RFD with the E and B field lines; (b) example of a 5 cell SW structure with centra coupler.

Table 5.17: SW single cell dimensions and parameters.

<i>Dimensions [mm]</i>	
a	20
b	60
t	9.5
d	52.5
Parameters	
Q_0	16000
$R_T [M\Omega]$	0.5
Max surf. E field $E / \sqrt{P_d} [V / mW^{-1/2}]$	$7.5 \cdot 10^4$

For the TW case we have considered multi-cell structures operating on the $2\pi/3$ mode.

The example of a TW structure with input-output coupler is shown in Figure 5.79. The main single cell parameters are reported in Table 5.18. In the table we have defined the *transverse series impedance* Z_T as:

$$Z_T = \frac{E_T^2}{P_{IN}} = \frac{\left| \int_0^D (\tilde{E}_x - c\tilde{B}_y) e^{j\omega_{RF}z/c} dz / d \right|^2}{P_{IN}} \left[\frac{\Omega}{m^2} \right] \quad (5-23)$$

where P_{IN} is the power flux along the structure and d is the cell period.

The RF deflectors parameters at the different energies are reported in Table III. In yellow there are remarked the choice we propose for the SPARX project.

The beam parameters and the measurement resolutions for the different charge working points at the different energies are reported in Table 5.20 to Table 5.22.

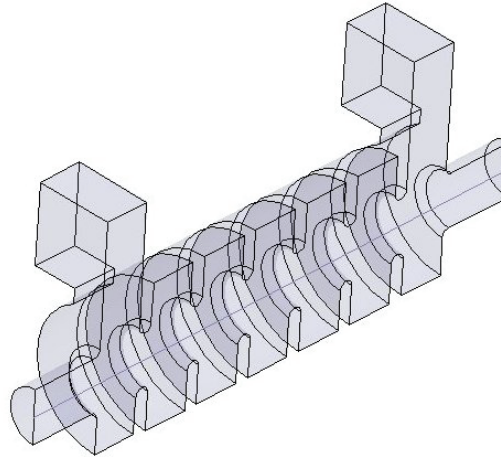


Figure 5.79: Example of a multi cell TW structure

Table 5.18: TW single cell dimensions and parameters.

<i>Dimensions [mm]</i>	
a	15
b	61.5
t	9.5
d	35
Parameters	
v_g/c	2%
$\alpha[1/m]$	0.1
$Z_T [\Omega/m^2]$	$5.7 \cdot 10^6$
Max surf. E field	$5 \cdot 10^3$
$E / \sqrt{P_{IN}} [V/mW^{-1/2}]$	

Table 5.19: Deflectors parameters at different energies.

DEFLECTOR PARAMETERS						
Beam Energy (E) [GeV]	0.150		1.5		2.4	
RF frequency (f_{RF}) [GHz]	2.856		2.856		2.856	
Max deflecting voltage (V_T) [MV]	4		10		40	
Deflector type	SW	TW	SW	TW	SW	TW
Number of cells (N_{TOT})	5	28	9	39	19	71
Total length (L_{TOT}) [m]	0.26	0.98	0.5	1.5	1.5	2.5
Max. input power (P_{RF}) [MW]	3.2	3.2	11	11	57	57
Filling time (τ) [μ s]	3.7 (¹⁷)	0.17	3.7	0.25	3.7	0.42
Max. surface E field (E_{max}) [MV/m]	60	9	83	17	107	37

Table 5.20: Beam and optics parameters at 50 pC.

BEAM PARAMETERS AND RESOLUTION						
Beam Energy (E) [GeV]	0.150		1.5		2.4	
Bunch length (σ_z) [μ m]	43		43		6	
Defl. input Power [MW]	2.5 (SW)		10 (TW)		50 (TW)	
Meas. Resolution (σ_{meas}) [μ m]	6.9		7.3		2.7	
Norm. vertical emittance ($\epsilon_{y,v}$) [mm-mrad]	0.5		0.5		0.5	
OPTICS PARAMETERS						
Distance defl.center-flag (L) [m]	3.8		4.7		4	
Beta function at deflector (β_r) [m]	17		15		10	
Beta function at screen (β_s) [m]	1		1		1	
BEAM DIMENSIONS AT SCREEN						
Deflector status	OFF	ON	OFF	ON	OFF	ON
RMS beam dimension at screen ($\sigma_{y,s}$) [μ m]	36.3	242.2	13	77	10	23

Table 5.21: Beam and optics parameters at 200 pC.

BEAM PARAMETERS AND RESOLUTION						
Beam Energy (E) [GeV]	0.150		1.5		2.4	
Bunch length (σ_z) [μ m]	160		160		20	
Defl. input Power [MW]	2.5 (SW)		10 (TW)		50 (TW)	
Meas. Resolution (σ_{meas}) [μ m]	8.3		9		2.7	
Norm. vertical emittance ($\epsilon_{y,v}$) [mm-mrad]	0.6		0.6		0.5	
OPTICS PARAMETERS						
Distance defl.center-flag (L) [m]	3.8		4.7		4	
Beta function at deflector (β_r) [m]	15.3		15		10	
Beta function at screen (β_s) [m]	1.2		1		1	
BEAM DIMENSIONS AT SCREEN						
Deflector status	OFF	ON	OFF	ON	OFF	ON
RMS beam dimension at screen ($\sigma_{y,s}$) [μ m]	44.6	$0.39 \cdot 10^3$	16	286	10	75

¹⁷ In the case of SW cavities we have considered 4 filling times.

Table 5.22: Beam and optics parameters at 1 nC.

BEAM PARAMETERS AND RESOLUTION						
Beam Energy (E) [GeV]	0.150	1.5	2.4			
Bunch length (σ) [μm]	900	250	50			
Defl. input Power [MW]	1 (SW)	10 (TW)	50 (TW)			
Meas. Resolution (σ_{\dots}) [μm]	52	13	4			
Norm. vertical emittance (ϵ_{\dots}) [mm-mrad]	1.2	1.2	1.2			
OPTICS PARAMETERS						
Distance defl.center-flag (L) [m]	3.8	4.7	4.3			
Beta function at deflector (β_r) [m]	14.6	15	15			
Beta function at screen (β_s) [m]	0.9	1	1			
BEAM DIMENSIONS AT SCREEN						
Deflector status	OFF	ON	OFF	ON	OFF	ON
RMS beam dimension at screen (σ_{γ_s}) [μm]	79	$0.95 \cdot 10^3$	23	446	16	186

5.3.9 Beam Position Monitors

Two types of beam position monitor (BPM) will be installed in the different sections of the machine, to fit with the vacuum chamber sections and available spaces.

Design of BPMs of the 'strip-line' type, developed for the SPARC photo-injector, has been modified to allow installation inside each quadrupole. They will be located in the LINAC, between each accelerating section and in the transfer lines. Beam based alignment will be used to determine and adjust the centers. The expected resolution is $10\mu\text{m}$ for a 0.5nC charge.

BPMs are composed by two pairs of metallic strips placed inside the vacuum chamber, the equivalent transmission line of each strip with the surrounding chamber is set to 50 Ohm by proper choice of the strips dimension.

The length of each strip is 130mm, the angular width of the electrode is 30° degree, 50ohm sma-type vacuum feed-through is connected to the upstream side, while downstream ends are short circuited to the chamber.

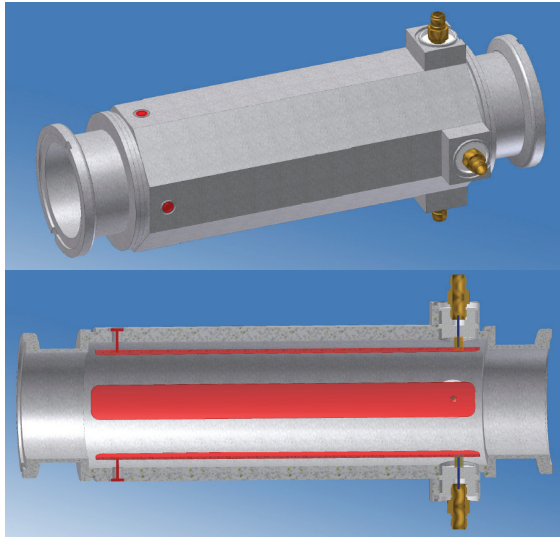


Figure 5.80: Stripline beam position monitor

The stripline frequency response is periodic with a sinusoidal shape. It presents a null at all frequencies where the strip length is equal to $n\lambda/2$, and the maximum where the strip length corresponds to a quarter wavelength. In our case the length has been chosen to have a maximum of the BPM transfer impedance as near as possible to the LINAC frequency.

The beam position will be deduced comparing the amplitude of the signals induced in the four striplines. Measurement and acquisition of these signals will be performed through dedicated detection electronics.

The proposed detection scheme is commonly referred as log-ratio detection: the signals from opposite electrodes are processed through independent channels with band pass filters and logarithmic amplifiers. The RF-bursts from the filters are demodulated through amplifiers which provide the log of the envelope of the signals.

The outputs are then applied to a differential amplifier to obtain the difference of the logs and hence a signal proportional to ratio of the logs. Externally triggered ADCs are the last stage to acquire the two signals to be processed with a reconstruction algorithm to extract the beam transverse position.

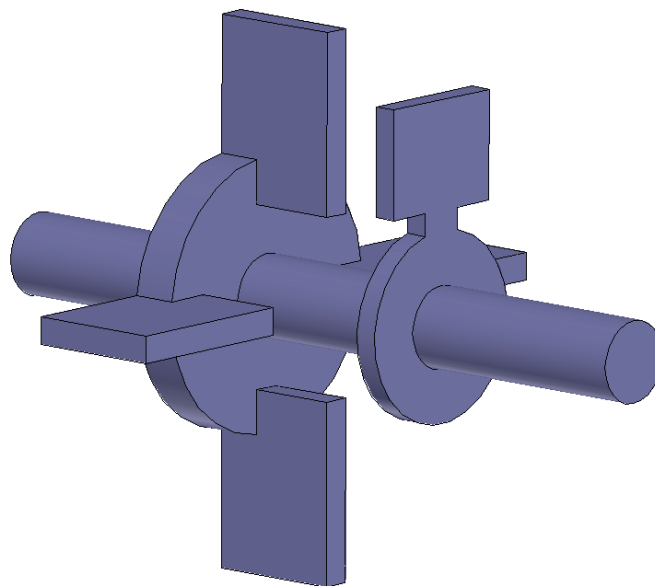


Figure 5.81: cavity BPM for the undulator sections

Between the undulator sections, the severe requirements for resolution and the limited diameter of the vacuum chamber ask for the adoption of a different BPM pickup. Cavity BPMs are used to provide the required 1 micrometer resolution basing on the excitation of a TM dipole mode when the beam passes off axis.

A pickup composed by two resonant C-band pill-box cavities has been numerically simulated (Figure 5.81) for use in the SPARX undulator sections.

Beam position will be extracted from amplitude and phase variations of the TM₁₁₀ dipole mode of the first cavity using as a phase reference signal the monopole mode TM₀₁₀ of the second cavity. The two cavities are designed to operate at the same frequency.

Four waveguides intercept the first cavity symmetrically, horizontally and vertically, coupling only with the TM₁₁₀ mode and rejecting the monopole mode.

When the beam passes off axis, the dipole mode is excited and its amplitude yields a signal proportional to the beam displacement while its phase, relative to the monopole mode reference, gives the sign of the displacement.

The receiver is a three channel heterodyne receiver. Signals from the two cavities are pass band filtered and down-converted from C-band to the IF frequency by means of mixers. Intermediate frequency signals are demodulated by I-Q demodulators which provide baseband signals proportional to beam displacement which are finally digitalized with A/D converters.

5.4 CONVENTIONAL MAGNETIC ELEMENTS

The beam transport in the LINAC requires more than 300 conventional electromagnets: dipoles, quadrupoles, solenoids and steering magnets. Table 5.23 summarizes the different magnetic elements of the LINAC beamline in terms of number, type and location (i.e. purpose). Wherever possible, the choice of grouping different magnets in a fixed transverse cross section configuration (but, eventually, with different magnetic lengths) has been made, hence minimizing the number of different elements to be produced, with evident gain on the economical point of view as much as in production speed up. Although reported in Table 5.23 as independent elements, steering magnets will be embedded within the quadrupoles' assembly, and in principle this is going to be a single mechanical assembly, but in terms of power supply they must be taken in account separately.

Table 5.23: Overview of the different electromagnets throughout the LINAC

<i>Magnet type</i>	<i>No. of Magnets (same cross section)</i>	<i>Operation area in the LINAC</i>
Dipoles	4	1.5 GeV
	16	BC/Dogleg
	8	2.4GeV
	3	Dump
	3	Dump
Solenoids	1	Gun
	12	Acc. sections
Quadrupoles	66	1.5 GeV line
	16	Intra undulators
	25	2.4GeV line
	36	Intra undulators
Steering magnets	143	Quad-embedded x/y

5.4.1 Design procedure

All magnets have been designed through the aid of finite elements analysis (FEA) computer codes. After an initial design through approximated analytical calculations, first dimensioning is made through the 2-D magnetostatic solver *Poisson* [62]. The result of 2-D simulations is then extended to a full 3-D model and analyzed through the code *Tosca* [63]. This tool allows for complete field evaluation in the whole space. Then, slight adjustments of magnet shape follow to adequate the model to the goals of final specifications. Magnets power supply requirements have been set in terms of working points, stability, tolerances, loads. Cooling has been also dimensioned to fit the feeding water flux facility of the tunnel. Analytical calculations and FEA code *Tempo* [63] have both been used for this purpose. Together with magnetic design of the elements, a preliminary mechanical assembly of the real model has been put together through computer aided design tools. Such a step can give an important feedback, because in principle, the actual magnetic field could undergo slight changes (e.g. screws supporting the electromagnet can

force adjustments of shape and positioning of coils) to be checked and corrected again through FEA codes.

5.4.2 Material choice and construction

An electromagnet suitable iron is necessary to withstand high magnetic flux density and guide the field lines following the design specifications. ARMCO iron (whose B-H curve is shown in Figure 5.82) has been used in all calculations so far, as a reference point (and without loss of generality), because it is a well established standard for particle accelerator electromagnets, and, moreover it is a product of wide availability. Anyway, all calculations can be easily tailored to fit a different type of iron. In general, forged iron or vacuum casted iron may be both suitable choices. All the magnets will be manufactured from solid blocks of high purity iron with an extremely low carbon content ($0.06\% \pm 0.02\%$ is the best choice [64]) as much as low percentage of other impurities [64], in order to guarantee high permeability up to a saturation level of magnetic induction of about 2 T and the proper hardness required to overcome the mechanical stresses generated by the magnetic field.

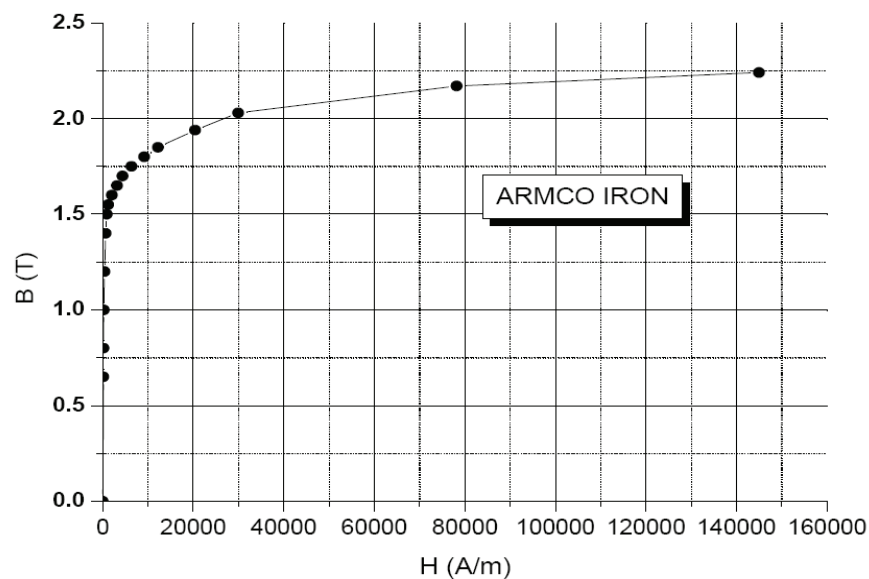


Figure 5.82: Typical magnetization curve for ARMCO iron

The final choice will be given by the best compromise between an economical point of view and ease and velocity of production/delivering of the whole magnetic elements set. No constraints in terms of magnets ramping are given: special laminations assembly is not requested by the operating conditions. Nevertheless lamination is usually the most viable choice in order to ensure the proper uniformity within the single magnet iron yoke, and, moreover, within the whole set of magnets. In fact, a proper randomized placement of the iron slabs within the final magnet assembly prevents the inhomogeneities present in different parts of the same iron yoke as much as mismatches between different iron yokes stocks to reflect in the final magnet yokes.

5.4.3 Single magnetic elements

Some of the most tight specified magnets are here outlined in a preliminary design.

Bunch compressors dipoles

A common dipole design based on a C shape profile has been chosen for ease of handling and easy insertion into the beam line. The dipole magnets for the bunch compressors require high fields plus high field quality over a wide horizontal range, so this was the most challenging case to test the choice of the C with respect to the H shape design. A summary of the main features of different bunch compressors dipoles are outlined in Table 5.24. Each dipole has a pole gap of 50 mm, pole trasverse width of 200 mm and a length of 300 mm. The maximum field strength is in the order of 1 T with a deflection angle of 70 mrad at 1.2 GeV. Figure 5.83 reports dipole field in the gap versus excitation current.

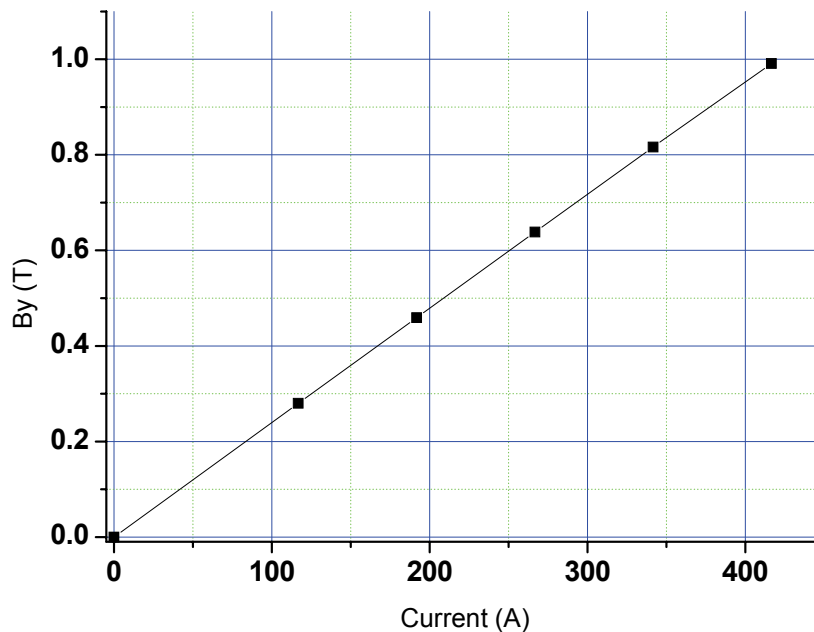


Figure 5.83: BC dipole, vertical B field vs. excitation current up to the maximum field required.

To minimize the increase of transverse emittance due to higher order multipole components in the dispersive region, the field quality has been specified quite high. Within a good field region of ± 20 mm distance from the center (both in vertical and horizontal direction) it is possible to achieve a field error (defined as $\Delta B/B_0$) in the order of 10^{-4} . Electrically, these dipoles will be arranged as a series circuit to guarantee equal field strength. Water cooled pancake coils (conductor dimension is 10 mm by 10 mm with squared cross section and circular inner duct for water flow cooling) have been chosen with a maximum current density of about 5 A/mm². The maximum foreseen power is 3.9 kW and the total number of windings (per magnet) is 96. Each coil cross section is composed by 8 horizontal by 6 vertical windings.

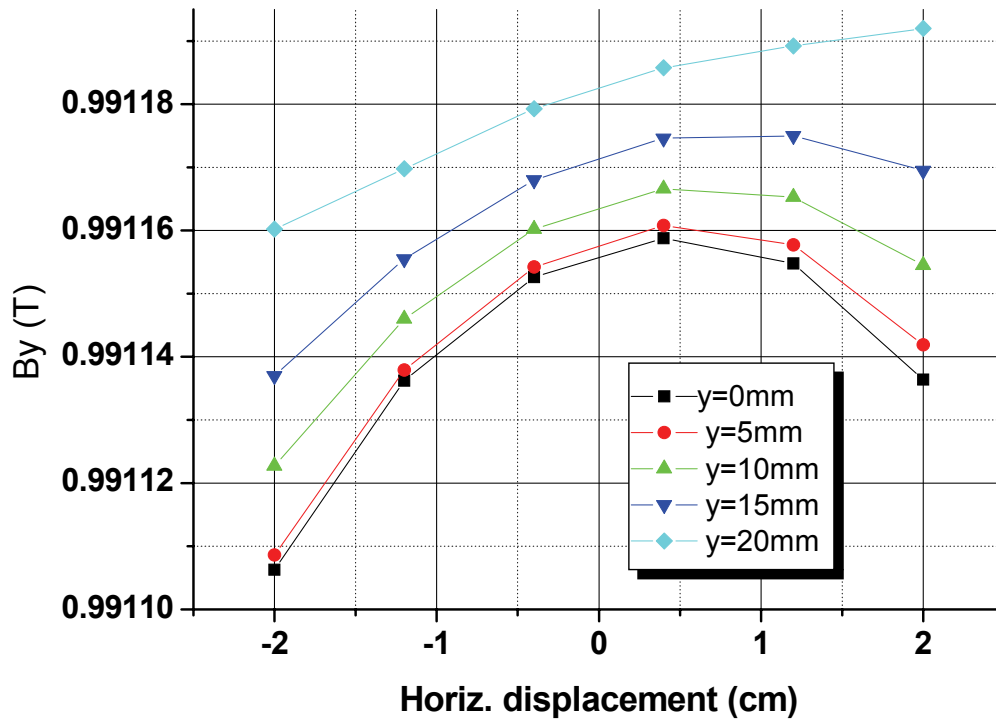


Figure 5.84: Vertical magnetic induction within the good field region

At maximum power the cooling scheme foresees a unique feeding for each single dipole, with 20 K of water temperature rise, for a maximum pressure drop of 4.4 bar (accounting for facility nominal water pressure and eventual losses from the line to the magnet) and a flux of 2.87 l/min. A typical field map inside the good field region of the magnet coming from 2-D simulation is shown in Figure 5.84, while 3-D evaluation of magnetic field inside the iron yoke is shown in Figure 5.85.

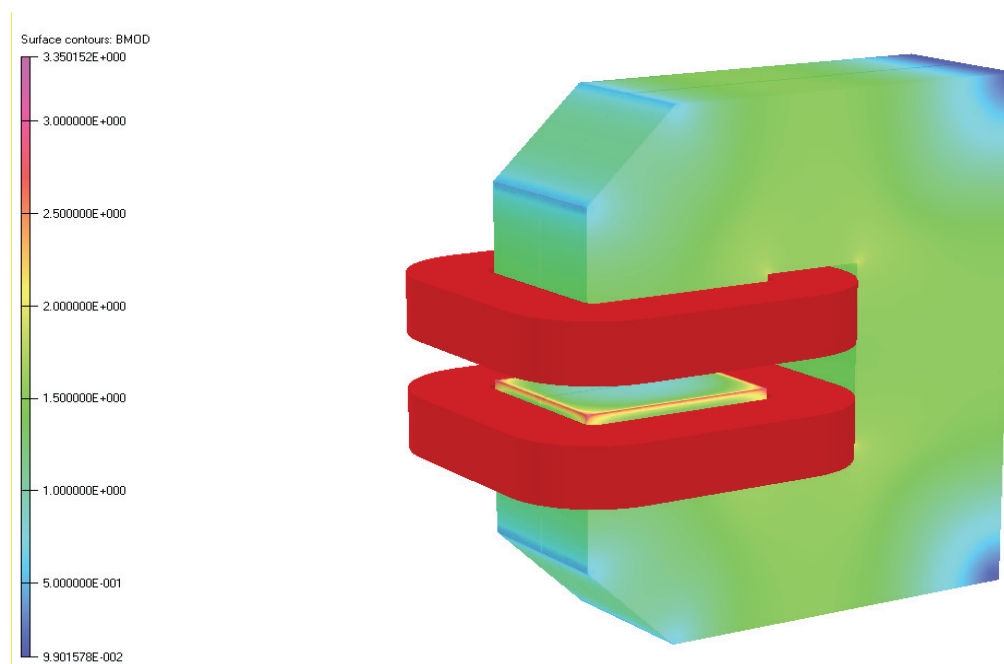


Figure 5.85: Tosca 3-D solid model of BC dipole. B field in the iron yoke for 0.8 T of field in the gap.

Table 5.24: Overview of the main features of the BC dipoles

<i>Element</i>	<i>Energy (MeV)</i>	<i>Deflection angle (mrad)</i>	<i>Gap Field (T)</i>	<i>Coil current (A)</i>	<i>Power (kW)</i>
<i>BC1</i>	300	150	0.816	342	3.2
<i>BC2</i>	600	50	0.744	312	2.9
<i>BC3</i>	1200	70	1.003	420	3.9

1.5 GeV Quadrupoles

Quadrupoles for the 1.5 GeV beam line have been designed with a larger bore radius (i.e. 28 mm) than requested by the vacuum pipe itself. Such an aperture, in fact, is aimed to hold a beam position monitor, and, moreover, each pole will be supplied of an additional coil, to act as an embedded steering magnet within the same mechanical assembly. This is an optimal choice on the point of view of beam orbit detection/correction; moreover such a composite element makes the whole beam line extremely compact, at the expenses of a bigger requested accuracy in terms of magnet alignment [65]. This means that beam orbit errors must be minimized in order to work within the good field region of the steering magnets (the most critical part within these elements), but, on the other side, the “shared joke” design guarantees an automatic superposition between magnetic center of quadrupoles and correctors. Obviously the increased bore radius brings further issues: at high gradient levels the power requested (and the heat to be removed by the cooling circuit) becomes large. At the same time the higher magnetic field necessary is likely to bring the iron yoke in deep saturation if this is not properly dimensioned.

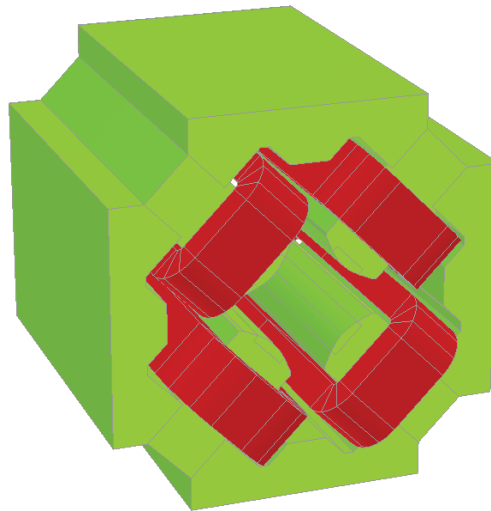


Figure 5.86: 1.5 GeV type quadrupole. 3-D solid model used in magnetostatic calculations in Tosca code

In terms of performances, maximum requested gradient of quadrupole is 25 T/m over a magnetic length of 300 mm. Field gradient versus feeding current is shown in Figure 5.87. Coils are assembled in 17 turns per each pole. A

copper conductor of squared cross section measuring 10 mm by 10 mm equipped with a circular hole for water cooling of 7 mm diameter has been used in power/cooling dimensioning. At the maximum gradient of 25 T/m with a single cooling circuit throughout the magnet, the power dissipated is 5428 W. 3.9 l/min is the water flux necessary to remove the heat from the magnet, with a pressure drop of 4.3 bar and temperature rise of 20 K.

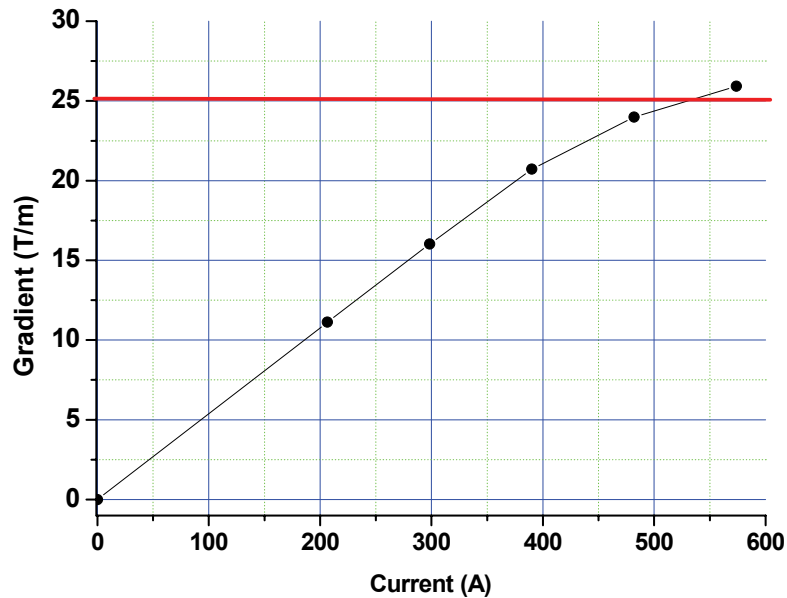


Figure 5.87: Quadrupole gradient vs. excitation current. The horizontal red line lies on the maximum requested gradient.

Dealing with field quality, some of the harmonic analysis results at the limit of the good field region (within a radius of 20 mm) are briefly shown in Figure 5.88 for different working points. No evident dependence of multipole content on current excitation (i.e. field level) is appreciable.

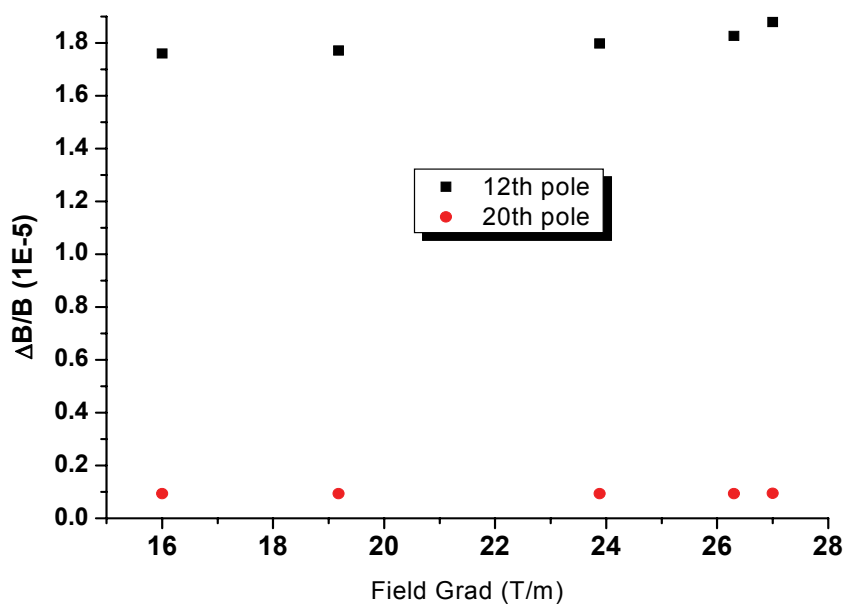


Figure 5.88: Field error coming from 12th and 20th pole contribution at 20 mm radius for different field gradients.

As before mentioned, steering action will be embedded inside the as described quadrupole by means of an additional coil per pole. This is going to be a small coil (same conductor cross section used for the quadrupole coil but with one single turn per pole) supplied with low current densities (cooling is not foreseen for such additional windings). It is important to estimate the operating zone of the steering magnet for its strong field dependence on trasverse displacement from the center. Electron beam along the beamline is confined inside an area of few hundred microns of radius. In principle beam extension plus eventual displacement errors should be taken in account. It has been stated that after a fine beam based alignment the area experienced will be contained inside a radius of 0.5 mm. As shown in Figure 5.89 (for a nominal field of about 1 mT) keeping the electron beam inside such a region brings to experience field errors ($\Delta B/B_0$) on the order of a few E-4, that is a good result for a composite magnet design. A first mechanical assembly of the magnet is also shown in Figure 5.90. This is going to be used as a model be test on final magnetostatic simulations.

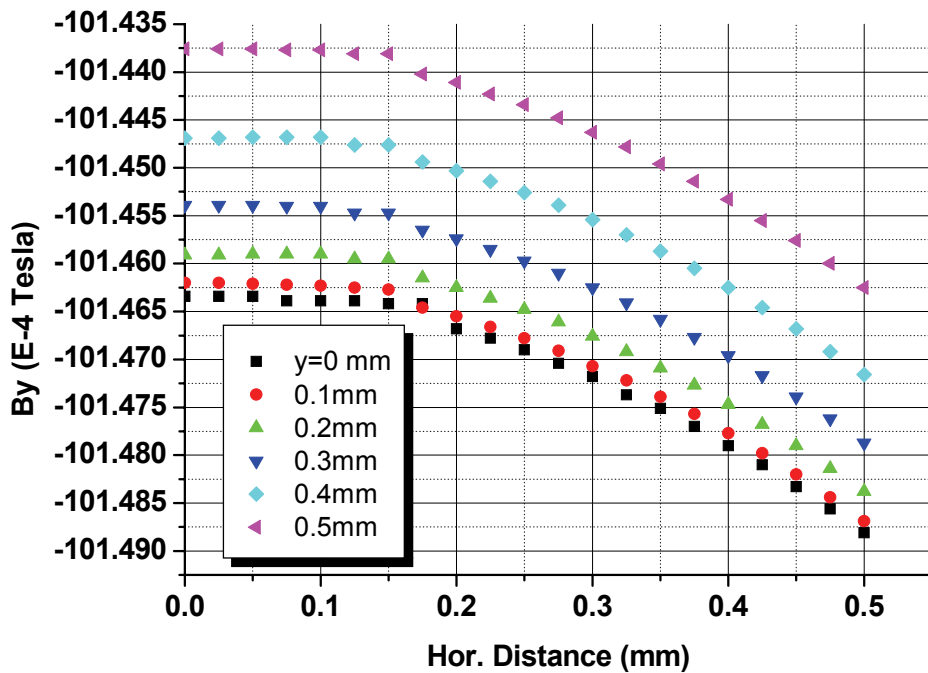


Figure 5.89: Embedded steering magnet field dependence on horizontal and vertical position within 0.5 mm radius.

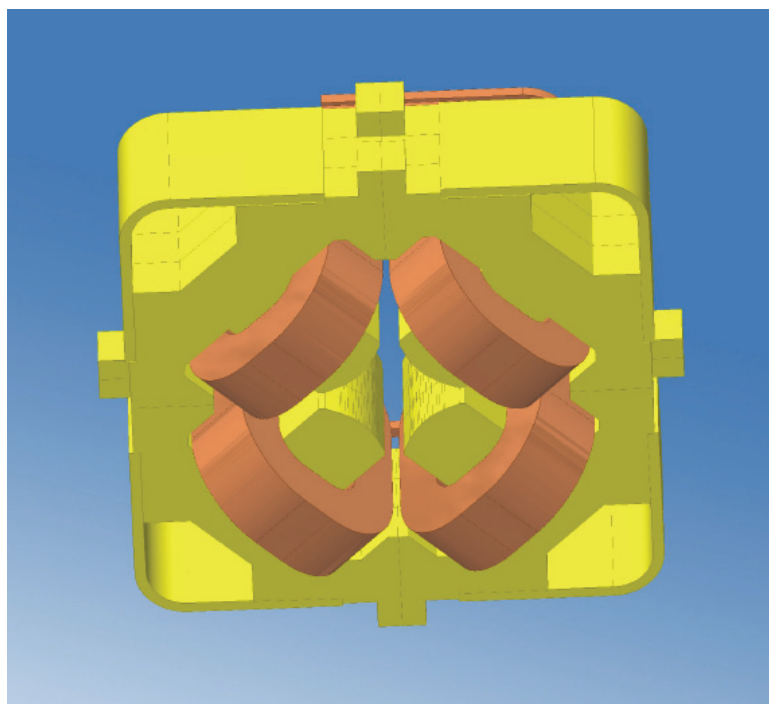


Figure 5.90: Actual mechanical assembly of the 1.2 GeV quadrupole

See also [66].

5.5 References:

- [1] <http://laacg1.lanl.gov/laacg/>
- [2] <http://www.ansoft.com/products/hf/hfss>
- [3] V.A. Dolgashev, "High Fields in Couplers of X-band Accelerating Structures", PAC 03, Portland, Oregon, USA, May 12-16,2003.
- [4] D.P. Pritzkau, "RF Pulsed Heating", SLAC-Report-577, PhD. Dissertation, Stanford Univ., 2001.
- [5] <http://www.ansoft.com/products/tools/ephysics>
- [6] T. Wangler, "RF Linear Accelerators", John Wiley & Sons, Inc. 1998.
- [7] J. F. Schmerge, "Reducing the heat load on the LCLS 120 Hz RF gun with RF pulse shaping", LCLS Technical Note LCLS-TN-02-7 (Stanford, 2002)
- [8] S. H. Kong, J. Kinross-Wright, D. C. Nguyen, R. L. Sheffield, Nucl. Instr. Meth. A, 358 (1995) 272;
- [9] L. Cultrera, C. Ristoscu, G. Gatti, P. Miglietta, F. Tazzioli, A. Perrone, J. Phys. D: Appl. Phys., 40 (2007) 5965;
- [10] M. Bellaveglia et. Al., Proceedings of FEL 2006 Conference, (2006) 637;
- [11] D. H. Dowell et al., Proceedings of FEL 2007 Conference, (2008) 276;
- [12] T. Srinivasan-Rao, I. Ben-Zvi, J. Smedley, X. J. Wang, M. Woodle, D. T. Palmer, R. H. Miller, Proceedings of PAC 1997 Conference, (1998) 2790;
- [13] L. Cultrera, G. Gatti, P. Miglietta, F. Tazzioli, A. Perrone, J. Nanoscience and Nanotechnology, in press;
- [14] D. Alesini et al., Nucl. Instr. Meth. A, 528 (2004) 586;
- [15] G. Gatti, L. Cultrera, F. Tazzioli, J. Moody, P. Musumeci, A. Perrone, Proceedings of PAC 2007 Conference, (2008) 995;
- [16] T. Srinivasan-Rao, J. Schill, I. Ben Zvi, M. Woodle, Rev. Sci. Instrum., 69 (1998) 2292;
- [17] X.J. Wang, M. Babzien, R. Malone, Z. Wu, Proceedings of LINAC 2002 Conference, (2003) 143;
- [18] L. Cultrera, G. Gatti, P. Miglietta, F. Tazzioli, A. Perrone, Nucl. Instr. Meth. A, 587 (2008) 7;
- [19] M. Ferrario et al. PRL 99, 234801 (2007).
- [20] J. Yang and al. J Appl. Phys. 92, 1608 (2002).
- [21] L. Palumbo and J. Rosenzweig, eds., Technical Design Report for the SPARC Advanced Photo-Injector (LNF-INFN 2004). <http://www.lnf.infn.it/>
- [22] W. Koehler, Solid State Laser Engineering, Springer-Verlag, Berlin, Heidelberg 1999.
- [23] C. Rulliere Femtosecond Laser Pulses, Springer Verlag 1998
- [24] P. Maine, D. Strickland, P. Bado, M. Pessot, G. Mourou, IEEE J. Quantum Electr., 24, 398, (1988).
- [25] S. Backus et al. High power ultrafast lasers, Rev. of Scie. Instr., 69 no. 3, 1207, (1998).
- [26] FERMI@ELETTRA CDR <http://www.elettra.trieste.it/fermi/>
- [27] S. Cialdi, M. Petrarca, C. Vicario, Opt. Lett. 31, 19 (2006) 2885-2887 and Virtual Journal of Ultrafast Science Oct. 2006.
- [28] F. Verluise and al, Opt. Lett. 25, 572 (2000).
- [29] A. M. Wiener, D. E. Leaird, J. S. Patel and J. R. Wullert Opt. Lett. 15, 326 (1990).
- [30] S. Cialdi, C. Vicario, M. Petrarca, P. Musumeci, Appl. Opt. 46, 22 (2007) 4959-4962.

- [31] S. Coudreau, D. Kaplan, and P. Tournois *Opt. Lett.* 31 1899 (2006).
- [32] C. W. Siders, J. L. W. Siders, A. J. Taylor, S. Park, and A. M. Sessler, *Appl. Opt.* 37, 5302-5305 (1998).
- [33] S. Zhou et al., *Appl. Opt.* 46, 35 (2007), 8488.
- [34] S. Cialdi, I. Boscolo, A. Flacco, *J. Opt. Soc. Am. B* 21, 9 (2004) 1693-1698.
- [35] C. Vicario et al. *Proceedings of EPAC 2004*, Lucerne, Switzerland, p.1300-1302.
- [36] A. Ghigo, C. Vicario, M. Petrarca and S. Cialdi, *Care Note 2007-Phin*
- [37] C. Vicario et al. *SPARC Technical note-LS-07/002*, <http://www.lnf.infn.it/>
- [38] D. Kaplan and P. Tournois *Private Communications*, (2008).
- [39] J. A. Hoffnagle and C. M. Jefferson, *Appl. Opt.*, 39, (2000), 5488.
- [40] <http://www.zemax.com/>
- [41] M. Born and E. Wolf, *Principles of Optics*, Cambridge Univ. Press, Rochester, New York, 1999.
- [42] M. Petrarca, C. Vicario, S. Cialdi, P. Musumeci, G. Gatti, A. Ghigo, M. Mattioli, *SPARC Note LS-06/002*, 2006.
- [43] A. Gallo et al. *Proc. Of Particle Accelerator Conference 2007*, TUPMNO36, Albuquerque, USA.
- [44] "The Stanford Two-Mile Accelerator", Stanford Univ. 1968. pp 95-160.
- [45] H. Matsumoto et al., "High Power Test of a SLED System with Dual Side-Wall Coupling Irises", *Proc. of the 1993 Particle Accelerator Conference*, pp. 959-961.
- [46] Zenghai Li et al., "Coupler Design for the LCLS Injector RF-Structures", *Proc. of the 2005 Particle Accelerator Conference*, pp. 2176-2178.
- [47] C. Vaccarezza, "SPARX Accelerator 1.2-2.4 GeV Layout 0.1" *SPARX Note to be published*.
- [48] P.Emma, "X-band RF Harmonic Compensation for Linear Bunch Compression in the LCLS", LCLS-TN-01-1, Nov. 14, 2001
- [49] *Traveling Wave Structure Optimization for the NLC*, Zenghai Li, Karl L. Bane et al., August 2002, SLAC-PUB-9049;
- [50] *SLAC/CERN High Gradient Tests of an X-Band Accelerating Section*, J. W. Wang, G. A. Loew et al., PAC95, SLAC-PUB-9977.
- [51] *Design of a 50 MW Klystron at X-Band*, E. Wright, R. Collins et al., July 1995, SLAC-PUB-95-6676;
- [52] *Development of the X-Band Klystron Modulator at KEK*, M. Akemoto, S. Anami et al., High Energy Accelerator Research Organization (KEK), 305-0801 Japan;
- [53] *Realization of an X-Band RF System for LCLS*, P. McIntosh et al., May 2005, SLAC-PUB-11270;
- [54] C. Lejeune and J. Aubert, *Adv. Electron. Electron Phys. Suppl. A* 13, 159 (1980).
- [55] L. Catani et al., *Rev. Sci. Instrum.* 77, 093301 (2006).
- [56] L. Catani, A. Cianchi, G. Di Pirro, K. Honkavaara, "A large distributed digital camera system for accelerator beam diagnostic", *Review of Scientific Instruments* 76, 73303 (2005)
- [57] H. Wiedmann, "Particle Accelerator Physics 1", second edition, ed. Springer 1999, pag 157
- [58] M. G. Minty, F. Zimmermann, *Measurement and control of charged particle beams*, ed. Springer, 2003, pag 104

- [59] E. Chiadroni et al "Non-Intercepting Electron Beam Transverse Diagnostics with Optical Diffraction Radiation at the DESY FLASH Facility" accepted by NIM B in publication.
- [60] M. Minty "Measurement and Control of Charged Particle Beams" Springer
- [61] C. Vaccarezza et al, "An RF deflector design for 6d phase space characterization of the sparx beam" Proc. of EPAC 2004, Lucerne (Switzerland) pag 2616
- [62] Poisson/SUPERFISH codes:
http://laacg1.lanl.gov/laacg/services/download_sf.phtml#ps0
- [63] Vector Fields Opera codes: <http://www.vectorfields.com/>
- [64] G. E. Fischer, SLAC-PUB-3726 July 1985
- [65] CTF3 TDR <http://doc.cern.ch/archive/electronic/cern/preprints/ps/ps-2002-008.pdf>
- [66] Bessy TDR
http://www.bessy.de/publicRelations/publications/files/TDR_WEB.pdf

6 UNDULATORS SYSTEMS

6.1 Magnet technology

Once the undulator beamline has been chosen (section 4.1), the first decision concerning the undulator is about technology to adopt.

There are different technologies which can be used for our purposes. The choice among them depends on opportunity, difficulty in problem solving, economic issues. Furthermore, we are compelled to choose among design, manufacturing techniques, which are readily available with extensive experience, and other ones which can be considered not yet reliable. Some of them have become mature and now commercially available.

The SPARX project expects *3 undulator beamlines* : we can choose different technologies to fulfill several radiation output requests

Furthermore, segmentation of undulator presents a number of advantages, apart a trivial manufacturing and transportation simplification :

- 1 If necessary, it is possible to exploit a step-tapering to maximize FEL extracted power
- 2 Opening to maximum gap, the effective electron-photon interaction length can be arbitrarily reduced
- 3 Difference between one segment and the next can be compensated by tuning the gap for the different sections

The properties of the X-ray beam (spectrum, polarization state, divergence etc.) depend on the magnetic field geometry. Most of the devices is based on high performance permanent magnet arrays placed symmetrically on each side of a narrow vacuum chamber or in vacuum.

In the following a brief review of some of different undulator technologies is reported.

Permanent magnet undulators at room temperature

Permanent magnet undulators NdFeB at room temperature have many advantages:

- Manufacturing techniques are readily available and extensive experience exists
- Fabrication errors can be controlled by high precision machining
- A number of high precision magnetic measuring techniques have been developed
- Field errors can be controlled by using shimming and tuning techniques
- Phase matching of undulator sections is possible
- Variable gap undulator are commercially available

and few drawbacks:

- There is a lower limit on the vacuum chamber aperture given by resistive wakefields effects. In a variable undulator a limit in the minimum gap (apart mechanical issues) thus occurs
- There is a lower limit on the minimum undulator period length in order to obtain sufficient magnetic fields
- Poor resistance to demagnetisation following exposure to high current electron beam

In order to overcome the limit of the minimum undulator period length, various approaches have been taken into account. First of all the in-vacuum undulator (IVU). The concept of the IVU is to installing the permanent magnet arrays inside the vacuum chamber: the vacuum gap is exactly the same as the magnetic gap. The main advantage of IVU is that the gap size can be reduced unless the beam is perturbed. Therefore, a short magnetic period can be achieved using small-size magnet blocks resulting in high energy fundamental radiation. At NSLS Brookhaven [1] a good performance mini gap undulator has been realized. Its characteristics are summarized in Table 6.1.

Table 6.1: NSLS BNL mini gap undulator characteristics

NdFeB with Vanadium Permendure poles	
Magnetic period	12.5mm
Number of poles	54
Minimum gap	3.3mm
Magnetic field strength	0.92T
Undulator parameter K	1.07

Although the design of IVU enables a short magnetic gap, there is a crucial limit in the performance of NdFeB material in terms of maximum magnetic field obtainable and resistance to demagnetisation following exposure to an electron beam as shown in Fig. 6.1.

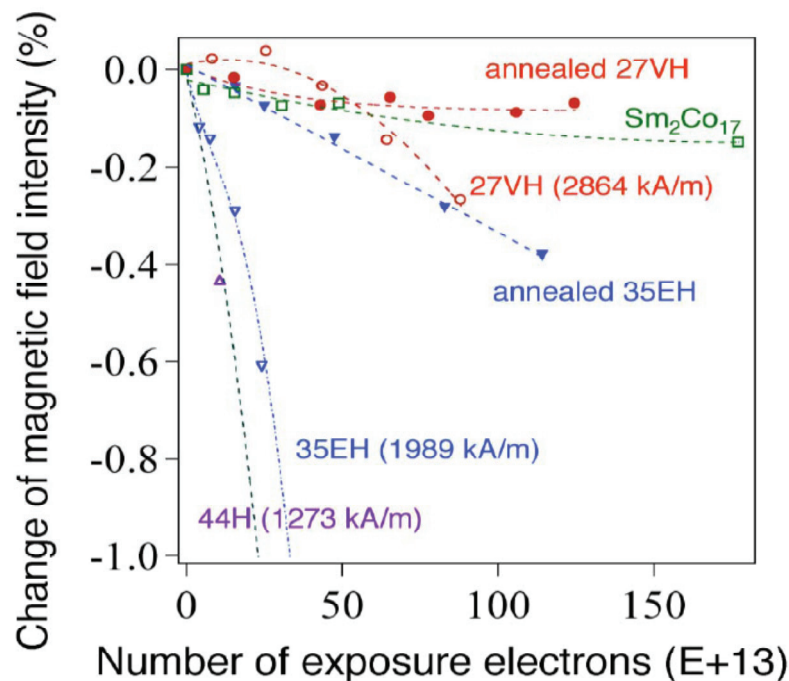


Figure 6.1: Demagnetisation of NdFeB vs. number of exposure electron (courtesy of H. Kitamura , SCSS [2])

Earlier concerns about demagnetization of NdFeB magnets are less of concern now with proper magnet selection after many years of successful

operation at Spring-8, NSLS without any signs of demagnetization. IVU can be a standard device for an X-ray source in a medium-scale facility. NdFeB with high coercivity or Sm₂Co₁₇ should be adopted.

Cryogenic Permanent Magnet Undulator

Cryogenic Permanent Magnet Undulator (CPMU) was first proposed in 2004 [2] at SPRING-8 and is based on the idea to expand the possibility of the in-vacuum undulator technology. The advantage of CPMU comes from the specific property of NdFeB, its negative temperature dependence of the remanence and the coercivity (Fig. 6.2 and Fig. 6.3): both increase as the magnet temperature decreases [3]. Such a gain in magnetic performance can be obtained by cooling down permanent magnets to a cryogenic temperature.

With high remanence it is possible to reduce undulator period. High coercivity increases resistance to radiation. CPMU can be used to extend the undulator spectrum to higher X-rays energies.

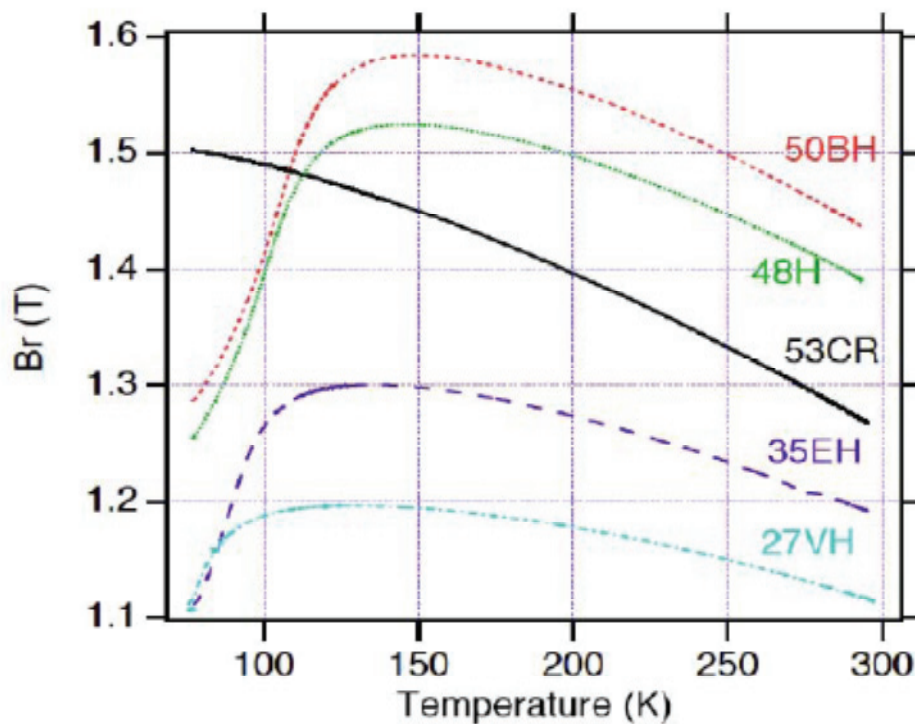


Figure 6.2: Temperature dependence of remanent field NEOMAX-XX (NdFeB coloured lines, PrFeB black line). Courtesy of H. Kitamura, SCSS [2]

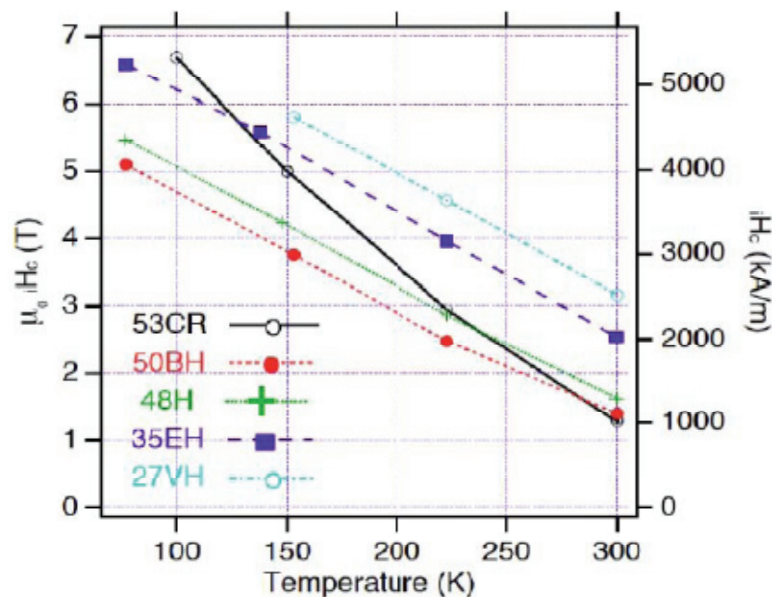


Figure 6.3: Temperature dependence of coercivity NEOMAX-XX (NdFeB coloured lines, PrFeB black line). Courtesy of H. Kitamura , SCSS [2]

Differently from the superconducting undulator technology, heat load problem is negligible [4]. We can expect much higher cooling capacity of cryocooler at liquid Nitrogen temperature (200W at 77°K) than the cooling capacity at liquid Helium temperature (~ 2W at 4°K) (the cold surface of magnets may suffer heat load from e-beam or synchrotron radiation).

One critical aspect is the mechanical deformation induced by temperature gradients along the magnetic assembly which results in local gap fluctuations. A possible solution has been proposed [5] which consists in using of aluminum girders together with adapted mechanical connection of the cooling pipes.

It has been also suggested that the use of the new material PrFeB magnet continually increases its remanent field as the temperature is decreased. It is under investigation [6] the use of Dysprosium poles for hybrid magnet structures which could potentially have a saturation level over 3 Tesla which can dramatically increase CPMU performance over the currently used material such as vanadium-permendure

Superconducting Undulators

Although superconducting undulator (SCU) has been developed about thirty years ago it is not yet a reliable technology. Some technical challenges exist, such as beam and/or radiation heating of the vacuum chamber. Heating can come from a number of sources such as thermal conduction into the chamber from the ends, radiation heat transfer from the ends, beam scraping, synchrotron radiation heating, and heating due to the beam image currents in the beam tube. Heat from most of the sources can be controlled.

Heating due to image currents from the beam may be the largest source of heat [7]. A promising solution has been proposed and realized [8]: a layer of high purity copper (~25µm) is plated on the inside of a stainless steel bore tube. For low temperature the anomalous skin depth effect depends on the residual resistivity ratio of copper layer which in this case is of the order of 100 and it reduces the beam heating.

Another issue for SCUs is phase error correction and field shimming. Notwithstanding a great effort has been made at ANKA [9] in cooperation with industry [10] and results are very encouraging (ANKA SCU characteristics are summarized in Table 6.2).

Table 6.2: ACCEL SCU main characteristics at ANKA
ACCEL SCU main characteristics at ANKA

Magnetic period	14mm
Magnetic gap (in steps variable)	8 - 12 - 16mm
Number of periods	100
Magnetic field	0.7T

6.2 Undulator design

The undulator is the core of any FEL device, which, along with the relativistic e-beam passing through it, realizes the relevant active medium. The properties of the radiation emitted by electrons in the undulator are important for different reasons, they may provide indeed a useful flux of radiation and can be used as a diagnostic tool for the e-beam itself and of the undulator field as well. A pictorial view of the arrangement of the undulator sections along with the electron beam transport line for a SASE FEL is shown in Fig. 6.4.

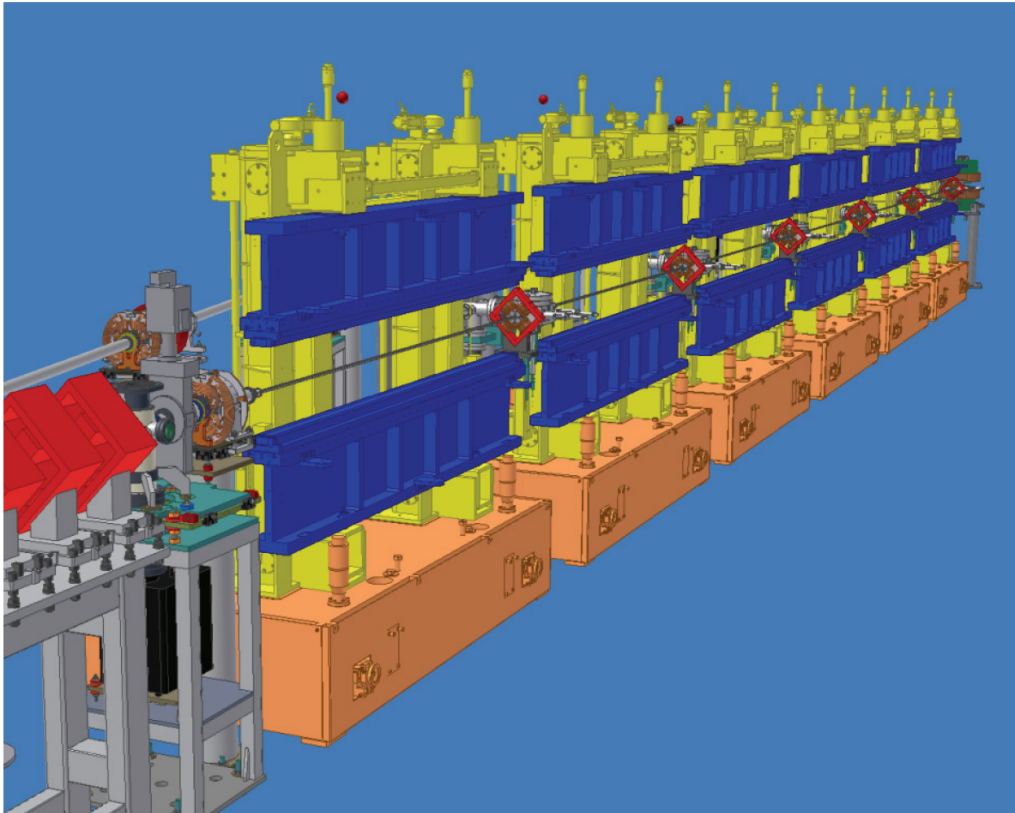


Figure 6.4 : Arrangement of the undulator sections (the undulator drawing is based on ACCEL design) with the relevant transport line.

These undulator sections are separated by empty gaps dedicated to the installation of quadrupoles for the e-beam transport, phase correctors for the compensation of the phase advance between electrons and fields in the longitudinal phase and for the installation of diagnostics for both the e-beam and the FEL radiation. The quadrupole responsible of the horizontal focusing is clearly visible in the picture Figure 6.5 . The electron beam transport in the undulator is indeed realized with a FODO lattice, where the focusing is provided in the vertical direction by the undulator field, and in the horizontal direction by quadrupoles between the sections.

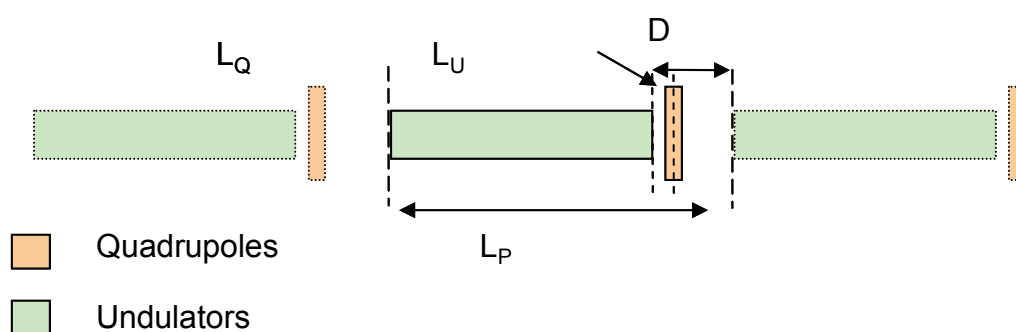


Figure 6.5: Layout of the undulator FODO lattice.

The SPARX VUV-EUV beamline (see section 4.1) consists of 10 identical undulator sections. A variable gap, pure permanent magnet NdFeB, linear undulator arranged to the standard Halbach configuration has been adopted for each section (see considerations in 6.1). In Table 6.3 the main undulator characteristics are summarized

Table 6.3: SPARX VUV-EUV undulator characteristics

SPARX VUV-EUV undulator characteristics	
Pure permanent magnet NdFeB (Halbach configuration)	
Magnetic period	34mm
Number of periods/section	67
Minimum gap	8.1mm
Undulator parameter K (max)	3.275
# of sections	11

The SPARX EUV-Soft X-Ray undulator beamline is composed by three different groups of sections, characterized by a period length decreasing toward the end of the structure (see section 4.1). Conventional magnetic technology can also be adopted. In Table 6.4 the main undulator characteristics are summarized

Table 6.4: SPARX EUV- X-ray undulator characteristics

	1 st group	2 nd group	3 rd group
Pure permanent magnet NdFeB	yes	yes	yes
Magnetic period	40 mm	28 mm	22mm
Number of periods/section	55	77	100
Minimum gap	8.1mm	8.1mm	6.1mm
K parameter (max)	3.27	2.3	1.9
# of sections	4	12	4

The second group of undulator sections matches exactly the period of existing SPARC undulators [18].

Hard X-ray beamline (0.62 nm – 3.1 nm)

In order to provide photons in the energy range 400 eV – 2 KeV an undulator with a very short period is necessary. We are analysing the performance of an FEL based on cryogenic permanent magnet undulator (SCSS like *1.5 cm period, K ~ 1.2-1.3 at 3.7 mm gap*) (see Table 4.15).

6.3 Undulator Tolerances

The aim of an accurate undulator design for SASE FEL is to investigate the possible sources of errors which can influence gain length and consequently the saturation length. There are many significant parameters in the system, and a deviation in any of these parameters will increase the saturation length. An accurate tolerance investigation for the various parameters has been carried out and it is based essentially on three classes of issues:

- Quality of the magnetic field
- Mechanical alignment of the undulator segment pole faces
- Mechanical alignment of the entire beamline

Quality of the magnetic field

Very strict tolerances are required on the magnetic field quality of the SPARX undulators in order to meet the condition of saturation and to ensure the design performances. The undulator is also responsible of the beam transport optics, which has to be correctly integrated in the transport system of the whole device. Two issues are of major concern:

- Accurate identification of the mechanical and magnetic axes and control of the gap tuning.
- Quality of the magnetic field, namely homogeneity of the transverse magnetic field components along the beam axis and minimization of the errors of the field integrals calculated along the beam axis.

A highly accurate magnetic field measurement system is therefore required for the undulator characterization and optimization.

Inhomogeneities of magnetization within the blocks, error of positioning of the blocks can induce peak field, period fluctuations as well as field shape deformation. Thus the B_y distribution on the axis field is no more provided by a pure sinusoid.

The Fourier spectrum of the measured undulator magnetic field can be used to have a first estimation of the deviation from the canonical value of the undulator parameter K as shown in [11]. It is evident from fig. 6.6 that the distribution is essentially a sine-function. Two extra harmonics (the 3rd and 5th) with a relative amplitude with respect to the fundamental of about 1% have to be considered.

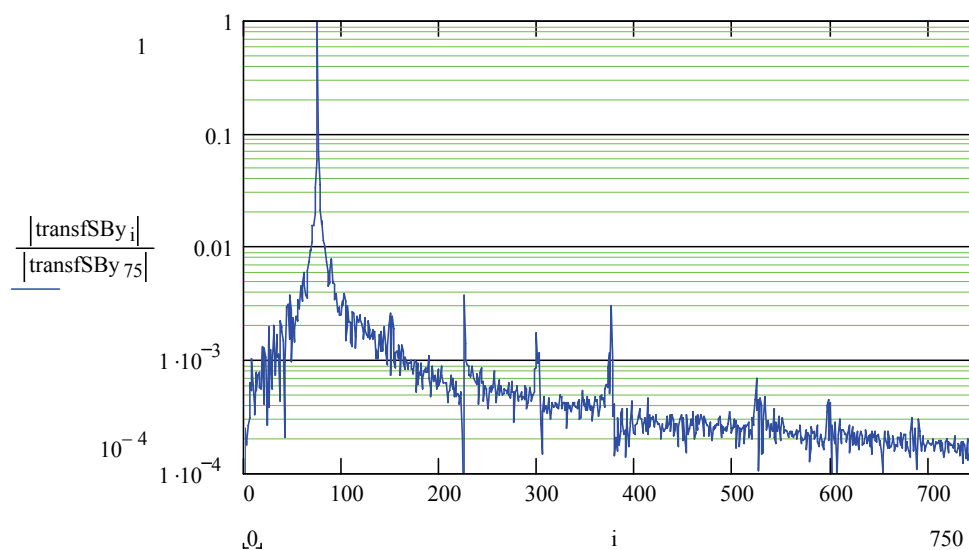


Figure 6.6: Fourier spectrum of the B_y magnetic field normalized to the 1st harmonic (measurements of the SPARC ACCEL undulator prototype carried out at the ENEA labs.)

The field in the y -direction on the magnetic axis is therefore provided by:

$$B_y = B_0 \left\{ \sin\left(\frac{2\pi}{\lambda_u} z\right) + 10^{-2} \left[\sin\left(\frac{6\pi}{\lambda_u} z\right) + \sin\left(\frac{10\pi}{\lambda_u} z\right) \right] \right\} \quad (6.1)$$

The K value due to this function contribution is given by [12] :

$$K = K_0 \sqrt{1 + \left(\frac{d_3}{3}\right)^2 + \left(\frac{d_5}{5}\right)^2} \quad (6.2)$$

We can therefore estimate a deviation from the canonical value given by

$$\frac{\Delta K}{K_0} \approx \frac{10^{-4}}{2} \left[\frac{1}{9} + \frac{1}{25} \right] \cong 10^{-5} \quad (6.3)$$

The correct “figure of merit” for undulator performance is the rms phase error that is the most important quantity in determining the radiation properties [13],[14],[15].

The undulator phase error is a phase advance per period, defined by the formula

$$\Phi(z) = k_u \left[\frac{1}{1 + \frac{K^2}{2}} \left(z + \frac{e^2}{m^2 c^4} J(z) \right) - z \right] \quad (6.4)$$

Where

$$\begin{aligned} k_u &= \frac{2\pi}{\lambda_u}, \\ J(z) &= \int_0^z I_1^2(\zeta) d\zeta, \\ I_1(z) &= \int_0^z B_y(\zeta) d\zeta \end{aligned} \quad (6.5)$$

the phase error is related to the deviation from the ideal K value induced by a non zero average angle from the on axis field due to non zero values of the first field integral [16]

$$\begin{aligned} \Phi(z) &= -\frac{\pi z}{2\gamma^2 \lambda} \left[K^2 - K(z)^2 \right], \\ K(z) &= \left(2 \frac{e^2}{m^2 c^4 z} \int_0^z I_1^2(\zeta) d\zeta \right)^{\frac{1}{2}} \end{aligned} \quad (6.6)$$

In [17] it is shown that the relative deviation from the canonical K value is linked to the phase error and reads

$$\frac{\Delta K}{K} \cong \frac{1}{2} \frac{\lambda_u}{\pi \cdot z} \frac{1 + \frac{K^2}{2}}{K^2} \Phi(z) \quad (6.7)$$

The phase error estimation (eq.6.4) strongly depends on the integral $J(z)$ determination accuracy, which in turns depends on the magnetic field first integral accuracy.

An alternative method for phase error evaluation has been considered which is independent of all most operating parameters but $B_y(z)$ measurements.

It consists in searching the zeros of the field integral $J(z)$, then in evaluating the standard deviation σ_T and mean $\langle T \rangle$ of the intervals between successive zeros:

$$\Phi = 2\pi \frac{\sigma_T}{\langle T \rangle} \quad (6.8)$$

Mechanical alignment of the undulator segment pole faces

Deviations from the ideal field will cause the average beam position to move away from a straight line into a random walk trajectory. Another contribution to random walk can come from misalignment of the undulator pole faces with respect to mid plane axis as shown in Fig. 6.7

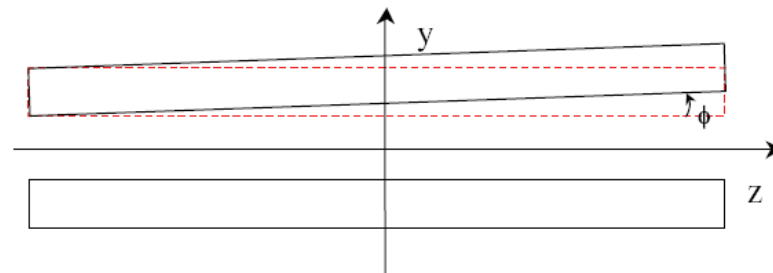


Figure 6.7: Misalignment of the undulator pole faces with respect to mid plane axis

The angular displacement shown in Fig. 6.7 leads to a variation of the on axis magnetic field for a single undulator section given by

$$B(z) = B_0 \left[1 \pm \pi \cdot z \frac{\delta}{L_u} \right] \quad (6.9)$$

See ref. [17] for the relevant field evolution

As the angular tolerances, we should include the effects due to an azimuthal tilt as shown in Figure 6.8

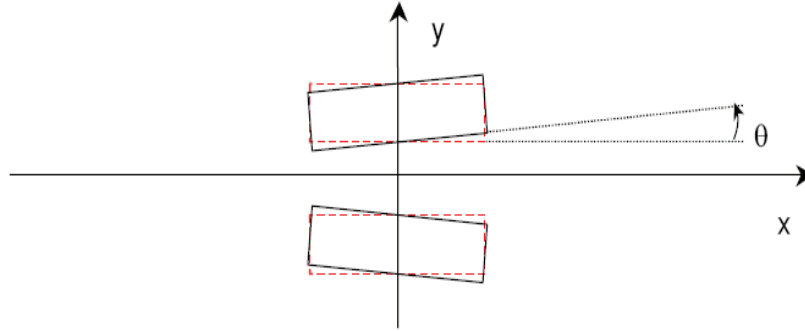


Figure 6.8: Transverse misalignment of the undulator pole faces with respect to mid plane axis

The relevance of this contribution does not appear particularly dangerous. They may affect the focusing properties of the magnet and the associated variation of K can be easily computed as

$$\frac{\Delta K}{K} = \pi \frac{L_T \text{tg}(\theta)}{\lambda_u} \quad (6.10)$$

which leads to the condition

$$\theta < \rho \frac{\lambda_u}{\pi L_T} \quad (6.11)$$

By keeping $L_T = 5$ cm, we find the upper limit for the azimuthal deviation given by $\theta < 3 \cdot 10^{-4}$ rad.

We can use a more rigorous argument based on the focusing properties of an undulator having the previously quoted tilt. We note indeed that the y -component of the magnetic field can be written as

$$B_y = B_0 \left(1 \pm \pi \frac{x\theta}{\lambda_u} \right) \sin(k_u z) \quad (6.12)$$

The relevant betatron equation along x -direction writes

$$x'' = \mp \frac{1}{2} \left(\frac{K}{\gamma} \right)^2 \pi \frac{\theta}{\lambda_u} \quad (6.13)$$

Which once integrated yields

$$x(z) = \mp \frac{1}{4} \left(\frac{K}{\gamma} \right)^2 \pi \frac{\theta}{\lambda_u} z^2 \quad (6.14)$$

This last relation can be exploited to get a condition at the end of the undulator as

$$\theta < 2 \frac{1 + \frac{K^2}{2}}{(KN)^2} \frac{x(L_u)}{\lambda \pi} \quad (6.15)$$

with λ being the resonant wavelength and N the number of undulator periods. By assuming that $x(L_u) \approx 10 \mu\text{m}$ we find $\theta < 1.5 \cdot 10^{-3} \text{ rad}$.

The third misalignment to be account for is that relevant to the horizontal deviation ψ between the faces, as shown in Figure 6.9.

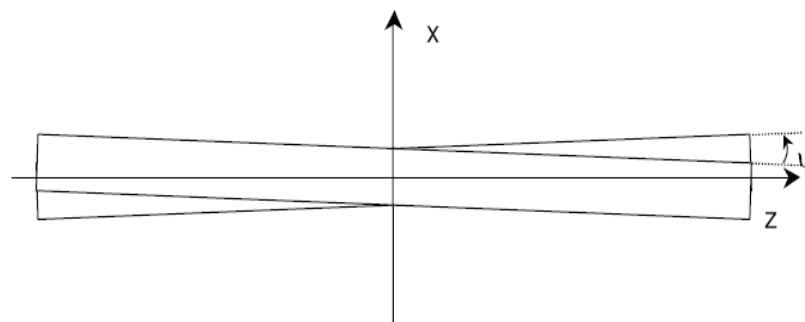


Figure 6.9: Misalignment of the undulator pole bars with respect to z axis

In this case the computation of the relevant effect is less straightforward. It provides an additional variation of K due to the fact that the magnets in the Halbach configuration with parallel magnetization, yields a contribution

depending on $\sin(\psi)$ which should be subtracted. With this assumption we may evaluate, by following the same procedure as before, an upper limit $\psi < 5 \mu\text{rad}$.

Mechanical alignment of the entire beamline

The design of a realistic undulator magnetic system for short wavelength high gain FEL requires consideration of an inhomogeneous magnetic system with focusing quadrupoles inserted into the breaks between undulator segments. Each section must foresee the necessary equipment to fulfil the following tolerances for the mechanical alignment of the complete beamline, according to the prescriptions shown in Table 6.5.

Table 6.5: SPARX undulator segment tolerance specification

Maximum error of vertical positioning	5 μm
Maximum error of horizontal positioning	5 μm
Maximum error of longitudinal positioning	50 μm
Maximum deflection angle θ	10 μrad
Maximum deflection angle ϕ	5 μrad
Maximum deflection angle ψ	100 μrad

Another contribution to random walk can come from transverse misalignment of the focusing quadrupoles. While undulator field errors will cause random walk mostly in one plane, quadrupole misalignment will produce a wander in two planes. Random walk trajectories need to be controlled by correcting the beam path using electron beam position monitors from which the trajectory's deviation from a straight line can be obtained.

One of the challenging issues is the required alignment of the electron beam axis to the radiation beam to a precision of few tenths micrometers over the full several tenths meters. Such an alignment requires sophisticated electron and photon beam based alignment techniques. Another issue is the measurement and tuning of such undulator segments by industry as well as verification of the required specifications by SPARX team in a laboratory purposely prepared for magnetic measurements.

6.4 Undulator measurement system

A Hall probe bench will be used. The bench consists of a Hall probe (Lakeshore model HMFT-3E03-VR) mounted on a movable cart, sliding over an

air cushion on a 3m long heavy granite beam (parallel to the undulator section) whose top surface is polished to a flatness of $\pm 5\mu\text{m}$ to reduce jolting. The cart is driven longitudinally by means of a gear wheel coupled to a cog rail mounted on the granite beam, controlled via a DC-servo motor drive with encoder PI mod. C136-10, which guarantees $1\mu\text{m}$ resolution. The longitudinal jitter/repeatability is estimated to $\pm 5\mu\text{m}$.

Transverse motion is attained by means of a x-y translation stage (Physik Instrumente model M 521 equipped with non contact linear encoder) mounted on the cart. The Hall probe is placed on the the tip of a conical , horizontal aluminium branch, mounted on the x-y stage. The stage linear table provides low friction, backlash-free positioning and guarantees $1\mu\text{m}/100\text{mm}$ straightness and flatness by using precision linear guiding rails with recirculating ball bearings.

All magnetic measurements will be carried out in a dedicated room with temperature control with a stability of $\pm 0.5^\circ\text{C}$. By means of an optical level (NAK2 by Leica) and a laser tracker (LTD 500 by Leica) an absolute horizontal plane has been defined in the hall and the granite block has been aligned to this plane with an error of $10\mu\text{m}/\text{m}$. A coordinate system has been defined with the axes aligned to the edges of the granite block.

To locate the reading area of the Hall Probe LS775 used to qualify the six SPARC's undulators sections [18] a new instrument was built consisting of a soft iron, square-shaped hollow yoke equipped with a set of carefully positioned cylinders made by the same material. The one end, the cylinders have a seat of shape and size designed for insertion of the cube mirrors of a laser tracker; on the other, they have conical head with a very sharp tip (diameter= $100\mu\text{m}$). The cylinders can be inserted in the yoke through four holes drilled at the median positions on each side. Around the cylinders a set of identical coils produce a magnetic field whose flux is conveyed by the cones' very small tips towards the device's central area. There, the field assumes a predictable multipolar configuration (dipole, quadrupole) depending on the sign of the currents flowing through the coils. The whole device was built to a high degree of mechanical accuracy ($10\mu\text{m}$), so that insertion of the Hall probe in the yoke between the cones' tips allow one to refer the reading area of the probe itself to the field's symmetry points, whose positions with respect to the seats of laser tracker's cube mirror can be easily derived.

In Figure 6.10, the geometry of the device as modeled with Radia software is shown. The segmentation corresponds to the maximum that proved to be viable both in terms of best accuracy achievable and reasonable number of iterations needed for the relaxation algorithm to converge. It is worth remarking, however, that we're not interested in absolute accuracy (i.e. the capability of the model implemented in Radia to reproduce the intensity of the fields actually measured) but rather to check that the field's map Figure 6.11, possess the expected symmetry and to what extent the position of the symmetry points can be reconstructed from experimental data. Sources of error (e.g. the effect of earth's field, misplacements of coils, differences in the shape/size/positions of relevant mechanical parts) should be considered, but only some of them will be included in the analysis.

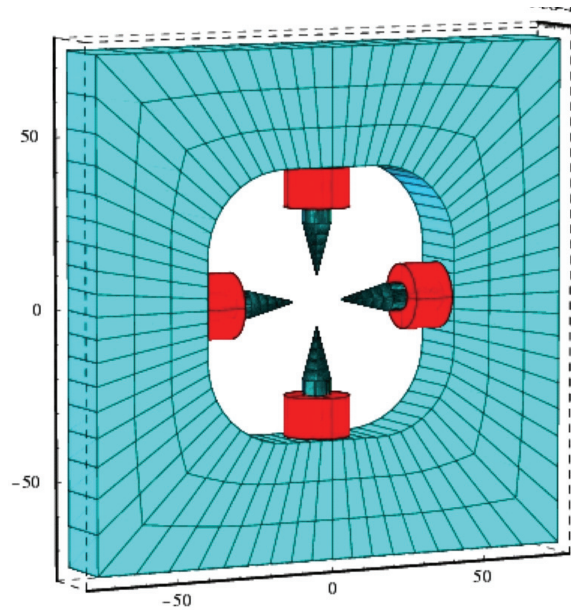


Figure 6.10: Instrument used to locate the reading area of the Hall probe

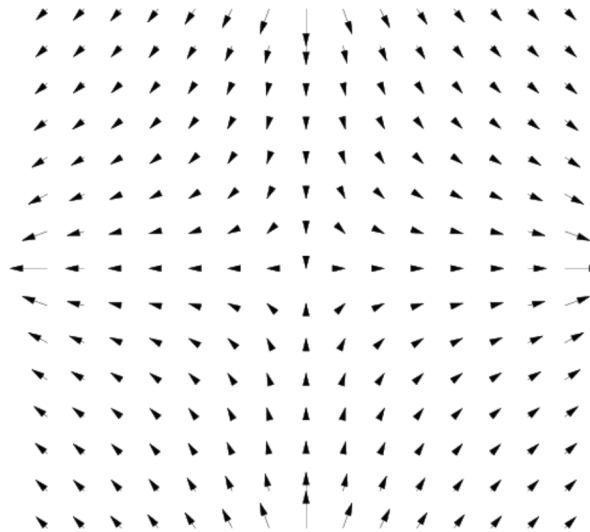


Figure 6.11: Field map

A very accurate alignment (within $10\mu\text{m}$) procedure has been developed at the ENEA labs for the SPARC undulators measurement [18], [19] to determine the undulator magnetic axis. Once the magnetic axis has been identified, repeated longitudinal scans are taken to check reproducibility in the evaluation of field 1st integral which in turns strongly depends on the Hall probe longitudinal position measurement accuracy. In order to enhance the accuracy, the longitudinal positions are acquired by means of a dual-frequency laser interferometer JENAer ZLM700 [20]

6.5 Phase shifter

In a single-pass FEL designed with segmented undulator, the gaps between each undulator segment introduce a phase shift between the electron transverse velocity and the phase of the electromagnetic field. Such a phase mismatch may cause the electrons to momentarily gain energy from the radiation field, interrupting the amplification process. The phase shift ϕ induced by a drift L_d between two segments is a function of the undulator K parameter

$$\phi = \frac{L_d}{2\gamma^2 \lambda_0} = \frac{L_d}{\lambda_u (1 + K^2/2)} \quad (6.16)$$

The main effect of a phase mismatch on the FEL dynamics is an increase of the saturation length. In order to compensate the phase error between two undulator segments in a variable gap device, a variable phase shifter is required. Now we recall the main results of this analysis. A phase mismatch of π is almost sufficient to inhibit the saturation process within the undulator length. Phase mismatches are even more effective in the case of seeded operation. In **Figure 6.12** it is shown the case of the SPARC FEL seeded at 160 nm. It can be observed that a phase mismatch of π induces a loss of about two orders of magnitude in the pulse energy. A phase mismatch has also significant effects on the spectrum of the seeded FEL source, which is not any more resembling those of the input seed.

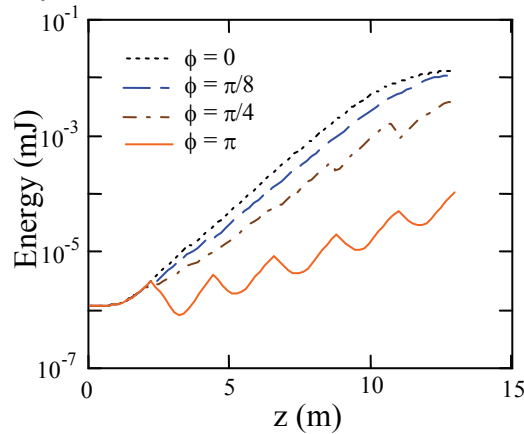


Figure 6.12: Energy along the SPARC undulator for different phase shifts ϕ at the gaps, in seeded mode ($\lambda = 160$ nm, 15 kW input power, 100 fs pulse see duration).

In addition to the correction of phase jumps at the undulator segmentations, phase shifter can be exploited to balance the growth of different harmonics of the FEL resonant wavelength. According to steady state

FEL simulations this method is very effective in suppressing the fundamental harmonic growth .

A phase shift is obtained by a magnetic chicane that delays the beam due to a longer path. This shift may be in principle realized as in the main undulator, with the same kind of permanent magnets, in a similar arrangement. The undulator is indeed capable of inducing a phase advance of 2π for each period. The possibility to vary the gap of this device, i.e. the electron beam path length, independently from that of the undulator allows to compensate for a given phase difference. The main requirement for such a phase corrector is that the field integrals must vanish independently of the specific undulator gap considered. The phase shifter design consists of two groups of permanent magnets, arranged as in the main undulator, in a variable gap magnet assembly which can be tuned independently of the main undulator gap. The simplest way to obtain this is to use a whole undulator period (four magnets). Two magnetic configurations are analysed, both capable of adjusting the phase and to fulfil the requirements in terms of field integrals. In the first one, the ending magnets have the same width but a reduced thickness. In the second one, they were vertically cut. In the final realization the first option will be selected. A RADIA model of the magnetic assembly is shown in Figure 6.13.

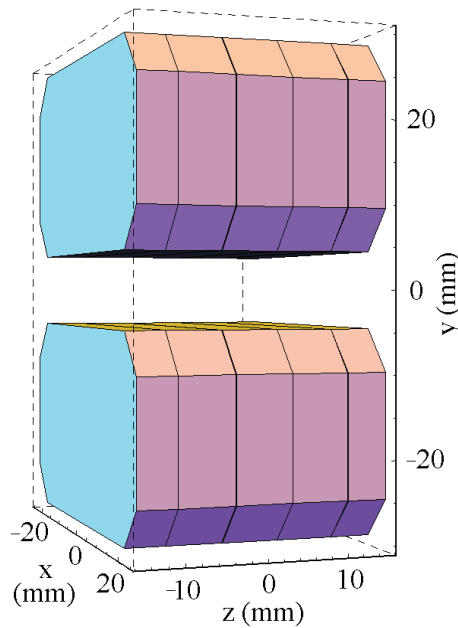


Figure 6.13:Phase shifter RADIA model (five horizontally cut magnets)

6.1 References

- [1] J.M. Ablett, L. E. Barman, C.C. Kao, G. Rakowsky and D. Lynch J. Synchrotron Rad. 11, 129 (2004)
- [2] T. Hara, T. Tanaka, H. Kitamura, T. Bizen, T. Seike, T. Kohda and Y. Matsuura Phys. Rev. ST Accel. Beams 7, 050702 (2004)
- [3] M. Sagawa, S. Hirose, Y. Otani, H. Miyajima and S. Chikazuma J. Magn. Mat. 70, 316 (1987)
- [4] T. Tanaka, T. Hara, T. Bizen, T. Seike, R. Tsuru, X. Marechal, H. Hirano, M. Morita, H. Teshima, S. Nariki, N. Sakai, I. Hirabayashi, M. Murarakami and H. Kitamura New J. of Phys. 8, 287 (2006)
- [5] C.Kitegi, J. Chavanne, D. Cognie, P. Ellaume, F. Revol, C. Penel, B. Plan and M. Rossat Proc. EPAC 2006, Edinburgh, Scotland
- [6] T. Tanabe, J. Bengtsson, D.A. Harder, S. Kramer, G. Rakowsky, J. Rank, Proc. EPAC 2008, Genoa, Italy
- [7] Green et al. Report LBNL-53721
- [8] A. Habl. Et al Accel IEEE Trans. On Appl. Superconductivity Vol 15,2,2005
- [9] T. Baumbach, A. Bernhard, S. Casalbuoni, G. Gerlach, M. Hagelstein, B. Kostra, R. Rossmanith, F. Schöck, E. Steffens, M. Weißer, D. Wollmann, Proc. EPAC 2006, Edinburgh, Scotland
- [10] D. Doelling, A. Hobl, H.U. Klein, D. Krischel, P. Komorowski, M. Meyer-Reumers, Proc. PAC 2007, Albuquerque, New Mexico, USA
- [11] E. Sabia , G. Dattoli, SPARC-FEL-07/002, available at www.sparc.it - Tech Notes
- [12] G. Dattoli, P.L. Ottaviani and S. Pagnutti SPARC-FEL-04/004, available at www.sparc.it - Tech Notes
- [13] B. Diviacco, R.P. Walker Proc. PAC89, IEEE Conference Record 89CH2669-0, p. 1259
- [14] B.L. Bobbs et al., Nucl. Instr. And Meth. A296 (1990) 574
- [15] R.P. Walker Nucl. Instr. And Meth. A335 (1993) 328
- [16] F. Ciocci, G. Dattoli, E. Sabia and M. Sassi SPARC-FEL-07/001, available at www.sparc.it - Tech Notes
- [17] F. Ciocci, G. Dattoli, L. Mezi and P.L. Ottavini SPARC-FEL-3/008, available at www.sparc.it - Tech Notes
- [18] AA. VV., SPARC Tech. Note SPARC-FEL-08/001
- [19] Technical report on measurement, alignment...
- [20] See <http://www.jenaer-mt.com/en/produkte/zlm800.php>.

7 RADIATION BEAMLINES

7.1 General Considerations

Three free-electron-lasers will be employed to produce radiation from 40 eV to 2000 eV (from 30 nm to 0.6 nm) to with extremely narrow bandwidths in very short time pulses (femtosecond regime). As a consequence of the high number of photons available in the short duration pulse of Free Electron Laser (FEL) emission an unprecedented high peak power up to gigawatts imposes severe constraints to the radiation handling in the beamline design. Special attention is required to avoid radiation damage on optics (mirrors, gratings, slit blades, etc.). Also the preservation of temporal duration of FEL pulses after photon transport and monochromatization is a new challenge imposed by these fascinating new sources. Some experiments are feasible by using the intrinsic energy resolution provided by the FEL source allowing to keep the pulse length at the shortest possible value. When a higher degree of monochromatization is needed, a lengthening of the pulse duration is to be paid. Consequently, the fundamental conflict between higher energy resolution and simultaneously short pulse availability should be faced in the beamline design according to the specific users' needs.

The SPARX FEL is designed to provide FEL radiation in seeded configuration [1] allowing to use very short (20-30 fs) and energy stable radiation pulses in the photon energy range between 40 eV and 2000 eV (30 nm - 0.6 nm). This will be done by means of three undulators U1, U2, U3 working at different electron beam energies and undulator gaps. U1 will be fed with electrons whose beam energy may be varied over the range from 0.96 GeV to 1.5 GeV, the U3 will operate with electrons in the range from 1.96 GeV–2.64 GeV while U2 will be able to work with both electron beam energy ranges allowing a very broad photon energy distribution. At the SPARX FEL facility we plan to have at least two different beamlines for each FEL source in order to maximize the users' accessibility. The two beamlines will be optimized for high photon energy resolution and for short-pulse handling. These two types of beamlines have been designed and optimized for the energy ranges of the three FELs: U1: 40 - 120 eV (30 - 10 nm); U2: 100 - 1000 eV (12 - 1.2 nm); U3: 1000 - 2000 eV (1.2 - 0.6 nm). Only one beamline at a time will be used at each FEL, and switching between them is accomplished by means of moveable mirror. This concept has been already used successfully at insertion device beamlines in many Synchrotron Radiation Facilities.

The aim of the project is to push the FEL source SPARX towards short radiation wavelength in order to face the challenging objective of performing the single shot molecular diffraction that will be the revolutionary scenario for biochemistry, pharmacology and molecular crystallography. To reach such a goal, is mandatory to increase the photon energy by implementing the linear accelerator energy towards 5 GeV, making accessible wavelength emission in the 0.1 nm range, at present stage reachable only by using higher harmonics, at expenses of the available photon flux. Table 7.1 reports the main SPARX FEL source parameters calculated by means of GENESIS and PERSEO at 1nC bunch charge.

Table 7.1: Parameters of the FEL sources available at SPARX laboratory

	Units	U1 (0.96-1.5 GeV)	U2 (0.96-1.5 GeV)	U2 (1.9- 2.6GeV)	U3 (1.9- 2.6GeV)
Wavelength/Energy	nm/eV	30-10/40- 120	15-4/80- 300	4-1.2/ 300-1000	1.2 - 0.6/ 1000-2000
Peak power	GW	1.7-3.4	2-9	3-20	0.8@2.4GeV
Average power	W	-	0.1-0.2	0.03-0.1	-
Photon beam size (FWHM)	μm	140	100		120
Photon beam divergence (FWHM)	μrad	33	20		17
Bandwidth (FWHM)	%	0.2	0.2-0.1	0.15-0.1	0.09@2.4GeV
Pulse duration (FWHM)	fs	200	250	70-30	70-80
Repetition rate	Hz	100-50	100-50	100-50	100-50
Number of photons per pulse	#	$1.0 \cdot 10^{14}$	$1.5-8.5 \cdot 10^{13}$	$5 \cdot 10^{12}$	0.5- $1.5 \cdot 10^{12}$
Peak brilliance	phot/(sec · mrad ² · mm ² · 0. 1 % bw).				
Average brilliance	phot/(sec · mrad ² · mm ² · 0. 1% bw).				

The photon beam characteristics that make different the design of standard synchrotron radiation (SR) with respect to FEL beamlines are mostly due to the very high peak energy reaching the optical elements, together with the extremely short pulse length. This differences requires modifications of the usual SR beamline designs as well as the choice of proper materials for optical coating and bulk. The peak energy density from the FEL is four to five orders of magnitude higher than what produced at 3rd generation synchrotron undulator beams. Such energy, delivered in sub-picosecond pulses, creates a large number of excitations and ionizations at surface atoms of the optical elements, inducing desorption (ablation) of surface layer atoms [2]. Such behaviour suggests to avoid strong focussing of the undispersed FEL radiation onto optical elements (slits included) and makes use of grazing incidence angles on the optical surfaces more suitable for photon transport. Finally, surface materials with as low as possible ionization cross section is preferred [3].

The radiation available at SPARX FEL presents a pulsed time structure ranging in 100 - 50 Hz repetition rates domain and pulse lengths of about 50 ÷

200 fs, with a peak power of $1 \div 5$ GW. The product of the pulse frequency and the pulse length for the given peak energy determines the total delivered power. Therefore, the integral power load delivered on the first optical element at each beamline ranges between 0.01 - 1 W. Also taking into account the power loads due to the spontaneous emission of the undulator, as well as, the radiation emitted by the bending magnet used to deflect the electron beam out of the photon trajectory very low values result for the average thermal load, values much smaller than what expected in typical SR beamlines, making conventional side cooling sufficient to remove the average heat load from optical elements.

The principal characteristic of the FEL radiation is its very short pulsed structure that should be preserved as much as possible passing through the optical elements along the whole beamline. In fact when this radiation pulses are energy dispersed by a diffraction grating its time distribution is inevitably modified. This is a consequence of two contributions: a) the different optical paths travelled by the individual photons within the same pulse and b) the mutual dependence of pulse length and energy bandwidth through the Fourier transform limit relation $\Delta T \Delta E \geq h/4\pi$

In the case of mirrors the optical path differences are close to zero and no energy dispersion is introduced in the photon pulse leaving almost unperturbed the pulse width. In the case of diffractive elements the light of wavelength λ illuminating a grating with N line density at an angle of incidence α is diffracted at angle β at first order. The diffraction pattern is determined by the interferences of rays which experienced a delay resulting in a path difference given by the grating equation $N\lambda = (\sin\alpha - \sin\beta)$. A pulse time width variation is roughly estimated to be equal to the path difference divided by the speed of light. According to beam divergences and the angles of incidence needed, the pulse width broadening will range from 0.01 to 10 ps depending on the requested photon energy resolution [4].

7.2 Power Load, Radiation Damage and Optical Design

7.2.1 Damage

While the average power is moderate, the peak power on the mirrors may be in the GW range. At these values, the principal problem may no longer be thermal distortion, but rather the possibility of plasma formation at the optical element surfaces, which affects the reflection efficiency and may even cause permanent damage. Formation of plasma will depend on the radiation dose per pulse, described as the energy absorbed per atom per pulse.

In the VUV and soft X-ray range, grazing angles of few mrad are commonly used to obtain good reflection efficiency and to reduce power per unit area on the mirror surface. The induced heat load, however, is related to the deposited energy per unit volume, i.e. the dose. This quantity becomes small only at incidence angles significantly larger than the critical angle α_0 for two reasons: 1) the penetration of the field into the mirror becomes roughly independent of the angle and no longer compensates the increasing size of the beam footprint, 2) the mirror also starts to reflect efficiently. Because the beam footprint and the reflectivity increases linearly with increasing α , the dose scales roughly with α^2 [5].

Table 7.2 shows the damage thresholds for several interesting bulk and coating mirror materials taken at FLASH FEL Facility [6], at two different photon wavelengths. The effects of surface damage should be avoided in order to preserve optics integrity. In order to guarantee long life to the optical coatings,

surfaces should be shined at sufficiently small grazing angle to ensure the energy density deposited onto the optical surfaces at least a factor ten less than the damage threshold. At the same time grazing incidence optics, increasing the reflectivity at smaller wavelengths, reduces the surface power load by absorption.

Table 7.2: Damage thresholds

$\lambda = 89 \text{ nm}$	mJ/cm^2	$\lambda = 32.5 \text{ nm}$	mJ/cm^2
Si	<4	Si	87 ± 45
a-C	<10	a-C	65 ± 30
		SiC	141 ± 70
		B ₄ C	197 ± 100
		CVD diamond	156 ± 75
Gold	<40		

7.2.2 Mirrors and Coatings

Generally, the reflectance of optical surfaces increases when reducing the grazing incidence angle θ [5]. At the same time the footprint of the incident beam spread on a larger area proportionally to $1/\sin\theta$. At first sight it seems that a reduction of the incidence angle always reduces the load on the optical surfaces but, if the effective layer thickness of the mirror coating is considered, the energy absorbed per atom at the surface may increase as the grazing angle is reduced. In some cases in the VUV and X-ray region the index of refraction of matter is smaller than its vacuum value allowing taking advantage of total external reflection from optical surfaces at incident angles higher than the critical angle θ_c . In this regime the penetration depth of radiation into materials is nearly independent on the incidence angle.

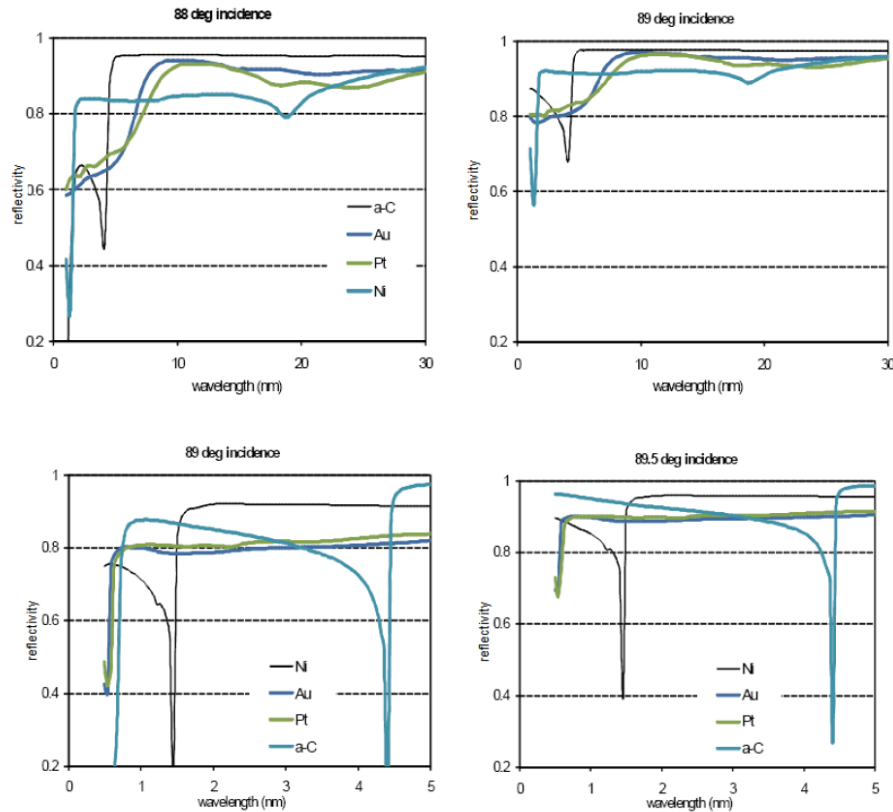


Figure 7.1: Reflectivity of some mirror coatings in the 1-30 nm region (upper panels) and 0.5-5 nm range (lower panels) calculated at different incidence angle.

This effect contributes to a further reduction of energy absorbed per surface atom which is still proportional to $1/\sin\theta$. The previous considerations indicate that in order to avoid damage of reflecting optical surfaces, smaller grazing angles are preferred, possibly in total reflection conditions.

The reflectivity behaviour is influenced by the inner shell absorption edges that introduce strong changes in the values of the optical constants of the surface mirror coating. Optical elements for VUV and soft X-ray radiation are, usually, coated with a material different from the substrate to enhance the reflectivity in a specific spectral range. Figure 7.1 shows reflectivity with respect to photon wavelength of some commonly used coating materials for soft X-ray optics [7].

Very strong structures in the reflectivity spectrum are evident in correspondence of the excitation energies at the K- and L-edges of the optical material due to the strong increase of the absorption cross section by more than one order of magnitude [8], enhancing the risk of surface damage. The reduced reflectance also precludes their use in these energy ranges; as a consequence the choice of the mirror coatings is dependent on the spectral interval we are interested in and should take into account materials with no absorption edges within the photon energy range of the beamline. Generally coating materials with small atomic numbers are more suitable to withstand the intense FEL beam.

The cross section of the low Z elements such as carbon are up to two orders of magnitude lower, for example, than high Z element like gold. Due to its damage resistance (see Table 7.2) and to the absence of absorption edges and high reflectivity, carbon is a very good coating material in the range from

20 to 270 eV (60 - 4.5 nm). At higher photon energy several candidates are possible, but the most promising coating material seems to be nickel. Its M- and L-edges at 70 eV and 850 eV, respectively, are far enough each other to provide an extended energy range for a soft x-ray beamline. At photon energies between 800 eV and 2000 eV (1.6 nm and 0.6 nm) carbon is again a suitable material together with Au and Pt.

Carbon has excellent thermal properties when used in its diamond modification. Assuming a grazing angle on the mirror as small as $\approx 0.5^\circ$, carbon coating reflectivity varies between 90 and 95% in the energy range 1 to 2 keV (1.2-0.6 nm). In the range from 500 eV to 2 keV (2.5-0.6 nm) carbon coating seems more suitable, in comparison with metal coatings, due to its better performance below 1 keV.

7.3 Photon Beam Transport

Figure 7.2 shows the general layout of the beamlines in the experimental hall. The electron bunches produced by the LINAC at 1.5 GeV and/or at 2.4 GeV are injected into three undulators with different characteristics as previously described. The three undulators produce radiation in different spectral ranges U1: 40 - 120 eV (30 - 10 nm); U2: 100 - 1000 eV (12 - 1.2 nm); U3: 1000 - 2000 eV (1.2 - 0.6 nm). The undulators are mounted at different angles with respect to the Linear Accelerator electron beam direction. U1 is shifted rightward and displaced of 2° . The U2 is also rightward shifted and deflected of 0.5° while the U3 undulator is leftward displaced with an angular deviation of 1° . A shielding wall separate the undulator hall from the experimental area. Before the FEL radiation passes the shielding wall, to feed the beamlines, a front-end section is met. After introduced into the experimental hall, the photon beam is deflected and energy characterized by a non destructive in-line spectrometer which acts also as the first deflecting mirror of each beamline, to remove the FEL photon beam from the direct observation of the undulator axes. For this reason the whole spectrometer is set inside a radiation safety hutch in order to avoid exposure to high energy bremsstrahlung radiation due to the scattering of accelerated electrons with residual gases in the undulator pipeline. Movable optics is designed for the characterization spectrometer, in such a way to allow the photon beam to pass undeflected to use high energy spontaneous emission. At the exit of the safety hutch the beam enters into a long pipe (10-20m) equipped, at the two ends, with differential pumping stage. This is the gas absorber stage that allows to control the intensity of FEL pulses and the high harmonic content of the "white" FEL photon beam, when working without monochromator spectral selection. At the end of the gas filter a second retractable mirror is met. This mirror, plane or concave, distribute the radiation into two different sections that usually have different monochromator performances, one with large bandpass, used to "clean" the pulse from any photons other than the selected harmonic, and one that allows to select narrow bandwidths. When a high-resolution monochromator is needed, the effect on the beam pulse duration is more evident, therefore, in the design of a monochromator the temporal lengthening has to be taken into account. The proposed designs are optimized with respect to groove density and angle of incidence in such a way to control the stretching of the pulse duration for Fourier transform-limit. After monochromatization the radiation from the exit slit is focussed onto the sample in the experimental chamber. Again the possibility of choosing different properties of the focussed beam are

considered and, where possible, two different focussing mirrors, working alternatively, are available.

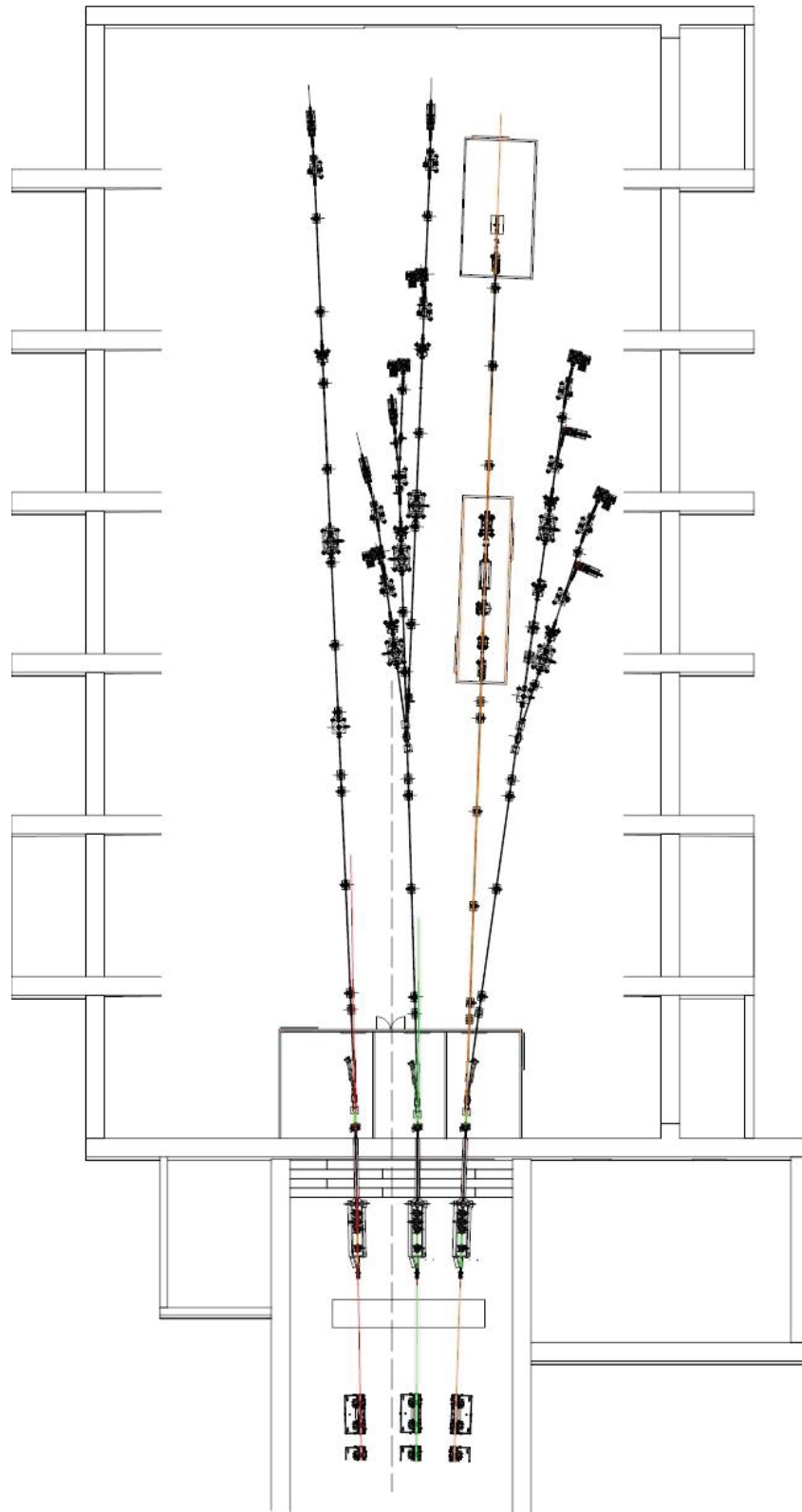


Figure 7.2: General layout of the beamlines at SPARX User Facility.

7.3.1 Front-end

The front-end is the interface between the photon source and the user beamline. It is designed to separate vacuum and for radiation safety purposes. It is the last equipment met before the FEL radiation enters the experimental hall and the beamline (a sketch is reported in figure 7.4).

A front-end must fulfil the following functions [9]:

Vacuum separation of the machine (LINAC and undulators) from the beamline. This is obtained by means of narrow pipelines equipped with remotely controlled valves.

2. Safety vacuum interlock system to regulate the manual opening and manual/automatic closing of separation valves.

3. Vacuum protection of the machine from sudden ventings that may happen somewhere in the beamline. This is made by means of a 3m vacuum delay pipe to break the pressure shock-wave and allow the action of a fast closing valve set in between the front-end and the undulator.

4. Radiation safety separation of the machine area from the experimental hall and the beamline. This is obtained by means of a beam shutter made of a tungsten alloy of suitable dimensions to strongly reduce the bremsstrahlung radiation from the undulator vacuum chamber; it will be placed before the radiation safety wall.

5. Definition of the optical path and suppression of scattered light between the machine and the beamline. A precision moveable diaphragm allows determining the propagation direction of the laser beam and defining the angular acceptance of the beamline. Variable acceptance angle is crucial in the suppression of scattered light from the source and in reducing the spontaneous emission content collected from the FEL source. Variable acceptance should be taken into account in case of front-ends that should allow collection of spontaneous emission from the undulator. Due to the strong power load experienced by surfaces shined by FEL radiation, movable apertures must be designed in such a way that the footprint of the FEL pulses results spread over a large area by using grazing incidence surfaces, typically of about 6° . Cooling of this devices could be taken into account to avoid desorption from surfaces maintaining the quality of vacuum into the front-end.

6. Diagnostics for determining the position and the emission angle of the radiation source (photon beam position monitors) should be also present in the frontend; these devices should be developed and must be able to perform $10\mu\text{m}$ spatial and $0.1\ \mu\text{rad}$ angular resolution.

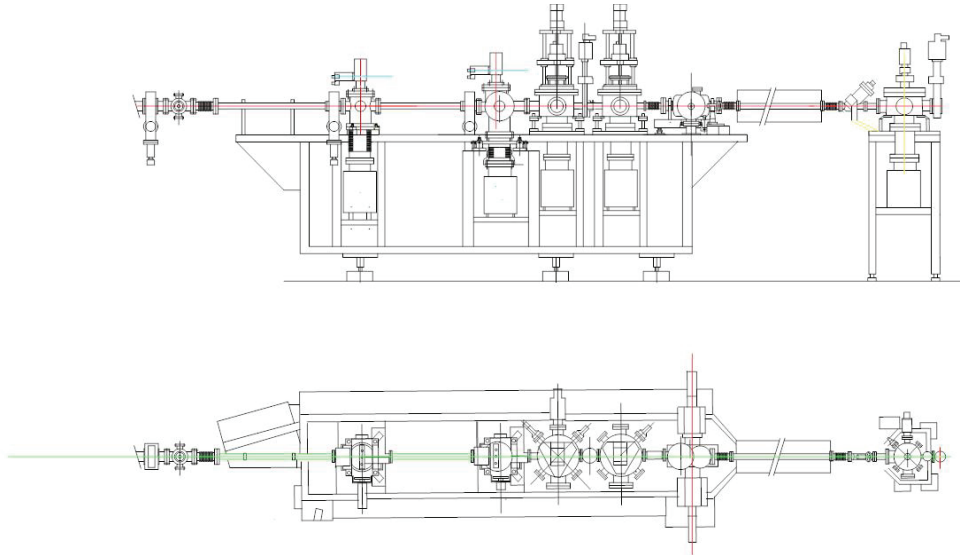


Figure 7.3: Sketch of a possible vacuum front-end for the FEL beamlines.

7.3.2 Vacuum

Table 7.3 reports the vacuum components of a generic beamline, sketched in Fig. 7.5, that fulfils the requirements of SPARX type beamline. The diameter of the vacuum pipes between devices, as well as the vacuum valves is 63 mm, where not differently specified. The valve along the beamline should be all-metal valve, to fulfil the necessary safety constrain toward accidental exposure of the closing surface to FEL and spontaneous radiation pulses. The first valve facing the source should be protected by a photon beam shutter (i.e. a copper block) enough massive and water cooled to support the power load of radiation coming from the undulator. The pressure demand for mirror and monochromator chambers will be in the $10^{□8}$ Pa range to minimize contamination. A beam-pipe diameter of 63 mm is chosen to reduce the number of pumps along the beamline. Ion pumps of nominal pumping speed of 120-250 l/sec are installed along the beamline in correspondence or close to the optical elements in order to reach the optimum value of residual gas pressure. Long pipelines for light propagation are additionally pumped with ion pumps of nominal pumping speed of 75 l/sec in order to get an average pressure not worst than $10^{□7}$ Pa. Vacuum gauges, residual gas analyzer and safety sensors are present all along the beamline in order to monitor pressure and vacuum quality.

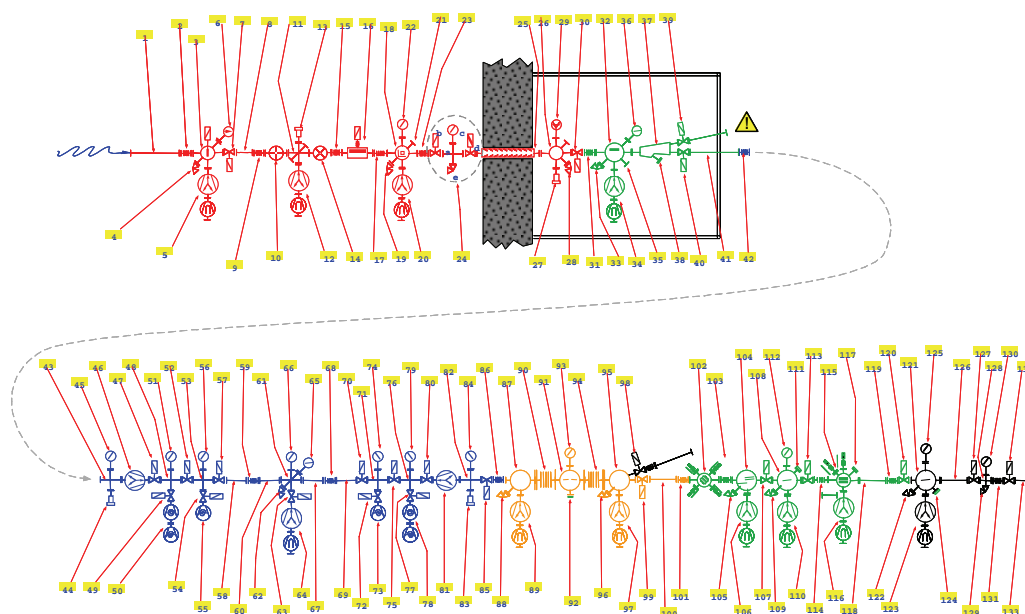


Figure 7.4: Vacuum structure of a generic beamline at SPARX

Six vacuum sections, separated by valves, are designed. The first one coincides with the front-end and has been previously described. The second is into the radiation safety hutch and consists of the vacuum section connected with the spectrograph for synchronous spectral analysis of the radiation pulses. The optical design needs a movable mirror chamber to allow switching of the mirror/grating position on the optical path. This is made by shifting the mirror chamber of 15-20 mm in normal direction with respect to the propagation of the photon beam. The next section guests the attenuation and filtering instrumentation for the FEL beam. It consists of a 10 m long gas cell of 40 mm diameter (CF40) which is filled with rare gases up to 10 Pa and, in order to fulfil vacuum requirements, towards both the front-end and the monochromator sides, should be equipped with appropriate differential pumping stages on the two ends of the gas cell. Each differential pumping section consists of diaphragms and capillary pipes for reducing conductance, turbo pumps to get enough pumping speed and suitable commercially passing through ion pump units able to support 10^{-5} pressure ratio between in and out port. A second switching mirror follows; it distributes the photon beam into two beamlines for spectral selection whose vacuum plants is very similar to the standard synchrotron ones. The next section is the last before the users and consists of one or two refocussing mirrors to produce a suitable light spot on the sample according with the experimental requirements. The end of the vacuum pipe should be equipped with tools that guarantee very good vacuum condition to the experiments (additional pumps) and protect (differential pumping stage) mirrors from critical operation in the experimental chamber.

Table 7.3: Vacuum components of the generic vacuum system of a SPARX beamline

N.	ELEMENT	ID	N.	ELEMENT
1	nipple		67	nipple
2	bellows		68	bellows
3	light beam stopper		69	nipple
4	right angle all metal valve	70	70	all metal gate valve
5	sputter ion pump+Ti sublimator	250 l/s	71	4 ways cross
6	ion gauge		72	gate valve
7	all metal gate valve	38	73	scroll
8	nipple	38	74	thermocouple vacuum gauge
9	bellows		75	gate diaphragm
10	beam position monitor 1 (special item)		76	4 ways cross
11	6 ways cross (special item)		77	gate valve
12	sputter ion pump+Ti sublimator	250 l/s	78	turbo+scroll
13	RGA		79	ion gauge
14	beam position monitor 2 (special item)		80	gate diaphragm
15	bellows		81	in line differential sputter ion pump
16	radiation beam stopper (special item)		82	4 ways cross
17	bellows		83	RGA
18	variable pin hole		84	ion gauge
19	right angle all metal valve		85	all metal gate valve
20	sputter ion pump+Ti sublimator		86	bellows
21	view port		87	4 ways manifold
22	ion gauge		88	right angle all metal valve
23	bellows		89	sputter ion pump+Ti sublimator
24	fast valve		90	bellows
25	vacuum safety retarding line		91	switching mirror chamber
26	6 ways cross (special item)		92	view port
27	RGA		93	ion gauge
28	right angle all metal valve		94	bellows
29	fast valve sensor		95	5 ways manifold
30	all metal gate valve		96	right angle all metal valve
31	bellows		97	sputter ion pump+Ti sublimator
32	switching mirror, spectrometer chamber		98	all metal gate valve
33	right angle all metal valve		99	all metal gate valve
34	sputter ion pump+Ti sublimator		100	nipple
35	view port		101	bellows
36	ion gauge		102	collimator
37	3 beams spectrometer chamber		103	all metal gate valve
38	view port		104	mirror + grating chamber

39	all metal gate valve	105	right angle all metal valve
40	all metal gate valve	106	sputter ion pump+Ti sublimator
41	nipple	107	bellows
42	bellows	108	focussing mirror chamber
43	4 ways cross	109	right angle all metal valve
44	RGA	110	sputter ion pump+Ti sublimator
45	ion gauge	111	view port
46	in line differential sputter ion pump	112	ion gauge
47	gate diaphragm	113	nipple
48	4 ways cross	114	bellows
49	gate valve	115	exit slit chamber
50	turbo+scroll	116	sputter ion pump+Ti sublimator
51	ion gauge	117	view port
52	gate diaphragm	118	nipple
53	4 ways cross	119	bellows
54	gate valve	120	all metal gate valve
55	scroll	121	post focussing mirror chamber
56	thermocouple vacuum gauge	122	right angle all metal valve
57	gate diaphragm	123	sputter ion pump+Ti sublimator
58	nipple	124	view port
59	bellows	125	ion gauge
60	nipple	126	nipple
61	6 ways cross (special item)	127	all metal gate valve
62	right angle all metal valve	128	4 ways cross
63	gate valve	129	right angle all metal valve
64	sputter ion pump+Ti sublimator	130	ion gauge
65	thermocouple vacuum gauge	131	bellows
66	ion gauge	132	all metal gate valve
		133	nipple

7.4 Beamlines lay-out

For the beam transport between undulator and experimental hall, a generic optical design of the beamline, which contains all needed elements to guide the FEL photon beam to the experiment, is defined.

This generic beamline consists of the estimated minimum number of components for this purpose. Special experimental needs may reduce the number of proposed devices in the generic part and add special optical devices close to the experiment. The elements in the generic beamline will provide the following functions:

- Radiation safety, collimation, diagnostics
- Transport of the photon beam from the undulator to the experiment, conservation of the beam properties, especially time duration and coherence.
 - Filtering
 - Monochromatization

- Focussing to fulfill the requests of the FEL users at the end-stations

These functions must take into account the various characteristics of the radiation such as pulse length preservation, monochromatization and energy resolution, source shifts compensation, focussing in the experimental chambers, beam splitting, etc. Obviously, different beamlines could have different needs that cannot be fulfilled simultaneously.

7.5 Splitting, Filtering, Monochromatization and Focussing

At present specialized design and complete description of the beamlines is in progress, but the leading possible solutions and some conclusions, that will be the guidelines along which the final project of the beamline will develop, are described in the following sections. The categories of experimental requirements, at present, can be collected into two main kinds: experiments in the time domain that requires as short as possible pulses and experiments that need high spectral resolution and ask for as narrow as possible photon energy bandpass. According to these two most requested features, a general scheme for a suitable beamline which is flexible and allow to match the needs from time and energy domain experiments, has been derived. Beamlines for very specific application can be developed from this general scheme or re-designed on the basis of the peculiar requests. The optical scheme of this generic beamline is sketched in Figure 7.6. It is constitute by a grazing incidence flat field spectrometer [10], this instrument allows to analyze, in-line, the single shot spectrum of the FEL radiation. Its role is also to deflect the FEL radiation horizontally enough to prevent unwanted radiation (bremsstrahlung, undulator x-rays, etc.) passing through and travelling along the beamlines towards in the experimental hall. This instrument can be easily adapted for the different spectral ranges available at the beamlines, by proper changes of the relevant parameters like: the angle of incidence, the average groove density and its density gradient, the coating reflectivity. The mirror-like reflection of the spectrometer will continue the photon beam forward, passing through the attenuation and filtering section, that consists of a 10 m gas cell, filled up to 10 Pa. The purpose of this section is to reduce the flux of FEL pulses over several orders of magnitude down to the level of the spontaneous emission radiation. Filtering is possible partially or over the full spectral region by using proper rare gases and their mixtures. After attenuation, radiation enters the spectral analysis section. The choice of time domain or high energy resolved experiments is made by using a switching mirror device that feeds the desired beamline for the experiment. The switching mirror consists of two flat mirrors (Figure 7.7) that sequentially reflects the radiation deflecting the photon beam of four times the grazing angle in the horizontal plane.

The monochromator stage take advantage of the reduced divergence of the FEL radiation (see Table 7.1) working without entrance slit (eventually a beam shaper). A variable incidence angle geometry [11] is adopted for the monochromatization of the radiation reached by combination of translation and rotation of a plane mirror that deflects the radiation on the grating surface that selects photons by proper rotation; the diffraction pattern is focussed onto the exit slit by a suitable mirror (spherical, elliptical or toroidal) according with the resolution limit to obtain.

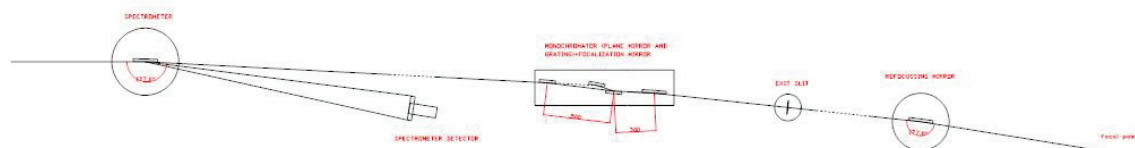


Figure 7.6. Generic optical lay-out of the SPARX beamlines (top view).

The monochromator design, discussed in the following, shows the possibility of performing the function of energy filter ensuring time duration preservation capability, selecting harmonics of the FEL emission with a bandpass larger than the natural spectral width of the FEL pulses. By choosing the proper parameters, the same kind of monochromator, in the energy ranges (40-2000 eV) of interest for the SPARX project, can reach a reasonable compromise between pulse lengthening (250-300 fs) and energy resolution (about 10000), as described later. A final refocussing section brings the monochromatized photon flux onto the sample. Due to the possible requests for different spot characteristics, a double focussing optics has been considered producing different spot quality for the experiments. The shape of the mirrors, angle of incidence and coatings are defined by the spectral range and spot quality requested.

7.5.1 Gas absorber

The request of intensity variation of FEL radiation at sample, could be fulfilled by a beam attenuator on the optical path. This is the role of a gas absorber placed before entering into the monochromatizing section. It consists of a 10 m long vacuum tube that can be filled with controlled rare gas flow in order to reach a proper pressure (up to 10 Pa) and regulate the transmission of the filter. The device is extensively described in the photon diagnostic chapter. The attenuator may operate in flat mode, that means an attenuation of the beam almost constant over the range of interest, or in a selective mode in which the inserted gas absorbs radiation with different attenuation factors in the spectral regions of interest. The selective mode of operation is used when small attenuation is desired on the first harmonic FEL photon beam and the intensity ratio between first and higher harmonics need to be enhanced. The flat mode fulfills the needs of global intensity variation over the full spectral range of radiation, as requested in radiation damage experiments and in non-

linear optical spectroscopy. The use of such a gas filter has some advantages here summarized:

- its response is almost insensitive to the incoming intensity.
- the attenuation factor can be easily varied in a very wide range ($1 - 10^{-8}$) by changing the gas pressure at fixed gas cell length.
- this attenuation method preserves the beam attributes such as coherence and pulse length.

The principal drawback is that the gas cell cannot be closed by windows and an efficient differential pumping system is required for a safe use of the device.

A suitable instrumentation, as described in chapter 8, is placed at the end of the gas filter in order to measure the radiation intensity before the monochromator section. This could be a calibrated gas ionization cell as described in chapter 8.

7.5.2 Switching mirror

The switching mirror that select the chosen beamline after the radiation passed the gas attenuator consists of two mirrors placed into the same chamber. The two mirrors are plane in shape and are placed in series in such a way to deflect the incoming light of a total angle that is shared between the two, this allows to use on each mirror a smaller grazing angle which ensure: a reduced power density shining the surface, to maintain the possibility of working in total reflection conditions and, especially for high photon energy to take advantage that, at fixed photon energy, the square of the reflectivity at θ is larger than the value of the reflectivity at 2θ . The twin mirrors may be moved in and out the radiation beam by means of a mechanism that displace the mirror vacuum chamber of a few centimeters. The optical scheme of this mirror chamber is reported in figure 7.8.

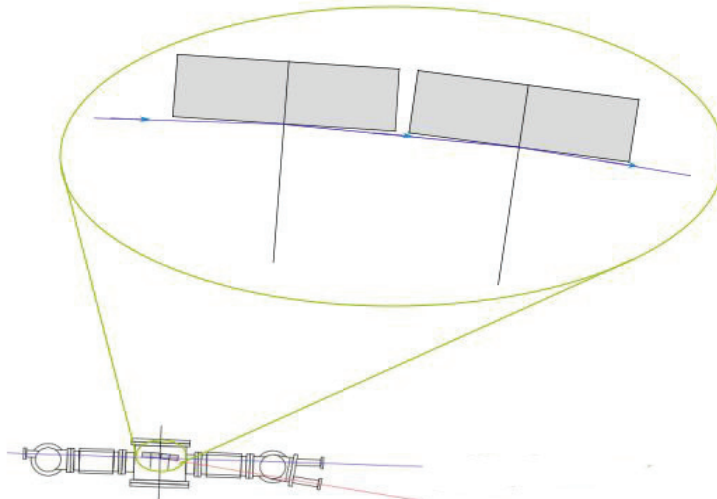


Figure 7.8 Optical scheme of the switching mirror chamber

7.5.3 Beamlines for short pulses

In this section the design of a beamline for filtering and focussing, to be used for the SPARX FEL radiation, is discussed following the guidelines described in the previous parts of the document.

The beamline consists of a low-resolution monochromator and a focussing section. The monochromator is used as a filter of the FEL radiation, either to increase the spectral purity of the source, e.g. suppressing the background when working with the FEL fundamental radiation, or to select the FEL harmonics and suppress the much more intense fundamental one. The focussing section consists of several mirrors with different focal length to change the spot size and the energy density at focus where the user accommodates the experimental chamber.

7.5.3.1 Low-resolution monochromator

The *filtering section* consists of a low-resolution grating monochromator with variable subtended angle, operating without an entrance slit since the requested spectral resolution is very low. In a block scheme it is divided into: 1) grating monochromator; 2) mirror to focus the radiation on the slit; 3) exit slit.

The use of a diffraction grating introduces a temporal broadening of the ultrashort FEL pulse because of the diffraction process. The broadening at the grating output has to be limited to less than 50 fs rms to avoid the degradation of the temporal resolution for pump-probe or dynamic experiments and the decrease of the peak intensity at focal spot. Since the temporal broadening depends on the wavelength and on the number of grooves that are illuminated by the radiation, it can be varied at a fixed wavelength by changing the incident angle on the grating. A design with variable subtended angle can then assure the flexibility required to minimize the temporal broadening. Furthermore, by changing the subtended angle the user can select different operating conditions at a given wavelength, either to maximize the efficiency or the spectral resolution.

A simple scheme with variable subtended angle is the plane mirror/plane grating configuration. The monochromator consists of a plane mirror reflecting the light to a plane grating with uniform line spacing. Both the optical elements are operated at grazing incidence. The wavelength scanning is performed by rotation of the grating around an axis passing through its center and parallel to the grooves. The mirror is simultaneously translated and rotated to change the subtended angle on the grating while maintaining a constant output direction. The mechanical design can be simplified by adopting the off-axis-pivot-point geometry [11].

The focussing section of the monochromator consists of a plane-elliptical mirror that focusses the radiation only in the plane of spectral dispersion. The design with plane-convex optics gives an astigmatic image on the exit slit, i.e. focussed only in the spectral direction, then reduces the energy density on the slit blades. Furthermore, it simplifies the alignment procedures. A less expensive spherical mirror can be adopted if a slightly lower resolution can be accepted at the long wavelength side of the spectral region of operation. The selection of the more suitable mirror (i.e. plane-elliptical, cylindrical or spherical) will be better considered in the advanced design phase.

The bandwidth at the monochromator output is chosen wider than the natural SPARX FEL bandwidth, to avoid fluctuations of the output intensity due

to variations of the FEL central energy and/or to source pointing instabilities. Furthermore, any clipping of the intrinsic FEL spectrum will cause a further temporal broadening of the pulse.

A schematic drawing of the spectral filtering section is shown in Fig. 7.9. The optical elements of the monochromator can be mounted in such a way that their surfaces deflect the output beam parallel to the floor itself making simpler the alignment of the following optical components of the beamline, such as the focussing section and the experimental chamber.

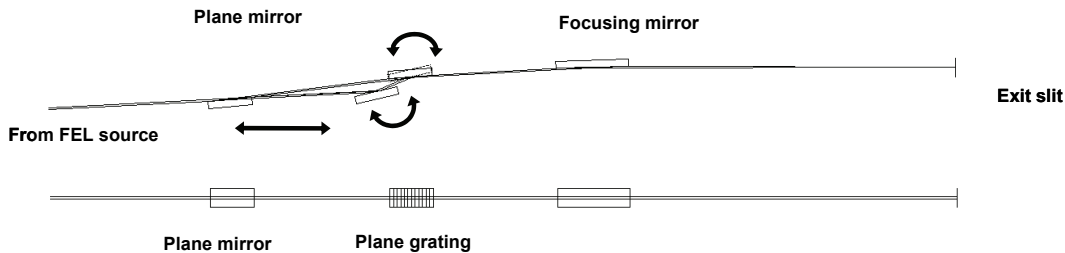


Figure 7.9: Optical layout of the low-resolution monochromator. The grating is rotated to perform the wavelength scanning, the mirror is simultaneously rotated and translated to change the subtended angle. Top: view on the vertical plane; bottom: view on the horizontal plane.

7.5.3.2 Focussing section

The *focussing section* adopts different mirrors to change the spot size, then the energy density, on the focal point. Several optical configurations will be tested in detail during the design phase, such as a single toroidal mirror, two spherical mirrors in the so-called Kirkpatrick-Baez configuration or two bendable mirrors.

The coatings of the optical elements will be chosen to maximize the reflectivity in the whole spectral region of operation. The reflectivity of some standard coatings in the 1-30 nm region is plotted in Fig. 7.2 [7]. In case of a broad spectral region of operation, a combination of different coatings should be adopted to maximize the efficiency in the whole interval. In case of selecting more than one coating, the optical components should have different coatings in horizontal stripes. The selection of the stripe to be illuminated is made through a linear translation of the element. Carbon and nickel are already used and considered among the best candidates in the 1.5-30 nm region.

Elements working at fixed angle of incidence, e.g. the focussing mirrors, should be set according to the shortest wavelength to be reflected. The angle of incidence on the elements operating at variable angle, e.g. the monochromator, can be varied depending on the wavelength of operation: the longer the wavelength, the smaller the incidence angle which gives yet high reflectivity.

7.5.4 Design of a beamline for the 1.5-15 nm spectral region

A preliminary design of a beamline for the 1.5-15 nm spectral region based on the previous considerations, is of interest for the operation of SPARX at 1.5 GeV.

As already stated, the surface of the optical elements of the monochromatizing section lay on the plane parallel to the floor to change the inclination of the FEL beam with respect to the horizontal. The focussing section is here assumed to consist on a single toroidal mirror with its tangential surface oriented in the vertical plane. A schematic view is shown in Fig. 7.10.

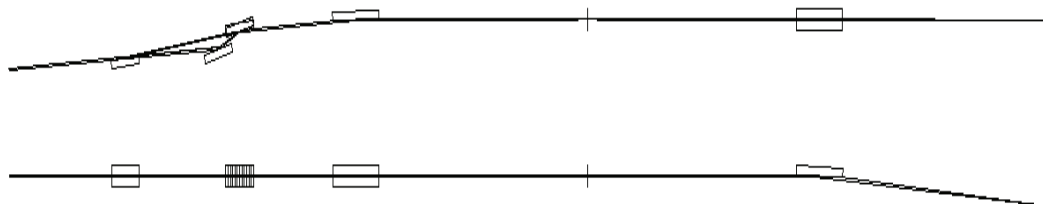


Figure. 7.10. *Optical layout of the beamline, including the low-resolution monochromator (three optical elements) and the focussing section (one toroidal mirror). Top: view on the vertical plane; bottom: view on the horizontal plane.*

Table. 7.10. *Characteristics of the source used for the simulation of the beamline in the 4.5-15 nm region*

Photon range	4.5-15 nm fundamental emission
Output pulse length	100 fs
Energy per pulse	1 mJ
Waist size	80 μm rms
Divergence	15 μrad rms @ 2 nm 20 μrad rms @ 5 nm 30 μrad rms @ 10 nm 35 μrad rms @ 13 nm
Bandwidth	0.15% rms @ 5 nm 0.20% rms @ 10 nm

The source characteristics used in the range of interest are reported in Table. 7.5.

Two different gratings are here assumed: 100 gr/mm density for the 4-15 nm region and 200 gr/mm density for the 1.5-7 nm region. The characteristics are resumed in Tab. 7.11. The plane mirror is supposed to be placed at about 40 m far from the FEL source.

The higher the subtended angle the higher the resolution and the temporal broadening. For a given wavelength, the subtended angle is selected as low as to give a temporal broadening lower than the FEL duration while maintaining high efficiency. The performances in terms of resolution, temporal broadening and grating efficiency are resumed in Fig. 7.11 and 7.12. The grating profile is assumed to be laminar. If a profile with extremely low blaze angle is considered, the grating efficiency increases by a factor ≈ 1.5 .

The grating section has also a plane mirror that can be inserted in the optical path. In such a case, the monochromator acts simply as a relay section with no filtering capabilities.

7.5.4.1 Effect of the slope errors

Both nominal resolution and flux transmitted are worse than the nominal ones because of the slope errors on the optical surfaces. Since the spectral resolution is rather low and the length of the exit arm is small, even in the case of tangential slope errors on the plane-elliptical mirror of $5 \mu\text{rad}$ rms, that are definitely higher than the present state-of-art for plane-concave mirrors, the decrease in transmission is lower than 5%. The decrease in resolution is almost negligible.

It can be concluded that the performances are not altered by the slope errors normally guaranteed for the optical surfaces to be used at grazing-incidence.

Table. 7.11. Characteristics of the monochromator

Plane mirror	
Subtended angle	165°-176°
Mirror size	120 mm × 20 mm
Plane grating	
	2 gratings
Subtended angle	Variable, 165°-176°, external order
Groove density	100 gr/mm (grating 1) 200 gr/mm (grating 2)
Ruled area	110 mm × 20 mm
Focussing mirror	
	Plane-elliptical surface
Incidence	88.5°
Mirror size	200 mm × 20 mm
Mirror-to-slit distance	1000 mm

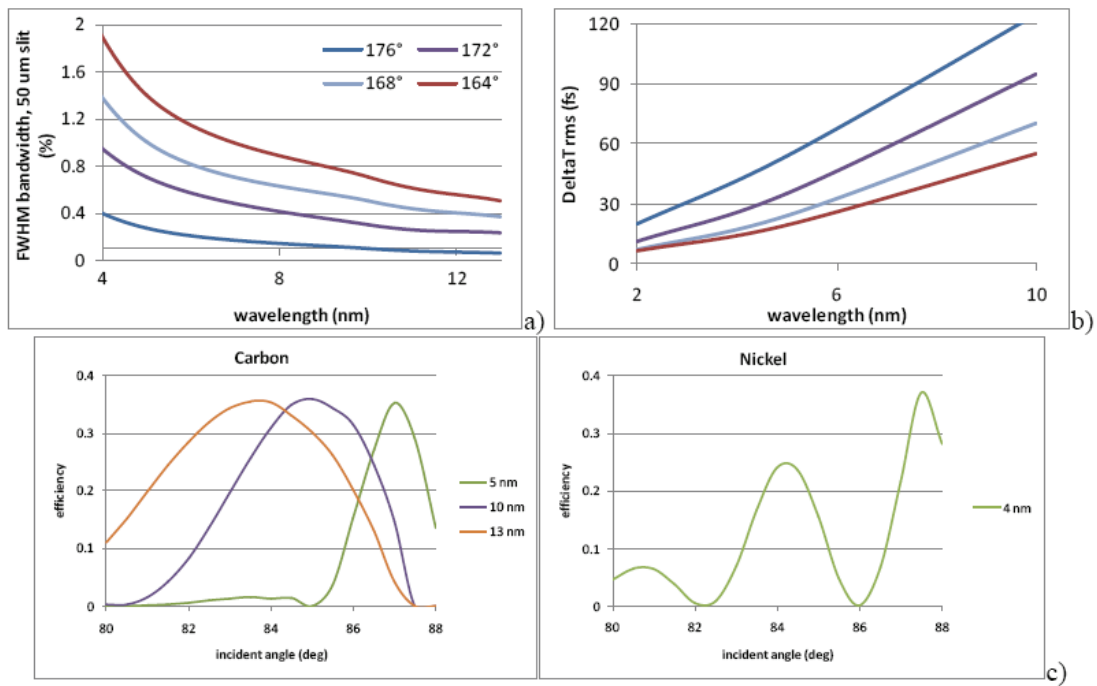


Fig.7.11. Performance of the monochromator, 100 gr/mm grating: a) FWHM bandwidth, 50 μm slit, b) Time broadening, c) Grating efficiency. The grating is assumed to have a laminar profile, 0.5 duty cycle, 30 nm groove height.

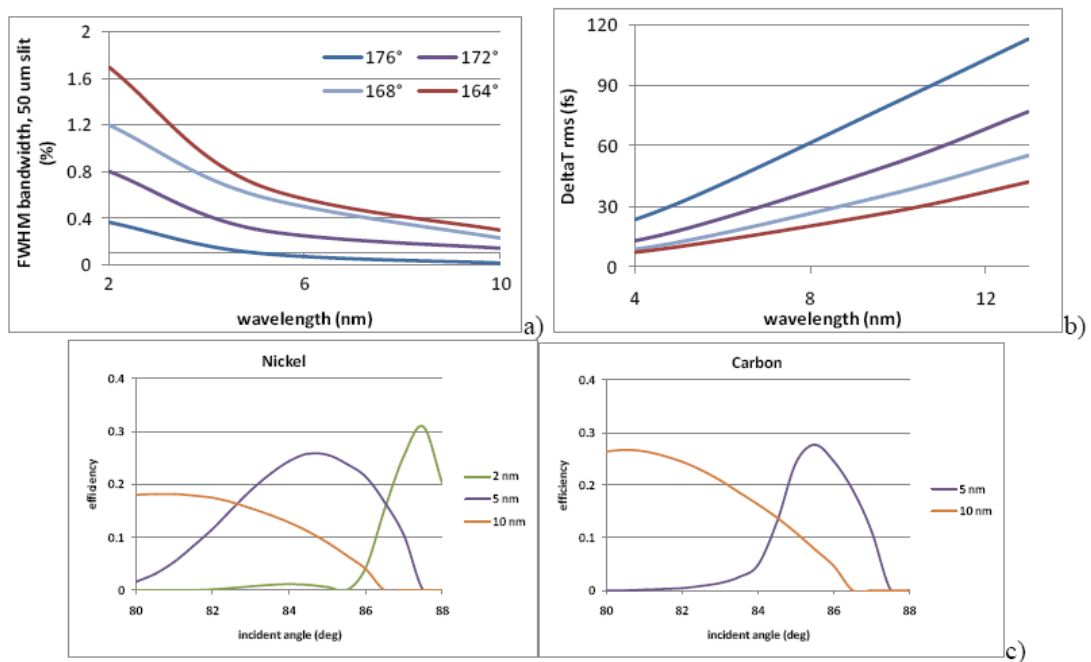


Fig. 7.12. Performance of the monochromator, 200 gr/mm grating a) FWHM bandwidth, 50 μm slit, b) Time broadening, c) Grating efficiency. The grating is assumed to have a laminar profile, 0.5 duty cycle, 13 nm groove height.

7.5.4.2 Operative conditions

Let us suppose to select the working condition at each wavelength that maximizes the efficiency. The performances in terms of throughput, spectral resolution and temporal broadening, are resumed in Table 7.12.

The temporal broadening is anyway below 50 fs rms, the spectral resolution is in the 0.3-0.4% FWHM range and the total efficiency is in the 0.2-0.25 range. Different grating parameters may give higher spectral resolution and longer temporal broadening or vice versa.

The efficiency of the monochromator used as a relay section, i.e. when the grating is substituted by a plane mirror, is shown in Table 7.13.

Table 7.12. Performance of the monochromator operated at the subtended angle that optimizes the grating efficiency at a given wavelength.

2 nm	
Grating	200 gr/mm, nickel coated
Subtended angle	176°
Spectral resolution	0.4% FWHM
Temporal broadening	20 fs rms (15 μrad divergence)
Total efficiency	0.20
5 nm	
Grating	200 gr/mm, nickel coated
Subtended angle	171°
Spectral resolution	0.4% FWHM
Temporal broadening	30 fs rms (20 μrad divergence)
Total efficiency	0.18
5 nm	
Grating	100 gr/mm, carbon coated
Subtended angle	176°
Spectral resolution	0.3% FWHM
Temporal broadening	30 fs rms (20 μrad divergence)
Total efficiency	0.22
10 nm	
Grating	100 gr/mm, carbon coated
Subtended angle	170°
Spectral resolution	0.4% FWHM
Temporal broadening	43 fs rms (30 μrad divergence)
Total efficiency	0.20
13 nm	
Grating	100 gr/mm, carbon coated
Subtended angle	167°
Spectral resolution	0.4% FWHM
Temporal broadening	50 fs rms (35 μrad divergence)
Total efficiency	0.20

Table. 7.13. Transmission of the monochromator used as a relay section

Wavelength (nm)	Transmission
2	0.60
5	0.80
10	0.80

7.5.4.3 Energy density on the optics and exit slit

The energy density on the optics has to be kept below the damage threshold of the coating. The reference damage thresholds are reported in Table 7.2. The calculated values, at two photon wavelengths on the optical elements of the monochromator operating as described, are reported in Table 7.14. The values are anyway well below the damage threshold of standard coatings. The energy density is high on the exit slit plane because of focussing. Since the slit aperture is kept wider than the FEL bandwidth, the FEL pulse is never focussed on the knives edges. The risk of damage is reduced by an astigmatic configuration of focussing, in which the source is focussed, on the slit plane, only in the spectral direction.

Table 7.14. Energy density on the optics of the monochromator.

<i>5 nm wavelength, 1 mJ/pulse, 20 μrad rms divergence</i>	
	Energy density (mJ/cm ²)
<i>Plane mirror</i>	1.6
<i>Plane grating</i>	1.3
<i>Focussing mirror</i>	0.1

<i>10 nm wavelength, 1 mJ/pulse, 30 μrad rms divergence</i>	
	Energy density (mJ/cm ²)
<i>Plane mirror</i>	0.7
<i>Plane grating</i>	0.6
<i>Focussing mirror</i>	0.1

7.5.4.4 Focussing section

For simplicity, the focussing section is here assumed to have a single grazing-incidence toroidal mirror that focusses the radiation on the experimental sample. As already stated, different configurations with more than one mirror can be studied and installed at the end of the beamline to offer alternative focus quality to the users.

Different mirror shape can be used to change the size of the focal spot and correspondingly the energy density on the sample; a toroidal mirror is here

considered to obtain a fine focussing; the characteristics of the mirror is reported in Table. 7.15. The separation between the mirror centre and the experimental point is 2.0 m that is long enough to accommodate the experimental chamber.

Table. 7.15. Parameters of the focussing section.

General parameters	
Incidence	87°
Mirror size	200 mm × 20 mm
Slit to mirror distance	2000 mm
Mirror to sample	2000 mm
Fine focus	Toroidal mirror
Radii	73 m (tangential) 100 mm (sagittal)
Spot size	30 μm rms @5 nm 50 μm rms @10 nm

7.5.5 Design of the beamline for the 1-5 nm region

The same design can be applied also for beamlines working in the 1-5 nm region (fundamental harmonic radiation). This FEL photon energy region will be available for the 2.4 GeV SPARX mode of operation at the U2 undulator. Since wavelengths as short as 0.5 nm are expected for the 3rd FEL harmonic, the incident angle on the optics has to be increased much closer to 90°. Beamlines with a similar design are already in operation in similar ranges at synchrotron radiation sources. A preliminary design of such a beamline here is discussed. The characteristics of the source used for the simulations are reported in Table. 7.16.

Table. 7.16. Characteristics of SPARX used for the simulation of the beamline in the 1.5-4.5 nm region

Photon range	1.5-4.5 nm fundamental emission
Output pulse length	30-70 fs
Energy per pulse	1 mJ
Waist size	80 μm rms
Divergence	10 μrad rms @ 1 nm 15 μrad rms @ 2 nm 20 μrad rms @ 4 nm
Bandwidth	0.15% rms @ 4.5 nm

The characteristics are summarized in Table. 7.17. The plane mirror is supposed to be placed at about 40 m far from the FEL source. The obtainable performances are detailed in Figure. 7.13.

The performances of the monochromator are not influenced by the usual slope errors contents of commercial optical surfaces for grazing-incidence application.

The performances, at each wavelength, that maximizes the efficiency, the optimized throughput, the spectral resolution and temporal broadening, are listed in Table. 7.18.

The temporal broadening is always below 50 fs rms, the spectral resolution is in the 0.3-0.4% FWHM range and the total efficiency is about 0.1. Changing the grating parameters, a higher spectral resolution and longer temporal broadening can be selected.

The efficiency of the monochromator used as a relay section, i.e. when the grating is substituted by a plane mirror, is shown in Table 7.19.

Table. 7.17. Characteristics of the monochromator.

Plane mirror	
Subtended angle	170°-177°
Mirror size	150 mm × 20 mm
Plane grating	
Subtended angle	Variable, 170°-177°, external order
Groove density	400 gr/mm
Ruled area	150 mm × 20 mm
Focussing mirror	
Incidence	89°
Mirror size	220 mm × 20 mm
Mirror-to-slit distance	1000 mm

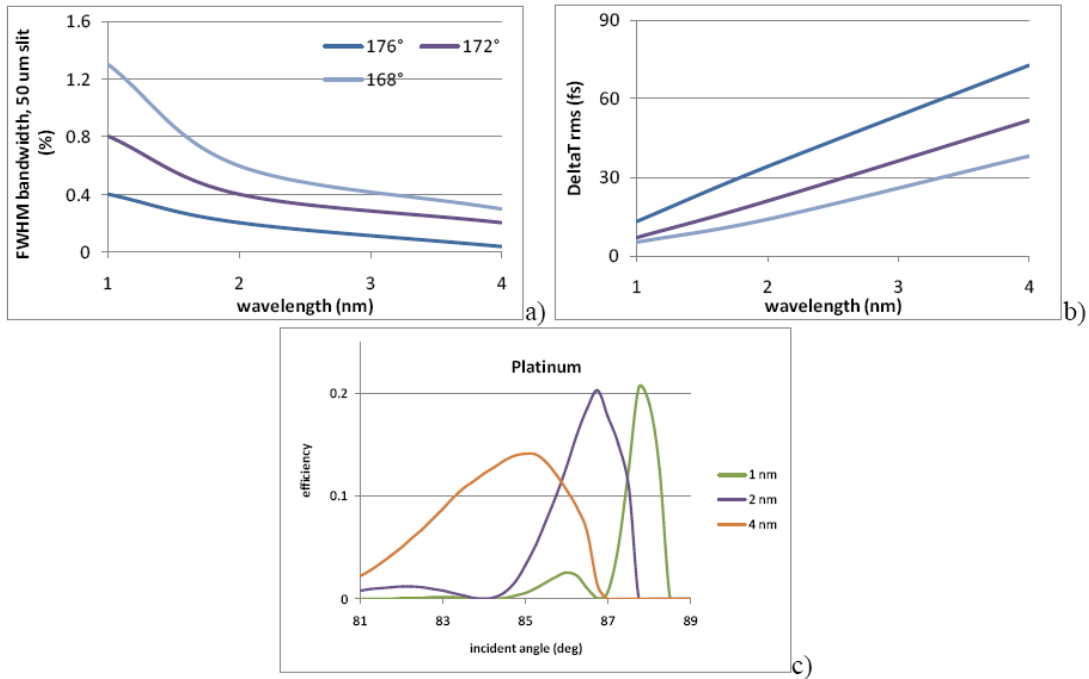


Fig. 7.13. Performance of the monochromator, 400 gr/mm grating
 a) FWHM bandwidth, 50 μm slit, b) Time broadening, c) Grating efficiency. The grating is assumed to have a laminar profile, 0.5 duty cycle, 10 nm groove height, platinum coating.

Table. 7.18. Performances of the monochromator operating at the subtended angle that optimizes the grating efficiency at a given wavelength.

1 nm	
Grating	400 gr/mm, platinum coated
Subtended angle	176°
Spectral resolution	0.4% FWHM
Temporal broadening	13 fs rms (10 μrad divergence)
Total efficiency	0.10
2 nm	
Grating	400 gr/mm, nickel coated
Subtended angle	174°
Spectral resolution	0.3% FWHM
Temporal broadening	27 fs rms (15 μrad divergence)
Total efficiency	0.13
4 nm	
Grating	400 gr/mm, nickel coated
Subtended angle	170°
Spectral resolution	0.3% FWHM
Temporal broadening	44 fs rms (20 μrad divergence)
Total efficiency	0.08

Table. 7.19. Transmission of the monochromator used as a relay section

<i>Wavelength (nm)</i>	<i>Transmission</i>
1	0.40
2	0.65
4	0.65

Table. 7.20. Energy density on the optics of the monochromator.

<i>2 nm wavelength, 1 mJ/pulse, 15 μrad rms divergence</i>	
	<i>Energy density (mJ/cm²)</i>
<i>Plane mirror</i>	2.0
<i>Plane grating</i>	1.6
<i>Focusing mirror</i>	0.1

<i>4 nm wavelength, 1 mJ/pulse, 20 μrad rms divergence</i>	
	<i>Energy density (mJ/cm²)</i>
<i>Plane mirror</i>	1.8
<i>Plane grating</i>	1.5
<i>Focusing mirror</i>	0.1

The effective energy densities on the optical elements are reported in Table. 7.20 at two wavelengths provided by the monochromator operating following conditions reported in Table. 7.17. The estimated values are always well below the damage threshold of standard coatings.

7.5.5.1 Focussing section

For simplicity, the focussing section is here assumed based on single grazing-incidence toroidal mirror that focusses the radiation onto the sample in the experimental chamber. As already stated, different configurations with more than one mirror can be studied.

Two different mirrors can be inserted on the optical path to change the size of the focal spot and correspondingly the energy density on the sample: 1) a toroidal mirror for $\approx 50 \mu\text{m}$ spot size; 2) a plane mirror for an unfocussed beam. The characteristics of the mirrors are resumed in Tab. 7.21. The distance between the mirror and the interaction point is 3.0 m that is considered large enough to accommodate the experimental chamber.

Table. 7.21. Parameters of the focussing section

General parameters	
Incidence	88°
Mirror size	220 mm × 10 mm
Slit to mirror distance	3000 mm
Mirror to sample	3000 mm
Unfocussed beam	Plane mirror
Spot size	2 mm rms
Fine focus	Toroidal mirror
Radii	311 m (tangential) 370 mm (sagittal)
Spot size	25 μm rms

7.5.6 Alternative designs: the grating in the off-plane mount

The off-plane mount of grating differs from the classical mounting in the orientation of the incident and diffracted wave vectors that result parallel to the grooves [12]. The geometry is shown in Figure. 7.14. The direction of the incoming rays is described by two parameters, the altitude and the azimuth. The altitude γ is the angle between the direction of the incoming rays and the direction of the grooves. The azimuth α of the incoming rays is defined to be zero if they lie in the plane perpendicular to the grating surface and parallel to the rulings, so $-\alpha$ is the azimuth of the zero order light. Let β define the azimuth of the diffracted light at wavelength λ and order m . The grating equation is written as $\sin\gamma(\sin\alpha + \sin\beta) = m\lambda\sigma$ where σ is the groove density.

The blaze condition of maximum efficiency is verified when the light leaves the grating in such a way that it performs a specular reflection on the groove surface, that is $\alpha = \beta = \delta$, where δ is the blaze angle of the grating. It has been theoretically shown and experimentally measured that the efficiency in the off-plane mount is close to the reflectivity of the coating, so much higher efficiencies than in the classical diffraction mount can be obtained in the soft X-ray region [5].

The efficiency of the filtering section may be increased by the use of gratings in the off-plane geometry, as already realized in instrumentation for ultra short pulses [13,14]. This option is a promising alternative to explore in detail for radiation filtering and time duration.

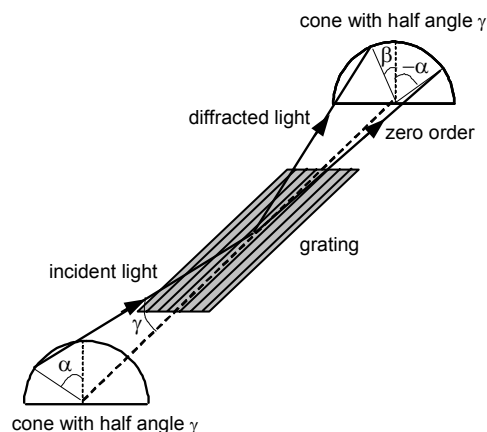


Figure. 7.14. Geometry of the off-plane mount

7.5.7 Beamlines for high-energy resolution

It is here presented the design of a beamline for experiments which require high spectral resolution on SPARX. The beamline consists of a section which focusses the FEL beam on the entrance slit of the monochromator, the high-resolution monochromator and the focussing section. The effects on the temporal duration of the pulse are discussed.

7.5.7.1 High-resolution on ultra short pulses

Let us consider the experimental problem of filtering an ultra short pulse with a high-resolution grating monochromator. Since the FEL pulse at the generation may be produced to be close to its transform limit, any modification of its spectrum results in a time broadening as described by its Fourier transform. For a Gaussian profile with no modulation of either phase or frequency, the product of the spectral width at half-height $\Delta\omega_{1/2}$ times the duration at half-height $\Delta\tau_{1/2}$ has a lower limit expressed by the relation:

$$\Delta\omega_{1/2}\Delta\tau_{1/2} = 4 \ln 2 = 2.77 \quad (7-1)$$

According to Eq.(1), it is clear that the monochromatization of the beam beyond its intrinsic limit increases the temporal duration of the pulse.

The monochromator can be modelled as a filter with a complex frequency response $K(\omega)$, that includes both the non-uniform spectral transmission and the distortion in the spectral phase. Since the variations of reflectivity of the coating within the FEL bandwidth are negligible, $K(\omega)$ can be considered constant, although lower than unity, taking into account of the total efficiency of the monochromator.

For a grating monochromator, the major mechanism that alters the time duration of the pulse is the difference in the lengths of the optical paths of the

rays diffracted by different grating grooves. In fact, a single grating gives inevitably a time broadening of the ultra fast pulse because of the diffraction: the total difference in the optical paths of the rays diffracted by N grooves illuminated by radiation at wavelength λ is $Nm\lambda$, where m is the diffracted order. This effect is negligible for picosecond or longer pulses, but is dramatic in the femtosecond time scale. Let us consider a 1200 gr/mm grating illuminated by radiation at 10 nm over a length of 30 mm; the total number of grooves involved in the diffraction is 36000, corresponding to a maximum delay in the first diffracted order of 360 μm , i.e. 1.2 ps. Once the spectral resolution $\lambda/\Delta\lambda$ has been defined, the minimum number of grooves to be illuminated to give such a resolution (Rayleigh criterion) is $N = \lambda/\Delta\lambda$. This gives the unavoidable minimum instrumental broadening of a grating monochromator. For resolving power in the range 8000-10000, the minimum broadening is of the order of 80-100 μm at 10 nm, i.e. 260-330 fs. For a high-resolution monochromator, this unavoidable instrumental effect has to be compared with the increase of the temporal duration of the pulse due to its narrower bandwidth.

It is possible to design grating monochromators that do not alter the temporal duration of an ultrafast pulse by using at least two gratings in a subtractive configuration to compensate for the dispersion [4]. In such a configuration, the second grating compensates for the time and spectral spread introduced by the first one. A scheme usable with normal incidence optics requires two equal concave gratings mounted with opposite diffraction orders: the incidence angle on the second grating is equal to the diffraction angle of the first grating. The spectral selection is performed by a slit placed in an intermediate position between the gratings, where the radiation is focussed by the first grating. This design has been proved to be very effective in time compensation of few femtoseconds for wavelengths longer than ≈ 40 nm, although with a rather low throughput. When working at grazing incidence, more complex designs have to be adopted [13,15]. A high-throughput time-delay-compensated grating monochromator for high-order harmonics with duration of few-femtoseconds has been recently realized with gratings in the off-plane mount [14].

Even if a time-delay compensated configuration can be designed for any grating configuration, its use is limited to low-resolution configurations. In fact, high resolution configurations usually require long paths (from several to tens of meters), then a time-delay-compensated configuration would require the double of the space. Furthermore, the duration of the pulse is intrinsically increased by the spectral clipping, then the concept of compensation of the optical path is somewhat relaxed. Here, we deal with conventional grating configurations with uncompensated time delay.

The optical layout of a general beamline for high resolution requires a pre-focussing section, a slit monochromator and a focussing section. The use of an entrance slit is necessary to guarantee the energy stability at the output of the monochromator. In fact, in case of operation without an entrance slit, any variation of the source pointing stability will reflect on a variation of the energy at the output.

If the source pointing stability is good enough, the monochromator could be operated without an entrance slit, as presently in most of the synchrotron beamlines. This simplifies the optical design since reduces the number of optical components.

7.5.8 Optical Layout of the beamline

7.5.8.1 Pre-focussing section

The pre-focussing section, if necessary, is a grazing-incidence mirror that creates an image of the FEL source on the entrance slit. The mirror focusses the radiation only in the plane of spectral dispersion, i.e. it creates an astigmatic image of the source. This reduces the energy density on the knives of the slit, hence the probability of damaging of the slit itself due to the high power density of the FEL pulse.

7.5.8.2 Monochromator section

The high-resolution monochromator consists of the entrance slit, the grating section and the exit slit. The optical design will give a highly resolved astigmatic image of the FEL source on the exit slit, again to avoid the focussing of the intense FEL beam on the knives of the slit.

As an example, it will be discussed a plane mirror/plane grating design with variable subtended angle. The use of a variable subtended angle gives to the user the flexibility of choosing different working conditions at a given wavelength, to optimize the efficiency, the resolution or the rejection of the higher orders.

Other designs both at variable and fixed subtended angle will be analyzed in detail once the characteristics of the beamline will be defined.

7.5.8.3 Focussing section

The focussing section creates a monochromatic stigmatic image of the FEL source on the experimental chamber. Different possible optical configurations will be studied in detail during the design phase, such as a single mirror or two mirrors in the Kirkpatrick-Baez configuration. Also bendable mirrors will be considered.

The coatings of the optical elements will be chosen to maximize the reflectivity in the whole spectral region of operation.

7.5.9 Design of a beamline for the 4.5-15 nm range

To validate the previously proposed solutions, in the following, the design of a beamline with a variable subtended angle monochromator using a plane mirror/plane grating configuration for the 4.5-15 nm spectral region is described. For simplicity, the source pointing stability is considered good enough to operate the monochromator without an entrance slit. The same design can be applied for different spectral region, both at long and short wavelengths.

The monochromator consists of a plane-parabolic mirror which collimates the light emitted from the FEL source, the plane mirror-plane grating section and a plane-parabolic mirror used as focussing element. All the optical elements are operated in grazing incidence. The wavelength scanning is the

same described in paragraph 7.4.3.1. The characteristics of the source used for the simulations are reported in Table. 7.10.

The first optical element is the collimating plane-parabolic mirror, that is supposed to be placed 40 m far from the FEL source. The grating parameters have to be chosen to give the desired spectral resolution with the minimum number of illuminated grooves. This can be performed by choosing the proper combination of groove density and length of the exit arm. Once the required resolution has been defined, the longer the exit arm, the lower the groove density. In the following calculations, the length of the exit arm has been limited to 8 m. Two different gratings are used: a 1200 gr/mm grating for the short wavelengths within the spectral interval of operation and a 600 gr/mm grating for the long wavelengths. The parameters are summarized in Table 7.22. The performances in terms of resolution and temporal broadening are resumed in Figure 2 and 3. The grating profile which maximizes the grating efficiency is a saw-tooth profile.

Table. 7.22. Characteristics of the monochromator.

Collimating mirror	Plane-parabola
Incidence	88.5°
Mirror size	200 mm × 20 mm
Mirror-to-source distance	40 m
Plane mirror	
Subtended angle	Variable, 163°-177°
Mirror size	120 mm × 20 mm
Plane grating	2 gratings
Subtended angle	Variable, 160°-174°, internal order
Groove density	1200 gr/mm (grating 1) 600 gr/mm (grating 2)
Ruled area	120 mm × 20 mm
Focussing mirror	Plane-parabola
Incidence	88.5°
Mirror size	200 mm × 20 mm
Mirror-to-slit distance	8000 mm

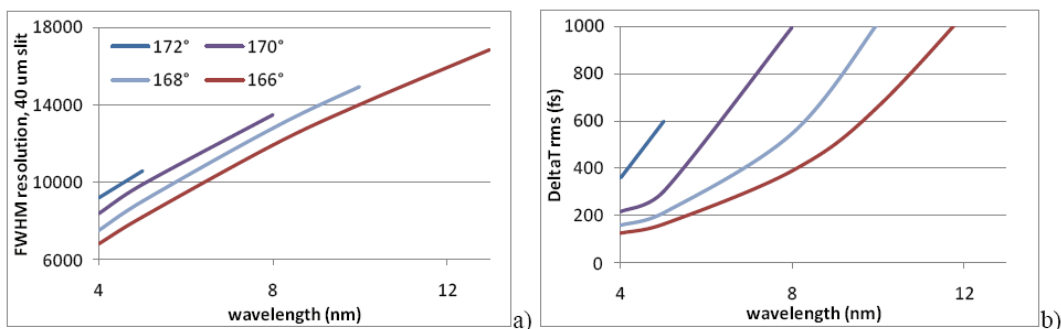


Fig. 7.15. Performance of the monochromator, 1200 gr/mm grating, a) FWHM resolution $\lambda/\Delta\lambda$, 40 μm slit, b) Time broadening

7.5.9.1 Effect of the slope errors

Both nominal resolution and flux transmitted are worse than the nominal ones because of the slope errors on the optical surfaces. For high-resolution instruments with long exit arms, the effect of the tangential slope errors on the optics has to be analyzed in details to quantify the corresponding decrease in resolution.

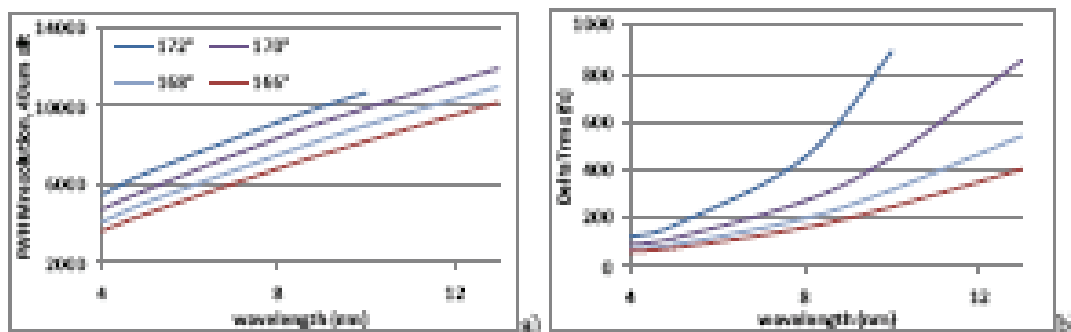


Fig. 7.16. Performance of the monochromator, 600 gr/mm grating, a) FWHM resolution $\lambda/\Delta\lambda$, 40 μm slit, b) Time broadening

7.5.9.2 Operative conditions

Let us suppose to select the working condition that maximizes the grating efficiency at each wavelength. The performances of the 1200 gr/mm grating are resumed in Table. 7.23.

7.5.9.3 Energy density on the optics and exit slit

The energy density on the optics has to be kept below the damage threshold of the coating as measured in existing FEL beamlines [6]. The energy densities on the optical elements are reported in Table. 7.24 when the monochromator is operated in the conditions reported in Table. 7.23. The values are anyway well below the damage threshold of standard coatings.

Table. 7.23. Performance of the monochromator operated at the subtended angle that optimizes the grating efficiency at a given wavelength.

5 nm	
Grating	1200 gr/mm, carbon coated
Subtended angle	168°
Spectral resolution	9000 FWHM
Temporal broadening	210 fs rms (20 μrad divergence)
10 nm	
Grating	600 gr/mm, carbon coated
Subtended angle	162°
Spectral resolution	12000 FWHM
Temporal broadening	405 fs rms (30 μrad divergence)

Table. 7.24. Energy density on the optics of the monochromator.

<i>5 nm wavelength, 1 mJ/pulse, 20 μrad rms divergence</i>	
	Energy density (mJ/cm ²)
<i>Collimating mirror</i>	0.6
<i>Plane mirror</i>	1.0
<i>Plane grating</i>	0.8
<i>Focussing mirror</i>	0.1

<i>10 nm wavelength, 1 mJ/pulse, 30 μrad rms divergence</i>	
	Energy density (mJ/cm ²)
<i>Collimating mirror</i>	0.2
<i>Plane mirror</i>	1.1
<i>Plane grating</i>	0.8
<i>Focussing mirror</i>	0.1

7.5.10 Design of a beamline for the 0.6-1.2 nm range

The configuration of the previously described beamline can be extended also towards higher photon energy and perform monochromatization in the 1000-2000 eV (1.2-0.6 nm) photon energy range. Such a beamline provides FEL radiation for experimental activity pivoted on coherent X-ray scattering, micro and nanoprobe and holography.

The same optical scheme of plane mirror/plane grating and focussing optics is used. In the suggested solution, attention has to be paid to the needs of very small grazing angles ($< 1^\circ$) on the optics and to the radiation divergence that makes the optical surface dimension along the light path, rapidly increasing. This makes necessary the use of a converging mirror instead of a collimator as first optical element. In this case the effect of the converging radiation on plane grating is to be considered. The grating groove density ranges between 600 l/mm and 1200 l/mm in order to achieve the proper resolving power (< 10000) in the energy range of interest. The focussing mirror to exit slit distance is of the order of 10 m. The final focus on the sample is, routinely, performed with a toroidal mirror. A complete design of such a beamline is under process.

Silicon single crystal material is a well established bulk material for the optical elements at lower photon energies and for grating applications. The bulk silicon material is masked with an appropriate thin film coating in order to avoid strong absorption at its K-edge at 1840 eV. Concerning coating properties, two coating materials seem to be optimal, carbon and chromium. Chromium is a well proven coating material, which forms very smooth layers, adheres very tightly to the bulk material and is often used as contact layer. Its strong absorption edges are at 574 eV and 584 eV out of the range of interest of the beamline. On the other hand carbon is a very light element showing no absorption edges above its K-edge at 285 eV. It has excellent thermal properties when used in its diamond modification but the coating quality of diamond layers on silicon is not yet as good as for chromium. The reflectivity

varies between 80% and 90%, in the energy range 1000 to 2000 eV (1.2 - 0.6 nm), for both carbon and chromium coatings.

Due to the spectral characteristics of this beamline and the high degree of spatial coherence of the emitted FEL radiation available, requests of micro- and nano- focussing from the users should be taken into account. In these cases, it is necessary to use extreme focussing optics to concentrate the beam onto micro/nanometer spotsize. Several solutions for the optics are currently used at third generation synchrotron radiation sources for nanometer focussing. They can be classified as i) reflective (mirrors, multilayers, waveguides); ii) diffractive (Fresnel Zone Plates, Bragg Fresnel or reflective Zone Plates).

- Reflective. Figured mirrors in Kirkpatrick-Baez geometry can now reach few tens of nanometer spot sizes, both as figured reflecting surface and figured multilayers [16,17]. The limit is still in the figure errors of the mirror surface. The advantage of mirrors is that they are achromatic (at least in a large energy range), and that at grazing angle they can stand high power loads. Moreover, they preserve the temporal structure. However, some wavefront distortion is unavoidable, which can create problems to coherent diffraction experiments.
- Waveguides are based on total reflection, but their behaviour is dominated by propagation of resonance (guided) modes, spatially confined by cladding layers [18]. Nanometer sized beams have been produced by waveguides, down to 10 nm, a record for hard X-rays [19]. Waveguides have several interesting properties for their perspective use with FEL: i) they preserve coherence, or even they can “clean” a beam whose coherence has been degraded by other optical elements, providing a beam with a well defined coherent curved wave-front; ii) they preserve the temporal structure of the incoming pulse [20]; iii) they can be fabricated with vacuum gap, thus allowing high transmission also for soft X-rays; iv) working in total reflection, with vacuum gap, the thermal load can be reduced to bearable levels; v) with proper operation, two coherent beams can be produced, allowing all X-rays pump&probe experiments, without the need of external trigger [20]. Waveguides have been used for microdiffraction with nanometer spatial resolution [21], for holography [22,23] and for Coherent Diffraction Imaging in Fresnel geometry using the curved wave front [23,24].
- Diffractive lenses as Fresnel Zone Plates (FZP) are largely used especially for imaging at very high resolution (15-20 nm) in the soft X-ray region [25]. Two problems potentially can limit their use with FEL: the intrinsic mechanism of image formation in FZP implies different optical paths, and hence pulse duration broadening; if this can be deleterious or not for a given experiment depend on the geometrical and physical conditions. The second problem regards the thermal load, because standard FZP work in transmission and therefore must stand the entire incoming power. Alternatives to overcome this problem have been studied, as Bragg-Fresnel and reflective FZPs [26].

7.5.11 Beamlines for spontaneous radiation

The unique opportunity to have access to the spontaneous emission from undulators used for FEL generation suggests to analyze the characteristics of this background radiation with the purpose of use it with dedicated beamlines. The complete emission spectrum from BESSY FEL source is reported, as an example, in Figure 7.17.

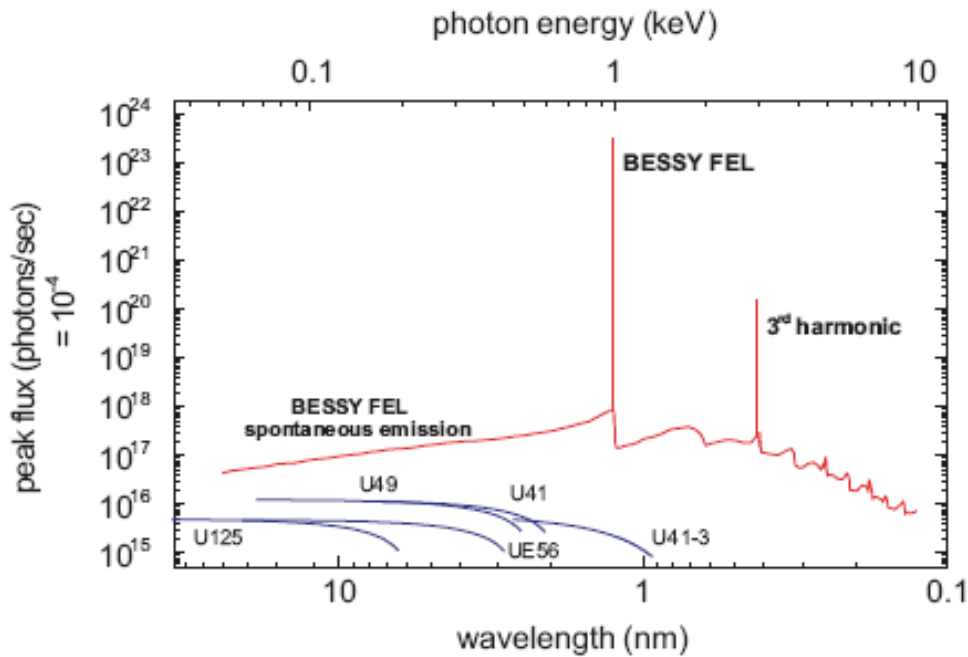


Figure 7.17: Spectrum of the BESSY SASE-FEL for a lasing photon energy of $h\nu = 1$ keV (1.2 nm) compared to the BESSY II performance. BESSY II: single bunch operation with 10 mA of average beam current at $E = 1.7$ GeV. BESSY SASE-FEL: $I = 5$ kA, $E = 2.25$ GeV and a planar undulator with $\lambda_u = 2.75$ cm and $N = 1450$ periods.

The spectrum is dominated by the intense laser harmonics but the background emission is still largely competitive with the present emission from standard undulators at Synchrotron radiation facilities. The spontaneous emission spread over a very large energy range up to hard X-rays and has the same time structure of the FEL emission (sub ps pulses) into a wider aperture emission cone. Coherence is comparable with that from standard Synchrotron radiation insertion devices. These specific features suggest to use the spontaneous emission from FEL undulator to cover hard x-ray range, that, at the first stage of the SPARX project, is not easily available. The spontaneous emission can be collected at each one of the undulators exit U1, U2, U3 by increasing the angular acceptance of the beamlines and allowing the X-ray photons to travel straight in the direction of the undulator axis. After collection from the insertion device the X-ray radiation pass through a gas filter 15 m long that allows to eliminate the low energy contribution from either the spontaneous emission and/or the FEL emission when the latter cannot be avoided from source. A further solid state filter (berillium foil or graphite sheet) can be inserted, after the gas attenuator, on the optical path before entering the experimental hutch. The optical hutch guests the monochromator in a preliminary start-up version only with a Si(111) double crystal providing a first monochromatic synchrotron radiation in the X-ray range between 2 keV (0.6 nm) and about 15 keV (0.08 nm) photon energy (expected bandwidth 0.1%). A three-segment Pt-coated toroidal focussing mirror converge the radiation into the experimental hutch. After lateral translation of the crystals, in alternative to the energy selected one also the "white beam" may arrive into the experimental hutch. The experimental activity span over the spectroscopic (absorption, fluorescence) and diffraction fields usually performed at X-ray beamlines, with the advantage of time resolved structure that allows to study dynamic

phenomena such as ultrafast structural changes in condensed matter. The pulsed structure of the spontaneous emission makes possible to reduce the time resolution from about some tens of ps, which is, at present, the synchrotron radiation limit from storage rings, to time resolutions ranging below 1 ps, by means of special streak cameras. The most favourable systems to be studied are structural changes that can be initiated e. g. by a short light pulse and represent reversible reactions, that reach the initial state after some relaxation time delay. However also irreversible reactions could be studied within the same time resolution provided the sample can be replaced continuously within two subsequent excitation and scattering events. This technique is well known in optical spectroscopy as pump-and-probe experiments, the unique thing being here an X-ray flash as probe signal.

7.6 References

- [1] Feldhaus, J.Arthur and J.B. Hastings, J. Phys. B 38 (2005) S799
- [2] L. Juha et al. Proceedings of SPIE 5917 (2005) 91
- [3] B.Steeg, S.Jacobi, R. Sobierajski, C. Michaelsen, J.Feldhaus, Technical Report TESLA-FEL 2002-06 DESY (2002)
- [4] P.Villoresi, Appl. Opt. 38 (1999) 6040
- [5] E.M. Gullikson, Experimental Methods in Physical Science vol. 31: Vacuum Ultraviolet Spectroscopy Academic press, (2000) 257
- [6] R. Sobierajski, 2nd meeting on Future X-FEL optics: “Damage threshold of Mirrors and Multilayers” Prague, Nov. 23, 2006; S. P. Hau-Riege et al, Appl. Phys. Lett. 90, (2007) 173728
- [7] See e.g. http://henke.lbl.gov/optical_constants
- [8] E.D. Palik, Handbook of Optical Constants of Solids, Academic Press (1985)
- [9] Q.H. Chen, F.De Bona, C.Fava, A. Gambitta, F. Mazzolini, A. Sednmach, A.Savoia, Rev.Sci. Instrum. 63 (1992) 451
- [10] P. Nicolosi et al, J. Elect. Spect. Rel. Phen. 145 (2005) 1055
- [11] G. Naletto and G. Tondello, Pure Appl. Opt. 1 (1992) 347
- [12] W. Cash, Appl. Opt. 21 (1982) 710
- [13] L. Poletto and P. Villoresi, Appl. Opt. 45 (2006) 8577
- [14] L. Poletto et al, Opt. Lett. 32 (2007) 2897
- [15] L. Poletto, Appl. Phys. B 78, (2004) 1013
- [16] <http://www.spring8.or.jp/wkg/BL29XU/solution/lang-en/SOL-0000000973>
- [17] O. Hignette et al., ESRF Highlights, (2005) 108
- [18] Bukreeva, A. Popov, D. Pelliccia, A. Cedola, S. Dabagov and S. Lagomarsino, Phys. Rev. Lett. 97 (2006) 184801
- [19] C.Bergemann, et al., Phys. Rev. Lett. 91 (2003) 204801
- [20] D. Pelliccia et al., Applied Optics 45 (2006) 1
- [21] S. Di Fonzo, W. Jark, S. Lagomarsino, C. Giannini, L. De Caro, A. Cedola and M. Müller, Nature 403 (2000) 638
- [22] C. Fuhse et al., Phys. Rev. Lett., 97 (2006) 254801
- [23] L. De Caro et al., Phys. Rev. B77 (2008) R 081408
- [24] L. De Caro et al., Appl. Phys. Lett. 90 (2007) 041105
- [25] W. Chao et al., Nature, 435 (2005) 1210
- [26] Erko et al., in «Modern developments of x-ray and neutron optics » chap. 28, A. Erko et al. Eds., Springer Series in Optical sciences – Berlin (2008)

8 PHOTON DIAGNOSTICS

8.1 Radiation based diagnostics in LINAC

A large amount of beam instrumentation, especially for electron beams, is based on the emission and detection of electromagnetic radiation. In this chapter we will illustrate some of these instruments and how they will be used to measure important aspects of the SPARX beam, allowing their commissioning to the designed values.

In particular we will describe the instruments used for measuring the beam transverse size along the LINAC and transfer lines and for measuring the bunch length especially after the various bunch compressors required to increase the beam peak current.

8.1.1 Beam size monitors

Fluorescent screens have a long history in the linear accelerators development, but it is with the improvement of imaging devices, in particular with the introduction of the digital CCD matrix, that their use has supplanted almost any other beam size measuring instrument. The on-board digitalization of the CCD, avoiding the noisy analog video signal, and with a depth of 12 or more bits has contributed to make this instrument not only a visual help for the operator, but a powerful means for a complete two-dimension beam reconstruction.

Two kinds of screens will be used on SPARX, depending on specific requirements as described in the LINAC diagnostics section: YAG:Ce fluorescent screens and Optical Transition Radiation (OTR) radiators.

One inch or larger radius Yttrium Aluminum Garnet (YAG) crystals, doped with Cerium, can be produced with a thickness as small as 100 μm . The fast decay time, less than 100 ns, avoids the possibility of intensity pile-up even at the highest repetition frequency. The emission spectrum, centered on the 550 nm wavelength, is well matched with the sensitivity of standard CCD devices. Being a single crystal, the YAG does not present intrinsic limitations to the spatial resolution due, by example, to the grain dimension as other fluorescent materials [1,2]. The resolution for these screen is mainly due to its transparency to the emitted radiation, so that the detector integrate the photons produced all along the particle trajectory inside the crystal, resulting in a "diffuse" image due to multiple scattering of the particle itself and depth of field of the optics. The reduced thickness of the crystal minimizes these effects, leaving the pixel size of the camera (6 - 10 μm) as the effective spatial resolution.

The high photon yield makes the YAG:Ce screen well suited for low electron density situations, but can give saturation effects in presence of high electron density (high charge, strongly focalized beams). In these cases the OTR radiators can be a better choice. Transition Radiation is emitted when a charged particle crosses a surface dividing two media with different refraction indexes, and OTR is the fraction of this radiation in the optical range. The emission of the Transition Radiation can be considered as the reflection of the pseudo-photons constituting the electromagnetic field of the particle by the discontinuity surface. As a surface phenomenon, it is almost instantaneous for the time scale of a bunch transit time, and, in its incoherent part, strictly proportional to the particle number. The radiation is emitted in a cone around

the direction of specular reflection of the particle trajectory, with zero intensity in this direction, allowing an easy extraction of the radiation from the vacuum pipe by means of a 45° screen. The theory of OTR is now rather well known, and the spatial resolution deriving both by its angular distribution and by the dimension of the emitting screen is well studied [3,4,5]. For the maximum energy of SPARX, no stringent limit to the spatial resolution obtainable from OTR is foreseen, the resolution being determined by the camera pixel size together with the optical magnification. The photon yield is, on the other hand, rather low, amounting to few photons for thousand electrons on all the optical range and on all the solid angle, from an interface between vacuum and an almost ideal conductor. This intensity is logarithmic dependent on the beam energy. Although this is not a real limitation for beam size measurements at high energy and for beam charge of 1 nC, it may require the use of special high sensitivity camera at low charge or in situations in which the beam size must be varied of a large amount.

8.1.2 Coherent Radiation Bunch Length Systems

The bunch length is a critical point for the FEL operation, and to avoid strong space charge effects it is reduced in two or more steps at different beam energies, and a measurement of the bunch length is mandatory after every bunch compression. There are different methods operating in the time domain to obtain the longitudinal bunch profile, and they are described in chapter 5. In this chapter we will illustrate a technique in the frequency domain that can be considered complementary to the time domain measurements, but that offer also advantages as a continuous and non-intercepting monitor of the stability of the bunch length. This technique is based on the measurement of the spectrum of the coherent radiation emitted by the electron bunches. Almost any type of radiation can be used for this purpose, but for practical reasons, typically only Coherent Transition Radiation (CTR) and Coherent Diffraction Radiation (CDR) are used.

If $\frac{dI_{sp}}{d\omega d\Omega}$ is the distribution of the radiation intensity emitted by a single particle, supposed concentrated in a narrow cone in the forward direction, the emission from a relativistic bunch of longitudinal profile $g(x)$ is normally written as

$$\frac{dI}{d\omega d\Omega} = \frac{dI_{sp}}{d\omega d\Omega} [N + N(N-1)F(\omega)] \quad (8-1)$$

in which N is the total number of particle in the bunch and $F(\omega)$ the “longitudinal form factor” of the bunch itself defined as

$$F(\omega) = \left| \int_{-\infty}^{\infty} g(x) e^{-i\frac{\omega}{c}x} dx \right|^2 \quad (8-2)$$

The coherent part of the radiation, proportional to N^2 , has a spectrum determined by the Fourier transform of the bunch longitudinal profile. The spectrum can be measured by interferometric methods and in particular, given the frequency range involved for standard bunch length in SPARX, by means of a Martin-Puplett interferometer.

Martin-Puplett interferometry of CTR and CDR has been extensively used on FLASH [6,7] for bunch length measurement, and a new interferometer is in

calibration phase for the same use on SPARC. A simplified sketch of a Martin-Puplett interferometer is shown in Figure 8.1. Compared to the better known Michelson interferometer, the beam splitter is replaced by a polarizing grid, whose wires are at 45° with respect to the horizontal plane when view along the beam axis. The grid reflects the field with polarization parallel to the wires and transmits the orthogonal one. The frequency range over which this effect is present depends on wires spacing and thickness. Furthermore, roof mirrors that rotate the polarization of the incident field upon reflection replace the plane mirrors.

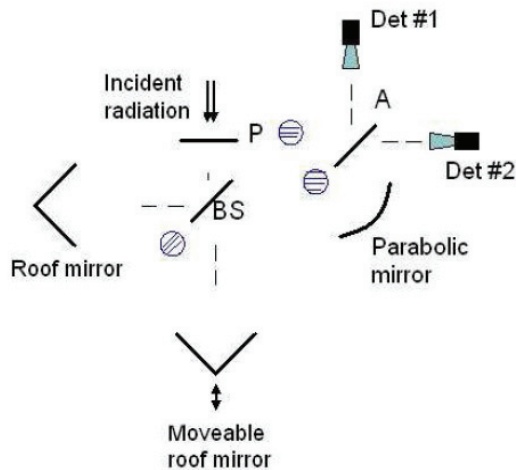


Figure 8.1: Schematic view of a Martin-Puplett interferometer.

The main drawback of this technique is that it gives direct access only to the square module of the bunch longitudinal charge distribution, cancelling any phase information. A method based on Kramers-Kronig dispersion relation and suggested in Ref. [8], can be used to retrieve the phase and eliminate the ambiguity in the reconstruction procedure. In principle, for this technique to be completely applicable, the whole frequency spectrum must be known. However, spectral techniques, even though they avoid the synchronization difficulty typical of time domain methods, typically suffer suppressions of the low-frequency part of the spectrum due to diffraction losses from the vacuum pipe and interferometer apertures, together with reduced acceptance and sensitivity of detectors at long wavelengths. Moreover, in case the experimental apparatus is not in vacuum, the transmission of the window as function of the frequency has to be taken into account, resulting in a high-frequency cut-off. Due to this frequency suppression, only a portion of the radiation spectrum is directly measurable, while the low and high part of the spectrum must be extrapolated in order to apply the phase retrieval technique, reducing the accuracy of the bunch profile reconstruction. Even with these limitations, this technique has shown to be very effective, giving its best results with shorter bunches, when the time domain measurement presents more difficulties. After each compressor is placed a vacuum chamber with an CTR radiator that can be opened in two half giving rise to a Diffraction Radiation screen through which the beam can pass undisturbed, while the CDR/CTR will be reflected across a z-cut quartz optical window with extended transmission in the sub-millimeter wavelength region. At the shortest bunch length a complete measurement with a Martin-Puplett interferometer placed outside the window in controlled atmosphere to avoid radiation absorption by the water vapor. The use of CDR

could make the measurement compatible with the contemporaneous FEL operation as has been demonstrated on FLASH [7]. At longer bunch length, where time domain techniques can be more effective, a single detector will measure the total intensity of CDR. The coherent radiation intensity, integrated from a given arbitrary value up to the shorter wavelength emitted, is an inverse function of the bunch length, and can be easily used to optimize the compression and/or to monitor continuously, without affecting the FEL operation, the stability of the delicate compression operation.

8.2 Radiation based diagnostics in undulators

For a correct and efficient operation of the FEL it is required a perfect alignment and transverse size matching between the electron beam and the radiation inside the undulator. To this purpose a quadrupole, beam steering and appropriate diagnostics are placed in the space between the undulator modules, as described in Chapter 6.

For the measurement of the electron beam transverse profile, OTR screens give the required resolution and, due to the possibility of making them very thin, at the level of one or few microns, the production of high energy bremsstrahlung radiation can be reduced, together with the beam multiple scattering.

The monitoring of the characteristics of the emitted radiation not only at the end of the undulator, but also along the undulator itself, is important to follow the evolution of the SASE-FEL emission process [9,10]. If it is possible to measure the way the radiation intensity increases along the undulator while the spectral bandwidth decreases, it would be possible to compare results with theoretical predictions, in order to tune the actual parameters of the undulator channel and to optimize the emission process. Photon diagnostics provide then an essential tool for the operation of the undulators independently from the electron-beam-based alignment procedures. Being the undulator divided in "sections", the emitted radiation has to be monitored only in the zones between the sections. The measurements can be summarized as intensity measurements, angular spread, spectrum and phase.

The concept of the photon-beam-based alignment procedure is based on variable-gap undulator segments which allow the sampling of the spontaneous radiation of each segment individually by switching off all other segments, i.e. opening their gap. The simultaneous measurement of photon beam position and angle will allow optimizing angle and position of the electron trajectory, tuning the k-parameter of the undulator segments and adjusting the phase match between adjacent undulators.

Photon diagnostic chambers equipped for intensity and angular spread measuring sections may be located between the undulator sections with beam position monitors, beam size monitors and intensity detectors. For a detailed description of the different techniques see Par. 8.3.3 and 8.3.4.

The photon diagnostic chamber for the monitoring of the spectrum can be located downstream of the last undulator after the e-beam dump. The spectrum can be acquired by a flat-field spectrometer consisting of the entrance slit, the diffraction concave grating and the 2D detector, such as an EUV-enhanced CCD camera or a phosphor screen coupled to a low-noise CCD camera. The deflecting mirror could be spherical to concentrate the light on the entrance slit of the spectrometer [11].

8.2.1 Radiation transport

The spectral range of SPARX imposes some constraints on the geometry of the radiation transport system. In fact, broad-band coatings have zero normal-incidence reflectivity at wavelengths below ≈ 30 nm and this requires to operate the optics at grazing incidence. For a given spectral region the incidence angle has to be higher than the critical angle to achieve non-zero reflectivity. Gold or platinum are used as metallic coatings for the soft X-ray region since they are stable in time and exhibit shorter cut-off wavelength for a given incident angle. Also highly-dense graphite is used for wavelengths above 5 nm because of its high reflectivity. Other metallic coatings as nickel, ruthenium or copper could be considered especially for the shortest wavelengths of the spectral range. As an example, the response of gold in the 0.6-30 nm region and of ruthenium in the 0.6-3.5 nm region for different incident angles is shown in Figure 8.2. The lower the wavelength of operation, the higher the incident angle that has to be used to extract the radiation.

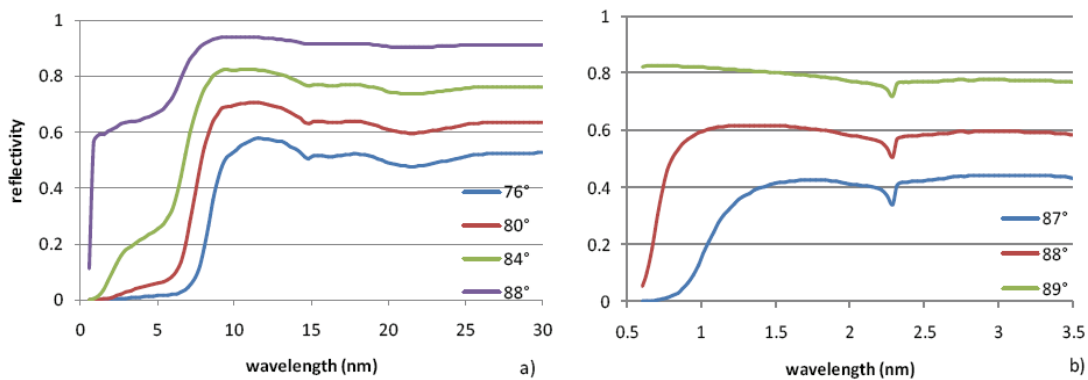


Figure 8.2: reflectivity of some metallic coatings in the XUV and soft X-ray region for different incident angles: a) gold, 0.5-30 nm region; b) ruthenium oxide (3 nm) on ruthenium, 0.5-3.5 nm region

The best geometry of the diagnostic chambers to be inserted between the undulator sections is the cylindrical one, so that it is possible to extract the radiation along any path passing through the section radius. It is possible to build a path with multiple reflections at grazing incidence that deflects the radiation out of the chamber at an angle in the 10° - 20° range. Let us suppose to accept an angular deviation of 8° - 10° . For wavelengths above 6 nm, a single reflection at 85° gives the necessary deviation with an overall reflectivity of more than 0.8 in case of carbon coating. For wavelengths in the 2-6 nm interval, two reflections at 87.5° on nickel will give an overall reflectivity of about 0.6. For wavelengths below 2 nm, gold or ruthenium coatings can be adopted but the number of reflections to achieve a large angular deviation increases: for a mirror operated at 88.5° , three reflections give an overall reflectivity of about 0.3 at 1 nm.

An alternative to metallic mirrors could be the use of multilayer mirrors that can provide high reflectivity in the soft X-ray region with a bandwidth of few % at almost normal incidence. In this case, the design of the diagnostic chamber would be simplified since it would be possible to deflect the radiation out of the chamber at 90° with a single reflection at 45° on the multilayer. Nevertheless, such mirrors are designed to operate at a specific wavelength and therefore they are not suggested for the use on a highly tunable machine like the FEL.

For the intense ultrashort FEL pulses, it is also important to limit the energy density on the optical elements and to keep its value below the damage threshold of the coating [12]. Once the pulse energy is defined, the energy density obviously decreases with the increase of the illuminated area. For a given beam section, the illuminated area is increased by the term $1/\cos(\alpha)$, where α is the incident angle. When working at grazing incidence with angles higher than 84° , the latter term is higher than ten, reducing considerably the energy density and then the risk of damaging of the coating. If needed, radiation focusing has to be performed using curved mirrors at grazing incidence.

The diagnostic chambers to extract the radiation between the undulator sections will be similar to those realized for the FEL SPARC project by ENEA Frascati and shown in Figure 8.3 and Figure 8.4. These chambers have mirrors operated at 45° with a total beam deviation of 90° and operate from the visible down to the EUV at ≈ 40 nm. The main difference with the SPARC design is that the radiation needs to be extracted at smaller angles and this makes a circular symmetry more suitable. The design shown in Figure 8.5 needs to be adapted to the new system, providing new light extraction devices.

Like in the SPARC system, it will be possible to insert different devices to intercept the beam by means of motorized stages mounted inside the chamber. With such devices it would be possible to monitor the e-beam position, the radiation transverse profile and to generate Coherent Transition Radiation for e-beam monitoring purposes. Being impossible the use of windows in the XUV and soft X-ray spectral regions, the radiation transport channels have to be performed in a vacuum pipeline connected directly to the diagnostic chamber.

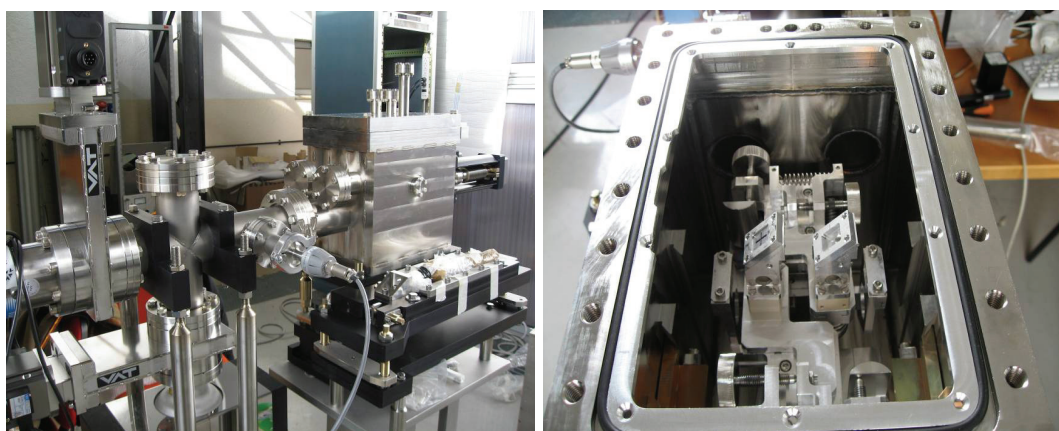


Figure 8.3: pictures of the diagnostic chambers realized for SPARC.

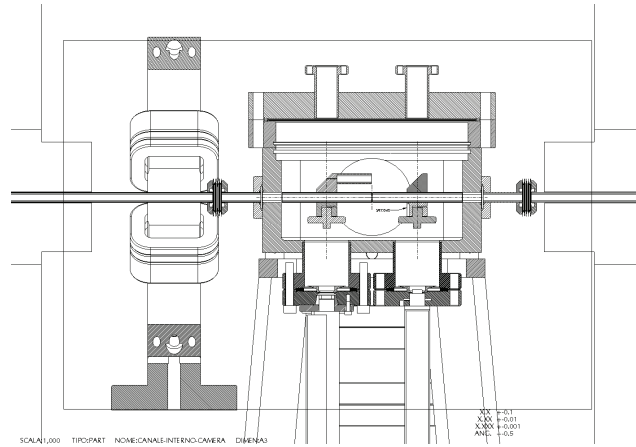


Figure 8.4: drawing of the diagnostic chamber of SPARC together with the focusing quadrupole

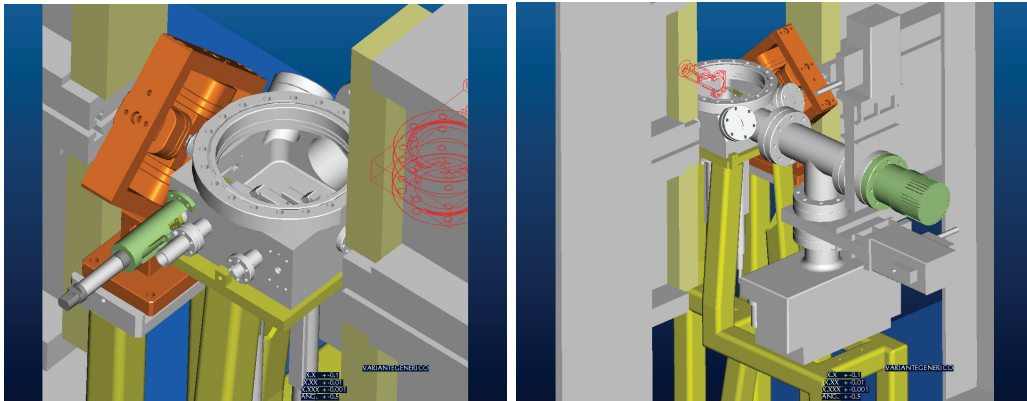


Figure 8.5: Drawings of the diagnostic chamber of SPARC between the two undulator sections

8.2.2 Spectral measurements

The measurement of the spectrum of the emitted radiation gives a way to compare the experimental results with the theoretical predictions and simulation codes. Bandwidth, relative amplitude of the spectral contributions, harmonic contents reflect contributions of homogeneous and inhomogeneous broadening mechanisms occurring in the FEL process.

The spectral measurement is important for two reasons. Since the contribution to the spectral spread comes from broadening processes associated with misalignments and deviations from the theoretical behavior of the magnetic field of the undulator, optimizing the emitted radiation bandwidth allows us to optimize the system alignment and to correct potential defects in the magnetic field configuration. Once the best possible situation is obtained, the minimum bandwidth is related to the gain coefficient g_0 and can provide useful information on the gain length and therefore on the saturation mechanism of the SASE FEL. Moreover, in the undulator regime the FEL emission wavelength depends on the angle θ of observation of the radiation respect to the magnetic axis (i.e. $\theta = 0$):

$$\lambda = \frac{\lambda_u}{2\gamma^2} \left(1 + \frac{K^2}{2} + \gamma^2 \theta^2 \right) \quad (8-3)$$

where γ is the relativistic factor, K is the peak value for the undulator parameter and λ_u is the undulator period. In order to correctly analyze the emitted

radiation, the maximum value of the angle θ is determined by the system geometry, being $\theta_{Max} = g/2L_u$, where g is the undulator gap and L_u the overall undulator length. Utilizing some of the parameters based on the data in this document, we obtain $\theta \cong 0.18$ mrad, corresponding to a wavelength spread of ≈ 0.54 nm around a central frequency of 18.7 nm.

The analysis of the spectrum can be performed through a grating flat-field spectrometer [11]. A compact and portable efficient spectrometer in the 1-m-class can be realized with a resolution $\lambda/\Delta\lambda$ in the 1000-2000 range. The spectrometer will be used for the commissioning phase of all the beamlines. Such a portable instrument is being realized at CNR-INFM LUXOR (Padova, Italy) for FLASH and could be realized also for SPARX.

Other radiation characteristics that provide information about the FEL operation are here listed:

- **Harmonics of the fundamental frequency.** The odd harmonic emission provides information about the undulator quality, together with a direct way to evaluate the e-beam emittance, while the even harmonics provides an indication about the e-beam misalignments and about possible multipolar contributions from the undulator.
- **Amplitude stability.** The radiation amplitude stability, once the signal is integrated in space and time, reflects the e-beam stability. It will be thus useful to monitor this stability to evaluate drifts in the short period (shot to shot), in the medium period (about 1 hour) and in the long period (about 1 day).
- **Beam pointing stability.** This measurement, to be performed utilizing an imaging tool, is aimed to evaluate the e-beam trajectory stability that depends on the magnetic optics current stability and on the beam pointing stability of the laser used for the photocathode
- **Synchronism analysis.** In the seeding experiment a streak camera will be used to verify the synchronism between the e-beam, the injected seeding radiation and the spontaneous emission. Such a measurement allows an evaluation of the relative jitter.
- **Phase measurements.** Utilizing correlation techniques it will be possible to evaluate the phase difference between different points inside the undulator chain, to provide a highest flexibility while matching phases of the different sections.

8.3 Radiation based diagnostics in beam lines

Photon diagnostics are essential not only to fully understand and characterize the performance of SPARX, but also to give to the users the necessary information on the experimental conditions. An ideal detector for SPARX has to cover a full dynamic range of several orders of magnitude from spontaneous emission to saturation, to be suitable for single-pulse measurements, to exhibit low degradation under radiant exposure in the XUV and soft X-ray region and to be ultra-high vacuum compatible and suitable for being assembled under clean room conditions. Furthermore, many experiments may require online diagnostics with minimum interference with the FEL beam: this means that the diagnostics should not block the FEL beam or alter some crucial beam properties such as coherence or intensity to an undesirable extent.

In the following, the main photon diagnostics to characterize the FEL emission both during the development phase and the experimental phase will be discussed. They will be routinely used by the SPARX operators to tune the FEL properties such as intensity, pointing direction and spectrum, and will provide to the users the measurements of the beam properties required to characterize the experiments. The instrumental developments for SPARX photon diagnostics will benefit of the large expertise developed on the diagnostics for FLASH that is at present the only FEL facility operating in the XUV, but also of collaborations in the framework of the other FEL projects currently under development.

8.3.1 In-line measurement of the FEL spectrum

The measurement of the SPARX spectrum is absolutely essential to understand the operating regime during the characterization phase and to give to the users the shot-to-shot pulse spectrum. This facility will be installed after the undulator section as a fixed photon diagnostics for each of the beamlines and is here described in details.

The spectrum is measured by a grazing-incidence flat-field spectrometer equipped with a variable-line-spaced (VLS) plane grating [13]. The polynomial law of variation of the groove density along the grating surface is selected to focus the radiation dispersed at the 1st diffracted order on an almost flat surface, where a plane detector acquires the spectrum. Since the length of the spectral curve is larger than the detector size, the latter is mounted on a linear stage and moved in the desired position to acquire the spectral interval of interest. Being the grating plane, the radiation reflected at zero-order propagates unperturbed to the following sections. The instrument gives the in-line single-shot spectrum of the FEL radiation. A schematic of the concept is shown in Figure 8.6.

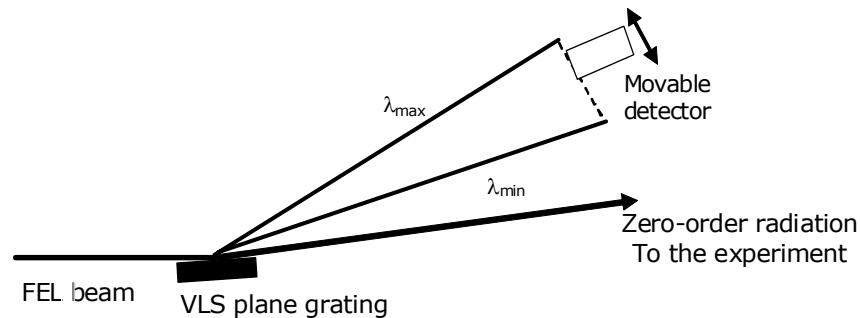


Figure 8.6: Schematic of the spectrometer; λ_{min} and λ_{max} indicate the minimum and maximum wavelength of operation.

The incident angle on the grating will be selected to have an energy density well below the damage thresholds of optical coatings. Let us suppose to have the grating 20 m far from the FEL source. In case of a 1 mJ pulse with 20 μ rad rms divergence, the energy density at 88° is 3 mJ/cm², that is more than one order of magnitude below the damage thresholds of optical coatings measured at 32.5 nm with the ultrashort FEL pulses at FLASH [12]. The operation at grazing angles in the 3°-1° range will assure a safe maintenance of the grating.

The other driving parameter of the incident angle is the coating reflectivity. The reflectivity curves at 88° and 89° incident angles in the 1-30 nm interval are shown in Figure 8.7 for some coatings used for grazing-incidence

optics in the soft X-ray region. It is evident that it does not exist the unique coating that can be used with the maximum performances in terms of reflectivity in the whole 1-30 nm region. Carbon is used in the 5-40 nm region for its high reflectivity and stability in time; it has also good performances in the 1-2 nm region especially at extreme grazing incidence. Nickel has a flat and high reflectivity in the 1.5-5 nm region. Platinum and gold are normally used as broad-band coatings although not optimized for the 1-40 nm region. Once the spectral region of operation has been defined, a combination of the proper coatings assures the highest throughput. If more than one coating is necessary to cover at best the spectral range of operation, the plane grating will be divided in horizontal stripes with different coatings. The selection of the portion to be illuminated will be performed through a linear translation of the grating in the direction parallel to the grooves.

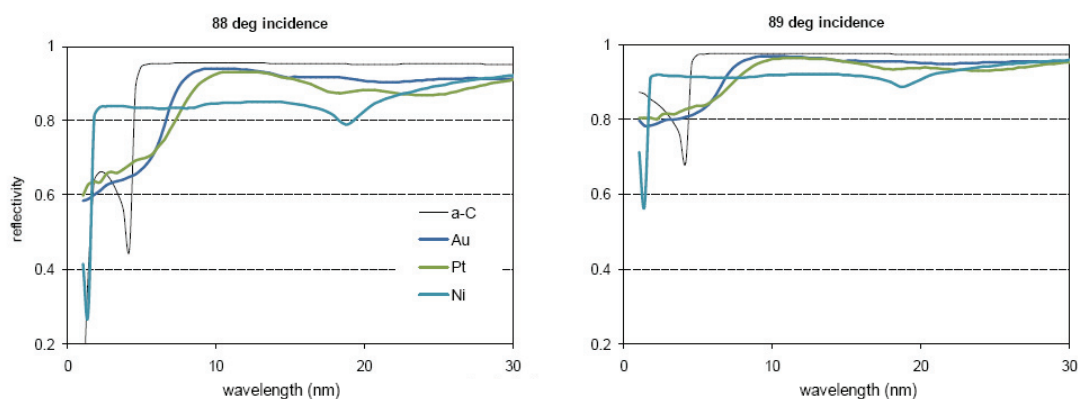


Figure 8.7: Reflectivity of some coatings in the 1-30 nm region.

8.3.1.1 Design for the 1.5–20 nm region

In the following, the design will be applied to operate in the 1.5-20 nm region for SPARX phase 1, where the lower limit is set to be the 3rd FEL harmonic of the fundamental at 4.5 nm. The spectrometer is assumed to be 25 m far from the source at 88.5° grazing angle. This corresponds to a deviation angle of the FEL beam of 3°. The coatings with the highest performances in the 1.5-15 nm interval are carbon for the 5-15 nm interval and nickel for the 1.5-5 nm interval. The grating for the spectral analysis should have two differently coated areas to optimize the throughput to the following experiments.

The optical element of the spectrometer is a long plane mirror ruled only on its central part. The size of the reflecting area is 180 mm (length) × 20 mm (height). The ruled area is only a small portion of this that is assumed to be 15 mm × 20 mm in size. The use of a small ruled area has several advantages: 1) since the reflectivity of a mirror is slightly higher than the efficiency of a grating at the zero-th order, the reflection coefficient of the beam which propagates unperturbed is maximized; 2) the optical performance of the spectrometer (e.g. aberrations, depth of focus) are improved; 3) the manufacturing cost of the grating is reduced. The grating is divided in two vertical stripes with different coatings, e.g. carbon and nickel, to optimize the efficiency in the whole 1.5-13.5 nm region. The central groove density is 1200 gr/mm. The parameters for groove space variations are chosen to have a flat spectral focal curve. The average length of the exit arm is 2 m.

Once the source has been tuned to the desired wavelength of operation, the spatial width of the FEL spectrum is in the millimeter range. A relatively

small detector is then required. Since the total length of the spectral focal curve in the 1.5-20 nm region is of the order of 250 mm, the detector has to be moved along the curve and centered on the spectral region to be acquired. Unfortunately a single straight line can not fit the focal curve with the necessary accuracy in the whole spectral region of interest. The required precision in the fit is obtained by two orthogonal linear stages, one fitting the spectral curve and used to bring the desired wavelength on the detector center, and the other mounted at 90° and used to change the grating-detector distance to the optimum value for the spectral focusing, as shown in Figure 8.8.

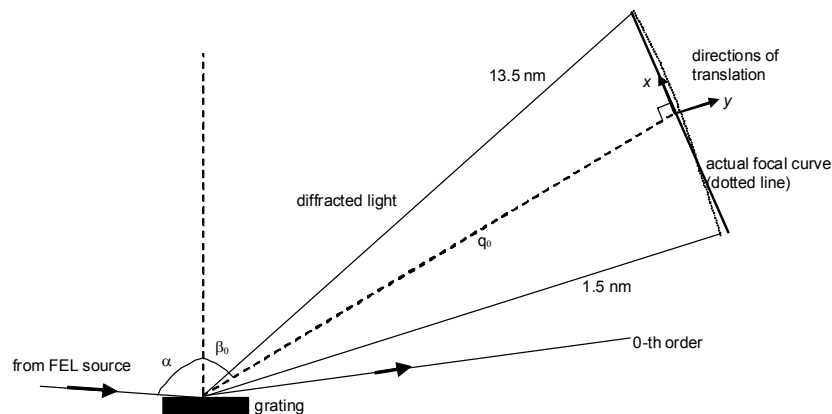


Figure 8.8: Detector mounted on two orthogonal linear stages.

As detector, a phosphor screen optically coupled to a CCD camera is adopted. For ultra-high sensitivity, the camera could be intensified. Such type of detector is used on the spectrometer currently used at FLASH [14,15]. This type of detector is more robust and safer than a UV-sensitive CCD or than a MCP intensifier with photocathode directly placed on the focal plane. In addition, a pulse with very short time duration such as the FEL signal could easily saturate the response of the MCP. The pixel size of such detectors is limited by the spreading of the light pulse generated by a point-like illumination on the phosphor. For example, the TPB (tetraphenyl-butadiene) phosphor can be easily deposited on a glass plate, it has excellent spatial resolution (several micrometers) and high quantum efficiency. With respect to the use of an EUV-enhanced camera looking directly at the spectrum, the use of the phosphor screen has some considerable advantages: the resolution is limited by the properties of the phosphor and not by the pixel size of the camera, since the latter is optically coupled to the phosphor screen and the magnification can be selected to project 10 μm from the phosphor screen to the camera pixel; on the contrary, an EUV-enhanced camera is directly mounted on the focal plane, and most of these cameras have pixel size larger than 10 μm . Furthermore, the camera acquires the signal emitted by the phosphor in the visible, so it is easy to find on the market different possibilities for cameras with high dynamic range, low noise and fast readout rates. Finally, the flux on the camera can be controlled by the aperture of the diaphragm of the objective: this can be useful if the diffracted signal is very strong. Assuming a 0.2% rms spectral width of SPARX and the geometrical parameters listed above, the spectrum is sampled at FWHM by 15 (@1.5 nm) to 80 (@10 nm) pixels, so the line profile can be reconstructed with good accuracy.

The efficiency of a 1200 gr/mm laminar grating is shown in Figure 8.9. The 0-th order efficiency is few % lower than a mirror, while the diffraction efficiency is in the 0.005-0.015 range. Then, the intensity profile of the beam

reflected to the experiment is almost unchanged with respect to the beam reflected by a mirror. The actual grating efficiency depends on the manufacturing process of the groove profiles and must be specified by the manufacturer.

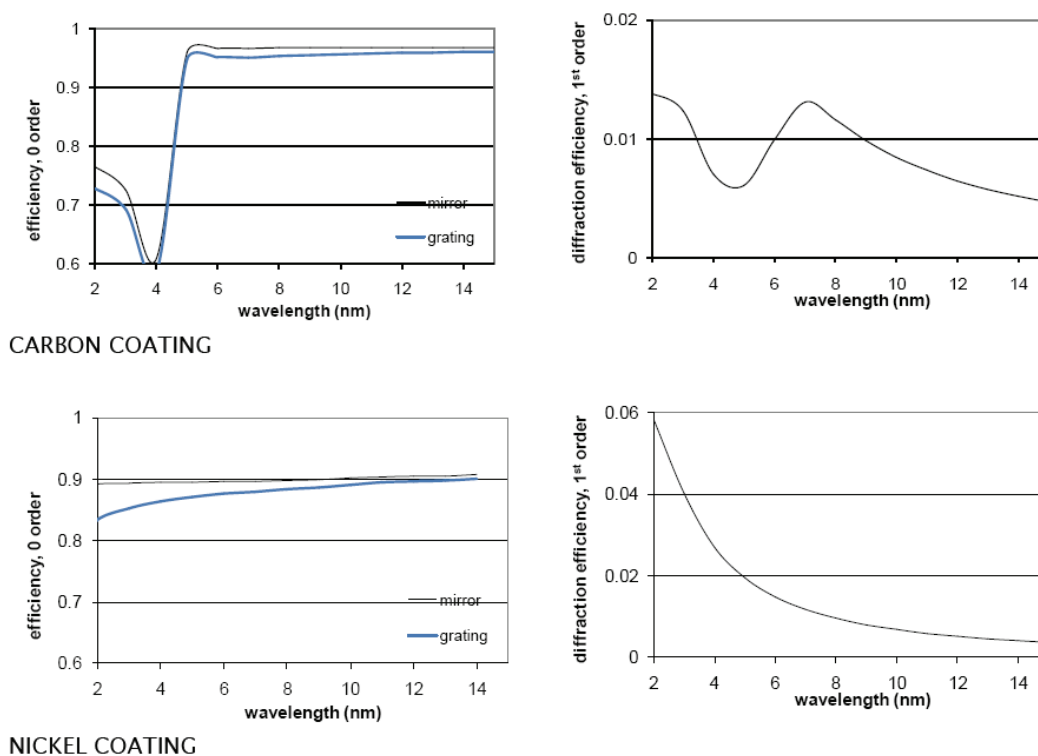


Figure 8.9: Efficiency of a 1200 gr/mm grating with laminar profile, duty cycle 0.5, groove depth 4 nm.

Let us estimate the throughput at the detector stage at three wavelengths.

- 1) 10 nm, $1 \cdot 10^{14}$ ph/pulse. We assume 0.13 of the flux on the ruled area, 0.008 grating efficiency, YAG efficiency of 0.6 photons over 4π per incident photon, a 100-mm f/2.4 objective, 0.5 CCD quantum efficiency, one digital count per 5.6 photons on the CCD. The flux on the diffracted order is about 2500 counts/pixel on an illuminated area of $80 \text{ px} \times 250 \text{ px}$.
 - 2) 5 nm, $5 \cdot 10^{13}$ ph/pulse. We assume 0.20 of the flux on the ruled area, 0.006 grating efficiency and YAG efficiency of 0.6. The flux is about 7400 counts/pixel on an illuminated area of $40 \text{ px} \times 170 \text{ px}$. In this case, the diaphragm of the objective has to be closed to avoid the saturation of the CCD camera.
 - 3) 2 nm, 3rd harmonics, $1 \cdot 10^{11}$ ph/pulse. We assume 0.20 of the flux on the ruled area, 0.05 grating efficiency and YAG efficiency of 0.7. The flux is about 200 counts/pixel on an illuminated area of $20 \text{ px} \times 150 \text{ px}$. In this case, the signal can be spatially binned to increase the signal-to-noise ration.
- It can be concluded that the flux on the detector is high enough to give spectra with high signal-to-noise ratio in the single shot when SPARX is operated at its nominal parameters.

8.3.1.2 Design for shorter wavelengths

The same optical design can be applied both in case of wavelengths longer than 20 nm and shorter than 1.5 nm. Let us consider the case of SPARX

in phase 2 which is expected to emit in the 1.5-5 nm spectral region (fundamental radiation). Diffraction gratings used at extreme grazing incidence have already been used for soft X-ray spectroscopy up to 7 keV, i.e. 0.17 nm [16,17]. Since wavelengths as short as 0.5 nm are expected for the 3rd FEL harmonic, the incident angle on the plane grating has to be increased much close to 90°. The reflectivity of some standard coatings for extreme grazing-incidence optics is shown in Figure 8.10. The working angle will be the 89-89.5° interval.

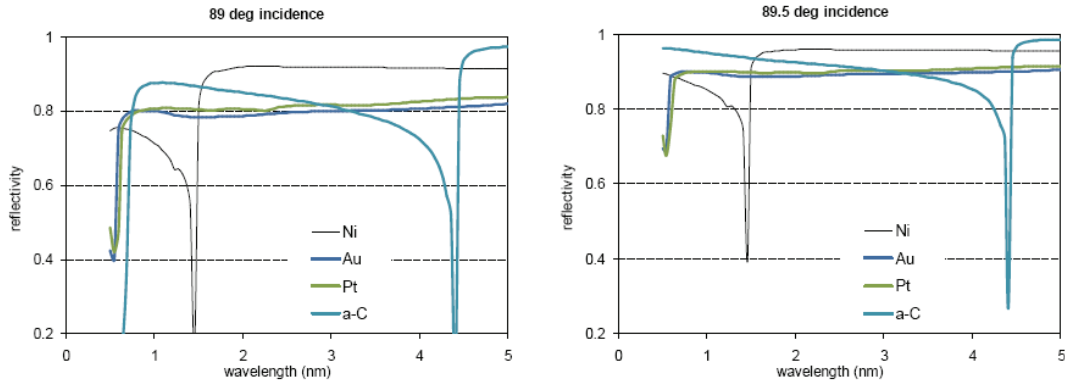


Figure 8.10: Reflectivity of some coatings in the 0.5-5 nm region.

8.3.1.3 Expertise of the team in realization of spectrometers for Free Electron Lasers

The CNR-INFM LUXOR laboratory, located in Padova (Italy), has a long experience in the realization of spectrometers for FEL radiation. In particular, it has been responsible of the realization of the spectrometer used at present to acquire the spectrum of FLASH in the 4-35 nm region [14,15]. Some pictures of the instrument are shown in Figure 8.11.

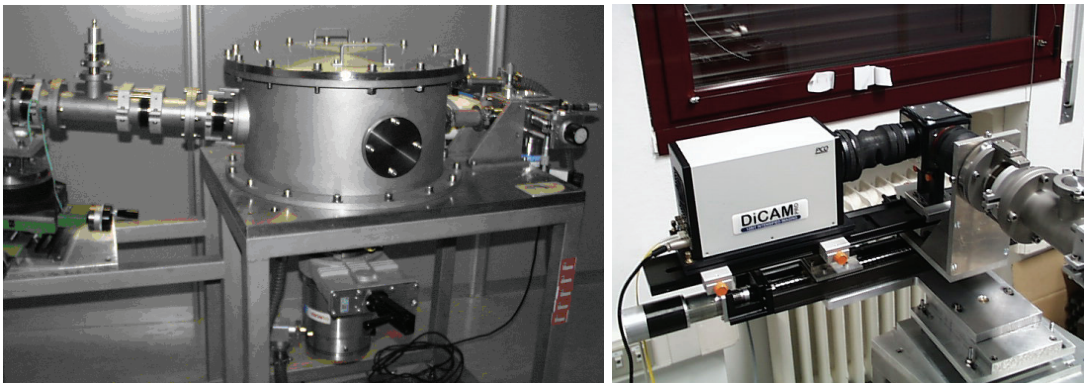


Figure 8.11: Images of the spectrometer realized in the LUXOR lab and installed at the FLASH facility since 2004 to monitor the FEL spectrum: left) the instrument; right) the detector

8.3.2 Controlled attenuation of FEL radiation using a gas absorber

Several experiments with FEL radiation may require different intensities on the sample, depending on the type of sample, e.g. gas or solid, and on the regime under investigation, e.g. linear or non-linear. It is then useful for the users to have available a simple method to control the intensity of the FEL beam on the interacting area. The ideal attenuator should have the following characteristics:

- It should work in the whole spectral region of operation of SPARX
- It should have a controlled and variable attenuation in the $1\text{-}10^{-5}$ interval
- It should preserve the beam attributes such as coherence, statistics and spectrum. Note that this is not possible if the attenuation is obtained by changing the LINAC settings.

A simple and effective attenuation system is the use of a gas cell filled with different gases and operated at different pressures [18]. The spectral region of operation drives the selection of the type of gas and the operating pressure controls the amount of attenuation. The gas absorber cell can be realized by a long tube (e.g. 10 m length, <40 mm internal diameter, CF40 flanges) filled with gas and placed after the undulators at the end of the FEL tunnel. Differential pumping sections placed at the two inputs of the tube will assure the UHV conditions both in the undulators and in the beamlines. The maximum operative pressure is 0.1 mbar. The pressure inside the tube has to be controlled and maintained with high accuracy to select the attenuation factor and keep it constant in time. This can be realized by an active system in which the injection valve and the vacuumeter form a feedback loop. The attenuation in the 3-30 nm region of typical gases to be used to fill the cell is shown in Figure 8.12. The operative conditions of the gas attenuators are resumed in Table 8.1.

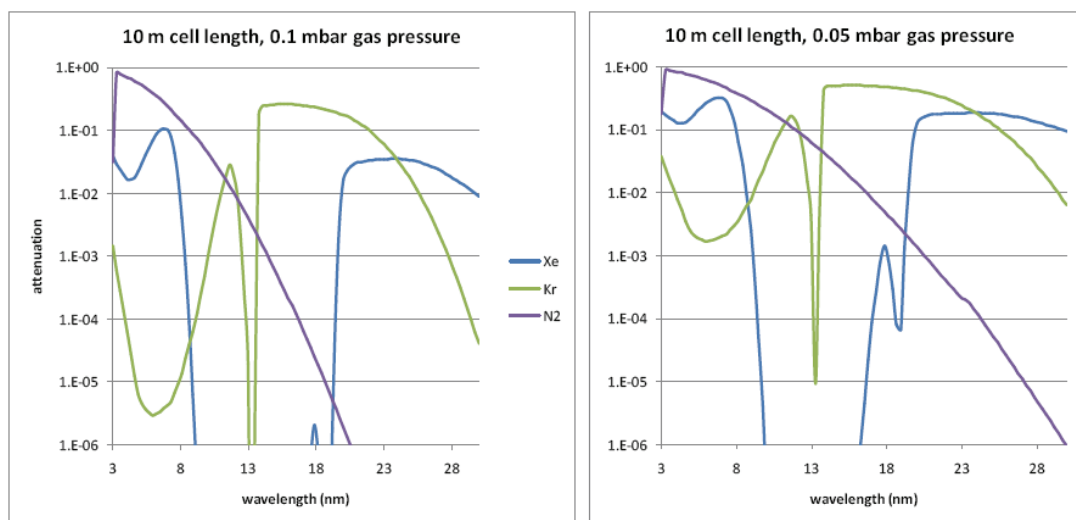


Figure 8.12: Absorption of Xenon, Krypton and Nitrogen in the 3-30 nm spectral region.

Table 8.1. Operative conditions of the gas attenuator, 10 m cell length.

<i>Spectral range</i>	<i>Gas</i>	<i>Pressure range</i>	<i>Attenuation</i>
3-10 nm	Kr	0.01-0.1 mbar	$10^{-1}\text{-}10^{-6}$
9-20 nm	Xe	0.01-0.1 mbar	$10^{-1}\text{-}10^{-7}$
20-30 nm	N ₂	0.01-0.1 mbar	$10^{-1}\text{-}10^{-6}$

8.3.3 Intensity monitor

An intensity monitor has to cover the full spectral range expected for SPARX, from 1 nm to 30 nm, as well as the extended dynamic range from spontaneous undulator emission to FEL emission at the saturation. The intensity of the individual FEL pulses can be measured with several detectors, such as gas monitor detectors [19], MCP-based detectors [20], thermopiles or photodiodes [21].

A well established method already used at the FLASH facility is the gas ionization detector [22,23]. It is an absolutely calibrated detector based on photoionisation of noble gases at a low target density and the detection of photoions and photoelectrons. The number of electrons/ions generated is proportional to the number of photons, to the target density, to the photoionisation cross section and to the length of the interaction volume. A schematic of the system adopted at the FLASH facility is shown in Figure 8.13.

This method has many advantages for the intensity measurement of SPARX: 1) it is almost transparent to the FEL beam and does not alter the beam properties; 2) it has a wide dynamic range; 3) it is independent from the beam position; 4) it has no saturation effects; 5) it can be absolutely calibrated within $\approx 10\%$; 6) , it can also be used to measure the beam position. The extended dynamic range of the gas-monitor detector is achieved by varying the gas pressure inside the cell and guarantees high linearity in the measurement of the non focused FEL beam even in the saturation regime. On the other hand, the device can be calibrated using synchrotron radiation at low photon intensities. The detector is typically operated with either nitrogen or a rare gas at low pressures of typically 10^{-6} mbar. Besides the intensity of the FEL beam, also its position can be monitored with the same gas cell. The detection electrodes are split allowing pulse-resolved determination of the horizontal and vertical beam position. This device can be placed at the end of the undulator section in front of the first mirror as a permanent intensity and beam position monitor common for all the beamlines.

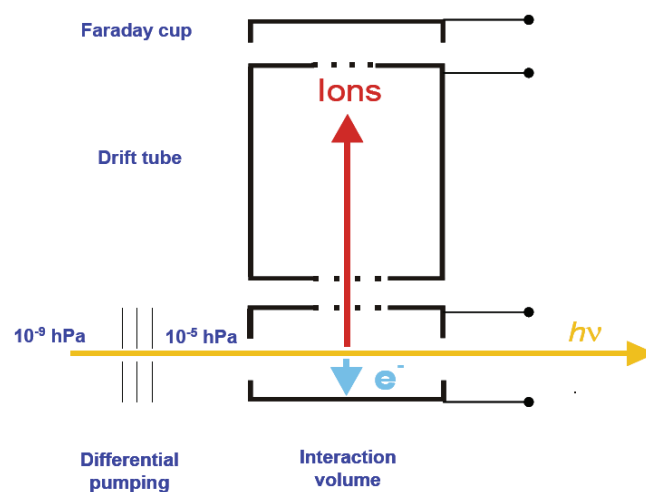


Figure 8.13: Schematic of the gas ionization detector adopted at FLASH (see Ref. 22)

Also MCP-based detectors have been already successfully used for intensity measurements at FLASH [9]. Briefly, the MCP detector uses a gold mesh with 0.65 transmission or alternatively a thin gold wire to reflect part of the FEL beam onto a calibrated MCP. Keeping the MCP in the low gain regime, it

is possible to determine the FEL gain with respect to spontaneous emission once the applied MCP voltage is known. By using an optimized geometry with small reflection angles and materials with higher reflectivity in the X-ray, such a detector can be used in a broad spectral region ranging from the XUV to the X-ray. With respect to the gas cell, the MCP-based detector alters the spatial properties of the FEL beam, since the gold mesh produces diffraction, resulting in an inhomogeneous intensity distribution at the sample position. The intensity monitor has to be installed after the gas attenuator to take into account of the actual attenuation introduced by the gas absorption.

8.3.4 Beam position monitor

The monitoring of the FEL beam position and profile is required to ensure pointing stability for the optical systems of the beamlines and optimum focusing at the experiment. Furthermore, the spatial and angular stability of the X-FEL radiation is very important for undulator alignment. Both OTR or fluorescent YAG:Ce screens can be employed during the alignment procedures. Screens will be placed behind each of the mirror stages to monitor the beam position. It will be essential for a correct alignment to have a laser reference that visualizes the optical path of the FEL.

On-line monitoring can be provided by beam position monitors (BPMs) of blade type (based on photoelectron emission from the blade material) that are current state-of-the-art for 3rd generation synchrotron sources. Since the information of the beam position is obtained from the halo of the undulator radiation, these detectors affect the photon beam spatial properties. Instead, BPMs based on the detection of electrons/ions generated by the photon beam in a gas cell do not alter the beam properties, since they are based on an indirect detection scheme without solid elements intersecting the beam [24]. In addition, the same detector gives the measurement of the FEL intensity, as already pointed out. The distance between consecutive BPMs will be fixed to give a transverse and angular resolution of the beam in the range of 10 μm and 1-2 μrad respectively.

8.3.5 Wave front measurement

The quality of the wave front of the FEL beam impacts directly on the performance of several kinds of experiments, such as phase contrast imaging experiments, which will suffer of a loss in resolution due to a distorted wave front, or high field experiments, which will suffer of a loss of intensity due to a degradation of the focus. The shape and slope error budgets of the reflecting surfaces (i.e. mirrors and gratings) required to preserve the wave front are really very demanding, at the limit of what can be done at present. Moreover, even a perfect optical surface may introduce distortions in the beam either by thermal load or by the mounting itself. It is then necessary to measure the distortion of the FEL wave front in-situ to fully understand the ultimate limits of experiments whose performances depend on the actual wave front.

A Shack-Hartmann sensor has been already used to characterize the XUV beam wave front and the focus of the beamline BL2 at FLASH [25]. The detector is based on the use of a diffracting element given by a two-dimensional hole array placed in front of an XUV-enhanced CCD camera. The use of such a sensor is of great importance during the commissioning phase of the beamlines to evaluate the performance of the optical elements. Furthermore, it can be used as an online shot-to-shot diagnostic in a parasitic way to an experiment, which does not block the primary beam.

8.3.6 Focus characterization

The determination of the spot size is essential for the beamline characterization, to assess both the peak intensity and the spatial resolving capabilities. Conventional methods like knife-edge [26] and fluorescent screen technique [27,28] have been successfully tested in the XUV with high-order laser harmonics to measure spot sizes of few micrometers, but they will not withstand the irradiance level of the focused SPARX beam.

Two methods have already been tested at FLASH to determine the spot size of the microfocus beamline BL2: wave front measurement [25] and atomic photoionization [29]. The former method has been already briefly described in the previous paragraph. The latter one is based on a saturation effect upon ionization of rare gases and manifests itself by a sub-linear increase of the ion yield with increasing photon number per pulse. The effect is due to a considerable reduction of target atoms within the interaction zone by ionization with single photon pulse.

8.3.7 Measurement of the transverse coherence

The methodology of characterizing coherence properties in terms of correlation functions is well developed and experimentally established. The transverse coherence will be measured by Young's double-slit experiments. This is routinely done at FLASH, as shown in Figure 8.14.

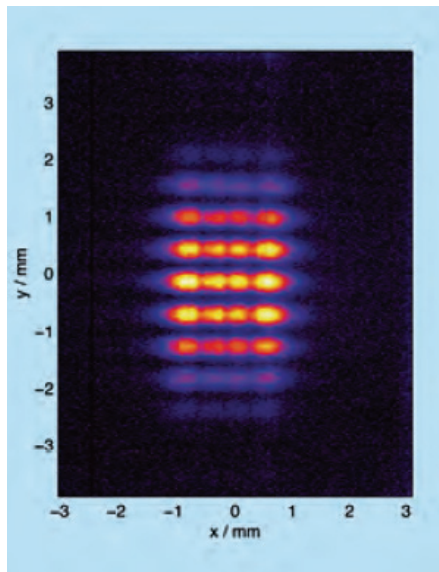


Figure 8.14: Double-slit diffraction pattern taken at FLASH at 100 nm with a slit separation of 0.5 mm (see [30]).

8.3.8 Temporal characterization

The temporal characterization of FEL pulses is a complex measurement although essential for a complete characterization of the FEL regime. Here the main scientific and technical aspects are discussed in details.

The characterization of ultrashort femtosecond pulses in the extreme ultraviolet (XUV) or soft X-ray spectral region depends on several parameters such as the pulse energy, pulse duration and reproducibility from shot to shot. In the following we will consider different schemes that could be successfully

implemented for the characterization of the pulses delivered by a SASE FEL operating between 4.5 and 30 nm.

The schemes usually applied for the temporal characterization of ultrashort pulses in the visible (VIS) and infrared region (IR) rely on the acquisition of an autocorrelation and/or a cross-correlation based on nonlinear effects (usually performed in nonlinear crystals). However these techniques have been extended only in the last years to the XUV spectral region and still represent a challenge for the experimentalists. The main difficulties for the application of autocorrelation techniques are given by:

- a) the absence of transparent nonlinear crystals in the XUV spectral region.
- b) the lack of suitable optics for splitting the pulses into two replicas.
- c) the cross sections for nonlinear effects (such as double ionization of Helium) in the XUV region are significantly lower than the corresponding ones in the IR and VIS region, requiring higher intensity (of the order of 10^{13} W/cm²- 10^{14} W/cm²) for a precise temporal characterization.

For this reason the characterization of XUV pulses has been mostly accomplished using a cross correlation technique between the XUV pulse to be characterized and a synchronized IR pulse; the signal in this configuration is the photoelectron spectra generated in the process of two color photoionization [31].

8.3.8.1 Cross-correlation measurements

For the temporal characterization of FEL operating in the SASE regime, one of the main problems is the absence of a synchronized IR laser. Moreover the stochastic nature of the SASE process determines a variation of the temporal characteristics of the XUV pulses on a shot to shot basis, so that multi-shot measurements can only give access to the average characteristics of the XUV pulses. Recent achievements in the synchronization of XUV FEL pulses and an independent laser system have reduced the residual time jitter down to about 100 fs, which is larger than the expected pulse duration of the XUV pulses (few tens of femtoseconds).

Recently, the temporal jitter of the XUV pulses generated at FLASH has been characterized by using the XUV-induced reflectivity change for visible light of GaAs samples [32]. The FEL pulses (39.5 eV photon energy, pulse duration shorter than 50 fs and energy up to 16 μ J) impinging onto a crystalline GaAs(100) crystal generate photo-excited carriers: Auger decay and auto-ionization convert the initial inner-shell excitation into valence excitation within a few femtosecond. Such valence excitations lead to ultrafast transient changes of the optical reflectivity in GaAs, which can be probed by a time-delayed visible pulse (400-nm or 800-nm central wavelength), produced by a laser source electronically synchronized to the electron accelerator. Since the intrinsic time constant of the initial reflectivity drop is small compared with the cross-correlation width (the duration of the visible pulse used in the experiment was 120-150 fs), this technique is suitable for cross-correlation measurement of the duration of the FEL pulse. Timing measurement of FEL pulses has been recently performed on a single-shot basis [33]. XUV pulses are crossed with visible pulses (400-nm wavelength) onto the GaAs target. The visible light reflected from the target is imaged onto a two-dimensional detector, as shown in Figure 8.15: the onset of the reflectivity change directly maps the delay between the FEL and visible pulse.

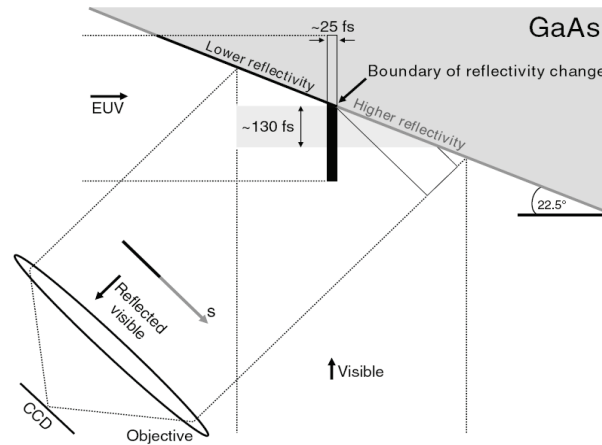


Figure 8.15: Experimental setup of the single-shot measurement (From Ref. 33).

The temporal characterization of the XUV pulses can be accomplished performing a two color photoionization using the synchronized IR pulse and the XUV pulse. Depending on the central wavelength of the XUV pulses different noble gases could be used as detection medium. When the two pulses overlap in space and time the photoelectron emitted by single XUV photon absorption can absorb or emit additional IR photons leading to the generation of the so called sidebands, separated in energy by an IR photon energy. It is important to point out that the sidebands can be generated only in the presence of both fields. The photoelectrons can be detected using different methods and configurations that can give access to different information. In the following we outline two methods whose combination could give complete information on the temporal characteristics and on the temporal jitter of the XUV pulses.

a) Perpendicular geometry [34]

The schematic experimental setup is shown in Figure 8.16. The XUV pulses are directed to a gas target, thus leading to photo-ionization. IR pulses propagate perpendicularly to the XUV beam. The XUV and IR pulses are linearly polarized parallel to the axis of the electron optics, and they overlap in space and time in the interaction region. The region of superposition of the two beams is imaged by using an electron detector (multi-channel plate + phosphor screen) and an electron lens system. This system must be provided with a high-pass energy filter, such as a retarding grid, in order to get rid of the electrons with energy below the first sideband; in this way it is possible to analyze only the electrons corresponding to the sidebands. In this configuration a relative temporal jitter between the XUV and IR pulses is mapped onto a vertical displacement of the cross-correlation giving access, on a single shot basis, to the time jitter characterization. Moreover, since the duration of the IR pulse can be measured independently, the XUV pulse duration can be obtained on a single-shot basis. If a multi-shots acquisition is performed, only average information about the timing of the pulses can be achieved.

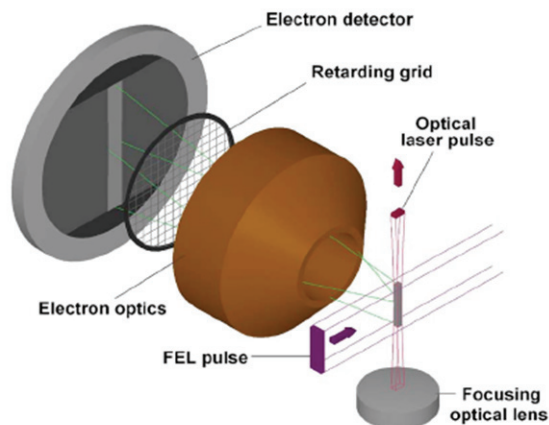


Figure 8.16: Setup of the cross-correlation measurement with perpendicular geometry (from Ref. 34)

b) Collinear geometry

In the collinear geometry the XUV and IR pulses must be combined in such a way that they propagate in the same direction. This can be accomplished using drilled mirrors (the XUV is usually transmitted through the central hole in the mirror, while the IR pulse is reflected by the external part) or using mirrors with different coatings (also in this case the XUV is usually reflected by the central part presenting an XUV multilayer coating and the IR by the external annular part with a dielectric or a metallic coating). The two pulses are then focused in the interaction region of an electron spectrometer (Time of Flight TOF, Magnetic Bottle, Velocity Map Imaging VMI spectrometer) and the electrons are finally detected using a MCP or an MCP coupled to a phosphor screen and a CCD camera. The energy of the electrons is determined either by their time of flight or by their impact position on the phosphor screen. Due to the collinear geometry a complete temporal characterization of the XUV pulse requires a delay scan between the two pulses; for each delay a complete photoelectron spectra must be acquired. From the width of the sidebands as a function of the relative delay, the duration of the XUV pulse can be determined (the duration and the intensity of the IR pulses must be independently measured). This technique is reliable for the characterization of fs XUV pulses as recently demonstrated by the characterization of 8 fs pulses at 36 eV [35]. However, using this method, it is not possible to disentangle the effect of the timing jitter between the two pulses and the effective pulse duration of the XUV and IR pulses on the temporal width of the sideband amplitude. A single shot sideband acquisition can be however implemented to determine the timing jitter between the two pulses, measuring the sidebands signal at a nominally fixed delay position [36]. For the application of this technique to the measurement of the XUV pulse duration, it would be necessary to compensate for the effect of time jitter, measuring it in an independent way using a second apparatus based either on the perpendicular or collinear geometry.

It is important to observe that in both geometries, the possibility to perform a single shot measurement requires a large number of electrons in a small volume; for this reason a careful numerical investigation based on the analysis of the electron trajectories would be necessary to avoid the presence of space charge effect that can compromise the energy resolution of the electron spectrometer.

A different approach, that gives the possibility to completely eliminate, at least in principle, the time jitter between the XUV and the other pulse to be used in the cross-correlation, is to use the electron bunch that generates the XUV light to produce an IR or even a far infrared (FIR) pulse, as well. This aim could be accomplished either by using an undulator matched for the generation of light in this spectral region or exploiting the radiation emitted by the electron bunch due to the acceleration caused by a bending magnet. In both cases, due to the common origin, the XUV and IR/FIR pulses are virtually jitter free and can be successfully used for the temporal characterization of the XUV pulses. In this case the collinear geometry, illustrated in the last section should be used.

The characteristics of the observed photoelectron spectra should depend on the ratio of the pulse duration of the XUV pulse ($FWHM_{XUV}$) and the optical cycle oscillation period of the IR/FIR field ($T_{IR/FIR}$). In general we can distinguish three different cases:

- 1) $FWHM_{XUV} \gg T_{IR/FIR}$. This condition is satisfied for IR pulses with a central wavelength $\lambda=0.8-1 \mu\text{m}$, taking into account that the expected pulse duration of a SASE FEL operating in this wavelength range is of few tens of femtoseconds. In this case the cross correlation between the two pulses leads to the generation of sidebands in the photoelectron spectrum. In this case, assuming as negligible the residual time jitter, it would be possible to estimate the duration of the XUV pulse.
- 2) $FWHM_{XUV} \ll T_{IR/FIR}$. This condition is realized for central wavelengths $\lambda > 15 \mu\text{m}$. In this configuration the effects of the FIR pulse on the photoelectron emitted by the XUV field is qualitatively different, and it leads to an overall upshift or downshift of the momentum distribution of the electrons depending on the relative delay between the two pulses. The process can be explained considering the emitted photoelectron wavepacket as a classical particle that, after ionization, is accelerated by the FIR electric field. At the end of the pulse the electron wavepacket has acquired an additional momentum that depends only on the vector potential at the release instant of the electron wavepacket. Analyzing the oscillation of the photoelectron spectra, as a function of the relative delay, a complete characterization of the XUV pulse can be achieved.
- 3) $FWHM_{XUV} \cong T_{IR/FIR}$. This case correspond to wavelengths in the range $1 \mu\text{m} < \lambda < 15 \mu\text{m}$. The effects of this radiation on the photoelectron wavepacket can be rather complex showing a transition between the sidebands formation (shorter wavelength) and the momentum shift (longer wavelength). However, also in these conditions, several retrieving algorithms can be successfully applied to determine the characteristics of the XUV pulse from the acquired trace.

It is important to notice that all these technique do not offer access to a single shot characterization of the XUV pulse, and for this reason the expected complex time structure characterizing a SASE FEL can't be completely resolved. These methods allow one to gain access to the average characteristics of the pulse train, such as pulse duration and, eventually, frequency variation as a function of time (chirp).

8.3.8.2 Autocorrelation measurements

As already discussed the lack of efficient nonlinear media in the XUV and soft X-ray region and the relatively low intensity of the sources operating in these wavelength region, have been challenging problems for a temporal

characterization based on an autocorrelation technique. However the recent progresses achieved in the field of High-Order Harmonic Generation (HHG) and the results obtained by different groups [37,38,39] have led to the first temporal characterization of XUV pulses using an autocorrelation method. The intensity required for the observation of nonlinear effects is in the range 10^{13} - 10^{14} W/cm² that can be accessed considering the expected high pulse energy of the SASE FEL. In the following, we will analyze the different aspects that must be considered to successfully apply an autocorrelation method to the characterization of the FEL.

a) Nonlinear medium

Nonlinear media with a nonresonant response over a large bandwidth are required for the temporal characterization of ultrashort XUV pulses. Different noble gases (Argon, Helium, Xenon) have been used for the demonstration of two-photon Above Threshold Ionization (ATI) using HHG radiation, and implemented for the complete temporal characterization of XUV pulses measuring the photoelectrons released by the absorption of two XUV photons. Recently, N₂ molecules have been used due to the larger nonlinear cross section [37]. In this case the absorption of two XUV photons leads to the formation of N₂²⁺ and subsequent dissociation in two N⁺ ions that can be measured using a time of flight electron spectrometer. Using this approach it has been demonstrated an interferometric autocorrelation of a train of XUV pulses. These techniques have been applied for XUV pulses with energy around 20.8 eV; their extension to different energy ranges will require a preliminary study to identify those atoms or molecules that present the highest nonlinear nonresonant cross section useful to perform a second order autocorrelation.

b) Beamsplitter

Another problem associated to the measurement of an autocorrelation trace in the XUV spectral region is the generation of two exact replica of the same pulse; indeed it is extremely difficult to produce efficient beamsplitters in this spectral region. Recently two different approaches have been developed:

- 1) a pair of silica plates closely placed (distance of 100 μm) and operating at grazing incidence for the XUV radiation, have been used as beamsplitter. The beam impinging on the two plates is divided in two replica that can be independently delayed moving one of the plates using a piezoelectrical stage. The two replica can be focused in the same focal spot using a toroidal mirror.
- 2) a multilayer mirror (Si/C) divided into two parts has been used to divide and to focus at the same time the XUV pulses into a Helium gas jet. Also in this case the delay between the two components can be independently controlled with high resolution.

c) Detection techniques

So far time of flight electron or ion spectrometer have been used. Depending on the cross section of the corresponding processes and type of characterization, the autocorrelation signal can be based on the measurement of electrons or ions. As already discussed the use of molecules, and therefore molecular ions, ensures higher count rates and shorter acquisition times giving access to a sub-cycle characterization of the XUV fields (interferometric autocorrelation). On the other hand the acquisition of electrons allows one to gain direct access to the frequency modulation of the XUV pulse and to extend techniques used in the VIS and IR range for a complete (envelope and phase) temporal characterization, such as the Frequency Resolved Optical Gating (FROG) also to the XUV range [40].

8.4 Proposal of novel diagnostic techniques

8.4.1 Electron beam transverse size effects in the transition radiation spectrum as a possible diagnostic tool in LINAC FELs

The present proposal aims at investigating possible effects due to the beam transverse size on the transition radiation (TR) energy spectrum by an electron beam in the short wavelength region - in particular, in the visible optical region (Optical Transition Radiation, OTR) - and to implement such experience in the beam diagnostics of a LINAC FEL. Typical OTR screens in an electron linear accelerator are in general not expected to produce spectral alterations of the TR intensity in the visible optical region. They behave indeed like an ideal conductor in the visible spectral region and can be suitably dimensioned so that possible diffractive cut-off of the spectrum due to the finite transverse dimension of the screen are in practice negligible even in case of ultra-relativistic electrons. For such an experimental condition, neither variations of the number of the OTR photons emitted at a given wavelength nor modifications of their angular distribution are, in principle, expected to be observed as a function of the beam transverse size under conditions of temporal incoherence. In fact, according to a well known theoretical model, under observation conditions of temporal incoherence, the OTR energy spectrum cannot bear information about the beam transverse size - i.e., about the relative distances of the electrons in the transverse plane - since it results from the linear addition of the spectral contributions from the N single electrons that are supposed to emit as isolated and individually radiating particles [41,42].

A recently proposed theoretical model [43,44] - based on the virtual quanta method originally formulated in terms of the electron density approach instead of the individual single electron - predicts that beam-transverse-size effects in the OTR spectrum may be observed. In particular, for fixed values of the beam energy and current, the number and the angular distribution of the OTR photons radiated at a given wavelength should increase and broaden, respectively, owing to a reduction of the beam transverse size.

On the basis of such a model, for a 10 ps long 1 nC electron bunch, the expected angular distributions of the radiation power integrated in the wavelength region 0.4-0.7 μm has been calculated - see Figure 8.17 - as a function of the beam transverse size for different values of the beam energy [45,46]. A standard OTR diagnostic station equipped with a focusing optical line and a detector (standard CCD camera for imaging both the OTR light spot and the OTR angular distribution, a power-meter or a photomultiplier for accurate power measurements) is suitable to the proposed measurements (see Figure 8.18 for a sketch of the experimental set-up).

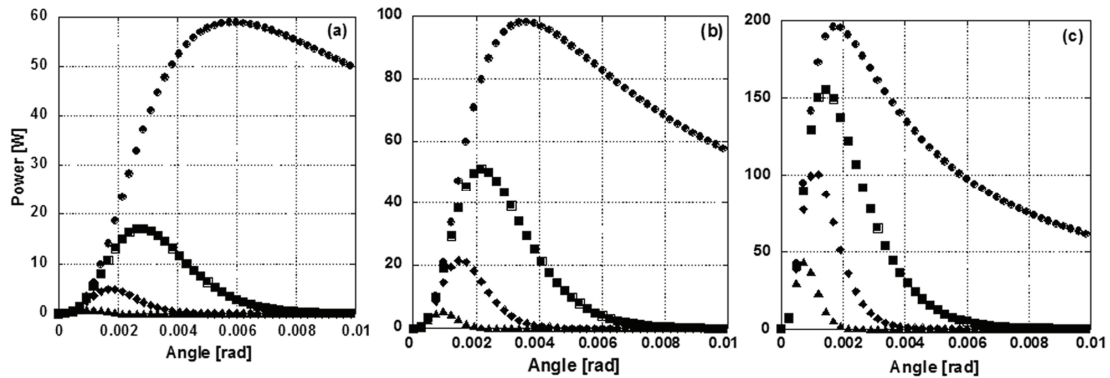


Figure 8.17: Polar angle distribution of the transition radiation power radiated in the band 0.4-0.7 μm by a 10-ps-long 1nC electron bunch with a cylindrical distribution for different values of the beam energy ($E=150$ (a), 250 (b) and 500 (c) MeV). In each frame, the radiation power expected for each energy is calculated for different values of the beam transverse size ($\sigma=100$ (\blacktriangle), 50 (\blacklozenge), 25 (\blacksquare) and 0 (\bullet) μm).

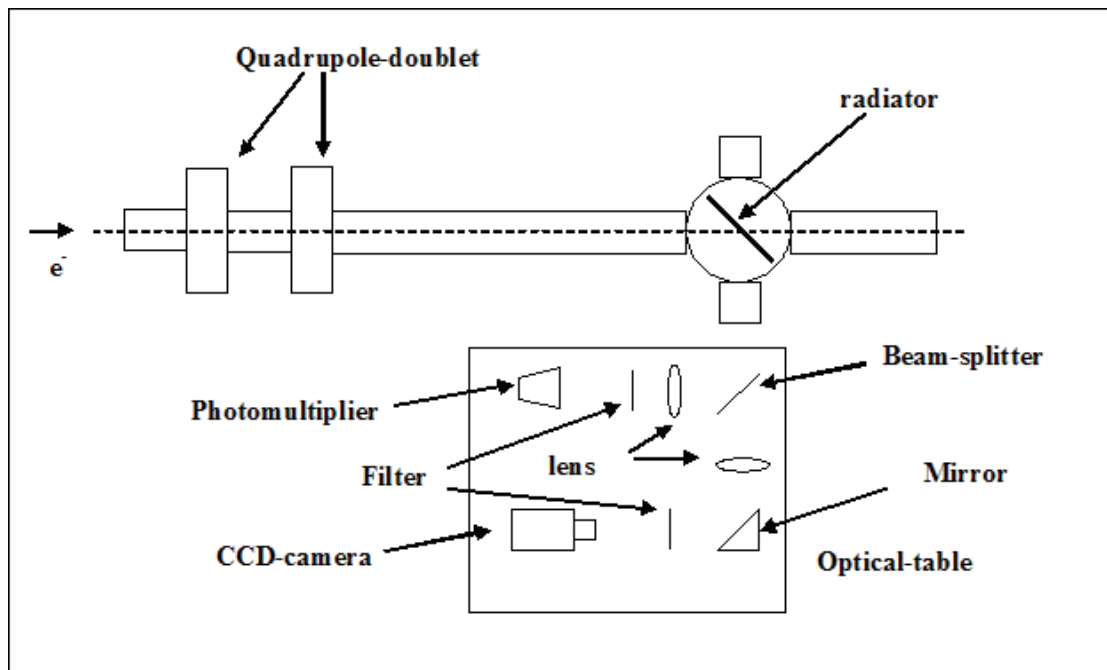


Figure 8.18: Top-view layout of the proposed OTR diagnostic station in an electron linear accelerator

The successful measurement of such an effect, that is not supported up to now by the standard theory, would have fruitful consequences in the development of a new dedicated OTR beam diagnostic methodology that meets the following criteria: (1) information about both the beam energy and transverse size can be estimated by means of a spectroscopic analysis of the angular distribution of the TR intensity even at a very short wavelength; (2) measurements of the beam energy and transverse size are not independent as long as the ratio of the beam transverse size to the observed wavelength is not negligible; (3) the smaller the beam transverse size, the higher the number of TR-photons emitted at a given wavelength and the wider the broadening of their angular distribution. Consequently, as the beam transverse size

approaches the spatial resolutions of a given CCD camera, a high precision measurement of the beam transverse size can be still performed if the same CCD camera is used to map the angular distribution of the OTR intensity instead of imaging the OTR light spot.

The experimental check of the beam-transverse-size effects in OTR and the complete investigation and development of the beam diagnostic applications of such effects in a FEL driver LINAC are the goals of the present proposal.

8.4.2 Pulse length measurements using incoherent synchrotron radiation fluctuations

Coherence properties of light always depend on the source. Given the type of source, its physical size, and bandwidth of emitted radiation, one can always calculate a coherence size for a given radiation wavelength λ_0 and a coherence time. The former deals only with the transverse source extension, indicating how big is the part emitting in phase at λ_0 . To quantify, the following formula can be used:

$$\sigma_x \cdot \sigma_{x'} = \frac{\lambda}{4\pi} \quad (8-4)$$

where $\sigma_{x'}$ is radiation *RMS* divergence and σ_x is the *RMS* coherent size. Coherence time is related instead to the physical mechanism producing radiation that fixes the bandwidth. If a source smaller than the coherence size emits radiation in a bandwidth $\delta\lambda$ around λ_0 radiation will be coherent only within a time [47]

$$\sigma_{coh} \leq \Delta\omega^{-1} \quad (8-5)$$

So, if source length and size are bigger, but commensurable with coherence length and size of radiation at a given λ_0 , coherence properties (such as interference patterns) can still be detected from incoherent light.

While being deviated by a magnetic dipole an electron emits synchrotron radiation over a large bandwidth. Looking to an entire beam circulating inside an accelerator, one can consider its macro properties, such as overall beam longitudinal shape, to be constant on a small time interval (minutes), while micro properties, such as single electron position inside the bunch and its arrival time, are changing at any turn. Selecting a frequency and a bandwidth (e.g. using a filter) a particular coherence length is fixed and the electron beam can be divided in longitudinal slices each being σ_{coh} long. By measuring the total radiation intensity, one will measure the sum of each single longitudinal mode intensity. These modes have 100% shot to shot fluctuation because of fluctuation on electrons number and relative position inside a coherent slice fluctuate, but the fluctuation of the sum will be proportional to the inverse number of modes in the radiation. Basically, once the standard deviation of total intensity is measured, the number of modes is known and so the pulse length.

Also transverse modes can be present if the beam's transverse size is not small enough; in this case fluctuation of the total signal decreases because the total number of modes is increased (multiplication of longitudinal and transverse modes, [48]). In pulse length measurement, transverse modes carry no information, and some experimental procedure, such as spatial filtering, can be used to remove them. Obviously filtering the signal will decrease the

intensity, which is further decreased by the frequency filter, so a very sensitive detector is needed. Suppose that the electron time of arrival in the magnet is t_j , the electron beam current will be [49]}

$$I(t) = e \sum_j \delta(t - t_j) \quad (8-6)$$

and the Fourier component of the emitted field will be:

$$E(\omega) = e(\omega) \sum_j e^{j\omega t} \quad (8-7)$$

where $e(\omega)$ is the Fourier transform of each individual particle's radiation field travelling through the magnet. In time domain, the electric field of the pulse on the detector can be written as [50]:

$$E(t) = A(t)e(t) \quad (8-8)$$

$A(t)$ being the pulse envelope:

$$A(t) = \sqrt{I(t)} \cdot e^{i\varphi(t)} \quad (8-9)$$

and $e(t)$ being a complex valued stationary process, i.e. its value at each t is a random variable. Obviously $e(t)$ is related to the electric field fast oscillations inside the envelope bringing information about the pulse bandwidth. The correlation function

$$K(\tau) = \langle e(\tau)e^*(t - \tau) \rangle \quad (8-10)$$

is then introduced, Fourier transform of which is the pulse radiation spectrum. Now, writing the electric field correlation function:

$$\Gamma(\tau) = \int E(\tau)E^*(t - \tau)d\tau \quad (8-11)$$

it can be shown [51] that fluctuations $d_\Gamma(\tau)$ of this function around its average carry information on the pulse envelope. The formula for $\tau = 0$ is:

$$d_\Gamma(0) = \int_{-\infty}^{+\infty} |K(\tau')|^2 d\tau' \int_{-\infty}^{+\infty} I^2(t) dt \quad (8-12)$$

For a gaussian pulse the current is

$$I(t) = I_0 e^{-\frac{t^2}{2\tau_b^2}} \quad (8-13)$$

where τ_b is the pulse length. Moreover, if a filter with gaussian bandwidth is used, then the normalized correlation function $K(\tau)$ is [51]:

$$\frac{K(\tau)}{K(0)} = e^{-\frac{\sigma_\omega^2 \tau^2}{2}} \quad (8-14)$$

where σ_ω is the filter bandwidth. In this case (which also will be the case of our measurements), the formula that links pulse length to intensity fluctuation is:

$$\left(\frac{\sigma_I}{I}\right)^2 = \frac{1}{\sqrt{1+(2\sigma_\omega\tau_b)^2}} \cong \frac{1}{2\sigma_\omega\tau_b} \quad (8-15)$$

Coherence length is fixed by the filter relative bandwidth. In the gaussian case one gets:

$$\begin{aligned} \sigma_\omega\tau_{coh} &= \frac{1}{2} \\ \tau_{coh} &= \frac{1}{2\sigma_\omega} \end{aligned} \quad (8-16)$$

Therefore the number of longitudinal modes inside the beam of length τ_b is

$$m_z = \frac{\tau_b}{\tau_{coh}} = 2\sigma_\omega\tau_b \quad (8-17)$$

Finally one gets:

$$\left(\frac{\sigma_I}{I}\right)^2 = \frac{1}{m_z} \quad (8-18)$$

If transverse modes are present, they will contribute to fluctuations:

$$\left(\frac{\sigma_I}{I}\right)^2 = \frac{1}{m_x m_y m_z} = \frac{1}{m_{tot}} \quad (8-19)$$

Once m_z is known, the pulse length can be calculated

$$\tau_b = m_z\tau_{coh} \quad (8-20)$$

Since the standard deviation of intensity has to be measured, a statistic is needed (multi-shot measurement). Errors will be therefore proportional to the inverse square root of numbers of data samples:

$$\varepsilon = \sqrt{\frac{2}{N}} \quad (8-21)$$

which means that the number of measurements has to be high enough.

A typical measurement setup is shown in Figure 8.19. The light from a bending magnet is collected and transported by means of optical elements to a detector (APD in figure). Along the line either spatial and spectral filters are applied in order to control the number of transverse and longitudinal modes.

The number of transverse modes should be minimized by the layout, since they contribute to the intensity fluctuations, but do not add information on the beam length; wrong evaluation of transverse modes can be a primary source of errors. The number of longitudinal modes has to be a compromise between the need of having a sensible signal variation shot-to-shot (intensity fluctuations are proportional to the inverse of the number of longitudinal modes) and the need of having high enough number of photons, to have an higher signal to noise ratio (quantum noise in the detector depends on the number of photons to be detected). After the APD a low noise amplifier increases the signal amplitude at a level which is compatible with the oscilloscope sensitivity.

Radiation in the visible spectral range is suitable for these measurements, making the setup easy and inexpensive, especially if compared with other bunch length measurement methods. Furthermore, there are no theoretical limitations to the measurement of very short bunches. The number of longitudinal modes can in fact be controlled by spectral filtering and shorter beams relax the request on the filter bandwidth.

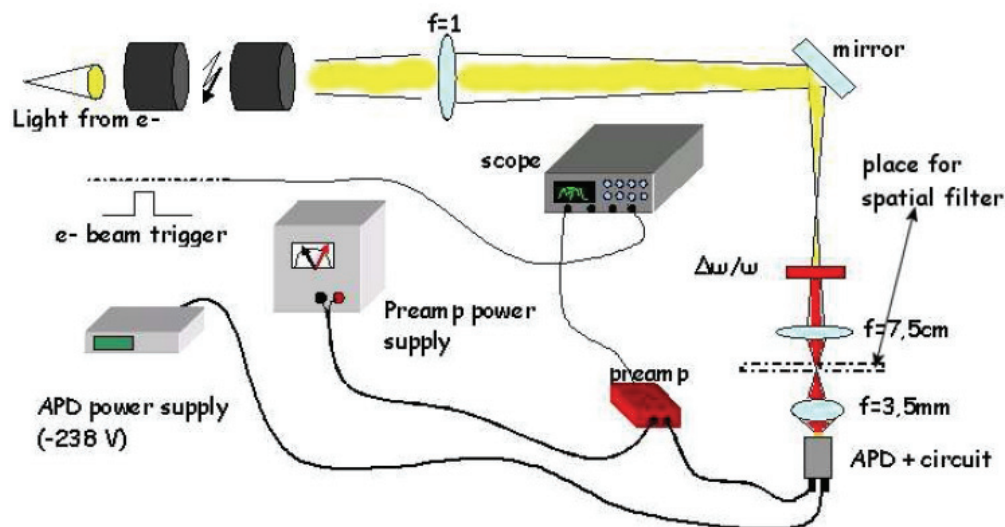


Figure 8.19: Top-view layout of the proposed OTR diagnostic station in an electron linear accelerator

8.4.3 Diagnostics using fast IR single element photodiodes and array detectors.

In attempt to measure the bunch lengths, the coherent emission and the beam emittance of the electron bunch at the first magnetic compressor as well in other points, the use of fast IR photodiodes and array detectors is proposed.

Recently photon uncooled infrared devices optimized for the mid-IR range based on HgCd(Zn)Te alloy semiconductors allows to obtain sub-nanosecond response times [52]. These devices can be used for fast detection of intense IR SR sources, such as third generation synchrotron radiation sources and FEL's [53]. Fast and promising photo-conductive and photo-voltaic IR detectors operating at near room temperature (from 300 K to 205 K temperature) are now available. These detectors are based on complex HgCdTe multilayer heterostructures structures grown by MOCVD (Metal-Organic Chemical Vapour Deposition) on (211) and (111) GaAs substrates. The devices are developed by VIGO SA, a leader manufacturer of fast uncooled IR photon detectors. Detectivity of thermo-electrically cooled optically immersed photodiodes approaches $1 \cdot 10^{10}$ cmHz^{1/2}/W at ≈ 10 μ m wavelength. The response times of photodiode detectors with a weak reverse bias is of the order of <100 ps. These devices are optimized for high frequency applications and are recommended for response time critical applications e.g.: laser diagnostics for ultrashort pulses from free-electron lasers (FEL) and quantum cascade lasers (QCL) [54].

A photo of an IR photo-conductive and of a photodiode detector is shown in Figure 8.20 (on left and on right, respectively). These devices are very compact, vacuum compatible, robust, easy to manage and low cost.



Figure 8.20: Pictures of fast IR photo-conductive (on left) and photodiode detector (on right).

Photo-conductive IR detectors have been tested at the IR beamline SINBAD of DAΦNE e^+/e^- collider [55,56]. Recently the pulsed emission of the electron bunches has been recorded with a fast IR uncooled photo-voltaic detector achieving a resolution time of about few hundred of picoseconds, as shown in Figure 8.21. Measurements were performed at room temperature although devices cooled at lower temperature (~ 205 K using three stage of Peltier coolers) could achieve a response time of the order of 100 ps or lower. These devices are going to be used for monitoring the bunch-by-bunch synchronous phase shift of the DAΦNE positron bunches within the *Time Resolved Positron Light Emission* (3+L) experiment [57].

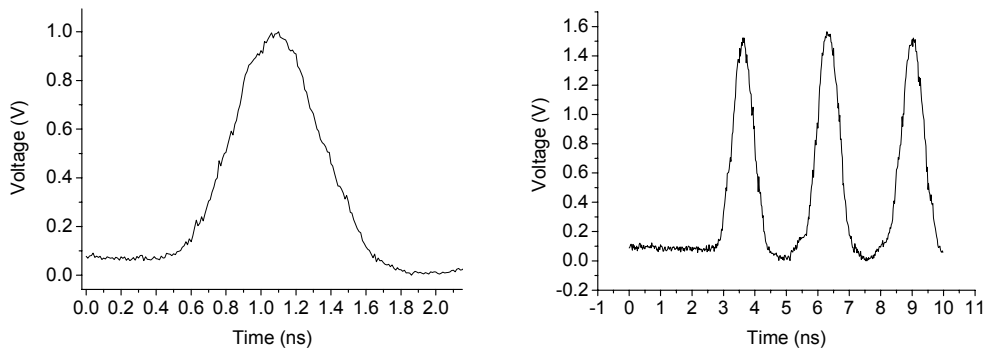


Figure 8.21: IR emission of e^- bunches measured at DAΦNE with a fast IR photodiode. The first bunch of the electron structure measured with a fast photovoltaic IR detector (on left). The first three bunches of the electron structure measured with an uncooled IR photodiode (on right).

In order to extract the IR light and to perform the diagnostics of the electron beam using fast IR detectors one or more exit ports can be set-up at the magnet compressor. An optical system composed by plane and a spherical mirrors working in air is proposed to focus the radiation on IR detectors. A similar optical layout is used on the 3+L experiment composed by 5 mirrors working in air, set after the IR window installed at the exit port of a bending magnet of the positron ring in the DAFNE hall. This optical layout uses four plane mirrors to transport 10×10 mrad² of the emitted radiation to the optical table where a spherical mirror focuses the radiation on fast IR detectors.

In order to perform the imaging of the source more complex optical system composed by a set of plane and aspherical mirrors is proposed at the exit port of the magnet compressor. The source will be focalize on a fast IR

array detector. This system will allow measuring the emittance of the electron beam at the exit port of the bunch compressor.

Nowadays fast IR array detectors are available. These array detectors are based on HgCd(Zn)Te alloy semiconductors and are constituted by photoconductive or photo-voltaic elements optimized for the detection of mid-IR range. In particular a first fast IR array detector has been developed in collaboration with the VIGO SA within the 3+L experiment. The array showed in Figure 8.22 is a customized uncooled IR photoconductive matrix constituted by 32x2 pixels.

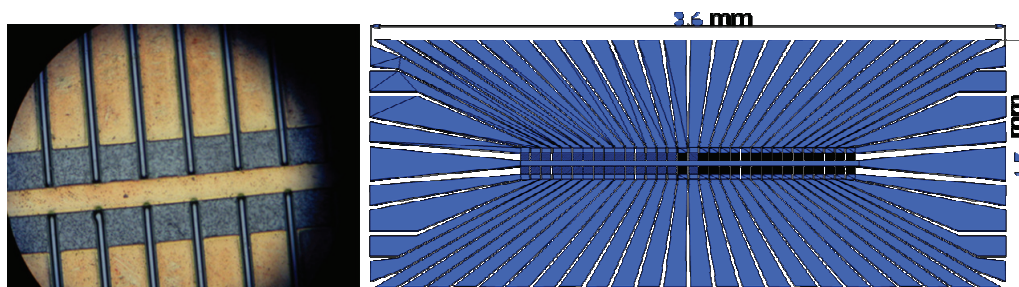


Figure 8.22: A small detail of the IR photoconductive array detector (on left). Layout of the array showing its real dimension (on right).

The size of each single pixel is about 50x50 micron and their response time is about 500 ps. A first experimental characterization of few pixels of the array has been performed on the SINBAD beamline. A complete characterization of the array can be carried out after the completion of the electronics that is foreseen in few weeks.

Faster and more efficient array detectors constituted by photodiode elements optimized to work at mid-IR wavelengths can be manufactured and customized by VIGO SA depending by the applications. With such device a bunch by bunch imaging of the IR source in order to measure the beam emittance of the bunch at the exit of the magnet compressor will be possible.

8.5 References

- [1] S. Ulc, W.S. Graves and E.D. Johnson, *BIW, Stanford, CA*, 4-7 May 1998
- [2] T. dLudziejewski et al., *Nucl. Instr. Meth. A* **398**, 287 (1997)
- [3] M. Castellano and V.A. Verzilov, *Phys. Rev. ST Accel. Beams* **1**, 062801 (1998)
- [4] M. Castellano et al, *Nucl. Instr. Meth. Phys. Res. A* **435**, 297 (1999)
- [5] G. Kube, TESLA-FEL 2008-01
- [6] M. Castellano et al, *Phys. Rev E* **63**, 056501 (2001)
- [7] E. Chiadroni, TESLA FEL 2006-9
- [8] R. Lai and A.J. Sievers, *Nucl. Instr. Meth. A* **397**, 221 (1997)
- [9] R. Treusch et al, *Nucl. Instrum. and Meth. A* **445**, 456 (2000)
- [10] K. Tiedtke et al., *AIP Conf. Proc.* **705** 588 (2004)
- [11] L. Poletto et al, *Rev. Sci. Instr.* **72**, 2868 (2001)
- [12] S. P. Hau-Riege et al, *Appl. Phys. Lett.* **90**, 173728 (2007)
- [13] R. Reininger et al, *AIP Conf. Proc.* **705**, 572 (2004)
- [14] L. Poletto et al, *SPIE Proc.* **5534**, 37 (2004)
- [15] P. Nicolosi et al, *J. Elect. Spect. Rel. Phen.* **145**, 1055 (2005)
- [16] A. Boscolo et al, *SPIE Proc.* **2805**, 260 (1996)
- [17] A. Boscolo et al, *Pure Appl. Opt.* **6**, L1 (1997)
- [18] K. Tiedtke et al, in *HASYLAB Annual Report 2006*, DESY (2006)
- [19] M. Richter et al, *Appl. Phys. Lett.* **83**, 2970 (2003)
- [20] A. Bytchkov et al, *Nucl. Instrum. and Meth. A* **528**, 254 (2004)
- [21] R. Treusch et al, *Nucl. Instrum. and Meth. A* **445**, 456 (2000)
- [22] K. Tiedtke, in *HASYLAB Annual Report 2003*, DESY (2003)
- [23] R. Treusch, in *HASYLAB Annual Report 2005*, DESY (2005)
- [24] H. Schulte-Schrepping et al, in *HASYLAB annual report 2003*, DESY (2003)
- [25] M. Kuhlmann et al, in *HASYLAB annual report 2006*, DESY (2006)
- [26] L. Le Déroff et al, *Opt. Lett.* **23**, 1544 (1998)
- [27] H. Mashiko et al, *Opt. Lett.* **29**, 1927 (2004)
- [28] H. Mashiko et al, *Appl. Opt.* **45**, 573 (2006)
- [29] A.A. Sorokin et al., *Appl. Phys. Lett.* **89**, 221114 (2006)
- [30] <http://www.lightsources.org/images/brochures/FLASHbrochure.pdf>
- [31] E. S. Toma et al., *Phys. Rev. A* **62**, 061801 (2000)
- [32] C. Gahl et al., *Nat. Phot.* **2**, 165 (2008)
- [33] T. Maltezopoulos et al., *New Journ. Phys.* **10**, 033026 (2008)
- [34] S. Cunovic et al. *Appl. Phys. Lett.* **90**, 121112 (2007)
- [35] L. Poletto et al. *Opt. Lett.* **32**, 2897 (2007)
- [36] P. Radcliffe et al. *Appl. Phys. Lett.* **90**, 131108 (2007)
- [37] Y. Nabekawa et al. *Phys. Rev. Lett.* **97**, 153904 (2006)
- [38] T. Shimizu et al. *Phys. Rev. A* **75**, 033817 (2007)
- [39] T. Sekikawa et al. *Nature* **432**, 605 (2004)
- [40] A. Kosuge et al. *Phys. Rev. Lett.* **97**, 263901 (2007)
- [41] V.L. Ginzburg and V.N. Tsytovich, *Transition Radiation and Transition Scattering*, Adam Hilger, Bristol (1990)
- [42] M.L. Ter-Mikaelian, *High-Energy Electromagnetic Processes in Condensed Media*, Wiley, New York (1972)
- [43] G.L. Orlandi, *Opt. Comm.* **267**, 322 (2006)
- [44] G.L. Orlandi, *Opt. Comm.* **211**, 109 (2002)
- [45] G.L. Orlandi, *FEL2005 Conf. Proc.*, 576 (2005)

- [46] G.L. Orlandi, ENEA Tech. Rep., C.R. Frascati, RT/2007/39/FIM (2007)
- [47] R. Loudon, *Quantum theory of light*, Oxford Univ. press, 1973
- [48] C.B. Schroeder et al, Phys. Rev. Lett. **82**, 1177 (1999)
- [49] V. Sajaev, in *Proc. of EPAC* (2000)
- [50] G.V. Stupakov and M.S. Zolotarev, *Proc. of PAC* (1997)
- [51] G.V. Stupakov and M.S. Zolotarev, *SLAC-PUB-7132* (1996)
- [52] J. Piotrowski, A. Rogalski, *Infrared Phys. Tech.* **46**, 115 (2004)
- [53] A. Piotrowski et al., *SPIE Proc.* **6542**, 65421B (2007)
- [54] http://www.vigo.com.pl/index.php/en/main_menu/aktualnosci/high_speed_ir_detectors
- [55] A. Bocci et al., *Nucl. Instr. Meth. Phys. Res. A.* **580**, 190 (2007)
- [56] A. Bocci et al., DIPAC'07, Venice, Italy, May 2007, <http://felino.elettra.trieste.it/papers/WEPB29.pdf>
- [57] A. Bocci et al., EPAC'08, TUPC008, Genoa, Italy, July 2008

9 EXPERIMENTAL ACTIVITY

9.1 Introduction and premise

The X-rays are used at present in a wide range of fields, from the fundamental and applied research, to the radiological diagnostic and to the analysis of industrial products. The SPARX source will take most current applications at new excellence levels and towards new directions. The disciplines involved will be numerous and of very different kinds. Novel methodologies based on X-rays imaging and on time-resolved studies in material science, in biology and in medicine will be developed. Many applications of non-linear optics will be extended to new spectral ranges and novel applications in the x-rays microscopy field will be explored, as well as new methodologies in the field of protein crystallography and of genomics.

The SPARX source will furthermore allow sending a huge power concentration on small areas of condensed and biological systems. This will make it possible the discovery of phenomena that cannot be forecast through a simple extrapolation of what already known. In particular, a series of results in the context of the photochemistry, which may have interesting industrial repercussions, can be expected.

The SPARX source will produce X-rays with absolutely unprecedented characteristics, among which three are particularly important: the space coherence of the radiation; its peak brilliance, about 10^{32} (in conventional units, c. u., that is photons/s/mrad²/mm², 0.1% band width); the duration of each pulse, about 100 femtoseconds. In the final project, possible experimental techniques to obtain even shorter pulses, i.e. few femtoseconds long, will be studied.

The use of higher harmonics (third and fifth) will allow a wide tunability of the energy between 10 nm and 2 nm (which includes the water window, 2-5 nm, of extreme interest in the biological field) and between 1.5 nm and 0.3 nm, respectively.

It is worth noting that the radiation produced by SPARX at the wavelength of 0.3 nm will have a peak brilliance of about 10^{27} c.u. (namely, still about five orders of magnitude higher than in the third generation sources). This will allow to apply the diffractive techniques with coherent radiation to both inorganic and biological materials and will give the possibility to make crystallography of macromolecules with a single pulse.

Another exceptional SPARX performance will be to deliver polychromatic spontaneous radiation down to 1 Ångstrom of wavelength, having a brilliance several orders of magnitude higher than that of the third generation sources. Taking into consideration that the spontaneous emission shares the same pulsed structure of the coherent component of the beam, a unique opportunity of investigating the dynamics of systems on the fs timescale will become available.

Clearly, it is impossible at the moment, even briefly, to evaluate all the possible applications of this new source. Three decades of research experience in the synchrotron radiation field teach that the actual applications of a new X-rays source are much wider than one can foresee. The extraordinary characteristics of this machine, such as the peak brilliance (up to 10^{33} c.u.), the collimation, the spatial coherence, the time-structure (duration of the pulses of the order of 100 fs) can be exploited in a series of application fields, which we

report in the following, along with a collection of the most significant experiments proposed.

9.2 Structural studies by using X-FEL radiation

9.2.1 Biological systems

Nowadays the complete genome structure of some organisms, from bacteria to man, are available and it is expected that the genetic material of other species will be sequenced in the next few years. The genome of a single organism code for a very large numbers of polypeptide chains, from about 1000, in simple bacteria, to a number that ranges from 30000 to 70000 in man. On the contrary, the three-dimensional structure of only a very limited subset of the proteins coded by the genome is available. It is important to stress that the function of a protein is strictly related to its three-dimensional structure, and not simply to its amino acid sequence: there are proteins that bear a very limited sequence homology but that present the same folding and possibly a similar function. This is the reason why the new frontier of research in molecular biology is proteomics, and in particular structural proteomics, i.e. the functional and structural characterization of all the products of the genome.

The determination of the three-dimensional structure of a protein using X-ray diffraction is still a quite long job, despite the enormous technological progresses of the last years. The rate-determining step of the process is the crystallization of the macromolecule, that is still more close to art than to a science. Moreover membrane proteins, that are estimated to represent about one third of a genome, in general resist crystallization and only for few of them the crystal structure is known. Another point which has to be considered is that proteins inside the cell do not act as single molecules in solution, but they are often organized in macromolecular complexes: this supra-molecular organization allows the kind of concerted actions that are necessary for the complex phenomena of living organisms. It is not necessary to add that macromolecular complexes are more difficult to crystallize than single proteins. On the other side NMR, the other technique that allows the determination of the 3D structure, does not need crystals but it is strongly limited by the size of the sample, i.e. only proteins smaller than about 30000 Da can be studied.

The traditional X-ray crystallography had as its aim the collection of diffraction data in correspondence of the reciprocal lattice points (that is the measurement of the *integer index reflections*), since the diffraction pattern of an ideal crystal having a size one thousands times greater than the unit cell period has a vanishingly small intensity amidst the Bragg peaks. On the other hand, a diffraction experiment on a single unit cell produces a continuous spectrum, usually referred to as *diffusion spectrum*. The nanocrystals show intermediate characteristics: Bragg peaks concentrated on the points of the reciprocal lattice and non-Bragg peaks, whose number depends on the crystal size, placed amidst them. The latter peaks can be defined as *fractional indexes reflections*. Analogously, the continuous spectrum produced in a diffraction measurement on an isolated molecule can be densely sampled and interpreted, also in this case, in terms of fractional indexes. The X-ray crystallography usually neglects the fractional indexes reflections because of the experimental difficulties connected to the diffraction from nanocrystals and/or single molecules.

In all the three cases, i.e. macrocrystals, nanocrystals and isolated molecules, the diffraction experiments do not provide any information on the phase of the diffracted radiation, since the measurements concerns its intensity only. This is the so-called phase problem, whose solution was obtained for small molecules only. The solution in the case of macromolecular crystals would produce enormous benefits in biology, structural chemistry and materials science.

The static properties of the fractional indexes reflections were studied by Giacobazzo, Siliqi et al. [1-8]. More recently the problem was discussed in terms of oversampling of the diffraction spectrum [9-12]. Practically the diffraction spectrum is oversampled with a spacing lower than the Nyquist distance creating, in this way, a “*non density*” region that surrounds the electron density region of the sample. It was shown that such a non density zone can be used to recover the information on the phase. Moreover, the present X-ray diffraction techniques do not allow in many cases, an experimental counterpart to the theoretical results discussed above. Indeed, the intensities of the fractional indexes reflections are much weaker than the Bragg peaks intensities and their measurement would require high doses of X-rays, which would imply severe damages to samples. This problem might be overcome by utilizing the ultra-short pulses of the SPARX source. Theoretical simulations showed that a macromolecule could suffer an X-ray flux of about 4×10^6 photons/Å² if the pulse duration is comparable to that of the X-FEL [13].

Each measurement carried out on a single molecule produces a 2D projection of its electron density. To reconstruct a 3D image several 2D projections must be combined, each one collected with a random orientation. Therefore, the use of an ultra-short and intense X-FEL pulse coupled with the X-ray pattern oversampling, should allow a direct determination of the 3D structure of a single molecule or of a macromolecular complex.

Since crystallographic studies on biological macromolecules require an atomic resolution, the fifth harmonic of the X-FEL (4 keV corresponding to a theoretical resolution of about 2 Å) enables, in principle, the determination of a 3D structure on atomic scale. Moreover, the continuous component of the X-FEL beam produced by spontaneous emission is about 3-4 orders of magnitude higher than that of a third generation synchrotron and might be used to perform these studies as well.

9.2.2 References

- [1] Venter J. C. et al., The Sequence of the Human Genome, *Science*, 1304-1351 (2001)
- [2] C. Giacobazzo & D. Siliqi *Acta Cryst. A* **54**, 957 (1998)
- [3] C. Giacobazzo, D. Siliqi, B. Carrozzini, A. Gagliardi & A.A. Moliterni *Acta Cryst. A* **55**, 314 (1999)
- [4] C. Giacobazzo, D. Siliqi, A. Altomare, G.L. Cascarano, R.Rizzi & R. Spagna *Acta Cryst. A* **55**, 322 (1999)
- [5] C. Giacobazzo, D. Siliqi & C. Fernandez-Castano *Acta Cryst. A* **55**, 512 (1999)
- [6] C. Giacobazzo, D. Siliqi, C. Fernandez-Castano & G. Comunale *Acta Cryst. A* **55**, 525 (1999)
- [7] C. Giacobazzo, D. Siliqi, C. Fernandez-Castano, G.L. Cascarano & B. Carrozzini *Acta Cryst. A* **55**, 984 (1999)
- [8] C. Giacobazzo, D. Siliqi, C. Fernandez-Castano & G. Comunale *Crystallographic Association* pp. 65-72 (2001)
- [9] Miao and Sayre *Acta Cryst. A* **56**, 596 (2000)
- [10] Miao, Sayre & Chapman *J. Opt. Soc. Am. A* **15**, 1662 (1998)

- [11] Sayre, Chapman & Miao *Acta Cryst.* **A54**, 232 (1998)
- [12] Miao, Charalambous, Kirz & Sayre *Nature (London)*, **400**, 342
- [13] Neutze, R., Wouts, R., Spoel, D., Weckert, E. and Hajdu, J., *Nature (London)* **406**, 752 (2000)
- [14] Hajdou et al. *AIP Conf. Proc.* **477**, 377 (1999)
- [15] Doniach, S. *J. Synchrotron Radiation* 116-120 (2000)
- [16] J. W. Miao, K. O. Hodgson, D. Sayre, *PNAS*, **98**, 6641-6645 (2001).

9.3 Time resolved X-ray diffraction: Pump&probe experiments

Reference proponent : V. Rossi Albertini, ISM-CNR, Roma

The undulator spontaneous emission SE accompanying the production of coherent radiation CE is usually regarded as a undesired byproduct of the latter and has to be removed by suitable optical systems (mirrors, filters, etc.). However, SE possesses some unique characteristics that can be utilised to perform experiments alternative to those based on the CE. Indeed, SE, while sharing the same temporal structure with the CE, spans over an energy range that can reach values two to three order of magnitude higher than SE. This means that, when a FEL is set to produce CE in the UltraViolet region, as in the first phase of SPARX (SPARX-VUV), the SE component may already reach wavelengths of diffractometric interest, thus providing a powerful and unexpected tool to carry out structural investigations on the 100fs timescale, from the very beginning of SPARX operations. In the frame of time-resolved experiments, diffraction plays a key role since it provides a direct insight in the atomic rearrangements mechanisms, with no need of theoretical models or adhoc methods to interpret data (see, for instance, the high time resolution studies by A. Zewail, accomplished by optical lasers transmission measurements). In addition, the integrated intensity of SE is comparable to the intensity of photons concentrated in the CE, so that single shot collections would be possible if a convenient setup was used. The details of this method, as well as the setup suggested to put into practice the theoretical discussion, constitute the subject of a contribution to the Scientific Case to which we refer the reader.

9.3.1 Coherent diffraction: X-ray holography

One of the main problems of diffractometry is that the diffraction pattern of a sample cannot be univocally associated to its structure. Actually, Fraunhofer theory of diffraction set a relationship (Fourier Transform) between the characteristics of scattered radiation and the geometric arrangement of the parts of the scattering system. In order to perform an exact Fourier transformation, both the magnitude and the phase of the electromagnetic field scattered by the sample has to be known in each point of the reciprocal space. Instead, ordinary diffraction patterns represent the scattered intensity only, so that the information on the field phase is lost. For this reason, just in a few cases it is possible to attain a structure from a diffraction pattern alone (see § 2.2.1). Generally other independent pieces of information are needed, such as the system symmetry, bond lengths or neighbors distances, configurational constraints. To overcome this limitation a technique capable to provide information on both the amplitude and the phase of the diffracted

beam should be used. In analogy with the visible light holography, an X-ray holographic method has been successfully used to investigate the structure of simple crystals, like cobalt oxide (see Figure 9.1 and Figure 9.2) [1].

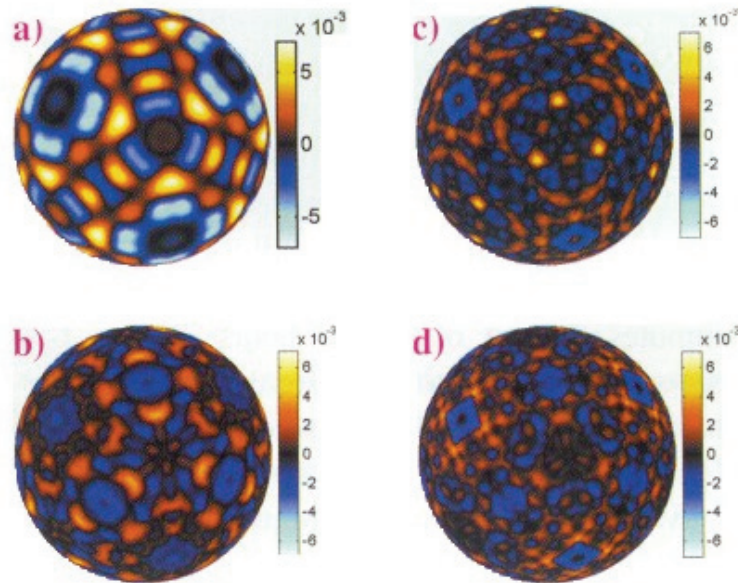


Figure 9.1: Holograms collected at various energies: 6.925, 13.861, 17.444, 18.915 keV. Four holograms were acquired in order to minimize the systematic errors [1].

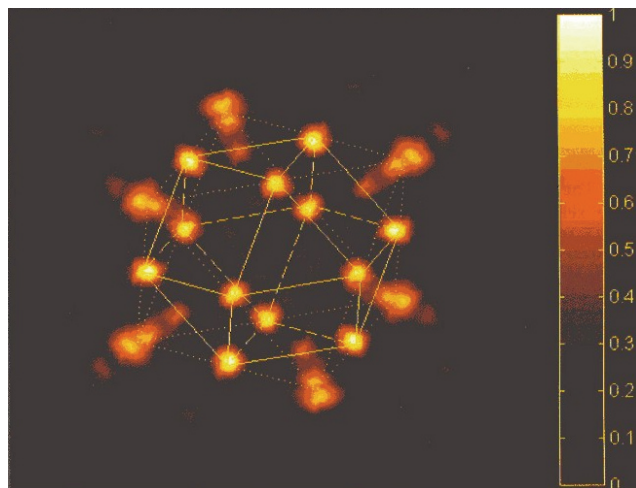


Figure 9.2: Spatial distribution of Co atoms calculated from the previous holograms [1].

To perform an X-ray holography measurement coherent X-ray beam is split and one of the two components is used to directly irradiate a detector, while the second is sent on the sample. The interference on the detector surface between the wave scattered by the sample and the reference produces an holographic pattern, allowing the reconstruction of the wave-front that contains the full information on the three-dimensional arrangement of the

sample atoms. At present, the drawback of this revolutionary technique consists of the difficulty of selecting a portion of the beam inside which the coherent component is not negligible. Indeed, the spatial (transverse) coherence of an X-ray beam emitted by an undulator at a third generation synchrotron is rather low and, to perform experiments of this kind, pinholes diaphragm as small as 10 μm must be used. This reduces the beam intensity very much, enormously dilating the experiment duration, so that a single acquisition currently lasts many hours [2].

Thanks to the full transversal coherence of its higher harmonics, the use of X-FEL for this purpose is the natural solution to this restriction for systems having long bond (or interplanar) distances. Needless to say, to couple the X-ray holography with the pump&probe diffractometric techniques mentioned above would open the way to unprecedented structural studies of the matter.

9.3.2 References

- [1] M. Tegze and G. Faigel, *Nature*, **380**, 49, (1996)
- [2] M. Belakhovsky et al., *ESRF Newsletter*, October 2000, p. 12

9.4 Coherent diffraction imaging, holography and nano-probes beamlines

Reference proponent: S. Lagomarsino, IFN-CNR, Roma

Spatial coherence is exploited by both x-ray holography and Coherent X-ray Diffraction Imaging (CXDI)

9.4.1 CXDI

Coherent x-ray diffraction imaging is one of the most promising techniques to study the structure and behaviour of non-periodic single objects or non-periodic assembly of objects at the nanoscale, being able, in principle, to achieve wavelength-limited spatial resolution overcoming the limitations imposed by the optical elements aberrations. This is the reason why CXDI is one of the most appealing methodologies for FEL installations, and the object of a recent striking experiment at FLASH in Hamburg [1].

CXDI was first introduced by Sayre [2], and demonstrated for the first time by Miao et al. [3]. It is based on phase retrieval of the diffraction pattern through iterative algorithms, under suitable oversampling geometry. Real space and reciprocal space constraints are applied to achieve convergence and retrieve the phase changes induced by the object, and hence the object density spatial distribution. Chapman et al. [1] have demonstrated at FLASH that even with femtosecond pulses it is possible to record a diffraction pattern before the sample is destroyed by Coulomb explosion.

In CXDI a fundamental pre-requisite is the spatial coherence of the incident beam. Initially a lens-less geometry, with planar incident waves was adopted [3]. However, this set-up suffers of the need of pinholes and beam stoppers. The first are used to reduce the spatial extent of the beam, but can distort the wavefront, the second ones are needed to stop the powerful incident beam, but limit the extent of the diffraction pattern in k -space.

Just recently, nonplanar waves have been used with success, proposing to extend CXDI in near-field Fresnel regime by the introduction of a “distorted object” for the calculation of the coherent diffraction pattern, to take into account the effects of Fresnel fringes [4,5]. A Fresnel-zone construction is embedded on an original object and then Fourier transformed to form a diffraction image. Simulated numerical examples have indicated that, also for near-field coherent diffraction, suitable Fourier-based iterative phasing algorithms can be realized [4,5]. CXDI experiments with non-planar wavefields have been recently performed in near-field Fresnel regime using either X-ray zone plates [6] and planar X-ray waveguides [7,8] as optical elements. The advantages of using nonplanar waves reside on a faster convergence of the iterative algorithm and on the possibility to avoid the beam stopper, hence recording holographic information on the object, which can be used as input for the direct space constraint. Another striking advantage has been pointed out very recently: the limited extent of curved wave fronts, as produced by suitable x-ray optical elements, such as the zone plates or the waveguides, allows to overcome the need of isolated objects illuminated by a larger beam in order to satisfy the oversampling requirement: the so-called keyhole coherent diffraction imaging (KCDI) in fact demonstrated that also extended objects can be retrieved by iterating measurements on adjacent portions of the extended object [9]. The KCDI has some analogies, but also important differences, with ptychographical algorithm [10] where a planar wave, limited by a pinhole, is used to illuminate different parts of an extended object, with large overlap between adjacent regions. In the case of ptychography the quality of the reconstruction depend on the extension of overlapping regions, and on the knowledge of the beam position on the sample at each location, whilst in the keyhole method each single diffraction pattern contains the useful information about the illuminated region.

Important fields of applications of CXDI are material science and biomedical. In the first case, nanomaterials, as isolated quantum dots or single magnetic particles, can be studied by CXDI exploiting the high brilliance of FEL. Dynamic studies can be carried out using its unique time structure. Even more exciting are the perspectives on studies of single biomolecules, viruses or protein complexes that cannot be crystallized. One problem can be that a single view gives only a projection in two dimensions of the three dimensional structure, and that the sample is damaged (or even destroyed) by the very intense x-ray beam. This problem can be overcome by exposing to the beam different copies of reproducible samples one by one in random orientations. A careful theoretical analysis of the needed statistics has been carried out [11].

In CXDI, the theoretical limit to resolution is just the wavelength, therefore atomic resolution can in principle be achieved with suitable photon energy. However, other effects must be taken into due consideration to evaluate the achievable spatial resolution. The first is a technical one related to the experimental set-up and in particular to the detector, because the ultimate spatial resolution is related to the detector numerical aperture and to the

visibility of the most external fringes. The second is a physical one, related to the radiation damage. Thorough theoretical studies have been carried out on the relation of the flux necessary to have information at a given spatial resolution, (the requiring imaging dose which scales up with the fourth power of the desired resolution) and on the threshold dose for damage (the maximum tolerable dose) [12]. From both, theory and experiments, it appears that 10 nm is the resolution limit before radiation damage destroys the sample. To overcome this limit, very short pulses must be used. The famous paper from Neutze et al. [13] used Molecular Dynamics simulation of the interaction between a very intense and short pulse and a biomolecule, to indicate that a pulse as short as few fs, if sufficiently intense, can deliver information on the protein structure before Coulomb explosion takes place. After that pioneering work, theoretical studies continued actively. The pulse requirements to achieve atomic resolution have been pointed out by Hau-Riege et al. [14], who indicated the best photon energy between 8 and 13 keV, and pulse duration of few fs if Angstrom resolution is desired. However, methods to improve situation are envisaged, as for ex. encapsulation of biomolecules in sacrificial layers to limit radiation damage [15].

9.4.2 Holography

In Fourier holography, the phase retrieval is carried out by an inverse Fourier transform, not by an iterative process as in CXDI. It is therefore a much faster process that however necessitates of a reference beam. In in-line holography the object reconstruction can be severely hindered by the twin image problem. Recently it has been demonstrated by two independent works [8,16] that the use of x-ray waveguides can overcome the problem of twin image, using an off-axis geometry.

Full field microscopy, scanning microscopy and nano-probe

In third-generation synchrotron radiation sources, many micro and nano-probes beam lines exist, working both in soft and in hard photon energies, dedicated to different methodologies, as imaging, micro-spectroscopy, microfluorescence, microdiffraction. To this purpose, extreme focusing optical elements are used. These can be classified as reflective (mirrors, waveguides), refractive (Compound Refractive Lenses) diffractive (Fresnel Zone Plates, Bragg-Fresnel and reflective Zone Plates). There are described in the "Extreme focusing elements" paragraph. The choice of one (or more) optical element with respect to others depends on the specific experiment, and different alternatives should be foreseen. For example, mirrors have high efficiency in providing small beams, but a certain wave-front distortion is unavoidable; Fresnel Zone Plates are preferred in imaging, but the high thermal load can seriously damage them, at least in transmission geometry; waveguides, at least in front coupling geometry, does not provide an effective gain, but coupled with other pre-focusing optics can assure a very important overall gain, with the advantage to provide a full coherent beam with curved wavefront, which can be very useful in holography and CXDI experiments.

The combination of different techniques, together with the unique properties of FEL, can give significant contribution in many scientific fields. As example, an interesting topic is the realization of bio-mimetic materials, whose properties must be thoroughly studied in comparison of real biological

materials. In this context, the problem of minerals formation by organism is still unknown regarding the influence of the organic macromolecule on the nano-scale hierarchical architecture of natural bio-composite. The main problem to investigate is the mutual arrangement of mineral phase and organic macromolecules (aragonite in mollusk shells, calcite in eggshells hydroxyapatite in enamel, vaterite in *Herdmania momus* ascidians).

Up to now, several differences are put in evidence between the behaviour of these biogenic materials and the geological crystals, or the usual ceramics, of the same chemical content. The tensile forces imposed by organic macromolecules on the mineral crystals or the decreases of the biogenic crystals blocks under heat treatment, are some examples of the unexpected observed differences.

In this regard, SPARX could give a significant impact to this research field:

The high- brilliance will allow the use of advanced X-ray optics to obtain nano-metric spatial resolution;

The spatial coherence will allow to combine phase contrast imaging and Small Angle X-ray Scattering (SAXS) measurement for a simultaneous analysis of the mineral and the organic contributions in the same micro-region on the sample.

The temporal structure will allow pump-probe measurement for the investigation of the sample response under local heating.

Concerning material science, studies on nanostructured materials and on magnetic nanostructures are interesting both from a fundamental and applicative points of view. In this respect, the range 500 eV-1 KeV is particularly suited, presenting L absorption edges of 3-d transition metals.

9.4.3 Optical components for coherent imaging

In some cases, it is necessary to use extreme focusing optics to concentrate the beam onto nanometer size spots. Several kind of optics are currently used at third generation synchrotron radiation sources for nanometer focusing. They can be classified as i) reflective (mirrors, multilayers, waveguides); ii) refractive (Compound Refractive Lenses); iii) diffractive (Fresnel Zone Plates, Bragg Fresnel or reflective Zone Plates).

- i) Reflective. Figured mirrors in Kirkpatrick-Baez geometry can now reach few tens of nanometer spot sizes, both as figured reflecting surface and figured multilayers [17,18]. The limit is still in the figure errors of the mirror surface. The advantage of mirrors is that they are achromatic (at least in a large energy range), and that at grazing angle they can stand high power loads. Moreover, they preserve the temporal structure. However, some wavefront distortion is unavoidable, which can create problems to CXDI experiments.

Waveguides are based on total reflection, but their behaviour is dominated by propagation of resonance (guided) modes, spatially confined by cladding layers [19]. Nanometer sized beams have been produced by waveguides, down to 10 nm, a record for hard x-rays [20]. Waveguides have several interesting properties for their

perspective use with FEL: i) they preserve coherence, or even they can “clean” a beam whose coherence has been degraded by other optical elements, providing a beam with a well defined coherent curved wave-front; ii) they preserve the temporal structure of the incoming pulse [21]; iii) they can be fabricated with vacuum gap, thus allowing high transmission also for soft x-rays; iv) working in total reflection, with vacuum gap, the thermal load can be reduced to bearable levels; v) with proper operation, two coherent beams can be produced, allowing all-x-rays pump&probe experiments, without the need of external trigger [21]. Waveguides have been used for microdiffraction with nanometer spatial resolution [22], for holography [23,24] and for Coherent Diffraction Imaging in Fresnel geometry using the curved wave front [24,25].

- ii) Refractive lenses are proposed for the hard region of the spectrum. For energies below few KeV the photoelectron absorption is too high.
- iii) Diffractive lenses as Fresnel Zone Plates (FZP) are largely used especially for imaging at very high resolution (15-20 nm) in the soft x-ray region [26]. Two problems potentially can limit their use with FEL: the intrinsic mechanism of image formation in FZP implies different optical paths, and hence pulse duration broadening; if this can be deleterious or not for a given experiment depending on the geometrical and physical conditions. The second problem regards the thermal load, because standard FZP work in transmission and therefore must stand the entire incoming power. Alternatives to overcome this problem have been studied, as Bragg-Fresnel and reflective FZPs [27].

9.4.4 Beam-lines description for coherence experiments

Two beam lines dedicated to coherent scattering and micro and nanoprobe are envisaged: one working mainly in the 300 eV-1 KeV energy, thus comprising the water window, to work with the U2 undulator, and one working with the U3 undulator in the 1-2 KeV region (with possible extension to higher energies if available).

The first one, at lower energy, will be mainly dedicated to coherent imaging. The second one, at higher energies, will also allow Coherent Diffraction Imaging and holography, but in addition will be also equipped with nanoprobe facilities, in order to allow for microfluorescence, microspectroscopy and microdiffraction (in particular Small Angle Scattering) experiments.

Both beamlines require the maximum distance from the undulator exit. Total reflection mirrors will be used to condition the beam at the entrance of the experimental hall. A plane grating monochromator, for experiments requiring monochromatisation beyond the natural band width, is foreseen. Either a moveable installation, either a division in two fixed branches is needed, in order to allow for both high flux and high energy resolution. The extreme focusing elements will be integrated with the instrument. Several possibilities must be foreseen, with easy exchange among them: k-B mirrors, waveguides and FZPs.

BEAM-LINE FOR COHERENT IMAGING IN THE WATER WINDOW (300 – 1000 eV on the U2 undulator)

The beam line is composed of a total reflection mirror (either plane or ellipsoidal for moderate focusing) to condition the beam, put at the entrance of the experimental hall. A plane grating monochromator, for experiments requiring monochromatisation beyond the natural band width, is foreseen. The monochromator will be moveable, to allow shifting from experiments requiring high flux to those requiring high energy resolution. Slits will be used to limit the beam divergence. Particular care will be devoted to preservation of coherence. A beam monitor is needed after the slits for intensity normalization. For high spatial resolution, several kind of extreme focusing elements will be used (KB grazing incidence mirrors, waveguides, Fresnel Zone Plates (either in transmission or in reflecting modes), the choice depending on the specific experiment to be carried out. In some specific cases, a system of collimation slits after the focusing elements is also foreseen. All the optical elements will be placed on the same antivibrating support of the sample holder. Cryo installation will also be included to limit the possible radiation damage produced by sample overheating. Other optical elements (for ex. objective lenses) are foreseen after the sample for some kind of imaging. The area detector must be very fast and with high dynamic range. The scheme below summarizes the main elements. All the beamline will be in UHV conditions.

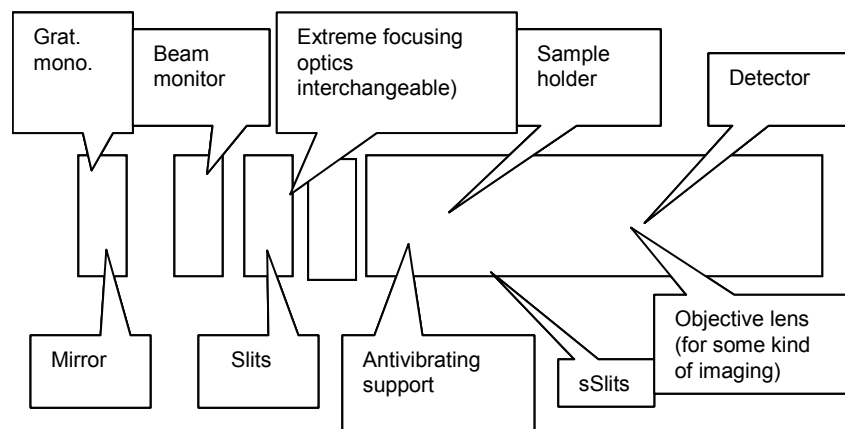


Figure 9.3: Scheme of the Beamline for coherent imaging in the water window.

BEAM-LINE FOR COHERENT DIFFRACTION, HOLOGRAPHY AND NANOPROBES IN THE 1-2 keV range (U3 undulator)

The beam line is composed of a total reflection mirror (either plane or ellipsoidal for moderate focusing) to condition the beam, placed at the entrance of the experimental hall. A crystal monochromator, for experiments requiring monochromatisation beyond the natural band width, is foreseen. The monochromator will be moveable, to allow shifting from experiments requiring high flux, to those requiring high energy resolution. Slits will be used to limit the angular divergence of the beam. Also in this energy range, particular care

will be devoted to preservation of coherence. To avoid radiation scattered by slits, several pair of slits with different apertures will be used. A beam monitor is needed after the slits for intensity normalization. For high spatial resolution several kind of extreme focusing elements will be used (KB grazing incidence mirrors, waveguides, Fresnel Zone Plates (either in transmission or in reflecting modes), the choice depending on the specific experiment to be carried out. Also lens-less coherent diffraction experiments will be allowed.

The same care as before will be used to limit heating damage and misplacements of optical elements.

Detectors are a crucial element of this instrument, in particular for Coherent Diffraction imaging. An area detector with a hole in the centre to allow transmission of the intense incident beam and a very high dynamic range is foreseen, but other detectors, both area detectors and energy-sensitive detectors for fluorescence measurements, are considered. The scheme below summarizes the main elements. All the beamline will be in UHV conditions.

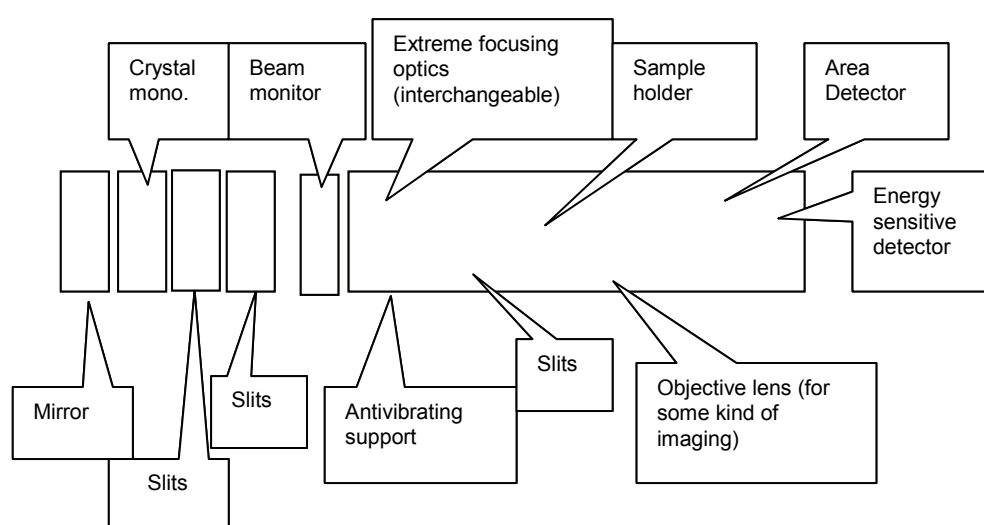


Figure 9.4: Instrumentation lay-out for the Coherent Diffraction, Holography and NanoProbe BL

9.5 Plasma Physics

9.5.1 Laser-plasma interaction: theoretical models

The study of the plasma produced by the action of the laser beam on different targets, needs theoretical methods specifically developed for non equilibrium systems. The use of such methods is necessary because the plasma produced will be characterized by a complex interaction between plasma-dynamics, transport processes and fast kinetics phenomena. In particular we expect a plasma in which the translational distribution of charged particles will deviate from the Maxwell law, and the population distribution of internal states of ions will not be characterized by the Boltzmann law. Accordingly, one can consider only kinetic models able to treat far-from-equilibrium cases, and possibly to abandon the approach based on population kinetics and consider quantum methods, and to consider coherence effects complicated by the

plasma-dynamic environment. Such phenomena, must be treated by a 'self-consistent' approach because of their reciprocal connection, and can not be solved separately. The goal will be the realization of a model for the beam-plasma interaction made up by the following interacting modules:

Electron and ion transport through the Boltzmann and Vlasov/Boltzmann equations

The module will consist of two sub-units which will be selected for homogeneous and non homogeneous plasma models, respectively. In the second case the detail of the results will be much higher, but also the computational cost. In the first case one unit will solve the quasi-isotropic Boltzmann equation (i.e. based on first-order expansion of angular part the electron/ion velocity distribution in spherical harmonics). In the second case one unit will solve the coupled Vlasov/Boltzmann problem for two or more species by the Particle in Cell/Monte Carlo (PIC/MC) method. In both cases we will consider the effect of charged particle collisions with excited species by coupling this module with the module described below. The Bari group was one of the pioneers in using this self-consistent approach for the Boltzmann equation [28,29] and one of the very few today to apply the same to the Vlasov/Boltzmann problem [30]. For very short times in which one cannot still neglect quantum effects for the conduction electrons in the solid metal target, we will consider an appropriately modified Boltzmann equation code recently developed by our group [31].

Collisional radiative model

This part of the project will study the relaxation of internal levels of atoms, ions and molecules coupled to the radiation field. In this system one finds two kinds of phenomena with different effects: e-A (electron/atom) collisions push the system towards local equilibrium, while the radiative decay, because of the spectrum of decay rates, produces non equilibrium conditions. The rate coefficients for e-A processes are functional of the electron energy distribution function whose relaxation, in turn, depends upon the population of internal levels. The strong non linearity of the problem asks for a self-consistent solution in the way cited above. The relevant equations can be corrected to include photon absorption [32]. In the case of very intense radiation we will also consider multi-photon and X-ray absorption, leading to excitation and ionization of internal level.

Density matrix and wavepacket dynamics for fast processes

For laser-target interaction times in the order of picoseconds it is no more possible to describe the absorption of laser radiation by the classical rate equations of population kinetics, since it is necessary to account for quantum coherence between internal states in the radiation field, working at the description level of the density matrix. At the same time, one has to consider the translational non equilibrium of plasma components described above, which affects the rate of de-coherence, and cannot be treated by traditional methods. Recently, a stochastic technique based on a new representation of the mixed classical (translational)/quantum(internal) state of the gas phase particles

[33,34,35] undergoing coherent kinetics during the gas-kinetic relaxation was developed. Such technique, suitably modified, will be applied to the case study of the project.

Plume expansion

A characteristic of the interaction of pulsed laser beams with solid targets is the production of plasma localized in a very small region of space, which expands at supersonic velocity (plume). Such a system can be applied to diagnostics (as a source of X lasers) as well as to material processing (to deposit thin films). We will provide a theoretical study of such system by solving the time-dependent Euler equations in the one-dimensional or quasi-one-dimensional approximation (which applies since the angular dispersion of the plume is very small) [36].

Because of the high expansion speed and the pressure gradient between the plume and the buffer gas, the characteristic times of the flow field can be compared to those of the atom kinetics. In such conditions, the coupling of the fluid dynamic equations with those of the collisional radiative model, thereby following the tradition of our group, becomes necessary for a correct description of the system. We will also consider the possibility to develop two-dimensional models.

Dynamics of elementary processes in atoms and molecules

The modeling of plasm-chemical systems in far-from-equilibrium conditions requires the knowledge of the cross sections involved in all the elementary processes determining the energy level population and the concentration of the single chemical species. Such elementary processes are represented by collisions between the different species present in the system like:

- collisions between electrons and molecules electronically and vibrationally excited, followed by electronic excitation, dissociation or ionization;
- electronic excitation induced by electron impact and followed by radiative decay;
- resonant collision between electrons and vibrationally excited molecules;
- electron-atom collisions;
- atom-atom collisions;
- atom-diatomic molecule and molecule-molecule collisions.

The cross section for these processes and the relative speed constants will be obtained through semi-classical and quantum methods [37,38,39,40,41,10-14]

We will also consider the case of diatomic molecules such as H_2 , N_2 , O_2 under laser radiation by simulating the evolution of a wave packet produced by coherent superposition of vibrational wave functions in electronic excited states, by solving the time-dependent Schrodinger equation. The simulation will describe the dynamics of the wave packet in the excited state including bound states, pre-dissociation and direct dissociation as well as the wave packet produced [42,43,44] by transferring part of the excited state wave packet to the ground state by a second, ultra-fast laser pulse.

A real system will be studied, including in the modeling effects due to the inharmonicity of the excited higher vibrational levels or to the dependence of the transition momentum (coupling the states involved in the dynamics) from the internuclear distance

9.5.2 some Laser-plasma experiments at SPARX

Reference proponent: L.A. Gizzi et al., Intense Laser Irradiation Lab., IPCF-CNR, Pisa ()

The interaction of short pulses of electromagnetic radiation with matter is widely used to investigate matter in extreme conditions of mass and energy density and to probe ultrafast phenomena. Intense optical, UV and X-ray pulses of duration below 100 fs or less, generated by chirped pulse amplification (CPA) of femtosecond pulses, by free electron lasers (FEL) or by alternative sources presently under development are considered today among the most powerful tools for the investigation of matter. A particularly enlightening example is the use of FEL pulses for the characterization, via X-ray diffraction, of the molecular structure of complex biological molecules. A pre-requisite for these techniques to work is that the duration of the electromagnetic pulses is shorter than the typical time of disassembling/modification induced in the sample by the intense radiation. Another important pre-requisite is that the temporal contrast of the pulse, i.e. the ratio between the peak intensity and the background (precursor) radiation is sufficiently high to avoid premature exposure to light.

First conceptual experiment: generation of warm dense matter (WDM)

High contrast, electromagnetic pulses focused on solid matter can be used to generate states of matter characterized by high mass density and relatively high temperature, normally referred to as WDM. This state of matter is the subject of intensive investigation due to its role in basic physics, but also for the implications in important applications like inertial fusion energy (IFE) and laboratory astrophysics. The key issue here is to deposit energy in significantly large volumes of matter in a time that is small compared to its expansion time.

High contrast optical CPA pulses are routinely used nowadays to activate WDM creation in the laboratory. However, optical pulses suffer from the small (skin) depth of penetration that limits the capability of optical pulses to densities that are 3-4 orders of magnitude smaller than the solid density. Another limitation is the temporal contrast of the radiation pulse, usually affected by ns-scale amplified spontaneous emission, that can lead to formation of a premature plasma corona before the target disabling interaction with the solid.

Alternative techniques based upon the use of (laser generated) focused proton beams have been suggested to produce WDM and preliminary experiments have already been carried out.

It is clear however, that intense ultra-short laser pulses of X-ray radiation (FEL) offer a unique opportunity to activate WDM via isochoric heating. In fact, provided FEL pulses exhibit a sufficiently high temporal contrast, their much shorter wavelength compared to CPA laser light will enable direct volume deposition of energy in the sample on a depth comparable with the attenuation length of X-rays in the sample. As an example, we assume a 1 keV FEL pulse with a pulse duration of 100 fs containing up to X-ray 10^{13} photons focused on

a sample in a spot of 10^{-6} cm². Considering that the attenuation length in gold is approximately 10^{-5} cm, we find that the density of X-ray photons in the volume is equal to the density of electrons. This is a unique interaction condition that involves ionization and transport phenomena in a new, rather unexplored regime in which new effects, including over-dense propagation of light are predicted to occur. A detailed understanding of this scenario is rather complex and very early stage modeling is available (JOURNAL DE PHYSIQUE IV **133**, 1097-1099 (2006) or Phys. Rev. E **73**, 066406 (2006)). However, initial experiments performed at soft X-ray FEL facilities are giving very encouraging results in view of experiments in the X-ray range that should finally enter the WDM regime. This experiment would require the FEL X-ray pulse only, with possibly low power femtosecond pulse to perform characterisation of the WDM plasma via reflectivity and absorption measurements in the pump and probe scheme.

Second Conceptual experiment: high density plasma interferometry

This is a technique widely used in experimental physics to measure the density of neutrals and free electrons via changes of its refractive index. In laser-plasma experiments, this technique is of a key importance to determine the density of free electrons and is generally carried out using frequency converted (second, third or fourth harmonic) of the fundamental optical laser radiation. At higher electron densities or in the presence of steep transverse (to the probe beam) density gradients, optical probing becomes ineffective and EUV or X-ray radiation must be employed.

X-ray plasma interferometry is still limited to the soft X-ray range where several X-ray laser schemes (laser-plasma or capillary discharge just to cite the most popular) are routinely generating beams of radiation sufficiently bright and short pulsed to enable plasma interferometry. The availability of shorter wavelength radiation will enable interferometry of the higher-density plasmas. An example is the over-dense plasma region above the critical density and including the ablation front of laser-irradiated targets. In fact, it is well known that this region is unstable to Rayleigh-Taylor instabilities, key issue in Inertial Fusion Energy, for example, where the instability leads to a growth of perturbations of initial density non-uniformities at the shell layer separation. Short pulse X-ray probing, combined with X-ray absorption/opacity measurements will enable a quantitative investigation of this mechanism. Such experiment would require the FEL X-ray pulse combined with one additional laser pulse, ideally a multi-joule, ≈ 100 picosecond pulse.

Third Conceptual experiment: fast electron transport in shock-compressed WDM

An extremely profitable use of FEL X-ray pulses concerns the investigation of fast electron transport in warm dense matter. This is a topic of very general interest that is also attracting attention due to the applicability to the so-called Fast Ignition Scheme for inertial fusion energy. The scheme, originally proposed by Tabak (Phys. Plasmas **1**, 1626 (1994)) is meant to provide a shortcut to ignition of compressed fusion pellets using massive currents of MeV electrons to spart-initiate the fusion process.

Using the scheme of production of WDM described above (experiment 1), it is possible to conceive an experiment in which the FEL pulse is used to generate the WDM sample that is then further compressed via shock wave by additional, optical laser pulses, possibly impinging from opposite sides of the sample. The WDM target produced in these conditions is an ideal medium for

study of transport of energy by fast electrons generated by a third, ultrashort laser pulse interacting at high intensities with the target. Using known scaling laws, it should be possible to investigate transport processes relevant to IFE conditions that are difficult to achieve otherwise. This experiment would require the FEL X-ray pulse combined with two additional laser pulses of medium power and energy. The shock-compressed pulse is ideally a multi-joule, picosecond pulse, while the fast electron generating pulse is multi TW, 100 fs laser pulse. Diagnostics include X-ray fluorescence imaging and spectroscopy, fast electron calorimetry and X-ray probing/interferometry from Experiment 2.

The Laser-Plasma Facility@ SPARX will host experiments based upon the combined use of the SPARX FEL radiation and ultraintense, ultrashort laser pulses from additional laser systems. Both laser pulses will be focused and synchronised on samples (solids, gases) using a *pump-and-probe* like configuration.

As discussed in the conceptual experiments, the X-ray pulse will be used either as a pump, for example to generate WDM (see conceptual exp.1), or as a probe, to diagnose plasmas (conceptual exp.2). Similarly, ultraintense laser pulses will serve as pump pulses, for example to generate large currents of fast electrons, or hot plasmas, and the FEL X-ray pulse will be used to probe the sample (exp.3).

A general layout of the facility will include a laser area and an experimental "target" area. The laser area will be equipped with a clean room (better than Cl. 10000) divided into a femtosecond CPA section and a ps, high energy section. One of the two areas, preferably the femtosecond CPA, will also serve as a laser beam handling and diagnostic laboratory, where synchronisation, laser beam control and optimisation will be carried out. The laser area will also host the high resolution delay line that will enable continuous scan of the relative timing between the main FEL X-ray pulse and the optical CPA/ps laser pulses.

The experimental target area will consist of a radiation shielded room capable of hosting a vacuum experimental chamber vacuum-connected with the high power vacuum compressor of the femtosecond CPA laser system. Radiation shielding should be effective against a primary radiation source consisting mainly of electrons with energy up to 100 MeV and charge up to 100 pC. The vacuum chamber will be equipped with dry pumps and turbomolecular pumps sized for a high rep-rate operation with gas-jet targets up to 1 Hz.

Focusing optics for both the main X-ray FEL pulse and the high power femtosecond CPA pulse will be available in the vacuum chamber. The X-ray pulse will be focused with curved gratings or alternative X-ray focusing configurations designed in collaboration with the X-ray Optics group of the IOQ (Jena). The femtosecond laser pulse will be focused with off-axis parabolic (OAP) mirrors now capable of achieving diffraction-limited performance with very high reflection efficiency (>90%). OAPs with three different numerical aperture, one small (F/1), one medium (F/5) and one long (F/10) will allow control of the spot size and depth of focus to meet the experimental requirements (from ultra-high intensity to long, plane-wave-like configuration).

The experimental chamber will be equipped with a range of diagnostic devices, directly attached to the vacuum chamber to allow detection of soft X-ray radiation. Among the main X-ray diagnostics, an ultrafast optical/X-ray streak camera will be mounted on the vacuum chamber for on-line, high rep-rate, high temporal resolution (<300 fs) measurements. An additional

“standard” diagnostic will consist of an optical interferometer for plasma density mapping with high temporal resolution. An X-ray interferometer will also be installed to allow higher plasma density measurements (see conceptual expt.2)

An additional on-line X-ray spectroscopic diagnostic will consist of a “single-hit” imager/spectrometer developed by the IPCF/CNR group in Pisa. The device is capable of producing spectrally resolved images with <100 eV, $5\mu\text{m}$ resolution, even on a single-event. This diagnostic will be of particular importance in the study of X-ray fluorescence from X-ray pumped multi-layer targets (conceptual expts. 1 & 3).

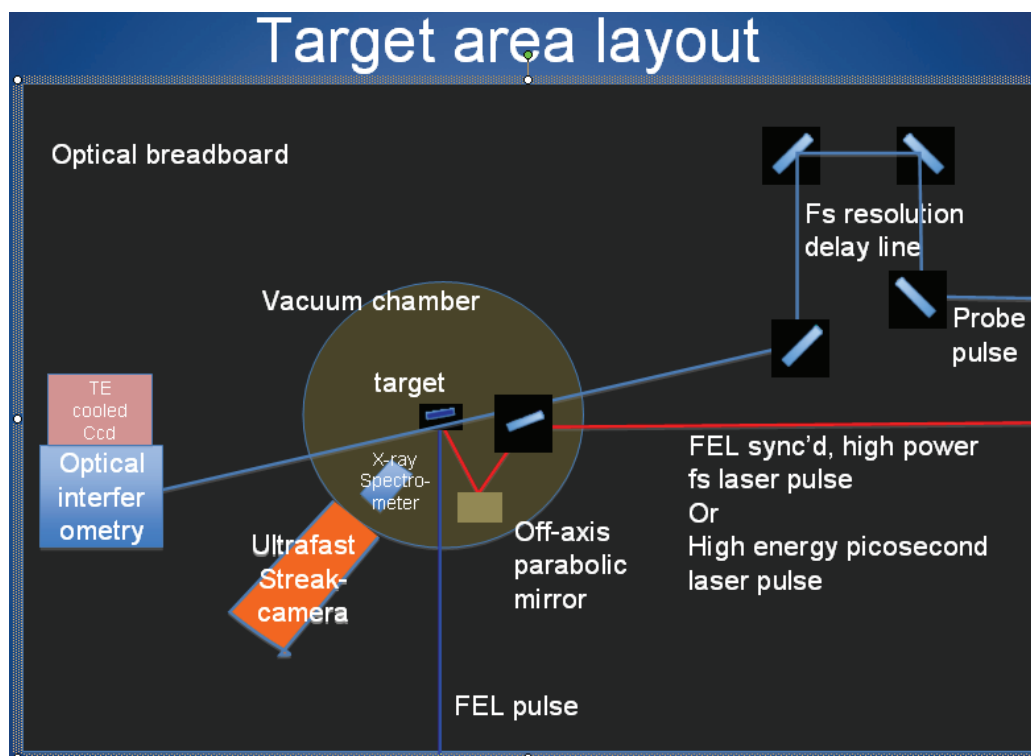


Figure 9.5: Target area layout.

9.6 Atoms , Molecules and Clusters

Basic atomic and molecular processes with short and intense FEL pulses

Reference proponent: Lorenzo Avaldi, IMIP-CNR, Roma

In the last twenty years lasers in the infrared, visible and UV region of wavelengths and synchrotron radiation sources in the VUV and X-ray range have become the most useful and versatile tools in fundamental and applied research, as well as in several branches of technology. Atomic, molecular physics and chemical physics largely benefited of the high flux and resolution of the third generation synchrotron sources as well as of the short and powerful pulses of fs laser sources . The first applications of the new built EUV FEL at Hamburg and Spring8 (Japan) have involved the investigation of the response of atoms and molecules to intense fields [45,46] . In the proposed X-

FEL facility the combination of pulses of few fs duration, a flexible time structure and a high peak flux in the X-ray region provides further opportunities and new challenges to this community. Indeed this source will allow the investigation of photon-matter interaction in a new regime, where inner shell electrons are the dominant “mediator” of the interaction.

Among the opportunities we can include the application of established methods and techniques which now will benefit of the high flux of the new source to tackle old topics with unprecedented accuracy or to investigate low density targets (clusters, radical and metastable species). Among the challenges all the unexplored topics which specifically make use of the characteristics of the new source and require the development of ad-hoc methods and instrumentation have to be included. Typical examples of the latter group are two (multi)-photon and “pump-probe” experiments on inner valence and core orbitals.

In the following some of these topics and the proposed experiments are sketched briefly, together with the experimental challenges that these studies with this new source put forward.

9.6.1 Two photon excitation, ionization and double ionization

Non-linear spectroscopy is a standard technique when applied by using high-power lasers in the visible and UV region. Multiphoton absorption spectra (single colour, 3-4 photons) have been reported for noble gases [47]. The number of photons per pulse in the FEL sources will make possible the investigation of two-photon processes in the soft X-ray region, too.

In this proposal we present three different kinds of processes based on two-photon absorption

1) Two-photon inner shell excitation in rare gases

The observable excited states of atoms by optical absorption are governed by selection rules. For single photon absorption, dipole rules apply while for two photon absorption, monopole and quadrupole rules apply. Thus different excited states are probed for these two cases, for example in the rare gases the np and nf series can be accessed on excitation of the outermost (n-1)p electron. Two-photon absorption is a non-linear process and thus requires a high power laser to occur. This will be the case at new FEL sources, where 10^{13} photons per pulse are foreseen.

Considering the range of wavelength available, the inner shell excitations from the Xe 4d (65 eV) up to the Ar 2p (240 eV) state appear to be the most suited candidates for these first studies in the different stages of the project. Eventually, also the region of Ne 1s (about 900 eV) might be accessed.

The only experimental information available on inner shell dipole forbidden transitions is provided by electron energy loss experiments. In figures 1a and b the energy loss spectra in the region of the Kr 3d excitations at two different scattering angles are shown. At the larger scattering angle, the dipole forbidden 3dns and nd are observed. However, their low cross section as well as the presence of the dipole allowed features hamper a clean characterization. This will be overcome in two-photon absorption experiments where the dipole allowed transition are completely suppressed.

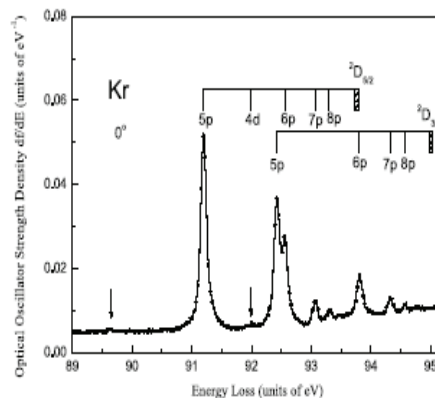


Figure 9.6

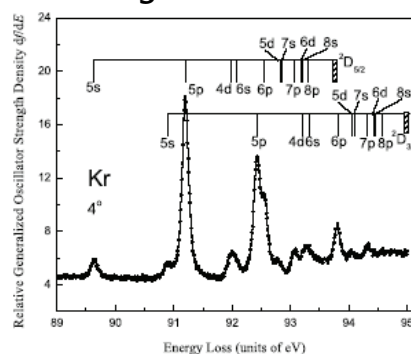


Figure 9.7: Kr 3dnl EELS spectra in dipolar (a) and non-dipolar (b) kinematics

Recently some calculations have been done in the case of the Ne 1s excited states by Novikov and Hopersky [48]. Using as a reference the values of cross section calculated for those cases (Figure 9.8), one can estimate that with an absorption path of about 2 cm, a cell pressure of 10^{-2} mbar and an average cross section of 10^{-54} cm⁴s, about 2400 counts per laser pulse (200 fs duration) are expected. Considering a repetition rate of 10 Hz with the typical gain of 10^6 - 10^8 of commercially available amplifiers, a current of few nA should be measured. However the main experimental issue will be the separation of signal from inner shell excited states from the direct ionization of the valence shell. Indeed, taking the Xe atom as an example, the absolute photoionization cross section at 30 eV is about 5 Mb. Thus, with 10^{13} photons per pulse, the single ionization will result in about 10^9 ions, with a signal/noise ratio of about 2×10^{-6} . The experiment therefore can not be done with the conventional experimental scheme of an absorption cell, but the use of a more selective detection scheme has to be envisaged. A possibility may be represented by the use of partial electron yield spectrometers.

Due to the limited energy tunability of the existing FEL facilities no two-photon excitation have been yet performed, but the results of two-photon ionization of He, Ne [49] and N₂[50] had already been reported. These results prove the feasibility of the proposed experiments, once the facility will allow an easy and continuous tuning of the energy.

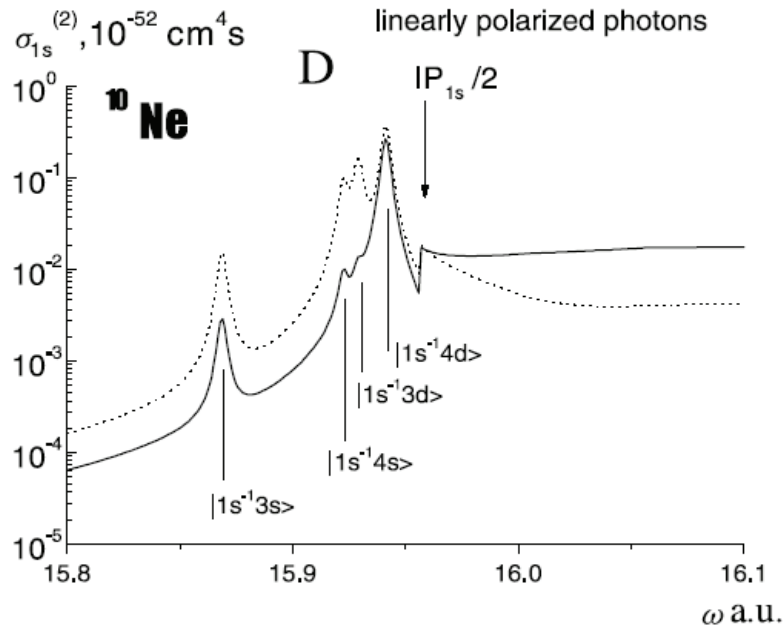


Figure 9.8: The two-photon cross section $\sigma(2)$ of the process of excitation/ionization of the Ne 1s shell by two linearly polarized photons calculated taking into account the effects of relaxation of the atomic residue in the field of the created vacancies with (full curve) and without accounting for this effect (dotted curve). In the figure the discrete final states are indicated.

2) Near threshold inner shell two-photon ionization

In the theoretical description of two-photon inner shell excitations, an important role is played by the interference between the processes of inner shell excitation/ionization and the decay of the created virtual hole. This is because the absorption of the two photons occurs in the duration of the pulse (10-100 fs) and this time is comparable with the lifetime of the core hole.

In the common wisdom, inner shell ionization and decay via an Auger process are treated as independent and incoherent processes. Recently the tunability and high resolution of third generation synchrotron radiation sources combined with the selectivity of electron-electron coincidence techniques have allowed us to investigate these processes in situations where the two-step approximation does not hold. Effects due to the final state interactions and exchange between the two electrons have been predicted [51-52] and experimentally observed [53,,56]. The question now is how these effects will show up in the energy and angular distributions of the photo- and Auger electrons, when the time scale of the absorption of the two photons is comparable with the relaxation (lifetime) of the inner hole.

The first experiments will study the photoelectron and Auger energy spectra and the corresponding angular distributions produced in the Xe 4d or Ar 2p ionization near threshold. By assuming a value for the two-photon ionization cross section of 10^{-52} cm^4 as for the Ne case, an interaction length of 2 mm, a solid angle of 10 millirad and an electron detection efficiency of about 30%, then about 10 counts per pulse are expected. This rises the question of how 10 counts produced in 200 fs can be managed by present

detectors. A possible way forward is to switch to charge measurements instead of pulse counting.

3) Two-photon double ionization

Double ionization is one of the basic processes in atomic and molecular physics. In the process the interaction of a single energetic photon may lead to the promotion of two electrons into the continuum. In this case, i.e. the so called photodouble ionisation (PDI), the driving force of the process is the electron–electron correlation in the initial state. The use of powerful Ti-sapphire lasers ($\lambda \approx 800$ nm, 1.5 eV) with ten femtosecond long pulses and intensities of several TW/cm^2 may lead to the double ionization of He, for example, by absorption of more than 50 photons. In the case of multiphoton double ionization the physics of the process is quite different. Since the first observation of double and multiple ionization by strong, linearly polarised pulses [57] a few experiments have been performed to elucidate the mechanism behind these processes. Two models have been proposed for multiphoton double ionization. One considers a rescattering process [58], in which the first ejected electron is accelerated by the laser field and later driven back by the field towards its parent ion. Then the second electron is ejected in an electron-ion collision. In the other one [59], a “shake-off” mechanism similar to the one active in the case of PDI by a single high-energy photon has been proposed.

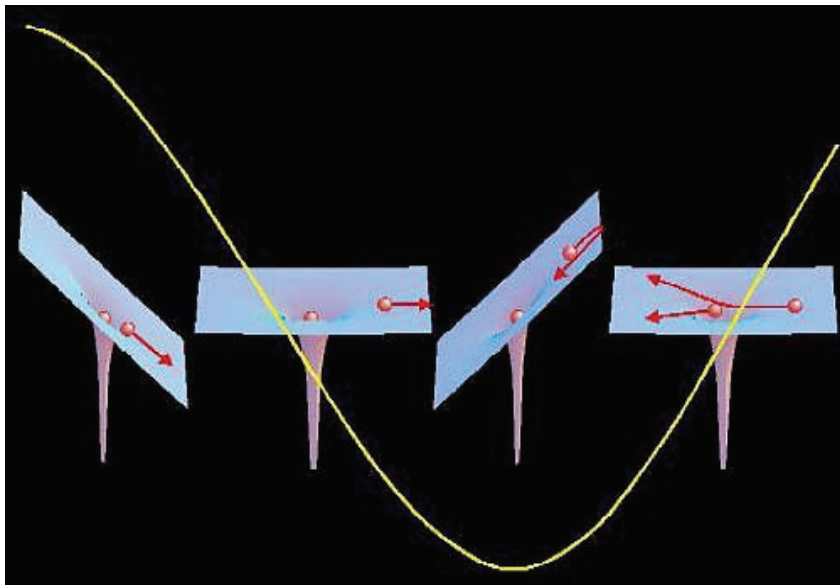


Figure 9.9: Rescattering and (e,2e) process

A series of experiments, where the momentum distribution of the two electrons ejected in the double ionization of Ar has been measured [60-62], have ruled out the hypothesis of shake-off. Moreover, experiments at different laser intensities have allowed to separate qualitatively within the framework of the rescattering model two contributions to double ionization. One is an (e,2e) like process in the ion field (Figure 9.9), while the other one is an excitation with subsequent tunneling of the second electron into the continuum. An intermediate step between PDI and multi-photon ionization in a strong laser field is represented by two-photon double ionization. In such a case the extension of our knowledge of PDI appears to be more straightforward. On the experimental side, the advent of the VUV-FEL sources would provide photons of

the proper wavelength and beams of enough intensity to tackle successfully the topic.

The advent of FLASH has triggered a series of theoretical studies on two-photon double photoionization of He. The status of the theoretical studies has been summarised in two recent works by Nikolopoulos and Lambropoulos [63] and Ivanov and Kheifets [64]. On the experimental side, two studies on two-photon double ionization of He have been performed : one in Japan using an HHG source at 42 eV [65] and the other one at FLASH at 42.8 eV [49]. Moshhammer et al.[66] have studied the double photoionization of Ne and Ar as a function of the intensity of the incident radiation. Their results show that non-sequential two-photon double ionization dominates up to about $6 \cdot 10^{12}$ watt/cm². Above this intensity three-photon processes occur. These experiments mainly focussed on the total yield of the process and its dependence on the power of the incident radiation. A systematic investigation of the two electron dynamics, as done in the case of single photon double ionization [67], is still missing. Only such experiments will allow to establish the link between a dynamics dominated by the Coulomb correlation, as in the case of the one photon process, and the one driven by the external field as, in the case of the multiphoton processes.

Several interesting feature are expected in the case of the coincidence angular distribution of the two electrons [64]. As an example, in Figure 9.10 the probability distributions of the two free electrons in the momentum space following one or more photon absorption at the Hamburg FEL frequencies and intensity ($\lambda=14-29$ nm and intensity 10^{16} W/cm²) as calculated by Parker et al. [68] is shown . The features observed in Figure 9.10 can be explained in this way: the vertical and horizontal lines correspond to events where the double ionization is reached via a two step process (first a single ionization and then the ionization of He⁺), the first half-circle corresponds to processes where an electron-pair is generated by the interaction with the laser, while the other half-circles correspond to events where the electron-pair in the continuum acts as a single “particle” and absorbs one or more photons like in the above threshold ionization [69].

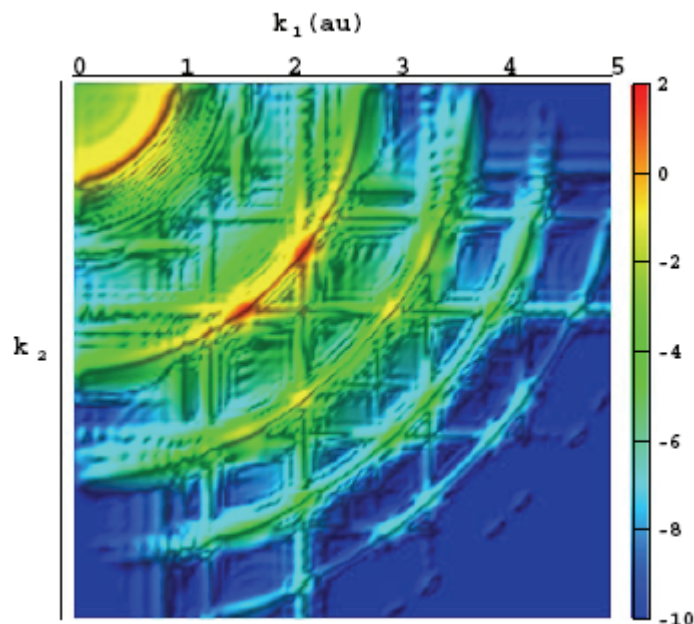


Figure 9.10: Log plot of the calculated probability distribution $P(k_1, k_2)$ of doubly ionizing electrons in momentum space after excitation with a 46 field period laser pulse of frequency 3.2 Hartrees and of peak intensity $2.0 \times 10^{16} \text{ W cm}^{-2}$. The units are arbitrary and the colour scale is mapped over 12 decades in magnitude.

We propose to perform the first experiments on the outer shell of the heavier rare gases like Ne and Ar. In a first stage, an existing multicoincidence apparatus [70], at present in use at the Gas Phase beamline at Elettra, might be used, however the building of an ad-hoc set-up that allows to collect simultaneously several energies and several angles [71] has to be planned.

The challenge is the construction of a set-up with a proper counting electronic to establish the time correlation among all the charged particles involved in the process and, at the same time, to stand the fluxes of the FEL.

9.6.2 Dissociation following the multiple ionisation of small polyatomic molecules

A topic that attracted some interest in the strong field community in the last two decades is whether, in the case of double/multiple ionization, the electrons escape the target “sequentially” or “non-sequentially”, i.e. if each electron absorbs the photons independently, or one electron absorbs the energy from the field and, then, shares it with the other electron via electron-electron correlation.

Very recently, Rudenko et al. [72] and Herrwerth et al. [73] answered this question performing measurements with PW lasers as a function of the intensity and of the wavelength, respectively. By imaging the process of ionization, they measured the ion-recoil momentum distribution in atoms [72,73] and molecules [73], isolating the regime of the double ionization induced by recollision from that induced by laser field (field or sequential ionization). In the case of the single ionization, a two step process is usually considered: in the first, the electron is set free by tunnelling through the

potential barrier created by the potential of the atom and the electric field of the laser. Then, depending on the phase of the laser field, the electrons can be accelerated and escape the molecular potential well or come back to the emitting atom/molecule. Upon recollision the electron can recombine and the atom emits Higher Harmonic radiation (HHG), or can be elastically or inelastically scattered with simultaneous excitation or ionization of the ion.

Our interest is the investigation of the role that the mechanism of the double/multiple ionization plays in the dissociation of a molecule. For a multi-electron molecule, the HOMO electronic state determines the characteristic of the bond and leads to the Potential Energy Surface (PES) experienced by the nuclei. The effect of the field is to modify the PESs of both bonding and dissociating states, affecting the motion of the nuclei. It is known that each dication state populated correlates only with one or more dissociating states. Thus different fragmentation channels can be followed, depending on the way the PESs are modified by the laser field. Among the studies on single and double ionization of polyatomic molecules, the work of Cornaggia et al. [74] regarding CO_2 , C_2H_2 (acetylene) and C_3H_4 (propyne) molecules is a milestone: it investigates the correlation between the single to double ionization rates as a function of the peak intensity of the laser. They established the regime of sequential (S) or non sequential (NS) ionisation comparing the ion yield with the different theoretical models. The FEL allows to extend these investigations to shorter wavelength and to compare one and two-photon processes directly in the same experiment. Varying the intensity regime (10^{13} W/cm²), and scanning the energy range, one can follow the double/multiple ionization and dissociation of these molecules from a regime dominated by the NS to the one of the S mechanism. The crossing from the NS to the S regimes will modify the population of the final ionic states and the path on the PES leading to the dissociation. This kind of study may explain why several dissociation channels identified with other techniques (synchrotron radiation, IR low intensity lasers) have not been recorded [74].

Another interesting topic to be addressed is the isomerization of molecules. Polyatomic molecules show nuclear oscillations in the form of stretching or bending modes which occur on 100 fs timescale. These modes are responsible for the isomerization in molecules. Indeed the isomerization time in acetylene di-cation (the time needed for the proton to migrate from one to the other end of the molecule) has been estimated to be around 60 fs [75]. Our interest here is to investigate the isomerization in small molecules (like acetylene and the propyne) when the dication state is populated by NS or S ionization. Indeed, beside the modification of the dication energy level, the new shape of the PES might speed up (or prevent!) the isomerization to take place.

Finally, above inner shell threshold, the Auger electron decay will compete with both the S or NS double ionization. Molecules like CH_3Br with the MNN Auger bands at 40 eV and 3d ionization potential at about 70 eV are the best candidates for these latter studies.

These studies can be performed specializing to the high intensity of the FEL a set-up in use at CNR-IMIP, Rome [76]. In this set-up, the time correlation among the different fragments produced in the dissociation of a molecular multicharged ion, can be established using a multi-coincidence electronics. Moreover, in the case of doubly charged ion formed after inner shell ionization, also the Auger electron can be detected. The challenge is to develop detectors and coincidence electronics fast enough to handle the bunch of charged particles produced by the short duration of the FEL pulse.

9.6.3 Main chamber, spectrometers and targets

To perform the experiments on low density matter (atoms, molecules and clusters), the basic equipment is formed by a versatile UHV chamber that can host several spectrometers. An example of such a set-up, with the proper extension to allocate one spectrometer, is sketched in Figure 9.11.

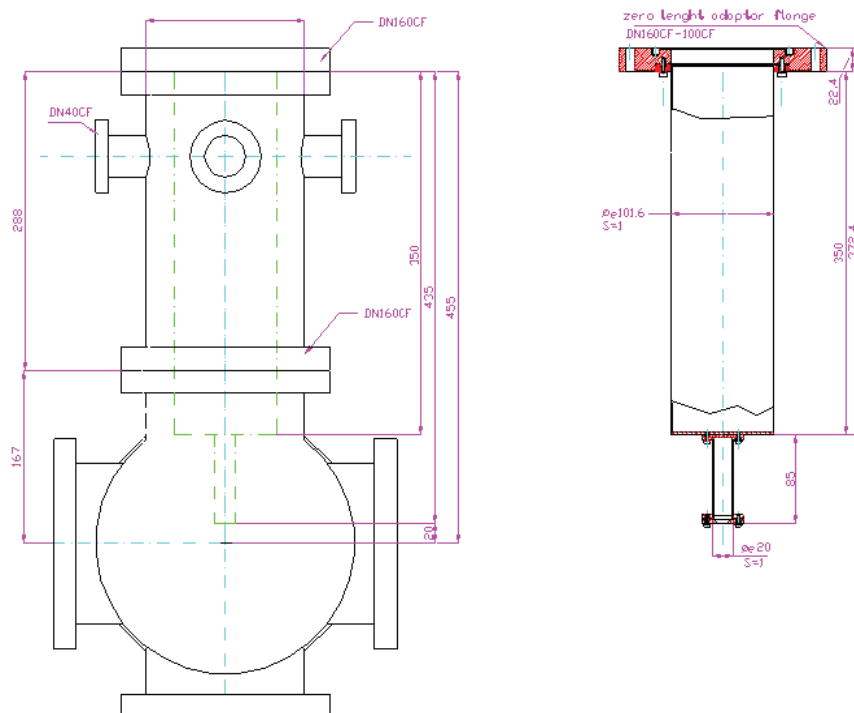


Figure 9.11: Schematic of the vacuum chamber and the electron time-of-flight spectrometer developed within the SPARC project to perform pump-probe experiment with a high harmonic generation source.

The core of the set-up is represented by a four- or six-way cross, where i) the electron and ion time-of-flight spectrometers, ii) the target source and iii) the pumping system have to be mounted. The pumping system has to be connected to the main chamber by means of a shock-absorber to eliminate any sort of vibration that may compromise the alignment of the optical elements used to perform pump-probe experiments (at time steps in the order of a few fs).

Due to the pulsed nature of the X-ray source, both electrons and ions will be detected by time-of-flight, TOF, spectrometers. They will be mounted one in front to the other (i.e. at 180°). In the first implementation, both the spectrometers will be equipped with microchannel-plate detectors, without any imaging option. In this configuration, the electron spectrometer will allow the characterization of X-FEL pulse via the measurement of the side-bands in the photoelectron spectra. On the other hand, the ion spectrometer will be used to perform total- and partial-ion yield measurements. As for the operation mode of the detector, both the counting and current operation modes will be implemented. It is expected that the intensity of each pulse and its duration will make the current operation the most suited mode. In such a case,

particular attention has to be paid to the acquisition system, which has to be based on fast (at least 1Ghz) digitizer units.

In a subsequent development, the two spectrometers will be replaced by fast imaging spectrometers that allow to simultaneously collect the energy and angular distributions of the photoelectrons, as well as to resolve the momentum of each fragment ion. The foreseen electronics of the detectors in this new configuration allows also to built up time correlation among the different charged particles. This option is crucial to study multionization processes and to follow the fragmentation of molecules and clusters.

Four different target sources are foreseen for this set-up. A conventional effusive gas inlet, a supersonic jet to produce cool targets, a furnace to evaporate powders (for example biomolecules) or solid samples (Figure 9.12), and a cluster source.

The monitoring of the incident beam will be achieved by a fast photodiode.

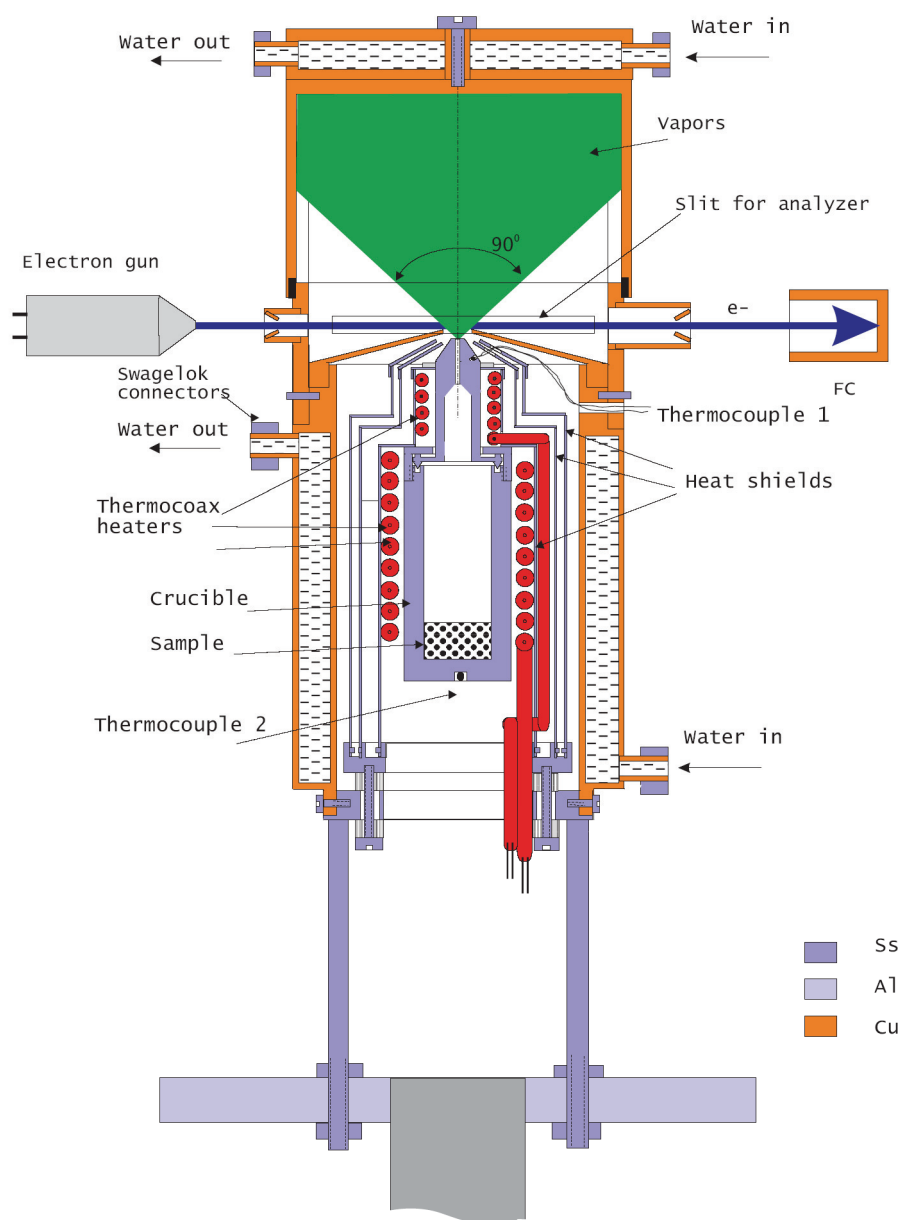


Figure 9.12: Schematic of an oven used in electron impact experiment

9.6.4 Characteristic of the beamline, monochromatization and beam diagnostic

A beamline hosting experiments with gas beam will be equipped with an end section devoted to the differential pumping to prevent any backstream of the gas target in the beamline. The experience of the operating FEL facilities has shown that the high vacuum used also in the gas phase experiments reduces this problem in comparison with synchrotron radiation facilities, where the experiments are operated at a gas pressure of the order of 10^{-5} mb. However, the installation of a differential pumping section guarantee a safer operation of the experiments.

The need of a further monochromatization of the X-FEL beam produced by the undulator depends on the duration of the pulse and the type of experiment. For pulse durations of the order of 100 fs and experiments at fixed wavelength no further monochromatization is needed. In the case of pulse durations shorter than 100 fs and experiments that need to scan the wavelength (like two-photon absorptions), a resolving power in the order 1000-5000 is desirable.

Due to the poor reproducibility of the FEL emission, the diagnostics of the photon beam needed for these experiments involve the measurement of pulse duration, of the intensity and of the space and time distribution in each pulse.

9.7 Some Nonlinear optics experiments at SPARX

Reference proponent: L. Poletto, LUXOR, INFN-CNR, Padova

STUDY OF OPTICAL NONLINEAR EFFECTS IN CONDENSED MATTER IN THE XUV REGION

The purpose of the present proposal is to explore the nonlinear response of condensed matter when excited by e.m. waves in the XUV region and the related e.m. fields resulting from the interaction.

So far, harmonic generation and, in general, nonlinear effects have been exploited and studied in dilute matter, typically gas jets, by using multiple nonlinear interaction from visible laser pulses. From the experimental point of view, the efforts of many laboratories have reached significant progress in the production (via multiple harmonic generation in gas jets) of X-rays wavelengths starting from ultra short high brilliance visible/IR laser pulses. In this way generation in the same tiny gas volume of multiple harmonic frequencies is achieved.

The advent of coherent X-ray pulsed sources such as FEL's opens up a completely new area of investigation since, in contrast to previous cases, coherent X-ray pulses are available at a single frequency and with brilliances giving rise to fields of intensity comparable with the atomic ones. The main difference is that the driving force for the nonlinearity is given by X-ray radiation rather than by visible one. The distinctive peculiarity of FEL radiation makes it an unique candidate for investigating the nonlinear optical properties of condensed matter in a new frequency domain.

While the single atom nonlinear response has been observed and studied thoroughly, very scanty results are present in the literature in the case of

condensed systems. A meaningful theoretical description of the nonlinear interaction in condensed matter appears to be a formidable task in which several groups are now active.

On the other hand, experimental activities in this domain are still in a initial phase and only recently systematic investigations are being carried on.

Nonlinear effects in condensed matter in the visible range are rather well understood and detailed theoretical frameworks which describe with fair accuracy the experimental results, have been developed. These phenomena are effective when the optical fields become comparable with the atomic field strength ($E \approx 10^8$ V/m) experienced by the relevant electronic levels. This occurrence imposes a minimum value for the brilliance on sample of the order of $2 \cdot 10^{14}$ W/m² for FEL operation at 150 eV. Short duration of the FEL pulses, besides helping in obtaining high intensities, is per se an attractive feature which allows time resolved measurements with X-ray pulses in temporal domains unexplored so far. The most promising time duration for coherent pulses is in the tens of fs, where a sufficient resolution is achievable on most electronic collective excitations.

But what are the main differences in nonlinear response in the visible and in the VUV-XUV regions? Moving on towards higher energies, radiation wavelengths start to approach characteristic distances of the crystalline lattice. Moreover, the photon energies start to exceed inner transition energies and shell ionization. Finally, collective excitations in bulk materials, such as plasmon coupling, may become resonant with the e.m. waves in the VUV. All this requires a new approach in the description of the interaction that has not yet been addressed from the experimental point of view.

The experiments in the present proposal fall naturally in three classes derived from the properties depicted above and can be scaled in frequency when they become available. Some of them will reach their full importance when spectral regions such as the water window or the absorption edges of relevant elements such as C or Si will become accessible. A non-exhaustive list of possible experiments is as follows.

9.7.1 Intensity driven (i.e. non linear optics) experiments

Harmonic generation in condensed matter. The problem of harmonic generation (HG) in the VUV and XUV regions has been explored by more than two decades now and coherent radiation has been generated from gaseous samples starting from visible laser pulses [77,78]. This approach has overcome the absence of coherent VUV or XUV sources and has improved our knowledge on the interaction of atoms with intense pulses of radiation.

This proposal addresses the complementary problem of the intrinsic nonlinearities in condensed matter in the range of energies that has not received much attention to date. In particular, direct measurements of the nonlinear susceptibilities in solid materials have not been attempted. We intend to exploit the SparX source in the VUV region by studying the nonlinear optical behaviour in a yet unexplored spectral region and identify role and importance of phonon and electron resonances. As a first approach to this issue, a systematic investigation of the non linear electronic response of the materials in the UV region allowed by the FEL source will be carried on. Surface and bulk contributions will be considered. Generation of second harmonic (SH) at surface and interfaces also between centre-symmetric materials is made possible by the reduced symmetry as demonstrated by a number of experiments carried out by visible lasers [79]. This fact opens a variety of spectroscopic opportunities

including the study of electronic and magnetic [80] properties of buried interfaces and in all the cases where discrimination against the bulk properties is crucial. We plan to detect and monitor the harmonic generation also through the observation of fluorescence photons and photoemitted electrons with the advantage of the inherent spatial resolution related with the SHG process. Moreover, the limits of the multipole expansion in the response of matter at higher photon energies will be tested. While detection will be mainly provided by the harmonic signal and by its dependence from the pump, here energy spectra of the photo-generated electrons, as well as possible fluorescent photons, are also available for further investigations. Applications of harmonic generation extends towards higher energy optical studies conducted so far, i.e. electronic structure studies, symmetry bonds in the XUV, buried interfaces, composition studies, search for material resonances, role of core electronic structure on $\chi^{(2)}$ and $\chi^{(3)}$.

9.7.2 Two photon absorption

Historically [81], from the advent of nonlinear optics, two-photon spectroscopy has been used to get access to electronic states not reachable with allowed single-photon transitions [82]. This technique, which makes use of virtual intermediate electronic states to reach the final real state will be used in the VUV and XUV regions as applied for instance to 3p shells of 3d metals, 4f shells of noble metals and also for the K shell excitation of light elements available in the SparX range. This latter occurrence is of particular relevance for electronic bond analysis since, by continuously tuning the FEL radiation, it could develop into a two-photon NEXAFS [83] for dipole forbidden final states.

9.7.3 $\chi^{(3)}$ effects

The exploitation of third order nonlinearities in the FEL-matter interaction is also part of this proposal. This nonlinearity results into, among others, Raman scattering and four-wave mixing. In the former case an extremely rich spectroscopy could be unravelled since one can get access to electronic states which are connected to the ground level via dipole forbidden transitions (as is the case in d-d transitions in transition metal oxides). On the other hand four-wave mixing generated directly by FEL radiation would selectively access the high k-values region of the Brillouin zone thanks to the short wavelength of the FEL which generates a high-pitched transient grating. This is complementary to optical probes which are suitable to explore the portion at low k-vectors of the Brillouin zone [84]. Both these experiments do not require time resolution.

In summary, novel spatial correlations of the atomic systems and new types of resonances of collective or single particle origin enter into play in the nonlinear interaction in this still unexplored energy range. They are central in the shaping of the nonlinear response and they knowledge and control will heavily affect the efficiencies of related effects as described for instance by the nonlinear susceptibilities.

Nonlinear optics experiments require: 1) a monochromatic FEL radiation without higher-order harmonics that can masque the harmonic emission from the sample and 2) a tight focus in order to reach the necessary intensity.

The filtering is ensured by the low-resolution monochromator which acts as a band-pass to increase the spectral purity of the FEL emission and by the focusing

section consisting of a grazing-incidence mirror with its focal point at the center of the experimental chamber. The characteristics of the output pulse are resumed in Table 9.1.

Table 9.1: Characteristics of pulse at the output of the beamline with the low-resolution filtering monochromator and the focusing section.

<i>SPARX 1</i>	
Photon range	4.5-15 nm fundamental emission 1.5-4.5 nm 3 rd harmonic emission
Output pulse length	100 fs rms
Energy per pulse	0.2 mJ (fundamental emission) 0.5 nJ (3 rd harmonic)
Spot size	30 μm rms @5 nm 50 μm rms @10 nm
Bandwidth	0.15% rms @ 5 nm 0.20% rms @ 10 nm

<i>SPARX 2</i>	
Photon range	1.5-4.5 nm fundamental emission 0.5-1.5 nm 3 rd harmonic emission
Output pulse length	100 fs rms
Energy per pulse	0.1 mJ (fundamental emission) 0.2 nJ (3 rd harmonic)
Spot size	25 μm rms
Bandwidth	0.15% rms @ 2 nm

The end station includes the experimental (scattering) UHV chamber and a preparation chamber for surface physics. They are connected in HUV; sample loading from the atmosphere is available through a load-lock. The scattering chamber is sketched in Figure 9.13. The lay-out allows optical experiments including reflectivity, absorption, fluorescence and transient luminescence flanked by electron spectroscopy (e.g. photoemission) in an UHV environment. Care will be devoted to optical stability and compactness. The whole object is thought as mounted on a single rigid basis, playing the role of an optical table. The solution satisfies optical stability and ease of roll-in-roll-out of the experimental station as a whole. Air cushion solution for movement can be envisaged.

The solutions proposed trace back to those adopted for the experimental station of the BEAR beamline at Elettra [83]. Most of the mechanical technology is available and transferable to the UNUS chamber.

Photodetectors (e.g. photodiodes) and electron energy analyzer (e.g. hemispherical analyzer, mean radius 60 mm) are installed on the detector arm. They cover a sphere of about 30 mm around the sample at the scattering center allowing the implementation of almost any scattering and incidence geometry. A second goniometer drives the in-air axis of the grating for fluorescence detector. Both goniometers driving the in-air axes of detector arm and grating are rigidly connected with the basis and mechanically decoupled with the walls of the vacuum chamber. The grating entrance and exit arms are of the order of 400 mm. The spectral image is formed on a MCP coupled with an optical intensifier. The optical signal is collected by an in-air lens and focused onto a CCD detector for parallel

acquisition. Six possible light outputs are foreseen for six corresponding grating positions corresponding to the CF63 ports shown in Figure 9.13 (axes at 15° with the horizontal plane). View ports can also be substituted with a with a continuous window. The in-air assembly of collection optics and CCD would follow the grating rotation.

The VIS/NUV monochromator for transient luminescence is indicated in two possible positions. Eventually the rod of the sample manipulator is indicated. It is supposed to feature - ensuring sample transferability and optical quality from the stability point of view - 6 degrees of freedom, sample heating/cooling facilities and facility for sample magnetization (e.g. horse-shoe device). The main in-air rotation could be accomplished by a goniometer according with the same scheme of detector and grating axes also mechanically decoupled from the vacuum vessel and making mechanical reference to the optical basis.

A surface physics preparation chamber (not shown in Figure 9.13) is connected with the scattering chamber through the port indicated in Figure 9.13. Also the preparation chamber is supposed to be on board of the single movable platform (e.g. on air cushion,) for ease of rolling in and out.

See also ref [85].

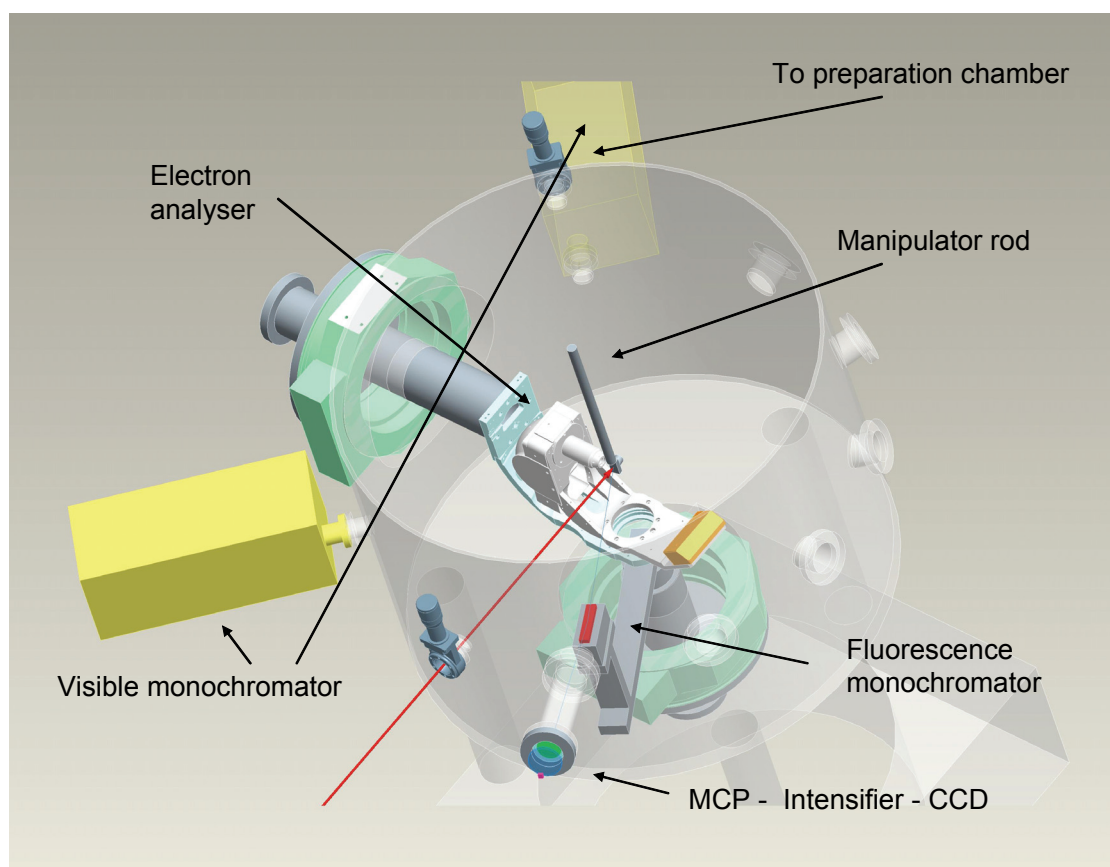


Figure 9.13: Scheme of the scattering chamber.

9.8 Condensed matter spectroscopy

9.8.1 Summary

In the last three decades synchrotron radiation in the soft X-ray region (100-1000 eV) has been extensively used for studies of chemical bonding and valence band structures by means of photoelectron emission spectroscopy. This energy region includes the so-called "water window" that is very useful for biological studies since the absorption coefficient of protein is about one order of magnitude greater than that of water, providing a contrast mechanism for hydrated biological specimen based on selective chemical fingerprints that does not rely on staining and fixation techniques. X-rays produced by conventional sources and synchrotrons are already used to probe the structure of biological molecules, but both systems are limited by the intensity and pulse length of their radiation. The short, high-intensity pulses from the new FEL should allow to overcome both of these limitations.

Soft X-rays are also used in spectroscopy of inner shell (core) electrons because they can reveal details of an atom's chemical bonding state and many surface reconstructions have been solved by such technique. A good characterization of the electronic properties of new materials (Silicon Carbide, high Tc superconductors), low-dimensional stripes (with organic and inorganic one-dimensional material) and dilute systems, like dopants in semiconductors or magnetic impurities in conventional superconductors, has also been obtained. In these last systems it is particularly relevant the usefulness of a new X-FEL source with the characteristic of higher brightness, small pulse width and full transverse coherence. It will be possible to obtain a higher spatial resolution (very important for low dimensional systems), a higher spectral and temporal resolution (important for surface reconstructions with complicated geometries and for dynamical studies) and higher coherence (very important for the investigation of disordered systems and for obtaining a higher contrast in microscopy).

9.8.2 X-ray Photon Correlation Spectroscopy on Superconductors

When coherent light is scattered by a disordered system it gives rise to a random diffraction (speckle) pattern due to the correlation of the scattering centers positions. In the case of a dynamic system (moving scattering centers) the speckle pattern will change with time. This phenomenon, currently applied for visible light using laser sources [86], is the base for the Photon Correlation Spectroscopy (PCS). Recently, third generation synchrotron radiation sources, providing a moderately coherent photon flux, have opened the experimental feasibility to studies employing coherent X-ray radiation.

The use of X-rays in photon correlation spectroscopy (X-ray Photon Correlation Spectroscopy technique, XPCS) allows to probe length scales down to the atomic resolution. In the hard X-ray regime this technique has been applied to several research fields: diffusion phenomena in complex liquids (colloids, polymers, melts...), phase transitions studies in alloys, magnetic domain dynamics in magnetic materials [87,88,89]. In Figure 9.14 we report as an example the speckle pattern recorded on a magnetic material. The use of soft ($\lambda=10$ Å) X-rays is also, in literature [89] in the study of medium range

ordered systems. On the other hand the very fast dynamic range is not accessible by present synchrotron radiation sources due to the time structure of the electron beam. The use of a Free Electron Laser source, even in the soft X-ray regime, will strongly widen the applicability of XPCS. If the X-ray source is suitably tunable (namely through the L edges of the IVth period transition metals) the use of resonant magnetic scattering for the observation of the dynamics of magnetic domains can be also envisaged. The feasibility of this class of studies, has already been demonstrated in literature [89]. The expected increased quality of the pattern due to the high flux of coherent radiation and the unique time structure of a FEL source will open the time domain of very fast dynamics.

This improved time scale feature could be applied in the investigation of charge fluctuation phenomena in hard condensed matter. This is a field of growing interest both from a theoretical and experimental standpoint. In fact, in the last few years several new effects in strongly correlated electron systems have been discovered. As an example we can take into account the observation of dynamic charge fluctuations (*stripes*) in high T_c superconductors. The cuprate superconductors are doped Mott insulators, with the undoped materials antiferromagnetic; a spin ordering has been found even in the superconducting phase. The Neutron scattering recently has resulted in an effective technique to get more information about the charge instability in high T_c superconductors. The picture which emerged is that there are fluctuating regions of antiferromagnetic order, separated by boundaries where the doping holes are confined. These features appear below a critical temperature and in most cuprate have been shown to be dynamic in nature. The role played by the stripes in the superconducting mechanism is matter of debate. A tool to investigate the dynamic of these charge fluctuations would result in an improvement of the comprehension of the strong correlated electron systems. The dynamic range needed for this type of investigation is in the 10^{-10} s and 10^{-13} s time scale [90]. The FEL, thanks to the high coherent photon flux and the unique time structure, will allow to observe the scattering from the charged regions. Using XPCS it would be possible to follow the dynamics of the formation of the charged boundaries of the stripes as a function of the sample temperature and the doping level. In fact, the presence of impurities in the crystal structure strongly influences the stripes dynamics and at certain level of suitable dopants it should be possible to freeze the stripes [91,92].

A possible experimental apparatus for this purpose could consist in a high-resolution soft X-ray monochromator [87] coupled to a delay line system [93]. The sample will be contained in a ultra high vacuum experimental chamber permitting normal and grazing incidence geometries. A challenging point is the development of a suitable detection system. Nonetheless, projects of detectors, based on pairs of time delayed pulses and exploiting well established technologies, capable to probe time scales in the 10^{-11} s regime have been presented in the past [93]. The technology in the fs time scale has to be proven but an X-ray detectors with a time resolution in the range of few fs has been proposed [94]. This conceptually new detector system is based on the depopulation of the valence band of a semiconductor by an intense ultra short laser pulse which can induce the absorption of monochromatic X-rays just below an absorption edge. The proposed device can operate as a detector by recording the fluorescence or Auger decay after the X-Ray absorption.

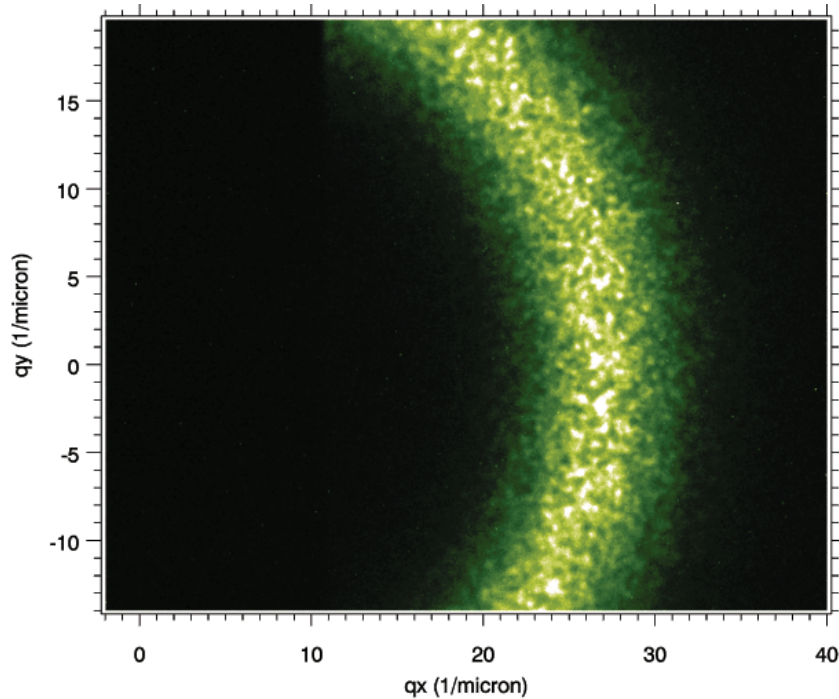


Figure 9.14: Magnetic speckle pattern recorded at ESRF on an amorphous sample of GdFe₂ (ref. 4).

9.8.3 Synthesis and study of nanophase materials

The mechanism of intense light coupling with solids and the process dynamics in pulsed laser ablation and deposition processes is still a matter of constant investigation. Conventional pulsed laser deposition processes rely on electronic excitation by ultraviolet nanosecond laser photons to initiate ablation and subsequent film growth. In many cases, it is desirable to have access to a plurality of parameters in order to avoid electronic excitations because of their photochemical consequences, or to obtain a very clean ablation process with no evidence of melted material.

The combination of unique parameters of a FEL (high average power, high repetition rate and ultra fast pulses) will offer an unique opportunity to gain significant improvements in the fundamental understanding of the desorption and growth mechanisms. These properties make the FEL also a powerful tool for the production of exciting new nanophase materials.

The systematic study of the influence of laser parameters (the role of the wavelength of the exciting radiation, the effect of the light pulse length and shape, the influence of the energy density), combined with the possibility of real-time optical diagnostic, will increase the base of knowledge in this field. The short duration of the FEL pulses will permit dynamic studies, and dissociation processes by using pump-probe techniques in combination with synchronized external femtosecond lasers.

We propose to use the innovative characteristics of the new FEL in order to study pulsed laser assisted growth of C-based tubular nanostructures. The most significant differences between the FEL beam and the tabletop laser currently used to produce nanotubes are:

the ultra-short (fs) pulse duration offer low ablation threshold, substantially

decreasing target damage and the elimination of particulate, typically generated by longer-pulse laser ablation, because the penetration depth due to thermal conductivity is negligible during the pulse;

the wide tunability of the wavelength, which should allow selective channeling of the reaction into specific molecular species.

The combination of the previous factors is expected to create a totally new and flexible environment for the growth of nanotubes. The effects of the pulse sequence (by selectively blocking or grouping pulses) on nanotubes growth and yield will be also studied.

In particular, real-time optical diagnostics should have to be incorporated into the growth apparatus in order to investigate the optical emission from the plasma. Spectra will be collected as a function of the time delay from the arriving of the FEL pulse and as a function of the position in the plume relative to the target. The spectra will be interpreted to measure the plasma temperature, the plume wavefront velocity, and to identify the presence of molecular species as a function of time and position. A further goal will be the identification of the spectroscopic signature in the plasma correlated with the weight-percent yield of Single-wall Carbon nanotubes in the deposit.

Advanced and complementary characterization techniques (SEM, STM, HRTEM, electrical transport and field emission properties, RAMAN spectroscopy and scattering) will be also applied to correlate the physical properties with the growth conditions.

9.8.4 Time resolved spectroscopy: pump-probe

In a pump-probe measurement (see dedicated section) it is possible to measure the change in absorption or reflectivity of the probe itself or indirectly by measuring the products of the interaction of the probe with the sample, like electron and/or ions. In both cases, in order to make a pump-probe measurement it is necessary to take into account a few fundamental requirements as:

- Amplitude stability of the pump and probe pulses
- Synchronization between pump and probe pulses
- Repetition rate of the pulses

Pump and probe amplitude stability defines the sensitivity of the measurements. As example pump-probe fluctuations of the order of few thousands lead to a sensitivity in absorption or reflectivity measurements not greater than a few percent. This condition can be partially released in case one observes products as result of the interaction (called background free detection). In this case it is possible to increase the sensitivity by another order of magnitude. The synchronization of the pulses is an important requirement for a pump-probe measurement: in fact one needs to determine the temporal superposition between the pump and probe pulses and control the relative delay. In the soft-X-ray spectral region many pump-probe schemes require the use of pulses in the visible frequency range. In order to determine temporal superposition cross-correlation techniques must be developed. The pulse repetition rate allows maximizing the signal/noise ratio, which increases as the square root of the frequency. However too high repetition rate (greater than 10 MHz) may cause severe problems in case of studying ultra fast processes which end up into metastable states (tens of nanoseconds more). In this case there is

a continuous accumulation of states with different initial conditions, which can alter the measurement.

The development of a versatile pump-probe set-up must take into account all previous requirements. Synchronization can be solved deriving the visible-infrared pulses from the same laser source, which has been used for the injector. Development of cross-correlation techniques, based on photo-electron spectroscopy, can provide useful means to control the temporal overlap of the pump and probe pulses. The effect of amplitude fluctuations can be reduced by using energy windows that refuse data which are taken out of the allowed fluctuation level.

Hereafter a few examples of experiments which can be performed with pump-probe techniques are briefly outlined.

9.8.4.1 Pump-probe: surfaces and interfaces

A relevant peculiarity of the new source is the short pulse width since with femtosecond time resolution we can directly observe polarization interactions and the localization of charge carriers in metal-semiconductor e/o insulator systems: in fact electrons in metals are usually free-electron like, whereas electrons in dielectric solids tend to be localized as small polarons [95]. Despite extensive study of charge localization phenomena, electron localization at interfaces between dissimilar materials remains largely unexplored. Understanding charge localization is important in determining the electronic and optical properties of applied materials and in the development of new materials. In this context, the combination of angle-resolved two-photon photoemission and femtosecond laser techniques provides a unique opportunity to study the dynamics of carrier localization at interfaces [96]. In this case a pump pulse excites electrons from occupied metal states into unoccupied interfacial states, and a probe pulse eject the excited electrons into the vacuum where the electron kinetic energy is measured at various angles. This allows the determination of the binding energy and the effective mass of the interfacial electrons. Also, if dielectric layers are grown on the metal substrate, one can explore the layer-by-layer evolution of the potential and the electronic structure of the interface as well as to control dynamics and localization phenomena by defects, doping or different layer material. Having a very intense photon flux from the new X-FEL source the above mentioned technique can be implemented to disclose information at the microscopic level taking images of the excited state as a function of the elapsed time by coupling with a Scanning Tunneling Microscope.

The study of ultrafast processes on surfaces has been a topic of increasing interest in recent years from both an experimental and a theoretical point of view. The prospect is of particular importance to processes such as heterogeneous catalysis where the interaction dynamics between the molecule and the surface are fundamental to the process. However in contrast to the case of gas or solution phase chemistry, where pump-probe transient absorption spectroscopy and more sophisticated techniques can be used to obtain a clear picture of reaction dynamics, experimental surface science techniques are more limited in their ability to give directly interpretable data. Past time-resolved surface studies have used two-photon photoemission, infrared spectroscopy, sum-frequency generation, and resonant Auger spectroscopy to monitor phonon and electron substrate-adsorbate coupling on ultrafast time scales. Photodesorption yield measurements and surface second

harmonic generation, have also been used to monitor the final state after completion of a chemical reaction, and have made it possible to measure the overall time scale of femtosecond laser induced desorption processes. All these experiments are limited in that the chemistry occurring at the surface itself has not been directly observed. The time resolved photoelectron spectroscopy in the UV is presently used to reveal variations in the valence bands of a surface adsorbed compound as a function of time [97]. This allows to directly observe the variations in the molecule chemical bonds, with a resolution of about one hundred femtoseconds, which is necessary to follow the entire evolution of the reaction. In the proposed experiment, a pump laser pulse, generated by a femto-second infra-red laser, will be used to excite a molecular species absorbed at a metal surface. Using ultrafast XUV light it is possible to monitor the change in the characteristic photo-emission spectrum from the surface as a function of time after the excitation by the pump. A change in the core level structure of the molecule-metal complex, is observed on a time scale of few hundreds femtoseconds.

From this measurement one can directly obtain information about the chemistry occurring at the surface such: the making and breaking of chemical bonds, the intermediate reaction steps and the existence of transient reaction products.

9.8.4.2 Ultrafast Pump-probe Experiments: Nanostructures

The characterization of quantum-confined nanostructures is quickly evolving with more stringent requirements in terms of spectral, temporal, and spatial resolution. As a concrete example, one may mention the large amount of applications that single-quantum-dot nanostructures (those displaying three-dimensional confinement) are finding in the fields of photonics and optoelectronics. Currently, there exists a large number of European projects focused on the study of quantum entanglement for applications in cryptography, or the use of nanolasers constructed from self-assembled quantum dots grown on semiconductor surfaces (e.g., InAs/GaAs).

This research proposal plans the study of the electronically excited states of single quantum dots by synchronous, two-color optical pumping using a (local) ultrafast IR laser and an X-FEL. The work scheme is similar to the one previously proposed by Haight, Bokor, and others [98], and schematically shown in Figure 9.15.

The characteristics of the X-FEL light source would allow the following: (a) an easy spatial selection of single quantum dots by beam focusing on spatial scales of ca. 100 nm; (b) reasonable signal levels arising from electron photoemission in coincidence with the local IR light source. Considering more recent experiments performed only with local laser sources [99], the ratio between the photon density per pulse of an X-FEL compared to that of a bench-top Ti:Sapphire laser is about ten orders of magnitude (10^{25} X-FEL vs. 10^{15} Ti:Sapphire). Such an increase in photon density will warrant positive results even after consideration of the various magnitudes for the excitation cross section as a function of the photon energy involved in the physical processes of interest.

The results obtained from these experiments will provide a detailed spectroscopy of the quantum-dot electronic energy levels and an ulterior characterization of single quantum nanostructures. By keeping fixed the

vacuum state, one can select the starting energy level by tuning the local laser light source to the desired emission feature. This type of experiment would require a high-pass electron detector (Faraday cup) or, preferably, a tunable electron analyzer. With such an additional means of discrimination, the temporal delay between the two laser pulses would allow the study of the single-quantum-dot picosecond decay dynamics, one electronic state at a time. Other experimental configurations are also possible.

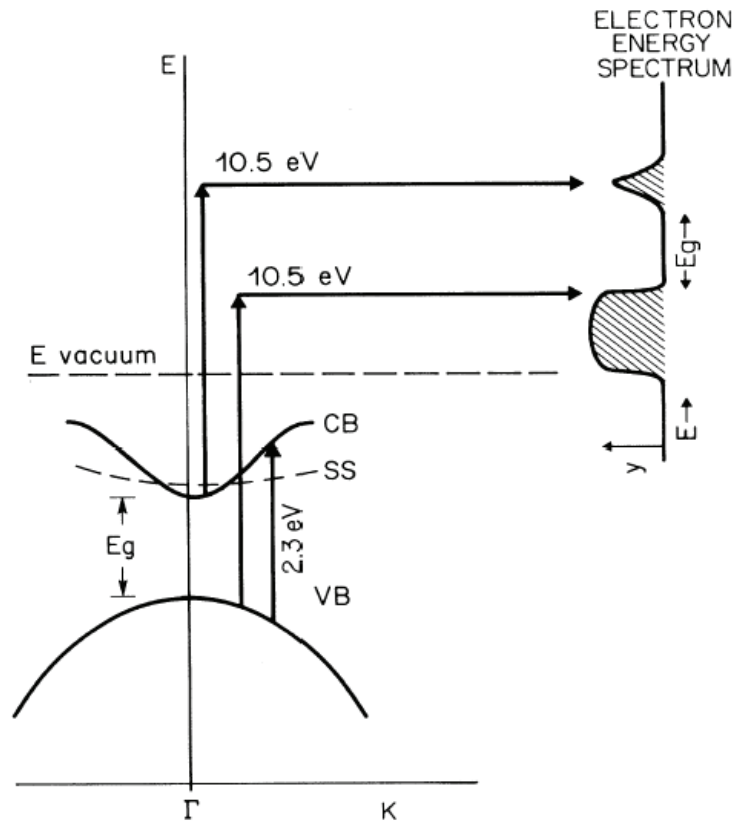


Figure 9.15: Schematic diagram of the pump-probe scheme (also see Ref. [98]).

9.8.5 Emission spectroscopy at the soft X-ray energies

Soft X-ray emission Spectroscopy (XES) is based upon a photon emission due to the decaying of a valence electron to a core hole originated by a primary electron excitation. XES is in fact a second order process bearing a complete information of the first order process (the photon absorption) and that of the de-excitation.

When the excitation is resonating at the edge of a core electron the methodology is called Resonant Inelastic X-ray Scattering (RIXS).

Recent studies have emphasized that RIXS is a two steps coherent process and moreover that final state resolution is not limited by the lifetime of the core level as it is in the absorption process.

The low quantum yield of the emission process is (<1 %) a serious limiting factor even in third generation synchrotron sources for a handy use of this methodology and fourth generation sources are called upon for this case.

An increase of several order of magnitude in brilliance with respect to that of the present sources will make RIXS of common use like nowadays the absorption or photo-emission spectroscopies, that have been the base for the interpretation of the electronic structure of matter.

Among the key points of RIXS it is useful to recall the following:

Selective excitations

In the soft X-ray regime it is possible to selectively excite different elements at energies which are well defined and separated from each other; the most important for several materials being those of the $1s$ states of C, N, and O, the $2p$ of Si, the $2p$ and $3p$ of the transition elements and finally the $3d$ and $4d$ of the rare earth elements. In the latter two cases indeed the $p \rightarrow d$ and the $d \rightarrow f$ transitions explore the states responsible of the magnetic properties of the materials.

Sensitivity to bulk properties

The absorption length in the soft X-rays is sufficient for the study of the bulk properties but does not allow an easy preparation of samples for a transmission absorption experiment. In this case the total electron yield current is recorded as a function of the impinging photon energy. This method is not applicable, anyway, to important classes of materials such as insulators and biological samples in wet environment, and it can introduce hardly interpretable effects in experiments that involve the use of electric and magnetic fields. Moreover the XES technique, by measuring photons emitted by the excitation process, allows to exploit the penetration length of soft X-rays, providing information about the bulk electronic properties. The low absorption coefficient of water in the soft x-ray region (water window) can ease the study of samples in wet environment. Moreover, the emitted photons are not sensitive to the sample charging and to electric and magnetic external fields.

Band structure

XES spectroscopies, although later supplanted by photoemission techniques for lack of intense sources, were among the first methodologies for band structure determination.

The RIXS technique [100] promises to be advantageous over angular resolved photoemission in that it is not limited to single crystal samples and can be used also with polycrystalline material. Moreover, it is bulk sensitive, and insensitive to electric and magnetic fields and to insulating samples charging, where the ARPES technique is strongly affected.

The high brilliance and the reduced dimensions of the source point image at the sample of the novel fourth synchrotron sources will definitely overcome those early studies and actually bring the present energy resolution limit from some hundred MeV to few MeV.

9.8.6 Low-dimensional systems

Recent investigations of strongly correlated electron systems have questioned the validity of one of the most fundamental paradigms in solid state

physics: Fermi liquid theory. This picture is based on the existence of quasiparticles which obey the exclusion principle and have lifetimes long enough to be considered as particles. This quasiparticle concept is restricted to zero temperature and a narrow region around the Fermi level. Angle resolved photoemission (ARPES) represents a crucial experimental probe for the presence or absence of Fermi liquid behavior. However, to be conclusive in the interpretation of the electronic structures around the Fermi level [101], such ARPES studies require very high energy resolution which requires exceptionally high photon fluxes (not achievable with conventional synchrotron radiation sources). In fact, a total energy resolution of the order of 1 MeV, which is essential for these studies, can be achieved with the high X-FEL brightness and an appropriate monochromatization. This experimental configuration will give an acceptable data acquisition time as compared with current synchrotron radiation sources. Such increase in spectral resolving power is necessary in these strongly correlated electron systems in order to be able to measure with the highest accuracy the lifetime width of peaks in the photoemission spectra. In fact, it is the energy dependence of the lifetime width in the vicinity of E_F that is a strong indicator of whether or not a material behaves like a Fermi liquid. Moreover, it is the excitation around the Fermi energy that is of prime importance for determining the origin of high-temperature superconductivity. Experiments made on model cuprate compound [102] have made a connection between stripes (see Figure 9.16), and the Fermi surface. Stripes are a phase with regular magnetic and charge ordering that has been observed in many high-temperature superconductors and in the case of some cuprates (Nd-LSCO) are stabilized with very low neodymium doping [102]. A Fermi surface can be extracted by integrating the photoemission spectra over an energy range near the Fermi level to obtain maps of the electron momentum distribution function. In this case the shape of the Fermi surface implies that the electron system is highly one-dimensional, i.e. the data are inconsistent with the more rounded Fermi surface calculated for two-dimensional copper-oxygen planes.

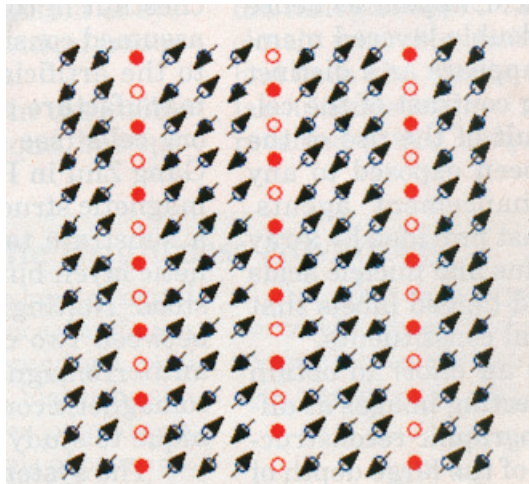


Figure 9.16: Stabilized phase of “stripes” in LaNdSrCuO_4 (ref. 2).

The high flux and the time structure of the of the X-FEL pulse will also be important in the study of solutions much diluted of atoms in solids or in

surfaces and interfaces, as dopants, adsorbate under the monolayer and defects. Submonolayer-monolayer adsorbate of organic self-assembled molecules on surfaces is an important example of very diluted samples. This research topic is relevant for its application in the fields of biosensors, corrosion inhibitors, mineral processing, and very recently, for the realization of prototype devices, in view of "plastic electronics" era [103,104,105,106,107]. Despite the growing interest in such systems, still open questions remain about the intimate molecule-to-substrate interface properties, the evolution of the electronic molecular levels (formation of extended band states, bandwidth) with the number of molecules on surface, the geometric arrangements of the molecules on the surfaces and the control of the transport properties (electron-phonon interaction and polaron effects). Much information regarding these systems can be achieved, in the photon energy range of the X-FEL, using photoelectron spectroscopy, both in angular integrated and resolved modes, photoelectron diffraction and near edge X-ray absorption fine structures (NEXAFS) spectroscopy for the edge of the light atoms constituting the organic molecules.

9.8.7 Highly correlated systems

Charge density fluctuations are essential in metals with small orbital extension and strong electron interactions. Their temporal evolution depends on the electron velocity, and is typically in the femtosecond regime. An interesting case occurs whenever the carriers are much heavier than the bare electrons. Indeed the strong renormalization reduces exponentially the electronic bandwidth and delays the coherent hopping. Therefore the dynamic of the charge fluctuations may evolve in fractions of picoseconds. That would open the possibility of imaging the electronic correlation with an X-FEL source. Remark that the study of this quantum effect is possible only if the fluctuating charge hides a broken ordered phase. In this case the scattered X-ray would produce diffuse peaks that can be distinguished from the incoherent phonon contribution. Under the irradiation of ultrafast X-rays the superlattice diffraction should present an internal structure made of fluctuating speckles.

In the following we propose an ideal system to study the dynamical charge ordering. Some of the Manganites display polaronic renormalization and superlattice peaks. Despite it, the signal diffused by these superstructures is weak and superimposed to a consistent background [108,109]. On the contrary quasi-one-dimensional (Q-1D) Peierls conductors produce strong charge density waves (CDW) with a coherence length dependent from the temperature [110]. In these materials the CDW is driven by the nesting properties of the Fermi surface. At room temperature the nanometric coherence length of the order parameter should diffract an ultrafast radiation into dynamical speckles. The characteristic time scale of the evolving pattern is fixed by CDW fluctuations. In the case of weak electron-phonon coupling these would be naturally associated to the thermal vibration of the lattice. On the contrary, strongly interacting electrons-phonon system would evolve on the time scale proper of the polaronic mass. Recently we proved that these metals display the spectroscopic signature of a polaron liquid [111]. It follows that the CDW fluctuations should be strictly related to the coherent motion of the electrons and lattice deformation. Consequently we expect that a temporal evolution slower than the unrenormalized band motion, but faster than the phonon diffused scattering.

9.8.8 Spectromicroscopy

Photoemission techniques like electron spectroscopy for chemical analysis are the leading electronic probes in material science, but their impact in the life science has been minimal. A critical problem is that the lateral resolution in ordinary photoemission is limited to several tens of a micron, which is nearly useless for most of the fundamental problems in biophysics and biochemistry, which deal with microstructures in the submicron range or smaller. This limit has been overcome with synchrotron radiation spectromicroscopy on third-generation soft X-ray synchrotron sources. In fact, spectromicroscopy represents a unique tool for the quantitative chemical microanalysis of material science and biological thin films by combining synchrotron radiation with the lateral resolution of a photoemission electron microscope [112]. All photoelectron spectromicroscopes fall in one of two groups: scanning focusing instruments [113], which achieve high lateral resolution by focusing the photon beam on the sample, and electron imaging instruments [114], which use an electron optics device. Such spectromicroscopy technique is able to distinguish quantitatively the different physical and chemical behavior with a laterally resolved determination of chemical composition. In fact photon energies in the soft X-ray energy range can be used to study all the chemical elements that have core levels (K or L edges) in this energy range. Recording a stack of images with CCD-cameras each obtained at a distinct energy, covering the whole absorption edge, results in two-dimensional spectroscopy with every point in the microscopic image that give rise to a microscopic spectrum. In this way the morphology and the local chemistry of biological specimens and material science samples have been investigated with a lateral resolution better than 100 nm and a spectral resolution of 0.1 eV [114,116,115]. As examples we can refer to works on diamond, where it has been possible to distinguish quantitatively between carbon phases with different hybridizations in a laterally resolved determination of chemical composition experiment [116], works on dodecahydro-dodecarborate where it has been possible to make chemical mapping images and spectra identifying the chemical contrast between Boron and Silicon by digitally subtracting different images taken with different photon energies [116] and works on neuronal cells to detect specific positions of the cells where metals was clustering after uptaking [114]. This again falls in the study of low dilute systems and the use of the enhanced intensity and brightness from the new X-FEL source opens the possibility to put a lot of light into a small spot which, together with the improvement of today available electro-optical systems can reduce the spatial and spectral resolution of a factor 10.

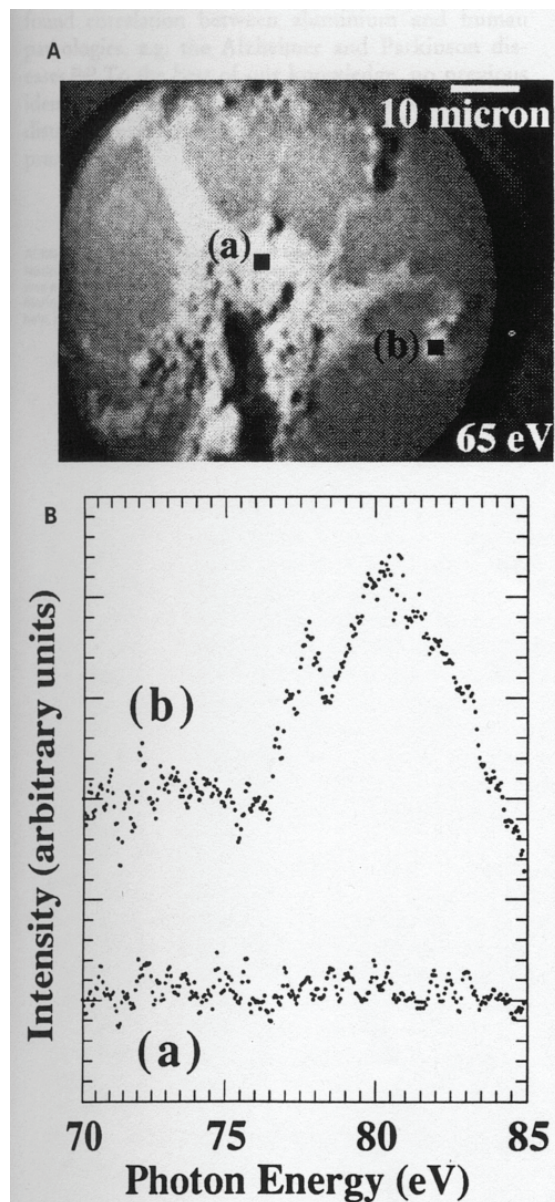


Figure 9.17: Microimage of neuronal cells doped with aluminum. The aluminum absorption spectra refer to different area of the cell. (ref. G. De Stasio et. al. Neuroreport 4, 1175 (1993)).

9.8.9 Biological samples

In the last few years big efforts have been dedicated in the so called "Genoma project" from the international scientific community, that is, in the systematic sequencing of the human DNA. The unbelievable amount of data obtained already started producing information in terms of better comprehension of the induction mechanisms of a few genetic disorders and a few pathologies. The first results already find applications direct for the safeguard of the health and make more concrete the perspective to produce more refined drugs with proteins directly interacting with the DNA. On the

other hand the sequencing of the genome also revealed the existence of thousands of unknown genes. The study of the proteins composition and of their functions is clearly critical to understand how the cells work or how the pathologies develop. For consequence, the experimental characterization of not very well known proteins is in continuous growth and in this context the introduction of new radiation sources like the X-FEL will bring important benefits. In fact, the soft X-ray radiation issued by the X-FEL is extremely useful in biological studies, thanks to the possibility of exciting resonances of the core levels, and to therefore know in a quantitative way the space distribution of selected chemical elements in the cells.

Furthermore, thanks to the time structure of the radiation of the X-FEL, all the parameters described above can be followed in their time evolutions with time-resolved experiments in the range which goes from femtoseconds to milliseconds, making in this way accessible a range of phenomena at present not investigable even with the more recent constructed synchrotrons.

This last aspect deserves a short widening; in the time scale femto and picoseconds the following phenomena happen:

- the atomic vibrations
- charge transfer phenomena that are often the key passages during the enzymatic catalyses or in the reactivity of the proteins
- the distortions of the chemical bonds for effect, for instance, of the application of external fields or during the chemical reactions.

In the time scale of the nanoseconds and microseconds the folding and unfolding processes take place and the transitions between various conformational states of the proteins and of nucleic acids that are the fundamental presuppositions for the chemical recognition and the functionality of these structures. In the time scale of the milliseconds falls, for instance, the diffusions of small metabolites.

At present, kinetics behavior of the proteins can be studied by experiments of flash-photolysis [117,118] in which an intense visible laser pulse induces a metastable state in the sample (for instance by breaking a bond of a ligand in an hemoprotein) and a delayed probe is used to analyze the relaxation of the sample (in the example the recombination of the ligand). The use of an opportune radiation from the X-FEL could allow to simultaneously probe the structure and the kinetic behavior of the sample with chemical specificity.

Other examples of applicability of the X-FEL are reported hereafter:

Adsorption of biomolecules and cells to surfaces.

This is a research field in strong development also due to the potential applications in the field of medicine, that concerns for instance the biocompatibility of prosthetic materials with osteoblasts or fibroblasts (with obvious consequences on the development of materials at low rejection level for implantation), or in the field of biotechnology, like the biosensors or biochips development.

Also under a more heuristic point of view several questions are still without answer. For instance, how the adhesion of proteins takes place (for ex. fibronectin, vitronectin, trombin etc.) in metals, glasses or polymeric materials? What are the crucial chemical bonds between the inorganic phases and the organic one? Does the molecular structure play a role? What are the bases of the molecular recognition?

These matters can find answers using X-rays spectroscopy by joining the high flux and the high spatial resolution of a source of radiation like the X-FEL.

Cellular metabolism.

Many fast metabolic events can be started or regulated by optic lasers pulses, even if their evolution can be followed only through a fast X-ray spectroscopic technique. Some aims which could be reachable are:

- follow the polymerization of proteins, the development of the DNA during the reading of the genetic code or from its state in the chromosomes and the opening and closing of the membrane channels;
- to study the dynamics of the native or perturbed plasmatic membrane channels for electroporation (analyzable also through imaging on the scale of the nanosecond) and the structure of the nuclear pores which regulates the transport of proteins, metabolites and hormones from and towards the cellular nucleus (see Figure 9.18);
- study the metabolic pathway of cellular messengers as the calcium ions in terms, for instance, of their release from sarcoplasmatics reticuli, or of the transit through the membranes both in physiological conditions and under the effect of external agents (for instance the application of electromagnetic fields) that interact with the normal metabolism of the calcium itself. Studies of this type will be possible with investigations in the X-rays region with a source which concurrently presents the time characteristics, the high space resolution and the chemical selectivity of the X-FEL radiation.

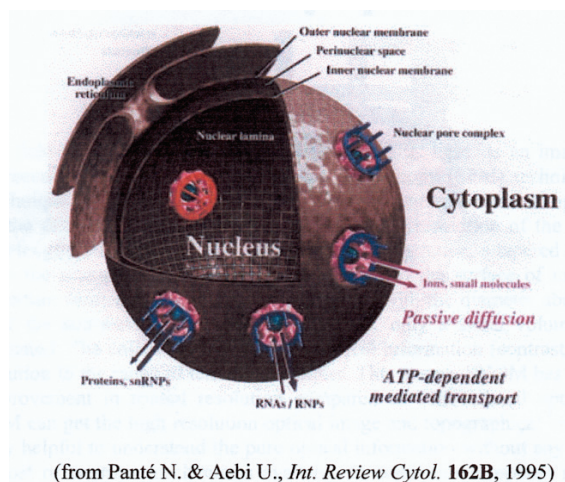


Figure 9.18: Scheme of a cell and its components.

9.8.10 Study of photosynthetic complexes and photochemical processes.

To the state of the art time-resolved studies of the pigments and of some photosynthetic complexes of the plants, often led “in vivo”, are essentially performed with fluorescence microscopy. Therefore the obtainable data suffer of the intrinsic limitation of the technique, that is the relatively poor resolution, due to the well known diffractive effects, typically limited to the order of 1 μm or not very lower. Under such a limitation, the experimental results are necessarily the effect of a space average on a big number of centers and photosynthetic processes taking place concurrently in the irradiated area. The future X-FEL radiation utilization will allow to keep or improve the time scale and to exceed the limitations due to the lateral resolution. Furthermore it will be possible to study the dynamics and the space distribution of the

photosynthetic centers directly "in vivo" in their natural location, e.g., on the thylacoid membrane.

Likely, combining the time resolution with the chemical selectivity coming from the possibility of exciting core levels, it will be possible to study the photochemical processes developed by chromophores containing heavy metals. This can contribute, for instance, to reveal the existence and the structure of the intermediate states of the photochemical processes.

9.8.10.1 The problem of radiation damage

The prolonged exposure to high flows of X-rays can give rise, already in the modern third generation synchrotrons, to modifications of the spectroscopic structures of the samples under study. Such an effect, observed several times in the last years, is especially critical in the case of the relatively delicate biological samples and it was identified as due to the damaging of the sample or to modifications of the components of the target for thermal effect induced by the electrons or by radio-lysis of the buffer [119,120]. It is clear that effects of this type are, all the more reason, expected also in the case of the X-FEL and, independently from the mechanism through which the modifications of the sample are produced, the sample safeguard strategies must be considered as key aspects in the design of biological experiments that foresees the use of the X-FEL radiation. In fact, once solved the problem of the damages, X-FEL radiation can support a new category of biological high quality experiments, many of which are not, at present, neither predictable.

However, it is good noticing that the production "in situ" of oxidative species, that generally constitutes a problem, can also turn out in a practical and powerful tool to induce and study the mechanisms and dynamics of the damaging induced by the X-rays in the cells. It is furthermore well known that the production of aggressive radicals takes place also "in vivo" and it is involved in processes as the natural ageing (for instance in the red blood cells) [121] and in the development of a big number of pathologies (included apoptosis and cancer). The artificial production of aggressive radicals will help understanding the radical-trapping behavior of compound (for instance glutathione or pyridinic drugs) [122,123] candidates for pharmacological applications.

Between the strategies used to reduce the damaging and to preserve the structural stability of the biological samples (proteins, nucleus, organelles, membranes, whole cells and tissues), during the exposure to the high doses of X-rays, we recall the fast freezing of the sample and the consequent analysis at low temperature. At present, hydrated 10 microns thick samples can be analyzed inside the wavelengths of the "window of water". For instance, the acquisition of microscopic images with nanometric resolution requires a dose of about 10^7 - 10^8 Gray while the tolerance of the biological samples can reach the 10^{10} Gray if the sample is exposed to shock-freezing [124]. Another simple strategy consists in analyzing various areas of the sample, for instance executing a scanning of the sample with respect to the beam of the X-FEL. Finally, when systems are studied in solution (proteins or nucleic acids), it is possible to keep them in slow flow using, for instance, peristaltic pumps.

Beyond the techniques mentioned above, it is worth to say that, recently, an analysis of the dynamics of the sample deterioration [125] was executed, in particular concerning simulations of the radiation induced damage as a function of the energy of the photons, of the length of the laser pulse and the dose absorbed by the sample. The work showed that the typical damage

threshold of about 200 photons (to 12 keV) for \AA^2 can be extended to very high doses and extremely short pulses as those of the X-FEL [125]. By consequence one can predict that single hydrated molecules, microcrystals or sub-cellular particles like nucleous, chloroplasts or rybosoms, opportunely manipulated and, in particular, once prepared in micro drops, can be analyzed, inside a time scale similar to the individual pulse of the X-FEL, i.e., the structural information can be collected before the damages on the sample take place.

9.8.10.2 Magnetic Materials

The unique properties of the FEL radiation offer unprecedented possibilities in the study and the manipulation of the magnetic behavior of matter. Open key questions in magnetism range from the quantum mechanical description of highly correlated electron systems, to the relation between the magnetic behavior, the morphology and the structure of nanosystems, and to the test of universality concepts in the physics of phase transitions. Moreover, the study of magnetic phenomena provides a guide to the engineering of new materials for innovative technologies. The functional properties of magnetic materials can be suitably tailored by purposely modifying the atomic geometry, the chemical composition, and the dimensionality. The impact of recent progresses in material science on industrial applications is exemplary testified by the introduction of artificial nanostructures in the technology of magnetic devices [126,127,128] as functional parts of novel types of magnetic sensors and information storages.

The research on magnetism and magnetic materials has largely profited in the past decade from the development of new investigation methods based on the synchrotron radiation from third generation storage rings. Wide-spread applications of various types of spectroscopy, magnetometry, diffraction, scattering and microscopy techniques have been specifically designed to exploit magnetic dichroic phenomena induced by circularly and linearly polarized X-ray radiation [129,130,131,132]. The high brilliance and the time structure of the FEL pulses (with $1 \text{ nm} < \lambda < 100 \text{ nm}$) will to lead to developments of these methods, capable of shedding light on the magnetic behavior of materials into yet unexplored microscopic and time domains. In the following we briefly outline some possible applications of the FEL radiation in the study of magnetic phenomena, that range from ultra-fast magnetic processes in response to light or magnetic field pulses, to the magnetic interactions in highly diluted systems, the spin-dependent charge transport and the imaging of the spin-dynamics in magnetic nanostructures.

The fast magnetization switching of individual miniaturized elements is a process intimately connected with the operation limit of magnetic and magneto-optical devices. The dynamics of the non-equilibrium states that follows a short magnetic field or laser pulse determines the ultimate timescale for writing and reading information in magnetic media. These characteristic times are fundamentally related to the thermalization transients of the electronic, spin and lattice excitations. Although these phenomena are also of obvious fundamental importance, their investigation has been so far hindered by the difficulty of following magnetic changes and electronic relaxation processes over ultra-short time scales. Magneto-optical Kerr-effect and photoelectron polarization studies [133,134] indicate that the dynamics of the

thermalization processes of a hot electron gas, excited with a visible laser pulse, can influence the magnetic states of thin films on a time scale ($10 \text{ fs} < \tau < 10 \text{ ps}$) apparently shorter than the electron-phonon relaxation time. Also, the possibility of achieving very fast magnetization reversal was demonstrated using ultra-short magnetic field pulses generated by a high-energy e-beam [135]. All present methods are not able to directly probe the evolution of the magnetization and of the magnetic moments, nor to examine in detail the electron relaxation mechanisms over these time-scale ranges. X-ray scattering techniques are powerful tools for the understanding of the electronic and magnetic properties of the matter. The tuning of the energy of the incident photon and the selection of the transferred momentum allows chemical selectivity via the core excitation and site symmetry exploring the k-space. Magnetic circular dichroism with soft-X-ray pulses produced by the FEL will make possible to follow aspects of the time-dependent response of a spin system to a ultra-fast perturbation, which are otherwise inaccessible to the investigation. This method is able to provide time-resolved and quantitative vectorial measurements of the size and orientation of the magnetic moments [147,148]. Moreover, through the selectively excitation of specific core transitions, it allows to separately probe the spin dynamics of the different chemical elements present in the system under investigation. Time-correlation techniques can exploit magnetic dichroism in absorption and reflection of polarized radiation using pump and probe schemes. A delayed X-ray circularly polarized pulse can act a probe of the evolution of the non-equilibrium magnetic states induced by a laser or a magnetic field pulse, or by high-pressure waves. The fastest dynamical range that can be explored is essentially limited by the time structure (ca. 150 fs) of the radiation pulses, while the use of seeding techniques will permit to probe time intervals shorter than 50 fs. The most relevant photon energy regions for these studies correspond to the ones of the $2p \rightarrow 3d$ thresholds (400-1000 eV) in 3d transition elements and the $4d \rightarrow 4f$ excitations (100-200 eV) in rare earth metals.

A further possible approach to the magnetization dynamics is the direct time-resolved imaging of the magnetic nanostructure. Various schemes can be envisioned to this purpose, combining pump-probe methods with photoelectron or X-ray fluorescence microscopy [136]. A possible experiment will consist of generating a short magnetic field pulse with a visible laser light, while a synchronized FEL pulse acts as a probe of the magnetic response. The detection of the photoelectron or X-ray fluorescence yield induced by the FEL pulse can be used to map the spatial distribution of the magnetization, and its ultrafast (fs-)time development following the magnetic-field pulse. While the spatial resolution achievable with synchrotron-radiation photoelectron microscopy is presently limited by the radiation flux to ca.10 nm (in static operation mode), the brilliance of a the FEL will allow to record an image with nm scale with a single radiation pulse. The systems of interest for these investigations include structurally complex materials, such as composite nanostructures for the spintronics, where the dynamics in both antiferromagnetic and ferromagnetic components could be followed by using linear and circular dichroism, respectively. The element specificity of the dichroic effects in X-ray absorption and emission will be able to separate the magnetic behavior of the chemical elements distributed within various functional nanocomponents. Magnetic microscopy operating with nm-resolution can address several other relevant issues, from the static and

dynamics of the magnetic structure within domain walls of thin films and surfaces, to slow magnetic fluctuations in the proximity of phase transitions.

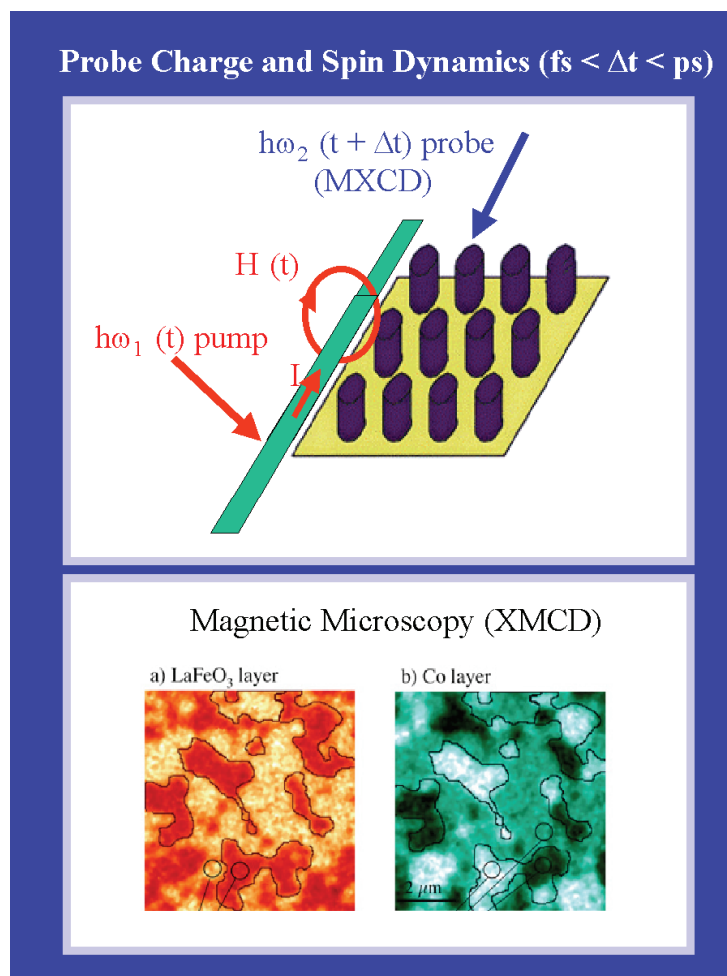


Figure 9.19

The increasing of the coherence and brilliance, together with the pulsed character, of the FEL radiation can bring to the full exploitation of other magnetic scattering techniques. The transverse and longitudinal coherence of the light allows precise phase relation between the light scattered by different domains. This phase relation is expressed in the scattered pattern in terms of "speckles" that are related to the domain distribution. Until now coherent scattering experiments are mainly domain of visible/near UV lasers. With the increasing of coherence in the light produced by undulators respect to the traditional bending magnets, it has been shown to be possible to investigate the effect of the coherence on the X-ray scattering [137]. The investigation scale of the scattering experiments is related to the wavelength. Moving towards the VUV/soft X-ray wavelength range the coherent scattering accesses to different characteristic lengths related with effects found in new class of materials. The soft X-ray wavelength is comparable to the size of nanostructured materials. The coherent soft X-ray scattering can enlighten the dynamic of magnetic domains, probe the interface effects in magnetic multilayers and nanostructures, put in evidence charge and orbital ordering

[138]. Moreover the soft X-rays are suitable for surface and near surface analysis because of the geometry less grazing than in the hard X-rays case, that need extended samples. The soft X-rays energy range includes the $2p \rightarrow 3d$ excitation of the transition metals, probing as final states the bands responsible for the magnetic properties. In the hard X-rays case the study of the magnetic properties is limited respectively to the $1s \rightarrow 3p$ and $2p \rightarrow 4d$ that are only indirectly involved in magnetism. Soft X-ray resonant magnetic scattering with polarized radiation represents another approach to the spin dynamics at surfaces and in nanostructures. The measurement of magnetic superstructures in the scattering of soft X-rays can probe the coherence of magnetically ordered structures with characteristic wave-vectors in the nanometer m-range [139]. Time-resolved scattering measurements would give a new way to access to the spin-dynamics of ordered array of magnetic dots, nanowires and stripes, as well as of surface domain structures.

The high brilliance of the FEL pulses can be exploited for investigation methods that are impossible or severely limited by photon brilliance of flux considerations at present synchrotron radiation sources. Circular polarized radiation from FEL pulses can give access to the magnetic dynamics and correlation of highly diluted impurity systems. Present detection limits in soft-X-ray absorption experiments are at concentration of $\text{ca. } 10^{12}/\text{cm}^2$ with electron yield measurements [140], and much lower (by about three order of magnitudes) for the soft-X-ray emission spectroscopy. Among the cases of high interest, which are hardly accessible with presently available methods, are the Kondo and heavy Fermion behavior of magnetic impurities, slow relaxation processes in spin glasses and amorphous magnetic metals, small (few atoms) clusters and molecular magnets, free and deposited on a surface. X-ray fluorescence detection methods appear most promising for many applications on diluted systems, as they permit with suitable energy filtering to effectively suppress the background signal from non-magnetic matrix hosts or other components.

The knowledge of the electronic structure in close proximity of the Fermi level is fundamental for understanding and properly engineering spin-dependent transport properties. The new emerging field of spintronics relies on the control of the spin-polarization of the carriers, rather than of their charge, for the information storage and transfer [141,142]. Spintronics devices consist typically of laterally patterned (on the submicron scale) film structures, integrating magnetic and semiconducting components. Among the potential applications of spintronics are non-volatile RAM nanoscale memories and spin transistors exploiting spin-dependent electron tunneling and scattering in thin magnetic films. Photoemission spectroscopy with analysis of the electron spin polarization is the most direct method in electronic-structure studies of magnetic materials, as it can determine all quantum numbers (E, k, σ) defining the electronic states. Complete (i.e. E -, k -, σ - resolved) photoemission experiments at third-generation synchrotron radiation sources are severely intensity-limited to an energy and momentum resolution of $\text{ca. } 50 \text{ meV}$ and 0.05 \AA^{-1} , respectively, due to the poor efficiency ($\text{ca. } 10^{-4}$) of all spin-polarization analyzers. The increase in average brilliance with a FEL source will allow to perform spin-resolved photoemission studies with energy resolution reaching 1 MeV and $\text{ca. } 0.01 \text{ \AA}^{-1}$ momentum resolution. The relevance of such a progress can be recognized from the role that spin-dependent low-energy excitations across the Fermi surface have for the polarized electron transport, for the magnetic reorientation driven by the magneto-crystalline anisotropy, and the coupling mechanism among nanomagnetic structures. Direct insights in the

electron relaxation processes can be achieved by pump and probe experiments, by measuring spin-resolved valence photoemission spectra with time resolution, following a visible laser pulse. In combination with magnetic dichroism experiments, these investigations will give a direct insight on the dynamics of electron and spin excitations in the ultrafast magnetic processes [143].

9.8.11 Nanoimaging

9.8.11.1 *Generalities*

The techniques and applications of X-ray microscopy have been the subject in the last year of a real revolution because of the novel features (in particular brilliance and spatial coherence) of the synchrotron radiation sources of third generation, both in the regions of medium and high energies. Among the most interesting results it is worth to remark the nanometric spatial resolution (30 nm for low energies X-rays and 100 nm for high energies [144,145]) and the development of novel techniques based on phase contrast. The fabrication of a free electron laser source of the SASE (Self Amplification Spontaneous Emission) type will bring to a similar breakthrough allowing the opening of novel research fields for the in-depth knowledge of matter (both biological and inert). In fact if from one side the brilliance and spatial coherence of the source SPARX will allow to improve the optics and measurement techniques already in use at the third generation synchrotron sources, its temporal features, based on the ultra-short pulses, will open a completely new direction of investigation also in the field of X-ray micro and nano-imaging.

9.8.11.2 *Optics*

In low energy X-ray microscopy (below 1 KeV) the most common optical elements are the Fresnel zone plates. They are made of concentric rings with alternating materials more or less transparent to X-rays. Through a diffraction effect, the incident beam is focalized in an extremely small region (few tens of nm).

The Fresnel lenses are currently used to fabricate both full field microscopes, and scanning microscopes. The present trend is from one side to improve spatial resolution, on the other to develop new concepts to improve the contrast, mainly in light materials as the biological ones. Concerning the improvement of spatial resolution, which in the soft X-ray region is of the order of 30 nm and is essentially limited by micro-fabrication, great interest has been raised by the development of zone plates modified by very small holes distributed among the rings [146]. The optics obtained in this way should reach a spatial resolution below 10 nm, but with relatively low efficiency. The use of sources with very high brilliance will allow to give enough fluxes, even with single pulses to obtain information with spatial resolution until now accessible only to electron microscopy techniques.

9.8.11.3 Phase Contrast

Another research theme deals with the optics and the techniques that allow to measure the spatial variations of the real part of the index of refraction instead than those of the imaginary part. In fact in the first case the phase of the wave front is concerned, while in the second the amplitude. Being the phase much more sensitive even to small variations of the index of refraction, it is possible to obtain a much stronger contrast. As a consequence X-ray optics and methodologies have been developed suitable to record phase contrast microradiographies. As an example recently have been fabricated interference contrast Fresnel zone plates with spatial resolutions of the order of $0.16\ \mu\text{m}$ which show, in PMMA structures, a contrast much stronger than that due exclusively to the absorption coefficient [147]. It is important to note that the improvement of the contrast allows to lower the absorbed dose, and therefore the damage in radiation sensitive biological materials.

Also other methodologies and special optics have been developed both in the low and the high energies to perform phase contrast micro-radiographies [148,149]. Since the beam spatial coherence is an essential requisite for this kind of techniques, they have been developed mainly in the synchrotron radiation sources. The SPARX source with its characteristics of coherence and brilliance, will allow an extensive use of the phase contrast techniques, improving their spatial resolution and efficiency, and adding at the same time the temporal dimension. In fact the ultra-short pulses will allow to follow the temporal evolution of complex phenomena both in biology and in material science on the time scale of picoseconds, a target presently unachievable with the present sources.

9.8.11.4 Spectromicroscopy

In spectromicroscopy the sharp variation of the absorption coefficient close to the absorption edge is exploited. Recording two images one just after the other at energies respectively slightly lower and higher than the edge (dual band imaging), and their mutual subtraction, it is possible to put in evidence only the presence of given elements [150].

Together with high spatial resolution this technique allows to accurately map the spatial distribution of the elements present in the sample. Even more interesting is the possibility to measure the valence state of a given element, due to the fact that the edge value is related to the valence state of the element. The SPARX source will allow to make this kind of analysis as a function of time, and therefore to follow the evolution of a chemical reaction or of a chemical-biological phenomenon both spatially and temporally.

See also ref [151].

9.8.12 Microradiology

9.8.12.1 Introduction

The advanced sources of X-rays are at the origin of a true revolution in the field of radiology, so for applications in materials science than for biological studies and, with every probability, for diagnostic uses [152,153,154]. The revolution has begun with the coming of sources of light type of synchrotron, and it will be definitely sped up by the arrival of the new pulsed SASE-FEL type sources.

The revolutionary character of the new radiological techniques can be understood on the basis of quite simple considerations [153,154]. Since the Röntgen discovery, radiology has been so long the principal area of application of the X-rays. The formation of images has always based on the different absorption of the X-rays in the various parts of the object. Pointing out that such absorption is very reduced is necessary: this property is at the same time the key for the success of the radiological techniques but also their principal limitation.

From one side, in fact, the low absorption allows radiology "to observe" the internal parts of the objects, including patients in diagnostic techniques. On the other side, however, this involves some differences limited in the absorption of various parts of the objects, and then to some contrast problems.

The problem is often resolved increasing the level of exposure and with it the signal. However this creates some serious problems: the dose of X-rays can damage the sample and, in the case of radiological diagnosis, it is simply unacceptable. The consequences are important also on the social plan. For instance, the precocious diagnosis of the breast cancer can today take to some very effective therapies – but unfortunately the systematic radiological diagnosis is still limited by the problems of contrast.

How to increase the contrast without increasing the dose? It is important to consider the interaction mechanism between X-rays and object in totality [153,154]. Excluding the absorption, the interaction mechanisms through the index of refraction of the material must be considered (or, more exactly, to the real part of the complex refraction index).

It is possible to imagine, for instance [154], a collimated beam of X-rays which reaches the border between two zones of the object with various refraction indexes. If the border is not of null width, the refraction takes to a local deviation of the beam which produces in the images some characteristics double fringes- and a very strong increase in the "visibility" of the border among the two zones. In an analogous way, the visibility of the borders can be increased by the mechanism, also bound to the refraction index, of the Fresnel border diffraction [153].

In principle, these types of interaction among X-rays and object can be more effective in producing contrast of the traditional mechanism bound to the absorption. In fact, the differences with respect to the vacuum of the indexes of refraction of the materials, though limited, are however comparatively bigger than the differences in the absorption. Such advantage is accentuated with the reduction of the wavelength.

A question could then rise: why, to beyond a century from the discovery of the X-rays, radiology is anyway principally based on the absorption? The answer is that the techniques related with the refraction index ask characteristics much advanced of the source of x-rays [153,154]. Specifically, the example mentioned above only works if the source emits a very much

collimated beam of X-rays, with low angular divergence. More in general, the mechanisms bound to the refraction index can be used only with high spatial coherent sources (the demands are more moderate as regards the time coherence) [153,154].

The conventional sources of X-rays offer a spatial coherence extremely limited: they are of big dimensions and produce divergent beams. These problems can be correct using some screens equipped with little holes. However the solution is not very effective, since it uses only a very little fraction of the X-rays emitted by the source (see dedicated paragraph).

9.8.12.2 Current programs

The true solution is provided by non-conventional sources such as the synchrotrons and, potentially, the FEL. Recently, some groups [153,154] in United States, Switzerland France, Germany Japan and other countries began experimental radiology not-conventional programs -- called generically (even if not completely corrected in way) "radiology with phase contrast". Italy is already to the vanguard in this field [153,154].

The results of these first programs are already very spectacular and have already passed the phase of development of the techniques. For example, Figure 9.18 shows a few images obtained in biological samples [155]. It is possible to notice the high contrast, obtained with very reduced doses of X-rays, typically 5-10 littler times than in the conventional radiology. The images of Figure 9.20 reveal also the exceptional level of lateral resolution of the new radiologies.

Simultaneously to the lateral resolution, radiology with phase contrast already reached a high level of time resolution which allows some analyses in real time of biological phenomena and in materials science. As shown in Figure 9.21, such technique can already be used in the real time study of living organisms (in the case at issue, a micro-ichthyic sample of the dimension of about 500 μm) [155].

The results are analogously spectacular in the field of materials science. It is possible to mention to such purpose the electrodeposition studies in real time and that of the fracture mechanisms in the leagues.

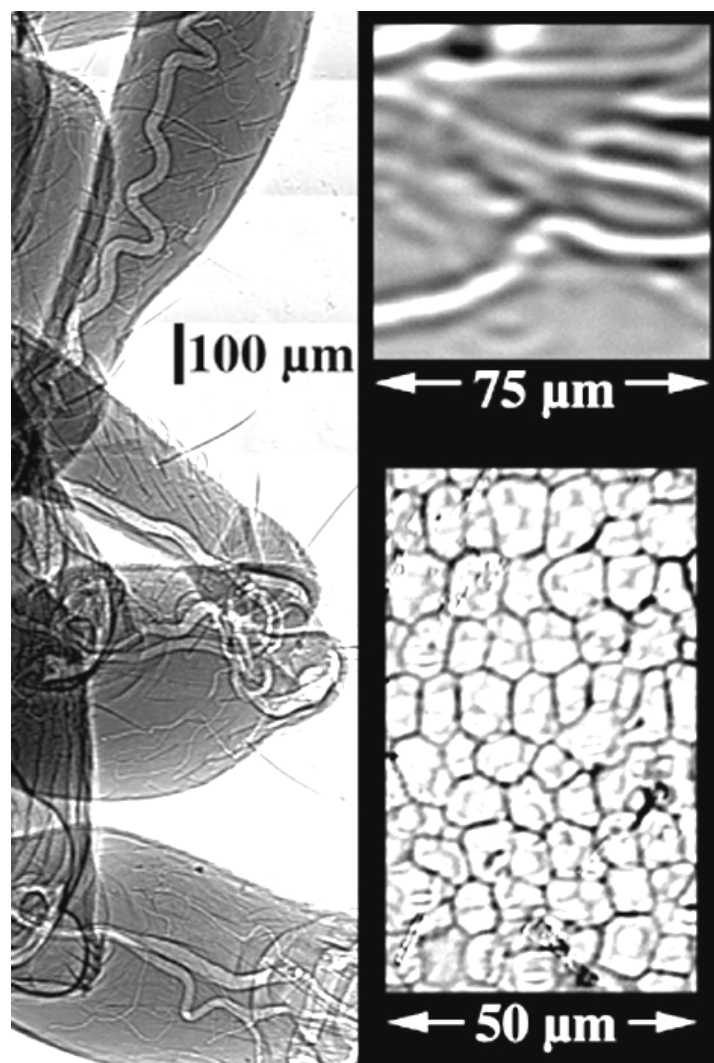


Figure 9.20: Examples of microradiology results with phase contrast. To left: image of an insect's leg, with (to right in high) a detail which shows the lateral resolution; right low: microradiography of a leaf [4].

Finally, it is worth pointing out the first attempts to use the new techniques in a tomographic way and, actually, tomographic images have already been obtained. The rebuilding problems present remarkable conceptual difficulties because of change in phase due to the interaction among X-rays and object. Therefore it is not possible to foresee all the future development of these lines: what is sure is that their potential applications are extremely important so in biology than in materials science and other fields like the archeometry or the study of artistic findings, historical and prehistoric.

Attempts [156] to obtain images in phase contrast in the regime of the anomalous diffusion, i.e., changing the wavelength in closeness of one of the thresholds of X-absorption of the constituents of the object. According to the Kramers-Krönig transformations, the quick change as a function of the wavelength of the absorption coefficient must correspond to quick changes of the refraction index. The corresponding modifications in the images could allow the analysis of the chemical constituents of the object on microscopic scale.

The first steps are very encouraging. Some effects were revealed and mostly justified on a theoretical base [156]. Therefore this new technique is likely to further increase the scientific impact of radiology with contrast by phase.

9.8.12.3 *The future: the SASE-FEL sources*

The new pulsed sources of this type will allow a further good quality jump in the non-conventional radiological techniques. An important element is the further increase in the spatial coherence at low wavelengths. On the other side, the most positive appearance is the very short duration time of the SASE-FEL pulses and their high energy.

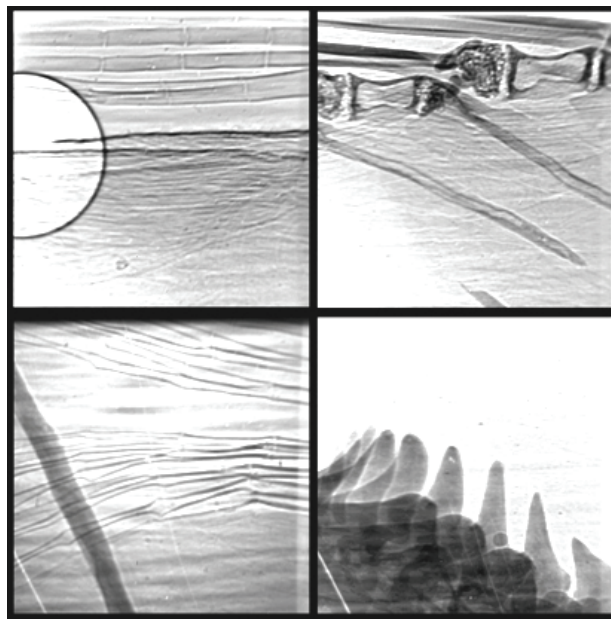


Figure 9.21: Microradiographies of details about a living fish of the dimension of about 0.5 mm [4].

These characteristics will take to non-conventional radiology experiments on time scales which are unreachable with the synchrotron sources. At the current state, the experiments in real time are led with scanning times of the order of a few milliseconds [153,154]. That allows the study of a long series of biological and chemical phenomena compatible with this time resolution - but excludes interesting phenomena on shorter scale.

The time resolution has not been optimized yet and could reasonably improve with today's sources, maybe 1-2 orders of magnitude. Further improvements would probably meet insurmountable obstacles. Such obstacles will be automatically eliminated from the SASE-FEL sources. Luckily, the time-coherence requests are, as already mentioned, quite limited [153,154], and also the use of very short pulses will not create problems.

Thanks to the possibility of accessing new time scales, the range of phenomena which will be able to be explored will be radically expanded. In the

scale from the microsecond at the nanosecond a series of important phenomena is in fact found in surface 'chemistry and, in general, material science. On lower time-scales, it is possible to assume the use of image formation techniques up to hundred of femtoseconds.

It is clear that the experimental strategies will have to be completely modified. In fact, the energy deposited by every single pulse will produce, with every probability, modifications on microscopic scale of the object. It will be needed to explore some techniques of image-acquisition in real time in which the damaging is not minimized but studied in its evolution.

This type of "one shot" strategy is not only important as measure technique but also as an intrinsic study. The problems of the damaging from radiation in regime of very high intensity on very short pulses is in fact all to explore, and the discoveries could be very important. For instance, the damaging processes could reveal positive and usable appearances for the industrial chemistry.

Finally, it is worth pointing out that the SASE-FEL sources will have a importing role also in other advanced radiology forms not with phase contrast. For instance, the digital radiology techniques at many wavelengths and digitally subtracted will be able to be implemented on very short time scale, while the tomographic techniques will take advantage of the improved characteristic of the source. Besides, it will be possible to acquire in short times a big number of tomographic images.

Adding this to the methodologies with phase contrast, these other techniques provide a further guarantee for a revolutionary impact of the SASE-FEL in radiology.

9.8.13 Nanolithography

The low energy beamline of the SPARX source, providing photons with wavelength between 10nm and 15nm, shows interesting features for nanolithography studies in the Extremely far Ultra-Violet (EUVL) range. The EUVL represents nowadays one of the most promising techniques in order to achieve a spatial resolution better than 70 nm [157,158,159]. In this kind of lithography, the chip circuit design on a Silicon wafer is obtained by projecting a mask by means of a suitable optical system. The wavelengths between 13 and 14 nm are the only region in the EUV range which can be used to build mirrors having a reflectivity of about 70%, suitable for industrial applications. It is just the short wavelength of the radiation used that makes possible to project the mask pattern on the wafer with a spatial resolution better than 70 nm, as it was demonstrated in preliminary experiments. Several consortiums have been started all over the world which are devoted to EUVL research, and the equivalent of hundred millions Euro have been invested in each of them. In particular, we want to cite:

- USA: industrial consortium. LLC (Motorola, Intel, AMD, Infineon, micron) + consortium of VNL research corporations (National laboratories Sandia, Berkeley and Livermore).
- Japan: ASET (Nikon) and CANON project.
- Europe: industrial consortium. MEDEA-plus (ASML, Philips, Zeiss, etc.) + European project EUNETE in submission phase (in February 2002).

Each of these three consortiums has the goal, to produce independently within 2006 a device based on EUV plasma-laser sources for manufacturing

microchips (stepper) using EUVL technology. The “roadmap” for microlithography in the development of semiconductor devices is shown in Figure 9.22.

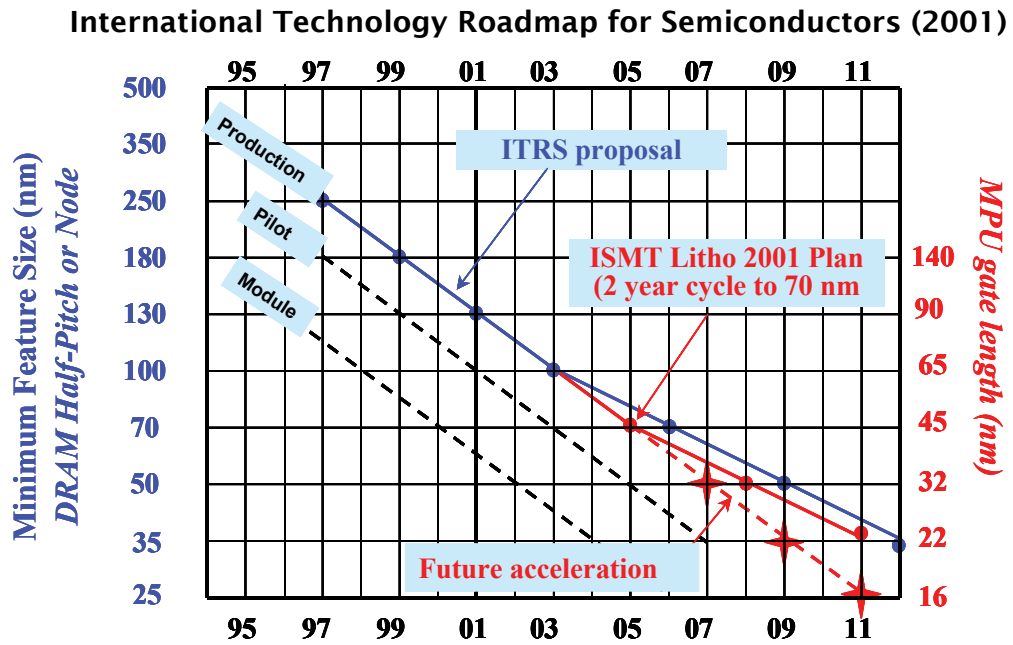


Figure 9.22: It is foreseen that the optical lithography will be used beyond 100 nm and 70 nm (DRAM Half-Pitch) by devices operating at the wavelength of 193 and 157 nm respectively. Details of 50 nm and 35 nm will require to use next generation devices, Next Generation Lithography (NGL). The candidate technology for this goal in the European programs MEDEA-plus and IST is the EUV lithography.

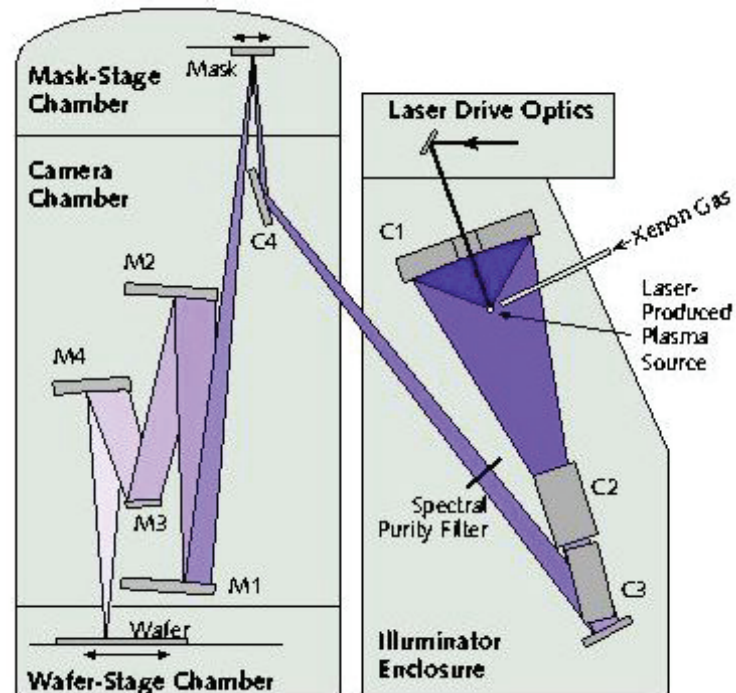


Figure 9.23: Device for the EUV micro-lithography (α -tool) developed by the American consortium LLC+VNL. The condenser mirror, C1, collects the EUV radiation over an angle of 1.8 sr. The C2 and C3 mirrors transform the beam in the ring-field geometry. The projection mirrors M1, M2, M3 and M4 project the mask image on the wafer with a 1:4 reduction. The α -tool is broken up into 4 separated chambers (source, mask, projection optics, wafer) so that the pollution produced by each chamber, i.e. the plasma-laser debris, the translation system residuals, the carbon outgassed by the steel walls and the molecules outgassed by the wafer photo resist respectively, is not diffused into the others.

In Figure 9.23 we show an outline of the aforesaid α -tool taken from [157], while in Figure 9.24 the reflectivity curve is reported relative to the best multilayer mirrors realized up to now in the EUV [160]. By using plasma-laser sources, i. e. wide emission spectrum ones, the 13.5 nm wavelength was universally acknowledged as the best for EUVL (based on the multilayer Mo/Si mirrors), as for this wavelength one obtains the optimized value for the integrated reflectivity (also known as system throughput) of the system, defined as $\int R^N(\lambda)d\lambda$, where $R(l)$ is the single mirror reflectivity and N is the whole number of mirrors in the optical system from the source to the wafer, including the mask. The use of a monochromatic source could change this choice, as pointed out in Figure 9.24, since in this case the peak reflectivity becomes more important than the integrated one.

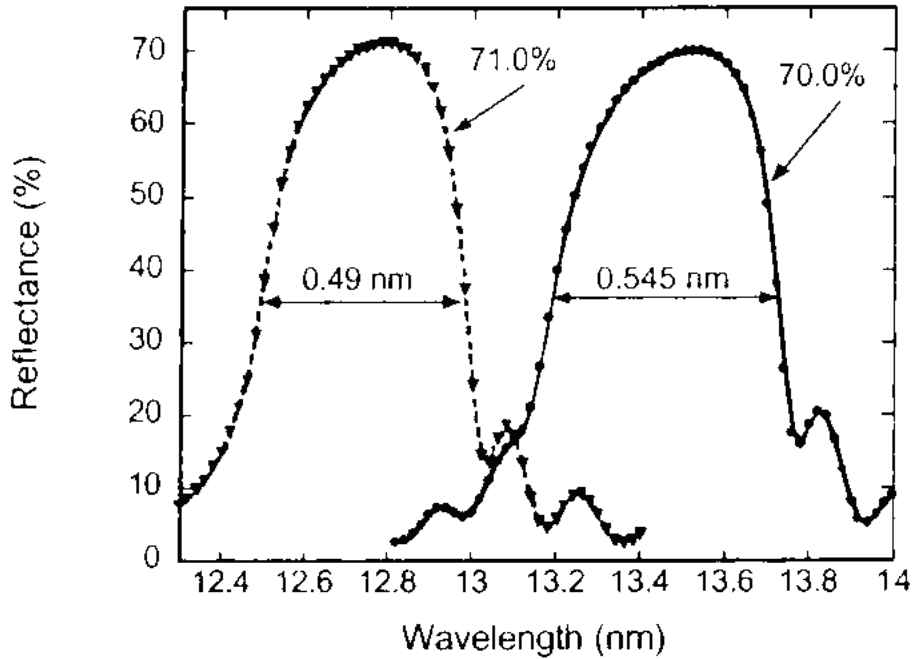


Figure 9.24: Reflectivity curve as measured on Mo/Si multilayer mirrors built according to ref. [7] and optimized in order to reflect at 12.8 and 13.5 nm. Between the Mo and Si layers (50 total periods) an insulating B4C layer (a few Ångstrom thick) was deposited to avoid diffusion problems. The lower reflectivity at 13.5 nm compared with the one at 12.8 nm is largely compensated by a wider bandwidth. This is important for wide-spectrum EUV sources such as the plasma-lasers.

The industrial applications of the EUV lithography require source features not presently obtained with the plasma-laser sources, but potentially achieved by a FEL-type source. In particular one requires (according to the European MEDEA+ consortium directions):

- Average power: 50-150 W in 2.2% bandwidth @ 13.5 nm, corresponding to the exposition of about 60 wafer-layer per hour
- Dose fluctuation per layer: < 2%
- Repetition frequency: >5 Hz
- Etendue: 0.4 - 0.8 mm²·sr
- Lifetime: 10¹¹ shots (one year @ 5 kHz)

Moreover the EUV source of the plasma-laser type (that are the most powerful available up to now) are necessarily debris emitters, namely metal clusters and single atoms coming from the target where the plasma is generated or from mechanical components (such as the nozzle from which the Xe vapor jet is emitted [161]) located close to the target. These fragments seriously limit the lifetime of the most delicate and expensive multilayer optical elements; in particular the lifetime of the first mirror (the so-called condenser), which must collect the EUV radiation from the source and send it to the mask, is affected.

The SPARX performance calculated for the low energy beamline allow the achievement of average power levels, emitted in the EUV at 12-14 nm, close to 50 W. These performance can be reached operating the photocathode laser in a

setup which implies a 35 pulses train with a mode-locking frequency of 100 MHz, repeated with a frequency of 100 Hz. In this configuration, the source is seen as a high performance device for pilot experiments on EUVL components and systems, which may also lead to the development of a dedicated source with suitable size and cost [162]. Such a source, moreover, would remove the debris problem, among the most important in the present development of stepper prototypes for the EUV lithography based on plasma-lasers.

Finally, the high monochromatization of an EUV laser beam would drastically reduce the problems of thermal overload and photoablation of the condenser mirror by the “out of band” radiation, i.e. the useless radiation emitted by the plasma-laser sources outside the reflectivity band of the mirrors.

The research to be performed in the EUVL field will be articulated in several directions:

- 1) Study and test of a diffusion optical device which leads the EUV beam emitted by the FEL to a ring-field geometry and with a power density tolerable by the Mo/Si multilayer mirrors for radiation in the 12-13 nm range.
- 2) Test of nanolithographic photoreproductions on wafers, obtained from the monochromatic radiation (12-14 nm) of the FEL laser.
- 3) Evaluation of the advantages/disadvantages of the illumination of an EUV stepper by FEL radiation compared to the incoherent illumination by plasma-laser sources.
- 4) Feasibility studies of a FEL laser optimized for the industrial applications of EUV lithography.

In particular, points 2) and 3) will be run in collaboration with international research laboratories on EUVL and with one of the main microelectronics firms located in Europe (e.g. ST - Microelectronics in Milan).

9.9 References:

- [1] H.N. Chapman et al., *Nature Phys.*, 2, 839 (2006)
- [2] D. Sayre, *Acta Cryst.*, 5, 843 (1952)
- [3] J. Miao et al., *Nature* 400, 342 (1999)
- [4] H. M. Quiney, K. A. Nugent and A. G. Peele, *Opt. Lett.* 30 1638 (2005).
- [5] X. Xiao and Q. Shen.. *Phys Rev. B* 72, 033103 (2005).
- [6] H. M. Quiney, A. G. Peele, Z. Cai, D. Paterson, and K. A. Nugent, *Nature Physics* 2 101 (2006); G. J. Williams, H. M. Quiney, B. B. Dhal, C. Q. Tran, K. A. Nugent, A. G. Peele, D. Paterson, and M. D. de Jonge, *Phys. Rev. Lett.* 97, 025506 (2006); G. J. Williams, H. M. Quiney, B. B. Dhal, C. Q. Tran, A. G. Peele, K. A. Nugent, M. D. de Jonge and D. Paterson, *Thin Solid Films* 515, 5553 (2006).
- [7] L. De Caro, C. Giannini, A. Cedola, D. Pelliccia, S. Lagomarsino, and W. Jark, *Appl. Phys. Lett.* 90, 041105 (2007).
- [8] L. De Caro, C. Giannini, D. Pelliccia, C. Mocuta, T. H. Metzger, A. Gagliardi, A. Cedola, I. Burkeeva and S. Lagomarsino, *Phys. Rev. B* 77-R 081408 (2008).
- [9] B. Abbey et al., *Nature Phys.* 4, 384 (2008)
- [10] Rodenburg et al., *Phys. Rev. Lett.*, 98, 034801 (2007)
- [11] G. Huldt et al., *Journal of Structural Biology* 144 219 (2003)
- [12] arXiv:physics/0502059v1
- [13] Neutze et al., *Nature*, 406, 752 (2000)
- [14] S.P. Hau-Riege, *Phys. Rev. E* 71, 061919 (2005)
- [15] S.P. Hau-Riege, *Phys. Rev. Lett.* 98, 198302 (2007)
- [16] C. Fuhse et al., *Phys. Rev. Lett.*, 97, 254801 (2006)
- [17] <http://www.spring8.or.jp/wkg/BL29XU/solution/lang-en/SOL-0000000973>
- [18] O. Hignette et al., *ESRF highlights*, p. 108 (2005)
- [19] I. Bukreeva, A. Popov, D. Pelliccia, A. Cedola, S. Dabagov and S. Lagomarsino, *Phys. Rev. Lett.* 97, 184801 (2006).
- [20] C. Bergemann, et al., *Phys. Rev. Lett.* 91, 204801 (2003).
- [21] D. Pelliccia et al., *Applied Optics* 45, 1-7, (2006).
- [22] S. Di Fonzo, W. Jark, S. Lagomarsino, C. Giannini, L. De Caro, A. Cedola and M. Müller, *Nature* 403, 638 (2000).
- [23] C. Fuhse et al., *Phys. Rev. Lett.*, 97, 254801 (2006)
- [24] L. De Caro et al., *Phys. Rev. B* 77-R 081408 (2008).
- [25] L. De Caro et al., *Appl. Phys. Lett.* 90, 041105 (2007)
- [26] W. Chao et al., *Nature*, 435, 1210 (2005)
- [27] A. Erko et al., ch. 28 in «Modern developments of x-ray and neutron optics », A. Erko et al eds, Springer Series in optical sciences- Berlin (2008)
- [28] M. Capitelli, C. M. Ferreira, B. F. Gordiets and N. Osipov “Plasma kinetics in atmospheric gases” Springer Verlag 2000
- [29] M. Capitelli, G. Colonna, A. Gicquel, C. Gorse, K. Hassouni, and S. Longo: “Maxwell and non-Maxwell behavior of electron energy distribution function under expanding plasma jet conditions: the role of electron-electron, electron-ion and superelastic electronic collisions under stationary and time-dependent conditions”, *Phys. Rev. E* 54,1843 (1996).
- [30] S. Longo: “Monte Carlo Models of Electron and Ion Transport in Non Equilibrium Plasmas”, *Plasma Sources Science and Tech.* 9, 468 (2000).

- [31] S. Longo, L. D. Pietanza, F. A. Tassielli and M. Capitelli “Non-equilibrium electron energy distribution function in Au under sub-picosecond laser irradiation: a kinetic study”, *Laser and Particle Beams* (2002) in press
- [32] G. Colonna, L. D. Pietanza and M. Capitelli: “Coupled solution of a time-dependent collisional radiative model and Boltzmann equation for atomic hydrogen plasmas: possible implications with LIBS plasmas”, *Spectrochimica Acta Part B* 56, 587 (2001); G. J. Pert: “The calculation of the electron distribution function following tunneling ionization using a Fokker-Planck method”, *J. Phys. B* 34, 881 (2001)
- [33] S. Longo: “Stochastic models for the kinetics of ensembles of two level systems”, *Physics Letters A* 267, 117 (2000); S. Longo, D. Bruno, M. Capitelli, P. Minelli: “A Monte Carlo model for the non-equilibrium coherent kinetics of ensembles of two level systems”, *Chemical Physics Letters* 320, 311 (2000).
- [34] S. Longo, D. Bruno, P. Minelli: “Direct simulation of non-linear inter-particle relaxation of ensembles of two level systems”, *Chem. Phys.* 256, 265 (2000).
- [35] S. Longo, D. Bruno: “Models for gas-phase coherent kinetics including correlations with flow quantities”, *Chemical Physics* 264, 211 (2001).
- [36] G. Colonna, A. Casavola and M. Capitelli: “Modeling of LIBS plasma expansion”, *Spectrochimica Acta Part B* 56, 567 (2001).
- [37] R. Celiberto, R. K. Janev, A. Laricchiuta, M. Capitelli, J. M. Wadehra and D. E. Atems, *Atomic Data and Nuclear Data Tables* 77, 1 (2001).
- [38] A. Laricchiuta, R. Celiberto, M. Capitelli, *Chem. Phys. Lett.* 329, 526 (2000).
- [39] R. Celiberto, A. Laricchiuta, U. T. Lamanna, R. K. Janev, and M. Capitelli, *Phys. Rev. A* 60, 2091 (1999).
- [40] F. Esposito, M. Capitelli, E. V. Kustova, E. A. Nagnibeda, *Chem. Phys. Lett.* 330, 207 (2000).
- [41] F. Esposito, C. Gorse, M. Capitelli, *Chem. Phys. Lett.* 303, 636 (1999).
- [42] V. V. Eryomin, I. M. Umanskii, N. E. Kuz'menko, *Chem. Phys. Lett.* 316, 303 (2000).
- [43] S. Meyer, M. Schmitt, A. Materny, W. Kiefer, V. Engel, *Chem. Phys. Lett.* 301, 248 (1999).
- [44] H. Schwoerer, R. Pausch, M. Heid, W. Kiefer, *Chem. Phys. Lett.* 285, 240 (1998).
- [45] J. T. Costello *J. Phys. Conf. Ser.* 88 (2007) 012057
- [46] T. Sato et al. *Appl. Phys. Lett.* 92 (2008) 154103
- [47] P.R. Blazewicz, J.A.D. Stocdale, J. C. Miller, T. Efthimiopoulos and C. Fotakis *Phys.Rev.* A35 (1987) 1092
- [48] S. A. Novikov and A. N. Hopersky *J. Phys. B:At. Mol. Opt. Phys.* 33 (2000) 2294
- [49] A. A. Sorokin et al. *Phys.Rev.* A75 (2007) 033411, 051402®
- [50] T. Okino et al. *Chem. Phys. Lett.* 432 (2006) 68
- [51] L. Vegh and J. H. Macek *Phys. Rev.* A50 (1994) 4031; L. Vegh *Phys. Rev.* A50 (1994) 4036
- [52] S.A. Sheinermann and V. Schmidt *J. Phys. B: At. Mol. Opt. Phys.* 32 (1999) 5205
- [53] N. Scherer, H. Lörch, T. Kerkau and V. Schmidt *Phys. Rev. Lett.* 82 (1999) 4615

-
- [54] S. Rioual, B. Rouvellou, L. Avaldi, G. Battera, R. Camilloni, G. Stefani and G. Turri Phys. Rev.Lett. 86(2001) 1470
- [55] J. Viefhaus, G. Snell, R. Hentges, M. Wiedenhöft, F. Heiser, O. Gessner and U. Becker Phys.Rev. Lett. 80 (1998) 1618
- [56] S. Rioual, B. Rouvellou, L. Avaldi, G. Battera, R. Camilloni, G. Stefani and G. Turri Phys. Rev. A61 (2000) 044702
- [57] L’Huillier A, L’Lompre A, Mainfray G and Manus C Phys. Rev. A 27 (1983) 2503
- [58] P. B. Corkum Phys. Rev. Lett. 71 (1993) 1994
- [59] D. N. Fittinghoff , P.R. Bolton, B. Chang and K.C. Kulander Phys. Rev. Lett. 69 (1992) 2642
- [60] Th. Weber et al. Nature 405 (2000) 658
- [61] B. Feuerstein et al Phys. Rev. Lett. 87 (2001) 43003
- [62] M. Weckenbrock et al. J. Phys. B: At. Mol. Opt. Phys. 34 (2001) L449
- [63] L.A.A. Nikolopoulos and P. Lambropoulos J. Phys.B40 (2007) 1347
- [64] I.A. Ivanov and A.S. Kheifets Phys. Rev. A75 (2007) 033411
- [65] Y. Nabekawa et al. Phys. Rev. Lett. 94 (2005) 04301
- [66] R. Moshhammer et al. Phys. Rev. Lett. 98 (2007) 203001
- [67] L. Avaldi and A. Huetz J. Phys. B: At. Mol. Opt. Phys. 38 (2005) S861
- [68] J S Parker , L R Moore , K J Meharg , D Dundas and K T Taylor J. Phys. B: At. Mol. Opt. Phys. 34 (2001) L69
- [69] P. Agostini, F. Fabre, G. Mainfroy, G. Petite and N.K. Rahman Phys. Rev. Lett. 42 (1979) 1127
- [70] R.R. Blyth et al. J. Electron Spectrosc. Relat. Phenom. 101-103 (1999) 959
- [71] M. Gisselbrecht and A. Huetz, M. Lavollée, T. J. Reddish and D. P. Seecombe Rev. Sc. Instr. 76 (2005) 013105
- [72] A. Rudenko et al. J. Phys. B : At. Mol. Opt. Phys. 41 (2008) 081006
- [73] O. Herrwerth et al. New J. Phys. 10 (2008) 025007
- [74] C. Cornaggia et al. Phys. Rev. A62 (2000) 023403
- [75] T. Osipov et al. Phys. Rev. Lett. 90 (2003) 233002
- [76] G. Alberti et al. Rev. Sci. Instr. 76 (2005) 073101
- [77] P. Jaegle', Coherent Sources of XUV Radiation (Springer, Berlin, 2006)
- [78] G.A.Reider and T.F.Heinz in "Photonic probes of surfaces" , Ed. P. Halevi, Elsevier (Amsterdam) 1995, and references there in
- [79] A.Kirilyuk, J.Phys. D.35, R189 (2002)
- [80] M. Goepfert-Mayer, Ann. Physik 9, 273 (1931)
- [81] M. Dagenais et al, Phys. Rev. Letters 46, 561 (1981)
- [82] J. Stohr "Nexafs Spectroscopy", Springer (Berlin) 1996
- [83] T. Feuerer et al, Science 299, 374-377 (2003)
- [84] S. Nannarone et al., AIP Conf. Proc. 705, 450 (2004)
- [85] L. Pasquali et al, AIP Conf. Proc. 705, 1142 (2004)
- [86] B.J. Berne "Dynamic Light Scattering With Applications" John Wiley&Sons, New York, 1976
- [87] A.C. Price, L.B. Sorensen, S.D. Kevan, J. Toner, A. Poniewierski and R. Holsty, Phys. Rev. Lett. 82, 755 (1999)
- [88] G. Grübel, D. Abernathy, T. Thurn-Albrecht, W. Steffen, A. Patkowski, G. Meier and E.W. Fischer, ESRF Newsletter July (1996)
- [89] J. F. Peters, M.A. De Vries, J. Miguel, O. Toulemonde and J.B. Goedkoop, ESRF Newsletter October (2000)
- [90] V. Kataev, B. Rameev, B. Buchner, M. Hucker and R. Borwski, Phys Rev. B 55, R3394 (1997)

- [91] H.A. Mook, D. Pengcheng, F. Dogan and R. D. Hunt, *Nature* 404, 729 (2000)
- [92] J.M. Tranquada, B.J. Sternlieb, J.D. Axe, Y. Nakamura and S. Uchida, *Nature* 375, 561 (1995)
- [93] J. Arthur, Proc. of the workshop "Perspectives of X-ray Photon Correlation Spectroscopy" June 1996 ESRF, Grenoble.
- [94] B. Adams, *Nucl. Instr. Meth. A* 459, 339 (2001)
- [95] A.L. Shluger and A.M. Stoneham, *J. Phys. Condens. Matter* 5, 3049 (1993).
- [96] N.-H. Ge, et al. *Science* 279, 202 (1998).
- [97] Lora Nugent-Glandorf et al., *Phys. Rev. Lett.* 87, 193002 (2001).
- [98] J. Bokor, R. Haight, R. H. Storz, J. Stark, R. R. Freeman, and P. H. Bucksbaum, *Phys. Rev. B* 32, 3669-3675 (1985)
- [99] S. Jeong and J. Bokor, *Phys. Rev. B* 59, 4943-4951 (1999).
- [100] Y. Ma, *Phys. Rev. B* 49, 5799 (1994); Y. Ma, N. Wassdahl, P. Skytt, J. Guo, J. Nordgren, P.D. Johnson, J.E. Rubensson, T. Boske, W. Eberhardt, S. D. Kevan, *Phys. Rev. Lett.* 69, 2598 (1992); S. Eisebitt, J. Luning, J. E. Rubensson, A. Karl, W. Eberhardt, *Phys. Stat. Sol. B* 215, 803 (1999)
- [101] T. Valla et al. *Science* 285, 2110 (1999)
- [102] Z.J. Zhou et al. *Science* 286, 268 (1999)
- [103] Jairo Sinova, John Schliemann, Alvaro S. Nunez, *Phys. Rev. Lett.* 87, 226802 (2001)
- [104] Franck-J. Meyer zu Heringdorf, M.C. Reuter and R.M. Tromp, *Nature* 412, 517 (2001)
- [105] Schön et al., *Nature* 413, 713 (2001); Schön et al., *Nature* 414, 470 (2001)
- [106] M.A. Reed, C. Zhou, C.J. Muller, T.P. Burgin, J.M. Tour, *Science* 278, 252 (1997)
- [107] M. Di Ventura, S.T. Pantelides, N.D. Lang, *Appl. Phys. Lett.* 76, 3448 (2000)
- [108] Vasiliu-Doloc L. et al, *PRL* 83, 4393 (1999)
- [109] Shimomura S. et al, *PRL* 83, 4389 (1999)
- [110] Sandre E. et al, *PRL* 86, 5100 (2001)
- [111] Perfetti L. et al, *PRL* 87, 216404 (2001)
- [112] Ch. Ziethen et al. *J. El. Sp. Rel. Phen.* 88-91, 983 (1998)
- [113] T. Warwick et al. *J. El. Sp. Rel. Phen.* 84, 85 (1997)
- [114] G. De Stasio et al. *Phys. Rev. E* 47, 2117 (1993)
- [115] G. De Stasio et al. *Rev. Sci. Instrum.* 69, 2062 (1998)
- [116] Ch. Ziethen et al. *J. El. Sp. Rel. Phen.* 107, 261 (2000)
- [117] Y. Imamoto, K. Mihara, F. Tokunaga and M. Kataoka, *Biochemistry* 40, 14336 (2001)
- [118] E. K. Wilson, A. Bellelli, F. Cutruzzola, W. G. Zumft, A. Gutierrez and N. S. Scrutton, *Biochem J.* 356, 39 (2001)
- [119] V. E. Prusakof, R. A Stukan., R. M. Davidov and K. Gersonde, *FEBS* 2673, 158 (1985).
- [120] V. Le Tilly, S. Pin, B. Hickel and B. Alpert, *J. Am. Chem. Soc.* 119, 10810 (1997)
- [121] P. Caprari, A. Scuteri, A.M. Salvati, C. Bauco, A. Cantafora, R. Masella, D. Modesti, A. Tarzia and V. Marigliano, *Exp Gerontol.* 34, 47 (1999)
- [122] M. Girasole, A. Congiu-Castellano, A. Arcovito, G. Amiconi and A. Cricenti, In "Epioptics 2000", proceedings of 19th course of the international school of solid state physics (Ed. A. Cricenti). World Scientific Publisher - Singapore. Pg. 52-63

- [123]R. Rossi, D. Barra, A. Bellelli, G. Boumis, S. Canofeni, P. Di Simplicio, L. Pascarella and G. Amiconi, *J. Biol. Chem.* 273, 19198 (1998)
- [124]G. Schneider, *Ultramicroscopy* 75, 85 (1998)
- [125]R. Neutze, R. Wouts, D. van der Spoel, E. Weckert, and J. Hajdu, *Nature* 406, 752 (2000)
- [126]P. Gruenberg, *Physics Today*, (2001).
- [127]Gary A. Prinz, *Science* 282, 1660 (1998).
- [128]F. J. Himpsel, J.E. Ortega, G.J. Mankey, & R.F. Willis, *Advan. Phys.* 47, 511 (1998).
- [129]B.T. Thole, P. Carra, F. Sette, G. van der Laan, *Phys. Rev. Lett.* 68, 1943 (1992).
- [130]P. Carra, B.T. Thole, M. Altarelli, X. Wang, *Phys. Rev. Lett.* 70, 694 (1993).
- [131]F. Nolting, et al. *Nature*, 405, 767 (2000).
- [132]H. A. Dürr, G. Y. Guo, G. van der Laan, J. Lee, G. Lauhoff, J. A.C. Bland, *Science* 277, 213 (1997).
- [133]E. Beaupaire, J. C. Merle, A. Daunois, and J. Y. Bigot, *Phys. Rev. Lett.* 76, 4250 (1996).
- [134]A. Scholl, L. Baumgarten, R. Jacquemin, W. Eberhardt, *Phys. Rev. Lett.* 79, 5146 (1997).
- [135]C. H Back, D. Weller, J. Heidmann, D. Mauri, D. Guarisco, E. L. Garwin, H. C. Siegmann, *Phys. Rev. Lett.* 81, 3251 (1998).
- [136]A. Scholl, J. Stöhr, J. Luning, W. Seo, J. Fompernyne, H. Siegwart, J. P. Locquet, F. Nolting, S. Anders, E. E. Fullerton, M. R. Scheinfein, H. A. Padmore, *Science* 287, 1015 (2000).
- [137]S. Eisebit, A. Karl, R. Scherer, W. Eberhardt, M. Adamcyk, T. Tiedje, C. Pistonesi, *Synchrotron Radiation News*, 11, N.5, (1998).
- [138]C. W. M. Castleton, M. Altarelli, *Phys. Rev. B*, 62, 1033 (2000).
- [139]H. A. Dürr, E. Dudzik, S. S. Dhesi, J. B. Goedkoop. G. van der Laan, M. Belakhovsky, C. Mocuta, A. Marty, Y. Samson, *Science* 284, 2166 (1999).
- [140]P. Gambardella, S. S. Dhesi, S. Gardonio, C. Grazioli, P. Ohresser, C. Carbone, *Phys. Rev. Lett.* 88, 047202 (2002).
- [141]B. Binasch, P.Grünberg, F. Sauerbach, and W. Zinn, *Phys. Rev. B* 39,4828 (1989).Baibich, J. M. Broto, A. Fert, F. Nguyen van Dau, F. Petroff, P. Etienne, G. Creuzet, A. Friedrich, and J. Chazelas, *Phys. Rev. Lett.* 61, 2471 (1988).
- [142]H. Ohno, *Science*, 281, 951 (1998); Y. Ohno, D. K. Young, B. Beschoten, F; Matsukura, H. Ohno & D. D. Awschalom, *Nature* 402, 79 (1999).
- [143]K. Maiti, C. Malagoli, E. Magnano, A. Dallmeyer, C. Carbone, *Phys. Rev. Lett.* 86, 2846 (2001).
- [144]J. Thieme et al., eds. "X-ray microscopy and spectromicroscopy" (Springer, Berlin, 1998)
- [145]S. Di Fonzo et al., *Nature*, 403, 638 (2000)
- [146]L. Kipp et al., *Nature* 414, 184 (2001)
- [147]T. Wilhein et al., *Appl. Phys. Lett.* 78, 2082 (2001)
- [148]S. Lagomarsino et al., *Appl. Phys. Lett.* 71, 2557 (1997)
- [149]F. Arfelli et al., *Phys. Med. Biol.* 43, 2845 (1998)
- [150]Ade et al., *Science* 258, 972 (1992)
- [151]G. R. Harp, *Phys. Rev. B* 42, 9199 (1990)
- [152]F. Arfelli, M. Assante, V. Bonvicini, A. Bravin, G. Cantatore, E. Castelli, L. Dalla Palma, M. Di Michiel, R. Longo, A. Olivo, S. Pani, D. Pontoni, P. Poropat, P. Prest, A. Rashevsky, G. Tromba, A. Vacchi, E. Vallazza, F.

- Zanconati, *Physics Medicine and Biology* 43 2845 (1998); F. Arfelli, V. Bonvicini, A. Bravin, G. Cantatore, E. Castelli, L. Dalla Palma, M. Di Michiel, M. Fabrizioli, R. Longo, R. H. Menk, A. Olivo, S. Pani, D. Pontoni, P. Poropat, M. Prest, A. Rashevsky, M. Ratti, L. Rigon, G. Tromba, A. Vacchi, E. Vallazza, F. Zanconati, *Radiology* 215 286 (2000); A. Snigirev, I. Snigireva, A. Suvorov, M. Kocsis, V. Kohn, *ESRF Newsletters* 24, 23 (1995); D. Chapman, W. Thomlinson, R. E. Johnston, D. Washburn, E. Pisano, N. Gmur, Z. Zhong, R. Menk, F. Arfelli, D. Sayers, *Phys. Med. Biol.* 42, 2015 (1997); A. Pogany, D. Gao, S. W. Wilkins, *Rev. Sci. Instrum.* 68, 2774 (1997); S. W. Wilkins, T. E. Gureyev, D. Gao, A. Pogany, A. W. Stevenson, *Nature* 384, 335 (1996); K. A. Nugent, T. E. Gureyev, D. F. Cookson, D. Paganin, Z. Barnea, *Phys. Rev. Lett.* 77, 2961 (1996); D. Chapman, W. Thomlinson, R. E. Johnston, D. Washburn, E. Pisano, N. Gmur, Z. Zhong, R. Menk, F. Arfelli, D. Sayers, *Physics in Medicine and Biology* 42, 2015 (1997)
- [153] G. Margaritondo, G. Tromba, *J. Appl. Phys.* 85, 3406 (1999)
- [154] Y. Hwu, H. H. Hsieh, M. J. Lu, W. L. Tsai, H. M. Lin, W. C. Goh, B. Lai, J. H. Je, C. K. Kim, D. Y. Noh, H. S. Youn, G. Tromba, G. J. Margaritondo, *Appl. Phys.* 86, 4613 (1999); G. Margaritondo, *Physics World* 11 28 (1998)
- [155] Y. Hwu, W. L. Tsai, T. H. Hwang., B. Lai, D. Mancini, D. Y. Noh, J. H. Je, H. S. Youn, M. Bertolo, G. Tromba, G. Margaritondo, unpublished.
- [156] A. Groso, G. Margaritondo, Y. Hwu, W. L. Tsai, J. H. Je, B. Lai, *Surf. Rev. Lett.* (in press).
- [157] Keit Diefendorff: "Extreme Lithography: INTEL backs EUV for Next-Generation Lithography", *Microprocessor Report*, 6/19/2000 (www.MPRonline.com).
- [158] David Attwood: "Soft X-rays and extreme ultraviolet radiation: principles and applications", Cambridge University Press, 1999.
- [159] R. H. Stulen and D. W. Sweeney: "Extreme ultraviolet lithography", *IEE Journal of Quantum Electronics* 35, 694 (1999).
- [160] Saša Bjt et al.: "Improved reflectance and stability of Mo/Si multilayers", *Contr. To the Int. Conf. San Diego July 2001*, SPIE 4506, (2001).
- [161] G. D. Kubiak et al., "High-power source and illumination system for extreme ultraviolet lithography", *Proc. SPIE* 3767, 136 (1999).
- [162] D. Dattoli, A. Doria, G. P. Gallerano, L. Giannessi, K. Hesch, H. Moser, P. L. Ottaviani, E. Pellegrin, R. Rossmanith, R. Steiniger, W. Saile, J. Wust: "Extreme ultraviolet (EUV) sources for lithography based on synchrotron radiation", *Nucl. Instr. And Meth. A* 474, 259 (2001)

10 TIMING AND SYNCHRONIZATION, CONTROL SYSTEM

10.1 Timing and synchronization: Introduction and General Architecture

The Timing and Synchronization central system is a very crucial part in a facility for SASE-FEL radiation production [1,2]. The physics of the FEL process requires an extremely accurate synchronization, at level of ≈ 100 fs or even better, among the various lasers (photocathode, heater, seeding,...) involved and the RF accelerating fields. Moreover, a relevant part of the beam diagnostics needs to be synchronized at the same level (bunch arrival monitors, streak cameras,...) as well as pump lasers whenever users perform pump and probe class experiments.

According to start-to-end simulations probing the sensitivity of the FEL process to the synchronization errors, the specifications that must be fulfilled for the various timing clients in order to guarantee an effective and reliable operation of the SPARX facility are reported in Table 10.1.

Table 10.1: Synchronization specifications for SPARX

Client	Jitter spec [fs]	Lock-in stability [fs]	Client Lock-in Bandwidth	Technology
Photoinjector Laser	200	240	5 kHz	SynchroLock (electro-opt or full opt.)
Laser Heater	150	130	5 kHz	SynchroLock (electro-opt or full opt.)
RF S-Band	150	130	1 MHz	Klystron Fast Phase Lock (LLRF)
RF X-Band	100	70	4 MHz	Klystron Fast Phase Lock (LLRF)
Seeding Lasers	100	70	5 kHz	SynchroLock (electro-opt or full opt.)
Streak Cameras	500	500	Full	Direct Seeding
Bunch Arrival Monitors	100	70	Full	Direct Seeding
Pump Lasers	100	70	5 kHz	SynchroLock (electro-opt or full opt.)

The timing clients are located over the entire facility, on a length scale of ≈ 400 m. Therefore the timing and synchronization system consists of three main parts:

- Timing generation and distribution. An ultra-stable reference signal generated in a central timing station will be distributed to the various clients through actively stabilized links. Due to the remarkable link lengths, an optical reference will be distributed to exploit the fibre-link low attenuation and the large sensitivity obtainable by optical based timing detection. The required stability of each link is ≈ 70 fs over any time scale, as it has been assumed in Table 10.1. The link stability is part of the synchronization budget assigned to each client.
- Client synchronization. Each individual client (laser systems, RF power stations, beam diagnostics hardware,...) has to be locked to the local reference provided by the timing distribution systems. The lock technique depends on the particular client (laser synchrolock, laser direct seeding, RF pulse-to-pulse or intra-pulse phase feedbacks,...) while the lock accuracy has been set in Table 1.
- Client triggering. Together with a continuous reference signal, low repetition rate trigger signals must be provided to some clients, which contain essentially the information on the timing of the macro pulses needed to prepare all the systems to produce and monitor the bunches and the FEL radiation pulses (laser amplification pumps, klystron HV video pulses, beam and FEL diagnostics, ...). The triggering system is a coarser timing line (≈ 10 ps required stability) that can be distributed either optically (through fibre-links) or electrically (through coaxial cables).

The proposed architecture for the SPARX timing and synchronization system to implement the illustrated general approach is sketched in Figure 10.1.

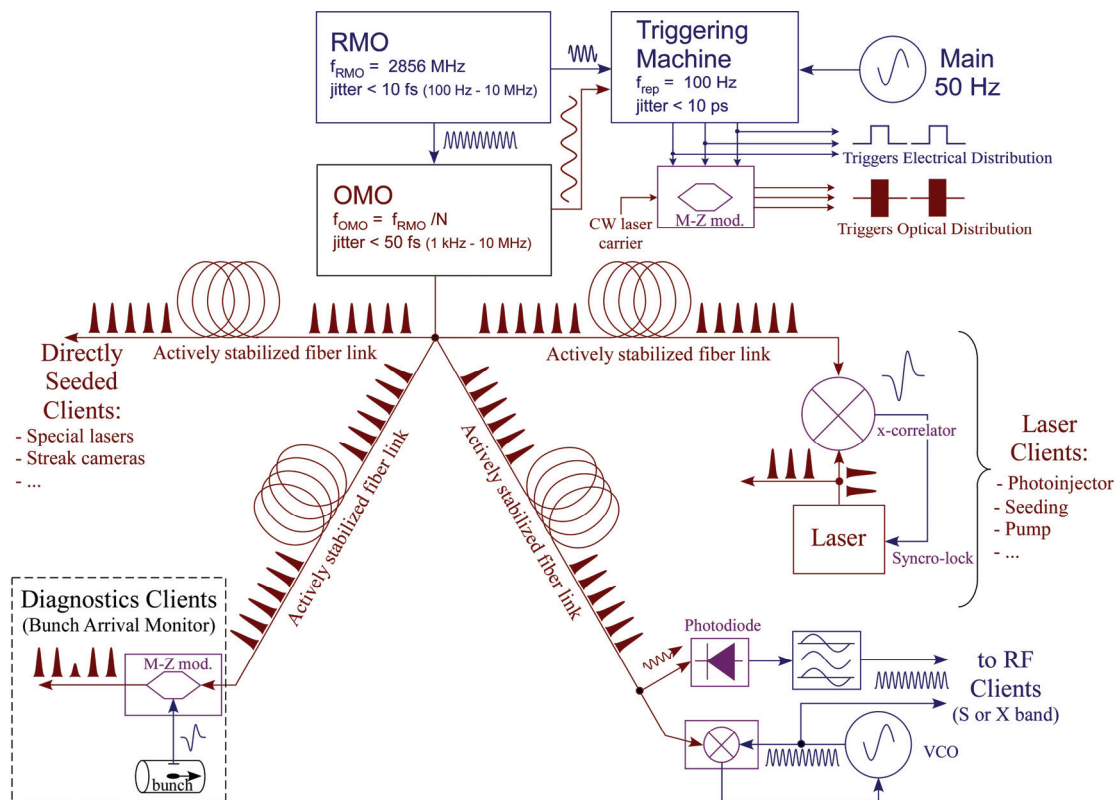


Figure 10.1: SPARX timing and synchronization architecture

10.1.1 Reference Master Oscillator (RMO)

The reference signal is originated by a Reference Master Oscillator (RMO) which is a μ -wave crystal oscillator with ultra-low phase noise characteristics. The role of this device is to provide a reliable reference tone to an Optical Master Oscillator which is a highly stable fibre-laser that encodes the reference timing information in the repetition rate of short optical pulse in the IR spectrum.

The RMO guarantees the long term stability of the OMO, and, through the OMO synchrolock system, imprints its low-frequency noise figure to the whole facility timing line.

The state of the art low-noise μ -wave oscillators can provide pure sine tones with phase jitter at few fs level over a spectral range from 10 Hz to 10 MHz [3]. As an example, the phase noise SSB spectra of sapphire oscillators commercially available from Poseidon Scientific Instrumentation (PSI) are reported in Figure 10.2.

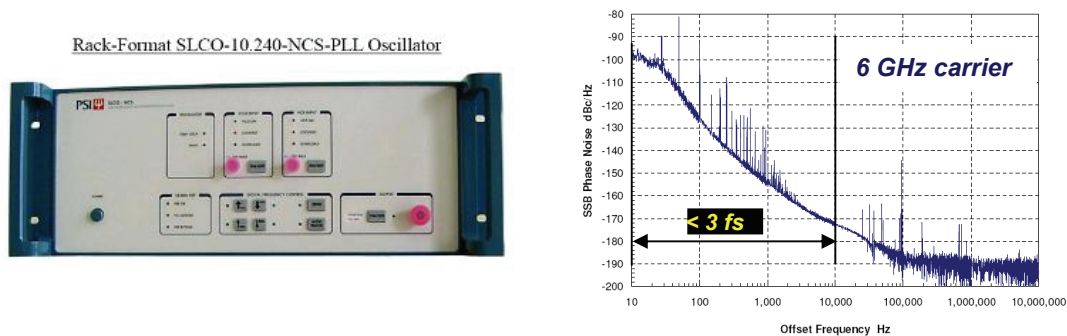


Figure 10.2: Ultra-low phase noise sapphire oscillator from PSI

In addition, since small reference phase oscillations at low frequencies should in principle produce only a common mode fluctuation for all the timing clients, high quality market available μ -wave oscillators with spectral purity about one order of magnitude worse than the state-of-the-art can be taken also into consideration. No major effects in the relative client-to-client synchronization are expected in this case, so that various cost effective solutions are available. As an example, the phase noise spectrum of a commercial frequency synthesizer (Agilent mod. E8257D [4]) is reported in the following figure.

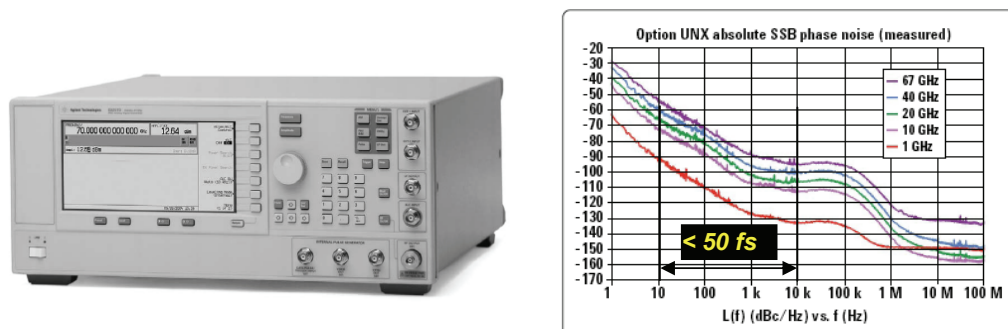


Figure 10.3: low phase noise Agilent E8257D analog signal generator

10.1.2 Optical Master Oscillator (OMO)

The timing reference will be encoded in an optical signal before being distributed over the whole facility through a glass fibre network. The μ -wave to optical conversion is accomplished by mode-locking a low noise fibre laser (the facility Optical Master Oscillator - OMO) to the RMO. The OMO to RMO synchronization is obtained by the Synchrolock™ system, which consists in a PLL scheme controlling the path length of the fibre laser cavity by stretching the fibre with piezo-controllers driven by the relative phase error between the two oscillators. This is a standard technique to synchronize also in-air laser oscillators to external references, with the piezos controlling the position of one or more mirrors in this case. Due to the limited frequency response of piezo-controllers, the Synchrolock™ loop gain rolls off typically around 5 kHz. Above this cut-off frequency the OMO retains its typical noise spectral properties, while below the cut-off frequency the OMO phase follows the RMO one, and the spectra of the two oscillators result to be very similar. However, the intrinsic phase noise spectrum of a good fibre laser oscillator above the Synchrolock™ cut-off frequency is comparable or even better respect to that of a μ -wave reference oscillator [5], as shown in Figure 10.4.

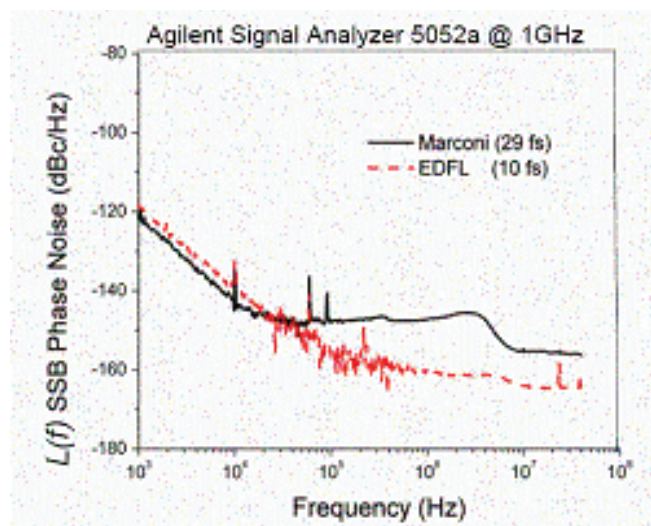


Figure 10.4: Comparison of phase noise spectra of an Erbium Doped Fibre Laser and a Marconi μ -wave oscillator

The overall phase noise of fibre laser OMO fairly locked to a high-class RMO can be as low as ≈ 100 fs in a wide spectral region spanning from 10 Hz to 10 MHz. The specifications of the OMO for the SPARX timing and synchronization reference distribution are reported in Table 10.2.

The OMO pulse repetition rate specified in Tab. II is 89.250 MHz, corresponding to the 1/32 of the LINAC RF frequency $f_{RF}=2856$ MHz. We used the RF sub-harmonic 32 because the frequency ratio can be obtained by using only by-2 counters, and the corresponding length of a laser optical cavity is quite ordinary.

Fibre lasers with characteristics close to the SPARX OMO specifications are already available on the market, needing only a limited customization to fully meet our requirements. As an example, two of such products [6,7] are reported in Figure 10.5.

Table 10.2: SPARX OMO specifications

Pulse width	τ_{pulse}	< 200 fs
Wavelength 1	λ_1	1560 nm
Wavelength 2	λ_2	780 nm
Pulse rep rate	f_{rep}	89.250 MHz
Pulse energy	E_{pulse}	> 2 nJ (~ 180 mW)
Phase jitter	τ_{rms}	< 100 fs rms (SSB Δf > 1 kHz)
Amplitude jitter	$(\Delta A/A)_{\text{rms}}$	< 0.05 % rms
Synchrolock BW	f_{cutoff}	> 5 kHz
Phase jitter relative to reference	τ_{rel}	< 10 fs rms (dc - 1 kHz)

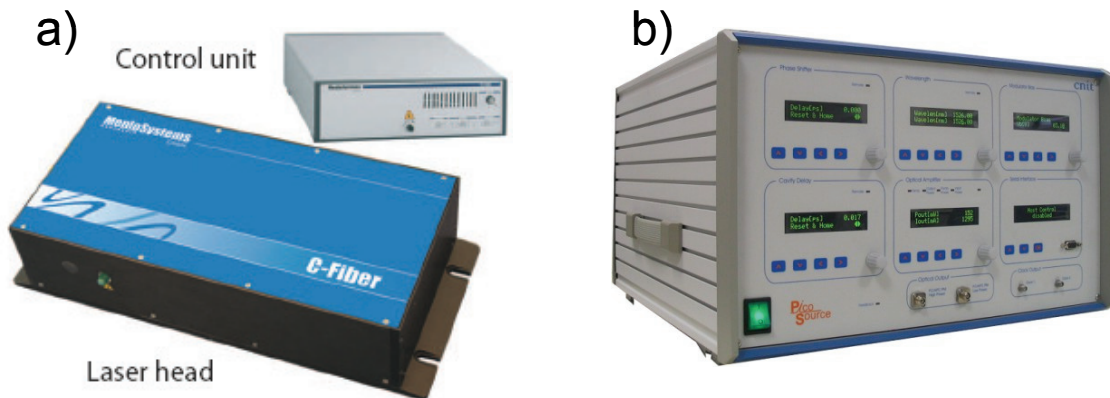


Figure 10.5: a) MENLO systems GmbH fibre laser C-Fiber 780 , b) PhoTriX active fibre laser harmonically mode-locked Pico Source

10.1.3 Optical Distribution of the Synchronization Reference

The distribution of the synchronization reference for SPARX must be realized using multi fiber optic channels. The source of the temporal reference signals for all the sub-systems is foreseen to be generated by an optical master oscillator (OMO) situated at a median position of the facility infrastructure. The channels extend from the source to the several end users up to 300 meters distance. The choice of optical waveguide channel to distribute the synchronization signals is motivated by a number of advantages of the optical link respect to the electrical cables. In fact the optical fibers offer THz bandwidth, immunity to electromagnetic interference and very low attenuation

[1]. These properties make the optical fiber a mandatory technology when one aims to synchronize a large scale facility at sub 100 fs level.

The layout of the synchronization source system is schematized in Figure 10.6. The OMO consists of a fiber optic oscillator generating soliton pulses. The cavity is designed to operate at repetition rate of 89.25 MHz as explained before. In a fiber oscillator the active medium is a portion of the fiber doped by Erbium and is, generally, excited through fiber-coupled diode. In the cavity, a portion of the optical path is in free space to allow the active control of the optical length. The fact that the cavity and the output coupling are realized within an optical waveguide determines a net improvement in the stability respect to a free space propagation laser. The output spectrum is centered at 1560 nm, because it is the standard wavelength for the telecom applications. The operating wavelength can be doubled, producing pulses at 780 nm. Since this wavelength matches the spectral gain of the Ti:SA it can be used to seed this kind of amplifier to achieve very high peak power.

The soliton passive mode locking OMO offer the possibility to produce and distribute a short pulse over long distance [8]. After the oscillator, the signal level needs to be augmented using an erbium doped fiber amplifier (EDFA) to achieve a proper power. At this point a fiber beam splitter will be used then to divide the signal to the different synchronization channels.

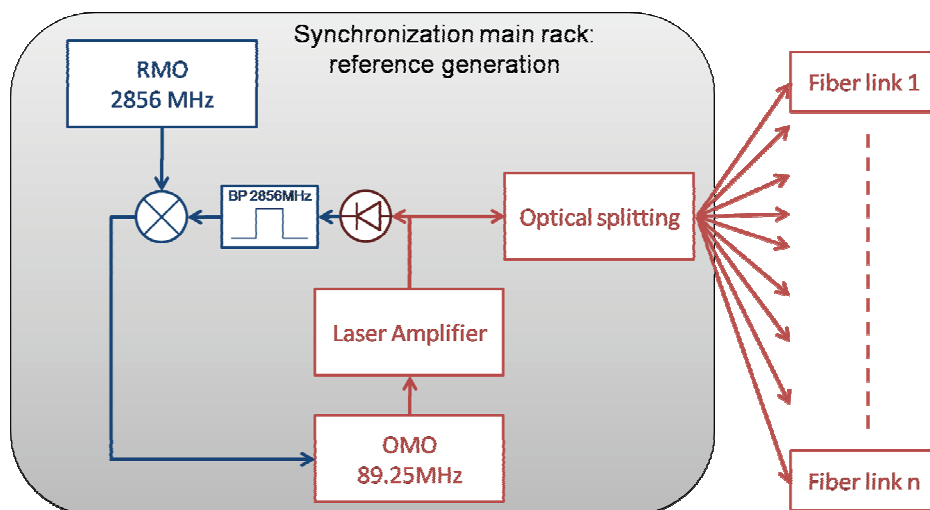


Figure 10.6: Schematics of the synchronization reference source and distribution.

The oscillator plus amplifier chain will be synchronized using a phase lock loop respect to the 2856 MHz μ wave reference synthesizer. At the output of EDFA the signal recorded from a fast photodiode (with the necessary bandwidth $> 3\text{GHz}$) will be sent to a narrow band pass filter at the 2856 MHz and, then, the result signal is then mixed with the reference to measure the pulse to pulse phase noise and generate the feedback toward the OMO. The oscillator repetition rate is kept constant using a piezoelectric actuator to drive a cavity mirror on the optical path of the cavity in air. The present status of the technology allows a jitter much lower than 100 fs rms. Since possible time jitters between the RF oscillator and the OMO are common mode disturb for all the SPARX subsystem, it is important to stress that the synchronization of the OMO is required in order to keep stable operating frequency on long term scale.

The optical signal will be sent to several fiber links with equalized optical length. The fiber optics will to be length-stabilized in order to deliver synchronous pulse to the end users. In fact the time of propagation in the fiber is in general affected by temperature drift and acoustic noise. The stabilization is achieved sending back a pulse from the end of the fiber and optically compare it with another pulse from the oscillator as schematized in Figure 10.7. To reflect part of the power a Faraday mirror can be used. In details the pulse to send through the fiber is divided with a polarization beam splitter: part of the pulse is sent to the fiber and the other is used as a reference for the optical mixing with the retroreflected pulse. The comparison between the reference and the other pulse is carried out with cross-correlator. The error signal will be used to drive a piezo path length stabilization unit and a stepper actuator to move trombone. The feedback aims to keep constant the pulse's propagation length.

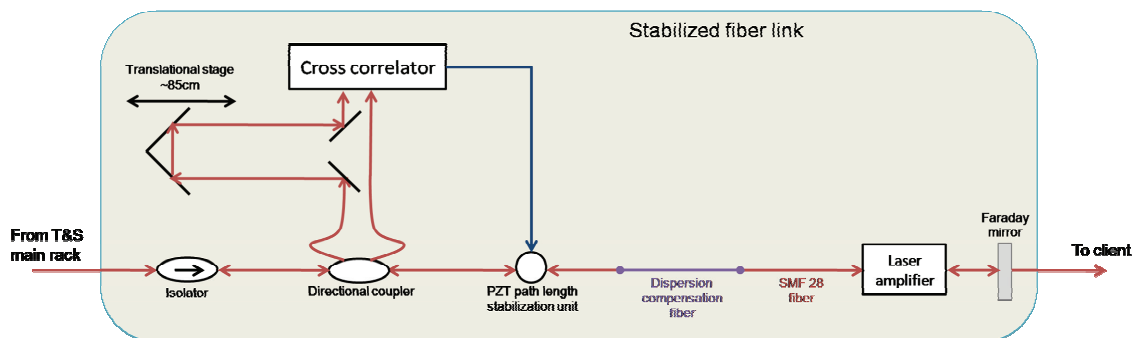


Figure 10.7: Layout of a path length stabilized optical link

A balanced cross-correlator is preferred for suppressing the laser amplitude noise and operates on a linear response of the optical mixer [9]. This technique demonstrated a stabilization better than 10 fs on 300 meter channel [10]. For low demanding end user the optical channel can be stabilized using electronic techniques based on high-speed photodetectors and microwave mixers. The limited timing resolution limits the stabilization to 100 fs level [11]. The cross-correlation or the electronic mixing requires more than half of the input pulse energy is not sent to the user. This set the required power per channel at level of 50 mW.

The propagation over hundred meters fiber induces a pulse broadening due to several mechanisms. The pulse broadening reduces the synchronization resolution for the end user and cross-correlator. Modal dispersion introduces an optical pulse broadening an unwanted effect that can be overcome with single mode fibers. A possible single mode fiber is the SMF-28. In fact this fiber is characterized by very limited attenuation: at 1560 nm the energy loss are 0.25 db/km that corresponds to an attenuation over 300 meters of less than 2% of power. Unfortunately this fiber shows a quite large dispersion 18 ps/(nm*km) that corresponds to a pulse broadening up to more than 130 ps for the typical oscillator bandwidth (25 nm) over 300 meters. To compensate the normal dispersion of the SMF-28 it is possible to use a fiber characterized by anomalous dispersion, named dispersion compensating fiber (DCF). A proper length DCF can completely balance the dispersion introduced by the normal dispersion fiber and produce a transform limited pulse to the end user and for the cross-correlation.

The price to pay for using a hybrid typology of fibers, are larger losses. In fact, the typical attenuation found in a DCF is three times higher than in standard

fiber and other losses are induced by the splicing losses between the two fibers. If one includes also the losses for match the fiber from the trombone delay line, the transmitted signal results to be very attenuated (up to 10 dB). To recover the energy losses at the far end of the optical link it is advisable to use an EDFA. The amplifier assures a good level of power for the final user and the cross-correlation. Insignificant time jitter is expected from the EDFA also because it is in the stabilized loop [12].

For better environment housing the OMO, the amplifier, the splitter and the fiber stabilizer should be controlled at better of ± 0.1 °C rms with a moderate air flow velocity. The stabilization of temperature and an optical table to dump possible acoustic noise is required when a total sub 100 fs are the target stabilization level. Moreover the optical fiber must be housed in a temperature controlled pipe (± 1 °C) to reduce the thermal effect during the propagation.

Finally the exposure of the optical link to radiation and particles induce a fiber darkening and therefore needs to be minimized.

10.2 Client Synchronization

10.2.1 Synchronization of SPARX lasers

In the SPARX photoinjector, a precise synchronization of the photocathode drive laser is necessary to have a fixed and stable time-of-arrival of the photons on the cathode with respect to the 2856 MHz RF field. This condition is very important to guarantee stability and shot-to-shot reproducibility of crucial beam parameters such as bunch charge, energy, energy spread, beam emittance, bunch time of flight and time of arrival across the LINAC, and to ensure a proper matching condition in the accelerator.

Other laser systems will operate at SPARX facility for seeding FEL regime, for electron beam diagnostic and for final FEL users synchronization. All the above laser sources are required to be synchronous with the RF field and the electron bunch. In particular the seeding laser is specified to be synchronized with the electron bunch time of arrival within 100 fs rms. The FEL user lasers should also be synchronous with the FEL pulse within 100 fs rms.

The RF frequency for the SPARX accelerator has been chosen to be the standard SLAC S-band of 2856 MHz, but typical laser oscillator repetition rates are between 70 and 100 MHz, so that the 32nd RF sub-harmonics $f=89.25$ MHz has been chosen for SPARX laser oscillators. A proper technique has to be adopted to compare the low and high frequencies to retrieve the phase error that is used to implement active synchronization loops. In fact, whenever various clients whose intrinsic repetition rate is the Nth sub-harmonic of the reference frequency are directly synchronized to the reference, their relative timing can differ by an integer number of RF periods. To avoid that, the synchronization has to be carried out also at the fundamental client frequency, to make different systems virtually overlap in time and space.

The synchronization between laser and RF fields has to be achieved at two different levels:

- a) by controlling that the laser emission happens at the time when the high power RF fills all the accelerating cavities (coarse timing – device triggering) and

- b) by phase-locking the laser optical oscillator with a the reference signal also at the N^{th} reference sub-harmonic, for real sub-ps synchronization (fine timing – device synchronization).

10.2.1.1 Laser Timing Description

All the SPARX laser system are based on Ti:Sa active medium. These systems have the same topology: an high repetition rate oscillator which provide pulse rate between 80 and 100 MHz with few nJ energy and a low repetition rate 10-100 Hz high energy amplifier. For more detail see the TDR chapter dedicated to the photocathode Laser. The amplifier consists of a regenerative pre-amplifier and two multipasses successive amplification stages. The pulse selection that reduces the repetition rate is accomplished by Pockel cells placed inside the regenerative cavity and switching with rise time of 1-2 ns. The regenerative amplifier is excited by a frequency doubled DPSSL (Diode Pumped Solid State Laser) at 1 kHz for better thermal stability. The multipass amplifiers are excited directly a 100 Hz.

The fine synchronization is carried out mainly at the laser oscillator level. The following amplification and manipulation introduce practically only a fixed delay. Fluctuations and drifts in the time of arrival of the laser on the cathode are mostly due to acoustic vibrations and/or thermal gradients, leading to slow drifts of the laser optical path that can be compensated by shifting the phase of the laser oscillator reference signal. Slow drifts among different laser systems can be compensated with motorized optical delay lines.

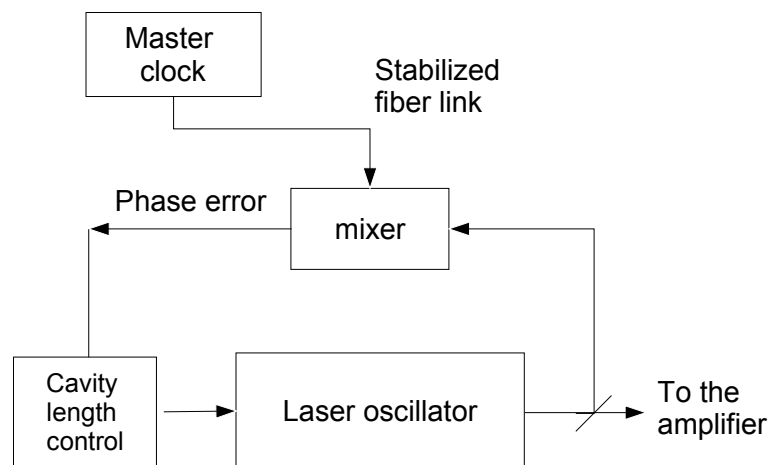


Figure 10.8: Schematic of the laser oscillator phase lock loop.

The repetition rate of the laser oscillator is equal to $c/2L$, where c is the speed of the light and L is the optical length of the cavity. In our case by design the cavity length L is equals to 1.68 m, giving a laser pulse frequency of 89.25 MHz, 32th sub-harmonic of the LINAC RF frequency. The chosen frequency is also a multiple of the facility repetition rate (100 Hz nominal).

The synchronization is achieved through an active feedback loop driven by the laser to reference phase error. In Figure 10.8 it is reported the conceptual scheme of the synchronization loop. The reference signal is generated by an optical master oscillator (OMO) and transmitted to the end users by a stabilized

fibre optic link. The phase error can be measured either with electronic or optical mixing. The electronic mixer requires two photodiodes, not drawn in the figure, as opto-electrical transducers: one placed at the laser oscillator exit and the other terminating the fibre link. The signals from the photodiodes can be filtered with a $< 1\%$ bandwidth bandpass filter centred at 2856 MHz, in order to reject all the harmonics but the 32nd and drive the mixer directly at the LINAC RF frequency. The use of an electronic harmonic loop (i.e. working at a frequency higher than the pulse repetition rate) increases the phase detection sensitivity. The only requirement is that the photodiode bandwidth extends to the chosen loop operational frequency. The intensity of the laser beam on the photodiode has to be optimized to reduce the amplitude-to-phase conversion present typically in the photodiode response near saturation.

As already mentioned, the ambiguity associated to the use of an harmonic loop derives from possibility of locking the laser at any of the 32 intermediate temporal positions corresponding to the harmonic periods within a period of the laser repetition frequency. This is not relevant whenever the laser has only to be locked to the RF field because the laser-to-RF synchronization is always guaranteed. But since the laser has to be synchronized also with other 89.25 MHz lasers, the use of a fundamental loop (i.e. working at the laser repetition frequency) in addition to the more sensitive harmonic loops is necessary.

Electric phase noise measurement can be performed with a resolution of ≈ 0.01 degree, which corresponds to ≈ 10 fs at 2856 MHz.

Optical mixing is obtained by mean of cross-correlators. In this kind of devices one pulse from the Ti:Sa oscillator and one from the OMO have to overlap inside a BBO (Beta Barium Borate BaB_2O_4) non-linear crystal at the fundamental repetition rate. It is possible to use either the fundamental wavelength at (1560 nm) or the second harmonic (780 nm) of the OMO for the optical mixing with the 800 nm from the Ti:Sa oscillator. At the output of the crystal the sum frequency at 530 or 390 nm is produced. The frequency sum pulse energy is proportional to the correlation signal $C(\tau) = \int S1(t)S2(t - \tau)dt$ calculated for the relative delay τ . Using a standard DC photodiode, it is possible to measure the pulse to pulse time jitter recording the variation of intensity of the sum optical frequencies. To reduce the effect of input amplitude jitter the cross-correlator is normalized to the intensity of the two input pulses. Recently it has been proposed a balanced cross-correlation configuration suppressing the effects of laser amplitude noise, showing also a linear characteristic response around the zero crossing [9].

The main advantages of the optical mixing respect to the electronic one are the intrinsic higher resolution and the need of less sophisticated acquisition and manipulation electronics (lower frequencies, 0-100 MHz). The cross-correlation allows resolving jitter with resolution that depends on the diode sensitivity and the input pulse length. The pulse from the oscillator is of the order of 100 fs rms and the signal coming out the fiber can be compressed to the same duration. This results in a resolution on the scale of the fs or even lower.

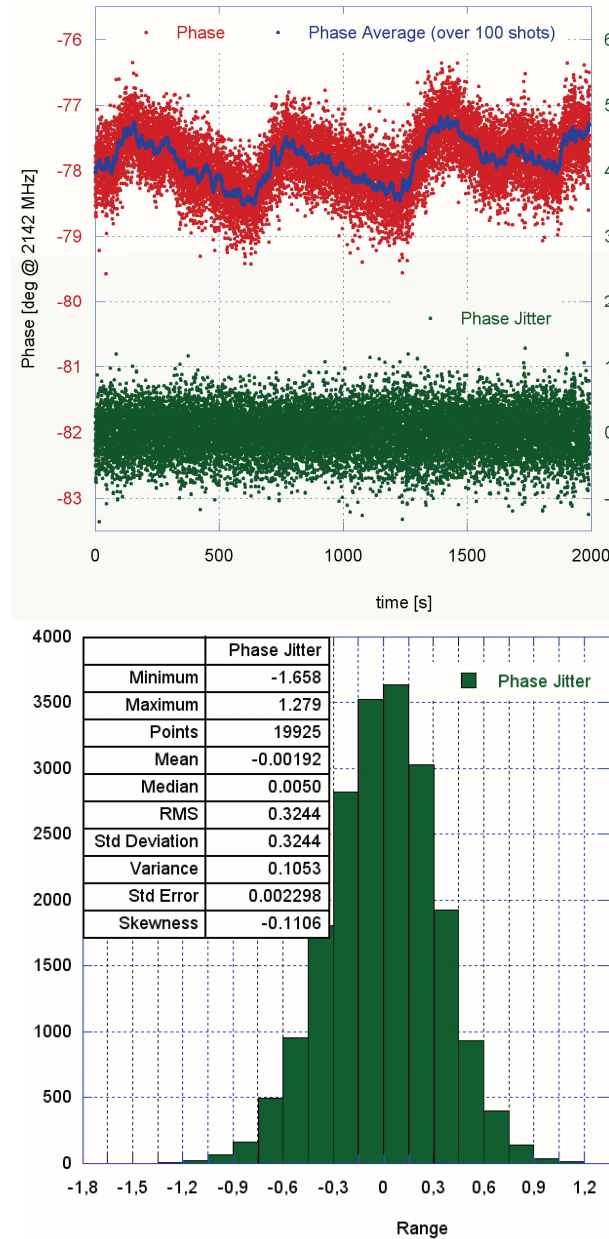


Figure 10.9: UV laser to RF relative phase jitter recorded at SPARC

The measured phase noise error is used to drive actuator to active control the oscillator's cavity length. In general high frequency piezo-electric transducers (PZT) are associated to a lower frequency galvanometer driven optical delay line and a DC motor. In general one of the cavity mirror is mounted on the DC motor with several mm stroke. The micrometer is positioned to minimize the frequency difference between the laser and the reference frequency with a coarse resolution of the order of 100 Hz. One cavity mirror is mounted on the PZT for high resolution frequency control. It has a typical range of few μm for voltages up to 100 V corresponding to a regulation range of few hundred Hz. The PZT frequency response extends up to 5-10 kHz. For long term stability a DC-magnet driven Galvanometer can be used to slowly adjusts the amount of glass in the optical path. This broadens the range of frequency correction of the PZT and allows to operate the piezo at its optimal DC voltage. The commercial active synchronization units guarantees the locking for temperature drifts of ≈ 10 degrees in a frequency range of 10 kHz.

As discussed above the actuator bandwidth fixes the maximum speed of the stabilization loop. Beyond this frequency, the laser is not anymore capable to follow the phase of the reference oscillator and therefore in this spectral region it behaves like a free-running oscillator, whose intrinsic stability contributes to the total phase noise of the locked device. The passive mode locking laser, such as the Ti:Sa oscillator, are in general less noisy at high frequency respect to the active mode locking where dedicated electronics guides the pulse formation.

An electronic synchronization loop following the Figure 10.8 scheme implemented with commercial devices has been extensively characterized at SPARC photoinjector using an RF cavity filter to measure the laser time of arrival after the laser amplification chain. An exponential decaying sine-wave produced by the impulsive excitation of an RF cavity is directly mixed with a portion of the reference oscillator voltage [13]. A sample of time jitter recorded after the amplification and the UV conversion is reported in the Figure 10.9 showing an rms value of ≈ 400 fs, a number very similar to the jitter measured at the laser oscillator level. The conclusions are that the resolution attainable with this kind of technique is well below the measured value (400 fs), and the laser amplification chain and the UV conversion do not add a relevant amount of jitter to the laser system.

10.2.1.2 Laser triggering scheme

In Figure 10.10 it is shown the layout of the laser timing. The sub-ps synchronization is obtained by locking to the 89.25 MHz OMO reference and has been already described. The regenerative diode pump solid state laser (DPSSL) works at 1 kHz and requires a trigger at this frequency from an external clock generator. The stability required for the pump laser is typically better than 5 ns. The 1 kHz clock can be used to initiate the time events. To generate the operating repetition rate, this signal is divided by 10. The 100 Hz signal generator is phased respect to the 50 Hz from the electrical power line. The locking with the line is done to limit the impact of line fluctuations and ripple on the shot to shot stability of the RF power plants and magnet power supplies which may affect beam parameters such as energy, position, sizes, etc. The 1 kHz clock generator is fed by 89.25 MHz pulses to synchronize the output pulse with the optical one and therefore to reduce the time jitter at less than 0.2 ns respect to the laser oscillator longitudinal modes.

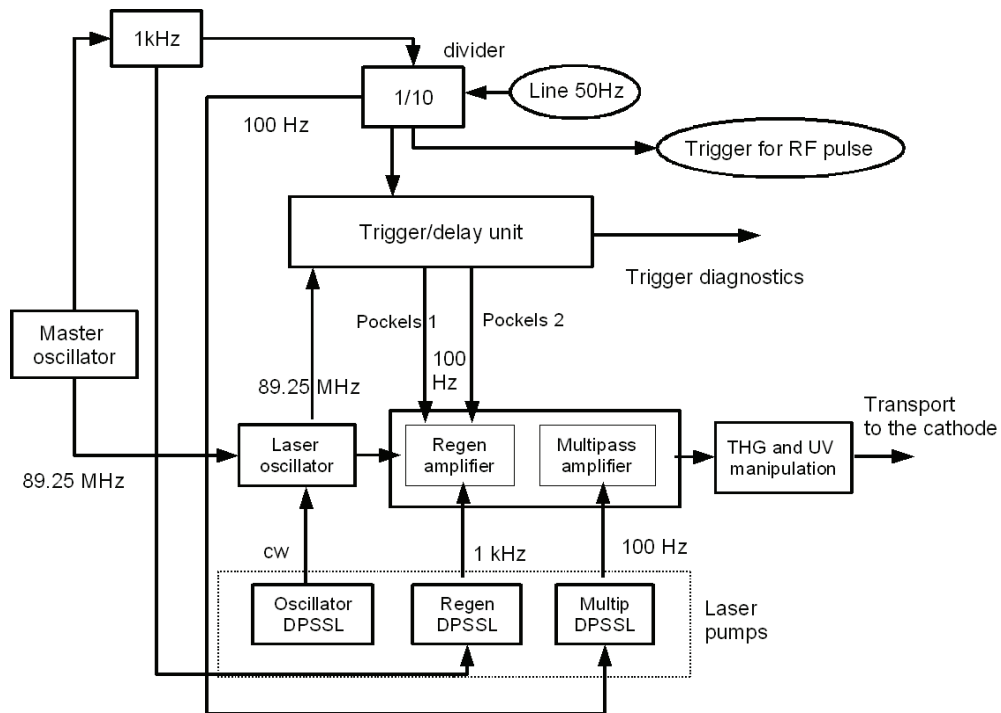


Figure 10.10: photocathode laser time and synchronization scheme

The trigger signal at 100 Hz (or at a lower frequency, since the machine will be probably commissioned at a reduced repetition rate) is sent to a trigger unit fan-out containing a multiple delay generator. One of the output trigger signals is sent to the Pockels cells in order to select one pulse out of the oscillator train. Proper trigger signals have also to be delivered to all the equipments requiring anticipated triggers, such as laser multipass pumps and the RF modulators.

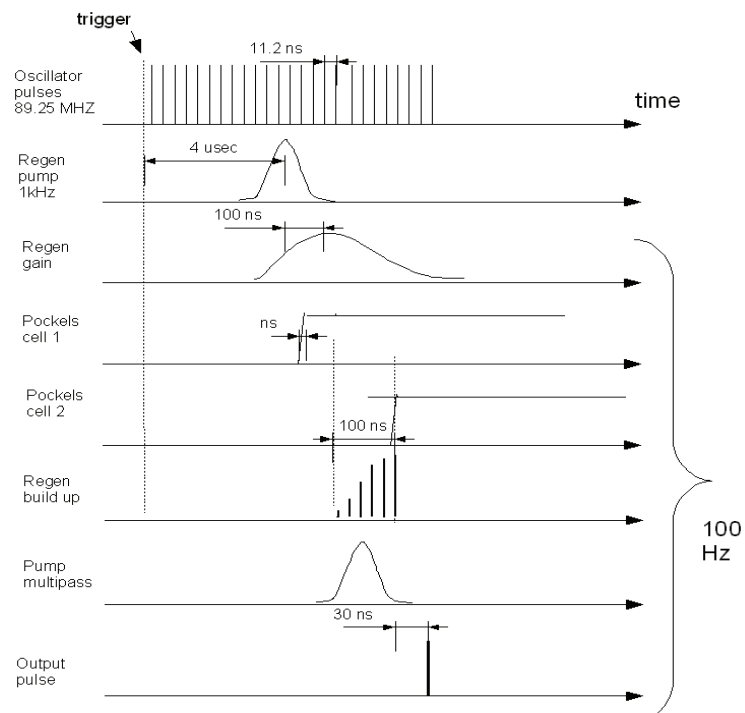


Figure 10.11: time diagram for the photocathode laser

Two Pockels cells are used as fast electro-optical switches inside the regenerative cavity to select and trap into the cavity one incoming pulse to be amplified. The first Pockels cell selects the seed pulse from the oscillator when the gain in the regenerative amplifier is at maximum $\sim 4 \mu\text{s}$ after the starting trigger. The Pockels cells are active for $\approx 100 \text{ ns}$, with a rise time of 2-3 ns. This fast rise time allows discriminating only one pulse of the oscillator pulse train. The first optical switch can be used to reduce the operating frequency at 100 Hz or less, selecting the right seed pulse, while the pump laser repetition rate is in general kept constant. The possibility to change the frequency should be implemented with a divider inside the trigger/delay unit. The second Pockels cell is delayed to extract the pulse when it reaches the maximum of the amplification, after about 10 passes in the regenerative cavity which is equivalent to $\approx 100 \text{ ns}$ later.

The timing diagram of the laser system is reported in the Figure 10.11. From a quick analysis of the scheme it is readily understood that the 1 kHz trigger initiates the chain of events that leads to the amplified laser pulse output. The regenerative optical pulse of about 100 ns is produced with a delay of $\approx 4 \mu\text{s}$ respect to the trigger. The pulse induces in the regenerative cavity a gain curve that sets the best point to inject the pulse, opening the first Pockels cell. After about ten round trips the optical pulse reaches the maximum intensity and can be extracted using the second Pockels cell. The Pockels cells require a trigger with sub-ns jitter (200 ps rms). To maximize the output energy the multipass DPSSL is triggered with few μs anticipation to realize the laser pulse few ns before the second Pockels cell is activated.

Table 10.3: Synoptic list of the required signals and jitters for the laser system.

Source	Frequency	End user	Anticipation	Jitter
Opt. master oscillator	89.25 MHz	Laser oscillator	CW	<1 ps
1 kHz generator	1 kHz	Regenerative pump	4 μsec	< 5 ns
1/10 divider	100 Hz	Multipass pump	4 μsec	< 5 ns
1/10 divider	100 Hz	RF pulse	4 μsec	< 5 ns
Trigger/delay unit	100 Hz	Pulse selection Pockels cell 1	250 ns	<0.2 ns
Trigger/delay unit	100 Hz	Pulse realize Pockels cell 2	150 ns	<0.2 ns
Trigger/delay unit	100 Hz	Laser diagnostics	> 50 ns	<0.2 ns

In Table 10.3 the signals necessary to drive the laser system are listed. Each signal is described in terms of source, end user and repetition rate. The expected jitter and anticipation respect to the laser arrival at the cathode is also reported.

10.2.2 Synchronization of the SPARX RF clients

The problem of keeping all the RF fields interacting with the beam always well synchronized among them and to the machine reference is obviously

crucial to obtain and preserve the beam quality. This subject is covered more extensively in the low-level RF paragraph of the LINAC chapter in this TDR, while here only basic concepts and features are summarized.

The RF driving signal for all the power sources (S band and X band) will be locally extracted from the OMO reference transported to each station by stabilized phase links. The optical to electrical conversion will be accomplished by photodiodes with proper bandwidth and/or Sagnac loop based Phase Locked Loops (PLLs) [14].

Samples of the RF voltages will be available all along the LINAC from directional couplers placed near the accelerating sections input/output coupling ports, and from RF probes located inside the standing wave cavities (RF gun, SW RF deflectors,...) to monitor the resonant fields inside. Directional couplers will be placed also near the output window of the klystrons to directly monitor the forward and reflected power on the tubes.

The low-level RF control will allow to demodulate some of the monitored RF pulses to work out amplitude and phase of the RF voltages, and monitor them on a pulse-to-pulse base at the rate of 100 Hz. Drifts and slow fluctuations of the monitored signals will be detected, and consequent actions to restore the optimal RF synchronization conditions will be done, essentially moving some variable phase shifters placed in the low-level hardware or in the waveguide network for independent phase control of different network arms. A sketch of the low-level control for a standard SPARX RF power station feeding 3 TW sections is shown in Figure 10.12. The reference RF signal to drive the whole RF chain is obtained from optical-to-electrical conversion of the OMO signal. The same reference is used to demodulate various RF pulses sampled over the network, and the whole station is re-phased in real time on the base of the measured values. The coaxial connections bringing the sampled signals to the demodulation board are out of the loop, so that any length variation will produce an error in the phase readout and a corresponding deterioration of the level of synchronization. Measures have to be taken to avoid these effects, such as reduction of the cable lengths, real time continuous calibration of the cable delays and use of thermally stabilized ducts to house and guide the cables along their paths.

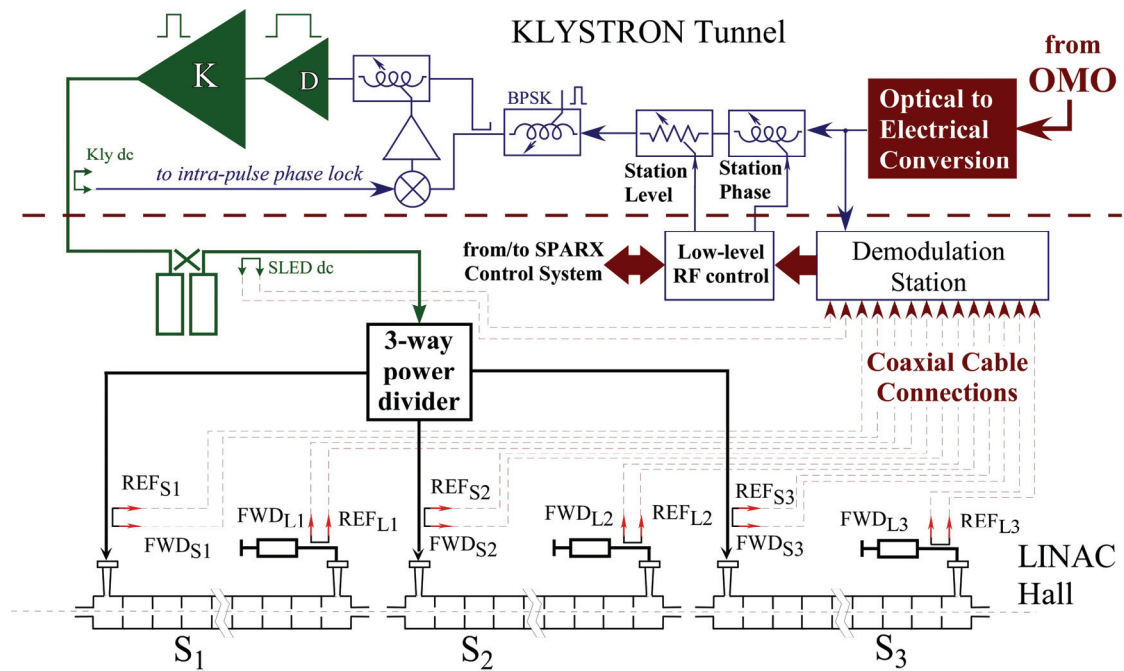


Figure 10.12: sketch of the SPARX low-level RF

Being 100 Hz the maximum repetition rate, phase stabilization loops based on pulse-to-pulse acquisition are intrinsically bandwidth limited to ≈ 50 Hz as a consequence of the sampling theorem. In order to overcome this limitation, an innovative intra-pulse phase lock scheme has been positively tested at SPARC [9] and will be implemented in the SPARX low-level RF control to push the RF synchronization to the best achievable specifications.

The intra-pulse phase lock scheme is a fast feedback loop with a response time of $\approx 1 \mu\text{s}$, capable to reach its regime condition within the time duration of each individual pulse ($\approx 4.5 \mu\text{s}$ for S-band modulators). Phase jitter extending its bandwidth beyond 50 Hz (power supply ripples, acoustic vibrations, etc.) is effectively reduced below 100 fs with this approach, as measured at SPARC and reported in low-level RF paragraph of the LINAC chapter in this TDR. However, the loop path length has to be reduced to the minimum in order to obtain the largest bandwidth in stable conditions. For this reason the loop can only encompass klystrons and RF driver amplifiers, while most of the waveguide network, SW cavities and TW sections can not be included and the phase noise entering the system at that level can only be cured by slower pulse-to-pulse feedback loops. The implementation of the intra-pulse phase lock also around the X-band station is very important to meet the tight synchronization specifications of such a client, but it will probably require some R&D because of the reduced time duration of the RF pulse ($\approx 1 \mu\text{s}$) in this case.

10.2.3 Synchronization of SPARX beam diagnostics

A large part of the LINAC beam diagnostics, (such as streak cameras, BPMs, striplines, video cameras, etc.) needs to be triggered and/or synchronized, as described in the dedicated paragraphs of this TDR. Instead this paragraph is dedicated to describe the instrumentation and the methods that we plan to use for the synchronization diagnostics, i.e. for measuring the

synchronization level achieved for various clients with respect to the main reference oscillator. Depending on the nature of the signal, we adopt different measurement techniques and devices. So we can classify our signal sources as follow:

- Long electrical macro-pulses: all kind of $\approx \mu\text{s}$ lasting RF pulses measured at the klystrons output, on RF gun, accelerating sections and RF deflectors monitors;
- High repetition rate optical signals: any type of laser oscillator as the ones of photoinjector, seeding and OMO laser systems;
- Low repetition rate pulses: signals probing the arrival times of the electron bunches or of amplified laser pulses.

All the phase noise or time arrival information will be stored in the control system and displayed in the control room and they can be used to set up feedback loops as the stretched fiber compensation links or the RF loops along the distribution lines.

10.2.3.1 RF Macropulses

Typical RF macropulses sampled from waveguide directional couplers and RF probes placed in the cavities last some μs . These signals are directly sent to RF demodulation boards where the I&Q components are extracted by mixing with a 2856 MHz reference signal. The resulting baseband signals are sampled with commercial digitizer cards (60Msamples/s, 12 bit typically) such as National Instruments PXI 5105. The phase of the RF sine-waves inside each pulse is locally calculated at the machine trigger rate (100Hz) and a mean value is calculated for each RF macro-pulse and stored in a data base. The number of RF signals sampled along the LINAC is quite large, so that to decrease the number of demodulation channels, we could consider to monitor only few selected pulses at a time (see the low-level RF paragraph in the LINAC chapter of this TDR). This measurement has been long time tested at LNF during the SPARC project commissioning phase obtaining satisfactory results.

10.2.3.2 High repetition rate optical signals

The synchronization information from the lasers oscillators can be obtained directly from the error signal generated by the balanced cross-correlator used to lock the “slave” laser under measurement to the master laser reference (see the previous paragraph 10.2.1). Of course to check if the locking system is working correctly, out-of-loop cross-correlation measurement of the laser oscillator phase with respect to the reference signal is desirable.

10.2.3.3 Short time pulses

This kind of pulses, with a duration in the range of picoseconds or less, need some special devices and measurement setup to be correctly detected.

10.2.3.3.1 Bunch arrival monitor (BAM) using an electro-optical modulator

This type of measurement, schematically shown in Figure 10.13 as already tested at FLASH facility [15], uses stripline pick up with several GHz bandwidth

to detect the passage of an electron bunch inside the pipeline. The output signal is used to drive a Mach Zender commercial Electro Optical Modulator (EOM) that modulates a copy of the optical master oscillator. A bias voltage will be applied to the EOM to choose a working point far from the zero crossing of the pick up signal (but still in the linear region). This will allow to have a bipolar error signal that discriminates whether the bunch arrives earlier or later. To extract information about the time arrival of the bunch, the EOM output is photo-detected and sampled with a fast ADC. To monitor continuously the measurement baseline, the ADC is clocked at the laser reference signal second harmonic.

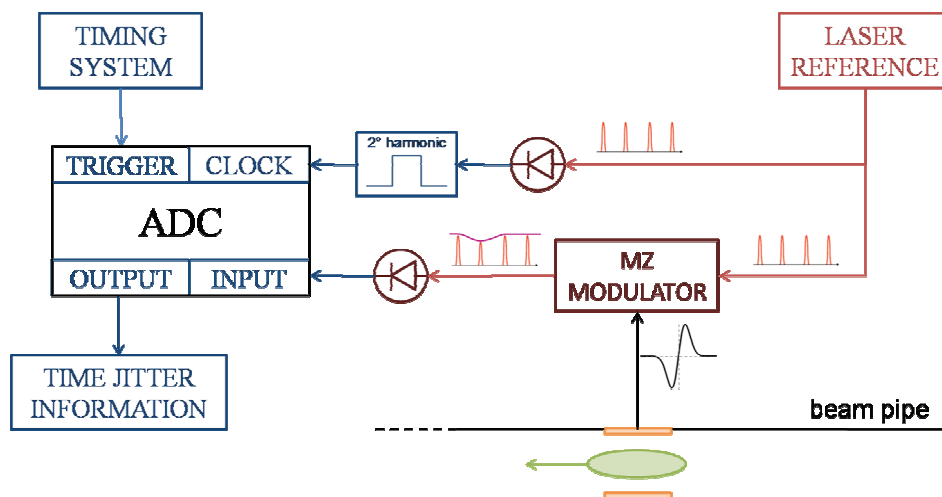


Figure 10.13: BAM based on bunch synchronous electro-optical modulation of the OMO

10.2.3.3.2 Bunch arrival monitor or laser arrival monitor using a resonant cavity

This kind of setup, described in the upper part of Fig. 14, has been already tested and implemented for the photo-injector laser arrival monitor in the SPARC experiment at LNF. A high voltage photodiode converts the amplified laser pulse in an electrical signal that excites an oscillation inside an RF cavity. The oscillation has a duration of some microseconds, thus the signal is sent to an I&Q mixer and sampled similarly to the RF macropulses. The demodulated RF phase of the cavity free-oscillations shows a linear time-dependence, being the slope of the line a measurement of the cavity detuning respect to the nominal frequency. The measure of the arrival time is obtained by measuring the initial phase of the oscillating mode inside the cavity. The same principle can be used to implement a resonant bunch arrival monitor, with the RF cavity embedded in the vacuum pipe of the accelerator and excited by the passage of the particle bunch (see the lower part of Figure 10.14).

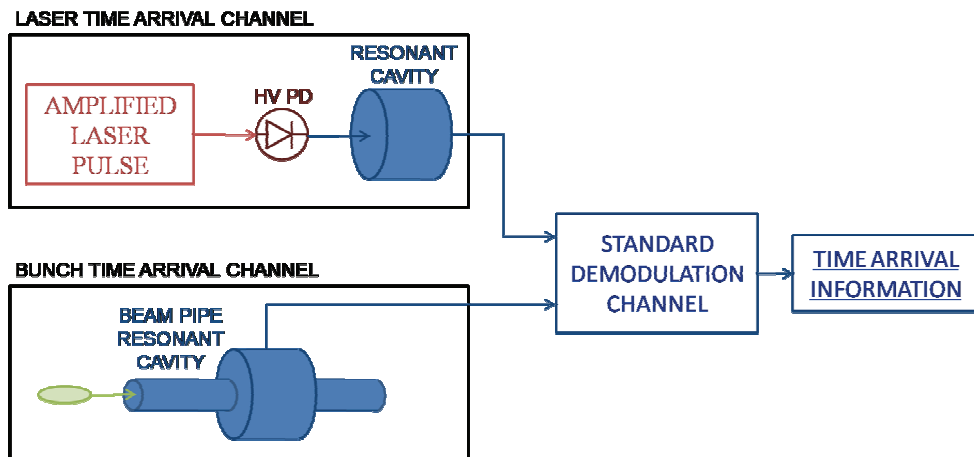


Figure 10.14: Resonant Laser and Bunch arrival monitors

10.2.3.3.3 SPARX Timing and Synchronization layout

A schematic layout of the machine Timing and Synchronization system is shown in

Figure 10.15. The central station containing the RMO, the OMO, the Trigger Event Generation and the origin of the actively stabilized fibre-link distribution network (including the fibre stretchers) is located near the machine barycentre, i.e. near the end of the 1.2 GeV LINAC. Receiving stations converting the optical reference in electrical one to drive RF power plant and demodulate RF pulses as well as beam and laser induced signals are placed in the vicinity of each RF station. Regeneration and manipulation of the triggers are also accomplished at this level. Laser and bunch arrival monitors are also located in some selected peculiar positions, monitoring the bunch synchronization at the beginning and at the end of the LINAC, as well as the synchronization of the photoinjector and seeding lasers.

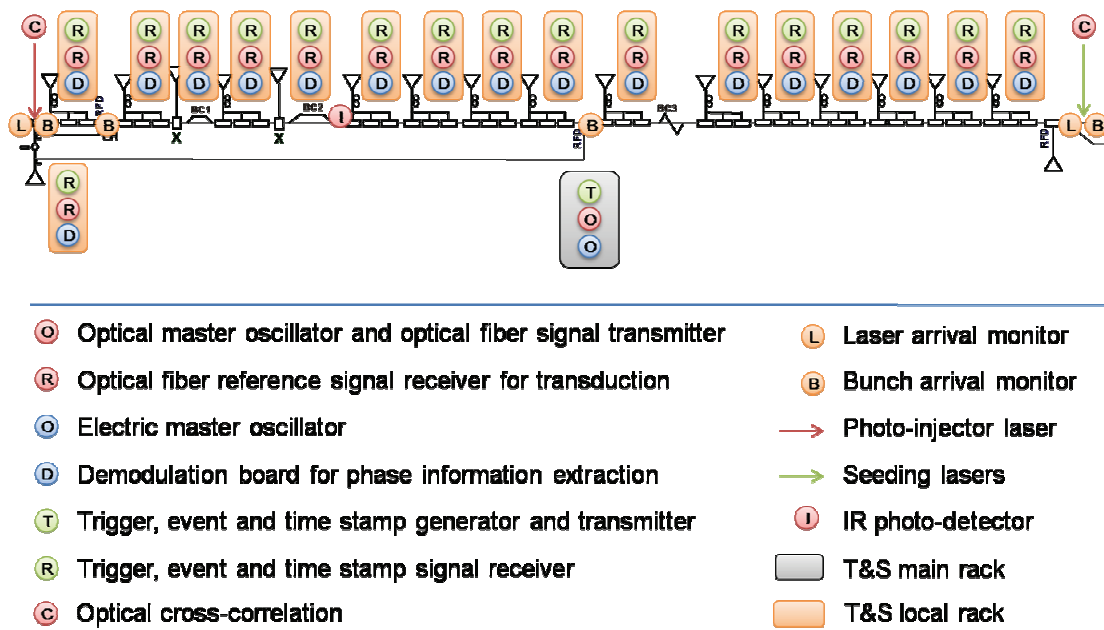


Figure 10.15: Layout of the SPARX time and synchronization

10.3 Triggers generation

10.3.1 Introduction and principles of operation

The trigger generator modules will have as input the RF frequency signals and the 50 Hz frequency from the main power supply (“the mains”) and will have to produce 100 Hz (or slower) output pulses and 1kHz signals. The requested precision is within ~10 ps rms jitter.

In principle, the input RF signal can be the S-band LINAC RF frequency (i.e. 2856MHz) coming from the RMO or the RF/32 (i.e. 89.25MHz) sent out by the OMO signal generator and used by the lasers.

The output signals generated shall be mainly pulses to manage the gun repetition rate (locked to the 50Hz from mains to be synchronous with the magnets ripple) and 1 kHz frequency for the laser systems. Both signals have to be generated with the necessary pre-triggers.

The low frequency trigger generation modules will be based on d-type flip-flop (used to divide by 2) and general purpose digital dividers.

Looking to the SPARX timing numerology, we see some integer results that can be easily used to produce frequencies locked in phase:

$$2.856.000 \text{ (kHz)} = (2^5) \cdot (5^3) \cdot 2 \cdot 3 \cdot 7 \cdot 17 \text{ (kHz)}$$

$$2.856.000 \text{ (kHz)} = 32 \cdot (5^3) \cdot 2 \cdot 3 \cdot 7 \cdot 17 \text{ (kHz)}$$

$$2.856.000 \text{ (kHz)} / 32 = 89.250 \text{ (kHz)}$$

$$17 \cdot 5 \cdot 3 = 255$$

$$5 \cdot 5 \cdot 7 = 175$$

$$89.250.000 \text{ (Hz)} / 175 / 255 / 2 = 1.000 \text{ (Hz)}$$

It is clear that combining different stages of dividers will be possible to produce all the necessary frequencies. In particular the 1 kHz signals can be derived from the 89.25 MHz using three stages of 8 bits dividers.

10.3.2 Comments on the main divider

Looking more in depth to the effects due to the OMO divider by N=32, it is evident that, if the trigger generation module would have as input the LINAC RF frequency, the timing system had two divider by n=32 with phase uncertainty between them at every power up. For this reason the flip-flop based divider (FAST_TIMING) module shall be used only for testing purpose.

Considering this point of the problem, we strongly recommend to have only one OMO divider in all the SPARX plant to maintain a constant phase difference between all the timing modules. If this is not the case, it would be necessary to design a fiducial reference module to give a low frequency reference signal locking in phase every OMO divider and the trigger generation module. It will be necessary also that every divider will have a phase reference input.

In the following we will consider the simplest case in which only one main divider (OMO or electronic) is foreseen in the SPARX system.

In this approach the trigger generation module will have this scheme:

- a) to receive in input the RF/32 frequency;
- b) to receive in input the main 50 Hz locked to the mains (of the ENEL network);
- c) to generate a 100 Hz frequency signal locked to the previous input and including a phase shifter with remote control;

- d) to generate, using flip-flop dividers, triggers at 1kHz frequency locked with the RF/32 input signal;
- e) to select, using the 100Hz signal locked to the mains, 100 pulses in a second from the 1kHz locked to the RF/32 and use this signal as 100 Hz signal for the bunch repetition scheme.

10.3.3 List of main trigger modules

To implement the trigger approach described above the design should include several modules that are described in the following.

The first module, GUN_REP_RATE, have to interface by a PLL circuit the 50 Hz from the ENEL network to produce in output software selectable frequencies in a range from 100 to 1 Hz or less. The output signal shall have a phase shifter software programmable feature to make the output phase correlated to the zero crossing magnet ripple at 100 Hz.

The second module is the FAST_TIMING board. In the case of 2856MHz input will be necessary to use last generation ECL dividers working up to 3-4 GHz as already implemented for the SPARC Timing System. The SPARC circuit (dividing by 36) can be re-used just changing the dip-switch setup to divide by 32 and to obtain 89.25 MHz frequency signal.

The third module, TRIG_1K_GEN, will implement the main three stage divisions to produce the 1 kHz signals and pre-triggers from RF/32 input clock. To implement TRIG_GEN, there are three possible design options to be evaluated:

- a) by using last generation ECL (Emitter Coupled Logic) based design producing for every division stage a very low jitter (of the order of 200fs r.m.s.); the flexibility of this choice is poor.
- b) by using FPGA (field programmable gate array) technology that allows a great flexibility because the circuits can be modified by a simple recompilation. Unfortunately this technology produces a bigger jitter respect to the ECL based design but probably less than 10 ps r.m.s. Some R&D is necessary to evaluate the real performance.
- c) a third design strategy can include both ECL and FPGA components in the same design. In this case should be possible to have low jitter and flexibility, at least in principle.

The TRIG_1K_GEN module, having in input the GUN_REP_RATE output signal, shall also select, from the 1kHz frequency, the pulses necessary to the gun repetition rate.

Other important and necessary modules will be the fanout boards, TIM_122 with NIM and differential ECL input/output and TIM_118 with TTL i/o. Both modules have been designed for the DAΦNE timing system [16], [17].

A module to convert the triggers from electrical to optical is also foreseen as described previously.

10.3.4 Event and time-stamp generator and receivers

The Timing System has to provide a complete timing distribution system including timing signal generation with only a few components. Throughout the design of the Event System any requirements of SPARX will be taken into consideration and, however, the system should be ready to cope with future upgrade.

According to international collaborations with important light sources facilities and laboratory as LCLS, APS, Swiss Light Source, Diamond, it is now possible to implement a complete Event System using commercially available boards and hardware. The hardware producer is the Micro-Research OY Finland (see <http://www.mrf.fi>).

. The software can be implemented in Labview or in EPICS. In the second case, it is possible to re-use easily the code developed by the international collaboration.

In the following, there are references to the system:

T.Korhonen, "Timing System of the Swiss Light Source", presented at ICALEPCS 2001, San Jose', USA

P. Krejčík, LCLS Facility Advisory Committee meeting, "Timing and Event System", Oct/12/2006.

S. Allison, "Event Displays for EVR IOCs", LCLS IOC meeting, March/20/2008.

<http://adwww.fnal.gov/www/icalepcs/abstracts/PDF/th3ac.pdf>

<http://www.slac.stanford.edu/econf/C011127/FRAT004.pdf>

<http://accelconf.web.cern.ch/Accelconf/e06/PAPERS/THPCH166.PDF>

<http://epaper.kek.jp/ica03/PAPERS/TU114.PDF>

Usually timing events are synchronized to a master clock reference e.g. the main acceleration frequency. Synchronization to the mains voltage phase is required, too, to keep the beam intensity and quality on the same level on consecutive triggers.

The Event System is capable of generating and distributing different frequencies, trigger signals and sequences of events, etc. synchronous to an externally provided master clock reference and mains voltage phase signal. Support for timestamps makes the system a global timebase and allows attaching timestamps to collected data and performed actions.

Event System components are available in VME form factor supporting standard VME and VME64x with hot-swap capability. Event Receivers are available also in PCI mezzanine card (PMC) form factor.

CompactPCI/PXI versions of both the Event Generator and Event Receiver can be used in the future.

Event System Structure

The Event System is part of the Timing System and consists of an Event Generator (EVG) which converts timing events and triggers to optical signals distributed through fanout units to an array of Event Receivers (EVRs). The Event Receivers decode the optical signal and produce hardware and software output signals based on the timing events.

By combining an event driven timing system with direct distribution of a set of signal the system achieves great flexibility. The system should utilise 256 event codes and allow distribution of eight simultaneous signals which do not

interfere with events. Events and the distributed bus signals are sampled with the event clock rate which e.g. for the VME products has to be at RF/32 (or in range 50 MHz to 125 MHz). The event clock may be generated on board by the EVG or, better, divided from an externally supplied clock reference, the RF/32 signal.

Event Receivers use a PLL circuit to lock precisely to the event clock of the Event Generator, so the hardware outputs are phase locked to the event clock and to the RF signal if applicable.

Event Generator

The Event Generator (EVG) is responsible of creating and sending out timing events to an array of Event Receivers. High configurability makes it feasible to build a whole timing system with a single Event Generator without external counters etc.

Events are sent out by the event generator as serialised event frames (words) consisting of an eight bit event code and an eight bit distributed bus data byte encoded using 8B10B encoding. The event transfer rate, the event clock, is derived from the external RF clock. An on-board fractional synthesizer is provided for testing purposes.

Event Sources

The Event system utilises eight bit event codes i.e. there are 256 codes available. Event code zero is sent out when there is no other code pending. There are several sources of events: trigger events, sequence RAM events, VME events and events received from an upstream Event Generator. Events from different sources have different priority which is resolved in a priority encoder. The different event sources and their priority are listed in the table below.

Priority	Event Source
highest	Trigger Event 0
	Trigger Event 1
	Trigger Event 2
	Trigger Event 3
	Event Sequencer 1
	Event Sequencer 2
	Trigger Event 4
	Trigger Event 5
	Trigger Event 6
	Trigger Event 7
	Upstream EVG Event
	Software Event
	Timestamping '0' Event
	Timestamping '1' Event
lowest	Timestamping Second Event

Trigger Events

There are eight trigger event sources that send out an event code on a stimulus. Each trigger event has its own programmable event code register and various enable bits. The event code transmitted is determined by contents of the corresponding event code register. The stimulus may be a detected rising edge on an external signal or a rising edge of a multiplexed counter output.

Trigger Event 0 has also the option of being triggered by a rising edge of the AC mains voltage synchronization logic signal.

Event Sequencer

Event sequencers provide a method of transmitting or playing back sequences of events stored in random access memory with defined timing. In the event generator there are two event sequencers. The 8-bit event codes are stored in a RAM table each attached with a 32-bit timestamp relative to the start of sequence. Both sequencers can hold up to 2048 event code - timestamp pairs.

Upstream EVG Events

Event Generators may be cascaded. An event code from an upstream EVG is transmitted when there is no higher priority event pending.

Software Events

Software events may be sent out by the IOC controlling the EVG.

Time-stamping Events

Time-stamping events may be used to transfer the precise real time to all event receivers.

VME Event Generator (VME-EVG-230)

The VME-EVG-230 is a successor of the EVG-200 which was design for the Diamond Light Source. (See <http://www.mrf.fi>)



Figure 10.16: VME-EVG-230 , event generator module

Main features:

- front panel RF input and programmable divider /1, /2, /3, ..., /12, /14, ..., /20
- bit rate 1.0 Gbps to 2.5 Gbps, event clock rate 50 MHz to 125 MHz
- front panel mains synchronization TTL input (ACIN)
- two front panel TTL inputs
- six front panel TTL outputs
- two universal I/O slots
- rear I/O

VME Event Receiver RF (VME-EVR-230RF)

The VME-EVR-230RF is a successor of the VME-EVR-200 which was designed for the Diamond Light Source. See <http://www.mrf.fi>. This board provides highest timing resolution and stability for most demanding subsystems.



Figure 10.17: VME Event Receiver VME-EVR-230RF

Main features:

- bit rate 1.0 to 2.5 Gbps, event clock rate 50 MHz to 125 MHz
- four programmable front panel TTL outputs
- two front panel TTL inputs
- three differential CML pattern outputs capable of RF recovery
- two universal I/O slots
- rear I/O
- jitter typically < 15 ps rms for TTL outputs, < 5 ps rms for CML outputs

VME Optical Fan-Out

Fan-out modules distribute the optical event stream generated by an event generator to an array of event receivers in star configuration.



Figure 10.18: 12-way VME-FOUT-12

Main features:

- Standard VME and VME64x compatible, supports hot-plugging in VME64x crate
- Takes only power from crate

- Small form factor pluggable (SFP) transceivers with LC connectors (850 nm short waveleght).

10.4 Control System

In a complex device like SPARX it important to manage the whole machine, from the gun to the radiation beam-line, with unique control system in Figure 10.19 show the control area. This means that the control system must be able to make the active elements execute the required commands as well as to integrate diagnostics to give as much information as possible to the operator. This implies that the control system must integrate all of the machine apparatus, being also able to follow the upgrades and the introduction of new elements.

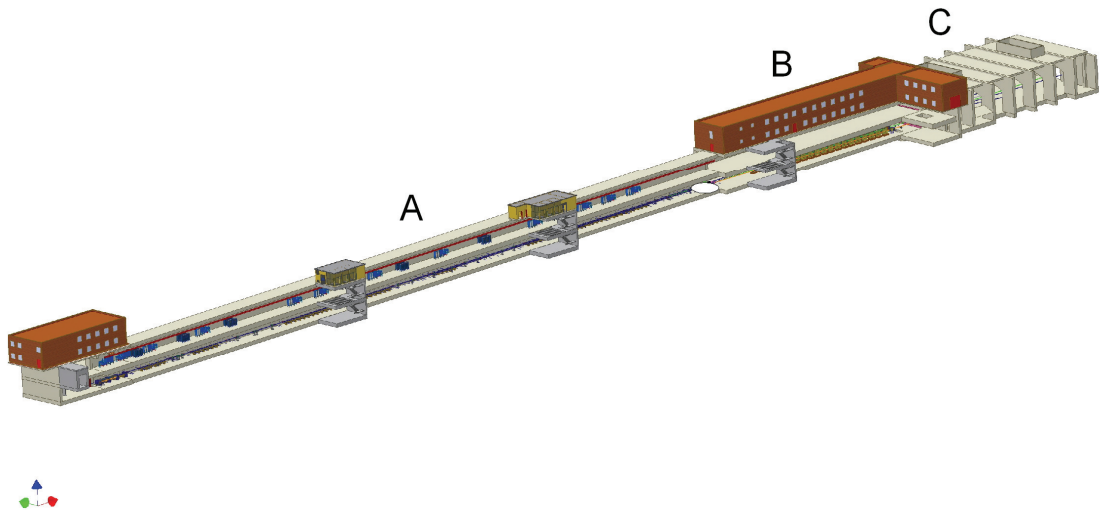


Figure 10.19: The SPARX area A) LINAC, B) undulator, C) beam-line

10.4.1 General Description

As above mentioned the control system should guarantee and simplify machine operation. In general the main operations in an accelerator control system are:

- data taking,
- display of information,
- analysis,
- command execution
- Storage.

The simplest more simple and functional is to have a control system with distributed processors on the machine area based on a classic three levels architecture.

- *First level*: at this level we find the console with their human interface to allow the operator to control the machine, a logbook to share information within the collaboration, a database to store all information coming from the machine and a serial web tools to help the management of the control system and to share some information outside the collaboration;
- *Second level* at this level we find the front-end CPU that executes commands and makes all the information about the status of the machine available for the first level. Meanwhile it automatically saves data from its various elements in two ways: the first is triggered on value changes, while the other is executed at fixed time intervals;
- *Third level* is the acquisition hardware where we find the appropriate acquisition board or the secondary field bus to acquire data from the real element.

The interconnection bus between the levels is an appropriate communication bus.

10.4.2 Hardware

First of all we decided that each distributed CPU controls only a certain type of elements. This simplifies the number and type of acquisition board assigned to the front-end processor. We want to use the right processor in depending on the element to control. We plan to implement in our system PXI bus, industrial pcs and real time processors.

At console level we need the maximum flexibility in terms of number of screens and possible remote connections. Also at this level, we plan to use small form factor PCs with at least 4 monitors each.

A storage facility for the whole system software and data is foreseen.

10.4.2.1 Network

This paragraph describes the network infrastructure foreseen for the SPARX facility. Given the size and the functional issues of the SPARX facility, it's useful to logically group the local network in Virtual LANs, to address issues such as scalability, security, and network management. In Figure 10.20 a hierarchical model of the network is presented. Three main areas are shown: the "Service" network, the "User" network, and the "Control System" network, connected in a star topology.

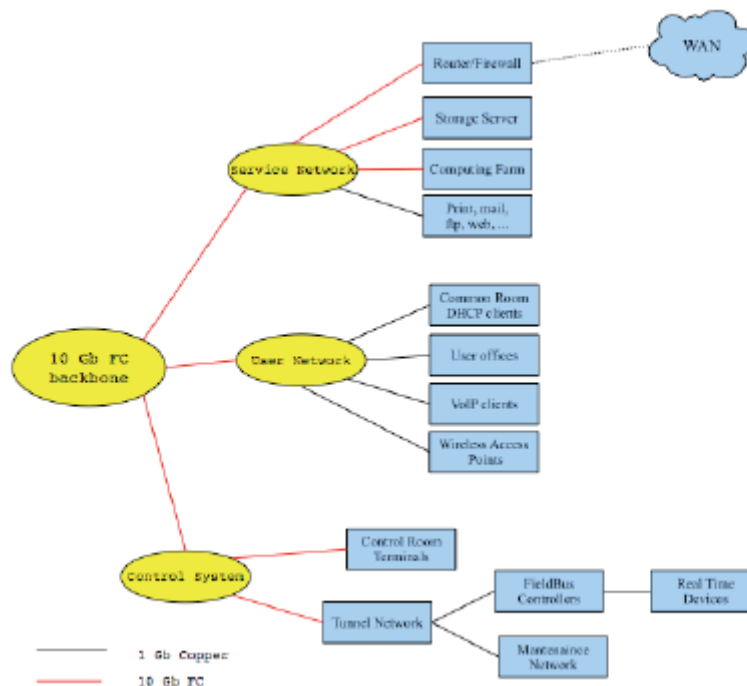


Figure 10.20: hierarchical model of the network

A dedicated technical room is foreseen, close to the Control Room, where all IT infrastructure components (e.g. routers, switches, servers, . . .) will be placed, as well as external WAN connectivity. This room should be powered by an uninterruptible power supply system and equipped with air conditioning system balanced with the expected thermal loads.

10.4.2.1.1 Network control system

The Control System is the ensemble of I/O peripherals, real time devices and controllers, dedicated hardware and software for the management, control and data acquisition of the accelerator components. The network associated to the control system connects all peripherals along both levels of the tunnel with the control room. In particular a 10Gbit Ethernet Fiber Channel backbone (with redundancy) is placed along the tunnel on level 1, with wiring closets placed every 30 m that brings Ethernet copper connectivity in the surrounding area through Layer 2 Gigabit Managed switches. These wiring closets contain, where needed, specific hardware for the control system, such as master CPUs for a fieldbus segment, and directly going through a copper Ethernet line on level 0 where real time devices are placed. In this way, approximately 15 switching sub-station are placed in the tunnel, providing also local access to the network for maintenance purposes.

For the control system different network topologies can be implemented (as shown in Figure 10.21), depending mainly on the expected data throughput and cabling issues. A first option is a simple line topology based on a dual fiber channel connection, with all the sub-station switches connected in cascade. A more traffic balanced option is a ring topology (with the constraint that switches should implement basic spanning tree algorithm), which is obtain by adding a second double line connecting the last station to the main backbone switch. If even more traffic is expected, the option of a tree topology can be considered. Such configuration can be obtained by dividing the network in three or more branches, with no more than 5 sub-station per branch.

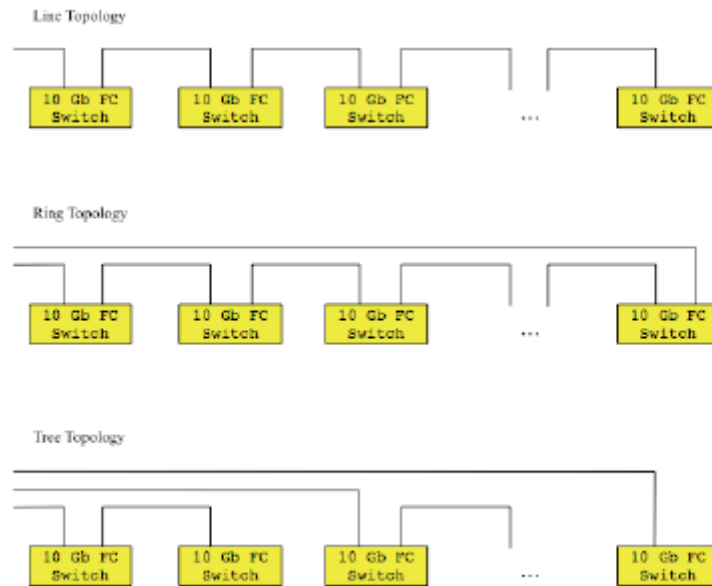


Figure 10.21: Example of topology for control system network

10.4.2.1.2 User Network

Under this label we group the network for users' connectivity along various areas of the building. Connectivity in the office rooms (at least 4 ports for each working person per room), would eventually include also VoIP service, as well as DHCP client connections. Wireless networking will be adopted where possible (office rooms, control room, experimental room).

10.4.2.1.3 IT Facilities:

In the data center technical room all the equipments providing services for the whole infrastructure are located: data storage, computing farms, network services (i.e. mail server, web server, DHCP server, print server), a videoconferencing facility in the control room. The storage facility can be arranged in a multi-level structure, with a first level dedicated to data acquisition for the control system, providing high performance and high reliability. Storage element, whose will be in the range of 5-10 TB will implement high performance technology such as iSCSI. The second level is characterized by high reliability and scalability in the range of 10-50 TB with such as SATA technology. This level is though as a resource for users and experiments, for example for backup purposes, scratch areas for data exchange. If needed, a third level of storage can be implemented, to be use as a long term data storage and for backup purposes, using a tape library or equivalent technology.

A computing facility can be implemented with one or more computing nodes, tightly connected (through Infiniband or Fibre Channel technology) together and to the storage elements. A peak computing power of 100 Gflops can be currently reached on a single computing node, and this value is expected to double every 1.5 years.

10.4.3 Software

In order to reduce the time of development of the SPARX control system, we decided to use well known Rapid Application Development (RAD) software. Labview became the natural choice for the following reasons:

- in the collaboration laboratories the use of National Instrument software is very popular (we can say it is a “standard”);
- Labview is used as development software in the DAFNE and SPARC control system. This choice allows us to re-use, when possible, already existing software;
- Labview is considered as reference software by many hardware manufacturers that write interface drivers in Labview.

Other software such as Matlab (whose integration with LabView is very well established), Mathematica or self-made will be introduced and integrated in the control system in order to help the online and offline analysis of the beam during the machine operation.

10.4.3.1 *Service Programs*

The SPARX collaboration involves different national and international research institutions. Some services are necessary to make all the information about the machine status and the work progress available to all involved people. The old system based on a logbook where the operator writes the data and glues picture on it can be useful but may not be available for remote researchers. We choose to use the same e-logbook already developed in SPARC. This logbook is on PostgreSQL database. The integration of the logbook system in the user interface helps the users in inserting entries and data in simple and homogeneous way.

During machine operation automatic data saving is mandatory. This mechanism can be useful both for machine maintenance and for offline analysis.

The data acquisition system will be based on a database with a possibility to communicate via TCP/IP.

10.4.4 Elements

The SPARX machine can be divided in three parts: the LINAC, the undulator and the radiation lines. Each part of the machine has its elements to control or display and its own or common subsystems.

10.4.4.1 *Laser*

To allow the optimization of the laser on the cathode, its remote control is essential. In order to implement this we need to control the maximum possible components of the laser apparatus. The main operation is the alignment of the light with the mirror, that can be controlled by means of a motor while the laser light is acquired through a video camera. Other parts can be controlled by means of standard interfaces such as Ethernet or serial.

10.4.4.2 *RF*

The RF section includes controls for the high power and the low power apparatus. The modulator can be controlled with Ethernet or serial interface with an appropriate protocol.

Signal monitoring and synchronization is designed using a demodulation board and digitizer cards in an PXI or compactPCI chassis, where data analysis

and device control are accomplished. The signal apparatus can be seen as a custom multi-channel digital scope, able to display in the control room all the demodulated signals coming from the RF structures placed along the whole machine.

Other devices such as attenuators, phase shifters, amplifiers and so on will be controlled with serial or Ethernet interfaces.

10.4.4.3 Magnets

In the accelerator we have a lot of different kind of magnets such as solenoids, correctors, dipoles and quadrupoles. Magnet control means controlling their power supplies. We decided to use as much as possible the same interface between the control and the power supply

The following specifications will be required to the power supply factory: Ethernet, RS232 or RS485 interface; the well defined communication protocol Modbus as standard interface protocol to the power supplies.

10.4.4.4 Vacuum

In the whole machine we need to display and control vacuum through different kinds of apparatus.

10.4.4.4.1 Pumps

The most widely used pumping systems for ultra-high vacuum (UHV) will be a combination of ion sputter pumps (briefly ion pumps) and titanium sublimation pumps (TSP). Control units for these pumps usually include a serial (RS-232 or RS-485) interface for remote control and a set of logical switches for alarm output to the control system. The brand and model of these controls, as previously indicated, should be the same for all the machine, in order to avoid duplication of software and spare parts. For particular sections (those requiring gas differential pumping) turbomolecular pumps with scrolling fore pumps will be required whose control units are again equipped with serial ports and switches. Turbo and scroll pump combinations will be also required for first stage of evacuation of each section, but in this case a remote control should not be needed.

10.4.4.4.2 Vacuum gauges

The vacuum gauges allow an accurate measure of the vacuum in different point of the machine. The most widely used ion gauges controls are equipped with serial ports or a FieldBus equipped with analog and digital channels. Unfortunately, at the time of this writing, these gauges are designed for industrial applications, and the required pressure range needed for radiation beam lines applications (in the 10^{-9} Pa scale) is not achieved, so the serial approach would be chosen. Some sections will require low vacuum gauges, such as thermocouples or Pirani heads, also generally equipped with control units having serial interfaces.

10.4.4.4.3 Valve controls

All the valves to be of the will be electro-pneumatic gate type. The control units, generally home made, will include a solid state switch for valve opening/closing and a couple of logical switches for valve status monitoring. All the valve control units will be logically (and in some case physically) connected to the vacuum gauge, ion pump and cooling system controls in

order to avoid valve opening in unsafe vacuum/cooling conditions and to close them automatically in case of vacuum/cooling alarms. Valves belonging to the switching mirror chambers will be also connected to the chamber position encoders, so that valves may be only opened on safe beam path conditions. Also, the correct opening and closing sequence will be ensured in order to avoid radiation directly hitting the front-end valves without the beam stoppers inserted. All these conditions imply hardware controls for the safety-related situations and realtime software controls in the other cases.

One special valve, designed for protecting the accelerator and the undulator from sudden venting of the beam lines, is the fast valve, which has its own sensor and control unit.

10.4.4.5 Diagnostic

The main machine parameter emittance, bunch length and energy in SPARX will be measured with images. Further information can be obtained by monitoring the undulator radiation. The use of a versatile camera system is strategic in the realization of this diagnostic. The rapid evolution in the image acquisition systems allows us to choose the camera and its own interface in a wide variety of products. The IEEE1394 or GvisionEth protocol gives us the possibility to interface different cameras with different specifications without changing the acquisition program. The cameras are acquired by different distributed personal computers that send data through a TCP/IP channel. The data transfer structure will be well defined to allow full integration of all cameras inside the control system.

Another important component in the diagnostic is the control of motors to move flags and slits to allow the acquisition of the beam image. The flag movement is allowed by the stepper motors.

The beam position and charge monitors depend on the pick up that we use. In general for this two kind of diagnostic we can use analog acquisition board with appropriate signal conditioning.

10.4.4.6 Motion and positioning

Most of the chambers holding optical elements, namely mirrors gratings and slits, but also the beam position monitor and the double slit inside the front-end, will require a motor system coupled with suitable position encoders. Depending on the accuracy required for positioning, stepper motors or CC motors will be used, coupled with optical encoders or potentiometric transducers respectively. In both cases, motor embedded encoders will not be used, relying on the motor reproducibility and on the external encoders. Motor control units are currently available with the most common interfaces such as Ethernet, CANopen, Profibus-DP, serial ports and so on. The latter three are also generally available for potentiometric transducers. Each motor will be equipped with a couple of switches (end of travel) to be used for both motor stopping and alarm generation.

10.4.4.6.1 Stepper motors and optica encoders

These will be required mainly on the grating actuators, in order to finely select the grating angle with the beam, and so the selected photon energy. Also the first switching mirrors, being a combination of mirrors/gratings, will need a stepper motor for grating grooves alignment on the radiation beam direction. Motor controls will be chosen according to their performance. In order to allow controlling the monochromators from the experimental stations during

experiments, the grating related motors will require real time and extremely low latency features. These will be the only motors requiring real time as we do not foresee to build spherical grating monochromators, which would require a moving exit (or entrance) slit in order to minimize aberrations. Optical encoders are usually read by serial interfaces.

Not only real time and low latency features will be needed, but a software interface will be made available for experimental station routines, in order to let the experimental groups insert the energy selection subroutines within their acquisition software

10.4.4.6.2 CC motors and resistive encoders

These will be used for all the other movements, where a positioning precision of less than few microns is not needed. Instead, a suitable motor power is required in order to move heavy vacuum chambers or mirror holders with the needed reproducibility.

10.5 References

- [1] J. Kim et al., "Femtosecond Synchronization and Stabilization Techniques", Proceedings of FEL 2006, BESSY, Berlin, Germany, p. 287
- [2] P. Craievich et al., "Jitter Studies for the Fermi@Elettra LINAC", Proceedings of EPAC 2006, Edinburgh, Scotland, p. 2880
- [3] Poseidon Scientific Instrumentation , PSI "Super Source" Performance Summary, private communication
- [4] Agilent E8257D PSG Analog Signal Generator Data Sheet; <http://cp.literature.agilent.com/litweb/pdf/5989-0698EN.pdf>
- [5] A. Winter et al. , "Phase noise characteristics of fiber Lasers as potential ultra-stable Master Oscillators" Proceedings of 2005 Particle Accelerator Conference, Knoxville, Tennessee p. 2521
- [6] http://www.menlosystems.com/pdf/cfiber780_web.pdf
- [7] <http://www.photrix.it/images/data-sheet%20picosource%20red.jpg>
- [8] G.P. Agrawal, "Nonlinear Fiber Optics", 3rd ed., Academic Press, San Diego, 2001.
- [9] T.R. Schibli et al., "Attosecond active synchronization of passively mode-locked lasers using balanced cross correlation", Opt. Lett. 28, 947 (2003).
- [10] J. Kim et. al., "Long-term femtosecond timing link stabilization using a single- crystal balanced cross correlator" Opt. Lett. 32, 1044-1046 (2007).
- [11] D. D. Hudson, S. M. Foreman, S. T. Cundiff and J. Ye, "Synchronization of mode-locked femtosecond lasers through a fiber link," Opt. Lett. 31, 1951 (2006).
- [12] F. Loehl et al Proceedings of PAC07, FROAC04, Albuquerque, New Mexico, USA (2007).
- [13] A. Gallo et al. , "Laser and RF Synchronization Measurements at SPARC", Proc. of 2007 Particle Accelerator Conference, Albuquerque, New Mexico, USA, p. 992
- [14] F. X. Kärtner et al. , "Progress in large-scale femtosecond timing distribution and RF-synchronization", Proceedings of 2005 Particle Accelerator Conference, Knoxville, Tennessee, p. 284
- [15] F. Loehl, et al., "A sub 100 fs electron bunch arrival-time monitor system for FLASH", Proceedings of EPAC 2006, Edinburgh, Scotland, p.
- [16] A.Drago, et al., "The DAFNE Timing System", EPAC96, Sitges, June 10-14, 1996. Published in *Sitges 1996, EPAC 96* 1775-1777. LNF-96/033(P).
- [17] A.Drago, et al., "Implementation and Performance of the DAFNE Timing System", EPAC 98, Stockholm, Sweden, 22-26 June 1998. Published in *Stockholm 1998, EPAC 98* 1661-1663. LNF-98/023(P).

11 VACUUM SYSTEM AND ALIGNMENT

11.1 Vacuum system

11.1.1 Introduction

The vacuum system of the SPARX project can be divided into five subsystems, that differ each other mainly on vacuum requirements. They can be schematically described as follows:

- LINAC & Radio Frequency Wave Guides
- Transfer Lines
- Undulators
- Experimental Stations

This distinction reflects the different vacuum levels and performances that are requested for each part of the facility and, as a consequence, the different components that will constitute each subsystem.

The mean vacuum working pressure for each subsystem is described in the following table

Table 11.1

<i>SUBSYSTEM</i>	<i>WORKING PRESSURE</i>
LINAC	10^{-7} Pa (RF Gun 10^{-8} Pa)
TRANSFER LINES	10^{-6} Pa
UNDULATORS	10^{-6} Pa
EXPERIMENTAL STATIONS	10^{-8} Pa
RADIO FREQUENCY WAVE GUIDES	10^{-6} Pa

11.1.2 General remarks

The performance of the SPARX machine depends strongly on the vacuum pressure. Extreme care must be adopted during each step of design, construction and assembling of all the vacuum system. An accurate ultra high vacuum technology practice must be adopted during each step of the design of each part of the vacuum chamber, only all metal components and devices are permitted as well as only oil free vacuum pumping systems. Special care must be adopted for the design of the RF Gun vacuum system, because of the high pollution sensitivity of the photo cathode.

11.1.3 Subsystems

11.1.3.1 LINAC

Based on our experience within the SPARC project, the vacuum levels requested for the operation of the SPARX LINAC will be the following:

RF-gun	$\sim 10^{-8}$ Pa
S-band accelerating section	$\sim 10^{-7}$ Pa
RF Waveguide	$\sim 10^{-6}$ Pa
Beam pipe	$\sim 10^{-6}$ Pa

Again the vacuum system of the LINAC itself it can be divided mainly in four parts:

- Vacuum chambers and beam pipe;
- Pumping system;
- Vacuum diagnostics;
- Pumps valves and ancillary systems;

In following sections these different sections will be described in details.

11.1.3.1.1 Vacuum chambers and beam pipe

The vacuum chamber of the transfer lines sections that are foreseen in between each accelerating structures will be made using stainless steel pipe with pumping station every 8 meter. Only sputter ion pumps will be adopted.

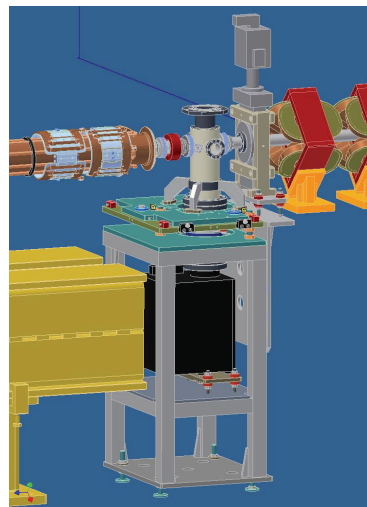


Figure 11.1: Pumping system

Based on the SPARX RF layout it is convenient to imagine a dedicated pumping system for the SPARC-like photoinjector that include the RF-gun, the first three accelerating sections and the RF sources and waveguide. For whom it concerns all the successive accelerating structures of the LINAC the pumping system will be described for a group of three accelerating section, their waveguide components and will be replicated for all the remaining sections.

11.1.3.2 RF-Gun

The RF-gun vacuum represents one of the most delicate parts of the whole system. In fact this structure should operate with very high electric fields gradient (about 120 MV/m) and high repetition rates (100 Hz) thus in order to decrease as much as possible the probability of discharge events the vacuum of this device has to be kept in the range of few 10^{-7} Pa during operation. Such low pressure is also required in order to keep the cathode surface free from contaminants that have been demonstrated to alter the photoemission properties of the cathode.

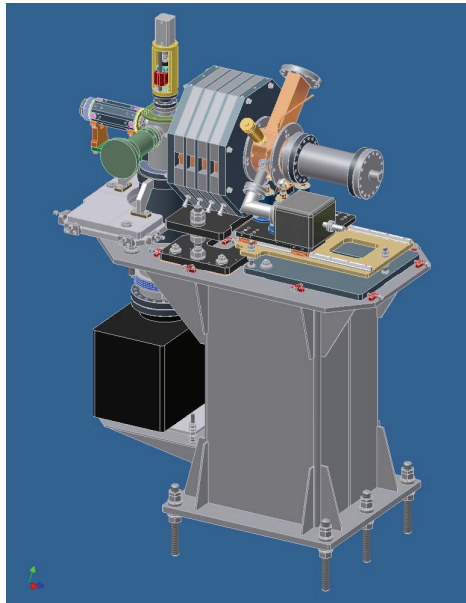


Figure 11.2

Considering the RF gun design that include a system of two waveguide RF coupler symmetrically connected to the full cell the pumping system of this device will be achieved by means of two sputter ion pump having a pumping speed of 50 l/s connected each to one of the RF coupler. Moreover in order to increase the pumping rate of hydrogen, which is not well pumped by ion pump, the use of a Non Evaporable Getter (NEG) is foreseen to be achieved using the back flange in the rear part of the gun.

Just after the gun focusing solenoid a 200 l/s ion pump is expected to pump down the vacuum chambers equipped with the diagnostic tools for the characterization of the electron beam before the injection on the TW accelerating structures.

The gun assembly (RF-gun, waveguide, diagnostic chambers and ion pumps) must be completed with a suitable backing system in order to perform an *in situ* degassing with the aim to remove all the residual water vapours that otherwise cannot be sufficiently eliminated avoiding the reaching of the requested vacuum level.

11.1.3.2.1 RF Waveguide

The radio frequency, needed to drive each accelerating section, flows through a complex system of copper wave guides operating under vacuum at a pressure of about 10^{-6} Pa. The vacuum is obtained by means of a certain number of titanium sputter ion pumps placed along the wave guides every about 10 meters. The RF connecting flanges will be of the CERN type.

11.1.3.3 Transfer Lines

A system of UHV transfer lines connects the exits of the LINAC to the undulators. The pressure in this section of the machine is maintained at a mean pressure of about 10^{-6} Pa by means of titanium sputter ion pumps. The vacuum chamber is made of stainless steel; all metal components and oil free vacuum pumps are installed in this section.

11.1.3.3.1 Vacuum diagnostics

Standard commercial vacuum diagnostics can be adopted on the SPARX LINAC. Vacuum gauges must be UHV compatible and must be able to read from atmospheric pressure down to 10^{-9} Pa. Moreover, in order not to disturb some beam diagnostic devices, UHV gauges must be of cold cathode type. Few residual gas analysers are foreseen to monitor the residual gas composition near some critical points of the LINAC, the RF Gun for example.

Table 11.2: LINAC vacuum components cost estimate (no VAT)

<i>Items</i>	<i>Unit number</i>	<i>Unit prices (k€)</i>	<i>Total (k€)</i>
Electro pneumatic valve	30	8	240
Manual service valve	43	2.5	107.5
Residual gas analyzer	2	6	12
Vacuum gauges	28	3	84
50 l/s Sputter ion pump	100	2.5	250
100 l/s Sputter ion pump	101	4	404
200 l/s Sputter ion pump	1	7	7
HV Power Supplies	14	5	70
HV Switching Boxes	14	8	112
NEG pump	1	10	10
Pump Connections	102	4	408
Vacuum Pipe	0.5/m	320 m	160
Fore Vacuum Karts	5	10	50
TOTAL			1914.5

11.1.3.3.2 Pumps valves and ancillary systems

On the LINAC the required vacuum pressure is obtained by means of a pumping system distributed along the LINAC itself. Besides the vacuum pumps, on the vacuum chamber some other components are foreseen: sector gate valves, manual service valves, fore vacuum systems.

In the following table a price estimate for the commercial vacuum components and the beam pipe is shown.

11.1.4 UNDULATORS

The vacuum system for the undulators, based on the scheme with two undulators of 16 magnets and one of 20 magnets, is able to reach and maintain a mean vacuum pressure in the order of 10^{-6} Pa. It is an all metal and oil free vacuum system.

11.1.4.1 Pumps

The vacuum pumps installed on the undulators section are titanium sputter ion pumps. Each magnet has its own chamber pumped by two 75 l/s ion pumps and at both ends a pumping station with a 150 l/s ion pump.

11.1.4.2 Vacuum diagnostics

Standard commercial vacuum diagnostics can be adopted on the SPARX Undulators section. Vacuum gauges must be UHV compatible and must be able to read from atmospheric pressure down to 10^{-9} Pa. Moreover, in order not to disturb some beam diagnostic devices, UHV gauges must be of cold cathode type. Three residual gas analysers are foreseen to monitor the residual gas composition, one for each undulator line.

11.1.4.3 Valves

Each undulator line has two electro pneumatic gate valves, one at its beginning and one at its end. Those valves are used to separate the undulator section from the rest of the machine in case of maintenance, fault analysis or emergency. In addition to the gate valves, some manual service valves are installed for fore vacuum pumps connection.

11.1.4.4 Beam transfer lines

A system of UHV transfer lines connects the exits of the LINAC to the undulators. The pressure in this section of the machine is maintained at a mean pressure of about 10^{-6} Pa by means of 150 l/s titanium sputter ion pumps. The vacuum chamber is made of stainless steel; all metal components and oil free vacuum pumps are installed in this section.

In the following table a price estimate for the commercial vacuum components and the beam pipe is shown.

Table 11.3: Undulator vacuum components cost estimate (no VAT)

<i>Items</i>	<i>Unit number</i>	<i>Unit prices (k€)</i>	<i>Total (k€)</i>
Electro pneumatic valve	6	8	48
Manual service valve	13	2.5	32.5
Residual gas analyzer	3	6	18
Vacuum gauges	13	3	39
75 l/s Sputter ion pump	104	2.5	260
150 l/s Sputter ion pump	65	4	260
HV Power Supplies	12	5	60
HV Switching Boxes	12	8	96
Undulator Chambers	52	5	260
Pump Connections	10	4	40
Vacuum Pipe	0.5/m	50 m	25
Fore Vacuum Karts	4	10	50
TOTAL			1188.5

11.2 Alignment

This section describes the procedures and methods used to position the SPARX components with their required accuracy. State of the art equipment and procedures can assure proper mechanical positioning. However, the position tolerances of the machine components, accelerators and undulators, are not achievable with standard procedures alone. With the conventional alignment methods an excellent pre-alignment is possible to achieve a sufficient initial accuracy for the following beam-based alignment.

The mechanical alignment will be realized using instruments such as laser trackers in combination with stretched wires and optical levels. A network of reference nodes will be built and will be qualified by referring the coordinates of each node to a properly chosen coordinate system. All components will be accurately fiducialized by means of either laser trackers or tactile probe measuring machines.

A stable site is obviously a crucial starting point for the alignment of a particle accelerator. For this reason maximum attention has been given to this aspect in the design phase in order to obtain good ground stability. Moreover it will be important to avoid the positioning of noisy vibrating equipment close to critical devices. From this point of view the choice of placing accelerator components and backing equipment in separate tunnels represents an advantage, also because it will allow the availability of more space dedicated and kept clear for the survey instrumentation and the measurement operations.

In the next paragraphs a more detailed description of the alignment method is given.

11.2.1 Reference Network

A network of reference nodes will be created inside the SPARX building. The nodes will consist of sockets fixed on brackets and pillars, or directly embedded in the walls and floor. The network is the reference frame for the alignment of the accelerator components. Therefore the network must be accurately qualified since it represents a limit for the overall accuracy. The qualification of the network is accomplished by means of free-standing laser tracker measurements and the precision of such measurements decreases linearly with the distance of the laser from the targets. Proper accuracy of qualification is only obtainable if the network is carefully designed and if the nodes are strategically distributed in the accelerator hall. High density and good spatial distribution of nodes will allow to reduce the uncertainty due to random laser tracker measurement errors. To uncover and reduce also the uncertainty due to possible systematic errors it will be necessary to perform redundant measurements using different instruments. For this reasons some of the network nodes will be referenced to one or more stretched wires. For redundancy of vertical measurements optical levels will be used.

A schematic layout of the SPARX reference network is shown in Figure 11.3. As it is possible to see, it will be made of primary nodes and secondary nodes.

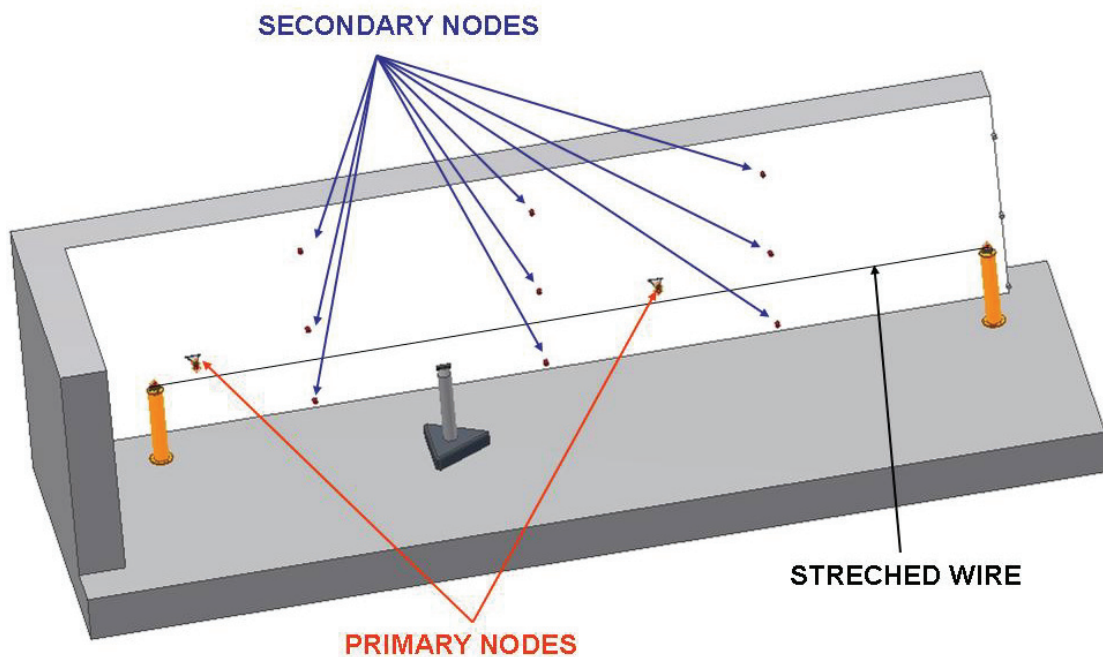


Figure 11.3: Schematic Layout of the SPARX Reference Network

The primary nodes will consist in CERN standard sockets mounted on pillars or brackets. Secondary nodes will consist in small cylindrical sockets, with 8mm precisely machined inner radius, embedded in the walls.



Figure 11.4: Primary (left) and Secondary (right) Node Sockets

The entire network will be made of approximately 50 primary nodes and 600 secondary nodes (1 primary node and 14 secondary nodes every 10m; the latter will be distributed on both sides of the hall and they will be placed at different heights). All nodes will be targeted both by laser trackers and optical levels. Only primary nodes will be referenced to stretched wires; their horizontal distances from the wires will be measured by means of CERN-built instruments (Figure 11.5). All node positions will be referred to a common right handed Cartesian coordinate system (SPARX coordinate system).

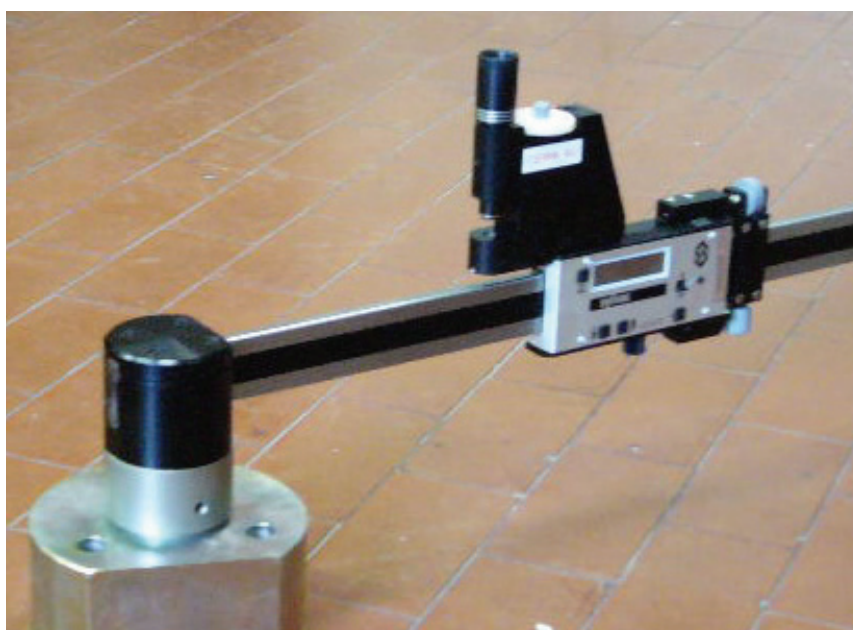


Figure 11.5: CERN built instruments for wire offset measurements

Despite the large scale of the project, the effect of the curvature of the earth on horizontal position differences between the projection of points on an equipotential earth gravitational surface and those on a local tangential plane may be neglected. In the vertical plane, however, it will have to be considered. With a reasonable approximation we can consider the earth gravitational equipotential surface as a sphere of radius $R=6372\text{km}$, and calculate the height differences between projection on the sphere and on the local tangential plane as $h=D^2/2R$, where D is the distance between the projection of the measured point and the point of tangency (Figure 11.6). In order to use and analyze clearly and easily both laser tracker and optical level

measurements, the height of the network nodes will not only be referenced to the SPARX coordinate system, but also to an earth gravitational equipotential surface.

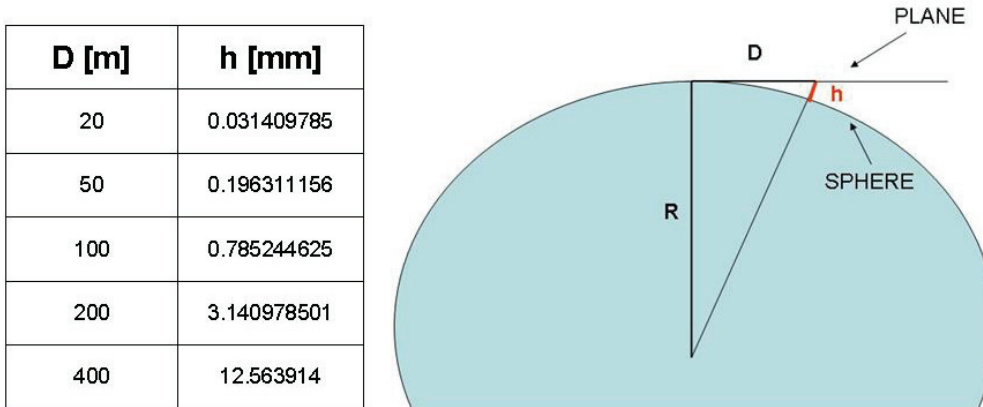


Figure 11.6: Earth Curvature Effect

11.2.2 Component Supports and Adjustment Systems

Generally a significant part of the uncertainty of the alignment is due to inefficiency of component supports and adjustment systems. To improve the accuracy all supporting structures will be carefully designed in order to assure a good rigidity. Furthermore a very accurate study, design and realization of the adjustment systems will be carried out. The latter will have to allow an adequately fine and sensitive regulation, and the possibility to block the components in position with minimum possible deformations. Moreover they will permit independency of horizontal and vertical movements.

11.2.3 Fiducialization

The process of referencing markers with respect to the axis of each component is called fiducialization. The correct fiducialization of components is as important as their correct positioning since an error in either task will affect the particles' trajectory and cannot be distinguished from each other. The design and realization of fiducial markers for all SPARX components will be carefully accomplished. The fiducials will have to be, first of all, clearly and comfortably visible during both fiducialization process and alignment operations in the accelerator hall. They will also have to be extremely stable and have, as much as possible, a symmetrical distribution around the component axis. The referencing of fiducial markers with respect to the geometrical axis of components will be performed by means of laser tracker measurements exploiting the tracking capabilities of this instrument and the versatility of leica Axyz software [1] which offers tools for many types of geometrical analyses. For some components this operation will be accomplished by means of tactile probe 3D coordinate measuring machines in outsourcing. In these cases data on fiducial marker positions, with certified accuracy, will be provided. For particularly critical magnetic components, which require high accuracy of alignment, the offset between magnetic and geometrical axis [2] will be measured by means of a hall probe machine [3] (Figure 11.7) or rotating coil. The positions of the fiducials on these components will then be referenced to the magnetic axis.



Figure 11.7: Hall Probe Magnetic Measuring Machine

11.2.4 Positioning of components

The positioning of SPARX components will be carried out in three main steps. At first the anchor hole positions for component supports will be marked on the floor and a rough and quick pre-alignment with an uncertainty of approximately 1 or 2mm will be done. Then, for precision alignment, free-stationed laser trackers, oriented to at least 6 neighbouring reference nodes will be used. The tracking capabilities of these instruments will significantly aid in facilitating the control of any alignment operation. At last, once the first positioning of all components is completed, they will be mapped for quality control. If any residuals exceed the given tolerances, smoothing operations and a subsequent quality control survey will be performed. A position accuracy of about ± 0.1 mm can be achieved.

11.3 References

- [1] www.leica.com
- [2] B. Bolli, S. Ceravolo, M. Esposito, P. Iorio, F. Iungo, M. Paris, C. Sanelli, F. Sardone, F. Sgamma, M. Troiani, G. Bazzano, I. De Cesaris: "Mechanical and Magnetic Qualification of the Focusing Solenoids for SPARC", ME-07/001, 02/03/2007
- [3] F. Iungo, M. Modena, Q. Qiao, C. Sanelli: "DAFNE Magnetic Measurement Systems", MM-1, 4/11/1993

12 RADIATION SAFETY

12.1 Introduction

High-energy electron accelerators are complex devices containing many components.

All facilities contain the same basic systems:

Accelerators structures

RF power components

Vacuum system

Magnetic system associated with steering and focusing the beam

Water-cooling

Etc

Prompt radiation and radioactivity induced by particle nuclear interaction in beam line elements and shielding structures represents the main radiation hazard of high energy accelerators.

The accelerator's design parameters are of crucial importance in the determination of the nature and magnitude of radiation source. The most important parameters are:

Particle energy

Beam power

Target material

Work load

Beam losses

12.2 Operating parameter

The SPAR-X project consists in an X-ray FEL facility in which an electron beam is accelerated at the energies of 1.5 and 2.4 GeV with peak current up to 2.5 kA (0.24 and 0.48 kW).

12.3 Machine protection

12.3.1 Electron losses

Even if the maximum power of the beam is quite low, an active machine protection system is under study to limit beam losses

12.3.2 Dose monitoring in the undulators section

The sensitivity of undulator magnets to radiation requires a dose monitoring in the undulator section. Active and passive systems are under evaluation.

12.4 Radiation Protection

12.4.1 Shielding outlines

The new machine general layout has been previously shown.

Using the previous operating parameters has performed calculations of shielding. Because of a great number of the precautions introduced, the results should be a conservative approximation of the doses actually expected. During the commissioning phase, the reliability of the assumptions made will be verified and, if necessary, additional precautions will be made.

12.4.2 Shielding Design Criteria

The shielding design criteria have been base on the text of the Italian legislation (D.Lgs. 230/95); according to European Directives as well as the recent ICRP recommendations (ICRP 103) According previous documents the individual limits are 20mSv/y for radiation workers, and 1 mSv/y for the members of the public.

Moreover the definitions of controlled and supervised areas are useful as guidelines. A controlled area is every area where 3/10 of the limits recommended for radiation worker may be exceeded. A supervised area is one area where the overcoming of 1/10 of the previous limit may occur.

Taking into account the dose levels normally found around accelerators, the thickness of the shielding was calculated maintaining the doses, within the areas outside the shield frequented by the staff, 1-2mSv/year and 0.25 mSv/year within the areas outside the shield frequented by members of the "public".

A shifting from these values could at most change the radiation classification of some areas.

In normal working condition the dose rate outside shielding should not exceed a fraction of $\mu\text{Sv/y}$

12.5 Source Term

For shielding evaluation purposes, three components of radiation field which are produced when an electron beam, with an energy of hundred of MeV both a vacuum chamber wall or a thick target have to be considered

12.5.1 Bremsstrahlung

Prompt photon fields produced by Bremsstrahlung constitute the most important radiation hazard from electron machines with thin shielding. Bremsstrahlung yield is very forward peaked, and increasingly so with increasing energy.

The following equation describes this behavior:

$$\theta_{1/2} = 100 / E_0$$

where $\theta_{1/2}$ is in the angle in degrees at which the intensity drops to one half of that at 0° , and E_0 is the energy of the initial electrons in MeV. In order to evacuate the shield thickness a "thick target", usually a target of sufficient thickness to maximize bremsstrahlung production, was considered. Photon yield from a thick target as a function of angle consists of two components: sharply varying forward component, described in equation , and a mildly varying wide-angle component. Forward (or zero-degree) bremsstrahlung

contains the most energetic and penetrating photons, while bremsstrahlung at wide angles is much softer.

The source term (per unit beam power) for bremsstrahlung at 90° is independent of energy.

12.5.2 Neutrons

Photons have larger nuclear cross-sections than electrons, so neutrons and other particles resulting from inelastic nuclear reactions are produced by the bremsstrahlung radiation. Neutrons from photonuclear reactions are outnumbered by orders of magnitude by electrons and photons that form the electromagnetic shower. However, some of these neutrons constitute the most penetrating component determining factor for radiation fields behind thick shielding.

12.5.2.1 *Giant resonance production*

The giant resonance production can be seen in two steps:

- 1) the excitation of the nucleus by photon absorption;
- 2) the subsequent de-excitation by neutron emission, where memory of the original photon direction has been lost.

The cross-section has large maximum around 20-23 MeV for light nuclei (mass number $A \leq 40$) and 13-18 MeV for heavier nuclei.

The angular yield of giant resonance neutrons is nearly isotropic.

The giant resonance is the dominant process of photoneutron production at electron accelerators at any electron energy.

12.5.2.2 *Pseudo-deuteron production*

At photon energies beyond the giant resonance, the photon is more likely to interact with a neutron-proton pair rather than with all nucleons collectively. This mechanism is important in the energy interval of 30 to ~300 MeV, contributing to the high-energy end of the giant resonance spectrum. Because the cross-section is an order of magnitude lower than giant resonance, with the added weighting of bremsstrahlung spectra, this process never dominates.

12.5.2.3 *Photo-pion production*

Above the threshold of ~140 MeV production of pions (and other particles) becomes energetically possible. These pions then generate secondary neutrons as byproduct of their interactions with nuclei. While substantially less numerous than giant resonance neutrons, the photopion neutrons are very penetrating and will be the component of the initial radiation field from a target (with the exception of muons at very high energies) that determines the radiation fields outside very thick shields.

Taking account all operating parameter as well as the foreseen beam losses (5%) and shielding design criteria, a roof of 1.5 m of ordinary concrete was chosen for machine tunnel (LINAC + undulators) and roof of 1 m of ordinary concrete was chosen for the modulator tunnel.

In following figure are reported the ambient dose equivalent rate at 6 m and 13 m from the source at 90° versus the thickness of concrete shield.

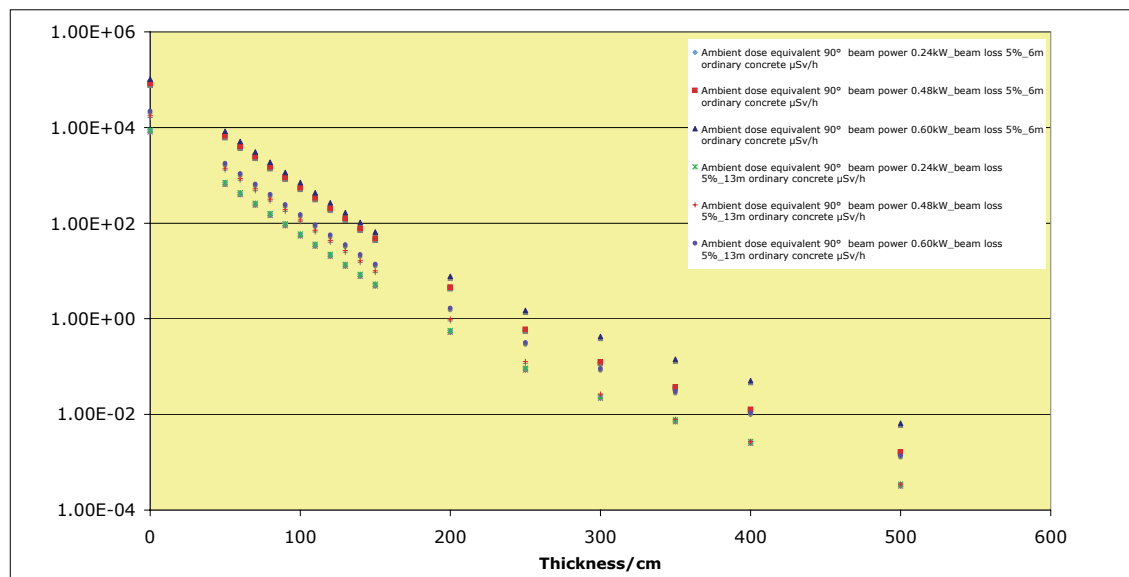


Figure 12.1: ambient dose equivalent rate.

Calculations are in progress in order to define the thickness of the whole shield, following the final layout, the final definition of the beam parameters and the beam losses.

12.5.3 Muons

Muon production is analogous to e^+/e^- pair production by photons in the field of target nuclei when photon energy exceeds the threshold $2m_m c^2 \approx 211$ MeV.

Above a few GeV the muon yield per unit electron beam power is approximately proportional to electron energy E_0 . Muon angular distribution is extremely forward-peaked, and this distribution narrows further with increasing energy. At energies of a few GeV adequate photon and neutron shielding will be also sufficient for muons. Calculation are in progress

12.5.4 Gas bremsstrahlung

The gas bremsstrahlung is produced by the interaction of the electron beam with residual low-pressure gas molecules in the vacuum pipe. Bremsstrahlung on residual gas is one of the main cause of beam loss in a storage ring and may represent a radiation hazard at synchrotron radiation facilities. This type of radiation has been thoroughly investigated at circular storage rings, where the beam current is much more intense. It is mainly in the straight section that a radiation problem could arise. At SPARX the straight length over which bremsstrahlung is produced will be not less 85 m.

Calculation are in progress following the final layout, the final definition of the operating parameters.

12.5.5 Induced Activity

Personnel exposure from radioactive components in the beam line is of concern mainly around beam lines, collimators, slots, beam stopper or beam dump, where the entire beam or a large fraction of the beam is dissipated continuously, while unplanned beam losses result from beam mis-steering due to inaccurate orbit adjustment or devices failure.

Beam losses induce activation in machine component as well as in

the beam pipe	(⁶⁰ Co, ⁵⁴ Mn, ⁵¹ Cr, ⁴⁶ Sc, ²² Na, ¹¹ C, ⁷ Be)
the cooling water	(³ H, ⁷ Be, ¹⁵ O, ¹³ N, ¹¹ C)
the air	(¹⁵ O, ¹³ N, ³⁸ Cl, ⁴¹ Ar)
the concrete walls	(¹⁵² Eu, ¹⁵⁴ Eu, ¹³⁴ Cs, ⁶⁰ Co, ⁵⁴ Mn, ²² Na)

The activation of soil as well as the groundwater by neutrons and other secondary particles can have an environmental impact but at electron accelerators the radioactivity levels are generally low and absolutely negligible with the previous beam parameters.

Calculations are in progress, following the final definition of the beam parameters and the beam losses and the characteristic of cooling water system, the air circulation system and the beam dump layout.

12.5.6 Machine accesses

During machine operation the LINAC tunnel will be an excluded area.

During no operation periods the LINAC tunnel will be a controlled area, due to the possible activation of the machine structure.

The technical areas behind the roof shield will be classified as controlled or supervised areas.

The experimental areas will be a free access area. Only areas close to the front ends or at the end of the beam line will be classified.

In order to protect workers in the experimental areas, the electron beam will be dumped below the floor after the FEL undulators. A deflection of 45° is effected by electromagnets.

For additional safety permanent magnets and active radiation detectors interlocked with the beam will be used.

12.5.7 Beam line radiation shielding design

For each shielding situation (insertion device white beam, radiation transport, monochromator, hutches etc.) the synchrotron radiation, the gas bremsstrahlung, the high-energy bremsstrahlung, from beam halo interactions with the structures of the machine, will be calculate for a representative geometry.

12.5.8 The operational radiation safety program

The purpose of the operational safety system program is to avoid life-threatening exposure and/or to minimize inadvertent, but potentially significant, exposure to personnel. A personnel protection system can be considered as divided into two main parts: an access control system and a radiation alarm system.

The access control system is intended to prevent any unauthorized or accidental entry into radiation areas.

The access control system is composed by physical barriers (doors, shields, hatches), signs, closed circuit TV, flashing lights, audible warning devices, including associated interlock system, and a body of administrative procedures that define conditions where entry is safe. The radiation alarm system includes radiation monitors, which measure radiation field directly giving an interlock signal when the alarm level is reached.

12.5.8.1 Interlock design and feature

The objective of a safety interlock is to prevent injury or damage from radiation. To achieve this goal the interlock must operate with a high degree of reliability. All components should be of high grade for dependability, long life and radiation resistant. All circuits and component must be fail safe (relay technology preferably).

To reduce the likelihood of accidental damage or deliberate tampering all cables must run in separate conduits and all logic equipment must be mounted in locked racks.

Two independent chains of interlocks must be foreseen, each interlock consisting of two micro switches in series and each micro switches consisting of two contacts.

Emergency-off buttons must be clearly visible in the darkness and readily accessible.

The reset of emergency-off buttons must be done locally.

Emergency exit mechanisms must be provided at all doors.

Warning lights must be flashing and audible warning must be given inside radiation areas before the accelerator is turned on.

Before starting the accelerator a radiation area search must be initiated by the activation of a "search start" button. "Search confirmation" buttons mounted along the search path must also be provided. A "Search complete" button at the exit point must also be set.

Restarting of the accelerator must be avoided if the search is not performed in the right order or if time expires.

The interlock system must prevent beams from being turned on until the audible and visual warning cycle has ended.

Any violation of the radiation areas must cause the interlocks system to render the area safe.

Restarting must be impossible before a new search. Procedures to control and keep account of access to accelerator vaults or tunnels must be implemented.

12.6 ELECTRON BEAM DUMP

The electron beam will be dumped below the floor at the end of the undulators in the LINAC tunnel. The beam deflection of about 45 degrees is made using permanent magnet for additional safety.

The layout of beam dump as well as the size and type of shielding materials is under study.

12.7 OTHER RADIATION SOURCES

The RF power sources for SPARX are 60 MW peak S-band klystrons.

The klystrons will arrive already shielded from factory.

Additional shield will be installed in order to eliminate and/or to reduce radiation escape. An interlocked fence around klystrons is foreseen in order to reduce as low as possible the radiation level behind the fence.

13 INFRASTRUCTURE

13.1 The Site

The SPARX X-FEL accelerator will be built in the Tor Vergata campus site, a few km southeast of the city of Rome. It will be disposed along a linear geometry, approximately 0.5 km long. The interested area is just alongside of the CNR territory and it is approximately a couple of km away from the ENEA and INFN sites in Frascati.



Figure 13.1: The Tor Vergata Campus Site

The ground in this region has volcanic origin; it came from the eruption of the Colli Albani volcano more than 600000 years ago. A geological analysis of the territory has been carried out and it has proved that the ground is made of very stable rock. The drilling tests performed in the nearby area, where the “Sports City” is under construction, show that the ground is made of a first layer of about 1m of soil, underneath which there is a second layer of brown pyroclastic rock, of approximately 10m of depth, composed of medium-grained volcanic sand and then a third layer, of approximately 15m of depth, of gray pyroclastic rock composed of coarse-grained sand (Figure 13.2).

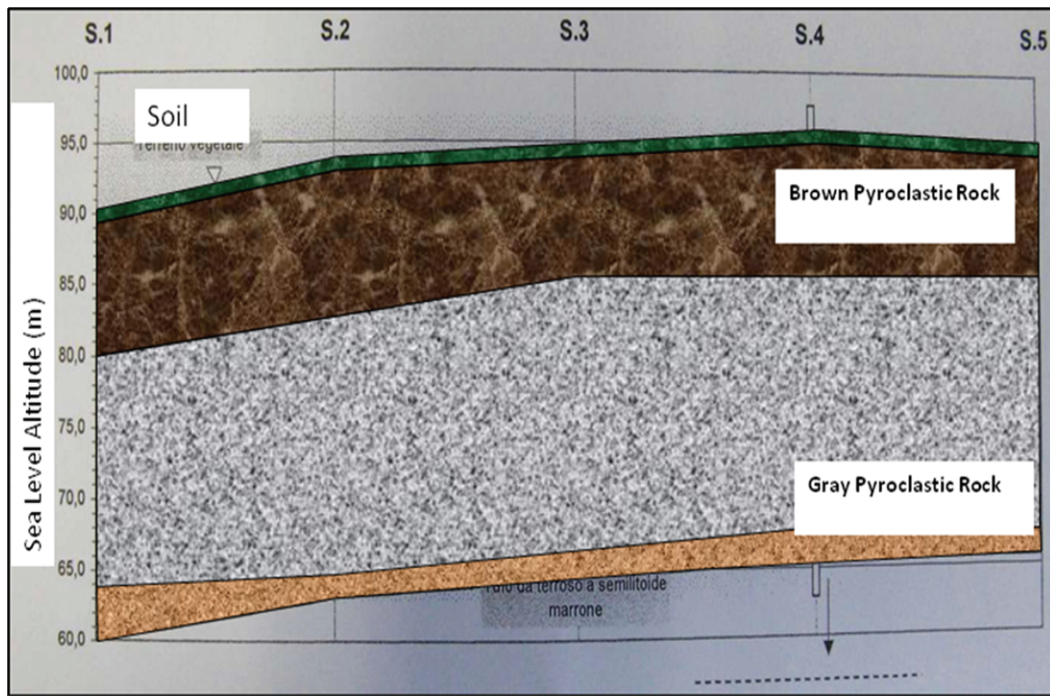


Figure 13.2: Composition of the Ground in the SPARX area

On the basis of the hydrogeological studies performed on this region, the area may be considered to have an extremely low level of hydrogeological vulnerability.

Seismic maps of the Italian territory, provided by the “Istituto Nazionale di Geofisica e Vulcanologia”, show that the area where the SPARX building will be built is geostatically stable (Figure 13.3). The maximum ground acceleration in the region of Rome and surroundings is comprised between 0.150 and 0.175 g, with a 10% probability of exceeding it in 50 years.

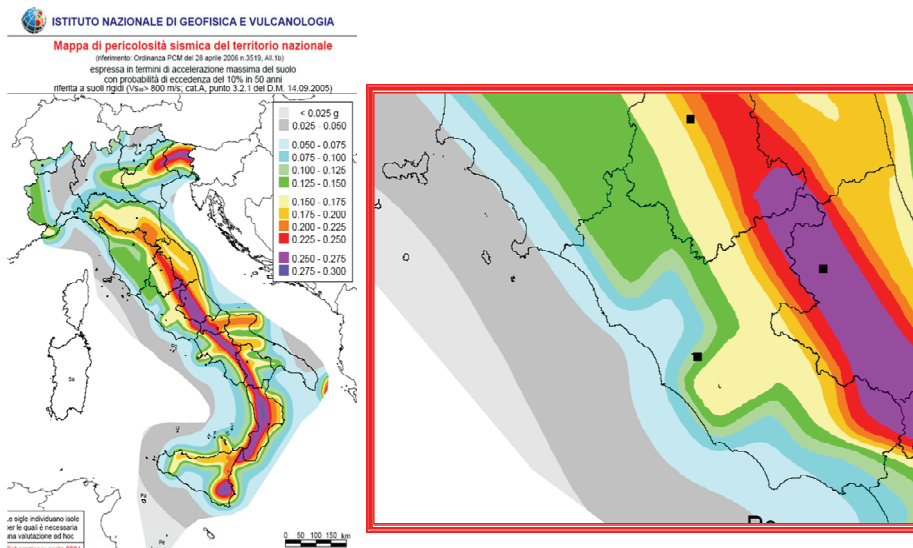


Figure 13.3: Seismic Map of the Italian Territory with a close-up on the Lazio Region

13.2 Buildings

The SPARX facility is housed in a complex of civil buildings, the most part of which are underground. The surface buildings have been reduced to a minimum in order to fulfil the town planning scheme of the Tor Vergata area, and they consist of a big building at the head of the facility and another one at the end of the LINAC, just above the undulator hall (Figure 13.4).



Figure 13.4: The SPARX buildings

The underground buildings consist of a service building at the beginning of the LINAC, and of three main halls for a total length of a bit more than 400m. The first hall will house the injector and the LINAC, the second hall will house the undulators and the third one will house the experimental lines and devices. LINAC and undulator halls will be divided in two overlapped tunnels. The lower tunnels will house the accelerator components, while the upper ones will house all the backing equipment such as klystrons and power supplies [1].

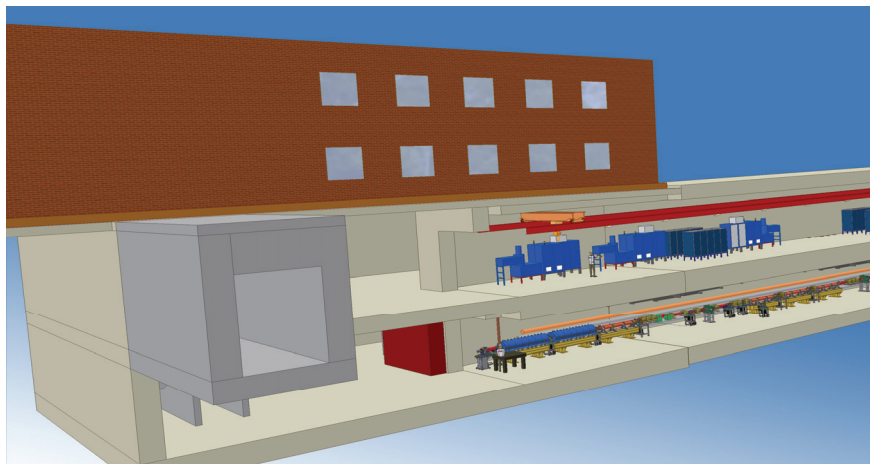


Figure 13.5: The Head Surface Building and the first part of the Klystron Hall and LINAC Hall

The choice of building two overlapped tunnels, for accelerator components and supporting devices respectively, instead of side by side tunnels, is dictated both by economical convenience (less excavation work will be necessary) and by the fact that it assures a greater structural rigidity with respect to vertical forces.

The underground buildings will be entirely built with reinforced concrete. The thickness of the walls will meet radiation safety requirements. The side

walls are 1m thick, the basement of the building is 1.2 m thick, while the two overlapped tunnels are separated by a 1.5m thick layer of concrete.

The LINAC tunnel is 5m wide and 4m high with a total length of 260m. Economical reasons have brought to the design solution of minimizing the height of the accelerator tunnel. The beam line is placed at 1.5 m from the left wall (Figure 13.6), leaving therefore enough space on the right side of the beam line for the transit of forklifts and small electrical lift trucks for the transport of components, supports and other material.

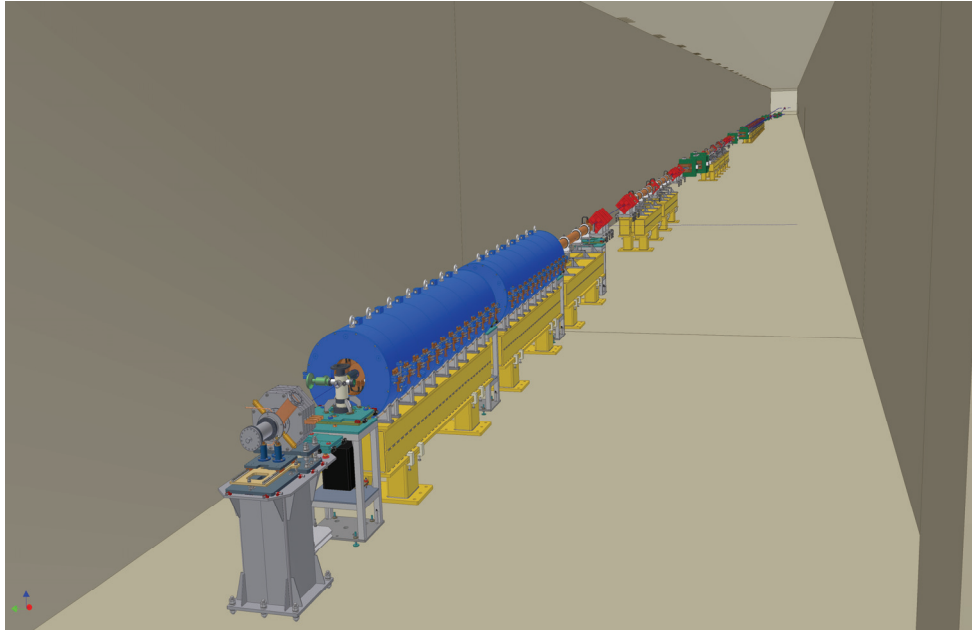


Figure 13.6: Position of the beam line inside the LINAC tunnel

The tunnel above the LINAC will house klystrons, power supplies and other supporting equipment. It will have same the width and length as the LINAC tunnel, but it will be 5.5m high. A 5t load capacity bridge crane will be mounted to facilitate the installation of klystrons and power supplies (Figure 13.7).

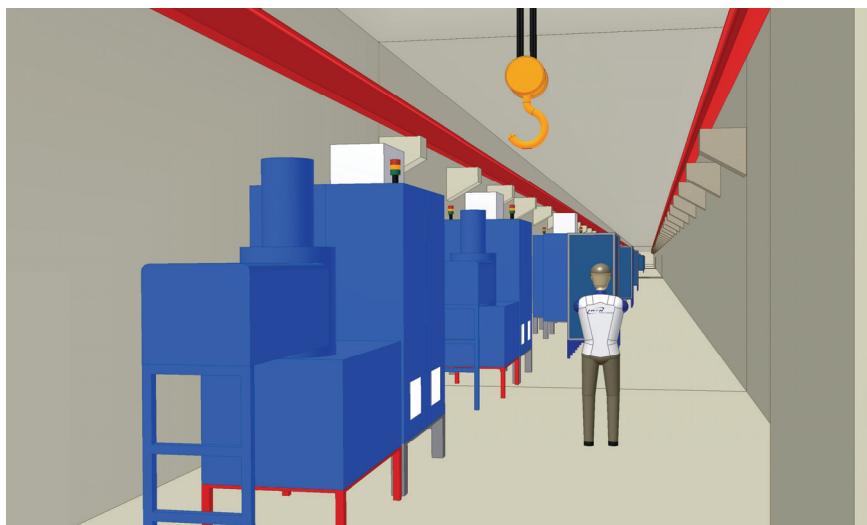


Figure 13.7: The Klystron Hall

The Undulator Hall will be 12m wide and 85m long. In the same way as for the LINAC Hall it will be divided in two overlapped tunnels. The lower one will have a height of 4m and it will house the machine components. The upper one will house a magnetic measuring machine and a workshop containing some supporting devices. The latter will be 5.5m high and a bridge crane will be installed in it.

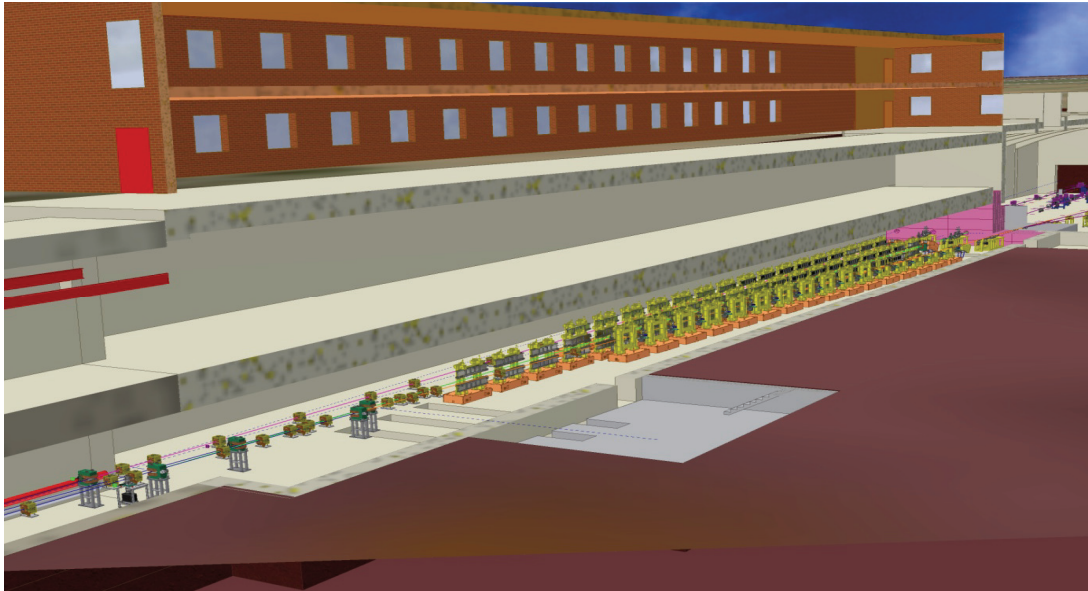


Figure 13.8: The Undulator Hall

The Experimental Hall will be 30m wide, 60m long and 10.5m high. The structure of the building will be reinforced by six arches, placed at a distance of 8.7m one from another. The latter will have a total width of 40m. By closing the external perimeter defined by the arches some more rooms could be obtained and used as supporting laboratories or storage rooms (Figure 13.8).

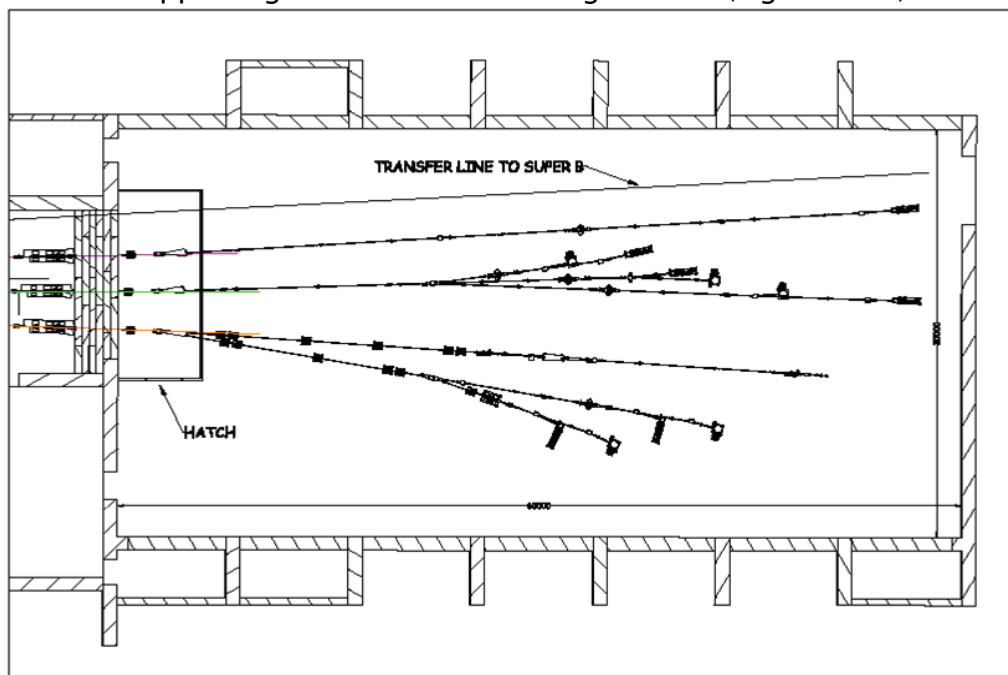


Figure 13.9: Plan of the Experimental Hall

The opening between the Undulator Hall and the Experimental Hall will be closed by a 3m thick shielding wall made of removable concrete blocks.



Figure 13.10: Cross-sectional view of the Experimental Hall with the experimental lines and devices

The SPARX facility will also include two main surface buildings. There will be a big building, housing the control room, above the Undulator Hall and a smaller one above the head of the LINAC. The control room building will also contain a meeting room and several offices for SPARX personnel and operating staff. A computing room will be foreseen and some storage rooms and laboratories will be realized and made available for:

- Vacuum tests;
- RF and electronics assemblies;
- Mechanical manufacturing;
- Alignment tests and calibration of metrology instruments;
- Radiation safety instrumentation;



Figure 13.11: The Control Room Building

The building at the head of the LINAC will have a big hall, accessible to trucks, where components and other equipment and material will be delivered. A bridge crane will be mounted and a pit will allow communication with Klystron Hall and LINAC Hall. This building will also house a few offices and the stairs that lead to the main entrance of the LINAC Hall (Figure 13.12). The Laser clean room will be in this building, at LINAC level, just aside the injector.

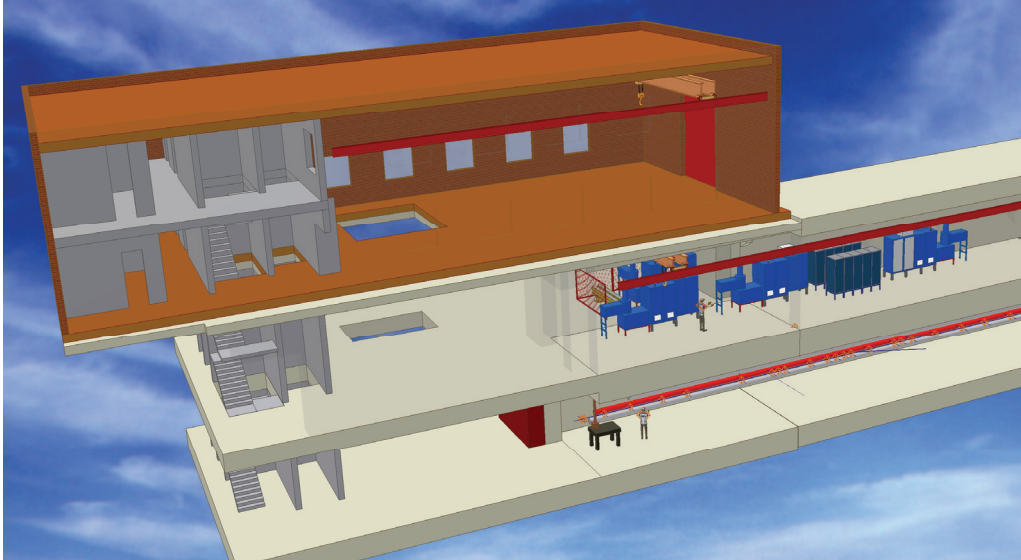


Figure 13.12: The Surface Building at the head of the LINAC

Five more emergency exits will be placed along the building, on the right side, at approximately 60m one from the other. Smoke filter areas will be realized and all safety standards will be respected.

At the side of the emergency stairs (at machine tunnel level and klystron tunnel level) there will be rooms available for conventional services equipment (cooling and air conditioning). At ground level there will be five surface buildings two of which will house the electrical substations necessary to power the entire facility.

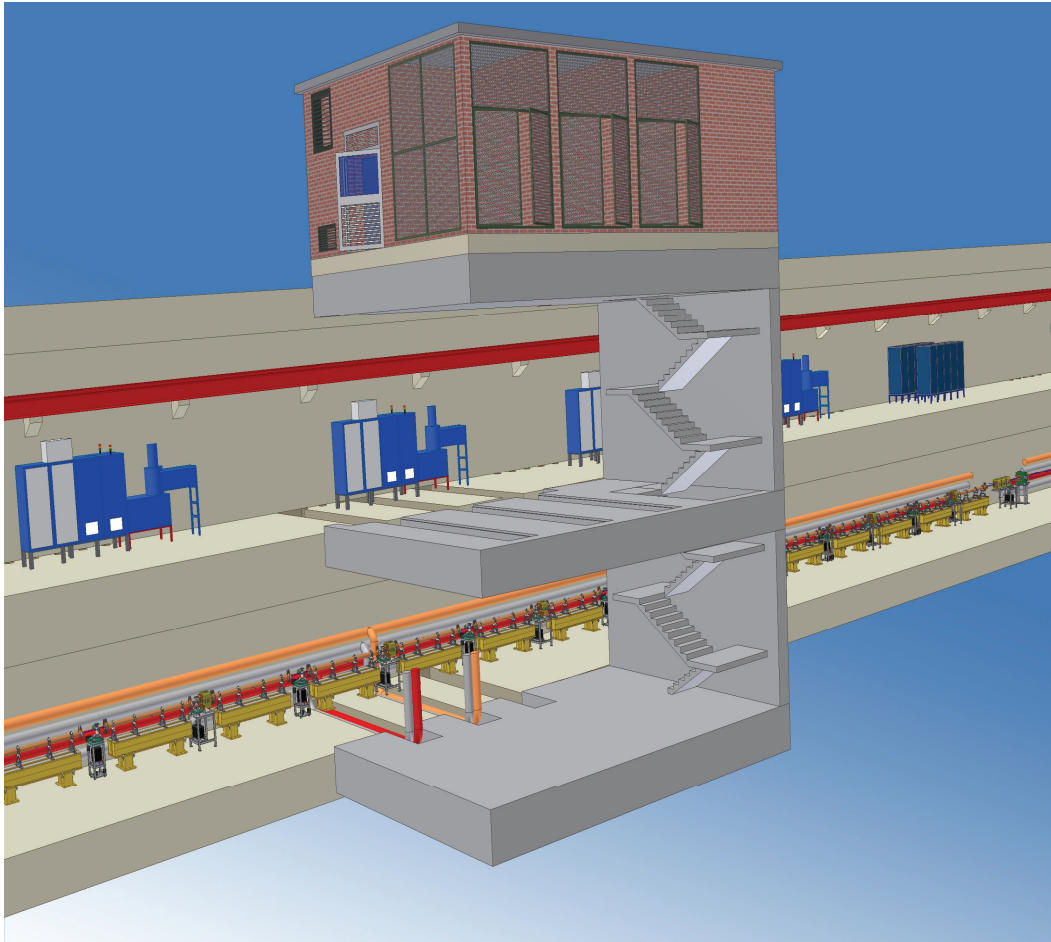


Figure 13.13: The Emergency Exit with rooms for cooling (machine level), air conditioning (klystron level) and surface building for electrical substation

13.3 Sparx Electrical Power supply

A modern 150 kV underground public network with two different HV substations supplies the Tor Vergata Campus area where Sparx will be built.

Sparx will be supplied by two 20 kV dedicated feeders connected to the two different HV substations a few hundred meters far from this installation.

Technical details in order to optimize the power quality level have been taken into account with the supplier (ACEA Distribuzione) and an historic survey of the quality delivered to the neighbour users will be performed.

Sparx facility expected power demand is about 7 MVA. In Table 13.1 a first load estimation is shown.

Table 13.1: First electrical load estimation

Stage 1	kVA
12 RF stations	1800
Magnets power supplies	540
Cooling system & HVAC	2000
Conventional Loads	300
Stage 2	
6 RF stations	900
Magnets power supplies	676
Total power demand	6216

The Sparx facility will be powered by two MV/LV substations equipped with 3 x1.6 MVA transformers each. The first substation will supply the first stage at 1,5 GeV and the cooling system, the second one will power the 2,4 GeV section, the Undulators, the experimental area and the external building.

The two substations will be located in two technical buildings at ground floor, close to the two central fire stairs and central with respect to the electrical load.

Oil filled 20/0.4 kV transformers will be housed in a out-door roofing area, in order to minimize cost and reduce the thermal load to be removed by HVAC.

Reactive power compensating system will be housed in the substations.

Some staging can be taken into account. The installation of two transformers of the second substation and cabling related to stage 2 loads can easily be postponed.

The technical areas for substations and the electrical installations as the cable tray occupancy have been integrated in the civil construction design.

13.3.1 Redundancy criteria

Fault redundancy has been taken into account for main components as the transformer bay and MV feeders. The unavailability of one component of a transformer bay, like MV or LV breaker, protection devices, auxiliary services, busbars, as well as the transformer, doesn't compromise the operation.

Transformers will be sized in order to be fully loaded in case of unavailability of one per substation. Otherwise they will be loaded at 50%.

A back-up generator will supply underground lighting, ventilation, auxiliary services and some UPS loads.

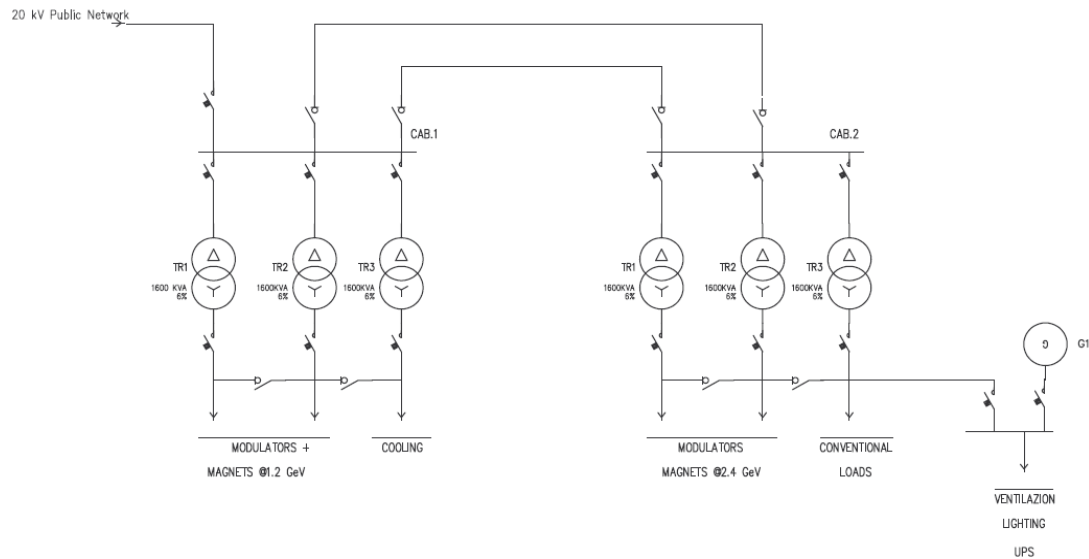


Figure 13.14: Sparx electrical power distribution system.

13.3.2 Low voltage power distribution

Power is distributed at level 400/230 V as TN-S distribution system.

LSOH Cables (fire retardant, Low Smoke – Zero Halogen) will be adopted for internal wiring.

Power cables will be drawn in metal ducting systems distinct and far from control and signal ducting system in order to minimize the electromagnetic coupling with electronic cables and devices.

Protection against indirect contact has to be achieved by overcurrent protective devices. Residual current devices will be adopted only on the load.

As a general consideration, important loads, over 125 A, will be fed by dedicated switch units of the low voltage main switchboard. Lower size devices will be supplied using 400 A busbars trunking systems that will serve all the power supply rooms. Busbar Tap-off units will be equipped with circuit breaker.

13.3.3 Electrical installation for the accelerator tunnel

Special care will be taken into account in order to minimize radiation damage against electrical devices. Radiation tolerant materials and low maintenance systems will be selected for every component that has to be installed in the beam area. Electronic devices not absolutely necessary will be banned by the accelerator area, like electronic ballasts and control devices.

With respect to lighting devices, polycarbonate and electronics suffer by radiations. Metal and glass luminaries with fluorescent bulbs with not electronic ballast will be adopted, and a central emergency lighting system will be preferred with respect to self-powered devices. Fire resistant cable FGT100M1 will be adopted for the safety lighting power distribution.

Reduced maintenance devices and solutions will be adopted in the radiation safety restricted access area. Electrical switchboards will be placed out of the beam area of influence.

13.3.4 Grounding, bonding and low voltage distribution system

The earth electrode, required for electrical safety, will be integrated with metal reinforcement of concrete and structural metalwork of all the building site. A meshed common bonding network (CBN) will be distributed with 250 mm² of copper bar in all the beam and power supplies area, and it will be used to bond all the devices in the beam line and the auxiliaries besides the proper earth protection.

The low voltage distribution system will be delivered as TN-S, with separate neutral and protective earth (PE) wires. The PE will be distributed and bonded on the CBN wherever is possible, in order to minimize conducted and radiated interference.

CBN will be the only reference potential inside the site.

13.3.5 Electromagnetic compliance

With respect to technical rules CEI-EN 50160, 61000-2-2 and 61000-2-12, electrical installations have to comply level 2 of CEI-EN 61000-2-4. Nevertheless, higher harmonic current distortion level has to be expected for power converter that will be powered by a “dirty” transformer bay.

13.4 Accelerator special fluid plants

This section is devoted to all the mechanical subsystems needed to remove the heat from the machine (water cooling), from its auxiliary equipments and their rooms (accelerator tunnel, modulators tunnel, undulators hall, experimental hall). In addition, here are comprised the water treatment systems, the clean room air conditioning system and the compressed gas production, storage and distribution.

The integration with the conventional building HVAC systems has to be discussed.

The aim of the design of these facilities will be a high level of performance and reliability, the energy effectiveness and the easiness of operation and maintenance.

The design of the whole system will allow to stage the installation according to the two phases foreseen for the accelerator.

13.4.1 Cold and hot fluids production

Based on the electrical power requested by the user, the total cooling load is estimated in about 5 MW, and it will be reasonably distributed in 4 MW in water and 1 MW in air. With respect to these estimation, based on the electrical needs, a certain redundancy will be necessary, to keep an adequate level of reliability and availability of the service.

The heat from the accelerator will be dissipated by dry coolers, where and when the ratio of cooling water temperature to external air temperature is favourable, and by air cooled chillers. This choice is due to keep as low as

possible the electrical consumption, with free cooling, and to avoid any continuous water use (no water source is currently available).

13.4.2 Air conditioning and ventilation of tunnels and halls

The air treatment will remove the heat from the accelerator rooms to keep a stable and suitable temperature and will supply fresh air to maintain a low level of pollutants. Because the first task is largely predominant, a double cold vector (water and air) is needed to keep passages as small as possible.

The equipment will consist in several Air Handling Units (AHU), placed outside of the tunnels and halls, and several internal water cooled appliances, or Fan Coils (FC).

The balance between the room occupancy along the tunnels and the users needs in term of temperature uniformity and stability will be studied to define the number and the size of these equipments.

The experimental hall and the undulators hall will be carefully studied from the air distribution point of view. A long range air jet nozzle row will be probably suitable for these large rooms. Detailed simulations are mandatory for the air distribution design.

This system has to be interfaced with the smoke extraction and with the emergency and safety subsystems.

13.4.3 Water cooling

Low conductivity, demineralized water is required to cool radiofrequency and magnetic components, to limit the corrosion of components, to keep adequate electrical insulation and for radiological reasons. Stainless steel will be mandatory for all the plant components (piping, valves, pumps, etc.).

A complete on-line treatment of de-gassing, UV hygienization and re-demineralization will be provided, as well as a demineralized water production unit.

An adequate pressure and temperature level will be set for each class of components; in general three thermal level will be provided for the accelerator:

- high (35 to 45°C) – it needs an additional heat source
- medium (30 to 35°C) – no needs of chilled water most of the year
- low (15 to 25°C) – it requires chilled water

along with the chilled water (7°C) and hot water (50-70°C) for AHU and air conditioning appliances.

Two pressure level will be available:

- low pressure (200 to 400 kPa)
- high pressure (500 to 800 kPa)

For special accelerator equipment, as RF accelerating sections, dedicated high accuracy cooling circuits will be realized. A stability of +/- 0.1°C could be achieved with special hardware and a careful design and commissioning.

A study will be requested to investigate the optimization of the temperature levels, to keep the electrical consumption and the plant construction cost as low as possible. A common temperature for the two higher level, around 35-40°C should be advisable.

Heat and cold recovery should be applied wherever possible.

13.4.4 Compressed gases

A central of production and storage of technical gases as compressed air, nitrogen, or others if required, will be installed, as well as a distribution network.

13.4.5 Energy efficiency

An efficiency evaluation of the whole installation will be performed.

In general:

- piping and users thermal insulation will be adopted to reduce losses;
- free cooling will be extensively used, as well as heat and cold recovery from the water and air flowing in and out;
- cold storage, associated with night cold production, will be employed to satisfy the peak of the variable heat loads;
- high return water temperature from appliances and accelerator components will be preferred to reduce passages and pumping energy and to increase the heat exchange efficiency;
- the use of any form of renewable energy will be promoted, as mandatory by italian law.

13.4.6 Users evaluation

A first screening of users needs in terms of cooling power, both in water and in air, has been done.

In the following tables the results are summarized.

<i>WATER cooling</i>	<i>POWER</i>	<i>FLOW</i>	<i>min. pipe ID</i>
SUB-STATION 1	kW	litri/min	cm
RF cooling control unit 1.1			
(demineralized water)			
Modulators Hall			
Mod.1 - Gun	75.0	537.5	
Mod.2 RF1-2-3	75.0	537.5	
Modulatore 18 (riserva)	75.0	537.5	
		225.0	1'612.5
			18.5
Accelerator Tunnel			
sez. acc.2 RF1-2-3	14.3	681.1	12.0
heaters regolazione RF	47.5		
loads	7.1	51.1	3.3
		68.9	
Power Supplies cooling 1.1			
(demineralized water)			
Modulators Hall			
Sol1	7.5	21.5	
Sol2	7.5	21.5	
Quad + correttori Sparc (10 quad @150 MeV)	0.4	1.1	
		15.4	44.1
			3.1
Magnets cooling 1.1			
(demineralized water)			
Accelerator Tunnel			
Sol1	67.5	193.5	
Sol2	67.5	193.5	
Quad + correttori Sparc (10 quad @150 MeV)	3.6	10.3	
		138.6	397.3
			9.2
Auxiliaries 1.1			
Demineralized Water treatment			
Demineralized Water production			
Compressed air			
Technical gases			
SUB-TOTAL			
	447.9		
FLOW FROM MAINS (ref. to 5°C deltaT)		1'284.0	16.5
HVAC 1.1			
raw chilled water circuits			
Clean Room FC	10.0	28.7	2.5
Clean Room AHU	6.9	19.8	2.0
Mounting Hall FC	30.0	86.0	4.3
Mounting Hall AHU	10.8	31.0	2.6
Modulator Hall FC	47.8	137.0	5.4
Modulator Hall AHU	4.9	14.0	1.7
Accelerator tunnel FC	16.7	47.9	3.2
Accelerator tunnel AHU	4.9	14.0	1.7
Electrical facilities halls FC	30.0	86.0	4.3
Electrical facilities halls AHU	3.0	8.6	1.4

Mechanical facilities halls FC	30.0	86.0	4.3
Mechanical facilities halls AHU	3.0	8.6	1.4
Chillers station MAINS	197.9	567.4	11.0
TOTAL POWER	645.8		
TOTAL FLOW		1'851.5	19.8

<i>WATER cooling SUB-STATION 2</i>	<i>POWER</i>	<i>FLOW</i>	<i>min. pipe ID</i>
--	--------------	-------------	-------------------------

RF cooling control unit 2.1			
Modulators Hall			
Mod.3 RF 4-5-6	75.0	537.5	
Mod 17 Banda X	75.0	537.5	
Mod.4 RF 7-8-9	75.0	537.5	
		225.0	1'612.5
			18.5
Accelerator Tunnel			
sez. acc.3 RF 4-5-6	14.3	681.1	
sez. acc.4 RF 7-8-9	14.3	681.1	
heaters regolazione RF	95.0		
			1'362.3
			17.0
loads	7.1	51.1	0.0
		130.7	1'413.3

Power Supplies cooling 2.1			
Quad LN1 (@1,5 Gev)	1.5	4.3	
BC1	0.9	2.5	
BC2	0.8	2.2	
Quad LN2 (@1,5 Gev)	1.0	2.9	
		4.1	11.9
			1.6

Magnets cooling 2.1			
Quad LN1 (@1,5 Gev)	13.5	38.7	
BC1	8.0	22.9	
BC2	6.8	19.5	
Quad LN2 (@1,5 Gev)	9.0	25.8	
		37.3	106.9
			4.8

Auxiliaries 2.1			
Demineralized Water treatment			
Demineralized Water production			
Compressed air			
Technical gases			

SUB-TOTAL	397.1		
FLOW FROM MAINS (ref. to 5°C deltaT)		1'138.4	15.5

HVAC 2.1			
raw chilled water circuits			
Modulator Hall FC	21.4	61.4	3.6
Modulator Hall AHU	4.9	14.0	1.7
Accelerator tunnel FC	6.6	19.0	2.0
Accelerator tunnel AHU	4.9	14.0	1.7

Electrical facilities halls FC	30.0	86.0	4.3
Electrical facilities halls AHU	3.0	8.6	1.4
Mechanical facilities halls FC	30.0	86.0	4.3
Mechanical facilities halls AHU	3.0	8.6	1.4
Chillers station MAINS	103.8	297.5	7.9
TOTAL POWER	500.9		
TOTAL FLOW		1'436.0	17.5

<i>WATER cooling</i>	<i>POWER</i>	<i>FLOW</i>	<i>min. pipe ID</i>
SUB-STATION 3	kW	litri/min	cm
RF cooling control unit 3.1			
Modulators Hall			
Mod.5 RF 10-11-12	75.0	537.5	
Mod.6 RF 13-14-15	75.0	537.5	
Mod.7 RF 16-17-18	75.0	537.5	
	225.0	1'612.5	18.5
Accelerator Tunnel			
sez. acc.5 RF 10-11-12	14.3	681.1	
sez. acc.6 RF 13-14-15	14.3	681.1	
sez. acc.7 RF 16-17-18	14.3	681.1	
heaters regolazione RF	142.6		
		2'043.4	8.5
loads	7.1	51.1	1.3
	192.5	2'094.5	
RF cooling control unit 3.2			
Modulators Hall			
Mod.8 RF 19-20-21	75.0	537.5	
Mod.9 RF22-23-24	75.0	537.5	
	150.0	1'075.0	6.2
Accelerator Tunnel			
sez. acc.8 RF 19-20-21	14.3	681.1	
sez. acc.9 RF 22-23-24	14.3	681.1	
heaters regolazione RF	95.0		
		1'362.3	6.9
loads	7.1	51.1	1.3
	130.7	1'413.3	
Power Supplies cooling 3.1			
Quad LN3 (@1,5 Gev)	2.2	6.2	
DL1	1.0	2.9	
BC3	2.5	7.1	
	5.7	16.2	0.8
Magnets cooling 3.1			
Quad LN3 (@1,5 Gev)	19.5	55.9	
DL1	9.2	26.4	
BC3	22.2	63.6	
	50.9	145.9	2.3

SUB-TOTAL	754.7		
FLOW FROM MAINS (ref. to 5°C deltaT)		2'163.5	21.4
HVAC 3.1			
raw chilled water circuits			
Modulator Hall FC	35.6	102.0	4.7
Modulator Hall AHU	4.9	14.0	1.7
Accelerator tunnel FC	12.5	35.7	2.8
Accelerator tunnel AHU	4.9	14.0	1.7
Electrical facilities halls FC	30.0	86.0	4.3
Electrical facilities halls AHU	3.0	8.6	1.4
Mechanical facilities halls FC	30.0	86.0	4.3
Mechanical facilities halls AHU	3.0	8.6	1.4
Auxiliaries 3.1			
Demineralized Water treatment			
Demineralized Water production			
Compressed air			
Technical gases			
Chillers station MAINS	123.8	354.8	8.7
TOTAL POWER	878.5		
TOTAL FLOW		2'518.3	23.1

<i>WATER cooling</i>	<i>POWER</i>	<i>FLOW</i>	<i>min. pipe ID</i>
SUB-STATION 4	kW	litri/min	cm
RF cooling control unit 4.1			
Modulators Hall			
Mod.10 RF 25-26-27	75.0	537.5	
Mod.11 RF 28-29-30	75.0	537.5	
	150.0	1'075.0	15.1
Accelerator Tunnel			
sez. acc.10 RF 25-26-27	14.3	681.1	
sez. acc.11 RF 28-29-30	14.3	681.1	
heaters regolazione RF	95.0		
		1'362.3	17.0
loads	7.1	51.1	0.0
	130.7	1'413.3	17.3
RF cooling control unit 4.2			
Modulators Hall			
Mod.12 RF 31-32-33	75.0	537.5	
Mod.13 RF 34-35-36	75.0	537.5	
	150.0	1'075.0	15.1
Accelerator Tunnel			
sez. acc.12 RF 31-32-33			
sez. acc.13 RF 34-35-36	14.3	681.1	
heaters regolazione RF	14.3	681.1	
	95.0		
		1'362.3	17.0

loads	7.1	51.1	0.0
	130.7	1'413.3	17.3
RF cooling control unit 4.3			
Modulators Hall			
Mod.14 RF37-38-39	75.0	537.5	
Mod. 15 RF 40-41-42	75.0	537.5	
Mod 16 RF deflector	75.0	537.5	
	225.0	1'612.5	18.5
Accelerator Tunnel			
sez. acc.14 RF37-38-39	14.3	681.1	
sez. acc. 15 RF 40-41-42	14.3	681.1	
RF deflector	14.3	681.1	
	142.6		
		2'043.4	20.8
	7.1	51.1	0.0
	192.5	2'094.5	21.1
Power Supplies cooling 4.1			
Quad TL1 @ 1,5 (fino a ond)	4.0	11.5	
Quad LN4 (@2,4 Gev)	20.0	57.3	
Dipoli DL2	1.0	2.9	
	25.0	71.7	3.9
Magnets cooling 4.1			
Quad TL1 @ 1,5 (fino a ond)	36.0	103.2	
Quad LN4 (@2,4 Gev)	180.0	516.0	
Dipoli DL2	9.2	26.4	
	225.2	645.6	11.7
Power Supplies cooling 4.2			
Quad TL1 @ 1,5 (fino a ond)	31.1	89.2	
Quad LN4 (@2,4 Gev)	5.8	16.6	
Dipoli DL2	5.0	14.3	
	41.9	120.1	5.0
Magnets cooling 4.2			
Quad TL @ 2,4 + TL 1,5-2,4 (@2,4 Gev)	280	802.7	
Quadrupoli ondulatori	52	149.1	
Dump 1,5 -2,4 GeV	45	129.0	
	377.0	1'080.7	15.1
Auxiliaries 4.1			
Demineralized Water treatment			
Demineralized Water production			
Compressed air			
Technical gases			
SUB-TOTAL	1'647.9		
FLOW FROM MAINS (ref. to 5°C deltaT)		4'724.1	31.7
HVAC 4.1			
raw chilled water circuits			

Undulators Hall FC			
Undulators Hall AHU			
Experimetal hall FC			
Experimetal Hall AHU			
Modulator Hall FC	55.7	159.6	5.8
Modulator Hall AHU	4.9	14.0	1.7
Accelerator tunnel FC	70.5	202.0	6.5
Accelerator tunnel AHU	4.9	14.0	1.7
Electrical facilities halls FC	30.0	86.0	4.3
Electrical facilities halls AHU	3.0	8.6	1.4
Mechanical facilities halls FC	30.0	86.0	4.3
Mechanical facilities halls AHU	3.0	8.6	1.4
Chillers station MAINS	201.9	578.8	11.1
TOTAL POWER	1'849.8		
TOTAL FLOW		5'302.9	33.6

In the following tables, the main Air Handling Units are listed:

<i>Air Handling Units – Station 1.1</i>	<i>Flow (mc/h)</i>	<i>Duct ID (cm)</i>
Clean Room	4'600.0	57.1
Mounting Hall	7'200.0	71.4
Modulator Hall	3'250.0	48.0
Accelerator tunnel	3'250.0	48.0
Electrical facilities halls	2'000.0	37.6
Mechanical facilities halls	2'000.0	37.6
TOTAL	22'300.0	
Air Handling Units – Station 2.1		
Modulator Hall	3'250.0	48.0
Accelerator tunnel	3'250.0	48.0
Electrical facilities halls	2'000.0	37.6
Mechanical facilities halls	2'000.0	37.6
TOTAL	10'500.0	
Air Handling Units – Station 3.1		
Modulator Hall	3'250.0	48.0
Accelerator tunnel	3'250.0	48.0
Electrical facilities halls	2'000.0	37.6
Mechanical facilities halls	2'000.0	37.6
TOTAL	10'500.0	
Air Handling Units – Station 4.1		
Modulator Hall	3'250.0	48.0
Accelerator tunnel	3'250.0	48.0
Electrical facilities halls	2'000.0	37.6
Mechanical facilities halls	2'000.0	37.6
Undulators Hall	10'200.0	85.0
Experimental hall	18'000.0	112.9
TOTAL	38'700.0	

A summary of data is resumed in the table below:

SUMMARY		
medium temperature total power	3'247.6	kW
CHILLED WATER TOTAL POWER	627.4	kW
WATER TOTAL POWER	3'875.1	kW
WATER TOTAL FLOW	11'108.6	liter/min
TOTAL AIR FLOW	82'000.0	mc/h

13.4.7 Electrical consumption

Assuming a Coefficient of performance of the chillers of about 2, a consumption of 50W (electrical) per kW (thermal) for the dry coolers, a mean pumping power and about 30% of chillers summer help to the dry coolers circuits, we will have about 1200 kW of electrical power required.

13.4.8 Open points

The general lay out, with space occupancy and passages through the walls has to be defined.

All the ambient thermal and hygrometric conditions, as well as their tolerances should be discussed. The same for the water cooling set points and quality requirements.

In the next design phase, detailed study should be carried out about air distribution along the tunnels and in the halls, about thermal stabilization for water and air, and about the level of reliability and service continuity.

A general standard has to be set for all the users and for the designers of water and air cooled accelerator components, as well as for the producers of power supply and electronics. Temperature, pressure, fittings, acceptance test and commissioning procedures, and so on, will be detailed in advance.

13.4.9 Rooms and spaces

A rough estimation of the room needed has been performed. Nevertheless, several design points have yet to be exploited, and they can heavily affect our evaluations.

At the moment, the plant has one external area for the chiller and the dry coolers, and four sub-central, placed along the tunnel. In the sub-central will be the pumping stations, the heat exchangers, the Air Handling Units, all their auxiliaries, the electrical boards, the water treatment systems, etc.

Care shall be paid about service and maintenance spaces.

	<i>Internal (m²)</i>	<i>External (m²)</i>
Main Central		800
Sub-Central 1	450	
Sub-Central 2	450	
Sub-Central 3	450	
Sub-Central 4	650	

For references, see also [2,3]

13.5 References

- [1] EMC - POWER CONVERTERS FOR PARTICLE ACCELERATORS A. Charoy
<http://cas.web.cern.ch/cas/Warrington/PDF/Charoy.pdf>
- [2] Earthing of High-Energy Physics Detector Systems F. Szoncsó CERN-TIS
http://szoncsó.home.cern.ch/szoncsó/EMC/Earth_new_Latin_020405.pdf
- [3] EMC for Systems and Installations, T. Williams - K. Armstrong Ed.
Newness (partially available in: <http://www.compliance-club.com/KeithArmstrongPortfolio.htm>)

14 PROJECT MANAGEMENT

14.1 Overview

The SPARX-FEL will be assisted by a project management and a project management office (PMO) that applies well established and proven best practice techniques as described in different handbooks and applied by specialized project management firms. The project management will take care of project organization, project scheduling, process tracking, status reporting, issue and change management. To do so, several tools are used that will be described later.

Project organization

The work within the SPARX-FEL Project will be organized in different phases that will be organized in Workpackages and Taskpackages. Each Taskpackage contains the different tasks that are carried out by the project team (see Figure 14.1).

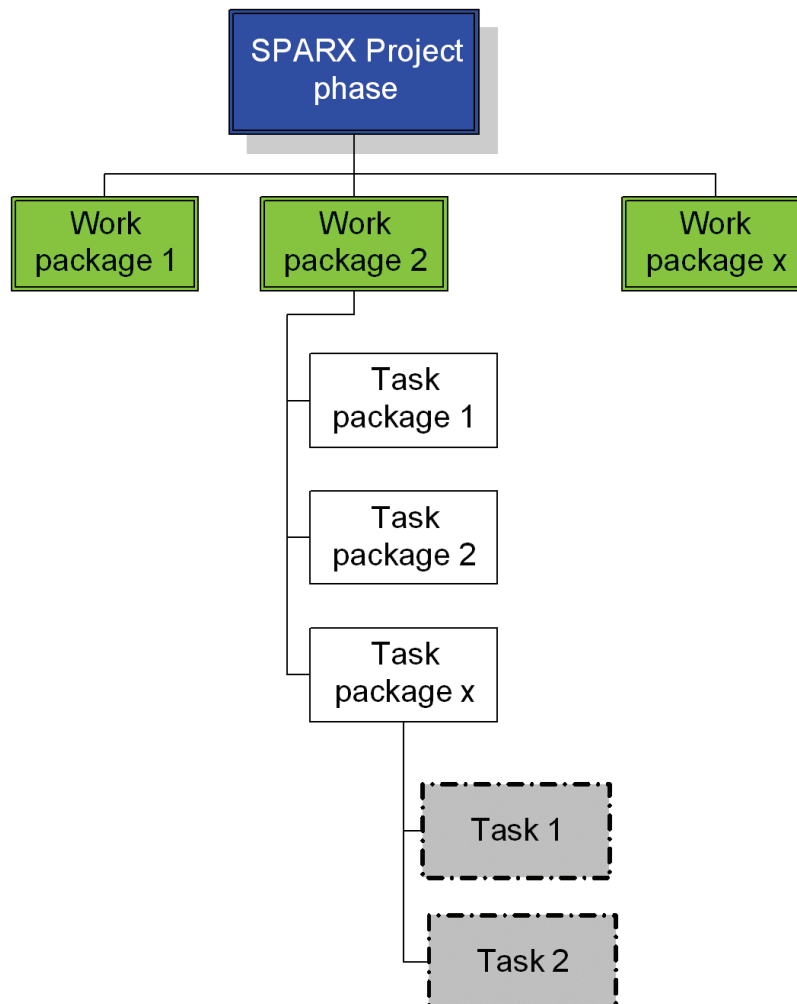


Figure 14.1: General organization of the work performed within the SPARX-FEL Project.

14.2 Organization

14.2.1 Premise

The aim of the SPARX-FEL project is to build a Free-electron laser X radiation source within the Campus of the University of Tor Vergata, Rome. The Ministry of Education (MIUR), the Regione Lazio, the CNR (Centro nazionale Ricerche), ENEA and INFN cooperate in the fulfillment of the project. The project is funded by the MIUR and the Regione Lazio and is coordinated by the INFN during the construction phase. The facility will be governed by a consortium in which the different above mentioned parties are involved and that is explained in detail later. The global organization is indicated as in Figure 14.2 and is explained hereafter.

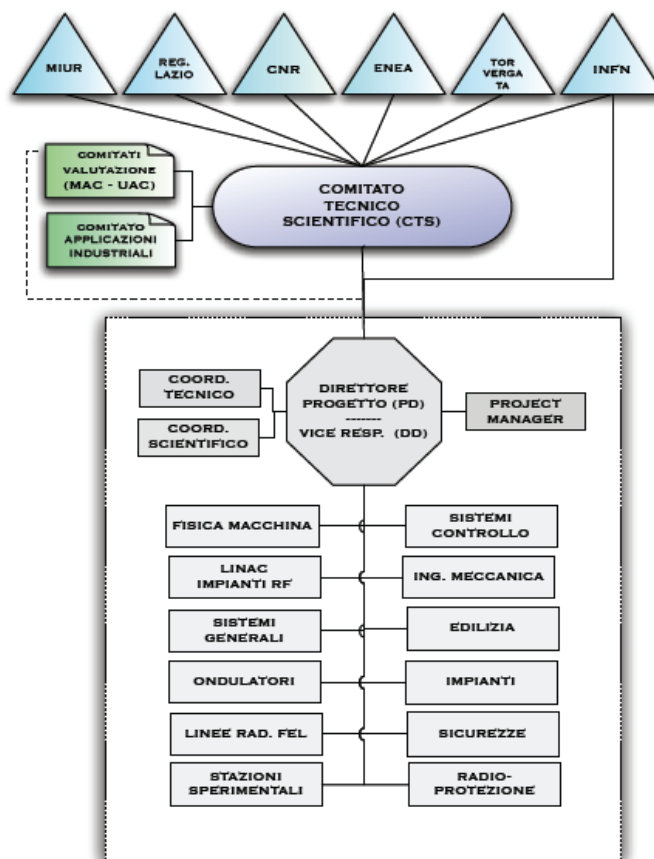


Figure 14.2: Organization of the SPARX-FEL Project.

14.2.2 Steering Committee (Comitato tecnico scientifico - CTS)

Each party involved in the SPARX-FEL project, i.e. MIUR, Regione Lazio, CNR, ENEA, University of Tor Vergata and INFN elects one representant that represents the project at the steering committee level (CTS, comitato tecnico scientifico). The aim of this board is to monitor the advancement of the project in its different phases and establish global synergies. Under the supervision of the the CTS, the parties have the role to coordinate the definition and the

execution of all technical-scientific aspects in its best way. The representative of the "Regione Lazio" is chair of this board. The board expresses a judgment relative to the accomplishment of the scientific and technical content and financial plan presented by the Project Director (defined hereafter). The Project Director also reports to the CTS the advancement of the project, either in terms of scientific-technical either in financial matters and informs the CTS about possible issues that could compromise the accomplishment of the goals and milestones of the SPARX-FEL project.

The CTS meets regularly with a minimum frequency of 3 months. The participation to the CTS is done on gratuity.

14.2.3 Project Team - PT

The project team is composed by experts belonging to the involved parties or externally and related to the different fields of the SPARX-FEL project (linear accelerator, undulators, beamlines, diagnostics, infrastructure, security). The PT has the mission to define the final project of the facility and establish a cost-estimate related to its operation (either in terms of financial or human resources). Roles and responsibilities of the project team can vary during the different phases of the project.

14.2.4 Directorate

The project team is coordinated by a Project Director - PD that has the responsibility to coordinate all phases of design and construction of the facility. The Project Director is appointed by the INFN after consultation with the CTS representatives of CNR, ENA and the university of Tor Vergata; The PD reports to the CTS the construction plans of the facility and the advancement of the project itself. The project director (PD) is assisted by a Deputy Director (DD) that acts in his absence and reports to the PD. The project director, after consultation with the CTS, also appoints

- 1) the project manager (PM), that assists in elaborating financial and temporal plans and is responsible for the project management (Cost control, Quality Control and Risk-Issue Management).
- 2) The scientific coordinator (SC) that acts as interface with the scientific and users community and ensures that those objectives are met within the SPARX-FEL project
- 3) The technical coordinator (TC) that acts as interface regarding all matters concerning the technical and construction aspects of the SPARX-FEL project during all project phases.

The DD, TC, SC and PM are appointed by the PD after
The following figures form the SPARX-FEL directorate:

- the project director
- the deputy director
- the scientific coordinator
- the technical coordinator
- the project manager

that are assisted by a team assistant.

The entire work of the SPARX-FEL project is subdivided in different Workpackages, that are coordinated and led by one Workpackage Leader (WPL).

WPL are appointed by the PD, after concertations with the scientific representatives of the CTS.

For each taskpackage the following informations needs to be provided:

- 1) Aim of the Workpackage
- 2) Deliverables
- 3) Milestones and scheduling
- 4) Cost estimate
- 5) Necessary resources
- 6) Dependencies with other Taskpackages and Workpackages
- 7) Documentation linked to the taskpackage

For the SPARX-FEL project, the following workpackages have been identified:

- 1-Machine Physics
- 2-Lay-Out Mechanical Engineering&Alignment
- 3-LINAC Design
- 4-Common machine system design
- 5-Undulators design
- 6-Radiation beam lines
- 7-Photon Diagnostics
- 8-Experimental stations
- 9-Control system design
- 10-Radiation safety
- 11-Infrastructure
- 12-Project Management
- 13-Editorial

The work inside the workpackages is organized by taskpackages that are coordinated and led by a Taskpackage leader (TPL), appointed by the Workpackage leader. TPL are responsible for the accomplishment of the assigned Tasks and report to the WPL.

For each taskpackage the following informations are given:

- 1) Aim of the Taskpackage
- 2) Deliverables
- 3) Milestones and scheduling
- 4) Cost estimate
- 5) Necessary resources
- 6) Dependencies with other Taskpackages and Workpackages
- 7) Documentation linked to the taskpackage

14.2.5 Evaluation committee

At least once a year, the project is presented to a board of national and international experts that evaluate the technical, scientific and organizational aspects of the projects. The evaluation is sent to the PD and the CTS. The following committee evaluate the project:

- Machine Advisory Committee - (MAC)
- User Advisory Committee - (UAC)

Committees are nominated in concertation between the different parties (CNR, INFN, ENEA, UNIVERSITA' di TOR VERGATA). The participation to this committees is done without remuneration.

Consulting committees

Besides the evaluation committee, a Industrial Advisory Committee (IAC) is established that has as mission to identify possible industrial applications either in national or international field related to the SPARX-FEL.

The committee is appointed by the Regione Lazio. This committee elaborates a report that is sent to the CTS. The participation to this committees is done without remuneration.

14.3 Roles and responsibilities within the SPARX project

In order to ensure an efficient organization of the project team, every team member has assigned roles and responsibilities to ensure that tasks and deliverables are accomplished.

14.3.1 Directorate

The role of the directorate is to ensure the correct accomplishment of the project (design and construction). The activity of the directorate is coordinated by the project director. The directorate is responsible also for all the communication related to the project, either internally as externally, in particular for the establishment of policies of communication (website, scientific publications, participation to conferences, technical reports, press, media and television).

14.3.2 Project Director

He has the responsibility of the coordination of all design and construction phases of the facility and acts as spokesman for the project towards the general public and the stakeholders. He guarantees the unity of the management of the project and ensures that processes are building synergy between each other. In the decisional process he ensures that decisions meet the mission of the project and in case of choice expresses the resuming decision.

His roles include:

Ensure that the goals and objectives of the project are met within the given timeframe

Ensure and organized the different working packages in accordance with the need of the project and phases

Perform cost control and ensure that budget is spent efficiently and in accordance with the rules

- Day to day decision making, problem solving of eventual arising issues or conflicts within the project

- Supervise the project team and foster good team spirit and working environment
- Establish collaborations with other partners and ensure that those generate benefit for the project
- Ensure and maintain the integrity of the project
- Communicate to the public and stakeholders in relation to the mission, the objectives and the status of the project

14.3.3 Deputy director

The deputy represents the project director in his absence.

His responsibilities are:

- Assist the project director in the preparation of the project objectives and in the supervision of the project team
- Foster good team spirit within the project team
- Communicate to the public and stakeholders in relation to the mission, the objectives and the status of the project

14.3.4 Project Manager

Manage the organization of the project and ensure that the project follows the general guidelines fixed by the project itself.

His responsibilities are:

Help and assist the directorate in the financial organization and scheduling, implementing – when needed – processes and tools for the monitoring

- Implement management and tracking procedures in order to do cost and human resources estimate.
- Propose a possible financial plan and do cost control during the project development, reporting issues to the responsible persons
- Implement procedures to monitor Quality control and Risk-issue management
- Coordinate the scheduling, implementation and activity between the different working groups
- Foster good team spirit and communicate to the general public in relation to his duties and in application with the given confidentiality level

14.3.5 Scientific coordinator

He acts as interface between SPARX-FEL and the scientific community including users in order to integrate the scientific objectives of the projects during the entire phase.

His responsibilities are:

- Assist the directorate in the definition of the scientific objectives in relation to the FEL radiation source that come from the user community
- Monitor the design and the construction of the facility with regard to the scientific objectives
- Propose and starts initiatives that elaborate and update the scientific case of the project
- Communicate to the general public in relation to his duties and in application with the given confidentiality level

14.3.6 Technical coordinator

He coordinates all technical activity for the design and construction of the facility during the different phases.

His responsibilities are:

- Assist the directorate in the monitoring of the project technical and construction advancement with regard to the objectives of the project
- Collaborates to the temporal and financial implementation in relation to the construction of the facility and the assignment of resources
- Communicate to the general public in relation to his duties and in application with the given confidentiality level

14.3.7 Executive Committee

The role of the Executive Committee is

- 1) Ensure a good coordination between the different activities of the Work packages (WP)
- 2) Ensure the advancement of the Workpackages
- 3) Monitor the reporting
- 4) Identify issues and propose solutions
- 5) Distribute the information between the different WP
- 6) Assistance to the directorate for technical and scientific choices

Members of the Executive Committee are:

PD, DD, PM, TC, SC, WPL

The project director can appoint new members to the executive committee in order to complete technical or scientific competences or to include representatives of other institutions that collaborate in the project.

14.3.8 Workpackage leader (WPL)

Organize and monitor the work assigned to his workpackage

His responsibilities are:

- Organize and monitor the work assigned to his workpackage
- Identify actual and potential problems (e.g. relative to human resources) monitoring the advancement of the work and comparing it to the forecasted scheduling, choosing appropriate actions when necessary or raising issues to the directorate
- Determine, monitor and adapt deliverables, timelines, costs, resources and scheduling relative to the advancement of the project
- Define the task packages, the aim of the task package, deliverables connected to it, milestones and timelines, costs and resources, links to other Work/Task-packages within the project and documentation or information related to it
- Supervise the Workpackage team and foster good working environment
- Communicate to the general public in relation to his duties and in application with the given confidentiality level

14.4 Project management tools and procedures

To ensure an efficient collaboration within the project team, several project management tools and procedures have been implemented. Since the project team consists of personnel dislocated over Italy and abroad (USA, Germany), the communication and management tools are done mostly web-based.

For the upload of documents and plans/layouts a specific intranet page has been developed (hosted by the Università "Tor Vergata") in which project members can upload their documents in the directories of their Work package. An automatic message is generated to inform selected team members or other people about the insertion of the document. This might be useful whenever a different team member needs to have this information. Documents, drawings etc. are uploaded with a specific nomenclature. For drawings etc. it has been agreed to use as nomenclature a string made of three fields. The first field indicates the zone where the machine part is located (e.g. LINAC 1, Undulator, etc) the second field indicates the type of element (Magnet, Beam position monitor, etc), the last field indicates the distance of the element from the beginning of the machine (i.e. the injector). An example of string is LI1_BPS_12345.

The activity within the SPARX-FEL group, is disseminated by a Calendar that builds on the Google Applications [www.google.com/a]. Workpackage leader and PMO can upload events and meetings and generate "Guest" in order to create invitations to the event and therefore simplify the organization of the event since participants confirm or deny their venue directly "online".

Email accounts and mailing lists are handled by the Google-applications that are linked to the specific domain, i.e. www.sparx-fel.it. The administration of the domain is handled by the PMO. For the consortium the following domain names have been registered:

www.sparx-fel.it
www.sparx-fel.eu
www.sparx-fel.org

All three domain names are redirected towards a server hosted in the Tor Vergata University campus.

Documents within the project are generated with Microsoft (MS) Office or equivalent software, for the monitoring and project timing MS Project is used, for designing of processes MS Visio.

For the general update of procedures, for cost/time scheduling, for the implementation and use of the project management tools, the PMO and PM are responsible

14.5 Human resources and recruitment policy

As general tendency, the idea of the upcoming Consortium agreement is that resources of the SPARX-FEL group should come from the involved parties (INFN, ENEA; CNR; Tor vergata) and therefore resources hired direct by the Consortium should be limited to a minimum. The common recruitment policies, including salaries are therefore subject to the general procedures of each party. As result of this recruitment policy, the project staff will consist of a balanced staff structure with respect to the involvement of the different parties. SPARX-FEL affiliated personnel will be working on the facility site when needed and with the time percentage that has been agreed between the responsible persons and the facility management.

Similar to other facilities, there will be open positions for technicians, scientist and administrative people coming from abroad. SPARX-FEL will provide them assistance for settling-in and adaptation. Particular benefits and incentives are foreseen to attract high-level personnel from other facilities/institutions.

Since the construction of the facility is given in outsourcing, additional needed personnel for those peak periods will be subcontracted. The personnel belonging to permanent or temporary staff of the involved parties will monitor the activity linked to their workpackage during the construction period. It is foreseen that temporary contract should cover the construction and commissioning phase (i.e. 3 years) in order to guarantee a delivery of on time.

During the entire phase, students, either undergraduate or PhD will be involved in the project to train newcoming scientist/technician for the future facility. Internships and temporary staff are foreseen as well.

14.6 SPARX Consortium and collaboration agreements between contributing institutes

In accordance with the Framework agreement (“Accordo quadro – progetto FEL”) signed between the parties CNR, ENEA, INFN e Università di Roma “Tor Vergata” on may 22, 2007, a SPARX-FEL Consortium is constituted. The consortium has as legal status that of a private company and is agreed between the parties for initially 50 years with possible renewal. The consortium will be the unique entity that manages financing of the SPARX-FEL infrastructure. The consortium is open to other partners, either universities or institutions.

The following engagements have been taken by the parties:

Università di Roma “Tor Vergata” hosts the facility and therefore transfers to the consortium the rights of use of part of her area for a surface of 1500 m

length and variable width (depending on the project needs) for a period of initially 50 years.

INFN is responsible for the injector of the SPARX-FEL and engages itself to provide the injector of the machine, either by using for this purpose the existing SPARC injector, either by financing a new, identical injector.

CNR is responsible for the beamlines and for the experimental stations of the SPARX-FEL facility.

ENEA is responsible for the undulators.

CNR is responsible for the radiation diagnostics in collaboration with ENEA.

14.7 Communication

It is vitally important for a national facility such as the SPARX-FEL, willing to operate in international scenario, to communicate efficiently with funding agencies, universities and research institutions, scientific community, general public and to provide the necessary tool for an efficient interaction between the stakeholders.

The objective of this work package, called “Communication”, is to develop, apply and use the tools and media necessary for dissemination for the above mentioned goals.

14.7.1 Tools and initiatives

In order to achieve the objectives the initiatives of the Workpackage are subdivided in the following Task packages:

- Website(s)
- Press, brochures and external media
- Workshops, schools, conferences and seminars
- Communication to general public and stakeholders
- Dissemination to a wider audience of scientific publications, contribution to conferences and workshops produced by the project members
- Communication within the IRUVX-FEL Consortium – WP5

More in detail, the packages include the following tasks and initiatives

- Develop, maintain and update the project website(s)
- Prepare press releases aimed at specific and identified audiences.
- Publish regularly SPARX-news within the identified communication channels
- Create and keep updated brochures related to the facility
- Promote and support workshops and conferences

- Publish highlights related to machine development and research activity
- Invite top-level researcher for dissemination of front-edge science
- Promote and support research schools related with the FEL and SPARX machine and science activity
- Develop communication in the framework of IRUVX-FEL Consortium - WP5

14.7.2 General Guidelines

The general guidelines of all communication, including technical and scientific content, are given by the SPARX-FEL-directorate (comitato di direzione, "directorate").

The Directorate will indicate a coordinator for the "Communication" workpackage ("WP Coordinator").

Taskpackages or subtaskpackages within the workpackage "Communication" are organized by selected committees and whenever necessary shall include one representative of each project partner. A committee member, assigned by the directorate, will coordinate the entire taskpackage activity ("TP Coordinator").

14.7.3 Webpage development and maintenance

A selected committee will develop and propose the detailed storyboard (including content) of the webpage(s) to the directorate for approval. The committee will take into consideration proposals coming from the SPARX-FEL-team, the web-committee members and any other useful source accepted by the committee.

Both, proposals of a new website and significant changes or updates of the webpage are presented to the directorate for selection, approval or discussion. Decisions are implemented by the selected committee under the guidance of the coordinator, if necessary within an iterative process with the directorate. The webpage will include the approval date for the last version accepted by the directorate and will include the contact person and the members of the committee.

The coordinator of the selected committee is responsible for the functioning and maintenance of the website while the directorate is responsible for its content.

14.7.4 Communication and scientific dissemination actions - Press and brochures

Any scientific dissemination activity related either to the SPARX-FEL project or its scientific and technical activities such as brochures and press campaigns (and significant changes or updates to existing ones) can be presented by any member of the SPARX-team and any other useful source accepted by the directorate. Proposals are presented to the directorate for selection, approval or discussion. Decisions are implemented by the proposer or any agreed actor under the guidance of the workpackage and/or taskpackage coordinator, or a designed representative, if necessary within an iterative process with the directorate.

14.7.5 Organization of workshops, seminars and schools

Workshops, seminars and schools can be organized and performed by any member of the SPARX-team and any other affiliated resource(s). Any activity of this taskpackage needs to be communicated for approval prior to organization to the directorate or a selected committee.

14.7.6 IRUVX-FEL

The taskpackage concerning the communication activity related to IRUVX-FEL (WP5) will be managed by a dedicated coordinator assigned by the directorate.

For references, see [1,2,3].

14.8 References

- [1] A Guide to the Project Management Body of Knowledge, Project Management Institute, Newtown Square, PA 19073-3299 USA.
- [2] Microsoft Project Enterprise, Microsoft Cooperation, <http://office.microsoft.com/en-us/FX011204851033.aspx>
- [3] www.microsoft.com / www.openoffice.org

15 PROJECT TIMELINE AND FINANCING

15.1 Overview

The realization of the SPARX-FEL facility will take place in two major phases and several steps:

- 1) Upgrade of SPARC electron beam energy up to 750 MeV for a UV source
- 2) Construction of the SPARX civil infrastructures
- 3) Increase of electron energy up to 1.5 GeV, installation of one undulator and one radiation beam line for UV and soft-X radiation **[Completion of SPARX phase 1]**
- 4) Installation of a second undulator and a second beamline
- 5) Increase of electron energy up to 2.5 GeV and installation of an additional (third) undulator and beam lines for experimental station for hard X-ray radiation (0.6 nm) **[Completion of SPARX phase 2]**

15.2 Timeline

The timeline for the completion of the SPARX phase 1 is indicated in Figure 15.1. It includes a first period dedicated to the finalization of the architectural/engineering/construction plans and preparation of tenders. This period is followed by a construction phase, in which digging of the tunnel is started and the laboratory's buildings are constructed. Successively, all parts of the infrastructure are built and the implementation of plants (electricity, fluid, etc) concludes the phase. Gradually, all parts of the FEL (from accelerator to experimental stations) are constructed and tested during the construction phase. Installation takes place when the underground infrastructure is ready.

The timeline for the completion of SPARX phase 2 is given in Figure 15.2. This phase includes an update of the civil infrastructure and plants, the increase of the linac electron energy to 2.64 GeV and the procurement of two additional undulators (including installation). The commissioning of new transfer lines using the new undulators and the new electron-energy-regime concludes the second phase.

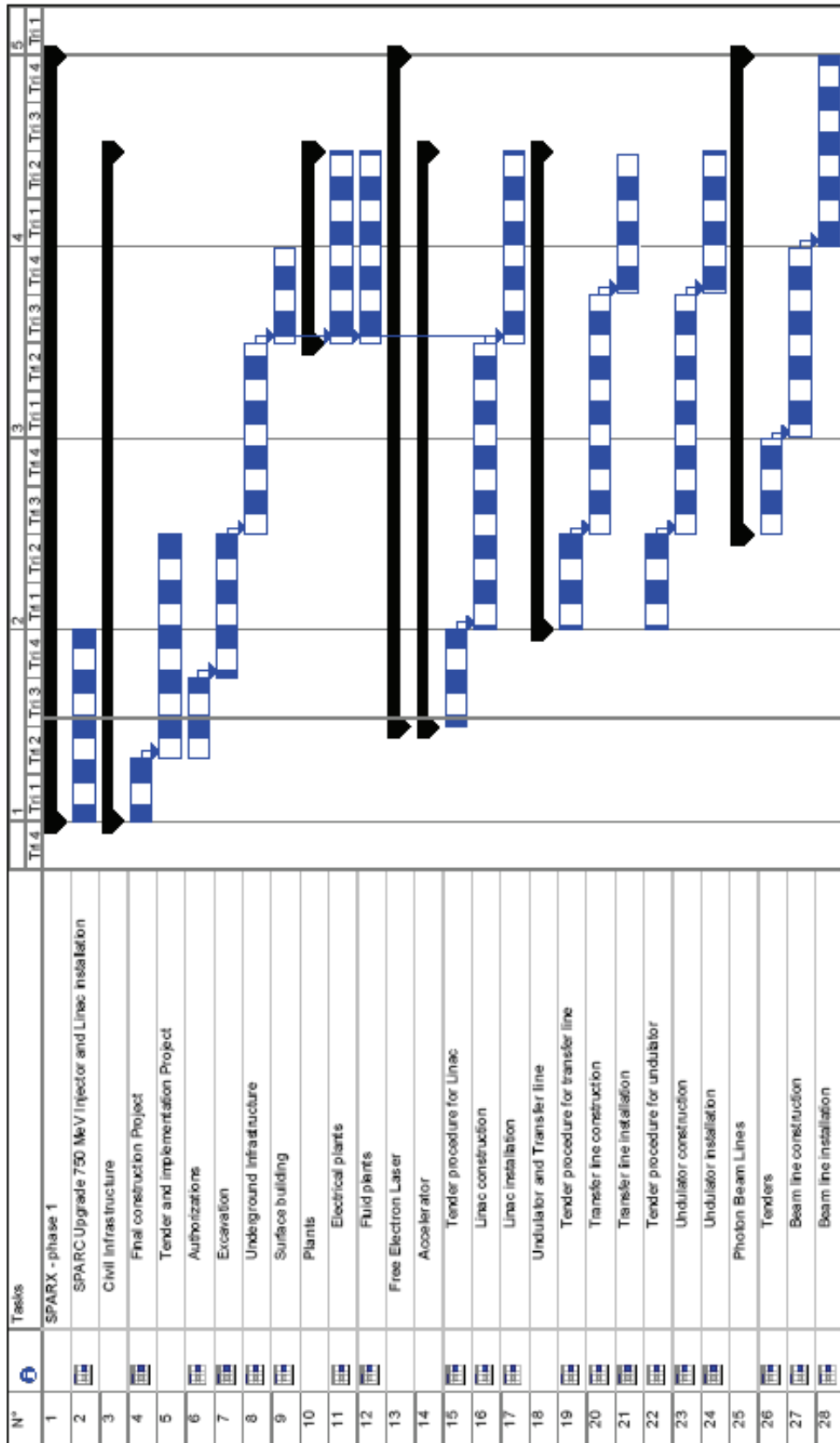


Figure 15.1: Timeline for the SPARX phase 1.

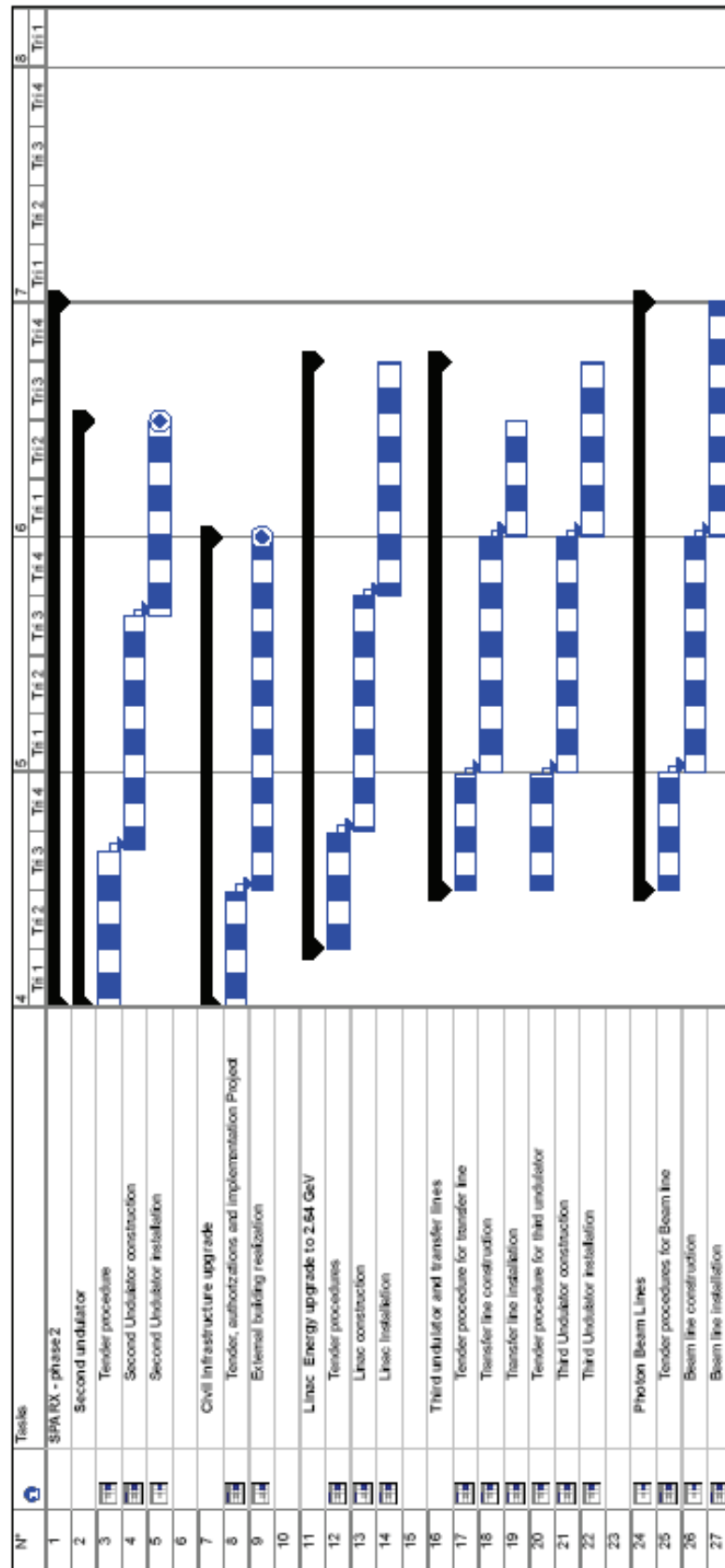


Figure 15.2: Timeline for the SPARX phase 2.

15.3 Construction Costs

The costs for the completion of SPARX, are detailed in the following tables which include the infrastructure, the technical plants (electricity, fluid, etc), the accelerator, the undulators, the transfer lines and the radiation beam lines. The costs of SPARX phase 1 are distributed over 4 years while those for SPARX phase 2 over 3 years. Currently it is planned that the first year of SPARX phase 2 overlaps with the last year of SPARX phase 1. As a result, both phases of SPARX-FEL should be realized within 6 years from the start of the project.

The tables below indicate the estimated costs (including VAT) for SPARX-FEL. The costs of the infrastructure have been estimated assuming that the core of the entire infrastructure will be build in the SPARX phase 1, which would in overall lower construction costs and optimize the timing.

The total costs of SPARX phase 1 are given by the table Table 15.1:

Table 15.1: Total costs for SPARX phase 1 (in M€, including VAT)

Completion SPARX Phase 1	
Infrastructure (entire)	25
Plants	7
Accelerator	25
Undulators and Transfer lines	8
Beam lines	5
Total	70

Total costs as given in Table 15.1 include the value of the existing infrastructure and funds at INFN laboratori di Frascati, SPARC project which are indicated in Table 15.2. Accordingly, the costs for the completion of SPARX phase 1 are given in Table 15.3.

Table 15.2: Value of existing infrastructure SPARC (in M€, including VAT)

Item	Value
Linac and transfer lines	8
Undulators	3
Beam line and diagnostics	1
Total	12

Table 15.3: Costs for the completion of the SPARX phase 1 (in M€, including VAT)

Completion SPARX Phase 1	Year 1	Year 2	Year 3	Year 4	TOT
Infrastructure (entire)	4	9	12	0	25
Plants			4	3	7
Accelerator	1	4	8	4	17
Undulators			2	2	4
Transfer lines			1		1
Beam lines			2	2	4
Total	5	13	29	11	58

For the phase 1, in the first year, costs occur mainly for finalizing the architectural plants, preliminary territorial studies and first digging. Most costs for the civil infrastructure occur in Year 2-4. Plants are foreseen to be installed in year 3-4. The accelerator costs occur during years 2-4, i.e. when the construction has been started, while undulator and transfer lines costs arise shortly after the accelerator has been started, i.e. in year 3-4. The costs for the beam lines conclude the budget and are due at the end of the construction phase, i.e. year 3-4.

Funding foreseen in the “Accordo Quadro” can cover at the moment 15 M€ from Regione Lazio for the infrastructure and 10 M€ from MIUR (Italian Ministry of Research and Education) which can allow the realization of an UV source based on the SPARC facility@750 MeV. In principle, there is a technical solution for a partial development of the civil infrastructure, using in the first phase only 15 M€. However, the realization of the entire infrastructure in one single phase, as assumed so far, is highly recommended.

Concerning SPARX phase 2 (see Table 15.4), the additional costs for the civil infrastructure occur in year 4-5, while those for the plants in year 5-6. The costs for the Linac upgrade are in year 4-6 while those for the two additional undulators year 5-6. The procurement and installation of the beam lines is done in the same period.

Table 15.4: Costs for the SPARX phase 2 (in M€, including VAT)

SPARX Phase 2	Year 4	Year 5	Year 6	TOT
Infrastructure	1	3		4
Plants		2	3	5
Accelerator @ 2.64 GeV	3	5	7	15
Undulators		6	8	14
Transfer lines		3	3	6
Beam lines		3	3	6
Total	4	22	24	50

The contingency not included in the above tables, is 5%.

15.4 Operational Costs

The annual operational costs are indicated in the table below (in M€ including VAT) and are divided in SPARX phase 1 (accelerator energy up to 1.5 GeV) and SPARX phase 2 (accelerator energy up to 2.64 GeV). Operations of the Linac are supposed to be at 100 Hz. Personnel costs include salaries for administratives, technicians, scientists and engineers, calculated on the basis of 30 FTE for the SPARX phase 1 and 40 for the SPARX phase 2, with average salary of 60 k€/year. The calculations for estimating the power consumption costs are detailed in Table 15.6.

Table 15.5: Operational costs for SPARX phase 1 and 2 (in M€, including VAT)

<i>Operational costs</i>	<i>Phase 1</i>	<i>Phase 2</i>
Personnel	1.8	2.4
Machine maintenance	1.0	1.5
General services	1.2	1.4
Consumables	0.4	0.5
Power consumption	2.6	4.2
Total annual operation costs	7.0	10.0

Table 15.6: Calculation of power consumption costs for SPARX phase 1 and SPARX phase 2 (units indicated in rows, costs including VAT)

<i>Power consumption costs</i>	<i>Phase 1</i>	<i>Phase 2</i>
LINAC power consumption (kW)	1500	2500
Transfer Lines / Undulators / Beamlines power consumption (kW)	300	500
Cooling and conditioning power consumption (kW)	450	750
Technical plants power consumption (kW)	150	250
General services power consumption (kW)	150	160
Total consumption (kW)	2550	4160
Working hours per year - 9 month, 24h/day, (h)	6480	6480
kWh	16524000	26956800
Price per kWh (as of April 2009 in Italy) (€)	0.157	0.157
Total Consumption costs (€)	2594268	4232218